NANOSTRUCTURES:
PHYSICS AND TECHNOLOGY

19th International Symposium

Ekaterinburg, Russia, June 20–25, 2011

Co-Chairs
Zh. Alferov
L. Esaki

PROCEEDINGS

Ekaterinburg, 2011

The International Symposium "Nanostructures: Physics and Technology" is held annually since 1993. The first Symposium was initiated by Prof. Zh. Alferov and Prof. L. Esaki who are its permanent co-chairs. More detailed information on the Symposium is presented on the World Wide Web **http://www.ioffe.ru/NANO2011/**

The Proceedings include extended abstracts of invited talks and contributed papers to be presented at the Symposium. By tradition this book is published before the beginning of the meeting.

The volume was composed at the Publishing Department of St Petersburg Academic University — Nanotechnology Research and Education Centre of the RAS from electronic files submitted by the authors. When necessary these files were converted into the Symposium style without any text revisions. Only minor technical corrections were made by the composers.

The Symposium is held under the auspices of
the Russian Academy of Sciences

Organizers

Institute of Metal Physics of the Ural Branch of the RAS
Ioffe Physical-Technical Institute of the RAS
St Petersburg Academic University — Nanotechnology Research and Education Centre of the RAS

in association with

Branch of Nanotechnologies, Information and Computer Sciences of the RAS
Branch of Physical Sciences of the RAS
Ural Branch of the RAS
The Government of the Sverdlovsk region
St Petersburg Scientific Center of the RAS

Acknowledgments

Location and Date

Symposium is held in Ekaterinburg, Russia, June 20–25, 2011.

Contents

Transport in Nanostructures

Excitons in Nanostructures

Nanostructure Technology

Metal Nanostructures

Microcavity and Photonic Crystals

Nanostructures and Life Sciences

Closing Plenary Session

Unprinted Papers

The papers listed below are included in the Symposium Program, but not printed in the Proceedings, as the authors had not submitted electronic files.

High-power single-mode bottom-emitting 960 nm VCSELs

S. A. Blokhin[1,2,4], N. A. Maleev[1,2], A. G. Kuzmenkov[1,2], J. A. Lott[3], M. M. Kulagina[1],
Y. M. Zadiranov[1], A. G. Gladyshev[1,2], A. M. Nadtochiy[1,4], E. V. Nikitina[4], V. G. Tikhomirov[5],
N. N. Ledentsov[1,3] and V. M. Ustinov[1]

[1] Ioffe Physical-Technical Institute, St Petersburg, Russia
[2] Connector Optics LLC, Shatelena Str. 26A , 194021, St Petersburg, Russia
[3] VI Systems GmbH, Hardenbergstrasse 7, D-10623 Berlin, Germany
[4] St Petersburg Academic University, St Petersburg, Russia
[5] St Petersburg Electrotechnical University "LETI", Prof. Popov Str. 5, 197376, St Petersburg, Russia

Abstract. We report 960 nm-range bottom emitting vertical cavity surface emitting lasers (VCSELs) with a record 15 mW of continuous wave single transverse mode output power that employ multiple aperture oxidation layers combined with a specific intracavity contact design. At relatively high operational currents the VCSELs switch from trivial multi-mode to single-mode operation with a SMSR >20 dB. We present detailed continuous wave and pulsed-measurements, and numerical modeling to investigate the crucial role of self-heating on the VCSELs unusual single-mode behavior.

Vertical cavity surface emitting lasers (VCSELs) are the key components for low-cost high speed local- and storage-area network (LAN/SAN) data communication systems. The rapidly increasing relevance of short reach optical interconnects and their continued penetration into traditional copper interconnect markets stimulate a strong research interest in high-speed VCSELs with single-mode emission. The extremely short cavity length of VCSELs leads to inherent efficient longitudinal mode selection, while devices have a strong tendency to operate in multiple transverse modes. Typically ultra-small current apertures are required for stable fundamental mode operation. These small oxide apertures have smaller gain volumes and this limits the VCSELs output power due to device heating and tends to increase failure rates due to increased operational current densities. By introducing the proper gain and optical confinement into the VCSELs microcavity or a selective loss profile into the DBRs as outlined in [1–5] one can enhance the transverse-mode discrimination. However these proposed epitaxial and post-growth techniques involve relatively complex extra processing, or a hybrid assembly configuration that is highly sensitive to misalignment and mechanical disturbances. Thus we continue to seek a reliable design and method to realize low-cost and high-power single-mode VCSELs to enable low-cost and high yield manufacturing. In this work we present our investigations of self-heating phenomena in bottom-emitting 960 nm VCSELs and discuss the attributes of our single-mode VCSEL design.

1. Design

The VCSEL structures are grown by metal organic vapor phase epitaxy on semi-insulating GaAs substrates and designed for emission near 960 nm. The active region consists of five, 4 nm-thick compressively strained $Ga_{0.8}In_{0.2}As$ quantum wells with 6 nm-thick tensile-strained $GaAs_{0.92}P_{0.08}$ barrier layers. We carefully design the layer thicknesses to set both the local and the global strain well below values critical for high quality growth. The distributed Bragg reflectors (DBRs) are primarily composed of $Ga_{1-x}Al_xAs$ ($x = 0.12$ and 0.9) with 20 nm-thick graded interfaces and quasi-periodic doping with C and Si to reduce the VCSELs resistance. The upper p-doped DBR has 30 periods including two 30 nm-thick $Ga_{0.02}Al_{0.98}As$ aperture
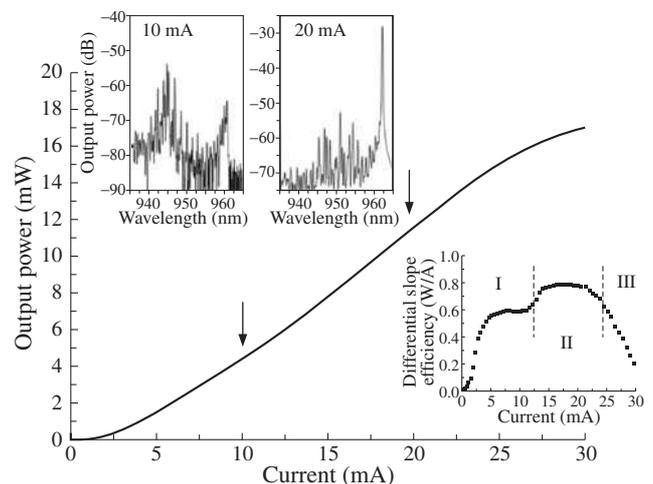
Fig. 1. Measured L-I-characteristics of the bottom-emitting VCSELs with 6–7 μm oxide apertures at RT in the CW regime. Inset: Differential slope efficiency as a function of current, emission spectra at 10 and 20 mA.

layers adjacent to the microcavity active region aimed to help reduce the VCSELs parasitic capacitance [Nishiyama]. The lower DBR resides on top of the S.I. substrate and is divided into a 5 period n-doped DBR, a 1.25λ-thick (n$^+$) GaAs intracavity contacting layer, and a 15 period undoped DBR.

The fabrication sequence begins with the lift-off deposition of circular p-type metal on the top surface, followed by annealing and a dry-etch down just past the microcavity active region and exposed aperture layers. The mesa etch is followed by the selective wet oxidation of the two oxide aperture layers and five adjacent capacitance reducing deep oxide layers. Next a second dry-etch is performed down to the top of the (n$^+$)GaAs intracavity contact/current spreading layer, followed by a selective etch to an etch-stopping layer and an n-type metal lift-off.

2. Results and discussion

Typical continuous wave (CW) light-current (L-I) characteristics from the VCSELs with oxide aperture diameters of 6–7 μm are given in Fig. 1. Devices show room temperature (RT) lasing in the CW regime with threshold currents of 2 mA and
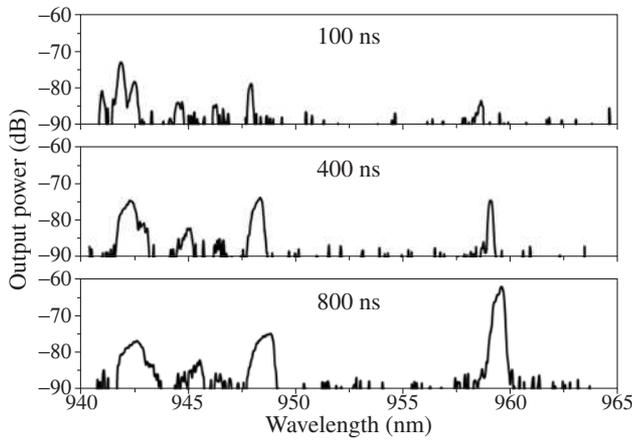
Fig. 2. RT emission spectra for bottom-emitting VCSELs with 6–7 μm diameter oxide apertures at 20 mA at different pulse widths (pulse ratio 1:100).

Fig. 3. Calculated thermal distribution of bottom-emitting VCSELs with 6–7 μm diameter oxide apertures. Temperature of the heatsink is 300 K and injection current is 20 mA, resulting in a 21 K temperature rise in the active region.

maximum output powers of 17 mW at 25 mA. The differential resistance slightly varies from 65 to 45 Ohms with current due to dissipated power. The relatively high threshold can be explained by absorption in the p-doped thick DBR and n-doped intracavity contact layer. According to the inset in Fig. 1, the dependence of differential slope efficiency on forward bias current has three parts: rapid increase and saturation at 0.58 W/A due to the appearance of lasing (region I); quick switching to lasing with 0.78 W/A (region II); and a monotonic decrease due to overheating (region III). In each of the three regions the differential efficiency depends on the injection efficiency, internal optical loss, and mirror loss. However the mirror loss is relatively insensitive to current due to the weak thermal dependence of the DBR layers refractive indices. Moreover we believe the injection efficiency remains practically constant because we do not observe kinks in the I-V-curves (not shown). Hence, we attribute the observed behavior to drastic changes in the VCSEL mode structure since each cavity mode has an individual intrinsic optical loss. Note that the VCSELs start working in region II at lower currents with temperature rise and, as a result, the region I fully disappears at temperatures higher than 60 K.

At low currents (<10 mA) in the CW regime the VCSELs show clear multimode operation at a peak emission wavelength of 945 nm via high-order modes (see insets in Fig. 1). However the subsequent increase of operational current results in the rapid increase of the side-mode suppression ratio (SMSR) and a switching to a single-mode lasing regime at a peak emission wavelength of 960 nm (region II). As a result, single transverse mode emission at a power of 15 mW and with a SMSR greater than 30 dB is obtained. To the best of our knowledge, this is the highest single-mode output power reported for any monolithic VCSEL to date.

The observed phenomena cannot be explained by oxide index guiding or non-uniform current pumping of the active region because these effects are hardly depend on forward bias current for our current VCSEL design. Fig. 2 depicts the emission spectra at a fixed current in the pulsed regime. At small pulse width (<400 ns) high-order modes dominate the lasing spectra (e.g. multi-mode operation). However the subsequent increase of pulse width results not only in a red-shift of the lasing wavelength, but also in a rapid increase of the optical power
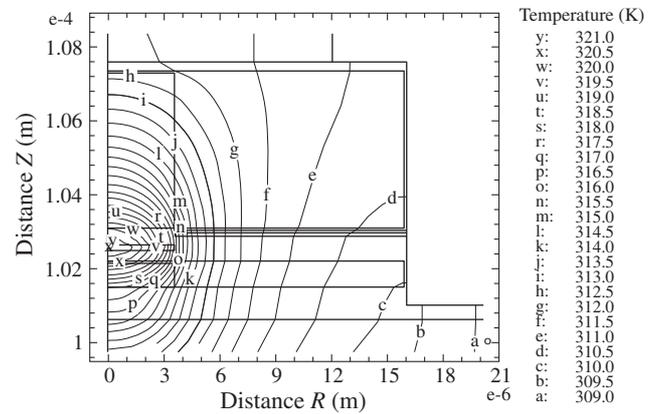
for the fundamental mode. These results demonstrate distinctly the crucial role played by ohmic dissipation (self-heating) in determining the CW modal behavior of the investigated VCSELs.

The 2D heat transport simulation of the device revealed a strong temperature gradient along the plane of the active region caused by effective lateral heatsinking. The temperature profile changes the refractive index of the cavity forming a thermal lens. Finally, the central region has an increased effective index profile creating an effective graded-index waveguide with a high index core. Such an effective waveguide leads to a stronger optical confinement of the fundamental mode, lower due to absorption in the nonpumped (passive) region and due to scattering from the multiple oxide apertures (via index discontinuities), and thus an increased SMSR.

To conclude, high-power single-mode oxide-confined VCSELs emitting near 960 nm were fabricated. We performed pulsed-measurements and heat transport modelling to clarify the physical nature of our VCSELs unusual single-mode behavior.

References

[1] C. Jung *et al*, *Electron. Lett.* **33**, 1790 (1997).
[2] Å. Haglund *et al*, *Photon. Technol. Lett.* **17**, 1602 (2005).
[3] H.J. Unold *et al*, *Electron. Lett.* **37**, 178 (2001).
[4] D. Zhou, L.J. Mawst, *J. Quantum Electron.* **38**, 1599 (2002).
[5] D.S. Song *et al*, *Appl. Phys. Lett.* **80**, 3901 (2002).
[6] N. Nishiyama *et al*, *Photon. Technol. Lett.* **12**, 606 (2000).

Features of antiwaveguiding oxide-confined 980 nm VCSELs

A. M. Nadtochiy [1,2], S. A. Blokhin[1], A. Mutig[3], A. V. Savelyev[2], A. G. Kuzmenkov[1], M. V. Maximov[2],
N. A. Maleev[1], N. N. Ledentsov[1,2], V. M. Ustinov[1] and D. Bimberg[3]

[1] Ioffe Physical-Technical Institute, St Petersburg, Russia
[2] St Petersburg Academic University, St Petersburg, Russia
[3] Technical University of Berlin, PW 5-2, Hardenbergstrasse 36, D-10623, Berlin, Germany

Abstract. 980-nm conventional and antiwaveguiding VCSELs with the same active region were investigated. Theoretical analysis of the antiwaveguiding design predicts enhancement of the oscillator strength for the VCSEL mode due to the suppression of the in-plane modes. Our experiments revealed additional positive effects of the antiwaveguiding design on both static and dynamic properties, which can be attributed to the decrease of the photon lifetime and increased thickness of the oxide aperture.

Introduction

During the last decade optical fiber data communication systems is gradually taking over copper interconnects and will become the leading technology in short distance datacom networks in the near future. Vertical cavity surface-emitting lasers (VCSEL) manifest themselves as reliable, ultra low-cost and high-speed light sources for Local/Storage Area Networks (LAN/SAN) [1]. At the same time continuous growth of transferred amount of information force telecom companies to seek more efficient, robust and faster light sources. This motivates efforts toward further optimization of VCSELs.

A common way to increase the bit data rate of the light emitter is to increase the modulation bandwidth of the device. The maximum achievable bandwidth in the absence of damping and electrical parasitic is proportional to frequency of relaxation oscillations, which is current dependent and can be defined for instance as [2]:

$$\omega_r^2 = \Gamma v_g a \left(I - I_{th} \right) / q V \, ,$$

where ω_r — frequency of relaxation oscillations, Γ — optical confinement factor, v_g — group velocity, a — differential material gain, I — operating current, I_{th} — threshold current, q — elementary charge, V — carrier volume.

From the equation given above and the given optimal operating current density (to avoid overheating and fast degradation effects) one can maximize ω_r by: 1) decreasing threshold current; 2) increasing differential material gain; 3) increasing Γ-factor; 4) reducing overheating. A numerous efforts were made to increase differential gain using strained quantum wells [3] or submonolayer quantum dots [4]. Another approach to is to minimization free carrier absorption and, thus, internal optical losses by applying proper doping profiles of the graded interfaces of DBR mirrors [5] or using intracavity contacts and undoped mirrors [6]. Other approach was demonstrated by Westbergh *et al* [7]. They have raised significantly modulation bandwidth by decreasing the photon lifetime.

1. Anti-waveguide conception

As was recently underlined [8] VCSEL may also suffer from in-plane waveguide modes, which originate due to the refractive index (RI) contrast between the GaAs-rich cavity and AlGaAs-rich DBR mirrors. In conventional VCSEL design spontaneously emitted light propagates not only in vertical direction and about 40% of all emitted power is attributed to the in-plane waveguide mode causing gain depletion and other parasitic effects like saturable absorption and the related self-pulsation.

Proposed antiwaveguiding concept [9] aims to suppress the guided mode intensity so that no optical in-plane mode having a significant overlap with the active region exists. In the present approach we use low RI cavity as compared to average RI of distributed Bragg reflectors (DBR). According to our calculations, in a such design optical power of the waveguide mode is redistributed to vertical VCSEL mode [8] and virtual tilted modes increasing their gain. In this work we analyze in details effect of antiwaveguiding design on VCSEL properties.

2. Experiment

Two VCSEL structures were grown on n+ GaAs (100) substrate by molecular beam epitaxy. The active region based on submonolayer InGaAs quantum dots [10] was inserted into a thin GaAs region and centered inside cavity. The conventional VCSEL design (ref-VCSEL) employs high index $Al_{0.15}Ga_{0.85}As$ λ-cavity, while the anti-waveguiding VCSEL (AVCSEL) design employs low index $Al_{0.2}Ga_{0.8}As$ $3/2\lambda$-cavity (Fig. 1a). Doped top/bottom $Al_{0.9}Ga_{0.1}As$/GaAs DBRs with 20/32 pairs and optimized electrical resistance with grating interfaces and modulation doping were used. The AlAs/$Al_{0.9}Ga_{0.1}As$ aperture layer was placed in a field intensity node on top of the cavity on the p-side. The VCSEL and AVCSEL devices with coplanar top contacts were processed using standard lithographic, metal deposition, dry etching techniques and wet oxidation.

3. Results and discussion

The idea of antiwaveguiding concept is illustrated on Fig. 1a, where refractive indexes and calculated optical fields of grown structures are shown. Using of low-index cavity allows one to remove parasitic waveguide mode (thin solid line) keeping high overlap of vertical mode (dashed line) with active area. In Table 1 light-current characteristics for both VCSELs are summarized. AVCSEL device has identical to ref-VCSEL threshold current (<0.3 mA) and slightly increased differential efficiency. At the above threshold conditions, the total

Table 1.

	I_{th} (mA)	Diff. eff. (W/A)	Max. power (mW)	I_{RO} (mA)
ref-VCSEL	0.28	0.55	3.6	10.9
AVCSEL	0.26	0.62	3.8	8.6

Fig. 2. Evaluated capacitance C_a as a function of aperture size. Inset: equivalent electrical circuit used to fit S11 curves.
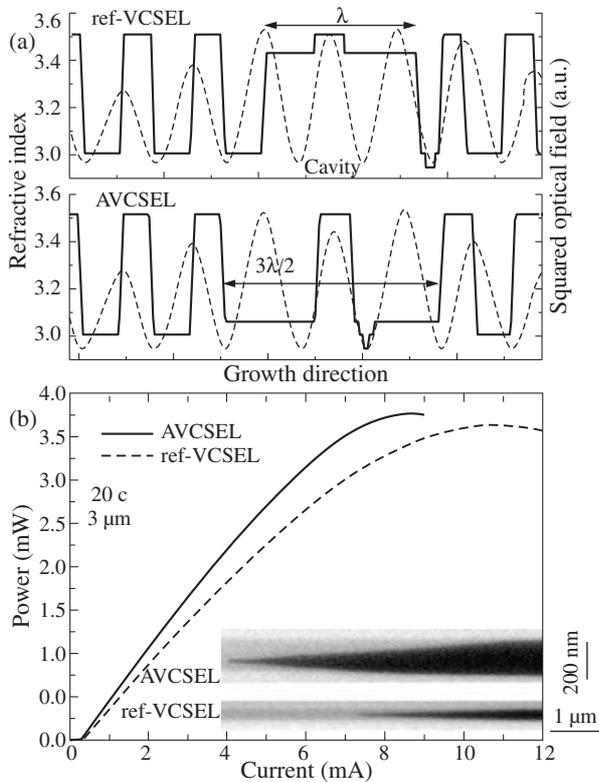
Fig. 1. a) Design of the devices. Bold solid line — refractive index; thin solid line — squared optical field for waveguide mode; dashed line — squared optical field for vertical mode. b) SEM images of oxidized apertures. Dark black corresponds to oxide, gray corresponds to AlGaAs material.

external differential efficiency depends on injection efficiency, internal optical loss and mirror loss [1]. The standard transmission matrix simulation revealed 25% increase of mirror loss in AVCSEL design as compared to that for VCSEL design (e.g. decrease of photon lifetime, which may be important for high speeds). This happens due to cavity-DBR RI contrast inverse. On Fig. 1b SEM images of apertures of both structures are shown. It is clearly seen that the total oxide thickness of aperture in AVCSEL is surprisingly 4-times thicker than that for VCSEL. This happens due to effect of vertical oxidation of low-index $Al_{0.8}Ga_{0.2}As$ layer from $AlAs/Al_{0.9}Ga_{0.1}As$ aperture layer. Thick oxide in AVCSEL results in strong index guiding effect and modifies lateral optical mode distribution causing mode to shrink in the center of active region area [11]. This implies optical mode overlapping with highly pumped central area of active region and reducing mode penetration into unpumped lossy side parts.

To analyze the effect of anti-waveguiding concept on high frequency properties of VCSELs the microwave reflection measurements were made. VCSEL high-frequency equivalent circuit [12] used for fitting is shown on the inset of Fig. 2. Evaluated values of VCSEL parasitic capacitance (C_p) and serial resistance (R_s) are 200 fF and 30 Ohm respectively. Equivalent resistance of active region (R_a) is about 3 times higher for AVCSELs as compare with ref-VCSEL (200 vs. 70 Ohm) due to thick low-doped $Al_{0.8}Ga_{0.2}As$ layer having lower conductivity. The evaluated effective capacitances of active region (C_a) as a function of aperture sizes are plotted on Fig. 2. Capacitance of the active area which is the sum of capacitance of oxide layers
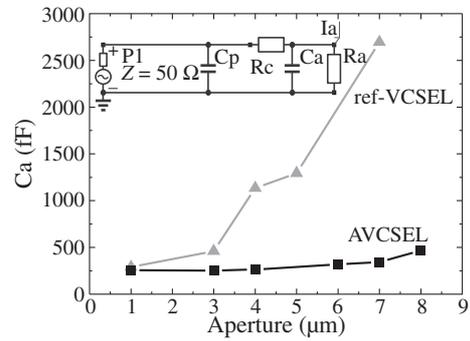
and junction capacitance [12] is found to be smaller and much less sensitive to the aperture size in the case of AVCSEL. This fact can be attributed to the thick antiwaveguiding layer which can be treated as a deep oxidation layer [12]. This leads to the significant reduction of the main part of parasitic capacitance of the active area — oxide layer capacitance.

Device capacitance results in increasing of the parasitic cut-off frequency for AVCSEL (11 GHz) as compare with reference VCSEL (6 GHz).

4. Conclusion

A 980-nm conventional VCSEL and antiwaveguiding VCSEL with the same active region were compared. The antiwaveguiding VCSEL demonstrated a higher differential efficiency and electrical parasitics cut-off frequency. These facts can be interpreted with the assistance of the positive effects of anti-waveguiding design, namely: smaller photon lifetime and the reduced capacitance of the active area.

References

[1] L.A. Coldren and S.W. Corzine, *Diode lasers and photonic integrated circuits*, (Wiley), 1995.

[2] J. Cheng and K. Dutta, *Vertical-Cavity Surface-Emitting Lasers: Technology and Applications*, (Gordon&Reach Publishers) 129 (2000).

[3] P. Westbergh *et al*, *Electron. Lett.* **44**, 907 (2008).

[4] A. Mutig *et al*, *Electron. Lett.* **44**, 1345 (2008).

[5] C.-H. Tu *et al*, *Proc. of SPIE* (San Diego, CA, USA, 2009), 7442216, 2009.

[6] V.V. Lissak and Y.-T. Lee *Proc. of SPIE* (San Diego, CA, USA, 2006), 63520Z, 2006.

[7] P. Westbergh *et al*, *Electron. Lett.* **46**, 1014 (2010).

[8] A.V. Savelyev *et al*, "Spontaneous emission in the anti-waveguiding VCSEL" *to be published*.

[9] N.N. Ledentsov *et al*, *Proc. of SPIE* (San Diego, CA, USA 2007), 64681O, 2007.

[10] S.A. Blokhin *et al*, *J. Quant. Electron.* **42**, 851 (2006).

[11] G.R. Hardley *et al*, *Opt. Lett.* **20**, 1483 (1995).

[12] Y.-C. Chang and L.A. Coldren, *J. Sel. Topics Quant. Electron.* **15**, 704 (2009).

GaN-based monolithic white LEDs

A. F. Tsatsulnikov[1], W. V. Lundin[1], A. V. Sakharov[1], E. E. Zavarin[1], S. O. Usov[2], A. E. Nikolaev[1],
V. S. Sizov[1], A. E. Chernyakov[2], A. L. Zakgeim[2], N. A. Cherkashin[3] and M. Hytch[3]

[1] Ioffe Physical-Technical Institute, St Petersburg, Russia
[2] Submicron Heterostructures for Microelectronics Research & Engineering Center, RAS, St Petersburg, Russia
[3] CEMES-CNRS — Université de Toulouse, Toulouse, France

Abstract. Monolithic white LED structures with active region based on several InGaN QWs emitting in different optical ranges were grown and investigated. Methods of the formation of nonuniform InGaN QWs which allow controlling structural and optical properties of the QWs were investigated. Effect of number of the QWs and barriers between QWs on optical properties of the monolithic withe LEDs was studied.

Introduction

Progress in the development of LEDs based on gallium nitride in the past two decades allowed creating highly efficient solid-state white light sources having long life time [1]. However, in general LEDs developed are based on conversion of blue light to white by phosphor. On the other hand, gallium nitride based LEDs can emit in whole visible range and, therefore, white light sources based on the concept of RGB mixing can be created. The most promising LEDs which use the concept of RGB mixing is a monolithic white LEDs containing in an active region several InGaN layers emitting in the range from blue to red. The main reason for the absence of these LEDs is low efficiency of the emission of InGaN QWs emitting at wavelengths longer 530 nm [2]. This is connected with high In content in the InGaN layers which is needed to shift emission toward long-wavelength side. Significant mismatch of the lattice parameters between GaN and InN results in generation of defects in such structures and worsening of the optical properties. In this work, we investigated methods of epitaxial growth of the InGaN/GaN active regions to reach emission in the yellow-green range and developed approaches to create monolithic white LEDs which contain multiple InGaN QWs in active region emitting at different wavelengths and mixture of these emissions produce white light.

1. Methods of the growth of active region for monolithic white LEDs

Design of LED structures based on combination of InGaN/GaN short-period superlattice (SPSL) and InGaN QWs was investigated to suppress effect of dislocations and improve carrier transport in the active region. These SPSLs with each layer thicknesses near 1 nm were fabricated using novel method based on cycle conversion of surface InGaN layer to GaN by applying of growth interruptions in hydrogen atmosphere [3]. SPSLs having total number of periods from 3 to 30 nm were in-
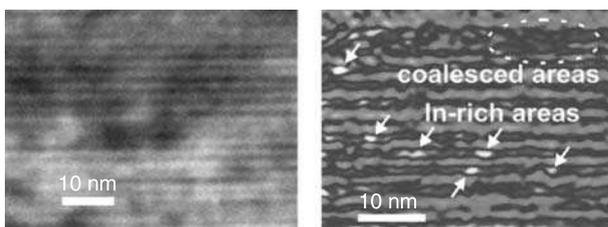
Fig. 1. TEM images of the SPSL.
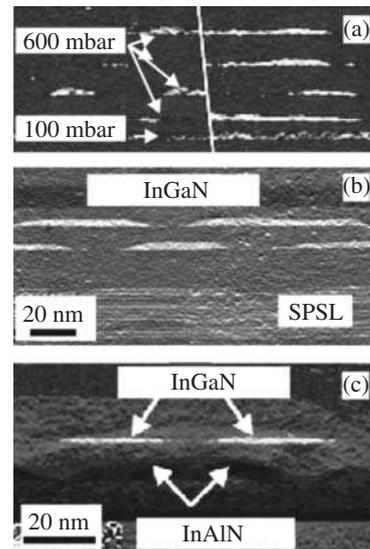
Fig. 2. TEM images of the InGaN layers, grown at different pressures (a), with growth interruptions (b), composite InGaN/GaN/InAlN structures.

vestigated by combination of optical methods, XRD and high resolution transmission electron microscopy (HRTEM) with geometric phase analysis. These investigations shown coalescence of neighboring InGaN layers in the SPSL and formation of local areas having increased thickness (Fig. 1). Besides, In-reach areas inside the SPSLs were revealed. These both effects result strong modification of emission with total number of period increase which accompanies shift of the peak position in the range of 410–470 nm. Temperature and excitation power dependences of the emission of the SPSLs were studied and effect of carrier transport inside the SPSLs on emission spectra was revealed.

Methods of fabrication of the active region of the monolithic white LEDs were investigated with point of view realization high color parameters of emission. Usually, main attention at development of the technology of epitaxial growth of active region for LEDs focuses on implementing high efficiency of emission at narrow line width. However, in the case of white LEDs based on mixture of colors the narrowness of the emission spectrum of individual colors will lead to a decrease of color rendering index (CRI) [3]. Since width of the emission line of the InGaN based active region depends on degree of the nonuniformity in atom distribution in the InGaN layers (the larger degree of the nonuniformity leads to increase in the width
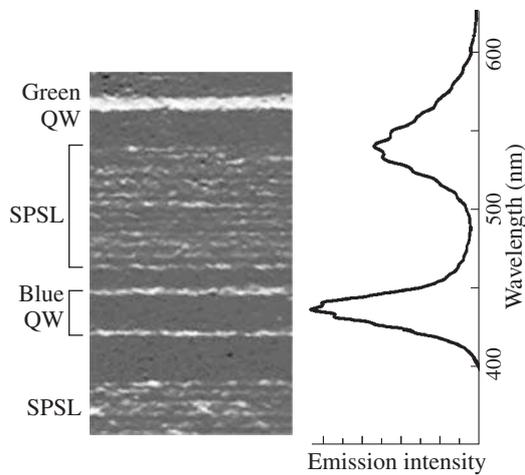
Fig. 3. TEM image of the active region and emission spectrum of the monolithic white LED.

Fig. 4. CIE color diagram of the monolithic white LEDs with 6 and 12 period SPSL barriers.

of the emission), different methods of synthesis of ultrathin In-GaN layers were investigated to reveal effect of the growth on structural and optical properties of these InGaN layers. Different approaches were investigated: effect of growth parameters (temperature, pressure); submonolayer formation of the InGaN layers; effect of deposition of the thin InGaN layer on the SPSL; transforming thin InGaN layer in the array of islands during growth interruption in nitrogen-hydrogen atmosphere; formation of composite InGaN/GaN/InAlN structures, based on the transformation of thin InGaN layer deposited on a wide band gap InAlN islands (Fig. 2).

These methods of growth of the InGaN layers were applied for growth of LED structures of blue and green-yellow ranges. It was shown that transformation of the continuous In-GaN layers to array of islands allows increasing external quantum efficiency and improving injection of carriers to active region [4]. Design of active region of LED structure emitting in green-yellow range based on single InGaN layer deposited on the SPSL was investigated [5]. Dependence of the external quantum efficiency on the parameters of the SPSL (number of periods, time of conversion, layer thickness) was revealed. It was shown that using of this design of active region leads to the increase of the maximal emission efficiency up to 16% at 540 nm and up to ~8% at 560 nm.

2. Monolithic white LEDs

On the basis of these studies different designs of the active region of monolithic LEDs were investigated. Two-color white LEDs based on the active region containing two blue InGaN QWs emitting at 440–450 nm and one "deep" green InGaN QW emitting at 540–570 nm range were investigated. As was mentioned above effective injection of carriers in all QWs should be realized. Nonuniform injection leads to the dependence of the emission intensity on the distance between QWs and decreases emission intensity with increasing of the distance between the InGaN QWs and p- and n-doped regions. This effect leads to the current dependence of the emission and, hence, dependence of color parameters on current. We proposed to use SPSL as a barrier between the QWs, emitting in the blue and green spectral regions (Fig. 3) [6]. It was shown that such SPSL can increase the efficiency of carrier injection into the InGaN QWs, located on significant distance from the p-doped
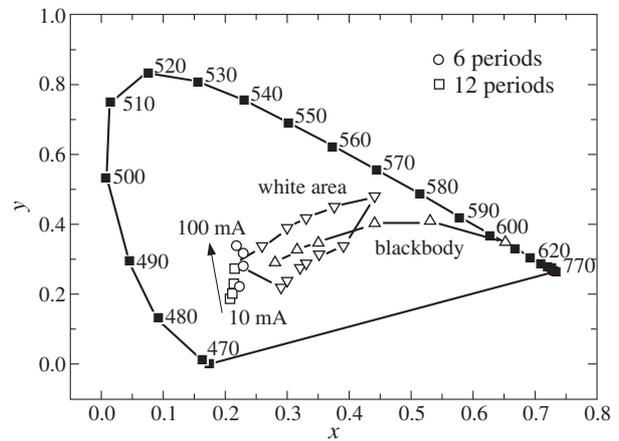
layer and improve emission efficiency of the monolithic LED structure. Optical properties of the monolithic LED structures were investigated in dependence on type (GaN or SPSL) and thickness of the barrier separating the InGaN QWs. LED structure having thin GaN barrier shown a higher value of external quantum efficiency that indeed is associated with a lower total In content in the structure. However, in the case of thin barriers intensity of the blue line is much higher than the intensity of the green line that leads to a high value of the correlated color temperature (CCT). For monolithic LED with SPSL based barrier intensities of the blue and green emission are comparable even at significant total thickness of the barriers (Fig. 4).

Dependence of the external quantum efficiency on the number of the InGaN QWs in active region was investigated. It was shown that deposition of the three InGaN QWs emitting at different wavelengths (450, 510, 560 nm) in active region leads to decrease of quantum efficiency on 20%. However, deposition of four InGaN QWs results in significant decreasing of the emission efficiency on 50%. For the processed two-color monolithic white LED better external quantum efficiency of 7–10% was achieved at CCT is in the range of 7000–10000 K.

References

[1] E.F. Schubert, *Light-emitting diodes*, Cambridge University Press (2003).
[2] A. Zukauskas, M. Shur, R. Gaska, *Introduction to Solid-State Lighting*, J. Wiley & Sons, NY (2002).
[3] N.V. Kryzhanovskaya, W.V. Lundin, A.E. Nikolaev, A.F. Tsatsul'nikov, A.V. Sakharov, M.M. Pavlov, N.A. Cherkachin, M.J. Hytch *et al*, *Semiconductors* **44** (6), 857 (2010).
[4] A.F. Tsatsulnikov, W.V. Lundin, A.V. Sakharov, E.E. Zavarin, S.O. Usov *et al*, *Semiconductors* **44** (1), 93 (2010).
[5] W.V. Lundin, E.E. Zavarin, M.A. Sinitsyn, A.E. Nikolaev, A.V. Sakharov, A.F. Tsatsulnikov *et al*, *EWMOVPE 13*, Ulm, 7–10 June 2009, Booklet of Extended abstracts, Inv. 2.
[6] A.F. Tsatsulnikov, W.V. Lundin, A.V. Sakharov, E.E. Zavarin, S.O. Usov *et al*, *Semiconductors* **44** (6), 837 (2010).

Carrier capture delay and modulation bandwidth in an edge-emitting quantum dot laser

L. V. Asryan[1], Yuchang Wu[1] and R. A. Suris[2]

[1] Virginia Polytechnic Institute and State University, Blacksburg, Virginia 24061, USA
[2] Ioffe Physical-Technical Institute, St Petersburg, Russia

Abstract. We show that the carrier capture from the optical confinement layer into quantum dots (QDs) can strongly limit the modulation bandwidth $\omega_{-3\mathrm{dB}}$ of a QD laser. As a function of the cross-section σ_n of carrier capture into a QD, $\omega_{-3\mathrm{dB}}$ asymptotically approaches its highest value when $\sigma_n \to \infty$ (the case of instantaneous capture). With reducing σ_n, $\omega_{-3\mathrm{dB}}$ decreases and becomes zero at a certain non-vanishing $\sigma_n^{\min}$. The use of multiple-layers with QDs considerably improves the laser modulation response — $\omega_{-3\mathrm{dB}}$ is considerably higher in a multi-layer structure as compared to a single-layer structure at the same dc current.

Introduction

Reducing dimensionality of the active region has been a key to developing low-threshold semiconductor lasers [1,2]. In commercial diode lasers, a two-dimensional active region (quantum well) is used [3]. In quantum dot (QD) lasers, an ultimate case of a zero-dimensional active region is realized [4,5]. While the steady-state characteristics of QD lasers have been extensively studied, their dynamic properties need to be further scrutinized. In particular, the potential of QD lasers for high-speed direct modulation of the output optical power by injection current should be clarified.

In [6], the highest modulation bandwidth attainable in QD lasers was estimated. For this purpose, an idealized situation of instantaneous carrier capture into QDs was assumed. In actual semiconductor lasers, carriers are not directly injected into the quantum-confined active region — they are first injected into the optical confinement layer (OCL) and then captured into the active region. Indirect injection adversely affects the laser operating characteristics — the threshold current is increased [7] and more temperature-sensitive [8], and the output optical power is decreased [9,10]. Due to a transport delay across the OCL and a capture delay from the OCL into the active region, the bandwidth of direct modulation of the output power by injection current is also reduced (see, e.g., [11] for quantum well lasers).

In this work, we study the effect of non-instantaneous capture of carriers into QDs on the modulation bandwidth of an edge-emitting QD laser.

1. Theoretical model

Our model is based on the following set of three coupled rate equations for free carriers in the OCL, carriers confined in QDs, and photons:

$$\frac{\partial n_{\mathrm{OCL}}}{\partial t} = \frac{j}{eb} - \sigma_n v_n n_{\mathrm{OCL}} \frac{N_{\mathrm{S}}}{b}(1 - f_n) + \sigma_n v_n n_1 \frac{N_{\mathrm{S}}}{b} f_n - B n_{\mathrm{OCL}}^2, \quad (1)$$

$$\frac{\partial}{\partial t}\left(\frac{2N_{\mathrm{S}}}{b} f_n\right) = \sigma_n v_n n_{\mathrm{OCL}} \frac{N_{\mathrm{S}}}{b}(1 - f_n) - \sigma_n v_n n_1 \frac{N_{\mathrm{S}}}{b} f_n$$
$$- \frac{N_{\mathrm{S}}}{b}\frac{f_n^2}{\tau_{\mathrm{QD}}} - v_g g^{\max}(2f_n - 1)n_{\mathrm{ph}}, \quad (2)$$

$$\frac{\partial n_{\mathrm{ph}}}{\partial t} = v_g g^{\max}(2f_n - 1)n_{\mathrm{ph}} - v_g \beta n_{\mathrm{ph}}, \quad (3)$$

where n_{OCL} is the free carrier density in the OCL, j is the injection current density, b is the OCL thickness, σ_n is the cross-section of carrier capture into a QD, v_n is the carrier thermal velocity, N_{S} is the surface density of QDs, f_n is the occupancy of the energy-level of a carrier confined in a QD, B is the spontaneous radiative recombination constant for the OCL, τ_{QD} is the spontaneous radiative lifetime in a QD, v_g is the group velocity of light, $g^{\max}$ is the maximum modal gain [7], n_{ph} is the photon density (per unit volume of the OCL) in the lasing mode, $\beta = (1/L)\ln(1/R)$ is the mirror loss, L is the cavity length, and R is the facet reflectivity.

In (1) and (2), the quantity $n_1 = N_{\mathrm{c}}^{\mathrm{3D}} \exp(-E_n/T)$ characterizes the carrier thermal escape from a QD to the OCL, where $N_{\mathrm{c}}^{\mathrm{3D}}$ is the effective density of states in the OCL, E_n is the carrier thermal excitation energy from a QD, and T is the temperature (in units of energy).

Strictly speaking, σ_n is the only parameter adequately describing the capture/escape into/from a QD. Using σ_n, two distinct characteristic times can be introduced – the capture time into an unoccupied QD ensemble [10] and the thermal escape time from an individual QD [7,10],

$$\tau_{\mathrm{capt},0} = [\sigma_n v_n (N_{\mathrm{S}}/b)]^{-1}, \qquad \tau_{\mathrm{esc}} = (\sigma_n v_n n_1)^{-1}. \quad (4)$$

Within the framework of the small-signal analysis of rate equations, we consider j in (1) in the form of $j = j_0 + (\delta j_m)\exp(i\omega t)$, where j_0 is the dc component and the amplitude δj_m of the time-harmonic ac component is small. We correspondingly look for n_{OCL}, $f_{n,0}$, and $n_{\mathrm{ph},0}$ in (1)–(3) in the form of $n_{\mathrm{OCL}} = n_{\mathrm{OCL},0} + (\delta n_{\mathrm{OCL}-m})\exp(i\omega t)$, $f_n = f_{n,0} + (\delta f_{n-m})\exp(i\omega t)$, and $n_{\mathrm{ph}} = n_{\mathrm{ph},0} + (\delta n_{\mathrm{ph}-m})\exp(i\omega t)$, where $n_{\mathrm{OCL},0}$, $f_{n,0}$, and $n_{\mathrm{ph},0}$ are the solutions of the steady-state rate equations at $j = j_0$ [9,10]. We thus obtain a set of algebraic equations in the frequency-dependent small amplitudes $\delta n_{\mathrm{OCL}-m}$, δf_{n-m}, and $\delta n_{\mathrm{ph}-m}$, the solution of which yields the modulation response function $H(\omega) = |\delta n_{\mathrm{ph}-m}(\omega)/\delta n_{\mathrm{ph}-m}(0)|^2$. Finally, we arrive at a cubic equation for the square of the modulation bandwidth $\omega_{-3\mathrm{dB}}$ — the frequency, at which $H(\omega)$ has fallen to half its dc ($\omega = 0$) value.

2. Discussion

The modulation bandwidth depends strongly on the capture cross-section σ_n. At a fixed dc component j_0 of the injection current density, with making slower the capture into QDs (reducing σ_n), $\omega_{-3\mathrm{dB}}$ decreases and finally becomes zero (Figs. 1
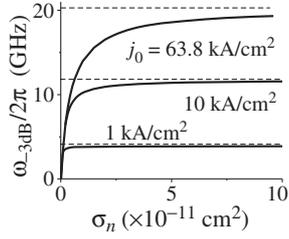
Fig. 1. $\omega_{-3\text{dB}}$ vs. σ_n. The horizontal dashed lines — instantaneous capture case.
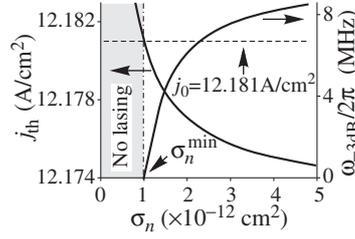
Fig. 2. $\omega_{-3\text{dB}}$ (at a very low j_0) and j_{th} vs. σ_n. Figs. 1 and 2 are for a single-layer structure. In Figs. 1–4, $T = 300$ K, $L = 1.1$ mm.

Fig. 3. $\omega_{-3\text{dB}}$ vs. j_0 in single- and 5-QD-layer-structures. $\sigma_n = 10^{-11}$ cm^2.

Fig. 4. Maximum $\omega_{-3\text{dB}}$ vs. σ_n. The horizontal line — instantaneous capture case [Eq. (9)].

and 2). As seen from Fig. 2, $\omega_{-3\text{dB}} = 0$ at a certain non-vanishing $\sigma_n^{\min}$. This is due to the fact that, at a given j_0, no lasing is attainable in the structure if $\sigma_n < \sigma_n^{\min}$. Indeed, while j_0 is fixed (the horizontal dashed line), the threshold current density increases with decreasing σ_n [7],

$$j_{\text{th}} = \frac{eN_S}{\tau_{\text{QD}}} f_{n0}^2 + ebB\left(n_1 \frac{f_{n0}}{1 - f_{n0}} + \frac{1}{\sigma_n v_n \tau_{\text{QD}}} \frac{f_{n0}^2}{1 - f_{n0}}\right)^2. \quad (5)$$

In order for the lasing to occur, j_0 should be higher than j_{th}. At a certain $\sigma_n^{\min}$, j_{th} becomes equal to j_0 (Fig. 2). At $\sigma_n \leq \sigma_n^{\min}$, $j_{\text{th}} \geq j_0$, which means that there can be no lasing and hence no direct modulation in the structure.

The minimum tolerable σ_n for the lasing to occur at j_0 is found from the condition $j_{\text{th}} = j_0$ and is given by

$$\sigma_n^{\min}(j_0) = \frac{1}{v_n \tau_{\text{QD}}} \frac{f_{n0}^2}{1 - f_{n0}} \sqrt{ebB}$$

$$\times \frac{\sqrt{j_0 - \frac{eN_S}{\tau_{\text{QD}}} f_{n0}^2} + \sqrt{j_{\text{th}}^{\text{eq}} - \frac{eN_S}{\tau_{\text{QD}}} f_{n0}^2}}{j_0 - j_{\text{th}}^{\text{eq}}}, \quad (6)$$

where $j_{\text{th}}^{\text{eq}}$ is j_{th} for the case of instantaneous capture [$j_{\text{th}}^{\text{eq}}$ is obtained using $\sigma_n = \infty$ in (5)].

With increasing j_0, $\sigma_n^{\min}$ becomes smaller, i.e., the lasing can occur and hence the direct modulation of the output power is possible at a slower capture. At high j_0 (when $\sigma_n^{\min} \to 0$), the asymptotic expression for $\omega_{-3\text{dB}}$ for σ_n in the vicinity of $\sigma_n^{\min}$ [$(\sigma_n - \sigma_n^{\min})/\sigma_n^{\min} \ll 1$] is

$$\omega_{-3\text{dB}} \approx 2\sqrt{r - 1} \, v_g g^{\max} \frac{f_{n0}(1 - f_{n0})}{2 - f_{n0}} \frac{\sigma_n - \sigma_n^{\min}}{\sigma_n^{\min}}, \quad (7)$$

where $r = 10^{0.3} \approx 1.995$.

As a function of j_0, $\omega_{-3\text{dB}}$ has a maximum (Fig. 3). In a single-QD-layer structure, the optimum value j_{opt} of j_0, at which $\omega_{-3\text{dB}}^{\max}$ is attained, is very high, i.e., $\omega_{-3\text{dB}}^{\max}$ is unattainable. As seen from the figure, there are two advantages in a multiple-QD-layer structure as compared to a single-layer structure: (i) $\omega_{-3\text{dB}}$ is considerably higher at the same value of j_0, and (ii) j_{opt} is considerably reduced, which means that $\omega_{-3\text{dB}}^{\max}$ is practically attainable.

At large σ_n, when $\tau_{\text{capt},0}/\tau_{\text{ph}} \ll 1$ [$\tau_{\text{capt},0}$ is given by (4) and $\tau_{\text{ph}} = [(v_g/L)\ln(1/R)]^{-1}$ is the photon lifetime in the cavity], both $\omega_{-3\text{dB}}$ at a given j_0 (Fig. 1) and $\omega_{-3\text{dB}}^{\max}$ (Fig. 4) asymptotically approach their saturation values corresponding to the case of instantaneous capture into QDs,

$$\left(\omega_{-3\text{dB}}\mid_{\sigma_n = \infty} - \omega_{-3\text{dB}}\right), \; \left(\omega_{-3\text{dB}}^{\max}\mid_{\sigma_n = \infty} - \omega_{-3\text{dB}}^{\max}\right)$$
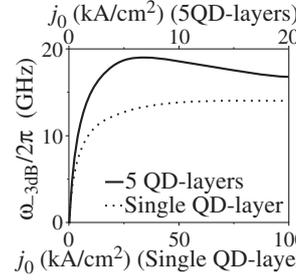
$$\propto \frac{\tau_{\text{capt},0}}{\tau_{\text{ph}}} \propto \frac{1}{\sigma_n}, \quad (8)$$
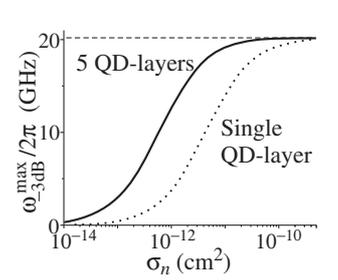
where $\omega_{-3\text{dB}}\mid_{\sigma_n = \infty}$ is given by Eq. (9) of [6] and

$$\omega_{-3\text{dB}}^{\max}\mid_{\sigma_n = \infty} \approx \sqrt{2}/\tau_{\text{ph}}. \quad (9)$$

As seen from Fig. 4, while the saturation value of $\omega_{-3\text{dB}}^{\max}$ at $\sigma_n \to \infty$ and at a fixed L [Eq. (9)] does not depend on the number of QD-layers, $\omega_{-3\text{dB}}^{\max}$ at a given finite σ_n is higher in a multi-layer structure as compared to a single-layer structure.

3. Conclusion

We have shown that the carrier capture from the OCL into QDs can strongly limit the modulation bandwidth $\omega_{-3\text{dB}}$ of a QD laser. $\omega_{-3\text{dB}}$ is highest in the case of instantaneous capture into QDs, when the cross-section of carrier capture into a QD $\sigma_n = \infty$. With reducing σ_n, $\omega_{-3\text{dB}}$ decreases and becomes zero at a certain non-vanishing $\sigma_n^{\min}$. This $\sigma_n^{\min}$ presents the minimum tolerable σ_n for the lasing to occur at a given dc component j_0 of the injection current density. The use of multiple layers with QDs has been shown to considerably improve the modulation response of the laser — $\omega_{-3\text{dB}}$ is considerably higher in a multi-layer structure as compared to a single-layer structure at the same j_0. At a plausible cross-section $\sigma_n = 10^{-11}$ cm^2 [12], $\omega_{-3\text{dB}}$ as high as 19 GHz can be obtained in a 5-QD-layer structure with $L = 1.139$ mm at a practical value of $j_0 = 7$ kA/cm^2.

Our analysis provides a basis for optimizing the QD laser design for high-speed operation.

References

[1] R. Dingle, C.H. Henry, U.S. Patent 3982207 (1976).
[2] Zh.I. Alferov, *Rev. Mod. Phys.* **73**, 767 (2001).
[3] W.T. Tsang, *APL* **40**, 217 (1982).
[4] Y. Arakawa, H. Sakaki, *APL* **40**, 939 (1982).
[5] A.E. Zhukov *et al*, *Phys. E* **17**, 589 (2003).
[6] L.V. Asryan, R.A. Suris, *APL* **96**, Art. No. 221112 (2010).
[7] L.V. Asryan, R.A. Suris, *Sem. Sci. Technol.* **11**, 554 (1996).
[8] L.V. Asryan, R.A. Suris, *IEEE QE* **34**, 841 (1998).
[9] L.V. Asryan, S. Luryi, R.A. Suris, *APL* **81**, 2154 (2002).
[10] L.V. Asryan, S. Luryi, R.A. Suris, *IEEE QE* **39**, 404 (2003).
[11] R. Nagarajan *et al*, *IEEE QE* **28**, 1990 (1992).
[12] O. Engström *et al*, *APL* **85**, 2908 (2004).

Dynamics of a photoluminescence in InGaAsSb/AlGaAsSb quantum wells

L. Shterengas[2], D. A. Firsov[1], *M. Ya. Vinnichenko*[1], L. E. Vorobjev[1], A. N. Sofronov[1], G. A. Melentyev[1],
G. Kipshidze[2] and G. Belenky[2]

[1] St Petersburg State Polytechnical University, 195251 St Petersburg, Russia
[2] Department of Electrical and Computer Engineering, State University of New York at Stony Brook,
New York 11794, USA

Abstract. Time resolved photoluminescence was studied by "up-conversion" method in heterostructures with
InGaAsSb/AlGaAsSb quantum wells. The optical phonon emission time was estimated from the analysis of the rise time of
the photoluminescence decay curves. The recombination rate was determined as a function of pumping level. The role of
the resonant Auger recombination was discussed. These heterostructures can be used in room-temperature operating laser
diodes of mid infrared spectral range.

Introduction

Heterostructures with InGaAsSb/AlGaAsSb quantum wells can be used in room-temperature operating laser diodes of mid infrared spectral range (wavelength more than 2 micrometers). Carrier recombination kinetics study is essential to improve performance of such devices. Present work is devoted to the studies of pico- and nanosecond range dynamics of photoluminescence (PL) in Sb-containing nanostructures with quantum wells (QW). Experimental data analysis allows to determine relaxation times and recombination mechanisms as well as to find out the role of Auger recombination in InGaAsSb/AlGaAsSb nanostructures.

Structures with ten QWs $In_{0.53}Ga_{0.47}As_{0.24}Sb_{0.76}/Al_{0.7}Ga_{0.3}As_{0.056}Sb_{0.944}$ with a QW width of 4, 5, 6, 7 and 9 nm have been grown on GaSb substrate. The resonant Auger recombination [1] worsens characteristics of injection lasers. Using the structures with different width allows to establish the role of resonant Auger recombination. According to the calculations the conditions of resonant Auger recombination $(E(e2) - E(e1) = E(e1) - E(hh1))$ should be satisfied in structure with a QW width of 6 nm (see Fig. 1).

1. Experimental

Photoluminescence spectra are shown in Fig. 2. With the increase of QW width the photoluminescence spectrum should

Fig. 2. Photoluminescence spectra of structures with different QW width measured at $T = 77$ K.

be moved to long wavelength range, which was confirmed in experiment. "Up-conversion" method was used to study PL dynamics in nano- and picosecond time ranges. The structures were pumped by pulses of radiation with 150 fs duration, 100 MHz frequency and quantum energy $h\nu_{ex} = 1.17$ eV (Fig. 1). Photons with this energy excite the electron-hole $(e - h)$ pairs only in QW due to transitions $hh1 \rightarrow e1$ and $hh2 \rightarrow e2$. Thus, in contrast to the work [2], where the photon energy corresponded to the excitation of $e - h$ pairs in the wave-guide (QW barrier) area, in our case concentration of $(e - h)$ pairs should be lower.

The time dependence of PL intensity was studied at the wavelength corresponding to electron transitions from the bottom of $e1$ subband to $hh1$ subband. Electrons which have received the high energy after excitation by optical pumping relax with emission of optical phonons until they reach the bottom of $e1$ subband. Time dependence of PL intensity rise is determined with this process. Analysis of this dependence (Fig. 3) allowed to estimate the optical phonon emission time (0.14 ps).

Weak minimum of PL intensity was observed at the times of 8–10 ps (Fig. 3). This can be explained by an optical escape of carriers. Electrons which were created by previous pumping pulse and have not recombined yet are excited from the bottom of $e1$ subband to higher energy states by light pulse, thus elec-

Fig. 1. The scheme of carrier energy spectrum in structure 590 with a QW width of 6 nanometers. Electron transitions corresponding to resonant Auger recombination are shown by dashed arrows.
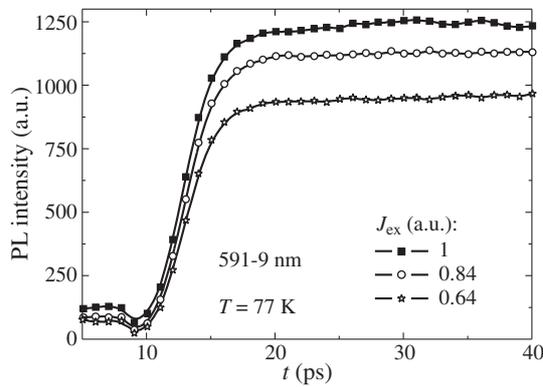
Fig. 3. Time dependences of PL intensity in picosecond scale for different intensities of excitation J_{EX} for sample 591–9 nm.
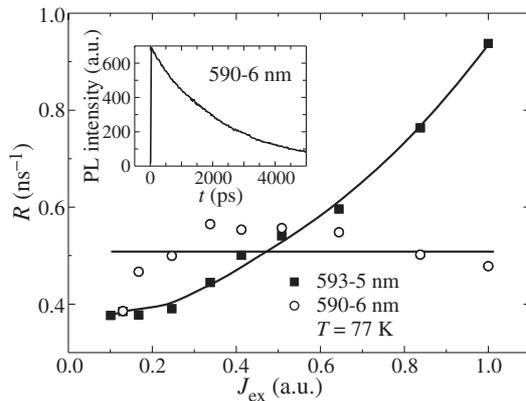
Fig. 4. Dependence of reciprocal lifetime on excitation level for two structures. On an insert — dependence of PL intensity on time.

tron population of $e1$ subband decreases which in turn partly suppress PL.

2. Carrier recombination

Analysis of PL decay curves (see for example Fig. 4, inset) allowed to calculate the carrier lifetime as a function of pumping level. The dependences of reciprocal lifetime $R = 1/\tau$ on pumping level J_{EX} for two structures with different QW width are shown in Fig. 4. At small pumping level Shockley–Read–Hall recombination is the dominating recombination mechanism. Corresponding lifetimes τ_{SHR} are equal to ~ 2 ns for QW width of 4–5 nm and ~ 3.5 ns for QW width of 7–9 nm. The reduction of τ_{SHR} with decreasing the QW width can be explained by the influence of heteroborders.

According to the calculations the energy spectrum of 590–6 nm sample most precisely meets the conditions of resonant Auger recombination (see Fig. 5). However the contribution of Auger recombination in recombination rate R, revealed as square-law dependence of R on pumping level J_{EX}, is observed in structure 593–5 nm. The possible reason of discrepancy between calculations (Fig. 5) and experiment (Fig. 4) is a nonparabolicity of the band spectrum which is especially strong at high electron energies and was not take into account in calculation. The observed increase of R with J_{EX} or carrier concentration is less than the theory [1] predicts. This can be explained by "degradation" of resonant conditions due to nonparabolicity of electron energy spectrum, anisotropy of hole energy spectrum, fluctuations of the content of the solid solutions.
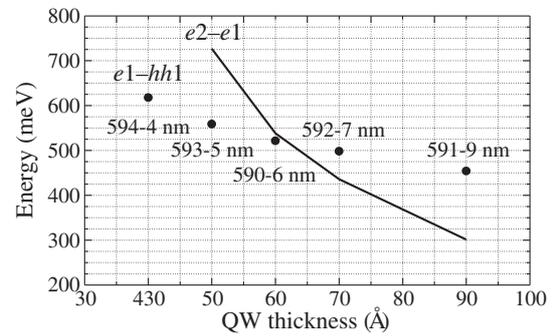
Fig. 5. The dependences of energy differences on QW width: $E(e2) - E(e1)$ (solid line, calculation); $E(e1) - E(hh1)$ (dots, experiment).

References

[1] L.V. Danilov and G.G. Zegrya, *Semiconductors* **42**, 550 (2008).
[2] L.E. Vorobjev, M.Ya. Vinnichenko, D.A. Firsov, V.L. Zerova, V.Yu. Panevin, A.N. Sofronov, P. Thumrongsilapa, V.M. Ustinov, A.E. Zhukov, A.P. Vasiljev, L. Shterengas, G. Kipshidze, T. Hosoda, G. Belenky, *Semiconductors* **44**, 50 (2010).

Power leaky-wave semiconductor laser with very narrow directional pattern

A. A. Dubinov[1], *V. Ya. Aleshkin*[1], *T. S. Babushkina*[2], *A. A. Biryukov*[2], *M. N. Kolesnikov*[2], *S. M. Nekorkin*[2] and *B. N. Zvonkov*[2]

[1] Institute for Physics of Microstructures, RAS, 603950 Nizhny Novgorod, Russia
[2] Research Physical-Technical Institute of the Nizhny Novgorod State University, 603950 Nizhny Novgorod, Russia

Abstract. A leaky-wave semiconductor laser diode has been developed based on the InGaAs/GaAs/InGaP heterostructure. This design made it possible to obtain a high radiation output in a narrow angular range (about $1-2°$) with an energy of 170 μJ in a laser with a cavity length of 0.8 mm and a stripe contact width of 360 μm, pumped by a single current pulse with an amplitude of 88 A and width of 5 μs.

Introduction

The technical (primarily, energetic) parameters of the currently used semiconductor lasers are close to the theoretical limit. Further development, expansion, and mastering of new areas of application of diode lasers is hindered by the high density of laser radiation at the output mirror, which is determined by the narrowness of the waveguide layer and significantly limits the output power. In addition, conventional lasers have a very wide output directional pattern in the plane perpendicular to the p-n junction, as a result of which the radiation deteriorates. One of the main reasons limiting the output power is the presence of ultimate light wave field in the cavity which leads to laser degradation. To reduce the electrical field in the cavity and to increase output power the either very wide cavities or two (sometimes three) successively located lasers, connected by a tunnel p-n junction are used [1,2]. However, the ultimate laser power can be increased in a different way. If most of the laser radiation leaks not through the mirror but through the substrate, which is several orders of magnitude thicker than the waveguide layer, the total power can be significantly increased. The radiation leakage through the substrate (leaky-wave regime) can be performed by reducing the thickness of the barrier between the waveguide layer and the substrate. Obviously, these lasers should have a high threshold current because of the high leak-induced loss. Therefore, many quantum wells must be incorporated into the laser active region to increase the gain. An important advantage of these lasers is the significant narrowing of the directional pattern in the plane perpendicular to the p-n junction. The purpose of this work was to develop and investigate a semiconductor laser with a wide waveguide and an active medium of enlarged volume, containing six InGaAs quantum wells inside GaAs waveguide. Optimization of this structure, aimed at providing conditions for radiation leaking mainly into the substrate, made it possible to obtain a very narrow directional pattern in the plane perpendicular to the p-n junction.

1. Experimental

A GaAs/InGaP/InGaAs heterostructure was grown by MOVPE under atmospheric pressure. Based on this heterostructure, we designed semiconductor lasers with an active region width of 360 μm and cavity lengths of 0.5, 0.8, 1, 1.3 and 2 mm. The temperature dependences of the threshold current density for
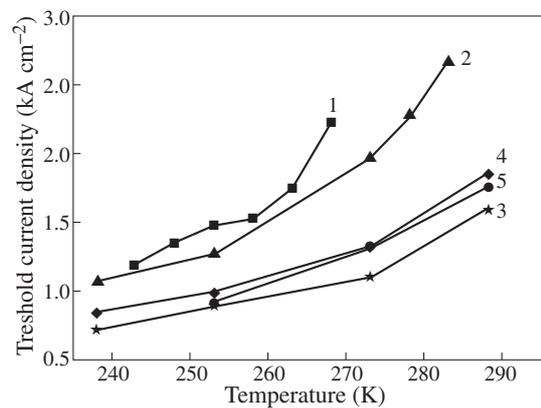
Fig. 1. Temperature dependencies of the threshold current density of laser diodes with cavity lengths of (1) 0.5, (2) 0.8, (3) 1, (4) 1.3 and (5) 2 mm.

the laser diodes are shown in Fig. 1. All samples exhibited a decrease in the threshold current upon cooling. Lasers generated at wavelength 0.977 μm at room temperature. These spectral measurements revealed that at liquid-nitrogen temperatures lasing begins under pumping by a dc current of 0.9 A (current density 250 A/cm^2); this is in agreement with the fact that the threshold current density tends to decrease upon cooling (Fig. 1, curve 3). We measured the directional patterns in the p-n junction plane and in the plane perpendicular to it. Fig. 2 demonstrates the directional radiation patterns for laser diodes with cavity length of 1 mm. The patterns of the laser diodes with cavity lengths of 0.5, 0.8, 1.3 and 2 mm in the plane perpendicular to the p-n junction had a single-lobe shape (as well as for the 1-mm cavity laser), with deviation by $10°$ from the normal toward the substrate. The width of the directional pattern at half maximum was $1-2°$. A comparison of the power of highly divergent radiation from the waveguide layer with the radiation through the substrate (characterized by a narrow directional pattern) showed that 84% radiation power is concentrated in a narrow angle. With an increase in the laser diode length to 2 mm an additional peak arises in the angular diagram, which is caused by the radiation reflection from the upper rough boundary of the substrate; as a result, the output radiation deteriorates. Note that the occurrence of additional peak is also determined by the substrate thickness (160 μm in our experiments).
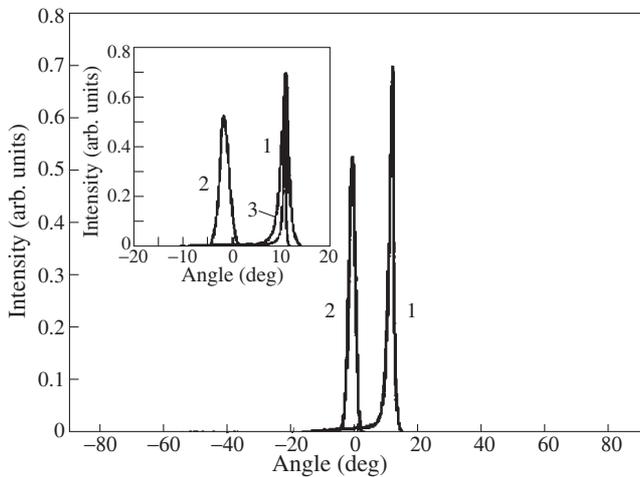
Fig. 2. Directional patterns of a laser diode (1) in the plane perpendicular to the p-n junction plane and (2) in the p-n junction plane (cavity length 1 mm, heat sink temperature 25 °C, pump current 7 A). The inset shows the same curves on the larger angular scale (curve 3 is the calculated directional radiation pattern in the plane perpendicular to the p-n junction).
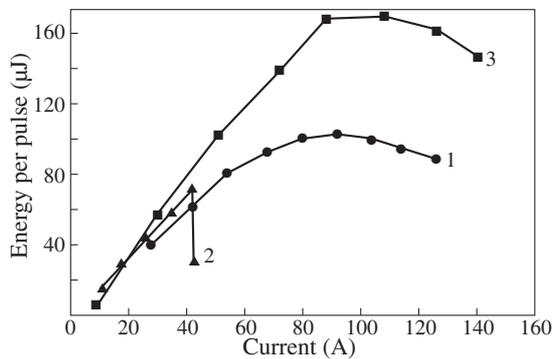
Fig. 3. Dependencies of the laser pulse energy on the pump current at a current pulse width of 5 μs for (1,3) a leaky-wave laser diode, without (1) and with (3) deposited reflection and antireflection coatings, and (2) a conventional laser diode (cavities lengths 0.8 and 1 mm, respectively).

The dependence of the pulse energy for a leaky-wave laser diode with a cavity length of 0.8 mm on the pump current for a 5-μs pump pulse is shown in Fig. 3 (curve 1). For comparison curve 2 shows a similar dependence for a conventional laser diode with a 1-mm cavity (the laser active region contained six QWs, its structure was similar to that of the lasers under study and differed only by the presence of a wide InGaP barrier between the waveguide and substrate). Deposition of reflection and antireflection coatings on the end faces of the leaky-wave laser made it possible to obtain a radiation energy of 170 μJ (Fig. 3, curve 3) under pumping by a single 5-μs current pulse with an amplitude of 88 A. As can be seen in Figs. 2 and 3, the radiation leakage through the substrate significantly reduces the electromagnetic field density at the mirrors, as a result of which a much higher output energy can be obtained at a higher pump current in comparison with conventional diode lasers. In addition, the radiation quality is significantly improved due to the very narrow directional pattern.

References

[1]   S.O. Slipchenko *et al*, *Fiz. Tekh. Poluprovodn.* **40**, 1017 (2006).
[2]   M.V. Zverkov *et al*, *Quantum Electron.* **38**, 989 (2008).

Double frequency generation in two-cascade interband laser

A. A. Dubinov[1], V. Ya. Aleshkin[1], T. S. Babushkina[2], A. A. Biryukov[2], M. N. Kolesnikov[2], S. M. Nekorkin[2]
and B. N. Zvonkov[2]

[1] Institute for Physics of Microstructures, RAS, 603950 Nizhny Novgorod, Russia
[2] Research Physical-Technical Institute of the Nizhny Novgorod State University, 603950 Nizhny Novgorod,
Russia

Abstract. The double frequency generation is obtained and investigated in new type injection heterolaser: interband cascade
laser with tunnel p-n junction separating two active regions with quantum wells located in common waveguide. Suggested
laser constriction have provided simultaneous generation of the first order TE mode with wavelength 1.086 μm and the
second order TE mode with wavelength 0.96 μm in the continuous wave lasing regime at room temperature.

Introduction

The two cascade semiconductor interband lasers have attractive
features which are lacking in ordinary laser diodes. The first of
all it is the possibility of simultaneous double frequency gener-
ation which can be used for the intracavity difference frequency
generation and to increase temperature stability of frequency
generation [1,2]. Moreover, the cascade laser containing two
injecting p-n junctions connected by tunnel p-n junction able
to generate the twice large power radiation in comparison with
ordinary laser diode containing one p-n junction [3]. How-
ever structure of cascade laser is similar to the thyristor and
therefore often has current voltage characteristics S-type and
current instability [4]. Current instability is undesirable, be-
cause prevents continuous generation. The reason it occurs is
too small width of the tunnel p-n junction. As a result, a p^{++}
region of the tunnel junction is injected with electrons which
don't recombine in the previous p-n junction, and n^{++} region
is injected with holes from further p-n junction. In the thyristor
structure is well-known effect of switching associated with the
injection of minority carriers in p-n junction, which occurs in
the laser structure. This work is dedicated to the creation and
study of interband two-cascade laser with a tunnel p-n junc-
tion with two types of quantum wells in a specially designed
waveguide for the simultaneous generation at the TE$_1$ and TE$_2$
modes in a continuous mode (Fig. 1). The design of the waveg-
uide and the position of the quantum wells were calculated so
as to generate TE$_2$ mode at the frequency corresponding to the
transition between the ground states of electrons and holes
in the thin quantum well, and the TE$_1$ mode at a frequency
corresponding to the transition between the ground states of
electrons and holes in the thick quantum well. The thick quan-
tum well located near the node of the short wavelength mode
and near maximum of long-wavelength mode. The thin quan-
tum well located near the maximum of the short wavelengths
mode. In this case, short wavelength radiation is not too much
absorbed in the thick quantum well, and the laser can generate
two frequencies. To eliminate the instability of thyristor type,
we introduced two additional thin layers of InGaP (on both
sides of the tunnel junction) in the waveguiding layer of GaAs
and to extend the tunnel junction.

1. Experimental

A GaAs/InGaP/InGaAs heterostructure was grown by MOVPE
under atmospheric pressure. The structures consisted of two
p-n junctions separated by a thin tunneling p-n junction (the
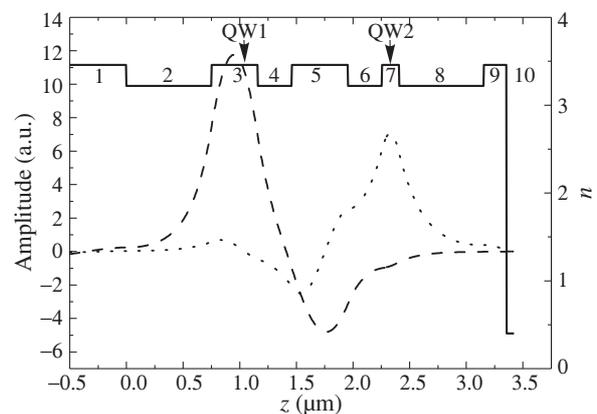
Fig. 1. Dependencies of the real part of the refractive index (solid
line) and the real part of electric fields in the modes TE$_1$ (dashed
line) and TE$_2$ (doted line) on the coordinate z (in the direction per-
pendicular to the p-n junction). Arrows indicate the positions of
the long-wavelength (QW1) and short-wavelength (QW2) quantum
wells in the structure. Layers in the structure consist of (1, 3, 5, 7,
9) GaAs and (2, 4, 6, 8) InGaP, (10) Au.

thickness of the heavily doped n- and p- type regions was 40
and 55 nm, respectively). The laser waveguide was formed by
a 0.75- μm-thick n-InGaP layer in the region of the lower p-n
junction and by a p-InGaP layer with the same thickness in the
region of the upper p-n junction. The short-wavelength QW in
the region of the upper p-n junction and the long-wavelength
QW in the region of the lower p-n junction were identical in
thickness (10 nm) but differed in the percentage of indium. In
order to form the active region in the plane of the p-n junction,
the structure was implanted with 80-keV hydrogen ions. Only
strips with the thickness of 100 μm were not implanted; it is
through these strips that the current exciting the laser oscilla-
tions passed. Cleaved faces of the structure served as mirrors.
The typical length of the laser's cavities was 2 mm.

In Fig. 2, we show the emission spectra of a laser for 4 values
of the pumping current. It can be seen from Fig. 2 that two
lines are observed in the spectrum. These lines correspond
to transitions between the first electron and hole subbands in
different QWs located in different p-n junctions.

In order to study the mode composition of emission, we mea-
sured the directivity diagrams of emission for all wavelengths
(Fig. 3). It can be seen from Fig. 3 that two clearly distin-
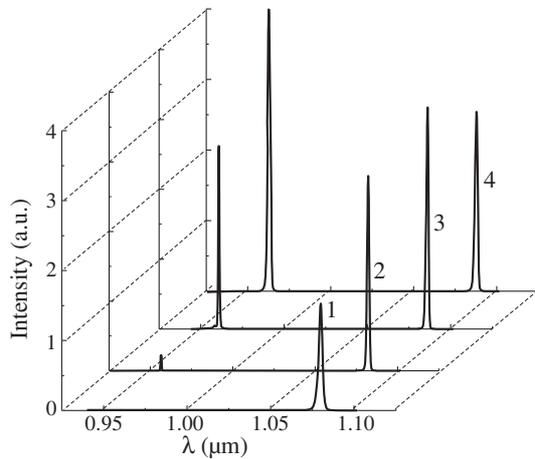
Fig. 2. The spectrum of laser generation for 4 values of amplitude of the current: 0.45 (1), 0.63 (2), 0.78 (3), 0.85 A (4).
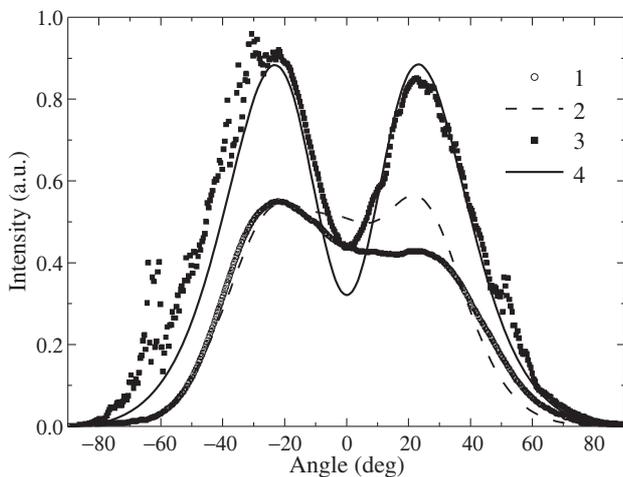
Fig. 3. Experimental (curves 1, 3) and calculated (curves 2, 4) directivity patterns for emission intensity in the plane of perpendicular to the p-n junction. The wavelengths are (1, 2) 0.96 and (3, 4) 1.086 μm.

Fig. 4. Measured spectra of generation of second harmonics (peaks 1 and 2) and sum frequency (peak 3).

References

[1] V.Ya. Aleshkin *et al*, *Semiconductors* **35**, 1203 (2001).
[2] V.Ya. Aleshkin *et al*, *Quantum Electron.* **39**, 727 (2009).
[3] M.V. Zverkov *et al*, *Quantum Electron.* **38**, 989 (2008).
[4] S.M. Nekorkin, *et al*, *Appl. Phys. Lett.* **90**, 171106 (2007).
[5] C. Flytzanis, *Phys. Rev. B* **6**, 1264 (1972).

guishable peaks exist for emission at the wavelength 1.086 μm in the plane perpendicular to the p-n junction. The positions and relative amplitudes of these peaks are consistent with those calculated for the TE$_1$ mode. In the case of emission with the wavelength 0.96 μm, a trapeziform peak is evident. This kind of directivity diagram corresponds to the diagram calculated for the TE$_2$ mode. The directivity diagrams for emission in the p-n-junction plane featured a single peak with the half-width of approximately 6° for all wavelengths. Thus, we may conclude that the choice of parameters of waveguide and arrangement of QWs made it possible to obtain genaration at the modes of specified orders.

In order to verify that two different frequencies in spatially crossing modes are interact, we observed the generation of the second harmonics and sum frequency. Mixing of frequencies in the laser's cavity occurs due to quadratic nonlinearity of the GaAs lattice parameters [5]. The results of observations are shown in Fig. 4. It can be seen that there are second harmonics for the modes with wavelengths 0.96 and 1.086 μm and also a signal with the sum frequency. This observation represents direct evidence for the possibility of mixing of frequencies with the laser's cavity and simultaneous lasing at two lines.

MOVPE grown ZnCdS/ZnMgS nanostructures and a longitudinal e-beam pumped UV laser based on them

P. I. Kuznetsov[1], G. G. Yakushcheva[1], V. A. Jitov[1], L. Yu. Zakharov[1], V. I. Kozlovsky[2], D. E. Sviridov[2] and M. D. Tiberi[3]

[1] Institute of Radioengineering and Electronics, RAS, 1 Vvedenskogo, 141190 Fryazino, Russia
[2] P.N. Lebedev Physical Institute, RAS, 53 Leninsky pr., 119991 Moscow, Russia
[3] Pricipia LightWorks Inc. CA, USA

Abstract. Cubic ZnCdS epilayers with lattice constant closed to GaP substrates were grown by metal-organic vapor phase epitaxy. The stabilization of cubic crystal lattice is realized at low growth temperatures (below 430 °C) and VI:II ratio near 1:1. ZnCdS/ZnMgS multi quantum well nanostructures were grown on (100) GaP substrates also. An etalon for vertical cavity surface emitting laser emitting in ultraviolet range was fabricated based on these nanostructures. Lasing at $\lambda = 358.4$ nm with 0.2 W in output power was achieved under longitudinal pumping by scanning electron beam at room temperature.

Introduction

Epitaxial layers of the wide gap A_2B_6 solid solutions such as ZnSSe, ZnMgSSe, ZnMgS and ZnCdS can be grown isoperiodic to GaP substrates. These layers are the good candidates for bandgap engineering of vertical cavity surface emitting laser (VCSEL) emitting in the ultraviolet spectral (UV) range. Up to now the epitaxial growth of wide gap A_2B_6 semiconductors are realized by MBE [1–4] and until our papers [5–7] there are only one [8] on using MOVPE for this purpose. For e-beam pumped VCSELs emitting in UV spectral range from 369 to 390 nm we used ZnSSe/ZnMgS [5,6] and ZnSSe/ZnMgSSe [5,7] nanostructures grown on (100) GaP substrates. The best results at RT were obtained using 30 ZnSSe/ZnMgSSe QW structures. However A_2B_6 solid solutions with anion substitution show broad emission lines via composition fluctuations and strong electron-phonon interaction [9]. The FWHM of ZnSSe and ZnMgSSe bulk layer emission lines are equal to about 90 meV [5]. We can expect more narrow emission lines for ZnCdS/ZnMgS nanostructures with cation substitution in solid solutions. Moreover we hope that these structures will be more stable under high excitation because of stronger chemical S-bonds. This should lead to improving laser characteristics.

In this paper we demonstrate first results on growth of ZnCdS/ZnMgS MQW structures and realization of e-beam pumped VCSEL on their base, emitting in UV spectral range.

1. Experimental

ZnCdS, ZnMgS epitaxial layers and periodic ZnCdS/ZnMgS MQW structures were grown by MOVPE on GaP substrates misoriented by $10°$ from (001) to (111)A. We used home-made horizontal quartz reactor with optical window for in situ reflectometry which allows us to realize the control of layer thickness and surface quality. Growth runs were carried out in a hydrogen at atmospheric pressure using $ZnEt_2$, $CdMe_2$, $(MeCp)_2Mg$ and t-Bu_2S as precursors. ZnCdS and ZnMgS epilayers were grown first to optimize growth conditions for each alloys matched to GaP lattice. For lasers with resonant-periodic gain ZnCdS/ZnMgS nanostructures were grown next. The different structures had from 20 to 28 periods (QWs). The thickness of ZnCdS QW with Cd content about 10% varied from 3 to 8 nm. Typical thickness of ZnMgS barrier layer was 132 nm.

As-grown structures were studied by photoluminescence (PL) cathodoluminescence (CL), X-ray diffraction, optical and AFM microscopy techniques. For PL excitation fourth harmonic of Nd:YAG laser ($\lambda = 266$ nm) was used. CL was measured at $T = 14$ K and RT, electron energy $E_e = 10$ and 30 keV, continuous current $I_e = 1$ μA and e-beam spot diameter $d_e = 1$ mm. Stepped etching in CrO3-HCl solution was performed for a set of nanostructures to analyze PL of QW and barrier layers along the structure depth.

To prepare the VCSEL the as-grown surface of nanostructure was coated by 8 pair quarter-wave Ta_2O_5/SiO_2 layer stack. Calculated reflectivity of the mirror was $R_1 = 0.99$. The sample was then glued by epoxy to a sapphire holder and the GaP substrate was removed by polishing, followed by chemical etching in KOH-$K_3Fe(CN)_6$ solution. A second mirror containing 7.5 pairs of SiO_2/Ta_2O_5 layers and a 0.1 μm thick Al layer ($R_2 = 1$) was deposited on the etched surface to complete the etalon. The cavity was pumped by a scanning electron beam with $E_e = 25-60$ keV, $I_e = 0 - 2$ mA and $d_e = 20-50$ μm, depending on E_e and I_e. The scan velocity was about 4×10^5 cm/s and the repetition rate was 50 Hz.

2. Results and discussion

2.1. Structure characterization

It is necessary to use the temperatures below 450 °C at growing of ZnCdS layers in the hydrogen atmosphere as at more high temperatures including of Cd in solid solution is strongly limited. Preliminary experiments showed on the other hand, that at the use of EtS, EtS2 and t-Bu2S as sulfur precursor only the last allows growing at temperatures suitable for growth of ZnMgS layers with high Mg content. Figure 1 shows the dependence of ZnCdS composition from the growth temperature. With increasing temperature the Cd content in layers falls sharply. According to X-ray data all layers had a cubic crystalline lattice. For the 1 μm thick $Zn_{0.86}Cd_{0.14}S$ layer the width of the rocking curve around the (004) reflection was 108 arcsec. All further runs we carried out at temperature of 420 °C. It was found that thick ZnCdS layers with mirror-like surface can be obtained at VI:II ratio close to 1:1. The same VI:II ratio is preferable also by growing thick ZnMgS layers. The grown ZnCdS and ZnMgS epilayers exhibit excellent PL and
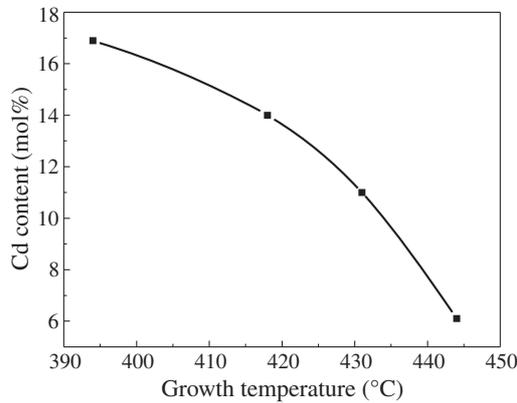
Fig. 1. Dependence of Cd content in ZnCdS epilayer on growth temperature.
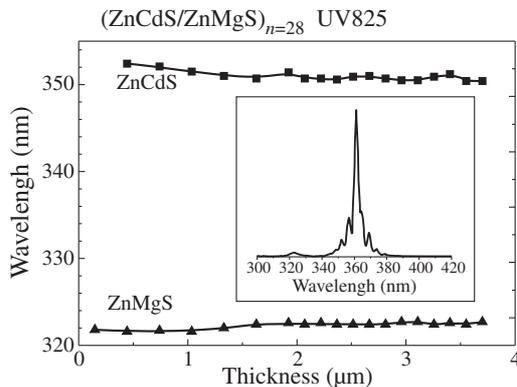
Fig. 2. Dependences of emission line peaks for ZnCdS QW and ZnMgS barrier layers on the depth of the ZnCdS/ZnMgS structure with 28 QWs and PL spectrum in the insert.

CL with effective band edge emission at both low and room temperatures.

The main problem of growing thick (4−5 μm) periodic heterostructures is keeping high uniformity of QW and barrier layer compositions along the structure depth. Earlier we faced with this problem at growing ZnSSe/ZnMgS heterostructures by using Et_2S_2 as a source of sulphur [5]. Here we found that much better uniformity of ZnCdS/ZnMgS can be achieved by using t-Bu_2S. Figure 2 shows the dependencies of emission line peaks for ZnCdS QW and ZnMgS barrier layers on the depth of the 28 ZnCdS/ZnMgS QW structure. They demonstrate high enough uniformity of both QW and barrier layers along the depth up to 4 μm. The PL spectrum of the heterostructure is presented in the insert of Fig. 2. The intensity of QW emission line is much higher than one of ZnMgS barrier emission line. This evidences on good transport of nonequilibrium carriers into the QWs. The PL spectrum shows strong interference fringes due to structure thickness although quality of growth surface was not very high. RMS parameter was about 8 nm.

2.2. Laser characteristics

The main laser characteristics are presented in Fig. 3. Lasing was achieved on one longitudinal cavity mode at 358.4 nm that was on long wave side of CL spectrum (Fig. 3a). The current threshold was 0.3 mA and output power was 0.2 W at $E_e = 45$ keV (Fig. 3b). Total angle of the main spot in the far-field pattern presented in the insert of Fig. 3b was about $10°$.
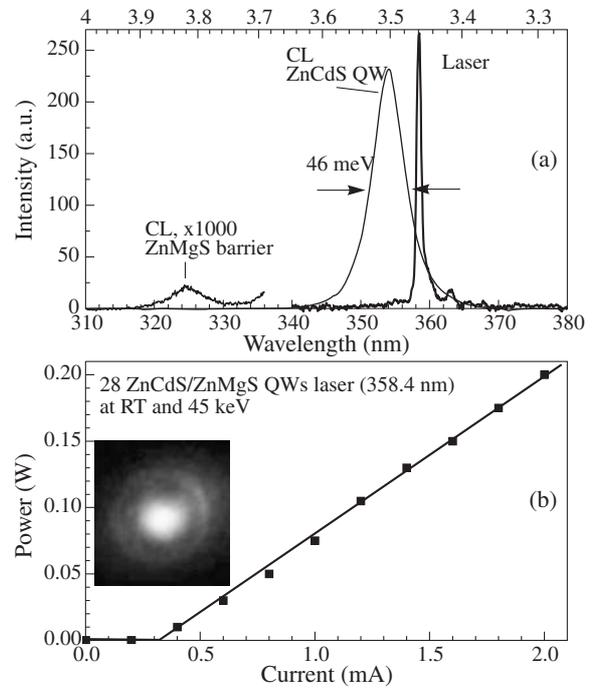
Fig. 3. CL and laser spectra (a), dependence of power on e-beam current (b) and far-field pattern (insert in (b)) at RT.

3. Conclusion

On GaP substrates thick ZnCdS and ZnMgS epilayers and ZnCdS/ZnMgS MQW structures were grown by MOVPE. The first UV (358.4 nm, 0.2 W) lasing was achieved with ZnCdS/ZnMgS MQW structures at longitudinal electron beam pumping. Further efforts should be done to increase laser power and efficiency.

References

[1] K. Ichino *et al*, *J. Crystal Growth* **214/215**, 135 (2000).
[2] I.K. Sou *et al*, *J. Electronic Materials* **30**, 673 (2001).
[3] S.A. Telfer *et al*, *J. Crystal Growth* **214/215**, 197 (2000).
[4] K.A. Prior *et al*, *J. Crystal Growth* **227**, 655 (2001).
[5] M. Tiberi *et al*, *Phys. Status Solidi B* **247**, 1547 (2010).
[6] G.G. Yakushcheva *et al*, *Phys. Status Solidi C* **247**, 697 (2010).
[7] P.I. Kuznetsov and V.I. Kozlovsky, *Proc. 7th Bel.-Rus. Workshop "Semic. lasers and systems" Minsk, June 2009*, p. 263.
[8] V. Sallet *et al*, *J. Crystal Growth* **220**, 209 (2000).
[9] S. Permogorov and A. Reznitsky, *J. Lumin.* **52**, 201 (1992).

Control of light polarization in a dual-wavelength vertical external cavity surface-emitting laser

Yu. A. Morozov and M. Yu. Morozov

Kotelnikov Institute of Radio Engineering and Electronics (Saratov Branch) RAS, 410019 Saratov, Russia

Abstract. The way to control the polarization characteristics of a dual-wavelength vertical external cavity surface-emitting laser (VECSEL) is proposed. It is shown that insertion of the retardation plate of special kind in the laser cavity allows one to cause the short-wavelength radiation to oscillate in *p*-polarized mode while the long-wavelength radiation oscillates in *s*-polarized mode. Due to this finding conventional anisotropic nonlinear crystals could be successfully applied to intracavity nonlinear frequency conversion to mid- or far-infrared spectral range in such a dual-wavelength VECSEL.

Introduction

Semiconductor dual-wavelength vertical external cavity surface-emitting laser [1] was shown to be a promising device for building a mid- or far-infrared $(5-30\ \mu m)$ oscillator based on intracavity optical non-linear interaction [2,3]. It was supposed in [2,3] that generation in the mentioned spectral ranges could be performed as difference frequency radiation of two fundamental waves (a pump and a signal waves in the terms of parametric generation) being simultaneously excited in the VECSEL cavity. Those fundamental waves of the dual-wavelength VECSEL [1] are presented in the form of two coaxial gaussian beams at wavelengths of $\lambda_S \approx 985$ nm and $\lambda_L \approx 1040$ nm. Both beams oscillate at dominant transverse cavity mode TEM_{00} and have nearly the same spot size. The wavelength corresponding to the difference frequency emission should come to approximately 18.6 μm. Taking into account a high value of intracavity beam power (about hundreds of watts in a continuous wave operation) together with a possibility of beams focusing into a nonlinear crystal, one could expect an effective nonlinear frequency conversion with the difference frequency power in the order of tens of milliwatts.

The publications [2,3] mentioned above deal with the analysis of nonlinear frequency conversion in a GaAs crystal revealing a nonlinearity of second order. Because of GaAs lacks for anisotropy of refractive index, the conventional methods of phase-matching are impossible [4]. Therefore, a GaAs crystal about a coherence length long was proposed to be inserted in the special sub-cavity tuned to the difference frequency [2]. The nonlinear optical mixing in the orientated-patterned quasi-phase-matched GaAs crystal has been analyzed in other paper [3].

It should be noted that an application of conventional (anisotropic) nonlinear crystals of mid (far) spectral range (e.g. GaSe, ZGP, Ag_3AsS_3) is hardly possible in the dual-wavelength VECSEL [1] because of both beams of the laser are strictly *s*-polarized. So, a phase-matching of type IIB (*e-eo* for negative crystals and *o-oe* for positive ones) could be only examined [4].

According to preliminary analysis, those crystals could be successfully applied for the difference frequency generation in the dual-wavelength VECSEL if one makes the conditions when the polarization planes of the beams are rotated regarding each other. In other words, one beam should ideally be *s*-polarized and the other one should be *p*-polarized. Then a more appropriate phase-matching of type I or type IIA could be used.

1. Jones matrix of the laser cavity with the polarization control elements

To control the polarization characteristics including the polarization azimuth β for both beams, we propose to use the retardation plate of special kind inserted in the cavity of the dual-wavelength VECSEL. Namely, the phase shifts of the retardation plate have to be as follows:

$$
\begin{aligned}
\varphi(\lambda_L) &= 2\pi(n_e - n_o)l_\varphi/\lambda_L &= 2\pi m\,, \\
\varphi(\lambda_S) &= 2\pi(n_e - n_o)l_\varphi/\lambda_S &= 2\pi m + \pi\,,
\end{aligned}
\tag{1}
$$

where m is the algebraic integer, n_e and n_o are the refractive indices for extraordinary and ordinary waves, respectively. According to estimations, such a retardation plate should be about 950 μm long provided that being made of crystalline silica.

The Jones matrix of the laser cavity forming a V-configuration (Fig. 1) with the nonlinear crystal and the retardation plate inserted can be written as follows (the reference plate is near the output coupler):

$$
A_J = M_3 F_\Phi(\delta) F_\varphi(\alpha) M_2 M_1 M_2 F_\varphi(\alpha) F_\Phi(\delta)\,.
\tag{2}
$$

Here $M_{1,2,3}$ are the Jones matrices of the gain mirror, the deflecting curved mirror and the output coupler, respectively; $F_\varphi(\alpha)$ and $F_\Phi(\delta)$ are the Jones matrices of the retardation plate and the nonlinear crystal [5]. The rotation angles of the retardation plate axis and of the nonlinear crystal axis with respect to plane ZX of the cavity are determined by α and δ.

2. Results

We have simulated the eigenvalues μ_i and the eigenvectors $\mathbf{E}_i$ of the Jones matrix A_J $(i = 1, 2)$. The value $L_i = 1 - |\mu_i|^2$ defines a relative power loss for the optical field of i-th configuration after one round trip along the cavity [5]. For the
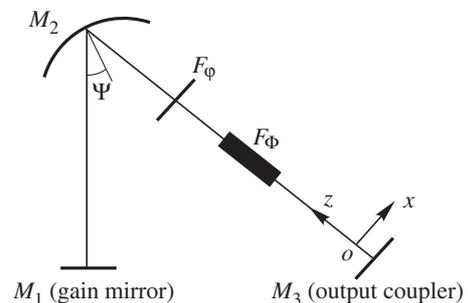
Fig. 1. Scheme of the laser cavity.
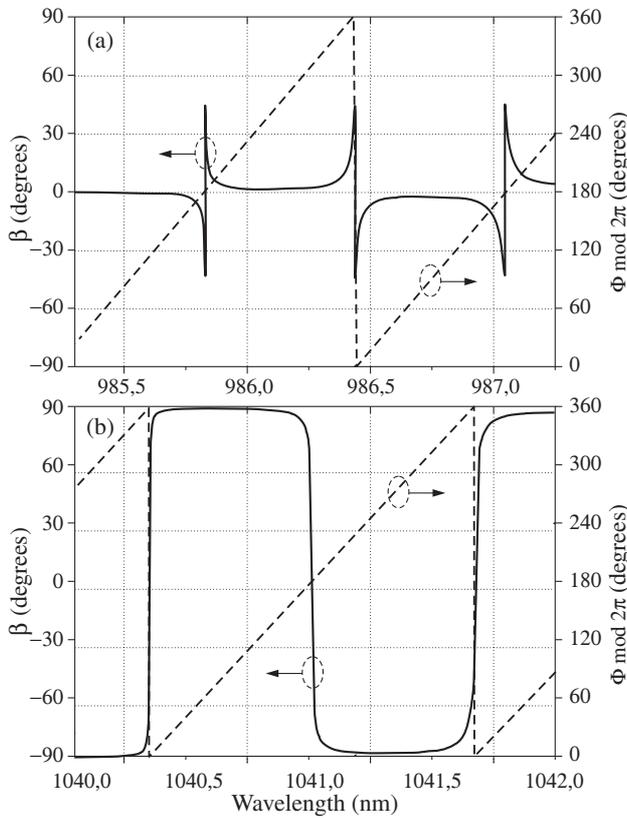
Fig. 2. Polarization azimuth β (solid line) and the phase shift Φ (dashed line) as the functions of wavelength varying near λ_S (a) and near λ_L (b).

Fig. 3. Polarization azimuth β of the short-wavelength radiation vs rotation angle α of the retardation plate.

eigenvector having minimal losses one can simulate the polarization azimuth β, i.e. the rotation angle of the polarization ellipse major semiaxis with respect to the coordinate system X-axis. Fig. 2 shows the polarization azimuth β and the nonlinear crystal phase shift Φ vs wavelength varying near λ_S (a) and near λ_L (b).

The simulation has been performed with the following parameters of the cavity: $l_\varphi = 936\ \mu m$, $l_\Phi = 8000\ \mu m$, $(n_e - n_o)_\varphi = 0.01$, $(n_e - n_o)_\Phi = -0.1$, $\alpha = 45°$, $\delta = 0°$, $m = 9$, $\Psi = 20°$. Note that the parameters with subscripts φ and Φ refer to the retardation plate and the nonlinear crystal, respectively.

One can see from Fig. 2a that the polarization azimuth of the short-wavelength emission remains near zero value (p-polarization) with the exception of the sharp spikes arising at the certain values of wavelength. These values of wavelength correspond to the phase shift Φ making up the multiple π. It is determined as well, that dramatic increase of loss L_i can be observed at the same values of Φ. So, the oscillations at the corresponding wavelengths could hardly be excited in the cavity. Fig. 2b shows that the polarization azimuth β of the long-wavelength radiation can be found near the values of $\pm90°$ (s-polarization). The abrupt change of these values appears at the phase shifts Φ forming the multiple π as well.

The polarization ellipticity, i.e. the ratio of magnitude of electric field components oscillating along the minor and the major semiaxes of the polarization ellipse, doesn't exceed a few hundredth parts of one percent at the wavelengths corresponding to slow variation of β. Thereby, both laser beams have linear polarization, one polarization plane is rotated rela-

tive to the other polarization plane by $\Delta\beta \approx 90°$, provided that the wavelengths of radiation are approximately correspond to equations (1) and $\alpha = 45°$, $\delta = 0°$.

If phase relationships (1) being violated, e.g. because of a wavelength tuning, the polarization azimuth is varied. Fig. 3 displays the polarization azimuth of the short-wavelength radiation as the function of rotation angle α of the retardation plate, though the wavelength has been tuned approximately by 1–1.5 nm regarding λ_S. The polarization azimuth of the long-wavelength radiation deviates from the optimal values $\pm90°$ by about the same quantity as for the short-wavelength radiation, provided that the comparable deviation of $\varphi(\lambda_L)$ exists from the value defined by (1).

The results of the analysis allow one to expect the efficient intracavity difference frequency generation in the dual-wavelength VECSEL with anisotropic mid-infrared nonlinear crystals inserted.

Acknowledgements

References

[1] T. Leinonen, Yu.A. Morozov, A. Härkönen, M. Pessa, *IEEE Phot. Techn. Lett.* **17**, 2508 (2005).

[2] Yu.A. Morozov, I.S. Nefedov, T. Leinonen, M.Yu. Morozov, *Semiconductors* **42**, 463 (2008).

[3] Yu.A. Morozov, T. Leinonen, V.V. Popov, M.Yu. Morozov, *Proc. of 6th Belarussian-Russian Workshop. Semiconductor lasers and systems (Minsk, Belarus, 2007)*, B.I. Stepanov Institute of Physics, 39, 2007.

[4] V.G. Dmitriev, L.V. Tarasov, *Prikladnaya nelineinaya optika*, (Moscow: Fizmatlit), 512, 2004.

[5] N. Hodgson, H. Weber, *Laser resonators and beam propagation. Fundamentals, advanced concepts and applications*, (Springer), 801, 2005.

InGaAs/AlGaAs-nanostructure based pulse laser pumped by electron beam of 3.5–15 keV energy

M. M. Zverev[1], N. A. Gamov[1], E. V. Zhdanova[1], *D. V. Peregoudov*[1], V. B. Studionov[1], A. A. Marmalyuk[2] and M. A. Ladugin[1]

[1] Moscow State Institute of Radio Engineering, Electronics and Automations, Vernadskogo pr. 78, 119454 Moscow, Russia
[2] RDI Polyus, 117342 Moscow, Russia

Abstract. The results of investigation of infrared spectral range lasers with electron beam pumping based on InGaAs/AlGaAs structures operating at room temperature are presented. Calculations of spatial distribution of non-equilibrium carriers in the structure and dependence of threshold pumping power on electron energy are performed. Parameters of lasers under pulse electron beam of duration 200 ns and electron energy 3–16 keV pumping are studied. Reduction of upper cladding layer thickness down to 30 nm allowed to reduce operation electron energy down to 3.5 keV. Minimal value of threshold electric current, equal to 0.35 A/cm^2, was measured at electron energies of 8–10 keV.

Electron beam pumping of semiconductor lasers allows to implement several exotic laser operation regimes: one- or two-dimensional scanning with laser beam, simultaneous or sequential generation with a number of different wavelengths, synchronization of light beam within subnanosecond accuracy. Output pulse power of such lasers could significantly exceed that of injection lasers. Practical usage of electron beam pumped lasers is inhibited by high value of electron energy (tens to hundreds keV) and big values of threshold current density, especially at room temperature (RT) of active element. Usage of different nanostructures as active elements allowed significant reduction of electron operational energy U_{min} for this type of lasers. Minimal value of $U_{min} = 3.7$ keV at RT was measured for green range laser on ZnSe-containing quantum-scale heterostructures [1]. Infrared (IR) range electron beam pumped lasers based on quantum-scale heterostruc-
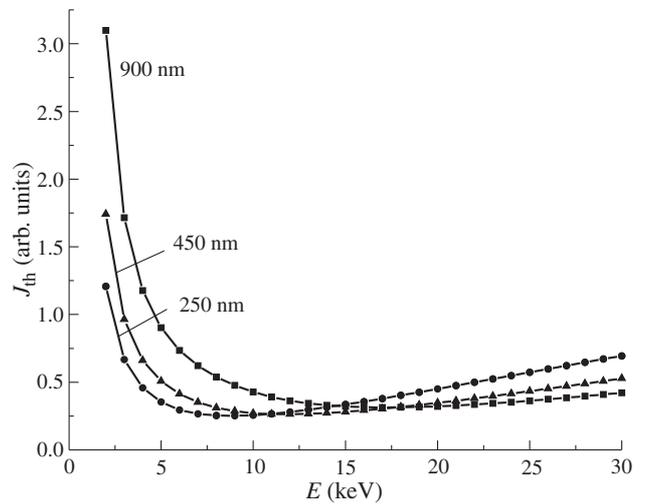
Fig. 2. Dependences of threshold current density on electron energy, calculated for waveguides with thicknesses of 900, 450 and 250 nm (the thickness stands near the curve).

tures are poorly investigated. Ultra small device based on Al-GaAs structures, operating at RT and beam energy of 10 keV is manufactured [2]. In our paper [3] it is shown that by pumping InGaAs/AlGaAs nanostructure with electron beam of energy 26 keV it is possible to obtain 90 W pulse power radiation, moreover, further pulse power increase is possible.

In the present paper the possibility of decreasing of operational electron energy for IR InGaAs/AlGaAs nanostructures based lasers by means of structure design optimization is investigated.

InGaAs/AlGaAs nanostructure with InGaAs quantum well, placed at the middle of 0.9 μm Al$_{0.27}$Ga$_{0.73}$As waveguide with Al$_{0.41}$Ga$_{0.59}$As cladding layers was grown by MOCVD on GaAs substrate. The size of Al$_{0.41}$Ga$_{0.59}$As upper cladding was 30 nm. The structure was used for fabrication of laser active element with cavity length of 0.9 mm.

The results of numerical simulation of waveguide fundamental mode spatial field distribution, of carriers concentration in InGaAs/AlGaAs quantum-scale structures with different active area design under electron beam pumping and calculation of threshold pumping power dependence on electron energy

Fig. 1. Calculated dependences of non-equilibrium carriers concentration in the structure, waveguide fundamental mode field and spatial distribution of electron energy losses in GaAs crystal for 10 keV electron beam. Upper edge of vertical line in the center of waveguide (concentration in quantum well) goes beyond the scale of figure by approximately three orders.

Fig. 3. Dependence of threshold current density on electron energy. $T = 300$ K. Waveguide cavity length 0.95 mm.

are presented (Figs. 1 and 2).

The transverse excitation geometry was used. The pulse electron beam (pulse duration time is of ~200 ns) with the energy of 3–16 keV was used as pumping sources. The experiments were carried out at room temperature.

The laser generation was observed for electron beam energies of 3.5–16 keV. Laser wavelength was equal to 0.89 μm at RT.

Experimental dependence of threshold current density on electron energy is shown on Fig. 3. Minimal electron energy necessary to obtain laser generation at RT was equal to 3.5 keV. Minimal value of threshold current density was equal to 0.35 A/cm^2 at electron energies in 8–10 keV range.

Thus the reduction of upper wide-band layer thickness to 30 nm allowed to reduce operation electon energy down to 3.5 keV. As one can see from simulation results (Fig. 2) further reduction of operation energy is still possible by optimization of waveguide thickness.

Acknowledgement

References

[1] M.M. Zverev, N.A. Gamov *et al*, *Techn. Phys. Lett.* **33(12)**, 1032 (2007).

[2] E. Molva, R. Accomo *et al*, *Appl. Phis. Lett.* **62**, 796 (1993).

[3] M.M. Zverev, N.A. Gamov *et al*, *Proc. of 14th International Conference "Laser Optics 2010"* (St-Petersburg, Russia, 2010), Optical Institute, 71 (2010).

The prototype of semiconductor maser using the spin-polarized conduction electrons

N. A. Viglin and V. V. Ustinov

Institute of Metal Physics, Ural Branch of RAS, 620990 Ekaterinburg, Russia

Abstract. A promising idea to use the spin-polarized conduction electrons transport in a magnetic hetero-structure for the inversion of charge carrier spin level occupancies in one of its layers to create an active environment for the electromagnetic radiation amplification has been realized in a number of FMC/SC structures, where FMC is a ferromagnetic conductor and SC is a semiconductor. The n-InSb single crystals, possessing high mobility of charge carriers, a narrow ESR line and an anomalously high absolute value negative g-factor ($g = -52$), were used as SC. The following materials were used as FMC playing a role of electron polarizer: (i) ferromagnetic semiconductors $EuO_{0.98}Gd_{0.02}O$ and $HgCr_2Se_4$, (ii) Heusler alloys Co_2MnSn, Ni_2MnSn and Co_2MnSb. We have demonstrated that the spin-polarized electrons injection into the n-InSb semiconductor from the above-mentioned ferromagnetic materials results in generation of the laser-type electromagnetic radiation.

Introduction

An idea of a quantum amplifier working on conduction electrons, the pumping in which is done by an injection of spin-polarized electrons from a ferromagnetic semiconductor into the InSb semiconductor, was suggested in [1]. The idea was based on the following well-known properties of these materials. Firstly, InSb possesses rather long spin-lattice relaxation time of conduction electrons, which allows observing stimulated transitions with electromagnetic energy absorption (the electron spin resonance of the conduction electrons). It was assumed that stimulated transitions with emission can occur in InSb due to the inversion of spin level population of conduction electrons. Secondly, in ferromagnetic semiconductors, such as $EuO_{0.98}Gd_{0.02}O$ or $HgCr_2Se_4$, conduction electrons are completely spin-polarized below Curie temperature. It was suggested that the injection of such polarized electrons from a ferromagnetic semiconductor into a semiconductor could result in an area with the inverse population of spin levels in the latter.

1. Experimental

Implementation of this idea required versatile studies to overcome technological and theoretical difficulties. In these investigations, the semiconductor pumping with spin-polarized electrons resulted in the electromagnetic radiation, the wavelength of which, λ, depended on an external magnetic field as:

$$\lambda = ch/g\mu_B B , \qquad (1)$$

where $|g| = 52$ is the g-factor of the InSb conduction electrons, μ_B is the Bohr magneton, B is the external magnetic field induction, h is the Planck constant, and c is the velocity of light. Such wavelength dependence on the magnetic field corresponds to the emission at transitions between the Zeeman levels of conduction electrons in InSb. The radiated power P dependence on the pumping current I and magnetic field B (determining parameters of damping and emission frequency)

$$P \propto \exp\left[\left(k_1 \sigma I p - k_2/B^2\right) L\right] \qquad (2)$$

is satisfactorily described within the framework of quantum light amplification theory, where σ is the cross-section for the stimulated transition between the levels, L is the sample length, k_1 and k_2 is a constant, p is coefficient of spin polarization [2].

A maser prototype containing a magnetic system, a cryostat and a current source meeting the following requirements has been designed. The working medium is a semiconductor crystal n-InSb in the form of a parallelepiped height of 1.5 mm and the size of the wide faces of 2.5×3.5 mm. Parallelepiped was made so that his wide face matched the planes $\{100\}$ crystal semiconductor, and the edges of wide faces are directed along $\langle 110 \rangle$. On one of the wide faces covered with a thin layer of dielectric MgO thickness of 2 nm and the film Heusler alloy Co_2MnSn thickness of 200 nm used as a spin polarizer.

The magnetic system is to create a magnetic field with the intensity ranging from 4 to 5 kOe (to obtain the wavelength of approximately 1 mm), directed parallel to the plane of a film spin polarizer (to minimize demagnetization of the film due to a shape factor). The source of current is to create the current ranging from 3 to 6 A (higher than the threshold current) across the heterostructure layers, and the cryostat is to cool the maser working medium down to the temperature below 180 K. The magnetic system (MS) construction must provide high-enough magnetic fields outside the MS to ensure the outlet of the emission spreading perpendicularly to the magnetic field. Based on the ideas of [3], the MS has been selected in form of a hexahedron with an axial working channel. The magnetization of each block is directed along a radius. This approximation to the optimal system capable of giving the maximum magnetic field above the MS plane has been selected based on a reasonable compromise between the desired field value and the construction complexity.

The Sm_2Co_{17}-based permanent magnets with the residual induction of $B_r = 1.05$ T ensuring high temperature stability were used for the MS. As shown by the experimental tests, the magnetic field component perpendicular to the MS plane (at a distance of 5 mm from the MS plane) is 4.9 kOe. The radial gradient magnitude is less than 20 Oe/mm. The longitudinal field gradient on the MS axis at a distance of 5 mm from the MS plane is approximately 250 Oe/mm. This structural feature of the MS results in the emission line broadening but it allows tuning the maser wavelength due to the working medium displacement along the MS axis. The MS parameters are as follows: an external radius is 40 mm, and the height is 40 mm.

Fig. 1. The mock-up of a solid-state quantum generator (maser) with spin-polarized electrons injection.

A cryostat is required for maintaining the temperature of the quantum generator working medium below 180 K. The cryostat construction is to allow magnetizing of the maser working medium in the spin polarizer plane and deriving the emission outside. In order to ensure the emission outlet through the cryostat wall, its Dewar flask was made of quartz tubes.

A method of maser working medium cooling through thermal contacts with two copper electrically isolated heat sinks was selected. The heat sinks have a shape of two halves of a cylinder cut along its longitudinal axis. The cylinder halves are again connected with each other through a thin dielectric plate forming a cylinder the length of 150 mm and the diameter of 8 mm. Both heat sinks have cuts in which the contact areas providing thermal and electrical contact with the maser working medium are located. The radiation outlet parallel to the plane of a spin polarizer film and perpendicular to the longitudinal axis of the cylindrical heat sink is provided as well. The device with working medium on one end is placed into quartz Dewar vessel the length of 100 mm with interior and outer diameters of 9 and 15.5 mm, respectively. The opposite end of the heat sink is immersed in liquid nitrogen, and conductors of current pumping are also joined to it. Thus, the problems of cooling, attachment in the cryostat and pumping by current of the maser working medium have been solved. When the heat sink was tested, a thermocouple was attached to the middle of the lateral face of a specimen perpendicular to the planes of thermal contact. A rectangular sample of $1.5 \times 2 \times 2.5$ mm made of InSb-semiconductor was used for testing. It took 7–8 minutes to decrease the specimen temperature from room temperature to 80 K.

The maser working medium is located at a distance of 5 mm from the MS plane so that the magnetic field the intensity of 4.9 kOe in the center of the working medium is directed parallel to the spin polarizer plane. The possibility of the working medium shift along the MS axis is provided, the magnetic field in the center of the working medium varying from 4.5 to 5.3 kOe. In accordance with expression (1), this range of the magnetic field variation ensures the emission wavelength, λ, tuning from 0.90 to 0.78 mm.

We used a quasi-optical scheme of power output with a focon parallel to the axis of emission propagation and the input and outlet diameters of 10 and 2 mm, respectively. To create one direction of emission we used a metallized segment of the Dewar flask cylindrical surface as a mirror. Such a quasi-optical scheme on our assumption is capable of deriving the emission with a very short wavelength (1 mm and less), which spreads along the focon axis or in parallel to it within the cone range of spread. The cone inlet diameter is 10 mm, which ensures the maser emission release and changing its wavelength by means of the working medium displacement along the MS axis. The distance between the focon axis parallel to the MS plane and the MS plane is 5 mm. Thus, the cone axis passes through the area where the magnetic field intensity is 4.9 kOe which corresponds to the central line of emission.

The maser electronic system includes a pulse generator of current and a temperature control unit. To reduce the Joules heat release in the maser working medium, it was pumped by short pulses the duration of 20 μs and repetition rate of 100 Hz. The amplitude control of current pulses from 0 to 6 A was provided. The temperature was measured by a thermocouple located on the copper heat sink near the working medium. The amplitudes of current pulses and temperature were displayed in the indication unit. Thus, a mock-up of a solid-state quantum generator (maser) of sub-millimeter range based on the InSb-semiconductor with the working medium pumping by spin-polarized electrons has been created (Fig. 1). According to our estimations, the output capacity of the maser is about 10^{-5} W at the working medium temperature of about 100 K, and the wavelength of emission can vary from 0.79 to 0.90 mm.

References

[1] V.V. Osipov, N.A. Viglin *et al*, *JETP Letters* **52**, 996 (1990).
[2] N.A. Viglin, V.V. Ustinov and V.V. Osipov, *JETP Letters* **86**, 193 (2007).
[3] S.V. Zhakov, *The Physics of Metals and Metallography* **96**, 562 (2003).

The CdSe/ZnSe QD pulsed electron beam and optically pumped lasers emitted in yellow spectral range

M. M. Zverev[1], N. A. Gamov[1], E. V. Zhdanova[1], *D. V. Peregoudov*[1], V. B. Studionov[1], S. V. Ivanov[2], I. V. Sedova[2], S. V. Sorokin[2] and P. S. Kop'ev[2]

[1] Moscow State Institute of Radio Engineering, Electronics and Automations, Vernadskogo pr. 78, 119454 Moscow, Russia
[2] Ioffe Physical-Technical Institute, St Petersburg, Russia

Abstract. The possibility of fabrication of semiconductor laser based on CdSe/ZnSe/ZnMgSSe structure with electron beam and optical pumping operating in yellow spectral range is exhibited. Lasing wavelength at room temperature of active element is as high as 568 nm. Maximal value of output pulse power under electon beam (with electron energy of 16 keV) pumping is 1.3 W and under N_2 laser pumping is 34 W.

The possibility of using ZnSe-based low-dimensional heterostructures for the green electron beam pumped (EBP) lasers was demonstrated during last decade. Due to significant decrease in electron energy the compact laser device operating in pulsed mode ($E_e = 10$ keV) has been realized at cryogenic temperatures [1]. The extremely low values of threshold current density at room-temperature ($j_{th} \sim 0.4-0.5$ A/cm^2 at $E_e = 8-10$ keV) were demonstrated for the structure with active region consisted of ZnSe quantum well (QW) centered with ZnSe/CdSe QD sheets [2]. However, the extension of spectral range towards the longer wavelength is of great importance because of the difficulties to cover this range by III-nitride based lasers. The yellow lasers could be used in navigation systems, traffic control systems etc. Up to date the maximum lasing wavelength for III-nitride pulsed laser diodes is limited by ∼532 nm, and there is a rapid increase in laser threshold with the increase of the lasing wavelength [3].

The transition to the yellow spectral range could be realized by the increase of CdSe nominal thickness in the active layer of laser structures similar to that used in Ref. [2]. However, this increase is strongly limited because of the stress relaxation via defect formation after exceeding a critical thickness (∼3 monolayer (ML) of CdSe), which is also accompanied by a sharp reduction of the photoluminescence (PL) intensity.

This paper presents the possibility of fabrication of yellow ($\lambda = 568$ nm) room temperature electron beam and optically
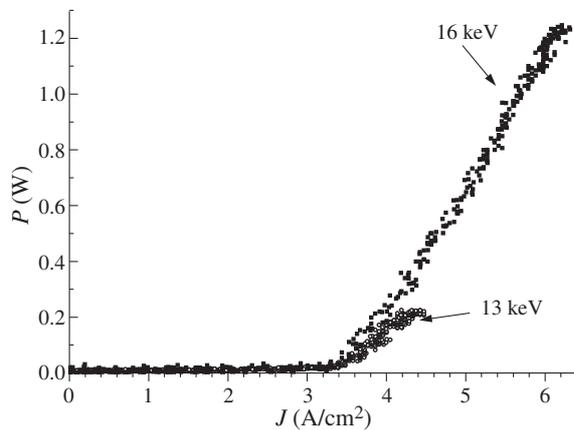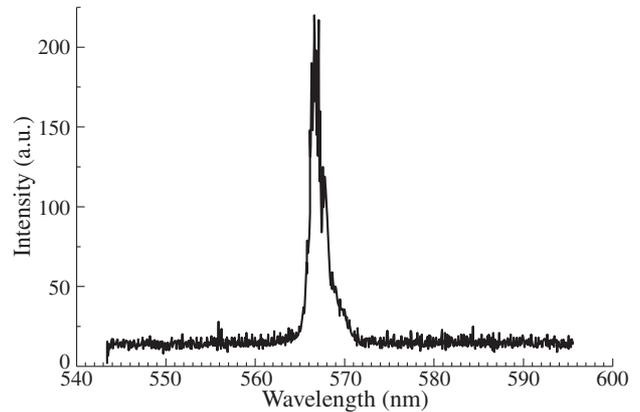
Fig. 2. The spectrum of laser generation under electron beam pumping.

pumped lasers with the CdSe/ZnSe QD active region. The CdSe/ZnSe/ZnMgSSe laser structure was grown by molecular beam epitaxy (MBE) pseudomorphically to GaAs (001) substrate at substrate temperature $T_S = 280$ °C. The structure consisted of a $Zn_{0.9}Mg_{0.1}S_{0.15}Se_{0.85}$ bottom and top claddings with the thicknesses of ∼1.7 μm and 20 nm, respectively, and 15 Å-$ZnS_{0.14}Se_{0.86}$/18 Å-ZnSe short-period superlattice (SL) waveguide lattice-matched to GaAs as a whole. The active region consists of ZnSe QW centered with CdSe QD layers with the nominal thickness slightly higher than 3ML. In spite of the CdSe nominal thickness is very close to or exceeds the critical value the structure demonstrates relatively bright PL both at cryogenic and room temperature.

The transverse excitation geometry has been used. The pulse electron beam (pulse duration time is of ∼200 ns) with the energy of 10–16 keV as well as pulse N_2 laser ($\lambda = 337$ nm) were used as pumping sources. The experiments were carried out at room temperature.

The laser generation was observed for electron beam energies of 10–16 keV. The threshold current density of the electron beam is of 3.5–4 A/cm^2 within the whole range of the e-beam energy. The dependencies of output pulse power on current density for different values of electron-beam energy are presented in Fig. 1 (the laser cavity length is of 0.55 mm). Maximum values of pulse output power under electron beam and optical pumping were as high as 1.3 and 34 W, respec-

Fig. 1. The dependencies of output pulse power on current density for different values of electron-beam energy.

tively. The lasing wavelength at room temperature is as high as 568 nm (Fig. 2).

The structure reveals rather high inhomogeneity, so both the emission parameters and the dependencies of pulse output power on time are strongly differed in different sample parts.

References

[1] E. Molva, R. Accomo *et al*, *Appl. Phis. Lett.* **62**, 796 (1993).

[2] M.M. Zverev, N.A. Gamov *et al*, *Techn. Phys. Lett.* **33(12)**, 1032 (2007).

[3] A. Avramescu, T. Lermer *et al*, *Appl. Phys. Express* **3**, 061003 (2010).

Rashba Spin-Orbit torques in ferromagnetic thin films

G. Gaudin[1], I. M. Miron[1,2], T. Moore[1,3], H. Szambolics[1], S. Auffret[1], B. Rodmacq[1],
L. D. Buda-Prejbeanu[1], A. Schuhl[1], S. Pizzini[3], J. Vogel[3], M. Bonfim[4] and P. Gambardella[2,5]

[1] SPINTEC, UMR-8191, CEA/CNRS/UJF/GINP, INAC, F-38054 Grenoble, France
[2] Centre d'Investigació en Nanociència i Nanotecnologia (ICN-CSIC), UAB Campus, E-08193 Barcelona, Spain
[3] Institut Néel, CNRS/UJF, B.P. 166, F-38042 Grenoble, France
[4] Departamento de Engenharia Elétrica, Universidade Federal do Paraná, Curitiba, Paraná, Brazil
[5] Institució Catalana de Recerca i Estudis Avancats (ICREA), E-08010 Barcelona, Spain

We investigate novel spin torque mechanisms based on spin-orbit effects in structurally asymmetric ferromagnetic metal layers. It is well known that spin-orbit coupling is ultimately responsible for magnetocrystalline anisotropy and damping. Under certain conditions, however, spin-orbit effects might either induce or enhance specific spin torque mechanisms. We analyze these effects by using two tri-layer structures (Pt/Co/Pt and Pt/Co/AlO$_x$) with similar magnetic properties but opposite structural inversion parity.

One of the effects of the Spin Orbit interaction is to induce deviations from pure conservation of angular momentum as an electric current is injected in a domain wall [1]. Therefore, besides the adiabatic spin-torque component, a second non-adiabatic component will appear. Due to its equivalence to an easy axis magnetic field, this second component is expected to be very efficient for inducing DW motion.

Quasistatic measurements of domain wall motion inside its local pinning center relate the observation of a 50-fold increase of the non-adiabatic component to the breaking of the structural inversion symmetry [2] (Rashba interaction). This enhancement is confirmed by the subsequent observation of DW displacements under ultra-short current pulses. We measure ultrafast DW motion with velocities approaching 400 m/s. Despite the strong pinning characterizing these samples, the DW displacements show high reproducibility demonstrating the potential for applications.

Moreover, besides these effects occurring in DWs, the Rashba interaction is also predicted to create a torque in the uniformly magnetized domains [3]. Unlike spin-transfer-torque, this second phenomena does not rely on injection of spin polarized current from another magnetic layer or adjacent domain. By the intermediate of the Rashba interaction, the conduction electron spin couples to the crystalline electric fields, and as a current is applied, a spin accumulation transverse to both the current direction and electric field is created. Further on, due to the *s-d* exchange interaction coupling the conduction electron's spins to the localized magnetic moments, the spin accumulation will act as an effective magnetic field on the magnetization.

To evidence such effects, we study the effect of current on uniform magnetization. We observe using a wide field Kerr microscope, how under the effect of 100 ns long current pulses, the magnetization relaxes from the uniformly magnetized metastable state to the demagnetized ground state. When applying an external magnetic field, the rate of nucleation is enhanced for a given direction of the current and decreased for the other direction. This asymmetry cannot be reconciled neither with the action of the Oersted field, which is parallel to — **y** and smaller than 1 mT, nor with simple thermal activation due to Joule heating.

Future directions of research in this field as well as the possibility of combining different spin-torque mechanisms in Rashba-type magnetic layers will be outlined.

References

[1] S. Zhang and Z. Li, *PRL* **93**, 127204 (2004).
[2] I.M. Miron *et al*, *PRL* **102**, 137202 (2009).
[3] A. Manchon and S. Zhang, *PRB* **78**, 212405 (2008).
[4] I.M. Miron *et al*, *Nature Materials* **9**, 230 (2010).

Single nanoparticle hysteresis: influence of morphology

N. Friedenberger[1], S. Stienen[1], C. Möller[1], Z.-A. Li[1], M. Spasova[1], F. Kronast[2], H. Dürr[2] and *M. Farle*[1]

[1] Fakultät für Physik and Center for NanoIntegration (CeNIDE), Universität Duisburg-Essen,
47048 Duisburg, Germany
[2] Helmholtz Zentrum Berlin für Materialien und Energie, 12489 Berlin, Germany

Abstract. The magnetic hysteresis loops of single cubic Fe nanoparticles with 18 nm side length were recorded using X-ray photoemission electron microscopy (XPEEM) at room temperature. The shape of the hysteresis loop changed when rotating the magnetic field from a magnetic easy axis (parallel to the cube edge) to a magnetic harder direction. To avoid surface oxidation the colloidal Fe cubes were coated by aluminum after removal of oxides and ligands in a hydrogen plasma. The experimental data where compared to micromagnetic simulations (OOMMF) using bulk Fe magnetization and magnetic anisotropy parameters as input. It is shown that shape imperfections of the Fe cubes on the nanoscale observed by transmission electron microscopy have a strong influence on the coercive field — reducing it by an order of magnitude compared to an ideal cube.

Introduction

The correlation of the magnetic response and electronic structure with the morphology and crystal structure of individual particles has been a long-time challenge. New developments in X-ray microscopies offer the promise of sufficient nanoscale magnetic resolution to address this question [1]. The advantage of X-ray microscopy with respect to other magnetic imaging techniques with high lateral resolution, e.g. magnetic force microscopy, is the combination of chemical and electronic spectroscopy with magnetic microscopy based on the X-ray magnetic circular dichroism (XMCD) effect. Recently we demonstrated the simultaneous recording of hysteresis loops for individual nanoparticles and different nanoparticle configurations utilizing X-ray photoemission electron microscopy (XPEEM) [2]. Here, in combination with transmission electron microscopy which offers imaging at atomic resolution we discuss the correlation of magnetic and morphological characterization of individual nanoparticles. By 3D tomography of selected Fe nanocubes the deviations from perfect cubic shape can be determined which influences the magnetic reversal behavior that is the coercive field and the shape of magnetic hysteresis loops. We demonstrate by micromagnetic simulations that coercive fields experimentally determined to be much smaller than expected for Fe nanocubes depend critically on details of the morphology of the cubes.

1. Experimental

Chemically synthesized Fe/Fe_xO_y nanoparticles with cubic shape and edge length of 18 nm [3] were deposited on Si-substrates. Highly diluted single layers of Fe cubes were obtained. Separations of the cubes discussed here were free of dipolar stray field effects from neighboring particles. Ligands and oxides on all particles were reduced using a soft plasma treatment. The metallic Fe cubes were subsequently in situ capped by a thin Al layer to prevent re-oxidation. For our experiments we used the XPEEM setup at the Berlin synchrotron facility BESSYII offering a lateral resolution for magnetic imaging of 25 nm. Magnetic hysteresis loops were recorded at room temperature in a field range of ± 18 mT [2,4]. Experimental results were compared to micromagnetic simulations using the Object Oriented Micromagnetic Framework (OOMMF) open source code [5].
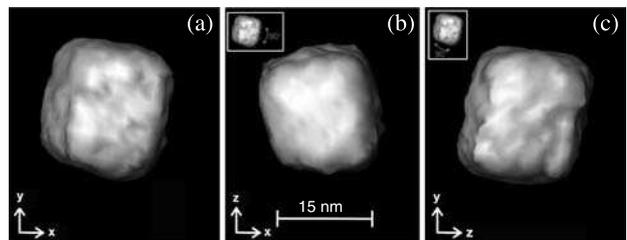
Fig. 1. Reconstructed tomography images of an Fe/Fe_xO_y nanocube viewed from three different directions.

2. Experiment and micromagnetic simulation

While in conventional transmission electron microscopy only two dimensional (2D) projections of three dimensional (3D) objects are imaged we employed 3D tomography measurements to obtain the three-dimensional morphology and shape of selected Fe cubes. As an example we show in Fig. 1a cube with nominal edge lengths of $x = 19 \pm 2$ nm, $y = 22 \pm 2$ nm, $z = 20.5 \pm 2$ nm.

Such a cube would look in a 2D projection like a nearly perfect square — as for example visible in Fig. 1 of Ref. [6]. The 3D tomography data have a resolution on the order of 1–2 nm showing topographic features viewed from three directions. Such topographic roughness is expected to have consequences on the local magnetic anisotropy and consequently on the reversal process of the magnetization. In the following we will use an approximate computer model of such a cube to understand the small coercive fields of single Fe nanocubes measured with X-ray magnetic circular dichroism. In Fig. 2a an exemplary room temperature hysteresis loop of a single Fe nanocube is shown. The coercive field H_C is about 2.5 mT and representative for several measured loops. A detailed investigation showed that the shape of the loops differ from particle to particle as may be expected for different orientations of the cubes with respect to the external magnetic field. Another critical parameter is the morphology of the particle as demonstrated in the following. From two-dimensional projection images a size distribution of 18.1 ± 0.8 nm edge length for the cubes was determined. Using the mean value as input parameter for micromagnetic simulations and using the magnetic anisotropy ($K_4 = 48$ kJ/m^3) and saturation magnetization ($M_S = 1700$ kA/m) for bcc Fe bulk we calculate hysteresis loops displayed in Fig. 1b showing a nearly 90 times bigger
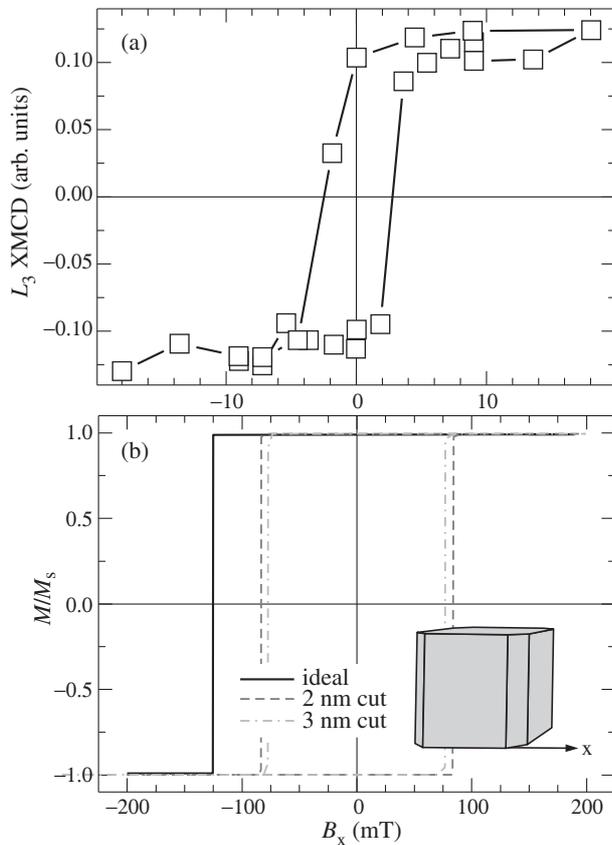
Fig. 2. (a) Hysteresis of an individual Fe nanocube measured at room temperature. (b) Simulated hysteresis loops for a perfect Fe cube and cubes with edge modifications as illustrated in the inset. The edge truncation (defined as sketched) is 2 and 3 nm, respectively.

coercive field (H_C = 125 mT) than the experimental one. For the calculation the idealized cube was discretized into 18^3 cells containing a magnetic volume of 1 nm^3 each. The field was applied along the facets of the cube. For an ideal cubic Fe particle a coercive field H_C = 125 mT is found. To obtain an insight of the effects of small morphological changes the cube edges were truncated by 2 and 3 nm, respectively, and the hysteresis loops were re-calculated.

As evidenced in Fig. 2b the truncation of the 18 nm cube by 2 and 3 nm at the edges reduces H_C by a factor of two. Considering that the experimental data were recorded at room temperature which is close to the blocking temperature of the Fe nanocube the smaller experimental H_C can be explained by a combination of a temperature dependent fluctuating magnetization and the complex modification of the nanocube's surface modifying the magnetocrystalline surface anisotropy contributions. Additional more detailed and temperature dependent calculations using the experimentally determined morphological data as input parameters for the simulation have to be performed in the future to obtain a quantitative agreement between experimental and calculated loop shapes.

3. Conclusion

In conclusion we presented an experimental hysteresis loop of a single Fe nanocube with 18 nm edge length. The comparison to micromagnetic calculations revealed that small changes of the idealized cubic shapes observed for real cubes results in a strong decrease of the coercive field approaching the small coercive fields measured in the experiment. One may conclude that the determination of magnetic anisotropy from hysteresis loops of single domain nanomagnets requires a detailed three-dimensional knowledge of the particle's shape and morphology.

References

[1] A. Dürr *et al*, *IEEE Trans. Magn.* **45**, 15 (2009).
[2] F. Kronast *et al*, *Nano Lett.* in print (2011).
[3] A. Shavel *et al*, *Adv. Funct. Mater.* **17**, 3870 (2007).
[4] F. Kronast *et al*, *Surf. Interface Anal.* **42**, 1532 (2010).
[5] OOMMF, http://www.math.nist.gov/oommf.
[6] A.V. Trunova *et al*, *J. Appl. Phys.* **104**, 093904 (2008).

Identification of optically induced nuclear spin transitions in (In,Ga)As/GaAs quantum dots

M. S. Kuznetsova[1], R. V. Cherbunin[2], I. Ya. Gerlovin[1], K. Flisinski[2], I. V. Ignatiev[1], M. Yu. Petrov[1], S. Yu. Verbin[1], D. R. Yakovlev[2,3], D. Reuter[4], A. D. Wieck[4] and M. Bayer[2]

[1] Physics Department, St Petersburg State University, 198504 St Petersburg, Russia
[2] Experimentelle Physik 2, Technische Universität Dortmund, D-44221 Dortmund, Germany
[3] Ioffe Physical-Technical Institute, St Petersburg, Russia
[4] Angewandte Festkörperphysik, Ruhr-Universität Bochum, D-44780 Bochum, Germany

Abstract. Orientation of electron spins in (In,Ga)As/GaAs quantum dots by light with circular polarization modulated at the frequencies resonant to that of nuclear spin transitions in transverse magnetic field is found to create a significant nuclear spin polarization. This technique allows us to identify the nuclear spin resonances for all nuclear isotopes comprising the quantum dots.

Introduction

Nuclear magnetic resonance (NMR) spectroscopy is known to be effective probe of the internal properties of solid-state materials. At the same time, low sensitivity of standard NMR technique makes difficult using it for studies of nanometer-sized semiconductor structures, such as quantum dots (QDs), which contain relatively small number of nuclei. Strong increase of the NMR sensitivity is achieved by the use of optical polarization of nuclear spins [1] or by the optical detection of resonant signal [2,3], which allowed to study nuclear resonances in thin semiconductor layers and quantum wells. No data, however, have been published till recently about nuclear resonances in semiconductor quantum dots [4,5].

In this communication, we report on observation of a number of nuclear spin resonances in self-assembled (In,Ga)As/GaAs QDs in the transverse magnetic field. The results are obtained using the method of selective optical pumping, which is based on the excitation of QDs by the light with modulated circular polarization and the registration of changes in nuclear spin polarization when the modulation frequency coincides with that of a nuclear spin transition. The analysis of experimental data allows us to identify resonances related to transitions between $|\pm 1/2\rangle$, $|\pm 3/2\rangle$, and $|\pm 5/2\rangle$ states in indium, gallium, and arsenic isotopes affected by strong quadrupole interaction in this type of QDs.

1. Experiment and discussion

A heterostructure under study contains 20 layers of (In,Ga)As QDs sandwiched between GaAs barriers with n-delta modulation doped sheets. Donor ionization supplies every dot with on average a single resident electron. The structure was grown by molecular-beam epitaxy on a (100) GaAs substrate an then annealed at a temperature 980 °C. The lowest optical transition in the QDs is at about 1.42 eV. We detected the changes in nuclear spin polarization via respective changes of electron spin orientation measured by all optical technique using the negative circular polarization (NCP) of QD photoluminescence (PL) [6,7]. The PL was excited by a continuous-wave Ti:Sapphire laser tuned to the energy of 1.481 eV corresponding to the wetting layer optical transition. An electro-optical modulator followed by a quarter-wave plate has been used to modulate helicity of optical excitation.
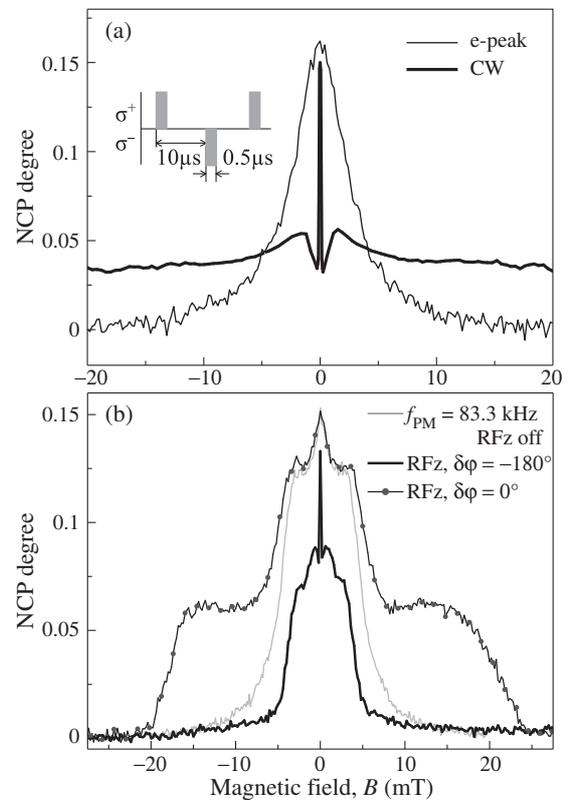
Fig. 1. (a) Hanle curves measured in CW regime (black curve), and amplitude modulation of excitation (e-peak). (b) Effects of RFz-field on Hanle curves. The black curve is measured at the antiphased Rfz-field. The black curve with symbols is measured at application of cophased RFz-field. The grey curve is measured with no RFz-field. $P_{exc} = 0.5$ mW, $T = 1.6$ K.

To study the electron-nuclear spin dynamics in the QDs, we have measured the dependence of NCP on magnitude of the transverse magnetic field (Hanle curve) at different excitation protocols (see Fig. 1). Optical excitation with one helicity of polarization and constant amplitude (CW) gives rise to well know W-structure in the central part of Hanle curve, which is an indication of dynamic nuclear polarization directed along the external magnetic field [2]. The amplitude modulation of ex-
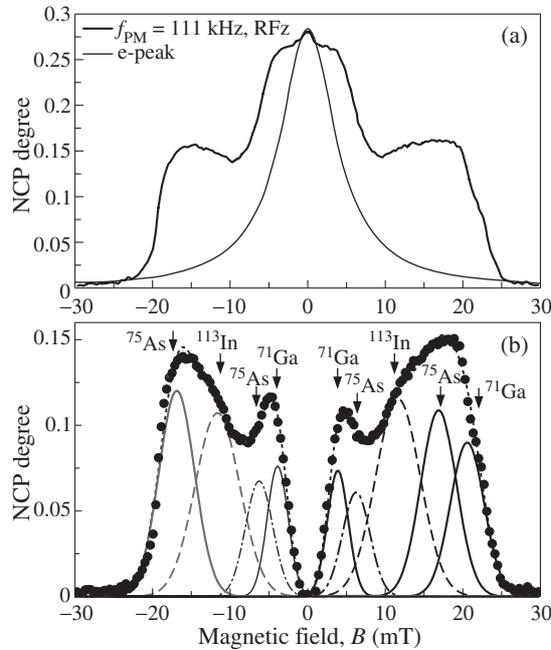
Fig. 2. (a) Hanle curves measured using amplitude modulation of excitation (e-peak), and modulated polarization of excitation (black curve). (b) Gaussian decomposition of the Hanle curve (symbols) with subtracted e-peak. Gray Gaussians are resonances $|+1/2\rangle \leftrightarrow |-1/2\rangle$, black Gaussians are resonances $|+3/2\rangle \leftrightarrow |-3/2\rangle$, which position are fitting parameters. $f_{PM} = 111$ kHz.

citing light does not create any nuclear polarization, the Hanle curve has a smooth shape with the width controlled by the light-induced dephasing the electron spin (e-peak).

The Hanle curve obtained at the modulated polarization of excitation shows strong additional maxima, which positions depend on the modulation frequency. Even stronger deformations of the curve arise when the radio-frequency (RF) field synchronous with the polarization modulation is applied to the sample as it is shown in Fig. 1. We applied the sinusoidal RF-field via a couple of Helmholz coils near the sample. The coils create magnetic component of RF-field along the optical axis with amplitude of fraction of milliTesla. The RF-field, $\Delta\varphi$, is applied either in-phase or anti-phase to the polarization modulation. As seen in Fig. 1, the cophased RF excitation considerably widens the Hanle curve, giving rise to new resonances and hysteresis-like behavior. As seen, the resonances are far beyond the electronic Hanle curve. The anti-phase RF, on the contrary, radically suppresses the NCP except the point $B = 0$.

Observed resonances can be explained by nuclear spin transitions in the QDs, which contain several types of nuclei (including isotopes), namely, ^{69}Ga, ^{71}Ga, ^{75}As, ^{113}In, and ^{115}In. Considerable part of the transitions is modified by large quadrupole splitting of nuclear spin states caused by the strain-induced gradient of crystal field as well as by the statistical population of crystal sites by Ga and In atoms. This consideration has been used for analysis of resonances observed in Hanle curves.

An example of the analysis is given in Fig. 2. The Hanle curve was measured for large enough modulation frequency and at application of cophase RF-field, see Fig. 2(a), where e-peak is also shown. For analysis, the e-peak is subtracted from

the Hanle curve and the remaining part is modeled by Gaussian-like resonances, see Fig. 2(b). In particular, the central part is modeled by resonances $|+1/2\rangle \leftrightarrow |-1/2\rangle$ and the wide part by resonances $|+3/2\rangle \leftrightarrow |-3/2\rangle$ for In and Ga nuclei, as well by resonances $|+5/2\rangle \leftrightarrow |-5/2\rangle$ for In nuclei. The resonance positions were considered as fitting parameters. This analysis was performed for all the experimental data obtained. We found that the resonance for ^{71}Ga can be identified most reliably and its magnetic field dependence is well described theoretically assuming that the quadrupole splitting is due to the strain aligned along z axis, $\varepsilon_{zz} = 0.01$. This value is in good agreement with that estimated in Ref. [4].

2. Conclusion

We have used the effect of resonant pumping of nuclear spins in QDs at joint action of rapid modulation of polarization of optical excitation and synchronous RF-field in transverse magnetic field to observe resonances related to transitions between nuclear spin states splitted by the magnetic field and quadrupole interaction. The resonances have been observed for large number of nuclear spin transitions in different species of nuclei in the QDs.

References

[1] S.E. Barrett, R. Tycko. L.N. Pfeiffer, and K.W. West, *Phys. Rev. Lett.* **72**, 1368 (1994).

[2] D. Paget, G. Lampel, B. Sapoval, and V.I. Safarov, *Phys. Rev. B* **15**, 5780 (1977).

[3] V.K. Kalevich, V.L. Korenev, and O.M. Fedorova, *Pisma Zh. Eksp. Teor. Fiz.* **52**, 964 (1990); [*Sov. Phys. JETP Lett.* **52**, 349 (1990)].

[4] K. Flisinski, I.Ya. Gerlovin, I.V. Ignatiev, M.Yu. Petrov, S.Yu. Verbin, D.R. Yakovlev *et al*, *Phys. Rev. B* **82**, 081308(R) (2010).

[5] M.N. Makhonin, E.A. Chekhovich, P. Senellart, A. Lemaître, M.S. Skolnick, and A.I. Tartakovskii, *Phys. Rev. B* **82**, 161309(R) (2010).

[6] R.I. Dzhioev, B.P. Zakharchenya, V.L. Korenev, P.E. Pak, D.A. Vinokurov, O.V. Kovalenkov, and I.S. Tarasov, *Fiz. Tverd. Tela (St Petersburg)* **40**, 1745 (1998); [*Phys. Solid State* **40**, 1587 (1998)].

[7] I.V. Ignatiev, S.Yu. Verbin, I.Ya. Gerlovin, R.V. Cherbunin, and Y. Masumoto, *Opt. Spektrosk.* **106**, 427 (2009); [*Opt. Spektrosc.* **106**, 375 (2009)].

Suppression of spin level coincidences under tilted magnetic fields in the HgTe quantum well as a manifestation of transitions into quantum Hall ferromagnetic phase

M. V. Yakunin[1], *A. V. Suslov*[2], *S. M. Podgornykh*[1], *S. A. Dvoretsky*[3] and *N. N. Mikhailov*[3]

[1] Institute of Metal Physics, Ural Branch of RAS, 620990 Ekaterinburg, Russia
[2] National High Magnetic Field Laboratory, Tallahassee, Florida 32310, USA
[3] Institute of Semiconductor Physics, 630090 Novosibirsk, Russia

Abstract. We report on observation of rich patterns of magnetic level coincidences under tilted magnetic fields in the magnetoresistivity of HgTe quantum well. Magnetic level crossings were found to turn into anticrossings within the quantum Hall range of fields with intensity of suppression of crossings nonmonotonously dependent on the spin- to cyclotron gaps ratio. This indicates the phase transitions into the quantum Hall ferromagnetic state as a possible nature of anticrossings.

Introduction

A strong spin-orbit interaction in HgTe makes it possible to realize wide spin gaps either with or without magnetic fields that leads to an effective g-factor g^* reaching in a two-dimension layer a value up to $|g^*| = 60$ [1] and its product on the effective mass related to the free electron mass exceeds 1: $g^*m^*/m_0 = 1.4$. The latter means that there are easy conditions to observe magnetic level coincidences under tilted magnetic fields in this material. While in a traditional heterosystem, like GaAs/AlGaAs, a large field tilt is necessary to reach even the first coincidence so that the field should deviate only a few degrees from the sample plane and the perpendicular field component is limited within the Shubnikov–de Haas range of fields, the first coincidence angle in HgTe is close to 60° and the coincidences may exist under fields high enough for the regime of quantum Hall effect (QHE) be reached.

1. Coincidences

We present the results on quantum magnetotransport under tilted magnetic fields in a symmetrical $Cd_xHg_{1-x}Te/HgTe$ quantum well, 20.3 nm wide, doped with In on both sides at the distances of about 10 nm. The electron gas density is about 1.5×10^{15} m^{-2} and a mobility of 22 m^2/V s.

Spin level coincidences appear due to that, at the fixed perpendicular field component $B_\perp$, the spin gaps may be increased

Fig. 2. Magnetoresistivity $\rho_{xx}(B_\perp, B_{||})$ at temperature 0.32 K. Straight beams ascending from zero correspond to fixed $r = 1, 2, 3, 4$ in Eq. (1). Beams descending from $B_{||}^0 = 16$ T correspond to Eq. (2) for $M = 1, 3, 5$.

by addition of field component $B_{||}$ parallel to the layers and occur at tilt angles θ such that the spin gap is an integer multiple r of the cyclotron energy (Fig. 1). This is reduced to a relation

$$\frac{g^*m^*}{m_0} = 2r\cos\theta_r, \qquad r = 1, 2, 3\ldots \qquad (1)$$

Experimentally the coincidences under QH regime are manifested in the picture of magnetoresistivity (MR) $\rho_{xx}(B_\perp, B_{||})$ as bridges at certain $B_{||}$ values through the MR minima of integer filling factors ν (Fig. 2). As seen in Fig. 2 the obtained coincidences are aligned on a set of straight beams ascending from zero and tilted the angles that fulfill Eq. (1) for $r = 1, 2, 3\ldots$. It means that a simple traditional scheme is acceptable here for description of coincidences in spite of the complicated nature of the conduction band in the HgTe 2D layer with inverted band structure. The same coincidences are also positioned on another set of beams descending from a point $B_{||}^0$ on the $B_{||}$ axis that correspond to a full spin polarization of the electronic system $g^*\mu_B B_{||}^0 = 2E_F$ with E_F — the Fermi level and μ_B — Bohr magneton. These beams correspond to a motion between integer ν values along the fixed upper spin sublevels on the

Fig. 1. The scheme of magnetic level coincidences under tilted magnetic fields in a one-particle model of a band identical to Γ_6.
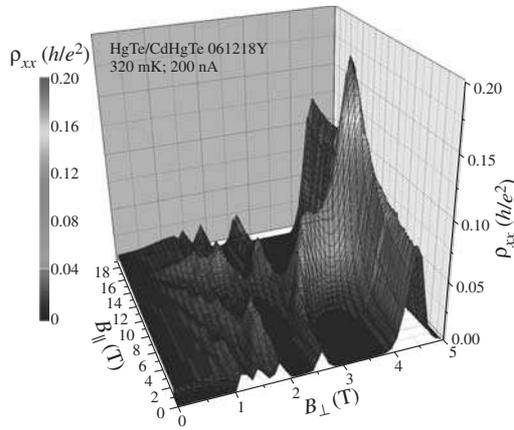
Fig. 3. The same as in Fig. 2 but in the bulk presentation. Well seen is how the coincidences are aligned along the traces of the second type (2). On the trajectory for $M = 1$ it is seen that the coincidence for $\nu = 3$ is suppressed stronger than the others.

scheme in Fig. 1 and at large enough tilts are described within the same simple model as

$$B_{||} = \frac{2}{g^* (m^*/m_0)} \, (B_1 - M B_\perp) \,, \, M = 1, 3, 5 \ldots \quad (2)$$

with $B_1 = h n_S/e$ — MR minimum position for $\nu = 1$, n_S — the electron gas density (Fig. 2). The second system of coincidences manifests in the experiment more pronouncedly than the first traditional one with the fixed angles θ_r (1): Fig. 3.

2. Anticrossings

In the high-perpendicular-field region, a complicated structure of the coincidence-related MR features is revealed with the MR peaks split into two components shifted from the integer ν in the valley center to the neighboring MR ridges with half-integer ν values leaving either lowered (Figs. 2, 3) or almost totally suppressed bridge at the integer ν (Fig. 4). Such a behavior means that the corresponding level coincidence is suppressed, i.e. the level crossing is changed for their anticrossing. Notable is that considerably stronger suppression is observed for the $\nu = 3$ coincidence than for those at $\nu = 2$ and $\nu > 3$. This is especially pronounced when, in our experimental pictures (e.g. Fig. 2), to go along the trace for $M = 1$ (see Eqn. 2) on the $(B_\perp, B_{||})$ plane thus moving from the partially depressed coincidence at $\nu = 2$ to the suppressed crossing at $\nu = 3$ and further to the well pronounced crossings at $\nu \geq 4$.

The level anticrossings in the coincidence effect under tilted fields may occur due to spin-orbit interaction [2]. The coincidence suppression at $\nu = 2$ could be described by this mechanism since Landau levels with numbers differed by 1 interact in this case. But levels with numbers differed by 2 participate in the coincidence at $\nu = 3$ (Fig. 1). The spin-orbit interaction between them may exist only in the second order thus the anticrossing should be much weaker in this case, contrary to the experiment. Another mechanism for the anticrossing may be connected with transition of the electronic system into a spin-polarized state when the Fermi level passes through the point of expected coincidence that is followed by a transition into a quantum Hall ferromagnetic state [3]. The coincidence suppression have been observed in the $Ga_{0.47}In_{0.53}As$ quantum well [4], but only for a single filling factor $\nu = 2$. The larger
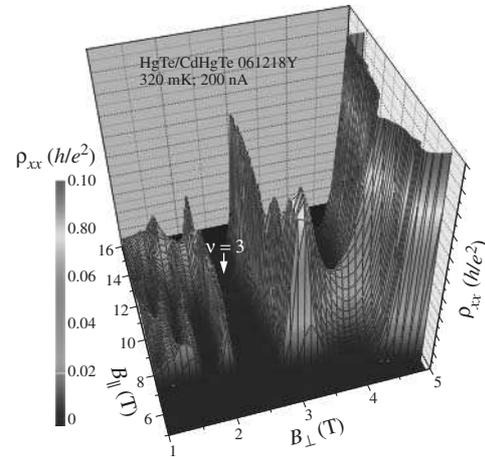
Fig. 4. Identical to Fig. 3 but in a state after IR-radiation. An increased mobility has led to a stronger suppression of the $\nu = 2$ coincidence and almost a total suppression of MR at the expected coincidence for $\nu = 3$.

$g^* m^*/m_0$ in HgTe makes it possible to observe coincidences at larger $B_\perp$ and thus to analyze a wider set of coincidences with larger ν, which are still within the QH regime. Just due to this we may see that the $\nu = 2$ state is not the only one suppressed under QH regime, but that the next state — $\nu = 3$ — corresponding to a larger number of spin polarized levels is still more suppressed. The observed recovery of coincidences at smaller $B_\perp$ may be explained in terms of overlapped levels that lead to a destruction of the QH ferromagnetic state [5]. Remarkable is that in $Ga_{0.47}In_{0.53}As$ [4] the recovery of coincidences have been observed already at $\nu \geq 3$, that supports the latter mechanism.

References

[1] M.V. Yakunin *et al*, *Physica E* **42**, 948 (2010).
[2] V.I. Fal'ko *et al*, *Phys. Rev. B* **46**, 4320 (1992).
[3] G.F. Giuliani *et al*, *Phys. Rev. B* **31**, 6228 (1985).
[4] S. Koch *et al*, *Phys. Rev. B* **47**, 4048 (1993).
[5] S. Yarlagadda *et al*, *Phys. Rev. B* **44**, 13101 (1991).

Aharonov–Bohm interferometer as a spin polarizer

P. M. Shmakov, A. P. Dmitriev and V. Yu. Kachorovskii

Ioffe Physical-Technical Institute, St Petersburg, Russia

Abstract. We study effect of spin-orbit interaction on tunneling transport of electrons through a single-channel quantum ring threaded by magnetic flux. We focus on the high temperature case, assuming that temperature T is much higher than level spacing in the ring and demonstrate that spin-orbit interaction leads to splitting of Aharonov–Bohm resonances. We calculate the spin-dependent transmission coefficient and show that unpolarized incoming electron beam acquires polarization after tunneling through the ring. The polarization degree depends on the strength of electron-electron interaction and reaches 100% (at certain values of magnetic flux) in the absence of interaction.

Introduction

It is well known that in purely 1D systems with spin-orbit (SO) interaction the spin degree of freedom may be excluded by unitary transformation. As a result, the effect of SO interaction on spin and charge transport is suppressed [1]. In this paper, we show that this is not the case for a tunneling transport through a single-channel quantum ring threaded by a magnetic flux Φ (Aharonov–Bohm interferometer). Though such a ring is actually 1D system, the interference between two waves (propagating clockwise and counterclockwise) makes the problem nontrivial. We will see that SO interaction may strongly modify transport properties of the ring. We focus on high temperature case, assuming that temperature T is much higher than the level spacing in the ring. In the absence of SO interaction this case was discussed in a recent work [2]. It was demonstrated that, in contrast to naive expectation, interference effects are not suppressed by thermal averaging. The manifestation of interference is quite interesting even in the case when electron-electron interaction is neglected. In particular, "noninteracting" Landauer conductance $G_0(\phi) = (e^2/2\pi)T_0(\phi)$ exhibits a sharp antiresonance in vicinity of $\phi = 1/2$:

$$T_0(\phi) = \frac{2\gamma \cos^2(\pi\phi)}{\cos^2(\pi\phi) + \gamma^2} . \quad (1)$$

Here $T_0(\phi)$ is the transmission coefficient averaged within the temperature window, $\phi = \Phi/\Phi_0$, $\Phi_0 = hc/e$ is the flux quantum, and $\gamma \ll 1$ is the transparency of tunneling contacts. This dependence is shown in Fig. 1. The dip at $\phi = 1/2$ is due to destructive interference of clockwise- and counterclockwise-propagating waves having the same winding numbers.

1. Main results

We assume that spin-orbit interaction is described by the following Hamiltonian

$$H_{SO} = (\alpha/2) \{[\mathbf{e} \times \boldsymbol{\sigma}], \mathbf{p}\} . \quad (2)$$

Here $\mathbf{e}$ is the unit vector parallel to built-in electric field, $\boldsymbol{\sigma}$ is the vector consisting of Pauli matrices, α is the constant of SO interaction, $\mathbf{p}$ is the operator of the electron momentum in the ring and $\{\cdots\}$ stands for anticommutator. The vector $\mathbf{e}$ has following components $(\cos\varphi\cos\theta, \sin\varphi\cos\theta, \sin\theta)$, where φ is the angle coordinate of the electron in the ring and θ is the angle between built-in field and the ring plane.

We will study the problem quasiclassically, assuming that $k_F L \gg 1$ and $\alpha p_F \ll E_F$, where L is the circumference of
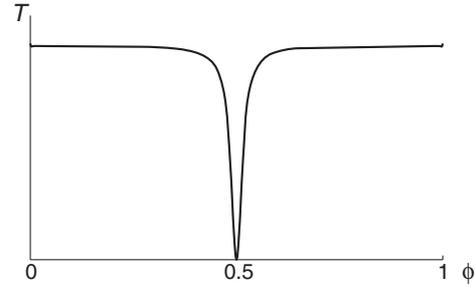
Fig. 1. Antiresonance in the transmission coefficient in the absence of SO interaction.

the ring. Within this approximation the effect of SO interaction can be fully taken into account if we consider rotation of the electron spin in the SO-induced effective magnetic field. We will neglect the Zeeman term $\hbar\omega_Z\hat{\sigma}_z$ in the Hamiltonian, assuming that $\omega_Z \ll \alpha k_F$.

Let us assume that an electron described by a spinor $|\sigma\rangle$ enters the ring at contact 1 and escapes from the ring at contact 2 in a spin state $|\sigma'\rangle$. If we neglect backscattering by contacts, the transition amplitude is given by a sum of amplitudes of clockwise and counterclockwise propagating waves $A^+_{\sigma'\sigma}$ and $A^-_{\sigma'\sigma}$. Each of the amplitudes $A^+_{\sigma'\sigma}$ and $A^-_{\sigma'\sigma}$ can be presented as a sum over winding number n:

$$A^+_{\sigma'\sigma} = |t|^2 \sum_{n=0}^{\infty} (t_{in})^{2n} e^{i(1/2+n)(kL-2\pi\phi)} \langle\sigma'|(\hat{M}^+)^n \hat{M}^+_*|\sigma\rangle, \quad (3)$$

$$A^-_{\sigma'\sigma} = |t|^2 \sum_{n=0}^{\infty} (t_{in})^{2n} e^{i(1/2+n)(kL+2\pi\phi)} \langle\sigma'|(\hat{M}^-)^n \hat{M}^-_*|\sigma\rangle. \quad (4)$$

Here k is the electron wave vector, t (t^*) is the tunneling amplitude to enter (exit) the ring, t_{in} is the amplitude to pass the contact without scattering and matrices $\hat{M}^+$, $\hat{M}^-$, represent operators of spin rotation after passing a full circle 2–1–2 clockwise and counterclockwise, respectively. The matrices $\hat{M}^+_*$, $\hat{M}^-_*$ correspond to spin rotation after passing half circle (1–2) clockwise and counterclockwise. Important feature of the SO interaction is that $\hat{M}^- = (\hat{M}^+)^{-1}$, so that these matrices can be written as

$$\hat{M}^+ = \exp(-i\sigma\chi/2) , \qquad \hat{M}^- = \exp(i\sigma\chi/2) , \quad (5)$$

where χ is a spin rotation vector corresponding to clockwise 2–1–2 process. One can also see that

$$\hat{M}^-_* = \hat{M}^- \hat{M}^+_* . \quad (6)$$
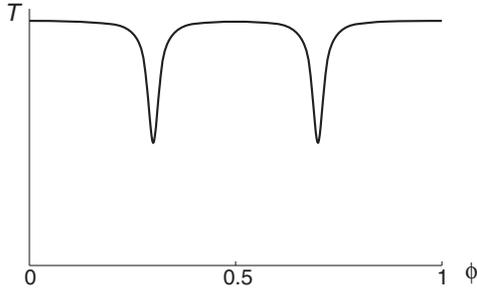
Fig. 2. Splitting of the antiresonance caused by SO interaction.

The spin-dependent transmission coefficient is given by

$$T_{\sigma'\sigma} = \langle |A_{\sigma'\sigma}^+ + A_{\sigma'\sigma}^-|^2 \rangle_k \,, \qquad (7)$$

where averaging over k is taken within the temperature window. Let us consider transmission of unpolarized electron beam through the ring. In this case, the total transmission coefficient T and the average spin of outgoing electrons S are expressed via $T_{\sigma'\sigma}$ as follows

$$T = \sum_{\sigma'\sigma} T_{\sigma'\sigma}/2 \,, \qquad S = \sum_{\sigma'\sigma} \sigma' T_{\sigma'\sigma}/T \,. \qquad (8)$$

Here sum is taken over $\sigma = \pm 1/2$, $\sigma' = \pm 1/2$. Introducing now spinor $|\tilde{\sigma}\rangle = \hat{M}_*^+|\sigma\rangle$ and using (6) we find that the spin dependent parts of $A_{\sigma'\sigma}^+$ and $A_{\sigma'\sigma}^-$ become respectively, $\langle \sigma'|(\hat{M}^+)^n|\tilde{\sigma}\rangle$ and $\langle \sigma'|(\hat{M}^-)^{n+1}|\tilde{\sigma}\rangle$. Since both total transmission and spin polarization contain sum over initial spin polarizations, one can replace sum over σ with the sum over $\tilde{\sigma}$. Now we can change basis choosing z axis be parallel to vector χ. Doing so we diagonalize both $\hat{M}^+$ and $\hat{M}^-$. Choosing the final spin polarization parallel (antiparallel) to χ, one can check that transmission coefficient summed over initial spin polarization coincides with one for spinless electrons but with the shift $\phi \to \phi + |\chi|/4\pi$ ($\phi \to \phi - |\chi|/4\pi$). One can also see that this conclusion remains valid if we take into account backscattering processes by tunneling contacts. As a result, we find that the total transmission and the average spin can be expressed in terms of $T_0(\phi)$ (see Eq. (1))

$$T(\phi) = \frac{T_0(\phi + |\chi|/4\pi) + T_0(\phi - |\chi|/4\pi)}{2} \,, \qquad (9)$$

$$S(\phi) = \frac{T_0(\phi + |\chi|/4\pi) - T_0(\phi - |\chi|/4\pi)}{4T(\phi)} \,. \qquad (10)$$

Using Eq. (2) one can find

$$|\chi| = 8\pi \frac{|\xi \cos\theta + \xi^2|}{1 + \sqrt{1 + 4\xi\cos\theta + 4\xi^2}} \,, \ \xi = \alpha m L/2\pi\hbar. \qquad (11)$$

Functions $T(\phi)$ and $S(\phi)$ are shown schematically in Fig. 2 and Fig. 3. It is worth stressing that the average spin reaches $1/2$ at certain values of ϕ. Its direction coincides with the direction of vector χ. Physically, the 100% polarization along χ is achieved when the transmission of the electrons with the opposite polarization is totally blocked due to destructive interference.

Let us now briefly discuss the role of the electron-electron (ee) interaction. This interaction leads to two effects [2]:
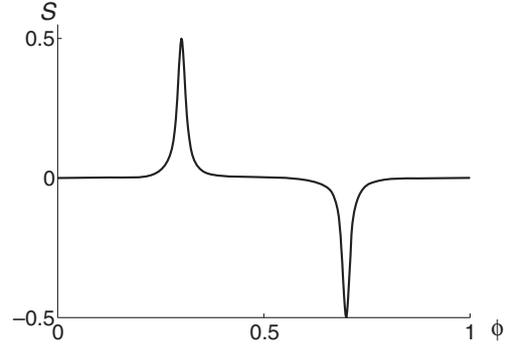
Fig. 3. Spin polarization after tunneling through quantum ring (incoming beam is unpolarized).

1) *Persistent-current blockade (PCB)*. As shown in [2] for interacting electrons $T_0(\phi)$ should be replaced with

$$T(\phi) = Z^{-1} \sum_{N_R, N_L} T_0(\phi - gJ)e^{-\epsilon_{N_R, N_L}/T}. \qquad (12)$$

Here N_R and N_L are the total numbers of right and left moving electrons in the ring, g is the dimensionless constant characterizing the strength of the ee-interaction, $J = N_R - N_L$ is the persistent current captured in the ring, $\epsilon_{N_R, N_L} = (\Delta/4K)[(N - N_0)^2 + K^2(J - 2\phi)]$ is the energy of so called "zero mode", $Z = \sum_{N_R, N_L} e^{-\epsilon_{N_R, N_L}/T}$, $N = N_R + N_L$, N_0 is the averaged number of electrons in the ring, Δ is the level spacing, and $K = (1 - g)^{1/2}/(1 + g)^{1/2}$ is the Luttinger constant. As a result of PCB, the Aharonov–Bohm anti-resonance (Eq. 1) acquires fine structure: it splits into a series of narrow peaks separated by distance g.

2) *Dephasing*, which leads to broadening of the peaks of the fine structure within the width Γ_φ/Δ, where Γ_φ is the dephasing rate. Here we restrict ourselves to the case when $g\sqrt{T\Delta} \gg \Gamma_\varphi \gg g\Delta$. In this case, the fine structure of resonances is not resolved, while the width and the height of resonances do not depend on Γ_φ and are determined by the Gibbs averaging in Eq. (12) [2]. One can show that the maximal average spin in this case is on the order of $\gamma/g\sqrt{T/\Delta} \ll 1$. We see that due to ee-interaction the maximal average spin becomes smaller than $1/2$.

2. Conclusion

In this work we demonstrate that the Aharonov–Bohm interferometer can be used as a spin polarizer. The maximal polarization, which can be achieved in such a polarizer is controlled by the strength of electron-electron interaction.

References

[1] M.V. Entin and L.I. Magarill, *Europhysics Letters* **68**, 853 (2004).
[2] A.P. Dmitriev, I.V. Gornyi, V.Yu. Kachorovskii, and D.G. Polyakov, *Phys. Rev. Lett.* **105**, 036402 (2010).

Surface anisotropy influence on nonlinear dynamics of Néel-type domain walls in magnetic films with in-plane anisotropy

M. N. Dubovik, B. N. Filippov and F. A. Kassan-Ogly

Institute of Metal Physics, Ural Branch of RAS, 620990 Ekaterinburg, Russia

Abstract. Within the framework of two-dimensional model of magnetization distribution and exact allowance for main interactions surface anisotropy influence on nonlinear dynamic behavior of Néel-type domain walls in thin magnetically uniaxial films with in-plane bulk anisotropy has been studied. Surface anisotropy of easy plane (easy axis) type proved to increase (decrease) time-average wall velocity and critical field value. Two possible wall internal structure dynamic rearrangement scenarios have been revealed.

Introduction

At present studying physical properties of nanosize objects has acquired a vital importance. Thereupon the investigation of nonlinear dynamics of domain walls in magnetic films with nanosize thickness b is of essential concern. Till recently studying domain walls motion based on numerical methods has being dealt mainly with the film thicknesses in which the stable static wall structure is two-dimensional vortex-like Bloch-type one. Dynamical transformation of two-dimensional Bloch-type domain walls internal structure [1] is of interest for nonlinear physics. In Permalloy films such walls exist at $b > 40$ nm. The only stable static wall configuration in the thinner films is one-dimensional Néel-type one. Despite the one-dimensional Néel-type wall static structure being simpler as compared with the two-dimensional wall one, recent investigation [2] showed the dynamic properties of walls in ultra-thin films to be nontrivial and of importance for better understanding the processes of domain walls motion in films. The present work deals with the surface anisotropy influence on the nonlinear dynamic properties of uniaxial films with in-plane anisotropy and of 8–35 nm thickness.

1. Statement of the problem and basic equations

Ferromagnetic film is considered to be a parallelepiped having thickness b along the y axis of Cartesian coordinate system and infinite dimensions in xz plane, with easy axis being parallel to the z axis. It is assumed that film magnetic state corresponds to two domains with uniform magnetizations oriented along $+z(-z)$ for $x < -a/2$ $(x > a/2)$. This implies that domain wall is concentrated completely in a region V of rectangular cross-section D in the xy plane having dimensions a and b along x and y respectively. Magnetization in region V is assumed to be a function of x and y: $\mathbf{M} = \mathbf{M}(x, y)$. Wall motion simulation is carried out using numerical integration of Landau–Lifshitz equation:

$$\frac{d\mathbf{M}}{dt} = -\gamma \left[\mathbf{M} \times \mathbf{H}_{\text{eff}} \right] - \alpha \frac{\gamma}{M_S} \left[\mathbf{M} \times \left[\mathbf{M} \times \mathbf{H}_{\text{eff}} \right] \right] . \quad (1)$$

Here t is the real time, α is the Gilbert loss damping parameter, γ is the gyromagnetic ratio, $\mathbf{H}_{\text{eff}}$ is the effective field which is determined by variational $\mathbf{M}$ derivative of full energy volume density. Because of $\mathbf{M}$ being independent of z domain wall
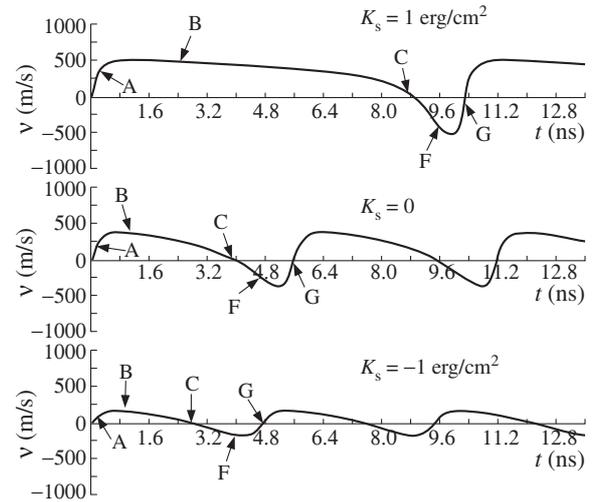
Fig. 1. Dependences of the average (over the film thickness) velocity of a domain wall motion on time for 15 nm thick film with basal parameters. $H = 40$ Oe $> H_c$.

energy per unit length along z can be written in the form

$$\begin{aligned}
\gamma_D &= \int\!\!\!\int_D \left\{ \frac{A}{M_S^2} \left[\left(\frac{\partial \mathbf{M}}{\partial x} \right)^2 + \left(\frac{\partial \mathbf{M}}{\partial y} \right)^2 \right] \right. \\
&\quad \left. - \frac{K}{M_S^2} (\mathbf{Mc})^2 - \frac{1}{2} \mathbf{M H}^{(m)} - \mathbf{M H} \right\} dx\, dy \\
&\quad + \int_{-\frac{a}{2}}^{\frac{a}{2}} \left[\frac{K_S}{M_S^2} \left(\mathbf{n M} \left(x, y = \pm \frac{b}{2} \right) \right) \right] dx . \quad (2)
\end{aligned}$$

Here A is the exchange interaction parameter, M_S is the saturation magnetization, K is the bulk anisotropy constant, $\mathbf{c}$ is a unit vector along the easy axis, K_S is the surface anisotropy constant, $\mathbf{n}$ is a unit vector normal to the film surface, $\mathbf{H}$ is an external magnetic field and $\mathbf{H}^{(m)}$ is the magnetostatic field determined from the magnetostatic equations. Initial distributions for numerical simulation of domain wall motion are obtained from the numerical minimization of (2) with $H=0$. For the details about the technique reader is refered to [1,3]. External driving field was applied along easy axis. Use was made of parameters typical for permalloy films: $A = 2 \times 10^{-6}$ erg/cm, $K = 10^3$ erg/cm³, $M_S = 800$ G, $\alpha = 0.01$. K_S was var-
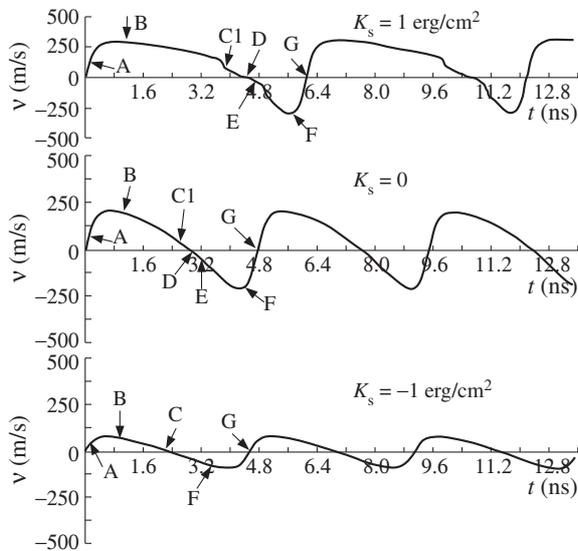
Fig. 2. Dependences of the average (over the film thickness) velocity of a domain wall motion on time for 25 nm thick film with basal parameters. $H = 40\,\text{Oe} > H_c$.

ied from -1 to $1\,\text{erg/cm}^2$. $K_S < 0$ ($K_S > 0$) corresponds to the surface anisotropy of easy axis (easy plane) type, with anisotropy axis normal to the film surface.

2. Results

When considering domain walls dynamic behavior two regions of external field H values should be distinguished, namely above and below certain critical field H_c. For $H < H_c$ the wall motion proves to be stationary and for $H > H_c$ velocity of motion changes with time (nonstationary motion), with time-periodic wall internal structure rearrangement occurring. Here we examine the letter case because of its being more interesting. Figures 1 and 2 show time dependences of wall motion velocities obtained for various film thicknesses. As stated above the only stable static wall type existing in Permalloy films of 8–35 nm having in-plane anisotropy is the one-dimension Néel-type wall. Nevertheless, the dynamic rearrangement of the internal wall structure at their nonstationary motion can occur, in particular, by the generation of vortex-like wall configurations, as shown in Fig. 3. Such a scenario of wall structure rearrangements is observed in 20–35 nm films (in absence of surface anisotropy) [2]. In thinner films the scenario alters substantially and the vortex-like configurations formation does not occur (see Figs. 1 and 3). In particular, at $b = 10$ nm instead of vortex-like states generation the precession of average magnetization of a wall about the easy axis lying in the film plane takes place. In this case, the scenario of dynamic rearrangement of the internal wall structure is very similar to that studied for the first time by Schryer and Walker [4] for the infinite medium case. Figures 1 and 2 show the presence of surface anisotropy of easy axis (easy plane) type to decrease (increase) the maximal wall motion velocity and the period T of wall internal structure rearrangement and hence decrease (increase) the time-average wall motion velocity. Such a dependence of T is connected with the surface anisotropy influence on the critical field H_c value. In particular, H_c increases in the case of $K_S > 0$ and decreases in the case of $K_S < 0$ as compared with the $K_S = 0$ case. As a result nonstationary wall motion can be completely suppressed by the surface anisotropy of easy-plane
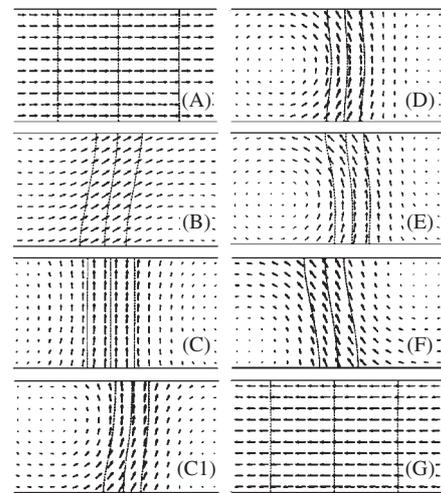
Fig. 3. Instantaneous wall configurations corresponding to points in Figs. 1 and 2. Arrows indicate the projections of **M** on the xy plane. Central dotted line is the level line $M_z = 0$; M_z varies by approximately 75% between the rest two lines.

type. Increasing H_c is of importance for obtaining big wall motion velocities and thus increasing possible film-based devises rate of operation. The presence of surface anisotropy also shifts the film thickness region boundaries where Néel-type wall nonstationary motion occurs with vortex-like states generation. In particular, in 25 nm thick film with $H_c = -0.5\,\text{erg/cm}^2$ such configurations formation does not take place.

References

[1] B.N. Filippov, L.G. Korzunin, F.A. Kassan-Ogly, *Phys. Rev. B.* **64**, 104412 (2001).
[2] B.N. Filippov, M.N. Dubovik, F.A. Kassan-Ogly, *Phys. of Metals and Metallogr.*, (in press).
[3] A.E. La Bonte, *J. Appl. Phys.* **40**, 2450 (1969).
[4] N.L. Shryer, L.R. Walker, *J. Appl. Phys.* **45**, 5406 (1974).

Ferromagnetic ordering in 2D semiconducting structures: GaAs/InGaAs/GaAs quantum wells with a remote Mn δ-layer

B. A. Aronzon[1,2], V. V. Rylkov[1,2], M. A. Pankov[1], V. Tripathi[3], K. Dhochak[3] and K. I. Kugel[2]

[1] RRC Kurchatov Institute, Kurchatov Sq. 1, 123182 Moscow, Russia
[2] Institute for Theoretical and Applied Electrodynamics, RAS, Izhorskaya Str. 13, 125412 Moscow, Russia
[3] Department of Theoretical Physics, Tata Institute of Fundamental Research, Homi Bhabha Road, Navy Nagar, Mumbai 400005, India

Abstract. We study experimentally and theoretically the electron transport and magnetism in GaAs/InGaAs/GaAs quantum wells with a remote Mn δ-layer. The existence of a ferromagnetic state is confirmed by the anomalous Hall effect, direct magnetization measurements, and by the observation of a peculiar hump in the temperature dependence of the sample resistance. This dependence was calculated taking into account effects of disorder, nonlinear screening, and magnetic interactions on electron transport. The theoretical results are in a good agreement with the observed local maximum. Our analysis shows that this peak lies significantly below the Curie temperature T_C in contrast to the three-dimensional case, where it lies above and close to T_C. The dependence of T_C on manganese content, depth of the quantum well, and the thickness of the spacer between quantum well and Mn δ-layer shed a light on the mechanisms of exchange interaction in such structures, which are discussed.

Introduction

Due to fundamental limits for further miniaturization of transistors in microprocessors and memory cells, electronic devices based on new physical principles are demanded. One of the most promising proposal is to transfer and process information not only through the charge but also through the spin of the electrons. This domain of research is called spintronics. In this context, Dilute Magnetic Semiconductors (DMS), mostly based on $A^{III}B^V$-type semiconductors, are currently the object of a widespread attention. However, two-dimensional (2D) structures, which proved to be suitable for electronics, are much less studied in the context of spintronics, and only recently some papers appeared, see for example [1,2,3]. For such structures, the possibility to achieve a spatial separation of magnetic dopants and charge carriers seem to be crucial and promising. Having this in mind, we have studied GaAs/InGaAs/GaAs Quantum Wells (QW) with a Mn δ-layer introduced into one of the GaAs layers and observed magnetic ordering and different manifestations of the spin polarization of the charge carriers. Unlike previous studies of $A^{III}B^V$-type DMS with Mn δ-layers, in our case the Mn layer and the conductive channel (the quantum well filled with charge carriers) are well separated from each other. This results in a relatively high mobility of the carriers, two orders of magnitude higher as compared to the DMS-based structures studied earlier [4,5]. As a consequence, unlike previous results, the hole spectrum is really 2D, as it is confirmed by the observation of Shubnikov–de Haas oscillations and quantum Hall effect, alongside with ferromagnetic behavior. Particularly, we have observed the anomalous Hall effect up to relatively high temperatures (140 K) [3]. The magnetic ordering in the structure under study was also detected by the presence of a hump in the temperature dependence of the electrical resistance $R(T)$ presented in Fig. 1, which is typical of systems with ferromagnetic ordering. The polarization of photo- and electroluminescence, proving the spin polarization of the carriers, was recently observed in similar structures [6]. Direct magnetization measurements were also performed. At high temperatures, the magnetization curves are typical of a
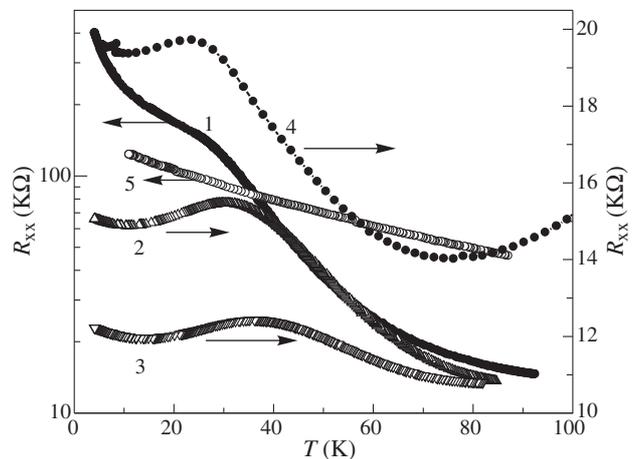
Fig. 1. Temperature dependence of resistance for the Mn doped heterostructures (1, 2, 3, and 4) with different carrier and doping densities and a carbon doped heterostructure (5).

magnetic cluster glass, while at low temperatures and at not high Mn content a hysteresis loop was observed. For structures with higher Mn content the exchange bias of hysteresis loop was observed also. That is due to spatial disorder of Mn distribution, which results in the existence of antiferromagnetic regions that could pin the magnetic moment of ferromagnetic areas.

1. Results

In this talk, the possible mechanisms of exchange interaction leading to the ferromagnetic state in these systems will be discussed. To shed light on this mechanism, we performed measurements at various Mn concentration, depth of the quantum well and thickness of the spacer separating the Mn δ-layer and the QW. These results presented in Figs. 2 and 3 prove two competing causes for spin polarization of carriers in the QW. First is related to the indirect exchange between carriers in the QW and Mn ions in δ-layer and second is due to affect of magnetization of Mn δ-layer on carriers while ferromagnetic ordering
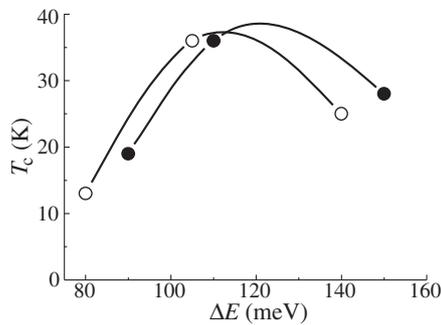
Fig. 2. Curie temperature versus depth of the QW for two sets of samples with Mn content 0.25 and 0.3 ML.
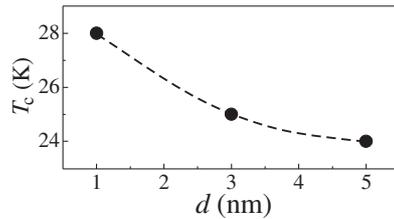
Fig. 3. Curie temperature versus thickness of the spacer for set of samples with Mn content 0.3 ML.

in this layer occurs itself without exchange with carriers inside the QW.

Our experimental results point out the intrinsic nature of the anomalous Hall effect in DMS with 2D geometry, which is related to the renormalization of carrier group velocity under the action of the spin-orbit interaction. The magnitude of the anomalous Hall effect and the change of sign when T rises are in a good agreement with the theoretical estimations for 2D structures [7].

2. Discussion and conclusions

Anomalies in the electrical resistance observed in both insulating and metallic structures can be interpreted as a signature of significant ferromagnetic correlations. The insulating samples turn out to be the most interesting as they can give us valuable insights into the mechanisms of ferromagnetism in these heterostructures. At low charge carrier densities, we show how the interplay of disorder and nonlinear screening can result in the organization of the carriers in the 2D transport channel into charge droplets separated by insulating barriers, similar to the earlier calculations of Gergel' and Suris [8]. Based on such a droplet picture and including the effect of magnetic correlations, we analyze the transport properties of this set of droplets, compare it with experimental data, and find a good agreement between the model calculations and experiment (see Fig. 4). Our analysis shows that the peak or shoulder-like features observed in temperature dependence of resistance of 2D heterostructures δ-doped by Mn lie significantly below the Curie temperature T_C unlike the three-dimensional case, where it lies above and close to T_C.

Acknowledgements
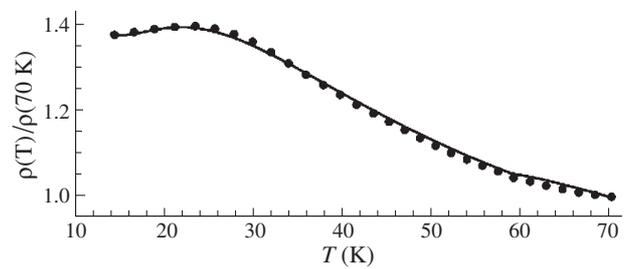
Fig. 4. Experimental and calculated temperature dependence of the resistance for sample 4.

References

[1] B. Rupprecht, W. Krenner, U. Wurstbauer, Ch. Heyn *et al*, *J. Appl. Phys.* **107**, 093711 (2010).

[2] Y. Nishitani, D. Chiba, M. Endo, M. Sawicki, F. Matsukara, T. Dietl, and H. Ohno, *Phys. Rev. B* **81**, 045208 (2010).

[3] B.A. Aronzon, M.A. Pankov, V.V. Rylkov, E.Z. Meilikhov, A.S. Lagutin, E.M. Pashaev, M.A. Chuev *et al*, *J. Appl. Phys.* **107**, 023905 (2010).

[4] T. Wojtowicz, W.L. Lim, X. Liu, M. Dobrowolska, J.K. Furdyna, K.M. Yu, W. Walukiewicz, I. Vurgaftman, and J.R. Meyer, *Appl. Phys. Lett.* **83**, 4220 (2003).

[5] A.M. Nazmul, T. Amemiya, Y. Shuto, S. Sugahara, and M. Tanaka, *Phys. Rev. Lett.* **95**, 017201 (2005).

[6] M.V. Dorokhin, Yu.A. Danilov1, P.B. Demina, V.D. Kulakovskii, O.V. Vikhrova, S.V. Zaitsev, and B.N. Zvonkov, *J. Phys. D* **41**, 245110 (2008).

[7] V.K. Dugaev, P. Bruno, M. Taillefumier, B. Canals, and C. Lacroix, *Phys. Rev. B* **71**, 224423 (2005).

[8] V.A. Gergel' and R.A. Suris, *Zh. Eksp. Teor. Fiz.* **75**, 191 (1978); [*Sov. Phys. JETP* **48**, 95 (1978)].

Modeling of nuclei-induced bunching effect in quantum dots

S. V. Yakovlev and M. Yu. Petrov

Physics Department, St Petersburg State University, 198504 St Petersburg, Russia

Abstract. We report on theoretical modeling of the electron-nuclear spin dynamics of semiconductor quantum dots in framework of both quantum mechanical and semi-classical approaches. Both the models allow us to simulate the effect of bunching in the electron spin dynamics induced by nuclear spins when pumping the ensemble of quantum dots by periodic pulse training.

Introduction

The spin of conduction-band electron localized in a quantum dot (QD) represents a natural two-level system supplying with a remarkably long coherence time and, therefore, attracts an interest for broad scientific community due to its fundamental interest as well as application potential [1, 2]. For strongly localized electrons, the spin coherence time is limited by its hyperfine interaction with surrounding $N \sim 10^4 - 10^6$ spins of lattice nuclei [3, 4]. A way to overwhelm this decoherence mechanism has been reported by Greilich *et al* (Ref. [5]). A series of short laser pulses has been used to transfer the nuclear spin system in a state, which focuses the electron spin precession in strong external magnetic field into modes synchronized with the laser pulses.

Dephasing of electron spin precession in strong transverse magnetic field might be caused either by spread of electron g factor in the QD ensemble [6] or by fluctuation of total field caused by the spread of the nuclear spin fluctuations [3]. Strongly periodic pulse training of electron-nuclear spin system gives rise to opposite effect of constructive interference of electron spin precession in the ensemble (bunching effect) caused by tuning the system to the pumping conditions. The bunching effect caused by the spread of electron g factor is well studied as experimentally as theoretically [6]. However, the role of nuclear spin fluctuations is theoretically analyzed only in framework of a phenomenological approach [5, 7].

In this work, we present the results of modeling the electron-spin dynamics in the ensemble of identical QDs initiated by a series of pulsed radiation. We show in quantum mechanical and semi-classical approaches that the periodic training of coupled electron-nuclear spin system can lead to synchronization of electron spin precession in strong external magnetic field. Both the models predict the nuclei-induced bunching effect in ensemble of identical QDs where the electron g factor spread is absent.

1. Model

The Hamiltonian of electron spin $\hat{\mathbf{S}}$ coupled to N nuclear spins $\hat{\mathbf{I}}^j$ ($j = 1, \ldots, N$) in the presence of external magnetic field $\mathbf{B}$ takes the form ($\hbar = 1$)

$$\hat{\mathcal{H}} = -\gamma_e \hat{\mathbf{S}} \times \mathbf{B} - \sum_j \gamma_n^j \hat{\mathbf{I}}^j \times \mathbf{B} + \sum_j A^j (\hat{\mathbf{S}} \times \hat{\mathbf{I}}^j), \quad (1)$$

where γ_e and γ_n^j are the gyromagnetic ratios for electron and jth nuclear spins, A^j is the constant of hyperfine interaction with jth nuclear spin. Unless we ignore the spatial dependence of hyperfine constants and assume the nuclear spins to

be similar to each other ($A^i = A^j \equiv A$, $\gamma_n^i = \gamma_n^j \equiv \gamma_n$, for all i and j) we introduce the total nuclear-spin momentum, $\hat{\mathbf{J}} = \sum_j \hat{\mathbf{I}}^j$, and rewrite Eq. (1) as

$$\hat{\mathcal{H}} = -\gamma_e \hat{\mathbf{S}} \times \mathbf{B} - \gamma_n \hat{\mathbf{J}} \times \mathbf{B} + A \hat{\mathbf{S}} \times \hat{\mathbf{J}}. \quad (2)$$

To derive the equations of motion (EOM) of the spin system, we substitute the reduced Hamiltonian (2) into the Von Neumann's equation, $\dot{\rho}(t) = i[\rho(t), \hat{\mathcal{H}}]$, and obtain

$$\frac{d}{dt}\langle \hat{\mathbf{S}} \rangle = A\langle [\hat{\mathbf{J}} \times \hat{\mathbf{S}}] \rangle + \boldsymbol{\omega}_e \times \langle \hat{\mathbf{S}} \rangle, \quad (3)$$

$$\frac{d}{dt}\langle \hat{\mathbf{J}} \rangle = A\langle [\hat{\mathbf{S}} \times \hat{\mathbf{J}}] \rangle + \boldsymbol{\omega}_n \times \langle \hat{\mathbf{J}} \rangle. \quad (4)$$

Here, $\langle \ldots \rangle$ denotes the quantum mechanical averaging over density matrix $\rho(t)$ and $\boldsymbol{\omega}_e = -\gamma_e \mathbf{B}$, $\boldsymbol{\omega}_n = -\gamma_n \mathbf{B}$ are the electron and nuclear precession frequencies about external magnetic field, respectively. The obtained EOM are quite complex because of presence of term $\langle [\hat{\mathbf{J}} \times \hat{\mathbf{S}}] \rangle$. Semi-classical approach consist in simplification of these EOM by factorization of this term to $\langle \hat{\mathbf{J}} \rangle \times \langle \hat{\mathbf{S}} \rangle$. By doing this, Eqs. (3) and (4) come into a system of EOM closed with respect to $S_\xi = \langle \hat{S}_\xi \rangle$ and $J_\xi = \langle \hat{J}_\xi \rangle$ ($\xi = x, y, z$).

The latter simplification is rough, therefore, we compare the results of calculation of S_ξ and J_ξ in this approach with those obtained within a quantum-mechanical model. In the quantum-mechanical approach, the density matrix of the coupled electron-nuclear spin system is represented in a block-diagonal form with each block, ρ_J, corresponding to the value of total angular momentum J. The dynamics of each block $\rho_J(t)$ can be evaluated according to the solution of the Von Neumann's equation with the reduced Hamiltonian (2). The resulting quantum mechanical averages for S_ξ and J_ξ can be calculated as $S_\xi(t) = \text{Tr}[\rho(t)\hat{S}_\xi]$ and $J_\xi(t) = \text{Tr}[\rho(t)\hat{J}_\xi]$. Further details of the model and numerical procedure can be found elsewhere (see Refs. [8] and [9] for details).

In both the models, we consider an ensemble of infinite number of identical QDs each containing one resident-electron spin. Starting from totally unpolarized nuclear spin states of each QD, the system is affected by a periodic pulsed radiation with period T_R. Each pulse orients the spins of the resident electrons in each QD along z axis and, simultaneously, does not affect the nuclear spin system of the QDs. This action simulates the process of optical orientation of electron spins by circularly polarized light. In the intervals between the pulse actions, there is a coherent motion in electron-nuclear spin system of each QD as well as the precession of electron and nuclear spins about the external magnetic field. Each pulse decouples electron with

nuclear spins, thus polarizing the nuclear spin system of each QD.

To simulate the unpolarized nuclear spin bath, which can be described in quantum mechanical model by the high-temperature density matrix $\rho_n(0) \propto \mathbb{1}$ ($\mathbb{1}$ is the unity matrix), in the semi-classical model, we initially generate many realizations of the nuclear momentum $\mathbf{J}_0^{(m)} = \left[J_{x0}^{(m)}, J_{y0}^{(m)}, J_{z0}^{(m)} \right]$ according to Gaussian probability distribution,

$$w(\mathbf{J}) = \frac{1}{\left(\sqrt{2\pi}\,\Delta \right)^3} \exp \left(-\frac{\mathbf{J}^2}{2\Delta^2} \right), \qquad (5)$$

where Δ is the variance of this distribution. Similar to Merkulov *et al* (Ref. [3]), it describes the frozen nuclear spin fluctuations in the QD ensemble. The initial state for electron spin at $t = 0$ is $\mathbf{S}_0^{(m)} = [0, 0, S_0]$. Within the semi-classical model, every initial vectors $\mathbf{J}_0^{(m)}$ and $\mathbf{S}_0^{(m)}$ are propagated in time according to the EOM [Eqs. (3) and (4)] until the next pulse event comes at $t = T_R$. At this time, this coherent process is interrupted and the new state of electron spin $\mathbf{S}^{(m)}(T_R) = \mathbf{S}_0^{(m)}$ is initiated. After that, until $t = 2T_R$, the evolution is described similarly by Eqs. (3) and (4). Repeating this procedure for each realization m and averaging over the initial probability distribution, we calculate the average values of S_ξ and J_ξ ($\xi = x, y, z$).

2. Results and discussion

We are interesting in the spin dynamics of electron spin polarization, i.e., $S_z(t)$, affected by interaction with nuclear spins in presence of strong external magnetic field applied in the direction transverse to electron spin orientation. We assume $\mathbf{B} = [B, 0, 0]$. We have chosen magnitude of B to be large enough so that the electron spin precesses many times during T_R about this field. At the same time, hyperfine constant A have been chosen to make the electron spin dephasing time to be of $0.2T_R$.

To compare two approaches, we have chosen for semi-classical model $\Delta = \sqrt{I(I+1)N/3}$ where N is the number of nuclear spins in quantum mechanical one and I is the nuclear-spin quantum number. The results obtained are shown in Fig. 1. As one can see from the figure, both the models give similar dynamics for electron spin polarization. Moreover, the dynamics between first two pulses coincides within the numerical error. However, after many periods of excitation, the semi-classical approach gives rise to considerably stronger bunching effect than the quantum mechanical one. This disagreement of two models is possibly due to factorizing the vector product in exact EOM [Eqs. (3) and (4)]. Further studies of this disagreement is required.

Summarizing, we have simulated the electron-nuclear spin dynamics of the QD ensemble in the presence of strong external magnetic field. The electron spin dynamics initiated by the periodic pulsed excitation in Voigt geometry is simulated in two models, the semi-classical and quantum mechanical approaches. Numerical analysis for limited number of nuclear spins, $N = 64$, shows that both the models give the quantitative agreement at the initial stage of excitation, when nuclear spins are unpolarized, and diverge after many training periods giving, however, qualitatively similar bunching effect induced. However, the applicability of phenomenological model
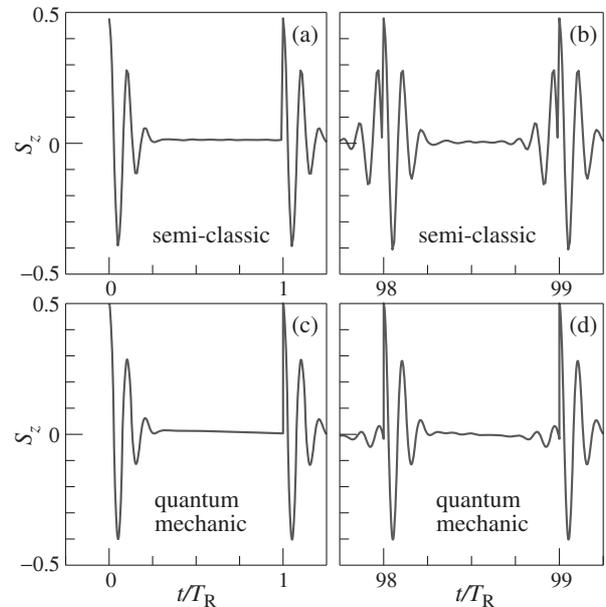
Fig. 1. The dynamics of z component of electron spin polarization between neighboring pulses calculated in semi-classic [panels (a) and (b)] and quantum mechanic [panels (c) and (d)] approaches. Note, good numerical agreement of both the models at the initial stage of "training protocol" [compare panels (a) and (c)]. Both the models predict the bunching effect (the increase of S_z just before next pulse) after long-time training the system, but the bunching amplitudes are different in different models [compare panels (b) and (d)].

for quantitative description still requires an additional investigation.

References

[1] *Spin Physics in Semiconductors*, ed. by M.I. Dyakonov (Springer-Verlag, Berlin 2008).
[2] *Semiconductor Quantum Bits*, ed. by F. Henneberger and O. Benson (World Scientific, Singapore 2008).
[3] I.A. Merkulov, Al.L. Efros, and M. Rosen, *Phys. Rev. B* **65**, 205309 (2002).
[4] A.V. Khaetskii, D. Loss, and L. Glazman, *Phys. Rev. Lett.* **88**, 186802 (2002).
[5] A. Greilich, A. Shabaev, D.R. Yakovlev, Al.L. Efros, I.A. Yugova, D. Reuter, A.D. Wieck, and M. Bayer, *Science* **317**, 1896 (2007).
[6] *Semiconductor Spintronics and Quantum Computation*, ed. by D.D. Awschalom, D. Loss, and N. Samarath (Springer-Verlag, Berlin 2002).
[7] M.M. Glazov, I.A. Yugova, and Al.L. Efros (unpublished).
[8] G.G. Kozlov, *Zh. Eksp. Teor. Fiz.* **132**, 918 (2007); [*JETP* **105**, 803 (2007)].
[9] M.Yu. Petrov, G.G. Kozlov, I.V. Ignatiev, R.V. Cherbunin, D.R. Yakovlev, and M. Bayer, *Phys. Rev. B* **80**, 125318 (2009).

Electron energy spectrum and persistent current in non-perfect one-dimensional quantum ring with spin-orbit interaction

I. A. Kokurin

Mordovian State University, 430005 Saransk, Russia

Abstract. The one-particle energy spectrum in the one-dimensional quantum ring with the Rashba spin-orbit interaction that contains the point δ-like defect is theoretically studied by means of numerical diagonalization of the Hamiltonian. The presence of the point defect leads to the reduction of the crossings into the anticrossings on the energy plot versus magnetic flux. The density matrix formalism is utilized for the persistent charge current calculation. Its dependence on the magnetic flux is studied. The persistent current dependencies on the magnetic flux are compared for the cases of perfect and defect ring. The new features observed for both perfect and defect rings that corresponds to the combined effect of Zeeman and Rashba splitting. The effect of finite temperature is discussed.

Introduction

The two-dimensional electron gas (2DEG) and the systems of reduced dimensionality based on 2DEG (quantum wires, dots, rings) attract much attention due to spin-orbit interaction (SOI). SOI allows to manipulate spin degrees of freedom by means of electric field that can be used for the application in semiconductor spintronics [1]. It is important for applications that the SOI strength for 2DEG structures can be tunable [2,3]. Note that for narrow-gap structures such as InAs-structures Rashba SOI [4] mechanism is dominant [3]. In general the Rashba SOI Hamiltonian has the form [4]

$$H_{\mathrm{R}} = \frac{\alpha}{\hbar} \left[\boldsymbol{\sigma} \times \mathbf{p} \right] \mathbf{n}, \tag{1}$$

where α is the Rashba SOI strength parameter; $\boldsymbol{\sigma}, \mathbf{p}, \mathbf{n}$ are the vector of Pauli matrices, the electron momentum and the unit vector of the normal to the 2DEG surface, respectively.

Among different spintronic device proposals it should be mentioned the one based on the quantum ring (QR) with Rashba SOI [5]. Moreover, the QR geometry is suitable for the observation of equilibrium effects such as the persistent charge current (PCC) [6]. PCC in the one-dimensional (1D) QR with Rashba SOI neglecting Zeeman splitting was theoretically studied in Refs. [7,8] (this case takes the place if effective g-factor is really small or in the Aharonov–Bohm geometry when there is no magnetic field in the ring area). Actually, in real narrow-gap 2DEG structures we cannot neglect the Zeeman splitting due to large effective g-factor.

The aim of present work is the theoretical investigation of the electron energy spectrum and PCC in 1D QR with Rashba SOI in the presence of the point δ-like defect in QR. We suppose the Zeeman splitting to be sufficiently large.

1. Model and Hamiltonian diagonalization

The Hamiltonian of the perfect 1D QR of radius a is given by [7,9]

$$
\begin{aligned}
H_0 = &\ \frac{\hbar^2}{2m^*a^2} \left(-i\frac{\partial}{\partial\varphi} + \frac{\Phi}{\Phi_0} \right)^2 \\
&+ \frac{\alpha}{a}\sigma_r \left(-i\frac{\partial}{\partial\varphi} + \frac{\Phi}{\Phi_0} \right) - i\frac{\alpha}{2a}\sigma_\varphi + \frac{1}{2}g^*\mu_B B\sigma_z, \tag{2}
\end{aligned}
$$

where m^* is the electron effective mass, $\Phi = \pi a^2 B$ is the flux of magnetic field $\mathbf{B} = (0, 0, B)$ through the ring, $\Phi_0 = 2\pi\hbar c/|e|$ is the flux quantum, g^*, $\mu_B = |e|\hbar/2m_0c$ are effective g-factor and Bohr magneton, respectively. Here we introduced the polar Pauli matrices, $\sigma_r = \cos\varphi\sigma_x + \sin\varphi\sigma_y$, $\sigma_\varphi = -\sin\varphi\sigma_x + \cos\varphi\sigma_y$.

The energy spectrum of perfect 1D QR with Rashba SOI is given by

$$
\begin{aligned}
\frac{E_{js}}{E_0} = &\ \left(j + \frac{\Phi}{\Phi_0} \right)^2 + \frac{1}{4} \\
&+ s\sqrt{\Lambda^2\left(j+\frac{\Phi}{\Phi_0}\right)^2 + \left[j+\left(1-g^*\frac{m^*}{m_0}\right)\frac{\Phi}{\Phi_0}\right]^2}, \tag{3}
\end{aligned}
$$

where $E_0 = \hbar^2/2m^*a^2$, $j = \pm 1/2, \pm 3/2, \ldots$, $s = \pm 1$, $\Lambda = 2\alpha m^*a/\hbar^2$. The energy spectrum of perfect ring as a function on magnetic flux is depicted on Fig. 1a.

The corresponding wavefunctions have the form

$$|js\rangle = \frac{1}{\sqrt{2\pi}} \begin{pmatrix} e^{i(j-1/2)\varphi}C_j^{(s)} \\ e^{i(j+1/2)\varphi}D_j^{(s)} \end{pmatrix}. \tag{4}$$

Here $C_j^{(+)} = D_j^{(-)} = \cos(\theta_j/2)$, $D_j^{(+)} = -C_j^{(-)} = \sin(\theta_j/2)$, $\tan\theta_j = \Lambda\lambda_j/(\Delta_Z - \lambda_j)$, with $\lambda_j = j + \Phi/\Phi_0$ and $\Delta_Z = \frac{1}{2}g^*\mu_B B/E_0 = g^*\frac{m^*}{m_0}\frac{\Phi}{\Phi_0}$.

Let us consider the short-range defect in the ring that is described by the δ-like potential $H_d = V_0\delta(\varphi)$. We find the spectrum of the Hamiltonian $H = H_0 + H_d$ utilizing the numerical diagonalization (calculating the matrix elements of $H_0 + H_d$ in the perfect ring eigenfunction basis). For this purpose we use 40×40 Hamiltonian matrix that ensures the perfect precision. After numerical diagonalization of the Hamiltonian $H_0 + H_d$ the crossings that take place in the spectrum of H_0 reduce into anticrossings (but gaps can be small and undistinguishable on the plot) on the $E(\Phi)$ dependence. The energy spectrum of the defect ring as a function of magnetic flux is depicted on Fig. 1b.

2. Persistent current

Let us first find the azimuthal velocity operator v_φ by means of Heisenberg equation of motion $v_\varphi = -\frac{i}{\hbar}[a\varphi, H]$ that leads to the following expression

$$v_\varphi = \frac{\hbar}{m^*a}\left(-i\frac{\partial}{\partial\varphi} + \frac{\Phi}{\Phi_0}\right) + \frac{\alpha}{\hbar}\sigma_r. \tag{5}$$
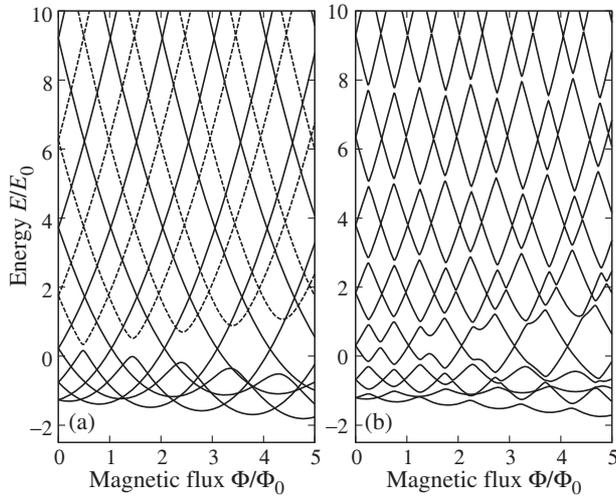
Fig. 1. (a) The energy spectrum of perfect 1D QR with Rashba SOI as a function of magnetic flux, $\Lambda = 2.3$, $g^* = -4.0$, $m^* = 0.05m_0$. The dashed (solid) lines correspond to $s = \pm 1$ levels, respectively. (b) The energy spectrum of QR with δ-like defect, $V_0 = 0.5E_0$.

Now we utilize the density matrix formalism in order to calculate PCC

$$I = \frac{e}{2\pi a} \, \text{Tr} \left[f_0(H) v_\varphi \right] , \qquad (6)$$

calculating the matrix elements of the velocity operator in H_0-basis (4). Here $f_0(E)$ is the Fermi distribution function.

Here we produce the numerical results for the case of the constant chemical potential μ that is the typical case (as we guess) for QR defined in 2DEG structure. It is well-known that PCC in the perfect ring has the following property $I(-\Phi) = -I(\Phi)$. This statement remains true in our case as well. For this reason we plot $I(\Phi)$ dependencies for positive Φ only. The $I(\Phi)$ dependencies are plotted on Fig. 2. The typical values of PCC are the following: I_0 is about 10 nA for the ring with $a = 50$ nm.

One can see on the Fig. 2a the usual PCC behavior: the monotonic decrease and the jumps on the $I(\Phi)$ dependence that corresponds to the alternation of the particle number. The V_0 increase leads to repulsion of the levels and the some reduction of PCC. More interesting features appear due to complex energy level structure for the chemical potential at the vicinity of $\mu = 0$ (see Fig. 2b). The solid arrow on Fig. 2b indicates the feature that corresponds to the level reduction due to the point defect. The dashed arrows on Fig. 2b indicate the features that appear due to the combined effect of Zeeman and Rashba splitting on the energy levels and electron velocity in the vicinity of the Zeeman gaps. These features become apparent both for perfect ring and defect one. As expected, the finite temperature leads to smoothing of the jumps on the $I(\Phi)$ plots (see Fig. 2c).

3. Summary

We have studied the energy spectrum and PCC in non-perfect 1D QR with Rashba SOI. The presence of short-range defect in the ring leads to drastic reduction of the 1D QR energy spectrum and PCC. There are two types of the features in PCC behavior (see Fig. 2b): (i) the first one deals with the defect on the ring, and (ii) the second one appears both in the perfect and
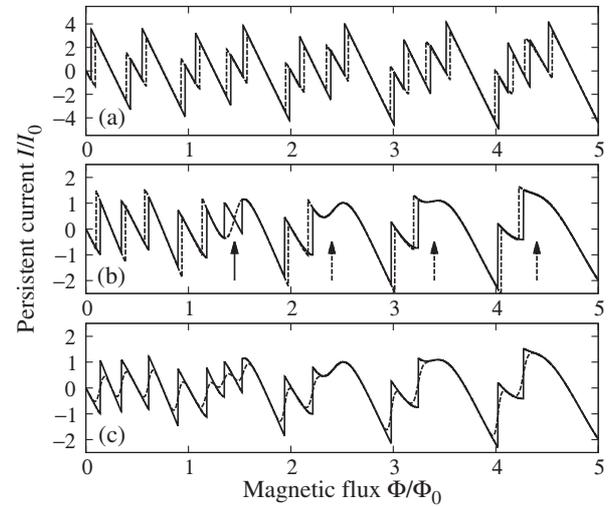
Fig. 2. PCC in 1D QR with Rashba SOI as a function of magnetic flux (QR parameters are the same as on Fig. 1), $I_0 = |e|\hbar/4\pi m^* a^2$. (a) $\mu = 3.5E_0$. The solid (dashed) line corresponds to perfect (defect, $V_0 = E_0$) ring, $T = 0$; (b) $\mu = 0.0$. The dashed (solid) line corresponds to perfect (defect, $V_0 = 0.5E_0$) ring, $T = 0$; (c) $\mu = 0.0$. The solid (dashed) line corresponds to defect ring at $T = 0$ ($T = 0.04E_0$), $V_0 = 0.5E_0$.

defect ring and corresponds to combined effect of Zeeman and Rashba splitting on the energy spectrum and electron velocity.

Since the electrons carry spin as well as charge then there is the persistent spin current (PSC) in QR and it can be detected by special methods [10]. The PSC components can be calculated in analogy with the charge current by means of replacement $ev_\varphi \to \frac{\hbar}{4}(\sigma_i v_\varphi + v_\varphi \sigma_i)$ in Eq. (6), ($i = r, \varphi, z$). These calculations and corresponding results will be published elsewhere (as well as the results for isolated ring that corresponds to the case of constant particle number).

References

[1] J. Fabian, A. Matos-Abiague, C. Ertler, P. Stano, I. Žutić, *Acta Phys. Slov.* **57**, 565 (2007).

[2] J. Nitta, T. Akazaki, H. Takayanagi, T. Enoki, *Phys. Rev. Lett.* **78**, 1335 (1997).

[3] D. Grundler, *Phys. Rev. Lett.* **84**, 6074 (2000).

[4] Yu.A. Bychkov, E.I. Rashba, *JETP Lett.* **39**, 78 (1984).

[5] J. Nitta, F.E. Meijer, H. Takayanagi, *Appl. Phys. Lett.* **75**, 695 (1999).

[6] M. Büttiker, Y. Imry, R. Landauer, *Phys. Lett. A* **96**, 365 (1983).

[7] A.V. Chaplik, L.I. Magarill, *Superlatt. Microstruct.* **18**, 321 (1995).

[8] J. Splettstoesser, M. Governale, U. Zülicke, *Phys. Rev. B* **68**, 165341 (2003).

[9] F.E. Meijer, A.F. Morpurgo, T.M. Klapwijk, *Phys. Rev. B* **66**, 033107 (2002).

[10] F. Schütz, M. Kollar, P. Kopietz, *Phys. Rev. Lett.* **91**, 017205 (2003).

Spin Hall effect induced by sound

I. I. Lyapilin

Institute for Metal Physics, RAS, 620990 Yekaterinburg, Russia

Abstract. The kinetics of conduction electrons in magnetic field that interact with the field of sound waves is studied. The balance equations for the macroscopic momentum, the component of spin, and energy are considered. The conditions for the realization of the spin Hall effect under sound waves are analysed.

Introduction

Among the effects, in which the spin-orbit interaction plays a dominant role and which recently have intensively been studied in low dimensional system it is worth noting the spin Hall effect (SHE) [1–3]. The effect is manifested in the form of a spin current directed perpendicular to the normal current, which takes place in an electric field. The SHE has been observed experimentally [4,5]. Note that upon the SHE external electric field which directly affects the kinetic degrees of freedom of electrons is transmitted to the spin subsystem through the spin-orbit interaction.

There are, however, mechanisms of interaction with external fields under which the energy of the external field is transmitted simultaneously to both electronic subsystems (kinetic and spin). One of these interactions is the interaction of ultrasonic waves with free conduction electrons. The interaction of electrons with the sound wave

$$\mathbf{u}\,(\mathbf{x}, t) = \sum_q \mathbf{u}(\mathbf{q})\,e^{iqx+i\omega t}$$

can be summarized as follows.

$$H_{\text{ef}}(t) = \sum_{in\mathbf{q}} \Phi_{-i}^{-n}(\mathbf{q})\,u^i(\mathbf{q})\,e^{i\omega t}\,T^n(\mathbf{q})\,, \qquad (1)$$

where $T^n(\mathbf{q})$ is the tensor operator, which depends on the group indices $n = (\mu, \alpha_1, \alpha_2, \ldots)$. $\Phi_{-i}^{-n}(\mathbf{q})$ is the c-number matrix. For the interactions which are independent from spin

$$T^n(\mathbf{q}) = \begin{cases} \sum_j e^{iqx_j} \equiv T^{\cdot\cdot}(\mathbf{q}) = N(\mathbf{q})\,, \\ \sum_j \{P_j^\alpha\,;\; e^{iqx_j}\} \equiv T^{\cdot\alpha}(\mathbf{q}) = P^\alpha(\mathbf{q})\,. \end{cases}$$

In other cases, the interactions with sound, depends both on the translational and spin operators, hence, the tensor operator has the form

$$T^n(\mathbf{q}) = \sum_j \{S_j^\mu\,P_j^\alpha\,;\; e^{iqx_j}\} \equiv T^{\mu\alpha}(\mathbf{q})\,. \qquad (2)$$

Here, $x_j\,P_j^\alpha\,S_j^\mu$ are the operators of coordinates, the momentum and spin of the j-th electron, respectively. The indices μ, α take the values $(0, +, -)$. The brackets $\{..,...\}$ denote the symmetrized product of operators. $A^\pm = A_x \pm i A_y$.

We have considered the system of conduction electrons in a constant magnetic field, which interact with the field of lattice displacements and impurities. We have examined the effects associated with the absorption and redistribution of energy between the subsystems of the kinetic and spin degrees of freedom in the vicinity of the resonance frequencies in the quadratic

approximation in the amplitude of displacements. The macroscopic equations for momentum balance, spin components and energy balance of subsystems are obtained by the nonequilibrium statistical operator $\rho(t)$ which is determined under the linear approximation in drift velocity and intensity of sound waves. The analysis of the macroscopical equations of balance is carried out which evidences the possibility of realization of spin Hall effect induced by sound waves (acoustic spin Hall effect). Besides, the resonant change of conductivity caused by various width of channels transferring the sound wave energy between electronic subsystems is studied.

References

[1] M.I. Djakonov, V. I. Perel, *Physics Letters* **35A**, 459 (1971).
[2] J. E. Hirsh, *Phys. Rev. Lett.* **83**, 1834 (1999).
[3] S. Zhang, *Phys. Rev. Lett.* **85**, 393 (2000).
[4] Y.K. Kato, R.C. Myers, A.C. Gossard *et al*, *Science* **306**, 1910 (2004).
[5] J. Wunderlich, B. Kaestner, J. Sinova *et al*, *Phys. Rev. Lett.* **94**, 047204 (2005).

Characterization and physical properties of the iron silicide nanostructures

S. G. Ovchinnikov[1,2], *S. N. Varnakov*[1,2], *A. S. Fedorov*[1], *S. A. Lyaschenko*[1,2] and *I. A. Yakovlev*[1,2]

[1] Kirensky Institute of Physics, SD RAS, Akademgorodok, Krasnoyarsk 660036, Russia
[2] Siberian Aerospace University, pr. im. gazety "Krasnoyarskii rabochii" 31, 660014 Krasnoyarsk, Russia

Abstract. The Fe silicide formation is studied both experimentally and theoretically. We have evaporated thin Fe film at the (100) single crystal Si substrate in the ultrahigh vacuum at different substrate temperature T_s with in situ characterization by high energy electron difraction (HEED), electron spectrometry, and ex situ by spectral ellipsometry. We have calculated ab initio electronic structure of β-FeSi$_2$ thin slab and β-FeSi$_2$/Si interface by the density functional theory method in GGA approximation and study the effect of the surface on the electronic properties of silicide.

Introduction

Ferromagnet/semiconductor nanostructures are promising class of new materials for spintronics which provides new properties beyond ferromagnet/metal structures with giant magnetoresistance. Among them magnetic nanostructures with Si spacer are very promising due to possible integration into the silicon technology. The Fe/Si nanostructures have been considered by several groups [1–3]. In addition to dimensional quantum effects and the effects of interaction between neighbouring layers, the physical properties of multilayered nanostructure (Fe/Si)n are governed by the iron silicide phases formed at the interface [4]. In this paper we study the Fe silicide formation both experimentally and theoretically. We have evaporated thin Fe film at the (100) single crystal Si substrate in the ultrahigh vacuum at different substrate temperature T_s with *in situ* characterization by high energy electron difraction (HEED), electron spectrometry, and ex situ by spectral ellipsometry. We have ab initio calculated electronic structure of β-FeSi$_2$ thin slab and β-FeSi$_2$/Si interface by the density functional theory method in GGA approximation and study the effect of the surface on the electronic properties of silicide.

1. Experiment

The samples were grown on the clean Si(100) 2×1 substrates by thermal evaporation in ultrahigh vacuum (UHV) at substrate temperature $T_s = 320, 450, 600, 750$ K using the modernized molecular-beam epitaxy "Angara" set-up. The base pressure in the growth chamber was 1.0×10^{-7} Pa. The component materials were evaporated from refractory (boron nitride) crucibles. The growth rate was checked-up in situ by a high-speed laser ellipsometer LEF-751M, and is equal to was 0.16 nm/min for Fe. The thicknes of Fe layer was 1.6–1.8 nm.

Earlier our high temperature SQUID measurements have revealed the silicides formation in the range $T_s = 400 - 650$ K from the irreversible temperature dependence of magnetisation [5]. To study the initial stage of the Fe silicides formation we have measured *in situ* HEED for different T_s value (Fig. 1 for $T_s = 450$ K).

The magnetic measurements on the Si(hkl)/SiO$_2$/Fe(d)/ Si(1.5 nm)/Fe(d)/Si(1.5 nm)/Fe(d)/Si(10 nm) films with various values of dFe (1.2, 1.6, 2.6, and 3.8 nm) were carried out using a SQUID magnetometer with applied fields up to 50 kOe. The measurements in the temperature range from 4.2 to 400 K were done with the standard plastic straw sample holder. From
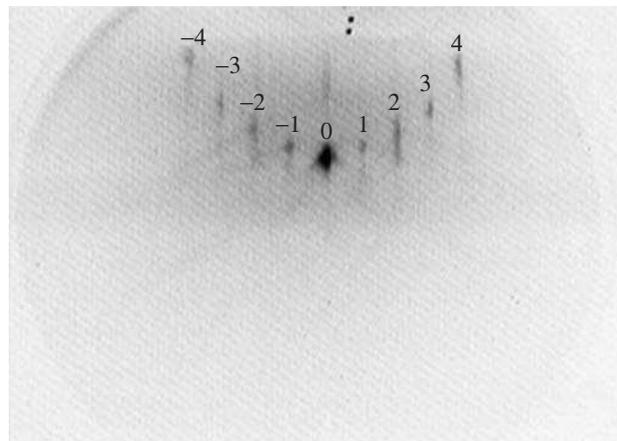
Fig. 1. HEED data for Fe/Si film at Ts = 450 K.

300 to 800 K the oven option was used with the sample holder consisting of a twisted thin aluminum foil sheet where the sample is located in the middle of the resulting rod. In the SQUID the sample was held in a helium atmosphere of 2 mbar pressure providing clean annealing and *in situ* measurements during the annealing.

The easy axis of magnetization is parallel to the film plane at zero field, as evidenced by the typical rectangular magnetization hysteresis loops measured with applied field H parallel to the film plane. The value of the coercivity for the samples ranges from 60 to 200 Oe. The magnetization M versus temperature T measurements for (Fe/Si)n multilayers were carried out in the external field $H = 700$ Oe sufficient to guarantee magnetic saturation. The diamagnetic contribution, determined in an independent measurement on a blank substrate, was subtracted from the data.

2. Results and discussions

We have performed the diffraction data analysis and found the following phases of silicides: β-FeSi$_2$ at $T_s = 450$ K, Fe$_3$Si or Fe$_2$Si and ϵ-FeSi at $T_s = 600$ K; α-FeSi$_2$, Fe$_2$Si, and Si (100) 2×1 at $T_s = 750$ K. This conclusion is preliminary, it agrees to some literature data and disagrees to other. The ellipsometry spectra for $T_s = 450$ K sample has been fitted in the model of the Fe silicide islands, the best fitting gives the FeSi$_2$ islands of the mean radii 100 nm and heights 5 nm with the 30% coverage. The temperature dependence of magnetization on the Si(hkl)/ SiO$_2$/Fe(d)/Si(1.5 nm)/Fe(d)/Si(1.5 nm)/Fe(d)/Si(10 nm) films
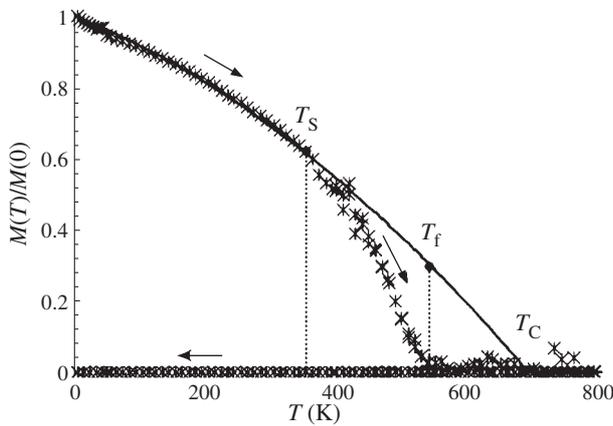
Fig. 2. The magnetization $M(T)$ as a function of temperature (in heating process) of the Si(100)/SiO$_2$/Fe(d)/Si(1.5 nm)/Fe(d)/Si(1.5 nm)/Fe(d)/Si(10 nm) samples.

Fig. 3. Layer resolution density of states in β-FeSi$_2$/Si.

with various values of dFe (1.2, 1.6, 2.6, and 3.8 nm) is presented in the Fig. 2. Magnetization is calculated as the ratio of the total magnetic moment of the sample to the total volume of Fe in the film. It is evident that both the absolute magnetization value and its temperature dependence are different in films with various dFe; with decreasing dFe the value of magnetization at $T = 0$, (M_0) decreases, and the slope of the low temperature dependence increases.

Analysis of our *in situ* high temperature annealing measurements reveals the irreversible process that starts in the temperature range of 400–650 K due to the formation of nonmagnetic silicides, causing modification of the magnetic properties of the sample. Indeed, the magnetization at RT, after cooling from the high temperature region, is totally lost for thin Fe layers below 2.5 nm on a Si(100) substrate. In contrast, for an Fe layer thickness larger than 2.5 nm on a Si(100) substrate, the RT magnetization is decreased but does not vanish.

At low temperatures the M(T) dependence is reservible and is described by the spin wave theory (the Bloch law)

$$M(T) = M_{s0}(1 - BT^{3/2} - CT^{5/2}).$$

It allows to determine such parameters as magnetization at 0 K M_0, and the value of exchange constant via parameter B. This magnetic characteristics are thickness dependent, for Fe(15 nm) $M_0 = (1750 \pm 2)$ Gs, $B = (4.9 \pm 0.2) \times 10^{-6}$ K$^{-3/2}$, $C = (1.35 \pm 0.01) \times 10^{-8}$ K$^{-5/2}$. With increasing Fe layer thickness we observe that the value of the activation energy seems to tend toward the value found for silicide synthesis in bulk layers of iron and silicon. The degree of silicide formation is strongly dependent on the crystalline quality of the multilayers and in particular on the interface roughness and structure. Therefore, the tendency for silicide formation is quite different for samples of different structural quality. The kinetic parameters for the silicide formation found here are related to our polycrystalline samples and are not universal for all types of Fe/Si multilayers. Nevertheless, the *in situ* method to study the magnetic properties by measurement of the high temperature SQUID measurements as Fe silicides form is universal.

To study silicide formation in the Fe/Si interface we have performed the ab initio calculation of the electronic structure of thin slab and β-FeSi$_2$/Si interface by the density functional theory method. The GGA band structure calculations of the thin
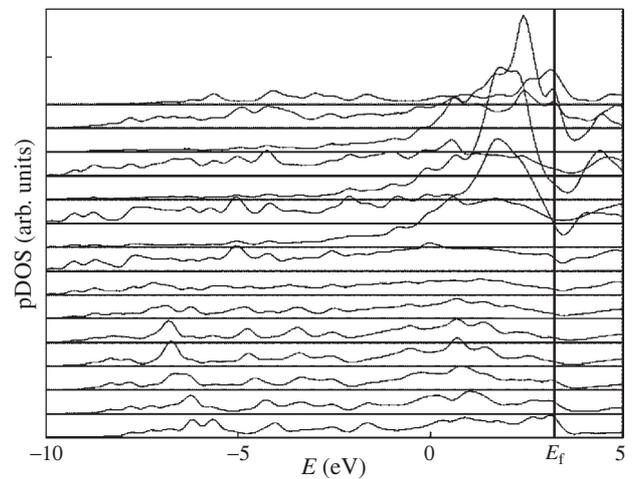
slab and have revealed metallic properties at both surfaces. For the β-FeSi$_2$/Si we have obtained the sharp interface between β-FeSi$_2$ and Si layers (Fig. 3), where the top layer is Fe, lower layers are Si.

3. Conclusions

In summary we have found that different iron silicides are formed depending on the substrate temperature. The β-FeSi2/Si interface may be sharp. Reconstruction of the surface states results in the metallic properties at the surface of β-FeSi$_2$. Preliminary results for HEED and ellipsometry data are published in [6] and of GGA calculations in [7].

References

[1] R.E. Cambley and R.L. Stamps, *J. Phys. Condens. Matter.* **5**, 3727 (1993).
[2] D.E. Burgler *et al*, *J. Phys. Condens. Matter.* **15**, S443 (2003).
[3] M.Yu. Gomoyunova *et al*, *Tech. Phys.* **50 (9)**, 1212 (2005).
[4] S.N. Varnakov *et al*, *Phys. Solid State* **49 (8)**, 1470 (2007).
[5] S.N. Varnakov *et al*, *J. Appl. Phys.* **104**, 094703 (2008).
[6] S.N. Varnakov *et al*, *Vestnik SibSAU* **30**, 45 (2010).
[7] A.S. Fedorov *et al*, *J. of Siberian Federal University. Mathematics and Physics* **4**, N2 (2011).

Electron mobility and high-field drift velocity enhancement in InAlAs/InGaAs/InAlAs quantum well heterostructures

G. B. Galiev[1], *I. S. Vasil'evskii*[2], E. A. Klimov[2], D. S. Ponomarev[2], J. Požela[3], K. Požela[3], A. Sužiedėlis[3],
V. Juciene[3], Č. Paškevič[3], S. Keršulis[3] and V. Stankevič[3]

[1] Institute of Microwave Semiconductor Electronics, RAS, 117105 Moscow, Russia
[2] National Research Nuclear University MEPhI, 115409 Moscow, Russia
[3] Semiconductor Physics Institute, 01108 Vilnius, Lithuania

Abstract. We report on experimental study of electron mobility enhancement by inserting thin (1–3 nm) InAs phonon walls in $In_{0.53}Ga_{0.47}As/In_{0.52}Al_{0.48}As$ quantum well (QW) as well as by increasing InAs content in $In_xGa_{1-x}As/In_yAl_{1-y}As$ heterostructures. The insertion of InAs phonon walls into QW gives the increase in electron mobility by a factor of 1.1–1.3, and enhances saturated high-field drift velocity up to 5×10^7 cm/s.

Introduction

The engineering of electron interaction with polar optical (PO) phonons by inserting thin layers into a quantum well (QW), which reflects PO phonons, is an useful instrument to regulate electron transport and photoelectric properties of heterostructure QWs [1–8]. In particular, there is a great interest to increase the mobility and high-field drift saturation velocity in $In_{0.53}Ga_{0.47}As/In_{0.52}Al_{0.48}As$ channels of HEMTs, which are the basic elements of the microwave electronics in the range of 10^2 GHz, and recently are used for detection and generation of THz range [7–9]. In $In_{0.53}Ga_{0.47}As/In_{0.52}Al_{0.48}As$ quantum well with thickness in the range of about 15–20 nm, the electron scattering by IF phonons is a predominant scattering mechanism. The electron-IF phonon scattering rate is the function of IF phonon frequencies, which are determined by a composition of interface semiconductor materials [5,6].

In the present study we report on the possibility to increase electron mobility and high-field drift velocity using two tools for the regulation of electron-PO phonon scattering rate in InGaAs/InAlAs QW channels: (1) the tuning of interface (IF) phonons by changing a value of InAs content in the ternary alloys of $In_xGa_{1-x}As/In_yAl_{1-y}As$ heterostructures; (2) the regulation of confined PO phonon by inserting InAs of 1–3 nm thick into $In_{0.53}Ga_{0.47}As/In_{0.52}Al_{0.48}As$ QW. These thin phonon walls are transparent for electrons but reflect confined PO phonons.

1. Calculation

The calculated dependence of electron-IF phonon scattering rate in $In_yGa_{1-y}As$ QW on the composition of $In_xAl_{1-x}As$ barrier layer is shown in Fig. 1. One can see that IF phonon scattering rate can be reduced several times by means of increasing the InAs content x in the barrier layer. The growth of the structure with increased InAs content in the barrier demanded the sufficient increase of InAs content in the QW layer too, in order to eliminate the mechanical deformations. The calculated scattering rate by IF phonons in the grown $In_{0.8}Ga_{0.2}As/In_{0.7}Al_{0.3}As$ structure is 1.4 times less than in $In_{0.5}Ga_{0.5}As/In_{0.5}Al_{0.5}As$ one (see Fig. 1). On the other hand, the increased InAs content should also lead to the decrease of electron effective mass by 1.4 times, and thus, to mobility enhancement. But calculations show an electron mobility increase as high as 1.8 times in $In_{0.8}Ga_{0.2}As/In_{0.7}Al_{0.3}As$ QW
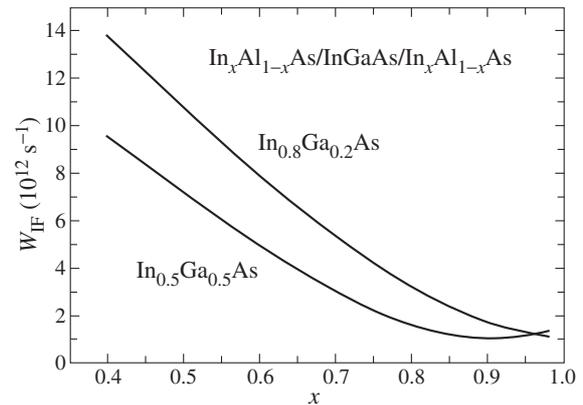
Fig. 1. The dependence of electron-IF phonon scattering rate in the $In_xAl_{1-x}As/In_yGa_{1-y}As/In_xAl_{1-x}As$ QW on x content of the In_x component in the barrier layer. The QW width is 16 nm.

compared with the $In_{0.5}Ga_{0.5}As/In_{0.5}Al_{0.5}As$ one.

So the increase of InAs content in the single QW $In_{0.52}Al_{0.48}As/In_{0.53}Ga_{0.47}As/In_{0.52}Al_{0.48}As$ structure should decrease electron-PO phonon scattering rate. The other possibility is the insertion of InAs phonon wall into InGaAs QW that divides confined phonon wall into several more narrower confined phonon walls. Confinement of PO phonons into several narrow phonon walls decreases the electron-PO phonon scattering rate radically.

2. Samples and the experiment

The samples were grown by MBE on InP substrates. Sample # 1 had single $In_{0.53}Ga_{0.47}As$ 17 nm thick QW. In the sample # 2 3.5 nm central InAs phonon wall was inserted. Sample # 3 had two 1.1 nm GaAs cladding walls at both QW interfaces, and in the Sample # 4 such GaAs walls were combined with two 1.2 nm thick InAs insertions in the QW. These GaAs thin layers in the samples # 3 and # 4 also could serve for the phonon confinement in the QW combined with more strong interface phonon mode origination. Sample # 5 with the high InAs content were grown with help of metamorphic technology and had $In_{0.8}Ga_{0.2}As/In_{0.7}Al_{0.3}As$ single QW with thickness of 16 nm. The mobility values at low fields (500 V/cm) were experimentally obtained from the geometrical magnetoresistance measurements. Sample essentials and the measured mobility and electron concentration are listed in Table 1. To

measure the current-voltage (I-V) characteristics of the structures, mesa structures with the width of 100 μm were fabricated with Au/Ni/Ge ohmic contacts 100×100 μm in area. The distance between the source and drain contacts varied from 5 to 100 μm. To prevent sample from heating the duration of the applied voltage pulse was less than 50 ns.

Table 1. Samples essentials and electron mobility μ and concentration n, $T = 300$ K.

#	x, InAs	Insertions	n (10^{12} cm^{-2})	μ (cm^2/V s)
1	0.52	—	3.4	5500
2	0.52	InAs	2.5	6100
3	0.52	2 GaAs	1.0	6200
4	0.52	2GaAs+2InAs	1.2	8400
5	0.52	—	1.4	12300

3. Results and discussion

To separate the contributions from the changes in electron mobility and electron density to the current dependence on the electric fields, the mobility was determined from magnetoresistance measurements in short 10 μm samples. The measured mobility and sheet electron concentration in the sample # 5 achieves 12 300 cm^2/V s at 300 K and 50 500 cm^2/V s at 77 K.

Figure 2 shows the field dependences of the mobility in the investigated structures. In the fields F of 0–4 kV/cm, the mobility in samples # 2 and # 4 with the inserted InAs, as well as in the samples with the increased InAs content in the sample # 5 are larger than that in the structures without the InAs barriers. At the field $F < 0.5$ kV/cm, the mobility in the sample # 5 is 1.7 times larger than in samples without the barriers. The large mobility increase coincides with the calculated decrease of interface (IF) phonon scattering rate in InAlAs/InGaAs structures [10]. The current non-linearity and saturation take place at the field of 1.5–2 kV/cm, which is significantly less than the threshold field ($F_t \approx 3.4$ kV/cm) for the intervalley $\Gamma - L$ transfer in bulk In$_{0.5}$Ga$_{0.5}$As.

For the drift velocity at 5 kV/cm, we obtained $v_s = 2.0 \times 10^7$ cm/s and $v_s = 3.2 \times 10^7$ cm/s in the samples # 3 and # 4, respectively.

Calculations showed that insertion of InAs phonon wall decreases the electron (with the energy of 45 meV) scattering rate by PO phonons 4.7 times in sample # 2 and 8.7 times

in samples # 3 and # 4. The total electron scattering rate by confined PO and IF phonons is approximately 1.2 times larger in the structures without the InAs barrier than that is in the structures with the InAs barrier.

References

[1] J. Požela, A. Namajunas, K. Požela, and V. Jucienė, *J. Appl. Phys.* **81**, 1775 (1997).

[2] J. Požela, V. Jucienė, A. Namajunas, and K. Požela, *Fiz. Tekh. Poluprovodn.* **31**, 85 (1997).

[3] J. Požela, K. Požela, and V. Jucienė, *Semiconductors* **41**, 1074 (2007).

[4] D.R. Anderson, N.A. Zakhleniuk, M. Babiker, B.K. Ridley, and C.R. Bennet. *Phys. Rev. B* **63**, 245313 (2001).

[5] G.B. Galiev, I.S. Vasil'evskii, E.A. Klimov, V.G. Mokerov and A.A. Cherechukin, *Semiconductors* **40**, 1445 (2006).

[6] J. Požela, K. Požela, A. Shkolnik, A. Sužedėis, V. Jucienė, S. Mikhrin and V. Mikhrin, *Phys. Status Solidi C* **6**, 2713 (2009).

[7] K. Onda, A. Fujihara, A. Vakejima, E. Mizuki, T. Nakayama, H. Miyamoto, Y. Ando and M. Kanamori, *IEEE Electron Device Lett.* **19**, 300 (1998).

[8] N. Dyakonova, A. El Fatimy, J. Lusakowski, and W. Knap, *Appl. Phys. Lett.* **88**, 141906 (2006).

[9] A.L. Orlov, and L.K. Orlov, *Semiconductors* **43**, 652 (2009).

[10] I.S. Vasil'evski, G.B. Galiev, Yu.A. Matveev, E.A. Klimov, J. Požela, K. Požela, A. Sužiedėlis, Č. Paškevič, and V. Jucienė, *Semiconductors* **44**, 898 (2010).
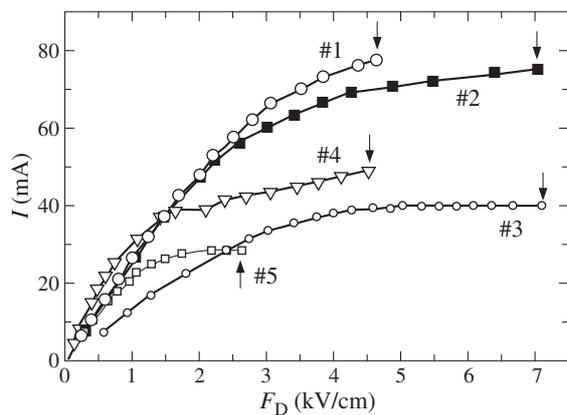
Fig. 2. Electric field dependence of the channel current in the QW samples # 1–# 5. The channel width is 100 μm.

Tunneling Hall effect

P. S. Alekseev

Ioffe Physical-Technical Institute, St Petersburg, Russia

Abstract. Electron tunneling in a semiconductor heterostructure with a barrier in a weak magnetic field applied parallel to the barrier interfaces is analyzed theoretically. A novel mechanism of the Hall effect in this structure is suggested. It is shown that the Hall current in the vicinity of the wide enough barrier is determined by the orbital effect of the magnetic field on the electron motion under the barrier, rather than by the electron $\mathcal{E} \times \mathcal{H}$-drift and scattering in the conductive regions lying to the left and to the right of the barrier.

In recent years, quite a number of papers have been devoted to studying the effect of tunneling through semiconductor barriers in the presence of a magnetic field. Attention to this issue is related both to the fundamental interest in various aspects of the physics of sub-barrier motion of particles, as well as to the fact that the application of a magnetic field gives great opportunities to determine different parameters of the structures. The effect of a non-quantizing magnetic field directed along the barrier interfaces on the tunneling current through a single barrier was experimentally and theoretically studied for the first time in [1]. The magnetic field leads to a slight modification of the tunneling current. The value of this modification was explained quantitatively in [1] in terms of a semiclassical pattern of the electron motion under the barrier modified by the magnetic field. Such an effect can be named the tunneling magnetoresistance.

Here I also consider the tunneling of 3D electrons through a single semiconductor barrier in a weak in-plane magnetic field. The tunneling probability depends on the wave vector in the plane of the interface. It is shown that this dependence gives rise to a surface current along the interface near the barrier. I demonstrate that the density of this current for realistic values of the heterostructure parameters may exceed the 3D Hall current density described by the Drude formulas. Such a generation of the in-plane electric current due to the cyclotron effect of the magnetic field under the barrier can be named the tunneling Hall effect [2].

Regions to the right and to the left of the barrier are equally strongly doped with donors and the temperature is low enough. If a bias U_0/e is applied to the structure, its main part falls on the dielectric barrier (see Fig. 1). The magnetic field is classical: $\hbar\omega_c \ll E_F$. Hence, an electron moves along the classical cycloidal trajectory in both the right- and left-hand regions. This motion is interrupted by scattering events on the chaotic potential of donors and/or on acoustic phonons (the corresponding scattering time τ is considered to be equal within a numerical constant to the momentum relaxation time). The tunneling current j_z flows along the z axis, being largely controlled by the barrier transparency, rather than by the electron scattering. Far from the barrier, the Hall current (or the Hall voltage) is due to the $\mathcal{E} \times \mathcal{H}$-drift and scattering and is given by the classical Drude formulas.

As the magnetic field is non-quantizing, it is true that $l_m k_F \gg 1$ and $r_c \gg k_F^{-1}$ ($l_m = \sqrt{c\hbar/e\mathcal{H}}$ is the magnetic length; $r_c = l_m^2 k_F$ and $2\pi/k_F$ are the cyclotron radius and the wavelength of a characteristic electron). Thus, electrons in the right- and left-hand regions can be described as classical wave packets with the width Δx, $r_c \gg \Delta x \gg k_F^{-1}$, and the center
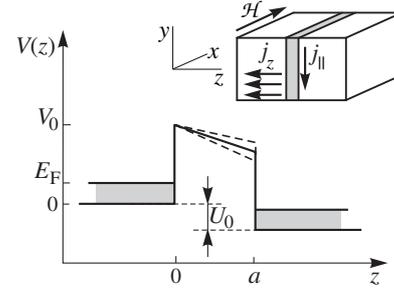
Fig. 1. Energy diagram of the heterostructure. The magnetic field modifies the barrier as shown by use of dashed lines. In the inset: heterostructure with a barrier, an in-plane magnetic field, and the directions of the tunneling current ($\mathbf{j}_z$) and the tunneling Hall current ($\mathbf{j}_\parallel$).

$\bar{\mathbf{r}}(t)$, moving as a classical particle. When the wave packet center $\bar{\mathbf{r}}(t)$ reaches the barrier (moment t_1), the wave packet is partly transmitted through, and partly reflected from the barrier as a quantum electron with the wave vector $m\dot{\bar{\mathbf{r}}}(t_1)/\hbar$. For this reason, the effect of the magnetic field on the electron motion outside the barrier should be neglected when we study the tunneling process. Thus, in further calculations I assume that the magnetic field exists only within the barrier.

The general concept of the tunneling Hall effect is following. Similarly to the usual "3D" situation, the electron motion under the barrier is accompanied by a cyclotron effect of the magnetic field in the (y, z)-plane. Quantitatively, this is reflected by the fact that the incident electrons with k_y and $-k_y$ have different tunneling and reflection amplitudes. Thus, it is reasonable to believe that, for some heterostructure parameters, the Hall (y-directed) current within a distance of about the scattering length l_{sc} from the barrier may be determined by a tunneling process, rather than by the 3D mechanism. It is noteworthy that a similar effect of the "filtering" of the electron wave vectors along the barrier interface was theoretically studied for the 2D electrons tunneling through the 1D "magnetic barriers" formed by the inhomogeneous magnetic field [3].

Let the barrier width a be substantially smaller than r_c: $r_c \gg a$. It is essential to assume that the values of E_F and U_0 are on the same order of magnitude and far smaller than the barrier height V_0. The barrier is considered to be wide, $k_0 a \gg 1$ ($k_0 = \sqrt{2mV_0}/\hbar$).

With the assumption of the absence of the magnetic field outside the barrier, the classification of electron states is the same as that in the absence of a magnetic field. The electron states in the right- and left-hand regions are plane waves partly transmitted through, and partly reflected from the barrier. It

is convenient to take a vector potential in the Landau gauge: $\mathbf{A}(\mathbf{r}) = 0$ in the left-hand region, $\mathbf{A}(\mathbf{r}) = -\mathcal{H}z\mathbf{e}_y$ within the barrier, and $\mathbf{A}(\mathbf{r}) = -\mathcal{H}a\mathbf{e}_y$ in the right-hand region. As the vector potential contains only the z space coordinate, the electron wave functions are the plane waves in the (x, y)-plane: $\psi_{\mathbf{k}}(\mathbf{r}) = e^{i(k_x x + k_y y)}u_{k_y,k_z}(z)$. It was shown that the effect of the magnetic field can by described as the weak k_y-dependent modification of the shape of the heterostructure potential $V(z)$ (see Fig. 1); this modification results in the dependence of the functions $u(z) \equiv u_{k_y,k_z}(z)$ on the magnetic field and k_y. The continuity of the zeroth and first derivatives of the functions $u(z)$, which are $u(z) = e^{ik_z z} + re^{-ik_z z}$ and $u(z) = t\,e^{ik_z^r z}$ in the left- and right-hand regions, should be maintained to find the tunneling coefficient $D = (k_z^r/k_z)|t|^2$. Here, the quantity $k_z^r = k_z^r(k_z, k_y)$ is the z component of the wave vector in the right-hand region modified by the additional potentials of the electric and the magnetic fields.

In order to simplify calculations, it is reasonable to accept the following additional restriction. Let me consider that the magnetic field affects the barrier transparency only by weak modifying the classical action in the argument of the functions "sh" and "ch" in the electron wave function $u(z)$ under the barrier: $\delta S_{\mathrm{mag}}/\hbar \ll 1$. It was confirmed that this situation takes place if the inequalities $k_F a \gg k_0/k_F$ and $(k_F a)^2 \ll k_0 r_c$ are satisfied. For this case, the transmission coefficient $D = (k_z^r/k_z)|t|^2 = 1 - |r|^2$ is:

$$D(k_z, k_y) = \frac{16\,k_z k_z^r}{k_0^2}\,e^{-2\tilde{k}_0 a}\left[1 + \frac{k_y\,a^2}{k_0\,l_m^2}\right], \qquad (1)$$

where $\tilde{k}_0 = \sqrt{2m(V_0 - U_0/2)}/\hbar$.

Let me restrict the analysis to calculation of the tunneling Hall current in the right-hand region, which is due to electrons tunneled from the left-hand region only, with the k_y-dependent reflection of electrons in the right-hand region disregarded. This corresponds to the case in which the applied bias is high enough: $U_0 > E_F$ (but, nevertheless, $U_0 \sim E_F$; see Fig. 1) and $T = 0$. The fact that the tunneling probability (1) depends on k_y results in that all the tunneled electrons, which had a symmetrical distribution function in the left-hand region, will have a nonzero mean y-directed momentum in the right-hand region. During the motion of the tunneled electrons in the z direction in the right-hand region, their scattering and, thus, the relaxation of their mean momentum will occur. So, a surface current will flow near the right-hand barrier edge in a layer with a width of about l_{sc}.

Following [4], I calculate the flux (in the z direction) of the y component of the velocity of tunneled electrons as a sum of values $v_z v_y$ multiplied by the transmission coefficient over all the populated states in the left-hand region with $k_z > 0$. The surface current $j_{||}$ is a product of this flux by $-e$ and τ. A simple calculation based on (1) gives:

$$j_{||} = -C_{||}\,\frac{e\,\hbar^2\,\tau\,k_F^8\,a^2\,e^{-2\tilde{k}_0 a}}{m^2\,k_0^3\,l_m^2}, \qquad (2)$$

where $C_{||} = C_{||}(U_0)$ is a numeric constant. Note that a similar calculation for the tunneling current density yields:

$$j_z = -C_z\,\frac{e\,\hbar\,k_F^6\,e^{-2\tilde{k}_0 a}}{m\,k_0^2}, \qquad (3)$$

where $C_z = C_z(U_0)$ is also a numeric constant.

On base of the Drude formulas and (2), it was shown that the 3D Hall current and the tunneling Hall current have opposite directions. The result (2) is linear in $\mathcal{H}$, whereas the magnetic field correction to j_z is quadratic in $\mathcal{H}$ [1].

The surface tunneling Hall current can be observed if its density exceeds that of the 3D Hall current. To estimate the tunneling Hall current density (near the barrier), $j_{||}$ should be divided by the scattering length $l_{\mathrm{sc}} = \hbar\langle k_z^r\rangle\tau/m$: $j_y^{\mathrm{tunn}} = j_{||}/l_{\mathrm{sc}}$, where $\langle k_z^r\rangle$ is equal to k_F by the order of magnitude. The Drude formulas for the 3D Hall current density lead to: $j_y^{3D} = j_z\,\omega_c\,\tau$. Using this equation, (2) and (3), we obtain: $[,j_y^{\mathrm{tunn}}/j_y^{3D}] \sim [(k_F a)^2/(k_0 l_{\mathrm{sc}})]$. Now, we can formulate a criterion for prevalence of the tunneling Hall current over the 3D Hall current: $k_F a \gg \sqrt{k_0 l_{\mathrm{sc}}}$. At the same time, it is necessary that $a < l_{\mathrm{sc}}$ for the ballistic tunneling picture to be relevant.

To summarize all the discussed conditions, the structure configuration must satisfy the inequalities: $k_F \ll k_0$ and $k_F a \gg k_0/k_F$. The scattering length must lie within the interval: $a < l_{\mathrm{sc}} \ll (k_F a)^2/k_0$. The magnetic field must have a cyclotron radius $r_c \gg (k_F a)^2/k_0$. Note that it follows from these inequalities that $a \gg k_F^{-1}$ and $r_c \gg a, l_{\mathrm{sc}}$.

In paper [1], a GaAs/AlGaAs-heterostructure with the parameters $V_0 = 43$ meV, $a = 25$ nm, $E_F = 12$ meV was studied. It was shown that for this structure, all the required inequalities can be satisfied with reasonable l_{sc} and $\mathcal{H}$. The surface current calculated using (2) is $j_{||} \sim 3 \times 10^{-7}$ A/cm for this structure at $l_{\mathrm{sc}} = 3 \times 10^{-6}$ cm and $\mathcal{H} = 1$ T.

It is reasonable to try to measure the suggested effect in a heterostructure with several barriers (i.e., in a superlattice with wide quantum well regions). If the distance between barriers is about l_{sc}, the Hall effect in the whole superlattice will be mainly due to the sum of the tunneling Hall effects near each barrier.

References

[1] P. Gueret, A. Baratoff, and E. Marclay, *Europhys. Lett.* **3**, 367 (1987).

[2] P.S. Alekseev, *Pis'ma v ZhETF* **92**, 872 (2010).

[3] A. Matulis, F.M. Peeters, and P. Vasilopoulos, *Phys. Rev. Lett.* **72**, 1518 (1994); G. Papp and F.M. Peeters, *phys. stat. sol. (b)* **225**, 433 (2001).

[4] S.A. Tarasenko, V.I. Perel', and I.N. Yassievich, *Phys. Rev. Lett.* **93**, 056601 (2004).

Relevant quantum corrections to conductivity of two-dimensional electron gas at classically strong magnetic fields

A. A. Greshnov

Ioffe Physical-Technical Institute, St Petersburg, Russia

Abstract. Quantum corrections to conductivity of the two-dimensional electron gas have been studied in the regime of classically strong magnetic fields, $\omega_c \tau \gg 1$. It is found that temperature dependence of the second-order quantum correction exhibits unexpectedly divergent behaviour, $\delta\sigma_2(T) \propto \ln^2 T$. This fact is in contradiction with the famous one-parameter scaling theory of conductivity [1] and results of the previous studies focused on the so-called unitary ensemble instead of Landau quantization [2]. Moreover, our results imply violation of the one-parameter scaling in the arbitrary magnetic fields, including classically weak.

Introduction

Initially, when hypothesis of the one-parameter scaling of conductivity had been introduced [1], it was implied to hold under quite general conditions, including presence of an external magnetic field. However, after discovery of the integer quantum Hall effect it became obvious that diagonal component of the conductivity tensor, σ_{xx}, cannot be scaled alone, without σ_{xy} [3]. This peculiarity, contradicting to phenomenological ideas of Ref. [1] and a theory of Ref. [2], was attributed to the non-perturbative corrections to σ_{xx} which are called instantons in the field-theory language [4]. Though Ref. [3] gives quite charming recipe of the two-parameter scaling to overcome inconsistency of the one-parameter version, it has never been confirmed by any experimental or numerical results [5]. In the present paper it is shown that violation of the one-parameter scaling occurs perturbatively, namely due to the quantum correction to conductivity of the second order in $1/(2N + 1)$, $N \gg 1$ being Landau level number associated with the Fermi surface. Though currently only the regime of classically strong magnetic fields ($\omega_c \tau \gg 1$) has been studied, we speculate that violation of the one-parameter scaling takes place in the arbitrary magnetic fields due to the analytical properties of σ_{xx}.

1. Theory

In order to calculate the diagonal component of conductivity tensor, σ_{xx}, we apply the usual impurity diagrammatic technique and Kubo formula

$$\sigma_{xx} = -\frac{e^2\hbar}{4\pi S} \overline{\text{Tr}\{\hat{v}_x(\hat{G}^R - \hat{G}^A)\hat{v}_x(\hat{G}^R - \hat{G}^A)\}}, \quad (1)$$

taking into account that only dissimilar (RA) contributions are able to give divergent contributions due to the diffuson ladder. Here S is a sample area, $G^{R,A}$ stands for the retarded and advanced one-electron (non-averaged) Green functions, and the overline implies averaging over the random impurity configuration. We consider the Gaussian model of disorder with the short-range correlator $\overline{U(\mathbf{r})U(\mathbf{r'})} = W\delta(\mathbf{r} - \mathbf{r'})$ and accept the self-consistent Born approximation [6] leading to

$$G_E^{R,A}(\mathbf{r}, \mathbf{r'}) = \sum_n G_n^{R,A}\left(\frac{E - \hbar\omega_c(n+1/2)}{\Gamma}\right) K_n(\mathbf{r}, \mathbf{r'}), \quad (2)$$

$$G_N^{R,A}(x) = \frac{2}{\Gamma}\left(x \mp i\sqrt{1-x^2}\right), \quad (3)$$

$$G_{N+\Delta}^{R,A}(x) = -\frac{1}{\Delta\hbar\omega_c} \mp i\frac{\Gamma\sqrt{1-x^2}}{2\Delta^2(\hbar\omega_c)^2}, \quad (4)$$

$$K_n(\mathbf{r}, \mathbf{r'}) = \sum_k \Psi_{nk}(\mathbf{r})\Psi_{nk}^*(\mathbf{r'}), \quad (5)$$

in the limit of $N \gg 1$, $\omega_c\tau \gg 1$. Here N is Landau level number corresponding to the Fermi energy E_F, $\Psi_{nk}(\mathbf{r})$ are eigenfunctions of the cyclotron motion [7], and the Landau level width Γ given by

$$\Gamma = \sqrt{\frac{4W}{2\pi l_B^2}} = \sqrt{\frac{2}{\pi}\frac{\hbar^2\omega_c}{\tau}} \quad (6)$$

appears not to be just $\hbar/\tau$ due to enhancement of scattering in the $\omega_c\tau \gg 1$ regime. Moreover, the Fermi wave-vector k_F and the scattering length l in this regime are substituted by $l_B^{-1}\sqrt{2N+1}$ and $r_c = l_B\sqrt{2N+1}$ so that $2N + 1$ gives an effective $k_F l$ value which is assumed to be large.

Since the logarithmical divergence of the first-order quantum correction to Drude–Ando conductivity

$$\sigma_0 = \frac{(2N+1)(1-x^2)}{\pi}\frac{e^2}{h} \quad (7)$$

is well known to cease in the presence of a magnetic field, hereafter we concentrate on the second-order correction $\delta\sigma_2$ which is given by a sum of the thirteen diagrams also known as Hikami boxes [2] (Fig. 1). In the case of zero magnetic field each of the diagrams (A–M) are proportional to $\ln^2 \varepsilon$ ($\varepsilon = \tau/\tau_\phi(T)$) but so that the total coefficient is zero and $\delta\sigma_2(B = 0) \propto \ln \varepsilon$ instead of $\ln^2 \varepsilon$. However, this cancellation ceases to work in the strong magnetic fields ($\omega_c\tau \gg 1$): in this case almost all the contributions except (B), (C) and (D) appear to be small in $(\omega_c\tau)^{-1}$. For example, the diagram (A) gives

$$\delta\sigma_A = \frac{1}{\omega_c\tau}\frac{1-x^2}{4\pi}\frac{\ln^2\varepsilon}{2N+1}\frac{e^2}{h}. \quad (8)$$

Skipping the explicit expressions for the contributions (E–M), which are also small in $(\omega_c\tau)^{-1}$, we focus on the diagrams (B–D). When these contributions are calculated using original Hikami boxes, i.e. with single impurity RR (AA) lines instead of the full arcs depicted at the bottom of Fig. 1, we obtain

$$\delta\sigma_{B+C}^{(0)} = \frac{1}{2\pi}\frac{\ln^2\varepsilon}{2N+1}\frac{e^2}{h}, \quad (9)$$

$$\delta\sigma_D^{(0)} = \frac{1-2x^2}{2\pi}\frac{\ln^2\varepsilon}{2N+1}\frac{e^2}{h}, \quad (10)$$
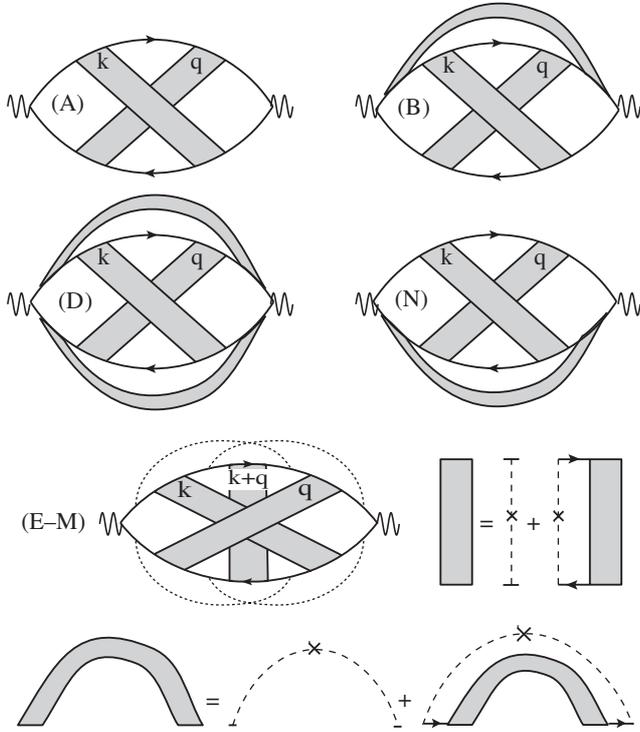
Fig. 1. Relevant diagrams for quantum corrections to conductivity of the second order in $1/(2N + 1)$.

so that its sum is just proportional to x^2. However, self-consistent Born approximation involves nesting of the impurity lines, this additional dressing of the diagrams gives the factors

$$B_N^{\mathrm{R,A}} = \frac{1}{1 - \left(\frac{\Gamma}{2} G_N^{\mathrm{R,A}}\right)^2} \qquad (11)$$

for the retarded and advanced arcs correspondingly. Taking this peculiarity into account we come to the final answer

$$\delta\sigma_{\mathrm{B+C}} = \frac{1}{4\pi} \frac{\ln^2 \varepsilon}{2N + 1} \frac{e^2}{h}, \qquad (12)$$

$$\delta\sigma_{\mathrm{D}} = -\frac{1 - 2x^2}{2\pi} \frac{\ln^2 \varepsilon}{2N + 1} \frac{e^2}{h}, \qquad (13)$$

$$\delta\sigma_2 = \frac{1}{8\pi(1-x^2)} \frac{\ln^2 \varepsilon}{2N+1} \frac{e^2}{h} = \frac{\ln^2 \varepsilon}{8\pi^2\sigma_0} \left(\frac{e^2}{h}\right)^2. \quad (14)$$

The plot of $\delta\sigma_2$ as a function of the dimensionless Fermi energy counted from the center of the corresponding Landau level N, $x = (E_{\mathrm{F}} - \hbar\omega_{\mathrm{c}}(N + 1/2))/\Gamma$, is presented in Fig. 2.

2. Discussion and conclusions

First of all, we note that according to Eq. (14) $\delta\sigma_2$ can be expressed as a function of σ_0 and ε which (at the first glance) confirms the scaling hypothesis. However, it is easy to check that equations of the renormalization group involves vanishing of the leading logarithms. While this condition (i.e. zero coefficient before $\ln^2 \varepsilon/(2N+1)$ in the perturbation series) is fulfilled at $B = 0$ as checked in Ref. [8], it is not the case at $B \neq 0$. Thus, we argue that application of external magnetic field violates the one-parameter scaling of conductivity, especially in
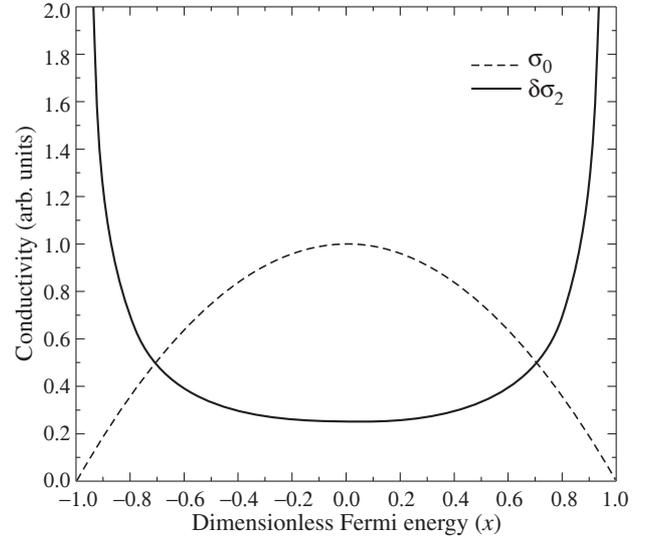
Fig. 2. Drude–Ando conductivity σ_0 and the second-order quantum correction $\delta\sigma_2$ as the functions of the dimensionless Fermi energy $x = (E_{\mathrm{F}} - \hbar\omega_{\mathrm{c}}(N + 1/2))/\Gamma$.

the region of classically strong magnetic fields, $\omega_{\mathrm{c}}\tau \gg 1$. Secondly, we see that sign of $\delta\sigma_2$ is always positive (except for the Landau level edges $|x| = 1$ where it diverges due to the constraints of the self-consistent Born approximation). This fact is even more shocking since σ_{xx} in the regime of the integer quantum Hall is believed to be always less than the "bare" Drude–Ando values, going with the decreasing temperature to zero except for the Landau level centers $x = 0$ (corresponding to the plateau-plateau transitions). Evidently, these quite unexpected features of the quantum corrections to conductivity of the leading order in $1/(2N + 1)$ shed more light upon the physics behind magnetotransport in the two-dimensional structures and challenge building a bridge between the phenomena of weak localization and the integer quantum Hall effect.

References

[1] E. Abrahams *et al*, *Phys. Rev. Lett.* **42**, 673 (1979).
[2] S. Hikami, *Phys. Rev. B* **24**, 2671 (1981).
[3] D.E. Khmelnitskii, *JETP Lett.* **38**, 454 (1983).
[4] H. Levine, S.B. Libby, A.M.M. Pruisken, *Phys. Rev. Lett.* **51**, 1915 (1983).
[5] A.A. Greshnov, G.G. Zegrya, *Physica E* **40**, 1185 (2008); A.A. Greshnov, G.G. Zegrya, E.N. Kolesnikova, *JETP* **107**, 491 (2008); A.A. Greshnov, G.G. Zegrya, Proc. 15th Int. Symp. "Nanostructures: Physics and Technology", Novosibirsk, 2007.
[6] T. Ando, Y. Uemura, *J. Phys. Soc. Jpn.* **36**, 959 (1974); T. Ando, *J. Phys. Soc. Jpn.* **37**, 1233 (1974).
[7] L.D. Landau, E.M. Lifshitz, Quantum mechanics, § 112, Pergamon, Oxford, 1977.
[8] L.P. Gor'kov *et al*, *JETP Lett.* **30**, 248 (1979).

TN.05o

Interaction correction to conductivity of double quantum well heterostructures near balance

A. V. Germanenko[1], G. M. Minkov[1,2], O. E. Rut[1], A. A. Sherstobitov[1,2] and I. V. Soldatov[1]

[1] Ural State University, 620000 Ekaterinburg, Russia
[2] Institute of Metal Physics, Ural Branch of RAS, 620990 Ekaterinburg, Russia

Abstract. The electron-electron interaction quantum correction to the conductivity of the gated double quantum well $Al_xGa_{1-x}As/GaAs$ structures is investigated experimentally. The analysis of the temperature and magnetic field dependences of the conductivity tensor allows us to obtain reliably the diffusion part of the interaction correction for the regimes when the structure is balanced and when only one quantum well is occupied. The surprising result is that the interaction correction does not reveal resonant behavior; it is practically the same for both regimes.

Double quantum well (DQW) structures exhibit a number of salient features (see, e.g., Refs. [1,2,3,4] and references therein). The quantum corrections to the conductivity are also expected to demonstrate peculiar behavior when the population of the quantum wells and/or the interwell transition rate is varied. The interference quantum correction in DWQ's is studied in [5,6,7,9], where the specific features of the interference induced magnetoresistance and dephasing processes are investigated both theoretically and experimentally. The correction due to the electron-electron (*e-e*) interaction is investigated significantly less [9,10].

The contribution of *e-e* interaction to the conductivity is determined by two terms: singlet and multiplet. Singlet term does not depend on interaction constant and it favors localization, i.e., it leads to the conductivity decrease with lowering temperature. In contrast, the contribution of the interaction in the multiplet channel depends on the interaction constant γ_2 and gives antilocalization correction for ordinary semiconductor structures. For diffusion regime ($T\tau \ll 1$, where τ is the transport relaxation time), the interaction correction to the conductivity is as follows [11]

$$\begin{aligned} \delta\sigma_{ee} &= K_{ee}G_0\ln(T\tau), \\ K_{ee} &= 1 + \left(4n_v^2 - 1\right)\left[1 - \frac{1+\gamma_2}{\gamma_2}\ln(1+\gamma_2)\right], \end{aligned} \quad (1)$$

where $G_0 = e^2/\pi h$, n_v is the number of valleys. The first and second terms correspond to the contributions in the singlet and multiplet channel, respectively. As seen the coefficient K_{ee} depends on the valley degeneracy. For the 2D gas with the single valley spectrum, $n_v = 1$, at $\gamma_2 = 0.28$, that corresponds to the electron density $n \simeq 10^{12}$ cm^{-2} [12], the multiplet contribution is less than the singlet one and $K_{ee} \simeq +0.6$. For the case of the two valleys electron spectrum, as it takes place in [100] Si-MOS 2D structures, the correction in the multiplet channel is larger than that in singlet one and the coefficient K_{ee} for the same electron density should have opposite sign, $K_{ee} \simeq -0.9$.

It seems that the double quantum well heterostructures based on single valley semiconductors should demonstrate analogous behavior. The crucial change of the interaction contribution should be observed when changing the relation between the electron densities in the wells with the help of gate electrode, for example. If one naively supposes that the total correction is the sum of the interaction contributions from each of the wells, the value of K_{ee} about $+1$ should be observed for particular case of the different but close electron densities in the wells, $n_1 \approx n_2 \approx 5 \times 10^{11}$ cm^{-2}. When the electron density is the same in the wells, $n_1 = n_2 = 5 \times 10^{11}$ cm^{-2}, we should deal with the analog of the two valleys structure, for which the coefficient in the multiplet term becomes equal to 15, the interaction contribution becomes antilocalizing with $K_{ee} \simeq -0.9$. Of course, such the giant change of K_{ee} can be observed in special structures only. Namely, the electron densities and mobilities in the wells should be close. Moreover, the scatterers should be common for the carriers in the different wells in the sense that each specific impurity should scatter the carriers of the lower and upper wells identically. In addition, the interwell distance d should be small, $\kappa d < 1$, where κ is the inverse screening length, but the interwell transition time t_{12} should be large, $t_{12} \gg 1/T$. In reality, it is very difficult to fulfil all these requirements. However, because the qualitative speculation presented above predicts very huge effect, it seems that significant change of the interaction correction in double well structure at varying of the density should be observed easily.

The results presented in this paper have been obtained for just the same samples, for which the weak localization effect has been investigated in [8]. The main parameters of the samples for two regimes considered here are listed in the Table. The regime when only the lower quantum well is occupied is referred as SQW regime. Balance is the regime of the equal electron densities in the wells.

The dependences of σ_i and $\Delta\sigma_i = \sigma_i(4.2\text{ K}) - \sigma_i(1.35\text{ K})$ ($i = xx, xy$) on the magnetic field taken for the structure 3243 at $V_g = -1.5$ V are presented in Figs. 1(a) and 1(b), respectively. One can see that $\Delta\sigma_{xx}$ decreases strongly up to $B = 1$ T therewith $\Delta\sigma_{xy}$ is not small. Such variations of $\Delta\sigma_{xx}$ and $\Delta\sigma_{xy}$ with the changing temperature and magnetic field is caused by the ballistic part of interaction correction, which renormalizes the mobility.

To extract the diffusion part of the interaction correction, we have used the unique property of the diffusion part of this correction: it contributes to the one component of the conductivity tensor, namely, to σ_{xx}, whereas $\delta\sigma_{xy} = 0$. Three differ-

Table 1. Parameters of the structures investigated.

Structure	#3243		#3154	
regime	SQW	balance	SQW	balance
V_g (V)	−4.1	−1.5	−3.6	−2.0
n (10^{11} cm^{-2})	7.0	7.5	4.0	4.5
μ (10^3 cm^2/V s)	14.5	15	4.8	6.5
$K_{ee} \pm 0.05$	0.60	0.57	0.53	0.50
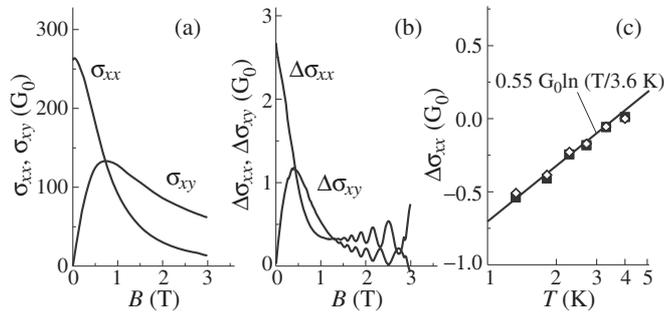
Fig. 1. (a) The magnetic field dependences of σ_{xx} and σ_{xy} taken at $T = 1.35$ K. (b) The magnetic field dependences of $\Delta\sigma_{xx,xy} = \sigma_{xx,xy}(4.2$ K$) - \sigma_{xx,xy}(1.35$ K$)$. (c) The temperature dependences of $\Delta\sigma_{xx} = \sigma_{xx}(4.2$ K$) - \sigma_{xx}(T)$ at $B = 1/\mu = 0.67$ T (squares) and that found from the Hall effect as described in text (diamonds). $V_g = -1.5$ V.

Fig. 2. The temperature dependence of the diffusion e-e interaction correction $\Delta\delta\sigma_{ee} = \delta\sigma_{ee}(T) - \delta\sigma_{ee}(1.35$ K$)$ for different magnetic fields near the balance (a) and in the SQW-regime (b). (c) The K_{ee} values plotted against the gate voltage. The line is obtained when sweeping the gate voltage at different temperatures.

ent ways have been used. They are the following: (i) analysis of the T-dependence of σ_{xx} at $B = 1/\mu$ (ii) obtaining of the interaction correction from the T-dependence of the Hall coefficient: $\Delta\sigma_{xx}/\sigma_{xx} \simeq -\Delta R_H/2R_H$ (iii) obtaining of $\delta\sigma_{xx}$ over the whole magnetic field range with the use of the method described in Ref. [13].

All three methods give the same results for both regimes, when the heterostructure is in the balance and when only the lower quantum well is occupied. In both regimes the correction $\delta\sigma_{ee}$ is logarithmic in the temperature and practically independent of the magnetic field [see Figs. 1(c) and Fig. 2]. In the balance, the experimental value of the parameter K_{ee} is 0.57 ± 0.05. In the SQW-regime, we have obtained $K_{ee} = 0.60 \pm 0.05$ that corresponds to $\gamma_2 \simeq 0.29$. This value is in a good agreement with the theoretical estimate $\gamma_2 = 0.31$ [12].

The surprising thing is that the value of K_{ee} in the balance practically coincides with that for the regime when only one quantum well is occupied. Such coincidence seems strange. It does not agree with our qualitative consideration in the beginning of the paper.

The resonant change of K_{ee} occurs quite possible within a very narrow range of V_g and we could overlook it measuring K_{ee} at fixed V_g. To check such an occasion we have measured ρ_{xx} and ρ_{xy} at fixed magnetic field $B = 1/\mu_b$, where μ_b stands for the mobility in the balance, and different temperatures sweeping the gate voltage. The dependence of K_{ee} vs V_g was found as the slope of the σ_{xx} vs $\ln T$ plot. As seen from Fig. 2(c) K_{ee} changes monotonically and exhibits no resonant feature within the sweeping V_g range.

Thus, all the results presented above show that the noticeable resonant change of K_{ee} to say nothing of change of its sign is not observed in the structures investigated.

One possible reason of the absence of the K_{ee} resonance can be the fact that the scatterers are not common enough in spite of our efforts to design special structures and despite proximity of the mobilities in the wells. The unavoidable variation in the scatterers positions with respect to the center of the barrier results in the fact that the specific impurity scatters differently the carriers of the lower and upper wells. Besides, the interwell distance is not sufficiently small in our case. The parameter κd, where d is the distance between the centers of the well, is equal to 3.6, so the interaction between the electrons in the different wells is noticeably weaker than that between electrons within

the one well.

On the other hand, the interaction correction for the structure with the large interwell distance ($\kappa d \gg 1$) should be equal to the sum of the correction in wells. The value of K_{ee} for the case when one well is occupied is 0.60 ± 0.05 for structure 3243 (see Table). So, at $V_g = -1.5$ V, when both wells are occupied and each of them has approximately the same density, the value of K_{ee} would be expected as large as $\simeq 1.2$. In reality the K_{ee} value is twice less. We conceive that this paradox can be resolved by taking into account the screening of the e-e interaction between the carriers in the one well by the carriers of the other one, which was not taken into account at qualitative consideration above. This screening reduces the e-e interaction strength and, consequently, diminishes the interaction contribution to the conductivity.

Thus, for the adequate understanding of the role of the e-e interaction in the double well structures, the theory, which properly takes into account the interaction in the singlet and multiplet channels and specifics of the screening for different interwell distances, is necessary.

References

[1] A. Palevski *et al*, *Phys. Rev. Lett.* **65**, 1929 (1990).
[2] N.E. Harff *et al*, *Phys. Rev. B* **55**, R13405 (1997).
[3] R. Fletcher *et al*, *Phys. Rev. B* **71**, 155310 (2005).
[4] N.C. Mamani *et al*, *Phys. Rev. B* **80**, 075308 (2009).
[5] N.S. Averkiev *et al*, *Fiz. Tekh. Poluprovodn.* **32**, 1219 (1998).
[6] O.E. Raichev and P. Vasilopoulos, *J. Phys.: Condens. Matter* **12**, 589 (2000).
[7] G.M. Minkov *et al*, *Nanotechnology* **11**, 406 (2000).
[8] G.M. Minkov *et al*, *Phys. Rev. B* **82**, 165325 (2010).
[9] I.R. Pagnossin *et al*, *Phys. Rev. B* **78**, 115311 (2008).
[10] Y.G. Arapov *et al*, *Low Temp. Phys.* **35**, 32 (2009).
[11] A.M. Finkel'stein, *Zh. Eksp. Teor. Fiz.* **84**, 168 (1983).
[12] G. Zala *et al*, *Phys. Rev. B* **64**, 214204 (2001).
[13] G.M. Minkov *et al*, *Phys. Rev. B* **67**, 205306 (2003).

Electric-field control of electron interference effects in semiconductor 1D nanostructures

V. A. Petrov and A. V. Nikitin

Institute of Radio Engineering and Electronics RAS, Moscow, 125009, Russia

Abstract. The influence of a constant transverse electric field on penetration of quantum-mechanical current density $j_x(x, z)$ under semi-infinite potential barrier in height V at the interference of the electron waves in semiconductor 2D nanostructures have been theoretically studied. We have considered a situation when in the 2D nanostructure at the left, from QW_1 the electronic wave of unit amplitude with energy $E_x < V$ on such barrier in QW_2 falls. We have shown, that in such structures the situation when under a barrier the quantum-mechanical current density $ej_x(x, z) \neq 0$ and its amplitude exponentially dumped at $x \to \infty$ is possible.

Introduction

At present, advances in nanotechnology allow to create semiconductor nanostructures in which linear dimensions 1D or 2D of the conductive channel in the direction of propagation of the electron wave are smaller than the mean free path of the electron. In such a channel particles move in a ballistic regime that allows to study experimentally the effects of ballistic transport in such structures, in particular, various electron interference effects [1]. A large number of theoretical works were devoted to the investigation of electron quantum ballistic transport in 1D and 2D nanostructures whose common feature is the presence in quantum channels of regions of a sharp (nonadiabatic) variation either of the channel's geometry or a potential relief in it [2–4].

The basic goal of our work is to theoretically investigate behaviour of the probability current density $j_x(x, z)$ (or quantum-mechanical current density $ej_x(x, z)$, e being an electron charge) at falling of the electron wave propagating along x-axis on semi-infinite potential barrier (a potential wall) in height V modified by a constant transverse (along z-axis; z-axis being the axis of the quantization) electric field with strength F in semiconductor 2D nanostructure. We have considered a situation when in 2D nanostructure at the left, from region 1 ($x < 0$, QW_1) the electronic wave of unit amplitude with energy $E_x < V$ on such barrier in region 2 ($x > 0$, QW_2) falls.

We have shown, that in a situation when the electron wave falls on the first quantum-confined electron subband in QW_1 and longitudinal energy E_x of the particle less than energy of the bottom of the second subband in this reg. 1 and reflection of the electron wave probably only on the same first subband the quantum-mechanical current density $ej_x(x, z)$ in reg. 2 equal to zero. However, if energy of the particle in reg. 1 is more than energy of the bottom of the second quantum-confined electron subband in QW_1 a situation because of the interference of the reflected waves cardinally varies. The possibility of the exit of the reflected wave on the second subband on $x \to -\infty$ results to the situation, when under a barrier the quantum-mechanical current density $ej_x(x, z) \neq 0$ (penetration of quantum-mechanical current density) and its amplitude exponentially dumped at $x \to \infty$. Thus under a barrier there are two zones of distribution of the $ej_x(x, z)$: the zone (2), in which $ej_x(x, z)$ it is directed in a positive direction of the x-axis and zone (1), in which $ej_x(x, z)$ has a return direction. On zone (1) there is an outflow of a charge from under a bar-

rier. Distinction of potentials $U_1(z)$ and $U_2(z)$ localizing a particle along the z-axis in regions 1 ($x < 0$) and 2 ($x > 0$) respectively provide nonorthogonality of the wave functions in these regions. It results to confuse of the electronic subbands in different regions and to appearance of the electronic interference effects. As is known [5], at falling of the free electron with energy E_x (the x-axis is the direction of propagation of the electron wave) on a rectangular potential wall in height V_0 ($x > 0$) under condition $E_x < V_0$ the quantum-mechanical current density $ej_x(x, z)$ in the reg. 2 is equal to zero, because of the real exponent of the wave function. Certainly, in this case exists exponentially dumped penetration of wave function of the particle into this region at $x > 0$.

1. Results

We considered the problem of scattering of a monochromatic unit-amplitude electron wave falling along the lower quantum — confined subband ($m = 1$) from region 1 ($x < 0$, rectangular QW_1) to semi-infinite potential barrier in region 2 ($x > 0$, QW_2) in semiconductor 2D nanostructure and that has the parameters of GaAs ($m^* = 0.067m_0$, where m_0 is the mass of a free electron). Width of the structure is $300\,\text{Å}$. The particle motion along all the coordinates is assumed to be separated, and a particle wave vector is directed along the x-axis. We also assume that the potential energy in each of the QWs does not depend on x varying jump-wise at the point of the joint of the QWs ($x = 0$). Assuming that the QWs are defined by a infinite-height-wall potential along the z-axis, the energetic spectrums in this direction are completely discrete.

We have obtained analytical expression for the longitudinal component of the probability current density $j_x(x, z)$ in the QW_2:

$$\frac{\eta}{2m^*}\left[\sum_{n,t} C_n C_t^* \varphi_n(z)\varphi_t^*(z)\left(k_n + k_t^*\right)\exp\left[i\left(k_n - k_t^*\right)x\right]\right]. \quad (1)$$

Here, $\{\varphi_{n,t}(z)\}$ are eigenfunctions of the Schrödinger equations in region 2, $C_{n,t}$ are constant coefficients defining the amplitudes of the waves passed to the QWR_2 through the subbands $E_{n,t}$; $k_{n,t} = [2m^*(E - E_{n,t} - E_c)]^{1/2}$ are the wave numbers corresponding to the motion of the particle along the x-axis in the QW_2. The energy is counted from the conduction band bottom E_c in the bulk material of the QWs. Let as note that if $E - E_c > E_{n,t}$ then $k_{n,t}$ are real, and the waves corresponding to them are spreading; at inverse inequality $k_{n,t}$
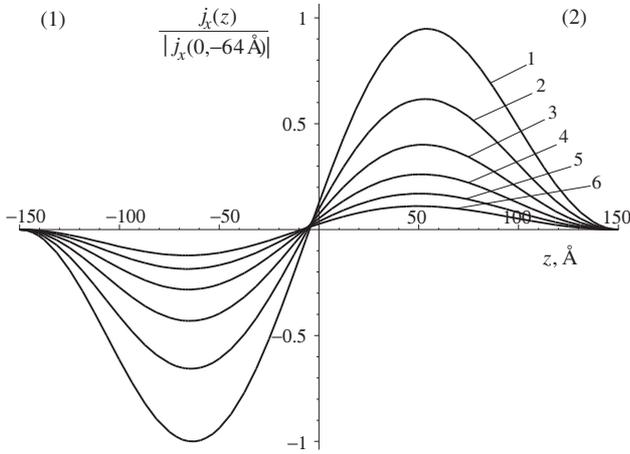
Fig. 1. The z-dependence of the normalized probability current density $j_x(x, z)/|j_x(0, -64 \text{ Å})|$ for the cross-section at the different $X_{1,2,3,4,5,6} = 0, 10, 20, 30, 40,$ and 50 Å in region 2 ($x > 0$, QW$_2$). $A = 300$ Å. The positively $j_x(x, z)/|j_x(0, -64 \text{ Å})|$ corresponds to the positive direction of the quantum-mechanical current density along x-axis; the negative $j_x(x, z)/|j_x(0, -64 \text{ Å})|$ corresponds to the current density in the negative direction x-axis. $F = 7 \times 10^5$ V/cm.

are imaginary, and the waves are damped, with typical lengths of $l_{n,t} = |k_{n,t}|^{-1}$. For the considered structures coefficients $C_{n,t}$ are defined from the system of equations following from boundary conditions for wave functions in regions 1 and 2 and their derivatives in point $x = 0$. Further on, while calculating the $j_x(x, z)$ we will only be interested in damped at $x \to \infty$ waves with imaginary k in the QW$_2$. The complete probability current density (or the complete quantum-mechanical current density) along the x-axis $J_x = \int j_x(x, z)dz$ as a consequence of the orthonormalized character of the functions $\{\varphi_{n,t}(z)\}$ has no coordinate dependence from x, as in Eq. (1) there are only terms with $n = t$ where the terms of the sum corresponding to subbands with $E_{n,t} > E$ and imaginary $k_{n,t}$ are equal to zero. It should be noted that the conductance of the structure $G = |J_x/V|$ does not depend on x.

We have considered a problem in two situations. 1. The particles kinetic energy $E = {}^1E_x : E_1^{(1)} < {}^1E_x < E_2^{(1)}$ in QW$_1$ and ${}^1E_x < V = V_0 + E_1^{(2)}$ in QW$_2$. 2. $E_2^{(1)} < {}^2E_x < {}_3^{(1)}$ in QW$_1$ and ${}^2E_x < V = V_0 + E_1^{(2)}$ in QW$_2$. The energies of the bottoms of three lower subbands in QW$_1$ are $E_1^{(1)} = 6.24$ meV; $E_2^{(1)} = 24.94$ meV and $E_3^{(1)} = 56.12$ meV at $E_y^{(1)} = 0$. The energies of the bottoms of two lower subbands in QW$_2$ are $E_1^{(2)} = 51.98$ meV and $E_2^{(2)} = 71.66$ meV. The built — in potential $V_0 = 36$ meV.

Situations 1. In situation 1 the quantum-mechanical current density $ej_x(x, z)$ in the reg. 2 is equal to zero, because of the real exponent of the wave function (as in standard situation [5]). Certainly, in this case there is exponentially dumped penetration of wave function of the particle into this region at $x > 0$.

Situations 2. In this case the kinetic energy of a particle $E = {}^2E_x$ in QW$_1$ was equal to 35 meV and was less than full effective height of a potential barrier in QW$_2$ $V = V_0 + E_1^{(2)}$ on 16.98 meV. Results of calculations in situation 2 are given

on the Fig. 1. In this situation under the barrier the quantum-mechanical current density $ej_x(x, z) \neq 0$ and its amplitude exponentially dumped at $x \to \infty$. In this case in the reg. 2 under a barrier there are two zones of distribution of the $ej_x(x, z)$: the zone (2), in which $ej_x(x, z)$ is directed in a positive direction of the x-axis and zone (1), in which $ej_x(x, z)$ has a return direction. On zone (1) there is an outflow of a charge from under a barrier. Figure 1 shows the results of calculation of a penetration effect for normalized probability current density $j_x(x, z)/|j_x(0, -64 \text{ Å})|$ under the barrier in the region 2 ($x > 0$, QW$_2$).

At present, there are methods for injecting the quasi-monoenergetic electron beams in 2D nanostructures. For example, Rauch *et al* [6] studied ballistic transport over minibands in a superlattice based on a GaAlAs–GaAs system by injecting a quasi-monoenergetic beam of hot electrons into the superlattice.

References

[1] D.K. Ferry and S.M. Goodnick, *Transport in Nanostructures*, Cambridge Univ. Press, Cambridge 1997.
[2] E. Tekman, S. Ciraci, *Phys. Rev. B.* **43**, 7145 (1991).
[3] Fernando Sols, M. Macucci, U. Ravaioli, and K. Hess, *J. Appl. Phys.* **66**, 3892 (1989).
[4] O. Olendski and L. Mikhailovska, *Phys. Rev. B* **66**, 035331-1 (2002).
[5] L.D. Landau and E.M. Lifschitz, *Quantum Mechanics* (*PNon-Relativistic Theory*), Pergamon Press, Oxford, 1977.
[6] C. Rauch, G. Strasser, K. Unterrainer, W. Boxleitner, K. Kempa, and E. Gornik, *Physica E* 2, 282 (1998).

Analysis of homogeneity of 2D electron gas at decreasing of electron density

A. A. Sherstobitov[1], G. M. Minkov[1], A. V. Germanenko[2], O. E. Rut[2], I. V. Soldatov[2] and B. N. Zvonkov[3]

[1] Institute of Metal Physics, Ural Branch of RAS, 620990 Ekaterinburg, Russia
[2] Ural State University, Ekaterinburg, Russia
[3] Physical-Technical Research Institute, University of Nizhni Novgorod, Nizhni Novgorod, Russia

Abstract. We investigate the gate voltage dependence of capacitance of a system gate — 2D electron gas ($C - V_g$). The abrupt drop of capacitance at decreasing concentration was found. The possible reasons of this drop, namely inhomogeneity of electron density distribution and serial resistance of 2D electron gas are discussed. Simultaneous analysis of gate voltage dependences of capacitance and resistance has shown that in heavily doped 2D systems the main role in the drop of capacitance at decreasing concentration plays the resistance of 2D gas. It is found that the investigated systems remains homogeneous down to the low temperature conductivity about $(10^{-2}-10^{-3})e^2/h$.

Introduction

The investigation of quantum effects in 2D systems has a great advantage due to the ability to control the concentration of charge carriers continuously by varying voltage on the gate electrode. With this variation, the role of electron-electron interaction changes as well as the role of disorder. The contribution from this interaction is determined by the parameter rs — the ratio of the coulomb interaction energy at an average distance $E_C = e^2 n^{1/2}$ to the Fermi energy E_F. The role of disorder is governed by the parameters h/τ and U, where τ is the momentum relaxation time and U is the characteristic energy scale of smooth random disorder. In all cases with a decreasing electron density the mobility decrease too. There are several different physical mechanisms of such behavior. When $E_C > h/\tau$, U, the decreasing of carriers concentration can lead to the Wigner crystallization. If, $h/\tau > E_C$, U, the Anderson localization plays the central role, and at low temperatures, one can get hopping conductivity over the states localized due to this effect. Finally, when the fluctuations of smooth random potential are significant ($eU > h/\tau$, $E^{\backprime}$), the decrease of electron density may cause the formation of droplet structures — "metallic" regions separated by barriers — and low temperature conductivity will be determined by carrier tunneling through those barriers. Usually, a decrease in the electron density causes all three parameters to change, thus, in order to appropriately interpret experimental data, one should know which of those mechanisms plays the main role. For example, in [1], the authors interpret the abrupt drop of conductivity σ (for $\sigma \leq 10G_0$, $G_0 = e^2/\pi h$) with decreasing electron density in terms of a "droplet structures" model. At the same time, in [2,3] the electron gas is believed to be homogeneous down to much lower values of conductivity ($\sigma = (10^{-2}-10^{-3})G_0$), and the strong temperature dependence was explained in terms of Anderson localization. So one need a method of analysis of homogeneity of electron gas to adequately interpret our data. We investigate the gate voltage dependences of the capacitance between gate electrode and 2D electron gas ($C - V_g$) on 2D GaAs structures with large disorder (with delta-doped quantum well, typical concentration 10^{12} cm^{-2}, electron mobility 1000 cm^2/V s) at different frequencies and temperatures.

1. Experimental details and discussion

Simultaneous analysis of gate voltage dependences of conductivity and capacitance shows that in the investigated structure the 2D gas remains homogeneous, at least until a conductivity of $10^{-3}G_0$, and that the drop in C^* takes place due to the increase of 2D gas resistivity instead of the formation of dielectric regions. It should be mentioned that such behavior (the fact that the 2D gas remains homogeneous while the value of conductivity is above $10^{-2}G_0$) is a consequence of the sample's features: high electron density and high scattering rate occur because of impurities which have been placed directly into the quantum well. In structures with remote impurities, the very similar behavior of * with decreasing electron density [4] is due to the formation of droplet structures. It becomes obvious, if one take a look at the value of conductivity, at which the drop of $1/(\omega \mathrm{Im}(Z))$ occurs. In [4] it happens at conductivity $(1-10)G_0$, when the resistivity of 2D gas has no influence on C^*, according to the distributed parameters theory. Thus simultaneous analysis of $C(V_g)$ and $R(V_g)$ dependencies allow us to test the homogeneity of 2D electron gas.

References

[1] S. Das Sarma, M.P. Lilly, E.H. Hwang, L.N. Pfeiffer, K.W. West, and J.L. Reno, Two-Dimensional Metal-Insulator Transition as a Percolation Transition in a High-Mobility Electron System, *Phys. Rev. Lett.* **94**, 136401 (2005).

[2] G.M. Minkov, O.E. Rut, A.V. Germanenko, A.A. Sherstobitov, B.N. Zvonkov, E.A. Uskova, and A.A. Birukov, Quantum corrections to conductivity: From weak to strong localization, *Phys. Rev. B* **65**, 235322 (2002).

[3] G.M. Minkov, A.V. Germanenko, O.E. Rut, A.A. Sherstobitov, and B.N. Zvonkov, Giant suppression of the Drude conductivity due to quantum interference in the disordered two-dimensional system GaAs/In$_x$Ga$_{1-x}$As/GaAs, *Phys. Rev. B* **75**, 235316 (2007).

[4] G. Allison, E.A. Galaktionov, A.K. Savchenko, S.S. Safonov, M.M. Fogler, M.Y. Simmons, and D.A. Ritchie *Phys. Rev. Lett.* **96**, 216407 (2006).

Energy relaxation rate of 2D hole gas in GaAs/InGaAs/GaAs quantum well within wide range of conductivitiy

I. V. Soldatov[1], *A. V. Germanenko*[1], G. M. Minkov[2], O. E. Rut[2] and A. A. Sherstobitov[2]

[1] Ural State University, 620083 Ekaterinburg, Russia
[2] Institute of Metal Physics, Ural Branch of RAS, 620990 Ekaterinburg, Russia

Abstract. The nonohmic conductivity of 2D hole gas (2DHG) in single $GaAsIn_{0.2}Ga_{0.8}AsGaAs$ quantum well structures within the temperature range of 1.4–4.2 K, the carrier's densities $p = (1.5-8) \times 10^{15}$ m^{-2} and a wide range of conductivities $(10^{-4}-100)G_0$ ($G_0 = e^2/\pi h$) was investigated. It was shown that at conductivity $\sigma > G_0$ the energy relaxation rate $P(T_h, T_L)$ is well described by the conventional theory (P.J. Price, *J. Appl. Phys.* 53, 6863 (1982)), which takes into account scattering on acoustic phonons with both piezoelectric and deformational potential coupling to holes. At the conductivity range $0.01G_0 < \sigma < G_0$ energy the relaxation rate significantly deviates down from the theoretical value. The analysis of $\frac{dP}{d\sigma}$ at different lattice temperature T_L shows that this deviation does not result from crossover to the hopping conductivity, which occurs at $\sigma < 10^{-2}$, but from the Pippard ineffectiveness.

In case of conductivity over delocalized states (diffusive conductivity) the electric field dependence of the conductivity originates from heating of 2DHG up to temperature T_h, greater than lattice temperature T_L. In the stationary conditions T_h is determined by the balance between incoming energy rate P_{in} and energy relaxation rate P. Therefore, studying the nonohmic conductivity, one can find the energy relaxation rate P, its dependence on T_L, T_h and determine the main mechanisms of the energy relaxation. Moreover, the study of the nonohmic conductivity provides an opportunity to find the conditions in which the diffusion conductivity changes to hopping conductivity with the change of density, disorder and temperature. It is possible due to the fact that in the hopping regime of conductivity $\sigma(E)$ dependence results not only from the change of the carrier distribution over energy, but also from the change in probability of hopes along the field.

Over the past 20 years there have been published a number of experimental papers, investigating heating of 2D electron gas in GaAs structures at high conductivities [1,2,3,4], 2D hole gas in SiGe [4], and a few papers studying heating of holes in GaAs [5,6], but only for lattice temperatures below 100 mK. To the best of our knowledge, there is no experiment within a wide conductivity range at higher temperatures in GaAs. In the present paper, we investigate the dependence of the energy relaxation rate on the carrier density and the strength of disorder in InGaAs based 2D hole structures in the temperature range of 1.4–4.2 K and a wide range of conductivities $(10^{-4}-100)G_0$. We have obtained the following results. It was shown, that at conductivities above G_0 the energy relaxation rate is well described in terms of scattering on acoustic phonons [7]. At lower conductivities $(3 \times 10^{-2}-1)G_0$ the energy relaxation rate deviates down from the theory in Ref. 7, while the regime of conductivity remains diffusive. This deviation is associated with the Pippard ineffectiveness of electron-phonon interactions. It was shown that a crossover to the hopping conductivity with lowering of σ occurs at $\sigma \sim 10^{-2}$.

From theory [7] it follows that besides coupling constants, temperatures T_h and T_L, the only sample parameter which the energy relaxation rate depends on is hole density. Let us analyze the dependence of the power ΔP required to heat holes from lattice temperature $T_L = 1.4$ K up to $T_h = 1.9$ K. It is seen that at densities above a certain value (different for each
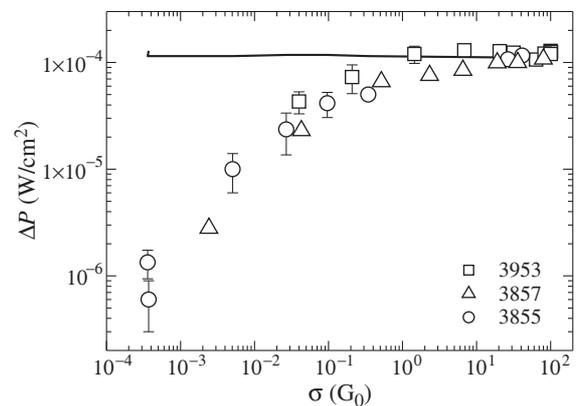
Fig. 1.

sample), the experimental data is in agreement with the theory. At lower densities the experimental energy relaxation rate significantly deviates downward from the theoretical value significantly. Such divergence for all the cases takes place when the conductivity of 2D gas falls below G_0.

A possible reason for such divergence could be the change of a conductivity mechanism (it is commonly believed that at $\sigma < \pi G_0$ conductivity is hopping), and in this case the described above treatment with P is not valid any more. To clarify the conductivity mechanism let us analyze the derivative $\frac{\partial P}{\partial T_h}$.

Hence, the conductivity remains diffusive at $\sigma(1.4 \text{ K}) > 3 \times 10^{-2} G_0$ and the drop in the energy relaxation rate at conductivity range $3 \times 10^{-2} G_0 < \sigma < 1 G_0$ is caused not by a crossover to the hopping conductivity. We believe that the it is caused by the Pippard ineffectiveness of the electron-phonon interactions, which takes place under the following conditions: i) the number of carriers within the length of the thermal phonon is sufficient to introduce the local conductivity [9] $\frac{q_t}{k_F} < 1$ (q_t is the wave vector of the thermal phonon), and ii) $q_t l < 1$, (l means free path). It was shown in Ref. [10], that the energy relaxation rate would decrease linearly in this regime. Indeed, in the investigated structures the linear decrease of the energy relaxation rate is observed. It begins at $\sigma(1.4 \text{ K}) \approx G_0$, when both conditions mentioned above are satisfied: $q_t l \approx 0.2$ ($q_t l = 1$ at $\sigma \approx 8G_0$). The parameter $\frac{q_t}{k_F}$ remains smaller than the unity the within whole range of temperatures. It should be

noted that the analogous behavior was observed also on n-type structures [11].

References

[1] E. Chow, H.P. Wei, S.M. Girvin and M. Shayegan, *Phys. Rev. Lett.* **77**, 1143 (1996).

[2] E. Chow, H.P. Wei, S.M. Girvin, W.Jan and J.E. Cunningham, *Phys. Rev. B* **56**, 1676 (1997).

[3] Y. Ma, R. Fletcher, E. Zaremba, M.D. Iorio, C.T. Foxon and J.J. Harris, *Phys. Rev. B* **43**, 9033 (1991).

[4] A.A. Sherstobitov, G.M. Minkov, O.E. Rut, A.V. Germanenko and B.N. Zvonkov, *Semiconductors* **39** 221 (2005).

[5] G. Braithwaite, N.L. Mattey, E.H.C. Parker, T.E. Whall, G. Brunthaler, and G. Bauer, *J. Appl. Phys.* **81**, 6853 (1997).

[6] X.P.A. Gao, G.S. Boebinger, A.P. Mills, Jr., A.P. Ramirez, L. N. Pfeiffer and K.W. West, *Phys. Rev. Lett.* **94** 086402 (2005).

[7] X.P.A. Gao, A.P. Mills, Jr., A.P. Ramirez, L.N. Pfeiffer and K.W. West, "Joule heating of dilute 2D holes in a GaAs quantum well", arXiv: cond-mat/0203151 (2002).

[8] P.J. Price, *J. Appl. Phys.* **53** 6863 (1982).

[9] A.B. Pippard, *Philos. Mag.* **46**, 1104 (1955).

[10] M.Yu. Reizer and A.V. Sergeev, *Zh. Eksp. Teor. Fiz.* **90**, 1056 (1986) [*Sov. Phys. JETP* **63**, 616 (1986)].

[11] A.A. Sherstobitov, G.M. Minkov, O.E. Rut, A.V. Germanenko, B.N. Zvonkov, E.A. Uskova and A.A. Biryukov, *Semiconductors* **37** 6, 705 (2003).

A model to describe the hump-like feature in CV-characteristics of MOS capacitors with oxide-hosted nanoparticles

V. A. Stuchinsky

Rzhanov Institute of Semiconductor Physics, 630090 Novosibirsk, Russia

Abstract. A numerical model was developed to explain the hump-like feature observed in the CV-characteristics of MOS capacitors with oxide-hosted Si nanoparticles. The model assumes that the majority carriers tunnel through the oxide along linear nanoparticle chains, with tunneling gaps in between nanoparticles being scattered in terms of width. Electrical characteristics of tunneling chains formed by up to six differently spaced nanoparticles were calculated to correlate the involvement of one or more variously located, differently penetrable 'bottlenecks' in the tunneling chains with the shape of the CV-curves of the MOS capacitors.

Introduction

Charge transport in dielectrics with nanoparticles is a matter of interest for creating favorable conditions for efficient electroluminescence in film structures, for developing multi-bit flash memory cells, etc. Measured CV-characteristics of MOS capacitors with oxide-hosted Si nanoparticles were reported to exhibit a 'hump' in the accumulation branch of the CV-curve; this feature normally emerges as a single capacitance peak or more intricately shaped structure [1]. Within this feature, measured MOS capacitance C can be notably in excess of the capacitance C_a of the ideal MOS capacitor (without oxide-hosted nanoparticles) in accumulation. The 'hump' emerges within a certain interval of bias voltages, this interval being preceded by a portion of CV-curve exhibiting a capacitance value close to C_a. With increasing bias voltage, measured MOS capacitance increases to reach some maximum value, and then it decreases to finally reach saturation at a lower capacitance level. The above behavior of CV-curves was attributed to penetration of majority carriers from semiconductor into oxide [1].

In the present work, we discuss a model for the formation of the 'hump' based on the following quite reasonable assumptions: (1) the majorities (for definiteness, holes) contained in the accumulation layer of the semiconductor may penetrate into Si particles (say, nanocrystals (nc's)), this penetration being promoted by the local electric field at the oxide-semiconductor interface; (2) the hole transport through the oxide proceeds along linear nc chains in a self-consistent manner with the establishment of local electric field in the dielectric; (3) in the nc chains the tunnel barriers are statistically scattered in terms of their width, so that the widest tunneling gap presents a 'bottleneck' for the hole current. As we measure a CV-characteristic, with raising the bias voltage the rate of hole tunneling from the accumulation layer into nc's adjacent to substrate grows in value while the rate of the reverse process, hole tunneling from the ns's to seconductor, decreases. For charging the nc's in the vicinity of substrate, some critical field is required, defined by the presence of empty hole states in downfield nc's level in energy with the valence-band edge of the semiconductor (with due allowance for the difference between the pre-exponential factors of the two processes). The latter circumstance accounts for the initial 'traditional' behavior of the CV-curve of the capacitor with nc's in accumulation at low bias voltages. With further increase of bias voltage, at a sufficiently low measurement frequency the nc's in between the bottleneck and the substrate in individual transport chains grow charged with injected holes,

and the capacitance C increases. This charging promotes an increase of the electric field in the least penetrable gap with subsequent elimination of the 'bottleneck', especially if emission of nc-bound holes into the valence band of the dielectric develops. After the 'bottleneck' is open, the hole current j_h flows along the chain in a state with a reduced oxide charge. With several bottlenecks in the chain arranged so that the width of widest gaps increases in the direction from substrate to metal the bottlenecks will turn gradually eliminated by increasing voltage in the direction from gate to substrate (since the field increases in the opposite direction). It can be speculated that each bottleneck opening will result in partial emptying of electronic states in nc's located in between the opening bottleneck and an upfield bottleneck, with the capacitance C decreasing in value.

In our study, we attempted making the above schematic model more tangible by performing calculation of ac and dc characteristics of MOS capacitors with oxide-hosted Si nc's evenly or unevenly distributed over the oxide thickness. Primary motivation was to correlate the structure of conducting chains with the shape of CV-characteristics of MOS capacitors. First, electrical characteristics of MOS capacitors with evenly spaced nc's were calculated to be compared with the same characteristics of an ideal MOS capacitor. Then, the width of one of the tunneling gaps was increased so that to trace the effect this increase will produce on the CV-curve. In further calculations, the effect was examined as a function of bottleneck position in the chain. In a similar manner, effects due to two or more bottlenecks differently arranged within one nc chain were examined.

1. Calculation procedure

In our calculations, we treated the case of MOS capacitors on p-Si substrates ($N_a = 10^{15}$ cm^{-3}) with oxide-hosted Si nc's arranged in layers. The sheet density of nc's in each layers was 2.5×10^{13} cm^{-2} (nc's sized 1 nm with lateral spacing 1 nm). In the MOS-normal direction various arrangements of tunneling gaps comprising one, two or more bottlenecks were considered. Continuity equations for the current coupled with field matching conditions were solved for nc chains comprising up to six nc's. Each nc was treated as a 1D rectangular quantum well. Since major attention in our study was focused on studying the effect due to nc arrangement in the chain, we did not treat the discrete electronic spectrum of nc's (and, hence, such things as the Coulomb staircase), assuming instead that each nc
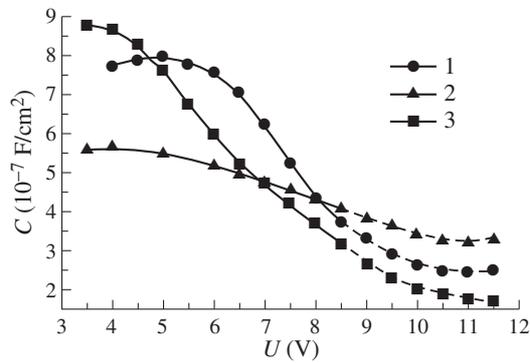
Fig. 1. The capacitance C of MOS capacitors 1–3 as calculated from the current j_d versus bias voltage. Oxide capacitance in capacitors 1–3 — 4.3×10^{-7}, 4.3×10^{-7}, and 4.1×10^{-7} F/cm^2.

had a uniform distribution of hole states over energy above the ground state of nc-bound hole. Physically, such smearing of the discrete hole spectrum in nc's could be thought of as resulting from dispersion of nc sizes. The energy density of states in the nc's was taken equal to the average energy density of hole states in 1-nm nc's. In a schematic model, the electric potential in the oxide could be assumed dropping only across the tunnel barriers, the drops across nc's being ignored. An nc-bound hole could tunnel, at constant-energy level, into a downfield nc provided that an empty state for this hole was available there. Alternatively, in high fields or at high occupations of host nc's tunneling emission of holes into the valence band of the oxide was possible. The emitted holes were assumed to rapidly drift to the gate without contributing to the space charge (in a simple version of the model, trapping of emitted holes at downfield nc's could also be ignored). The equation system for the dc quantities was a system comprising, for n nc's, $n + 1$ linear and $n + 1$ nonlinear equations. This system was solved using the MATHCAD software by applying a minimization procedure to some target function. For generating a first-guess initial approximation for the MATHCAD iterative process, in some cases the relaxation method was employed. The ac quantities were found by solving the system of linearized equations. Then, the total current (displacement plus hole current) could be calculated at each cross-section in oxide to finally obtain the capacitance C.

2. Results and discussion

Figure 1 shows the low-frequency CV-characteristics of MOS capacitors with nc chains comprising six nc's as calculated from the displacement current j_d in the gap between the metal and the nc layer nearest to the metal. In capacitors 1 and 2, the nc's were spaced evenly (at 1-nm spacing) except for one gap located in between the fourth and fifth nc (as counted from semiconductor) in capacitor 1 and in between the second and third nc in capacitor 2; the width of this gap was increased to 2 nm. In capacitor 3, the nc chain contained two bottlenecks, of widths 1.5 and 2 nm, provided at the same locations (the 2-nm bottleneck closer to the gate). We adequately covered with our calculations the range of bias voltages from 4 to 8–10 V, in which the space charge accumulated in the oxide grew in value with V. At lower and higher voltages, we met difficulties in generating successful guesses for the solution, presumably because to involvement of too many local minima in the function whose minimization was used in solving the nonlinear equa-

tion system in 14 variables. At $V > 8$ V the calculated C-data were additionally affected by inaccuracies in the calculated reactive component of the current $j_h^{\sim}$, small against the active component yet at many calculated points comparable in value with the displacement current. Yet, at points calculated to best achieved accuracy the C-values calculated with allowance for the current $j_h^{\sim}$ proved to lie close (within 10%) to the data represented in Fig. 1 with solid lines. It is seen from Fig. 1 that obtained data closely resemble known experimental findings. The dashed portions of the curves in Fig. 1 show less reliable data. Seemingly, at $V > 8$ V the capacitance C calculated from the displacement current in the gap between the fifth and sixth nc goes below C_a, possibly reflecting the fact that incremental voltages applied to the capacitor first preferred to drop across the oxide layer in between the bottleneck and the metal and afterwards, when the charge accumulated in the dielectric started decreasing, to a greater extent in between the bottleneck and the semiconductor. We believe that taking the current $j_h^{\sim}$ into account would compensate, at least partially, the dip in the CV-curves at voltages $V > 8$ V. Interestingly, the maximum capacitance in calculated capacitors 1–3 was observed at relatively low voltages (≤ 4 V) although the films kept accumulating holes up to 10–12 V. With one bottleneck available in the chain, the closer lies the bottleneck to the metal the more pronounced is the capacitance peak. In moderately thick films, involvement of two bottlenecks in the tunneling chain does not alter appreciably the general shape of CV-characteristics. We also tried to calculate an nc chain with evenly spaced nc's (1-nm spacing). In the latter case, the capacitance due to current j_d remained at a level of 5.5×10^{-7} F/cm^2 up to $V \approx 21$ V, at which depletion with holes started developing in the nc chain from the side of the metal. However, in the latter situation the inaccuracies in determining the hole current $j_h^{\sim}$ largely deteriorated the C-values calculated from the total current.

Generally, the hole charge accumulated in the oxide screens the local electric field at the oxide-semiconductor interface, thus diminishing the injection capacity of the contact. With electron injection out of metal being substantial, good conditions for efficient electroluminescence in films with nc's could be produced in an nc system formed by two counter-inserted 3D comb structures with teeth having alternate tunneling coupling either with metal or semiconductor. However, in the absence of well-established methods for nanoscale structuring of dielectrics in lateral direction a closest approximation to the latter configuration still remains given by film systems with randomly scattered nc's.

The present approach can be employed in treating more complicated transport models involving electron injection out of metal, electron-hole recombination in nc's, and trapping of free carriers at downfield nc's. It can also be used in examining the effect due to dead-end side branches of conducting chains and in calculating more evolved tunneling configurations.

References

[1] M.D. Efremov *et al*, *Fiz. Tekhn. Poluprov* **39(8)**, 945 (2005).

Conductivity of nanocrystalline carbon materials (fullerite, graphite and single-wall carbon nanotubes) at pressures 20–50 GPa

G. V. Tikhomirova, A. N. Babushkin and Y. Y. Volkova

Ural State University, 620000 Ekaterinburg, Russia

Abstract. Conductivity of fullerite C_{60}, single-wall carbon nanotubes (SWNT) and graphite have been studied at pressures 20–50 GPa and temperatures 77–400 K. The kinetics of resistivity of C_{60} at changing pressure was also studied. Transport phenomena were used as a tool for revelation and interpretation of phase transitions arisen under high pressure.

During last ten years, carbon materials under high pressure have been the subject of considerable studies. The pressure range below 20 GPa was studied in details. Attention has been mainly focused on the structure of high-pressure phases. In most works, the samples were previously agglomerated under high pressures and high temperatures, i.e., in fact, ones studied a new material rather than initial material during the pressure treatment. Many investigators noted that appearance of different phases of fullerenes depends on pressure treatment duration; nevertheless, the temporal processes of phase transformation were not ascertained up to now. Electrical properties of fullerenes C_{60} and carbon nanotubes under high pressure are not adequately explored, and available data are contradictory [1].

In this work conductivity of fullerite C_{60}, single-wall carbon nanotubes (SWNT) and graphite has been studied at pressures 20–50 GPa and temperatures 77–400 K. The kinetics of resistivity of C_{60} at changing pressure was also studied.

Three types of SWNT samples were investigated: samples produced by the graphite thermal dispersion method (SWNT percentage is 70%), the chemical vapor deposition method (SWNT percentage is 80%) and HiPco method (SWNT percentage is 90%).

Transport phenomena were used as a tool for revelation and interpretation of phase transitions arisen under high pressure.

High pressures have been generated in the high pressure cell with synthetic carbonado-type diamond anvils [2]. The anvils are good conductors and can be used as electric contacts making
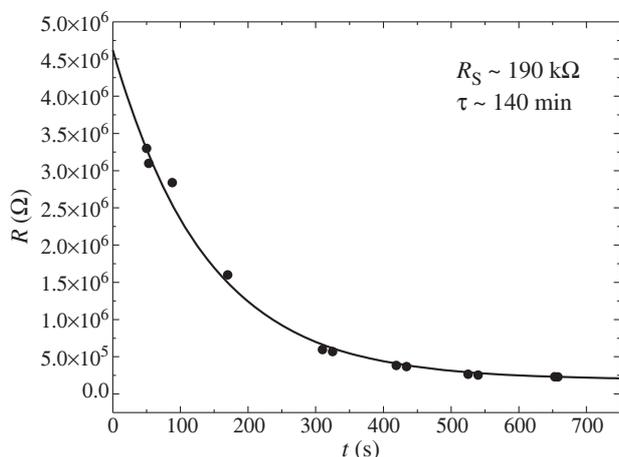
Fig. 2. Time dependence of resistance of graphite after increase the pressure from 17 to 47 GPa. Room temperature.

possible to measure temperature and pressure dependences of resistance. The method used allows us to study the same sample at successive increasing and decreasing pressure and also to keep it loaded during a long time.

Resistivity peculiarities were identified with the known phase transitions of fullerite. Successive phase transitions of fullerite C_{60} appeared in the course of HPHT treatment were accompanied by changes in resistance, which can be of quite different magnitude (from hundreds Ohm to hundreds MOhm) and of different temperature dependence.

The scheme of consequent phase transformation under high pressures and/or temperatures is suggested to be as follows: the molecular crystal C_{60} (fcc structure) → polymerized 2D and 3D conductive phases → a mixture of polymerized and amorphous phases → an amorphous phase.

1. The transition from "dielectric" state (with resistivity more than 100 MOhm cm) to a conductive state. A hysteresis in dependences of the resistance of fullerite on pressure and temperature, as well as growth of fluctuations and the increase in relaxation time near the transition point show that this is the first-kind phase transition. At not so long pressure treatment, this transition is reversible.

2. A transition to low-resistivity (∼200 Ohm) phase at the pressure above 45 GPa, which is attributed to formation of polymerized phases of fullerite. This phase is metastable and disappears after long exposure under pressure.

3. The resistance of phase appeared after long pressure and/or temperature treatment is of semiconductor character and

Fig. 1. Time dependence of resistance of C_{60} after increase the pressure from 47 to 49 GPa. Room temperature.
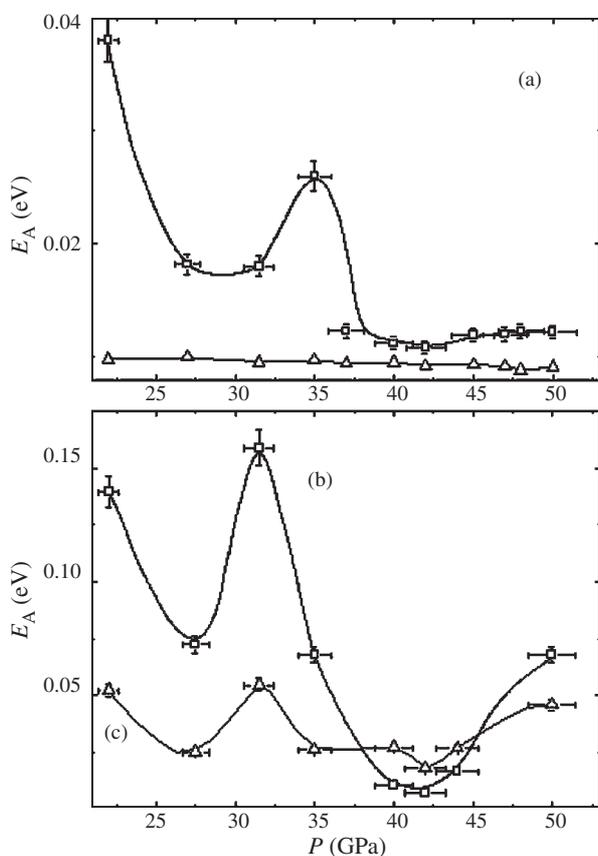
Fig. 3. Baric dependences of activation energy for the samples with 70 (a) and 90 (b) SWNT percentage at the temperatures $T > 250$ K (triangles) and $T < 250$ K (squares).

characteristics of SWNT rather than with the impurities contained in the sample. The irreversible changes of the electric properties of the samples observed in the pressure range 27–45 GPa can be connected with both the structure modification and partial destruction of the sample.

In the pressure range from ∼16 to ∼30 GPa, the sharp change in the termo EMF value of graphite was observed. Impedance measurements of graphite were carried out by means of RLC-2000 impedance analyzer at room temperature in the frequency range of 1–200 kHz. The impedance features found for all samples at pressures of ∼18 to ∼32 GPa confirm also the existence of the phase transition in this pressure range, which is confirmed by previous data obtained at d.c. conditions. The transition is irreversible.

Acknowledgements

References

[1] B. Sunqvist, *Adv. Phys.* **48**, 1 (1999).
[2] L.F. Vereschagin *et al*, *High Temperatures, High Pressures* **6**, 99 (1974).

can be attributed to an amorphous state of C_{60}.

Figures 1 and 2 show the temporal dependence of resistance of C_{60} and graphite at room temperature. It is seen that relaxation time of resistivity of fullerene is about two hours. The relaxation time for graphite after change of pressure was much shorter than that for fullerene. Even after increase in pressure from 17 up to 47 GPa, the time for conductivity saturation does not exceed 1 minute.

Critical pressures for the transitions depended on conditions and duration of preliminary HPHT treatment. This fact, as well as smeared character of the transitions are connected with long relaxation times, which turned out to be of ∼140 min. The different phase compositions of fullerite obtained after preliminary HPHT treatment may be a result of the existence of the long relaxation times.

Three types of SWNT samples were investigated. Electric properties of the samples under high pressure were dependent on SWNT percentage. The electric characteristics of SWNT samples remained of the same character with the increasing of SWNT percentage, but the additional features appeared (intermediate region in the temperature dependences of resistance; additional extremums in the baric dependences of activation energies in the pressure range of 40–45 GPa).

As an example, the baric dependences of activation energies for the samples with 70 (a) and 90 (b) SWNT percentage are shown in Fig. 3 at temperatures $T > 250$ K (triangles) and $T < 250$ K (squares).

Thus, the dependences obtained are connected with electric

Electrical conductance of C_{60}-adsorbed Si(111)α-$\sqrt{3}\times\sqrt{3}$-Au surface

D. A. Tsukanov[1,2], *M. V. Ryzhkova*[1], *D. V. Gruznev*[1], *A. N. Matetsky*[1], *L. V. Bondarenko*[1], *E. A. Borisenko*[1], *A. V. Zotov*[1,2] *and A. A. Saranin*[1,2]

[1] Institute of Automation and Control Processes FEB RAS, 690041 Vladivostok, Russia
[2] Far Eastern State University, 690000 Vladivostok, Russia

Abstract. Changes in surface electrical conductance of Si(111)α-$\sqrt{3} \times \sqrt{3}$-Au surface phase have been studied at deposition of gold atoms and fullerene molecules. Deposition of Au onto Si(111)α-$\sqrt{3} \times \sqrt{3}$-Au with 3 ML of adsorbed C_{60} has been reason of smooth increase in conductance up to 3 ML of Au. Adsorption of C_{60} on Si(111)α-$\sqrt{3} \times \sqrt{3}$-Au doesn't lead to any changes in electrical conductivity. Conductance changes were explained by changes in concentration of charge carriers in surface space-charge layer.

Introduction

It is known fullerenes make thin films consisting of large well-ordered domains on some surface phases, for example on Si(111)$\sqrt{3} \times \sqrt{3}$-Ag [1] and Si(111)$\sqrt{3} \times \sqrt{3}$-B [2]. Nevertheless fullerene's influence on electrical conductivity of silicon surface phases was studied only in [3]. We also haven't the clear answer on question: is the layer of C_{60} makes conductance channel like surface states or surface space-charge layer? In which way C_{60} molecules influence on electrical conductivity: either fullerenes change concentration of charge carriers or they make changes in carrier's mobility? To avoid latter case it is chosen system with layers of fullerenes with relatively ordered structure observing in STM and weakly bond with underlying surface. We have chosen Si(111)$\alpha-\sqrt{3} \times \sqrt{3}$-Au (hereafter $\sqrt{3}$-Au) because deposition of C_{60} onto it leads to well-ordered layers of fullerenes without any visible in STM degradations of $\sqrt{3}$-Au surface (Fig. 1a).

In this paper we studied electrical conductance of systems containing fullerene layers which weakly bond with underlying surface. Passivation of surface with $\sqrt{3}$-Au allows avoiding strong interaction C_{60} and silicon surface.

1. Experimental

In this paper, we report our results in measuring of electrical conductance Au/C_{60}/$\sqrt{3}$-Au system by four-point probe method. Probes have around 1 mm spacings and arranged on cones of square. Electrical conductance was measured in situ in ultra-high vacuum chamber equipped with low energy electron diffraction (LEED) and evaporation sources. We used silicon wafers $15 \times 5 \times 3$ mm^3 in size and 2–15 Ω cm resistivity of n-type. All data presented here were obtained at RT. $\alpha\sqrt{3}$-Au was prepared by depositing of 0.9 ML gold atoms on silicon surface with Si(111)7×7 surface phase at 520 °C. The Au coverage was calibrated with Si(111)5×2-Au phase with adsorbate coverage of 0.4 ML [4]. Fullerenes were evaporated from Knudsen cell with deposition rate 0.1 ML/min. 1 ML of C_{60} corresponds to full coverage layer formed on $\alpha\sqrt{3}$-Au and it's structure has been visible in LEED pattern presented on Fig. 1b. This LEED pattern corresponds to wholly covered surface by 1 molecule of fullerene in height which has been visible in STM (Fig. 1a). The scanning tunneling microscope images were recorded in separate UHV chamber equipped with LEED system. All conductance measurements were carried out at
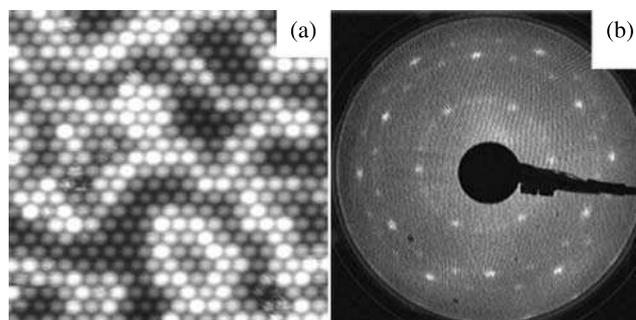
Fig. 1. STM image of $\alpha\sqrt{3}$-Au with fullerene monolayer, 20×20 nm^2 (a), LEED pattern of sample with 1 ML of fullerenes on $\alpha\sqrt{3}$-Au, source energy was 24.3 eV (b).

RT after 1h cooling down of samples with prepared surface phases. Then additional Ag, Au atoms or C_{60} molecules were deposited.

2. Results and discussions

Fig. 1a shows STM images of $\alpha\sqrt{3}$-Au with monolayer of fullerenes. It is seen that deposited fullerenes form ordered layer without any visible reconstruction of $\alpha\sqrt{3}$-Au. Fullerene layer is very ordered though $\alpha\sqrt{3}$-Au is characterized by presence of domain walls [5]. Therefore it is supposed that fullerenes don't change surface bonds in the phase. It could be supposed that we observe physisorption of C_{60} on this surface phase. Nevertheless this proposal requires careful consideration and additional experimental evidence from photoemission spectra. Monolayer of C_{60} molecules on $\alpha\sqrt{3}$-Au has lattice of 1 fullerite's layer, following layers grow in the form of fullerite with fcc lattice and intermolecular spacing 1.005 nm. It is known that fullerite has energy gap 1–1.5 eV [6]. Therefore it can be supposed that electrical conductance through layers of fullerenes would be very low in comparison with conductance of $\alpha\sqrt{3}$-Au. It is confirmed in Fig. 2b. Opened squares represent electrical conductance depending on fullerene coverage (upper abscissa in graphics). Adsorption of fullerenes doesn't change electrical conductivity of sample with surface phase.

Fig. 2a shows STM image of $\alpha\sqrt{3}$-Au with 1 ML of fullerenes on which gold atoms were deposited. Gold adatoms penetrate under the layer of fullerenes due to weak bonding of latter with substrate as one can see on STM image.
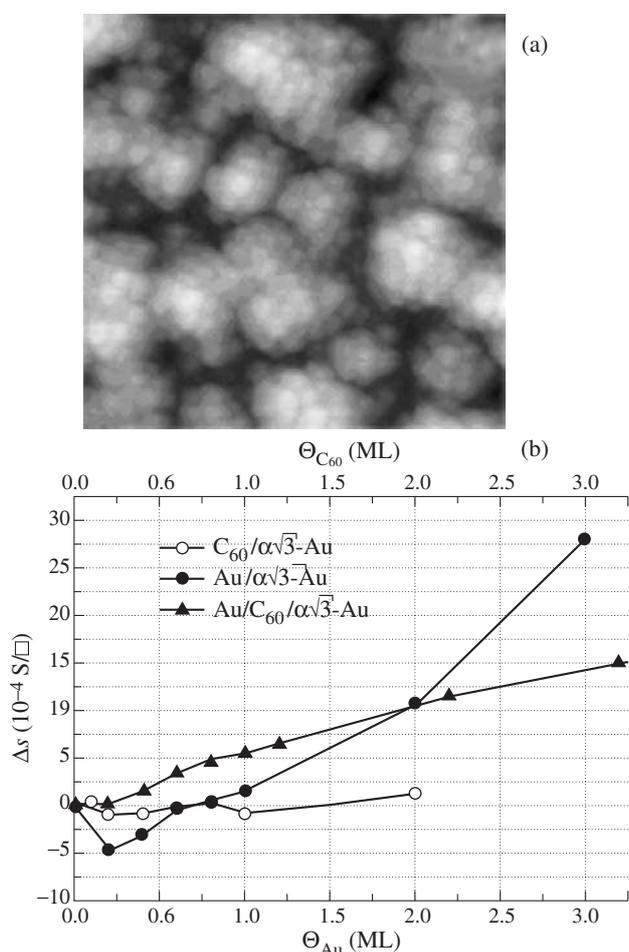
Fig. 2. STM image of $\alpha\sqrt{3}$-Au with fullerene monolayer after deposition of 4 ML of gold atoms (a), electrical conductance changes after deposition of Au and/or C_{60} onto $\alpha\sqrt{3}$-Au (b) at the stages shown in Fig. 1.

Fig. 2b shows measured conductance changes of the sample depending on adsorbate coverage up to 3 ML gold atoms or 2 ML fullerenes. Deposition of gold atoms onto $\alpha\sqrt{3}$-Au shows negative change in conductance up to around 0.7–1 ML of adsorbate coverage. Then conductance increases steeply. In the case of deposition of gold atoms onto $\alpha\sqrt{3}$-Au with 2 ML of fullerenes deposited previously it can be seen that conductance increases starting with very small coverage of Au.

We have carried out measuring conductance after deposition of various amounts of gold atoms on $\alpha\sqrt{3}$-Au. Electrical conductance data of specimen with gold surface phase during Au adsorption were obtained by Hasegawa *et al* [7]. In the same work it has been proposed the explanation of such behavior. $\alpha\sqrt{3}$-Au have so strong band bending that the surface Fermi level is very close to the valence band maximum, meaning hole-accumulation layer under the surface. The surface phase has surface state which lying at Fermi level and is observed only at several regions in k space, and its density of states is very small revealing a weak metallic character. In spite of said above conductance through surface space-charge layer makes main contribution in to electrical conductance of $\alpha\sqrt{3}$-Au [7]. It has been proposed that this layer changes to depletion layer by additional Au adsorption due to charge compensation leading to decreasing of measured conductance. In this case gold

adatoms play role donors of electrons. Minimum conductance we can observe at about 0.2 ML. With further adsorption of Au, the space-charge layer returns to hole-accumulation layer, and simultaneously a metallic Au-silicide layer is formed, resulting in the steep increase in electrical conductance. As noted in the mentioned work, this explanation demands direct photoemission studies of Si 2-p core-level signal for determination of band bending. But in the next experiment we showed that this conductance decreasing cannot be explained in terms of destruction surface states of $\alpha\sqrt{3}$-Au and creation of gold silicide layer.

In Fig. 2a conductance changes of $\alpha\sqrt{3}$-Au with 2 ML fullerenes depending on adsorbate coverage up to 3 ML gold atoms are shown. It can be seen that there is no any decrease in conductance during gold deposition and the electrical conductance increases starting with very small coverage of adsorbate. It could be supposed that gold atoms donate their valency electrons to fullerenes. This proposal requires additional photoemission spectra evidence from fullerenes. Therefore C_{60} plays role as acceptor adsorbate for Au adatoms. There is no charge compensation in space-charge layer in this case as seen from conductance measurements.

References

[1] T. Nakayama *et al*, *Phys. Rev. B* **50**, 12627 (1999).
[2] T. Stimpel *et al*, *Mater. Sci. Eng. B* **89** 394 (2002).
[3] S. Hasegawa *et al*, *Appl. Surf. Sci.* **162**, 42 (2000).
[4] V.G. Lifshits *et al*, *Surface Phases on Silicon*, Wiley, Chichester, UK (1993).
[5] D.V. Gruznev *et al*, *Phys. Rev. B* **73**, 115335 (2006).
[6] L.N. Sidorov *et al*, *Fullerenes* (in russian), Eksamen, Moscow (2004).
[7] S. Hasegawa *et al*, *Prog. Surf. Sci.* **60**, 89 (1999).

Dynamics of exciton and trion photoluminescence in GaAs/Al(Ga)As quantum wells

V. G. Lyssenko[1], V. Ya. Aleshkin[2], *L. V. Gavrilenko*[2], D. M. Gaponova[2], Z. F. Krasil'nik[2], D. I. Kryzhkov[2],
D. I. Kuritsyn[2], S. M. Sergeev[2] and C. B. Sorensen[3]

[1] Institute of Microelectronics Technology and High Purity Materials, RAS, 142432 Chernogolovka,
Moscow Region, Russia
[2] Institute for Physics of Microstructures, RAS, 603950 Nizhny Novgorod, Russia
[3] Mikroelektronik Centret, Danmarks Tekniske Universitet, DK-2800 Lyngby, Denmark

Abstract. In this work exciton and trion kinetics in quantum wells have been investigated under different excitation power and temperature. The study of trion photoluminescence dynamics helps us to separate exciton formation time and cooling time.

Introduction

The process of free electron-hole pairs binding into excitons and trions (charged excitons) has been debated for more than ten years and is not completely clear yet. Dependencies of exciton formation time on the concentration of photoionized charge carriers have been considered in different works (see, for example, [1]) and to a first approximation this dependence is following: formation time is proportional to n^{-1}. This dependence has been determined from the photoluminescence (PL) rise [1]. But authors of recent works [2] report of the opposite power dependence of the exciton formation time on excitation power at low power. Note that in III–V semiconductors optical methods are sensitive to a subset of excitons with momentum $K = 0$ only, revealing information about exciton thermalization rather than formation. Therefore the measurement of the exciton formation time is a quite difficult task, as hot excitons are not take part in PL process. But trions can participate in PL even with $K \neq 0$ due to the third particle takes away momentum excess. It enables us to separate exciton formation time and cooling time using trion PL dynamics investigation.

In comparison with excitons, the PL dynamics of trions has been even less studied. It is largely believed that trions can be formed only if a population of excess carriers is trapped in the well, producing exclusively trions with the same charge. But authors of [3] suggest a double path mechanism for the formation of trions. This directly implies that both negatively and positively charged excitons coexist in a quantum well, even in the absence of excess carriers. In this work exciton and trion kinetics in quantum wells (QW) and asymmetric double coupled quantum wells (DQW) have been investigated under different excitation power and temperature.

1. Experimental details

Our GaAs/Al(Ga)As n-i-n heterostructure consisted of 5 DQW (AlGaAs/GaAs/AlAs/GaAs/AlGaAs) placed in i-region and separated by $Al_{0.3}Ga_{0.7}As$ barriers of 300 Å width. Widths of each QW and thicknesses of AlAs barriers between them differed from pair to pair (GaAs/AlAs/GaAs: 121/11/124, 99/17/102/,85/23/88, 73/28/76, 62/34/65 Å) that allowed us attribute peaks in spectra to fixed DQW and coordinates in the sample depth. Besides that near highly doped GaAs layers (with concentration of 10^{18} cm^{-3}) undoped GaAs QWs of 300 and 350 Å width were situated. The lithography-made mesas with metal
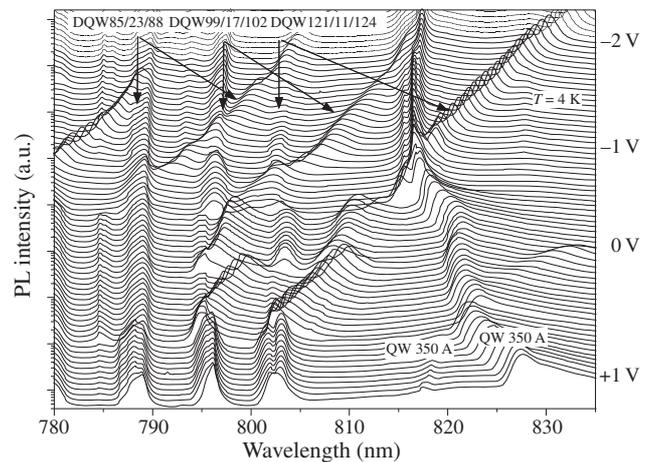
Fig. 1. The general view of PL spectra under various bias voltage at 4 K and excitation power 0.5 mW. Voltage values and corresponding QW and DQW widths are noted. Arrows point out separated and fixed lines for each DQW (see text below).

contacts were on surface of the sample. The sample was cooled down to 4–50 K and photoexcited with 100 fs-long pulses by a tunable Ti:sapphire laser with wavelength of 730 nm. The PL was energy- and time-resolved by a synchroscan streak camera in conjunction with a spectrometer. The setup enables us to determine the spectral positions with 0.2 nm accuracy. The time resolution was 10 ps in substructive spectrometer mode and about 70 ps in mode without dispersion compensation. The excitation power was varied from 0.1 up to 5 mW.

2. Results and discussions

Figure 1 shows the general view of PL spectra at different bias voltage. The corresponding width of QW and DQWs (GaAs/AlAs/GaAs) are lettered near the spectra lines. It is seen that one peak separates from each DQW peak group and shifts linearly with bias to long-wavelength side. This peak corresponds to indirect exciton in DQW while fixed peaks are attributed to direct excitons. The wide QWs (QW 300 Å and QW 350 Å) contain residual electron concentration which varies from 10^{16} up to 5×10^{17} cm^{-3} with applied field. In Figure 2(a) one can see changes in PL spectra under various electric field at low carrier's concentrations. Peaks X_{lh} and X are light hole and heavy hole excitons, correspondingly. Trion peak is lettered with T. It is seen that PL type is mainly excitonic at
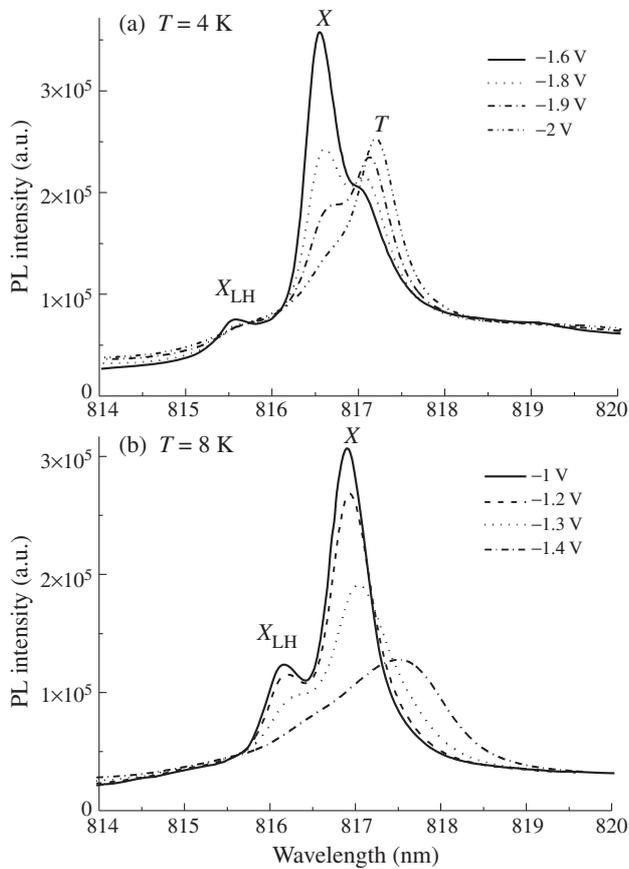
Fig. 2. PL spectra of 300 Å wide QW under various bias voltage at 4 K (a) and 8 K (b). Lines X_{lh} and X are light hole and heavy hole excitons, correspondingly. Trion line is lettered with T.

Fig. 3. PL kinetics of 300 Å wide QW under various bias voltage at 4 K and excitation power 0.5 mW (a) and 5 mW (b).

bias voltage $U > -1.6$ V and is mainly trionic at $U < -2$ V. Trion line shifts with bias voltage due to quantum confined Stark effect. Under high concentration the long-wavelength peak form at 4 K differs from trionic and by now is the subject of discussion (see Fig. 1 for $U > 0$ V). Note that trion peak disappears if temperature grows up to 8 K (see Fig. 2(b)).

Kinetic measurements show that at transition from excitonic to trionic luminescence radiative lifetime decreases from approximately 1 ns down to 0.3 ns which is in agree with [3–5] (see Fig. 3(a)).

We also investigated the power dependence of exciton and trion PL kinetics characteristic rise time. For exciton in QW and DQWs the rise time increases with power in power range 0.1–5 mW. This dependence is opposite to results of [1] but is in according with work [2]. Fig. 3(b) shows PL kinetics of the same QW in bias region of exciton-trion transition (it looks like in Fig. 2(a) but the bias voltage is different) at higher excitation power (5 mW). It is clearly seen that this curves are resulted by both kinetics: excitonic (slow) and trionic (fast). And long rise time component appears when kinetic become mostly excitonic. Note that trion kinetics rise time almost has not changed with excitation power. So we suppose that increase in the exciton rise time is manly concerned with the slower carriers cooling at higher excitation power due to phonon recycling processes.

References

[1] J. Szczytko, L. Kappei, J. Berney *et al*, *Phys. Rev. Lett.* **93**, 137401 (2004).

[2] E. Kozhemyakina, K. Zhuravlev, A. Amo and L. Vina, *Journal of Physics: Conference Series* **210**, 012002 (2010).

[3] M.T. Portella-Oberli, J. Berney, L. Kappei, F. Morier-Genoud, J. Szczytko and B. Deveaud-Pleodran, *Phys. Rew. Lett.* **102**, 096402 (2009).

[4] D. Sanvitto, R.A. Hogg, A.J. Shields *et al*, *Phys. Rev. B* **62**, R13 294 (2000).

[5] A. Esser, E. Runge, R. Zimmermann, W. Langbein, *Phys. Rev. B* **62**, 8232 (2000).

Polariton wave dephasing in quantum well by external electric field

D. K. Loginov, E. V. Ubyivovk, *V. G. Davydov*, Yu. K. Dolgikh, Yu. P. Efimov, S. A. Eliseev, V. V. Petrov, O. A. Yugov and I. V. Ignatiev

Physics Department, St Petersburg State University, Ulyanovskaya 1, Petrodvorets, St Petersburg, 198504, Russia

Abstract. Excitonic waves propagating in thick GaAs/AlGaAs quantum wells form an interference pattern, which is observed as oscillations in the reflectance spectra. Coherence of these waves can be disturbed by an external electric field thus destroying the interference. An experimental observation of this effect as well as its theoretical modeling are presented.

Introduction

Effect of electric field on the bulk excitons in semiconductors as well as on the two-dimensional excitons in thin quantum wells was studied previously [1–4]. Progress in growth technologies and experimental researches of polaritonic states in thick quantum wells allows one to observe in reflectance spectra excitons with large wave vector and to study effects of various fields on them. In particular, the effect of *magnetic* field was studied in Refs. [5,6].

In this work we present the results of experimental and theoretical studies of the *electric* field effect on the exciton energy in the quantum well whose width $L \gg a_B$ where a_B is the Bohr radius of free exciton.

1. Experiment

A GaAs/AlGaAs heterostructure containing quantum well of thickness $L = 330$ nm was grown on the silicon-doped GaAs substrate. To apply an uniform electric field, a transparent indium-tin oxide electrode was deposited on the sample surface. Reflection spectra were measured under normal incidence, that is the light propagated collinearly with the electric field. The sample temperature was $T = 10$ K. Polaritonic states were studied in the $1.510 \leq \hbar\omega \leq 1.530$ eV spectral range, where the energy of fundamental transition of GaAs bulk exciton is $E_X = E_g - R_X = 1.515$ eV. Here E_g is the bandgap and R_X is the exciton binding energy.

The reflection spectra (see Fig. 1) demonstrate oscillations caused by an interference of exciton-light (polariton) modes in the GaAs/AlGaAs quantum well similar to those studied previously [6]. Dominating spectral feature (that with maximum amplitude) corresponds to the anti-crossing between exciton-like and photon-like dispersion branches where wave vector $K \approx 0$. Smaller oscillations diverge and diminish towards higher energies. They originate from the interference of the heavy exciton-like polariton branch and correspond to the excitons whose wave vector K is much larger than that of photons [6]. Upon application of an electric voltage U to the sample, the oscillation amplitude gets smaller until they vanish completely. Meanwhile, the main spectral feature near $K \approx 0$ is observed at any value of U. The effect takes place for both positive and negative voltages U.

2. Theory and discussion

The simplest explanation of disappearance of the oscillations could be the exciton wave scattering on free carriers injected in the structure by an electric current. Whereas such an effect

indeed takes place (and is responsible for the earlier disappearance of oscillations at positive U), it is not sufficient to explain all the observed phenomena.

There is another fundamental reason for dephasing of the excitonic wave propagating along the electric field vector $\mathcal{E}$ and in reverse direction. To describe this effect theoretically, let us choose Z-axis along the [001] crystallographic direction, as it is in the experiment. Thus the components of excitonic wave vector are: $K = K_z$ and $K_x = K_y = 0$. Similarly, electric field has the components: $\mathcal{E} = \mathcal{E}_z$ and $\mathcal{E}_x = \mathcal{E}_y = 0$.

Using expressions for excitonic Hamiltonian [7], it is possible to derive an expression for excitonic energy in the presence of electric field. It contains, apart of standard terms, also a matrix element proportional to $K\mathcal{E}$:

$$E = E_g - R^{(n)} + \frac{\hbar^2 K^2}{2M} + \frac{2e\hbar^2}{(cM)^2} K\mathcal{E}, \quad (1)$$

where M, c, and e are the exciton mass, the light velocity, and the electron charge, respectively.

It follows from equation (1) that the dispersion law of excitons in electric field deviates from symmetric parabola. Namely, it depends not only on K^2, but also on K, and hence depends on the direction of wave vector. This brakes the symmetry between exciton propagation in the direction of electric field and in opposite direction for $K \neq 0$. Effect is absent for $K = 0$, as it follows from (1). This asymmetry destroys the interference of excitonic-like waves with $K \neq 0$ in quantum wells. In optical spectra this will manifest itself in destruction of high-energy oscillations, whereas the main feature at $K \approx 0$ should not be affected by the electric field (at least to a weak field approximation), which agrees with experimental findings.

To verify the model described above we calculated reflection spectra using the theory of interference of the polaritonic waves in thick quantum wells [6] and taking into account equation (1). For these calculations, we used the following material parameters of GaAs crystal: the dielectric constant $\varepsilon_0 = 12.56$ [8], and the mass of heavy hole exciton is $M = 0.52m_0$ [9,10]. The electric field magnitude was adjusted to reproduce the experimentally observed oscillation's damping. Results of these calculations are shown in the Fig. 1b and labeled by corresponding values of the electric field. The total extinction of oscillations is obtained in the calculations at the field of $\mathcal{E} = -20$ kV/cm, which qualitatively agrees with the voltage $U = -2$ V applied to the 1 μm undoped layer of the structure.

The developed theory predicts the symmetric oscillations damping for positive and negative voltages. However in the
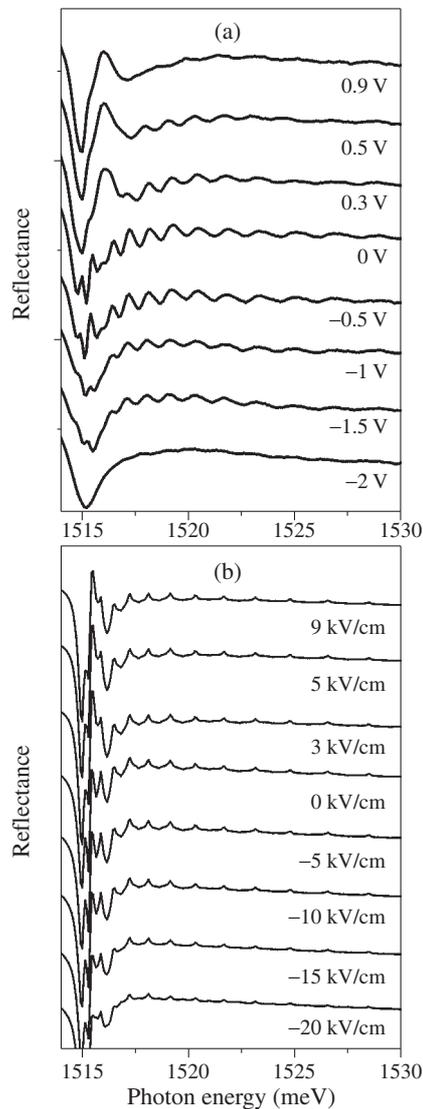
Fig. 1. Experimentally measured (a) and theoretically calculated (b) reection spectra of a structure with the $L = 300$ nm GaAs/AlGaAs quantum well. The electric bias ranged from -2 V to 0.9 V was applied to the sample surface.

experiment they decay considerably faster under positive bias. We attribute this effect to the additional scattering of excitons on free carriers of the electric current, which was observed to rapidly grow at positive voltages.

References

[1] L.V. Keldysh, *JETP* **34**, 1138 (1958), in Russian.
[2] W. Franz, *Z. Naturforschung* **13**, 484 (1958).
[3] D.A. Miller, D.S. Chelma, T.C. Damen, A.C. Gossard, W. Weigmann, T.H. Wood, C.A. Burrus, *Phys. Rev. B* **32**, 1043 (1985).
[4] R.T. Collins, L. Vina, W.I. Wang, L.L. Chang, L. Esaki, K. v. Klitzing, K. Ploog, *Phys. Rev. B* **36**, 1531 (1987).
[5] J.J. Davies, D. Wolverson, V.P. Kochereshko, A.V. Platonov, R.T. Cox, J. Cibert, H. Mariette, C. Bodin, and C. Gourgon, E.V. Ubyivovk, Yu.P. Efimov, S.A. Eliseev, *Phys. Rev. Lett.* **97**, 187403 (2006).
[6] D.K. Loginov, *Sol. St. Phys.* **52**, 58 (2010), in Russian.
[7] K. Cho, S. Suga, W. Dreybrodt, and F. Willmann, *Phys. Rev. B* **11**, 1512 (1975).
[8] M.S. Skolnik, A.K. Jain, R.A. Stradling, J. Leotin, J.C. Ousset, S. Askenazy, *J. Phys. C: Solid State Phys.* **9**, 2809 (1976).
[9] R. Romestain and C. Weisbuch, *Phys. Rev. Lett.* **45**, 2067 (1980).
[10] P. Lawaetz, *Phys. Rev. B* **4**, 3460 (1971).

Spectral features in reflection of thick quantum wells

V. A. Maruschyuk[1], B. S. Kulinkin[1], *V. G. Davydov*[2] and V. A. Gaisin[2]

[1] St Petersburg State Medical University, 6/8 Leo Tolstoy st., St Petersburg 197022, Russia
[2] Physical Faculty, St Petersburg State University, Ulyanovskaya ul. 1, Petrodvorets, St Petersburg, 198504, Russia

Abstract. Excitonic waves interference in thick GaAs/AlGaAs quantum wells is observed as oscillations in the reflection spectra. In the high quality samples this oscillations can be observed in broad spectral range with enough accuracy to perform sophisticated analysis of their energies, amplitudes and even shapes. This analysis yields details of the dispersion law of the interfering entities, in particular dependence of their mass on the energy.

Reflection spectra of the epitaxial GaAs/AlGaAs heterostructures were studied previously [1] at $T = 4.2$ K. The samples contained a 333 nm GaAs layer embedded between AlAs/GaAs superlattices. Reflection spectra were recorded using femtosecond Ti:sapphire laser as a source of spectrally broad ("white") light. Reflection was observed under Brewster's incidence angle in P-polarization in order to suppress background reflection from bulk GaAs. Monochromator MDR-23 equipped with homebuilt CCD camera was used as recording device giving resolution of about 80 μeV. Obtained spectra demonstrate a series of prominent oscillations in the 1.516–1.530 eV energy range. High optical quality of heterostructures under study (and hence small linewidth of the reflection lines, comparable with resolution of the experimental setup) allowed to perform an analysis of the spectra with enough accuracy to determine the quantization mechanism — interference of the polariton waves in thick quantum layers — and to interpret the observed features. Quantum numbers n were determined and their energies $E(n)$ and increments dE/n were plotted against n^2. From the analysis of this plots it follows that an effective mass of the excitonic state depens on the transition energy.

Here we present results of the same type of analysis of the oscillations in photo- and electroreflection spectra of another sample containing 150 nm GaAs quantum well between AlAs/GaAs superlattices which were measured in the previous work [2] covering wider spectral range 1.516–2.1 eV. The spectral dependense of the effective mass is quite similar in both samples, but not identical, as can be seen from Figure 1. Physical mechanisms of the observed anomaly is discussed.

References

[1] S.V. Poltavtsev, V.A. Gaisin, B.S. Kulinkin, V.A. Marchuk, T.S. Shamirsaev, Features of potoluminescence spectra of InAs/GaAs and InAs/AlAs quantum dots and GaAs/AlGaAs heterostructure containing thick GaAs layer. in: *Proc. of 18th Int. Symp. "Nanostructures: Physics and Technology"*, St Petersburg, 108 (2010).

[2] I.A. Yugova, V.G. Davydov *et al*, Spectroscopy of the high energy quantum confined excitonic states in the thick GaAs quantum wells, in: *Proc. of 8th Int. Symp. "Nanostructures: Physics and Technology"*, St Petersburg, 276 (2000).
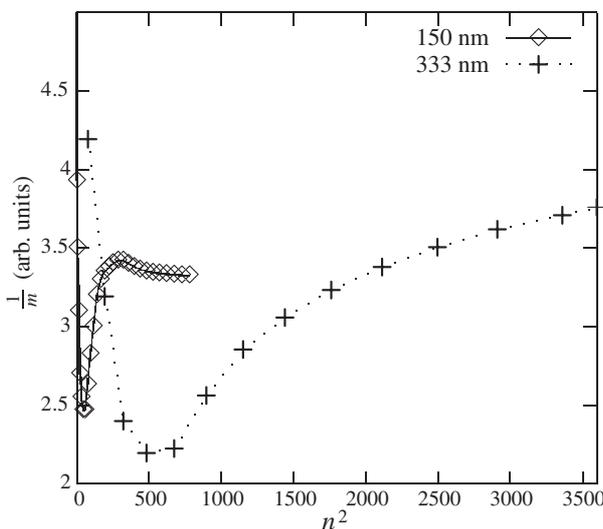
Fig. 1. Dependence of the inverse mass $\frac{1}{m}$ on the square of quantum numer n^2 for two different quantum wells (widths indicated).

Exciton luminescence in CdTe/MnTe/CdMgTe quantum well structures

V. F. Agekyan[1], G. Karczewski[2], E. S. Moskalenko[3], A. Yu. Serov[1] and N. G. Filosofov[1]

[1] V.A. Fock Institute of Physics, St Petersburg State University, 198504 St Petersburg, Russia
[2] Institute of Physics of the Polish Academy of Science, 02-668 Warsaw, Poland
[3] Ioffe Physical-Technical Institute, St Petersburg, Russia

Abstract. Exciton luminescence was studied in CdTe quantum wells with ultrathin MnTe interface layers on the temperature range 5–50 K. Magnetic shift of the luminescence bands in the narrow quantum wells shows linear dependence up to 5 T in Faraday configuration. This proves a weak frustration in magnetic MnTe 2D layers. The exciton localization parameters change strongly under the increasing magnetic field at low temperature.

Introduction

A growing interest in semiconductor 2D structures with specifically arranged ultrathin magnetic interlayers ranges from fundamental physics to the promising applications in nanoelectronics and spintronics [1]. The magnetic planes with the nominal thickness about several monolayers (ml) are able to impart some new properties to the quantum well (QW) structures depending on magnetic component concentration, thicknesses and their position relative to the interfaces. Moreover, such studies help to elucidate the peculiar properties of the 2D magnetic layers, in particular, their magnetization in the external field, as well as evaluate the magnetic atoms vertical diffusion beyond the magnetic layer. In this work we present the data concerning optical and magnetooptical characterization of MBE grown QW structures CdTe/CdMgTe with the ultrathin layers MnTe incorporated on the interfaces.

1. Experimental

Growth was carried out by MBE on GaAs (100) substrate. We grew the 4 μm CdTe and 1.4 μm CdMgTe buffer layers and four CdTe QW with varying thicknesses bounded by layers MnTe and separated by the barriers CdMgTe with Mg concentration about 35%. We studied two structures with the following nominal parameters:
Sample #1: 1 ml MnTe/31 ml CdTe/1 ml MnTe/62 ml CdMgTe/ 1 ml MnTe/16 ml CdTe/1 ml MnTe/62 ml CdMgTe/1 ml MnTe/ 8 ml CdTe/1 ml MnTe/62 ml CdMgTe/1 ml MnTe/4 ml CdTe/ 1 ml MnTe/62 ml CdMgTe.

Sample #2 is identical with the Sample #1 but the thickness of MnTe layers is 2 ml.

The ultrathin interface layer MnTe not only imparts the new magnetic properties to the structures under consideration but also contributes to the interface quality. Cation ionic radii $R(Cd^{2+}) = 0.099$, $R(Mn^{2+}) = 0.091$, $R(Mg^{2+}) = 0.074$ nm, that is the interface manganese layer is able to attenuate the strains caused by the lattice mismatch between CdTe and CdMgTe.

2. Temperature dependence of QW luminescence

The comparison of the emission spectra of QW_1 in samples #1 and #2 yields the following results (Fig. 1). In sample #1, the only band E_2 originated from the localized states is observed at $T = 5$ K. The band E_1 which corresponds to the light emission from the "regular" area of QW_1 appears at higher temperatures,
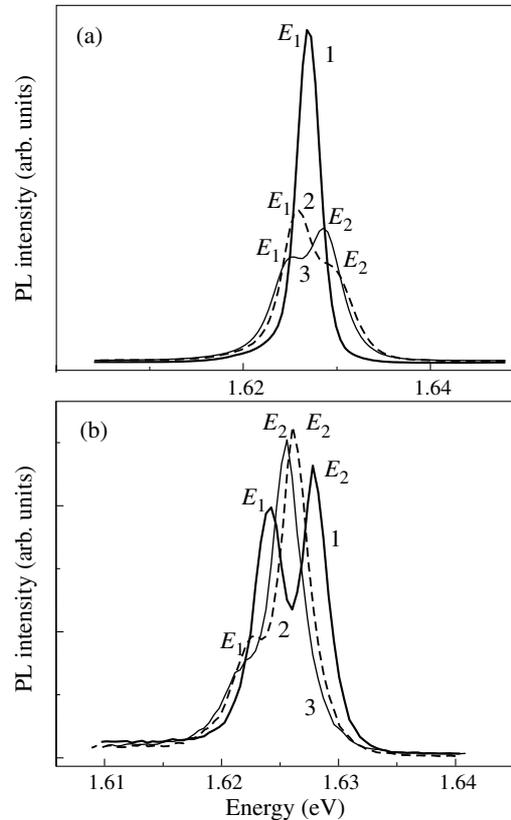
Fig. 1. Temperature dependence of QW_1 exciton emission (a — sample #1, b — sample #2). $T = 5$ (1), 30 (2) and 40 K (3).

the bands E_1 and E_2 becoming equal at $T = 35$ K. In Sample #2, both bands E_1 and E_2 are observed just at $T = 5$ K and they are equal at $T = 20$ K. This suggests that the increase of MnTe thickness on the interfaces is favorable for the extended exciton states, that is potential fluctuations decrease. The QW exciton localization is due to 1) QW width fluctuations, and 2) barrier potential fluctuations. In the case of thick QW1 the wave function penetration in the barrier is weak, thus the first mechanism is a dominant one. One can conclude that CdTe/CdMgTe interface quality is better when the ultrafine MnTe layer is incorporated between the QW and barrier.

3. QW luminescence in magnetic field

The study of light emission in the external magnetic field H makes it possible to clarify the influence of MnTe internal field
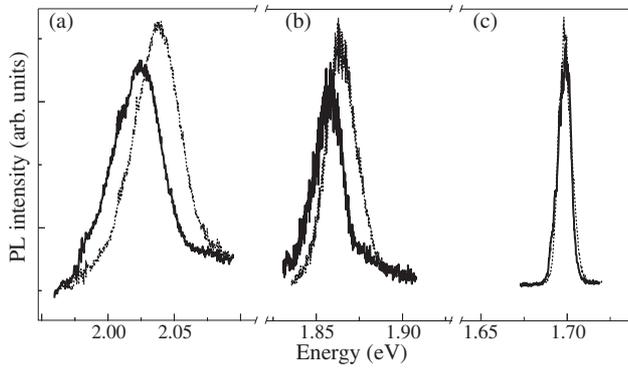
Fig. 2. Magnetic shift of the exciton bands in Sample #1: QW_1 (a), QW_2 (b), QW_3 (c). Dotted line — $H = 0$, Solid line — $H = 5$ T.
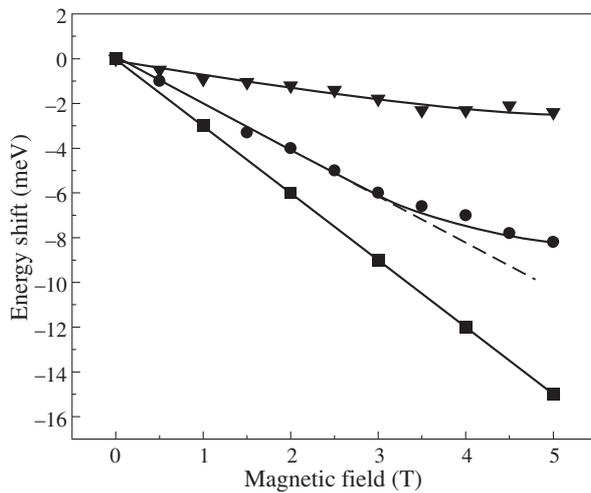
Fig. 3. Energy shift of the exciton band maximum versus magnetic field for QW_4 (1), Sample #1, WQ_3 (2), sample #2, WQ_2 (3), Sample #2; $T = 2$ K.

Fig. 4. Exciton emission from QW_1 (Sample #2) at $H = 0$ (dotted line) and $H = 5$ T (solid line); $T = 2$ K.

on the QW exciton states. This influence depends, firstly, on the magnetic layer structure and, secondly, on the amplitude and gradient of the exciton wave function on magnetic layer. The MnTe Layer magnetization can be modified significantly by a vertical diffusion of the Mn^{2+} ions in QW and barrier due to an appearance of noncompensated moments which impart the paramagnetic properties to our system.

The exciton emission bands from QW_3 and QW_4 show a strong low-energy shift which is stronger in the Sample #2. It is well known that the exciton magnetic polarons (MP) form in diluted magnetic (paramagnetic) semiconductor systems at low temperature [2]. The external magnetic field about 5 T suppress MP effect completely resulting, in particular, in a strong exciton band narrowing [3]. The Fig. 2 makes it clear that the shape and width of the symmetric exciton bands are not affected noticeably by the magnetic field in our case. The energy shift of the exciton bands in QW_3 and QW_4 (Sample #1) depends linearly on the magnetic field value (Fig. 3) whereas the exciton Zeeman splitting is already saturated in the diluted magnetic semiconductors at $H = 5$ T. These two points indicate that the samples under consideration do not exhibit the paramagnetic behaviour. On the contrary, the ordered 2D magnetic layer produces the internal field which depends linearly on the external field value in Faraday configuration [4].

Surely, a small portion of the Mn^{2+} ions penetrates in QW as determined by a weak magnetic shift of the wide QW_2 exciton band which saturates at H which exceeds 3 T (Fig. 4).

The peak energy of emission band maximum E_1 does not depend noticeably on magnetic field up to 5 T because a weak Zeeman shift of the QW_1 exciton lowest component is compensated by its diamagnetic shift. As expected, the exciton states in wide QW_1 are only slightly affected by the magnetic field due to low wavefunction amplitude on the MnTe interface layers. However, the magnetic field modify strongly the luminescence from localized states, namely, the emission band weakens and its maximum shifts towards the band E_1 (Fig. 4). The relative increase of the high-energy band E_1 is explained in the following way. The magnetic field deflects the photocarriers thus restricting their diffusion in the QW plane, and consequently their access to the localization areas. Moreover, the island-like monolayer fluctuation is able to localize the exciton if its radius is about three times larger as compared to the exciton radius. The exciton size reduces significantly in Faraday configuration, and as a consequence the smaller fluctuation is able to capture the exciton. The concentration of fluctuation depends inversely on their size, when the Gauss distribution is the case. In such a situation an average localization energy decreases along with an exciton shrinkage in the increasing field.

References

[1] C. Drexter *et al*, *Appl. Phys. Lett.* **97**, 182107 (2010).
[2] D.R. Yakovlev *et al*, *Solid State Commun.* **82**, 29 (1992).
[3] V.F. Agekian *et al*, *Solid State Commun.* **86**, 205 (1993).
[4] Yu.E. Lozovik, O.I. Notich *JETF Pisma* **54**,94 (1991).

Radiative decay rate of excitons in high-quality InGaAs quantum wells

V. G. Davydov, S. V. Poltavtsev, V. V. Ovsyankin, A. V. Trifonov, Yu. K. Dolgikh, S. A. Eliseev,
Yu. P. Efimov and V. V. Petrov

Physics Department, St Petersburg State University, Ulyanovskaya 1, Petrodvorets, St Petersburg, 198504,
Russia

Abstract. Excitonic reflection in InGaAs single quantum wells has been measured using Brewster's geometry. Record values of resonant excitonic reflection coefficient up to 0.24 were found. Experimental data were used to determine the dependence of radiative decay rate of excitons on indium fraction and quantum well width. Obtained values of radiative decay rate are weakly dependent on these parameters and in average give magnitude 65 ± 10 μeV. This value is correspondent to radiative lifetime of excitons 10 ps.

Introduction

Semiconductor nanostructures with quantum wells are considered as a promising material for devices that can process digital information in a pure optical way [1]. To realize this task the nanostructures should possess of very high efficiency of resonant interaction with light and high stability of optical properties. In this communication we present the results of detailed study of coherent optical properties of excitons in InGaAs quantum wells by means of well-developed method of resonant excitonic reflection using the Brewster's geometry [2, 3]. In particular, we have measured the value of radiative decay rate of excitons, $\hbar\Gamma_0$, which is universal property of individual quantum well. This parameter is proportional to the specific oscillator strength and is one of the most important parameters required for creation the digital cell based on the excitonic systems coherently interacting with light. In the Lorenz approximation the ratio between this quantity and exciton linewidth (FWHM) taken from optical susceptibility spectrum of quantum well reflects the fraction of coherence conserved during the processes of optical excitation and radiative recombination of excitons.

We have studied the dependence of radiative decay rate, $\hbar\Gamma_0$, on two main parameters of $In_xGa_{1-x}As$ quantum well, indium concentration, x, and well width, L_Z.

1. Samples and experimental technique

To obtain this dependence the reflection spectra from 15 samples containing totally 29 single quantum wells were measured and analyzed. The indium fraction and quantum well width values were in the ranges of $x = 0.02 - 0.1$ and $L_Z = 1 - 31$ nm, respectively. x-Range is limited because of the requirement of good stoichiometric growth of (In,Ga)As/GaAs heterostructures.

The reflection spectra were measured in the Brewster's geometry using p-polarized femto-second (fs) pulses of Ti:Sa Tsunami laser and CCD-based spectrometer with apparatus function FWHM of 20 μeV. Samples were mounted in closed-cycle cryostat and cooled down to temperature 8 K.

Using of the Brewster's geometry of excitation allows to obtain spectra without background associated with light reflection from sample surface. As a result, recorded spectral lines of HH-excitonic transitions rather well conformed to Lorenz curves. Fig. 1 shows resonant reflection spectra measured on
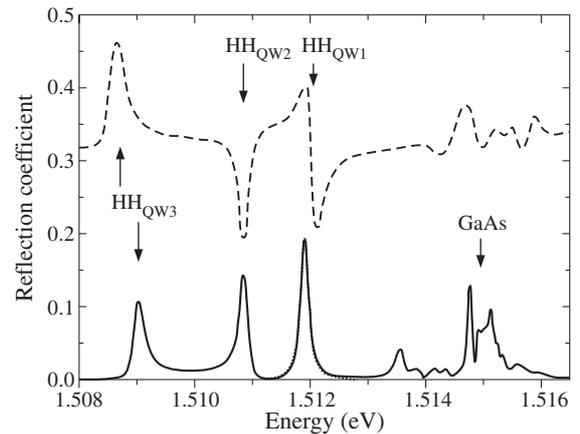
Fig. 1. Reflection spectra taken from two spots of P550 sample containing three quantum wells having following parameters: QW1: $x = 0.03$, $L_Z = 2$ nm; QW2: $x = 0.03$, $L_Z = 3.3$ nm; QW3: $x = 0.036$, $L_Z = 4$ nm. Dash-dot line — normal excitation geometry; solid line — Brewster's geometry; dot line — fitting of HH_{QW1} exciton line with Lorenz curve having FWHM 165 μeV and amplitude 0.19. Difference in HH_{QW3} line positions is, apparently, due to large spatial variation of indium concentration.

high-quality P550 sample containing three quantum wells with $L_Z = 2$, 3.3 and 4 nm and indium fraction of about 3%. To illustrate the Brewster's geometry advantage, the figure shows also a reflection spectrum measured in traditional normal geometry. It is seen that the last is much harder for analysis. Spectral lines observed at energies higher than 1.513 eV are, presumably, connected with LH-excitonic transitions as well as GaAs bulk excitonic transition.

The values for radiative decay rate are extracted from reflection spectra in the same way as it was done earlier on GaAs quantum wells [2]. Namely, we use Lorenz approximation while analyzing spectral lines of excitonic resonances. Then, the value of $\hbar\Gamma_0$ can be calculated using formula derived for normal light incidence on quantum well (the formula for amplitude reflection coefficient is given in [4]):

$$\hbar\Gamma_0 = \sqrt{K_{RR}}\,\hbar\Gamma_{total}\,,$$

where K_{RR} is the peak resonant reflection coefficient (the line amplitude), and $\hbar\Gamma_{total}$ is FWHM of spectral line. We do not take into account the modification of $\hbar\Gamma_0$ associated with exci-
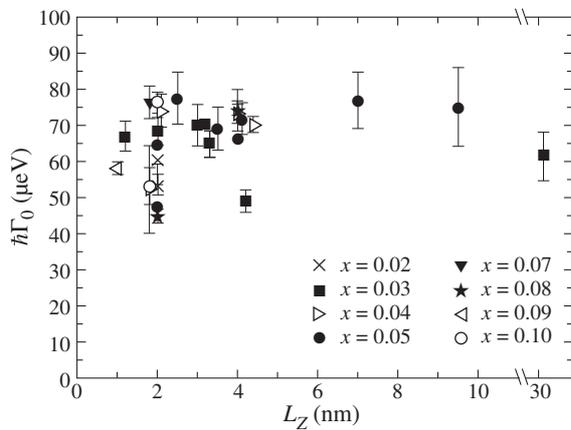
Fig. 2. Experimental values of $\hbar\Gamma_0$ with scatters for different indium fractions x and quantum well widths L_Z.

References

[1] I.Ya. Gerlovin, V.V. Ovsyankin, B.V. Stroganov and V.S. Zapasskii, *Nanotecnology* **11**, 383 (2000).

[2] S.V. Poltavtsev, V.V. Ovsyankin, B.V. Stroganov, Yu.K. Dolgikh, S.A. Eliseev, Yu.P. Efimov, and V.V. Petrov, *Optics and Spectroscopy* **105** 4, 511 (2008).

[3] S.V. Poltavtsev and B.V. Stroganov, *Physics of the Solid State* **52** 9, 1899 (2010).

[4] L.E. Vorob'ev, E.L. Ivchenko, D.A. Firsov, V.A. Shalygin, *Opticheskie svoystva nanostruktur* St Petersburg, Nauka, p. 98 (2001).

tation geometry: light refracted by the sample surface travels through heterostructure under the incidence angle of about 16°, which is small enough to neglect it. Absolute scale for reflection coefficient is obtained by normalizing spectra measured in *p*-polarization to the spectrum of fs-pulses reflected in *s*-polarization from sample surface.

2. Results

The magnitude of K_{RR} measured for a number of samples at temperature 8 K has a significant spread. For highest-quality samples it reaches the record value of 0.24. Narrowest spectral line has FWHM 130 μeV. For comparison, best parameters for GaAs single quantum wells measured earlier with the resonant reflection spectroscopy were 0.1 and 290 μeV for K_{RR} and FWHM, accordingly [2, 3].

Results of $\hbar\Gamma_0$ measurements for all samples under study are shown on Fig. 2. Each experimental point is averaged over approximately 10 measurements performed in different spots of the sample. Standard deviations are indicated.

As opposed to GaAs quantum wells, where monotonic growth of oscillator strength with diminishing of quantum well width was observed [2], here we do not see any evident dependence of this quantity on both parameters, x and L_Z. Resultant average value of radiative decay rate is $\hbar\Gamma_0 = 65 \pm 10$ μeV. This value corresponds to radiative lifetime of excitons $T_0 = 10$ ps.

Detailed analysis of reflection spectra over the samples surface revealed that large scatter of $\hbar\Gamma_0$ values caused by presence of large-scale growth defects which strongly influence the local optical properties of excitons. Surprisingly, this defects do not result in inhomogeneous broadening of spectral lines which are quite narrow and reach in the highest-quality samples width of 70 μeV.

Over 1.3 μm emission from (B)InAs/GaAs quantum dots capped by InGaAs strain-reducing layer

Qi Wang, Xiaomin Ren, Xin Guo, Tianhe Li, Pengyu Wang, Xia Zhang, Yongqing Huang, Xiaofeng Duan and Shiwei Cai

Key Laboratory of Information Photonics and Optical Communications (Beijing University of Posts and Telecommunications), Ministry of Education
Zh.I. Alferov Russian-Chinese Joint Laboratory of Information Optoelectronics and Nanoheterostructures, Beijing 100876, China

Abstract. Uniformity improvement of InAs/GaAs QDs caused by boron incorporation was oberved. 1.32 μm room temperature photoluminescence emission from BInAs/GaAs QDs capped by $In_{0.16}Ga_{0.84}As$ SRL was reported.

Introduction

Recently, the incorporation of boron into conventional III–V binary and ternary compounds (e.g., GaAs, AlAs, GaP and In-GaAs) has gained special attentions of many research groups to develop novel material systems for various potential applications [1–3]. Unfortunately, very limited experimental studies on boron incorporation into InAs quantum dots (QDs) are available [4,5]. In this paper, low pressure metalorganic chemical vapor deposition (LP-MOCVD) growth of boron-incorporated self-assembled InAs/GaAs QDs was reported. Particularly, the effects of boron incorporation on the critical thickness and uniformity of InAs QDs were investigated, and 1.32 μm room temperature photoluminescence from BInAs/GaAs QDs was demonstrated.

1. Experimental procedure

Samples were grown on exactly-oriented silicon-doped (100) GaAs substrates by LP-MOCVD. All the growths were performed in a vertical reactor with the constant pressure of 133 mbar (100 Torr). Triethylboron (TEB), trimethylindium (TMIn), trimethylgallium (TMGa) and pure arsine (AsH$_3$) were used as B, In, Ga and As precursors, respectively. A 400 nm GaAs buffer layer was first grown at 650 °C. The substrate was then cooled down to 530 °C for the growth of self-assembled QDs. In this study, InAs QDs with nominal coverage of 2.4, 3.0 and 3.6 ML were grown under S-K mode, respectively. Moreover, in order to form BInAs QDs as comparison, TEB source with flowrate of 6.8×10^{-6} mol/min was simultaneously introduced into the reactor during InAs deposition. Growth rate of 0.06 ML/s and V/III ratio of 10 were fixed during (B)InAs/GaAs QD growth. For the surface morphology characterization, the uncapped (B)InAs/GaAs QDs were cooled down to room temperature rapidly. For the photoluminescence measurement, after 30 seconds growth interruption (GRI) under AsH$_3$ ambient, (B)InAs/GaAs QDs were capped with 5 nm $In_{0.16}Ga_{0.84}As$ strain-reducing layer (SRL) deposited at 530 °C and additional 50 nm GaAs deposited at 600 °C, respectively.

2. Results and discussions

AFM images of uncapped InAs QDs (sample A, C) and BInAs QDs (sample B, D) are shown in Fig. 1. When InAs coverage was increased from 2.4 to 3.0 ML, the dot density decreased from 4.93×10^{10}/cm^2 to 3.65×10^{10}/cm^2 (not counting large
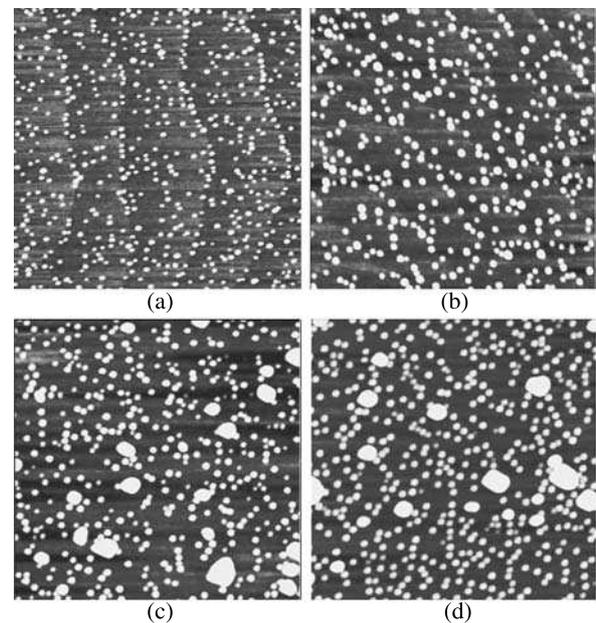
Fig. 1. 1×1 μm^2 AFM images of uncapped (a) 2.4 ML InAs QD, (b) 2.4 ML BInAs QDs, (c) 3.0 ML InAs QDs and (d) 3.0 ML BInAs QDs.

islands), and several large coalesced islands were observed. In addition, InAs QDs grown in this study have a bimodal size distribution. Meanwhile, the reduction of InAs QD density and improvement of the uniformity caused by the boron incorporation have been found. For BInAs coverage of 2.4 and 3.0 ML, the dot density was reduced to 3.28×10^{10}/cm^2 and 2.73×10^{10}/cm^2, respectively. This result demonstrated that boron incorporation caused the increase of critical layer thickness, which was attributed to the decreased lattice mismatch between BInAs and GaAs.

Room-temperature PL (RT-PL) spectra of InAs QDs (samples E) and BInAs QDs (sample F) grown using the nominal coverage of 3.6 ML are shown in Fig. 2. We obtained the peak wavelength of 1328 nm and FWHM value of 44 meV from PL of InAs QDs. Beside the reduction of PL intensity, the peak wavelength was blue-shifted to 1322 nm and FWHM value was narrowed to 40 meV after the boron incorporation. These results also demonstrated the decrease in the density and height as well as the improvement in the uniformity of QDs.
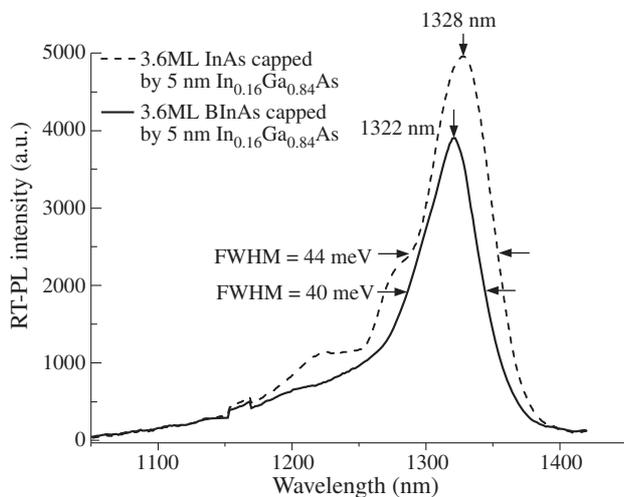
Fig. 2. Room temperature PL spectra of 3.6 ML InAs QDs (dash line) and 3.6 ML BInAs QDs (solid line). (B)InAs/GaAs QDs were capped by 5 nm $In_{0.16}Ga_{0.84}As$ SRL and 50 nm GaAs capping layer.

3. Conclusions

In summary, the experimental results show that boron incorporation can improve the uniformity of self-assembled InAs/GaAs QDs. Further investigations on the growth mechanism and key properties of BInAs/GaAs QDs are still ongoing.

References

[1] Q. Wang, X. Ren, *et al*, *Microelectron. J.* **39**, 1678 (2008).
[2] Q. Wang, X. Ren, *et al*, *Microelectron. J.* **40**, 87 (2009).
[3] Q. Wang, X. Ren *et al*, *J. Alloys Compd.*, (2011),
     doi:10.1016/j.jallcom.2011.02.104.
[4] X. Ren, Q. Wang *et al*, *18th International Symposium on Nanostructures: Physics and Technology (Russia, 2010)*, 2010.
[5] V.M. Danil'tsev *et al*, *J. Surf. Invest.* **2**, 514 (2008).

New technologies for nano-and optoelectronics based on layers with varied optical parameters — GeO$_2$ films with Ge-nanoparticles

K. N. Astankova[2], A. N. Aksenov[1], E. B. Gorokhov[2], I. A. Azarov[3], D. V. Marin[2,3] and V. A. Volodin[2,3]

[1] Novosibirsk State Technical University, 630092 Novosibirsk, Russia
[2] Institute of Semiconductor Physics, SB RAS, Lavrentieva av., 13, Novosibirsk 630090, Russia
[3] Novosibirsk State University, Pirogov str. 2, 630090 Novosibirsk, Russia

Properties of semiconductor nanoparticles (quantum dots — QD), embedded in the wide-gap dielectric matrix, are of interest as from the fundamental point of view and for device applications. Based on these structures one can create: a memory with the capture of charge carriers in quantum wells (flash memory), the single-electron transistors, optical interference filters, diffraction gratings, optoelectronic devices working on the effects of luminescence (light-emitting diodes, lasers, quantum dots displays — QD-LED), photonic crystals, the volume holograms. Analysis of the properties of GeO(s) layers and heterolayers, consisting of GeO$_2$ dielectric film with embedded Ge-nanoclusters (GeO$_2$⟨Ge-NCs⟩), shows that from the position of the physics and technology requirements they are promise for making of the most of the above devices [1]. Give examples.

By variation of the properties of GeO$_2$⟨Ge-NCs⟩ heterolayers one can create optical interference filters based on multilayer systems, where not only the optical constants of alternated layers vary widely, but a new effects reveal that can not be achieved using traditional materials and technologies. New properties can be given to such filters due to layers with refractive index changed in thickness [2], or forming a layer system, in which the complex refractive index varies smoothly and continuously from layer to layer. Taking into account that
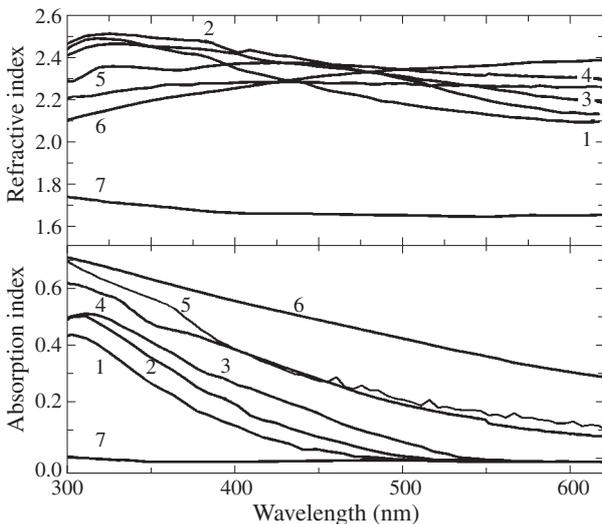
Fig. 2. Photo, scheme and transmission spectra of interference filters on the base of GeO$_2$⟨Ge-NCs⟩/SiO$_2$ multilayer system on glass, recorded in different point.

such filters are one-dimensional photonic crystals, the interest to this effect increases.

The optical constants of GeO$_2$⟨Ge-NCs⟩ heterolayers can be widely varied by three main technological methods:

— variations in chemical composition (i.e. part of each component in the GeO$_2$⟨Ge-NCs⟩ system);
— using of 3D quantum confinement effect in Ge-nanoparticles and their crystallization;
— chemical and structural modifications of the GeO$_2$ matrix in heterolayers due to easily activated chemical reactions at its contact with different inorganic agents (gases and condensed matters such as NH$_3$, SiO$_2$, Si$_2$N$_4$, etc.).

On the basis of GeO$_2$⟨Ge-NCs⟩ heterolayers a working prototypes of multilayer interference filters and diffraction gratings have been fabricated. The optical filter was made of alternating thin CVD SiO$_2$ layers (8–9 nm) and GeO$_2$⟨Ge-NCs⟩ heterolayers (from 10–13 to 25–30 nm) on the glass. In Fig. 2 is shown the photo of such filter, scheme of its layers and transmission spectra registered in two points with different thicknesses of GeO$_2$⟨Ge-NCs⟩ layers. Changes in the light transmission at these points are caused by the differences of interference conditions due to different thicknesses of heterolayers. With the growth of Ge-nanoparticle size by annealing, the absorption of filter increases in the UV region.

Diffraction gratings is formed by dry, maskless femtosecond (fs) laser lithography, where GeO$_2$⟨Ge-NCs⟩ heterolayers used as a resist. Its local modification was induced when scanning by a focused beam of pulse fs laser. They were 2 types

Fig. 1. Variation of *n* and *k* of GeO$_2$⟨Ge-NCs⟩ heterolayers after annealings due to 3D confinement effect in Ge-nanoclusters and growth of their sizes: 1, 2, 3, 4 — GeO(s) as deposited and annealed at 260, 290, 320 °C, 5 — LP CVD GeO$_2$⟨Ge-NCs⟩, 6 — Bruggeman model, 7 — thermal GeO$_2$.
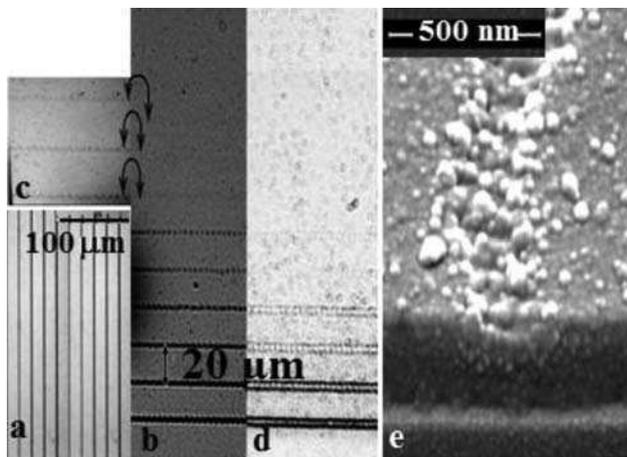
Fig. 3. GeO$_2$⟨Ge-NCs⟩ heterolayers as material for diffraction gratings formation: a, b, c — optical micrograph; d, e — SEM image.

References

[1] V.A. Volodin *et al*, *Quantum Dots: Research, Technology and Applications*, edited by Randolf W. Knoss, Nova Science Publishers Inc. New York, chapter 9, pp. 333–372 (2008).
[2] P.V. Adamson, *Pis'ma v JTF* **26** 22, 55 (2000).
[3] N.A. Vlasenko *et al*, *Technical Physics Letters* **4** 9, 619 (1978).

depending on the laser beam energy. High laser beam energy activated partial or complete "evaporation" of the resist material due to the reaction GeO$_2$ + Ge → 2GeO (gas). In this case, grooves were formed in the resist layer, which are easily detected by SEM (Fig. 3d and e) and optical microscopy. The minimum width of visible grooves was 200 nm. Scanning on the resist when the energy of the laser beam was below the threshold of its evaporation, in the bulk the beam could initiate other local chemical and structural modifications of second type. They were easily observed under an optical microscope (Fig. 3a, b and c) because in the resist layer the optical constants were changed locally. But such processes are slightly distorted the topography of GeO$_2$⟨Ge-NCs⟩ layer and the SEM couldn't reveal the traces of them. The process of the second type includes the decomposition of atomic net of metastable GeO(solid) layer, the nucleation and growth of amorphous Ge-nanoparticles and their crystallization, shrinkage of heterolayer and, seem, the crystallization of the GeO$_2$ matrix. These processes can also be used for the formation of diffraction gratings (the minimum width of the diffraction lines ∼15 − 30 nm).

New data were obtained in favor of application of GeO$_2$ ⟨Ge-NCs⟩ heterolayers and germanium monoxide (GeO(s)) layers in 2D and volume holography as shown in 1978 [3]. According to estimates, when the thicknesses of the studied films ∼0.3 − 0.6 μm, the Klein parameter $Q \sim 10$ (the theoretical criterion of the degree of voluminosity of the elementary holograms), while the threshold energy of most processes in these films activated by radiation does not exceed 40–60 mJ/cm^2 (which should speed up the recording of holograms, a minimum of the line width of the diffraction ∼15−30 nm (Fig. 3e)).

1. Conclusion

Approaches to the formation of some elements of modern optical devices based on thin films of GeO(solid) and GeO$_2$ were found. It was shown that unique properties make them promising materials for nano-and optoelectronics. The use of heterolayers consisting of an insulating matrix GeO$_2$ and embedded in it Ge-nanoclusters for fabrication of new types of diffraction gratings, interference filters and holograms were demonstrated. These technologies are a simple and low cost, that indicates a high efficiency of their using in development of nanoindustry.

GeO(s) films — new resist for nanolithography

K. N. Astankova[1], *E. B. Gorokhov*[1], *K. V. Bulah*[2], *A. A. Chouprik*[2], *A. I. Kuznetsov*[3] and *A. V. Latyshev*[1]

[1] Institute of Semiconductor Physics, SB RAS, Lavrentieva av., 13, 630090 Novosibirsk, Russia
[2] Moscow Institute of Physics and Technology, Institutskii per. 9, 141700 Dolgoprudny, Russia
[3] Laser Zentrum Hannover, Hollerithllee 8, 30419 Hannover, Germany

Introduction

Traditional optical lithography will reach its limit in the near future. The transition from optical lithography to other kinds of nanolithography goes through the search for new materials that can serve effectively as a resist in these processes. So, one uses both well-known common resists and completely new materials, whose properties appear suitable for this role in a particular lithographic problem. It is obvious that there is no universal resist for all kinds of nanolithography. But the complex of properties of some materials makes them especially favorable for use under certain conditions of nanolithography. As such material we study thin layers of germanium monoxide (GeO(s)), which can be used in intensively developed SPM and laser nanolithography. Curiously, that GeO(s) layers attract attention due to its property, which is not allowed to take them a notable place among other traditional protective dielectrics used in microelectronics — the structural, chemical, thermal and electrical instability of GeO(s). In spite of this, the preliminary results of applying GeO(s) and GeO_x layers ($x = 1, 2$) as a resist in SPM and laser nanolithography appeared have much promise. Thanks to structural instability, GeO(s) layers have low thresholds for modification and ablation processes under local impacts. In the film there is no too many chemical elements which could be responsible for undesirable chemical activity of the resist while the local modifications in it. This restricts the range of possible chemical and structural transformations in the resist layer that facilitates their separation, processes control and management.

1. GeO(s) films — as a resist for SPM nanolithography

The new experiment on the patterning of GeO(s) layer, used as a positive nanoresist, was performed in MIPT (Moscow). The lithography process includes three operations:

1) AFM-tip-induced local anodic oxidation (LAO) of GeO(s) layer: $2GeO(s) + O_2 \rightarrow 2GeO_2$;
2) thermal decomposition of GeO(s) layer into GeO_2 and Ge throughout the substrate: $2GeO(s) \rightarrow GeO_2 + Ge$;
3) removal of GeO_2 by selective etching from the decomposed GeO(s) layer, which converts into a matrix of GeO_2 with Ge-nanoclusters ($GeO_2\langle Ge\text{-}NCs\rangle$).

Homogeneous nondecomposed layer of GeO(s) (of ~9 nm thick) was obtained on Si-substrate by re-evaporation of GeO_2 $\langle Ge\text{-}NCs\rangle$ heterolayers in a high vacuum. Electrostimulated AFM modification of GeO(s) layer was carried out by probes DCP11 (curvature radius 50 nm, with a heavily doped conductive diamond-like coating). The lithography process was performed in contact mode of AFM at a constant voltage ($-V$) on the probe with respect to the substrate. Modification of the
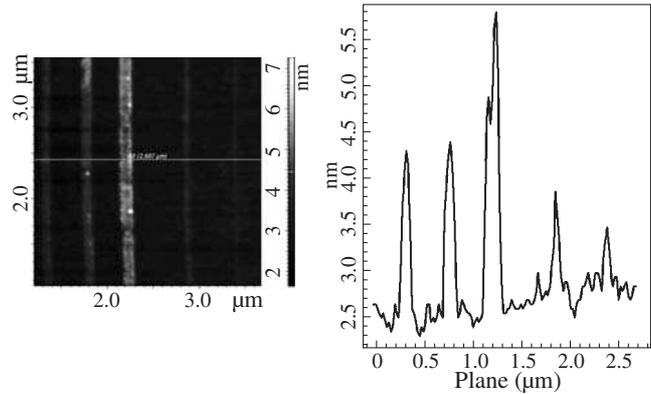
Fig. 1. AFM image of GeO_2 strips in GeO(s) resist formed by LAO method and their relief profile.

local details of the resist relief, formed by the probe, was controlled step by step. The average roughness of the film didn't exceed ~0.4 nm at the beginning and 0.8 nm in the end of the nanolithography process. By LAO method the strips of GeO_2 were formed, which was prominent above the surface of the GeO(s) resist. Their heights, depending on the probe voltage, varied from 0.8 to 3 nm, while the minimal width of strips was ~78−90 nm (Fig. 1) and spacing between them ~35−40 nm. After the operation (3) a thin layer (~3−3.5 nm) of agglomerated together Ge-nanoclusters is formed throughout the substrate. In places where GeO_2 strips were selectively removed from resist, grooves of ~1.5−3 nm in depth remained in Ge-agglomeration layer. Their minima width was ~30−60 nm (Fig. 2). Further optimization of the lithography regime described is possible. There is different way of SPM nanolithography, where GeO(s) film can be used as a negative resist [1].

2. GeO(s) films — as a resist for laser nanolithography

The best way to use of GeO(s) layers or $GeO_2\langle Ge\text{-}NCs\rangle$ heterolayers as a resist in dry, maskless laser nanolithography is a local initiation by beam of the reaction of their "evaporation" (i.e. GeO(s) transformation into vapor GeO(g)): $2GeO(s) \rightarrow GeO_2 + Ge(I) \rightarrow 2GeO(g)(II)$. For GeO(s) the process has **I** and **II** stages, and as for $GeO_2\langle Ge\text{-}NCs\rangle$ heterolayer — stage **II** only. In GeO(s) and $GeO_2\langle Ge\text{-}NCs\rangle$ heterolayer ultra-short laser pulses cause the processes of structural reconstruction and chemical reactions such as: film shrinkage; decomposition of GeO(s) layers due to the reaction **I**; Ge-nanoparticles growth and their crystallization in heterolayer; crystallization of glassy GeO_2 matrix; the reaction of GeO vapor formation (**II**) from matter of $GeO_2\langle Ge\text{-}NCs\rangle$ heterolayer; the films and substrate ablation (i.e. an explosive destruction) [2]. All of these processes take place at irradiation of studied layers by
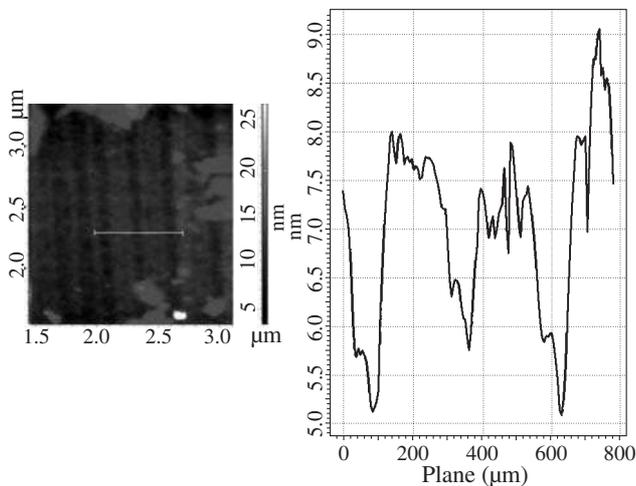
Fig. 2. AFM image of grooves in Ge-agglomeration layer after operation 2 and 3.

Fig. 3. a — Gaussian energy distribution; b and c — SEM image of local foaming of $GeO_2\langle Ge\text{-}NCs\rangle$ heterolayer without cap layer.

femtosecond (fs) Ti:Sa laser with $\lambda = 800$ nm ($h\nu = 1.55$ eV) and pulse duration of 30 fs. In different layered structures and conditions of irradiation with increasing of fs pulse energy these processes of modification of the film structure are excited by one to another.

Laser radiation is absorbed in heterolayers $GeO_2\langle Ge\text{-}NCs\rangle$ only by Ge-nanoclusters, which have a relatively narrow effective optical gap $E_g^{eff}(Ge\text{-}NC) < 2$ eV whereas matrix GeO_2 have optical gap $E_g^{eff}(GeO_2) \sim 4.5-5$ eV. So one can quickly heat only Ge-nanoclusters and leave "cold" the carrier matrix. But Ge-NCs could be heated so that they will react due to reaction (**II**) with matter of glassy GeO_2 surrounding of them. Thus released the gaseous GeO should be localized around each Ge-cluster in the form of nano-bubbles. Then without freedom of exit, hot GeO(g) can push by its pressure the heated glassy GeO_2 which became viscous. When Ge-nanoparticles heating by laser pulses stops, bulk glassy GeO_2 cools and hardens. Herewith viscosity of the glass will grow very rapidly, so that nanocavities in GeO_2, formed by hot gas, have no time to collapse to the end. As a result it is expected to obtain a layer in the form of frozen nano-foam from the mass of glassy GeO_2 with nano-bubbles filled with GeO(g).

Unprotected $GeO_2\langle Ge\text{-}NCs\rangle$ heterolayer of 70 nm thick were scanned by fs laser beam, focused to a spot size $2r_0 \sim \lambda \sim 1$ μm. Sample was placed perpendicular to the beam on the optical bench, which vibrated with amplitude of ~ 1 μm in the sample plane and vertically. With vertical vibration of the sample the focus of the laser beam in first turning point 1 (Fig. 3b) was on the film, and when turn back (point 2) focus lifts over the surface. In the point 1 the spot had a minimal diameter on the sample ($2r_1 = 2r_0 \sim \lambda$) and top energy E'_{max} in the center of beam exceeded threshold of foaming (E_1) in $GeO_2\langle Ge\text{-}NCs\rangle$ heterolayer and threshold of its evaporation (E_2) (Fig. 3a). In point 2 defocused beam on the film surface had the largest diameter $2r_2 > 2r_1$ and the minimum value of $E'_{max} < E_1$ and E_2. Therefore, in these points both processes didn't proceed in heterolayer, while in the points 1 they were activated by beam. Passing the points 1, the beam evaporated the material of heterolayer (along motion of its center on the film), opening in it up to the substrate a nanosize holes ($\sim 11-45$ nm) in the form of circular or long cavities (Figs. 3b and 3c). For tens or hundreds of nm away from the cavities
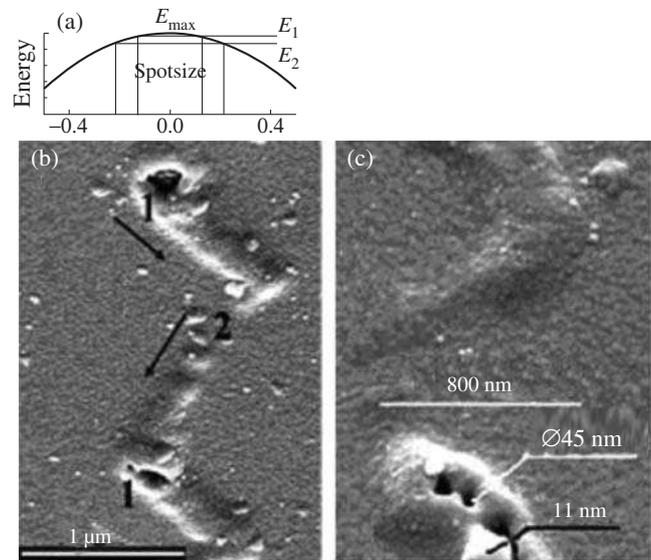
in $GeO_2\langle Ge\text{-}NCs\rangle$ heterolayers the process of their transformation into nano-foam proceeded. The length of the holes in heterolayer was not great because beam, shifting, was defocused. Vibration revealed a high sensitivity of the processes, activated by a scanning beam in heterolayers, to weak variations of its local intensity, the flexibility and rate of reaction to these changes.

3. Conclusions

Thus the possibility to form nanoscale cavities in a thin GeO(s) layer was proved, when the size of the focused beam and its wavelength in 20–70 times exceed cavity width. All data obtained on this effect surely showed promise of using these layers as resist in laser nanolithography. Confinement effect in a semiconductor quantum dots was used not in the format of study of details of the transfer kinetics in the electron subsystem of the solid, but for the chemical and structural modification of its state. Thin GeO(s), GeO_x layers and $GeO_2\langle Ge\text{-}NCs\rangle$ heterolayers also can be used as a resist in SPM nanolithography.

References

[1] K.N. Astankova *et al*, *Journal of surface investigation. Xray, synchrotron and neutron techniques* **3**, 773 (2009).
[2] E.B. Gorokhov *et al*, *Proceedings of SPIE* **7994**, 79940W (2011).

Growth of n-doped and p-doped GaAs nanowires by Au-assisted metalorganic chemical vapor deposition: effect of dopants flux rates

Jingwei Guo, Xiaomin Ren, Hui Huang, Shiwei Cai, Xia Zhang, Xin Guo, Qi Wang and Yongqing Huang
Key Laboratory of Information Photonics and Optical Communications Ministry of Education
Beijing University of Posts and Telecommunications, 100876 Beijing, China

Abstract. N-doped and p-doped GaAs nanowires (NWs) are grown on GaAs (111) B substrate by means of vapor-liquid-solid (VLS) mechanism in a metalorganic chemical vapor deposition (MOCVD) system. It is found that for n-type doping NWs growth rate is proportional the flux rates of dopant and the structure is pure zinc blende without any stacking faults. For p-type doing, in high II/III ratio range, there exists a critical length, beyond which the kinking takes place.

Introduction

In recent years, semiconductor nanowires (NWs) have drawn considerable interest due to their potential applications in electronic and optoelectronic devices [1]. Nanowier-based lasers, photo detectors, field effect transistors, and single-electron memory devices have already been demonstrated. The vapor-liquid-solid (VLS) mechanism, using gold (Au) nanoparticles as catalyst, is a commonly used method for semiconductor NWs growth [2]. GaAs NWs used for lasers and photodetectors is one of the most popular NWs.

In this paper, the growth and characterization of n-doped and p-doped GaAs nanowires are investigated. The related growth mechanisms are discussed.

1. Experimental procedure

The growth was performed in a THOMAS SWAN CCS-MOCVD system at a pressure of 100 Torr. Prior to NWs growth, an Au film with thickness of 4 nm was deposited on the GaAs (111) B substrate by magnetron sputtering. Then the Au-coated substrate was loaded into the MOCVD reactor and annealed in situ at 650 °C in arsine and hydrogen ambient for desorption of surface contaminants and formation of alloy droplets as catalyst. After ramped down to the growth temperature, GaAs NWs were firstly grown for 500 s at 470 °C. Trimethylgallium (TMGa, 15 sccm, sccm = stand − ard cubic centimeters per minute) and AsH_3 (30 sccm) were used as group III and V precursors for GaAs NWs. The carrier gas was hydrogen (H_2). During n-type doping, the flux rates of dopant SiH_4 were 80 and 40 sccm for sample A and B, respectively. For comparison, undoped GaAs NWs sample C was grown at the same conditions.During p-type doping, the flux rates of dopant diethyl zinc (DEZn) were 80, 40 and 1 sccm for sample D, E and F, respectively.

The morphologies of as-grown NWs were studied using a HITACHI S-5500 scanning electron microscope (SEM). The structure of single NW was characterized using JEOL 2100F and FEI TECNAI F30 field-emission transmission electron microscope (TEM). The acceleration voltage was 300 kV. For TEM samples preparation, the NWs were removed from the substrate by sonication into ethanol suspension for 2 minutes. A small volume of the NWs suspension was left to dry onto a holey carbon film supported by a Cu mesh TEM grid.

2. Results and discussions

SEM images of as-grown NWs are shown in Fig. 1. It shows that all n-doped NWs are vertical to the substrate and there is no lateral growth occurs. The average lengths of samples A, B and C are 6.3, 6.1 and 5.3 μm, respectively. The growth rates of samples A, B and C are 12.6, 12.3 and 10.6 nm/s, respectively. The growth rate is proportional the flux rates of n-type dopant SiH_4. Larger SiH_4 flux rate results in larger growth rate of NWs.

For VLS growth, there are two major contributions, i.e., direct impingement of the precursors onto the alloy droplet and adatom diffusion from the sidewalls and substrate surface to the top. It has been demonstrated that the adatom diffusion will result in lateral overgrowth and tapering when the wire length is longer than the diffusion length of adatom, and the growth rate inversely dependent on the diameter. In Fig. 1 (a)–(c), it is observed that lateral overgrowth and tapering of NWs do not occur, since the NW has a constant diameter from base to top. Thus, it can be concluded that NWs were grown with negligible contribution from adatom diffusion and main contribution from catalytic pyrolysis of the precursors impinging onto the alloy droplet. In other words, the droplet acts as a catalyst rather than a collector of adatom.

For p-type doing, with large DEZn flux rate (more than 10 sccm), there exists a critical length, beyond which the kinking takes place, as shown in Fig. 1(d) and 1(e) for sample D and E, respectively. A possible reason may influence on the bending of p-GaAs nanowires is that excess Zn atoms may segregate on the sidewalls forming deformation area.

From the top view SEM image (not shown), it is found that the sidewalls of all samples are hexagon and the sidewall facets belong to (112) families of planes, which are the same as Moewe [3] and Wacaser [4]. It is a different result than the one reported by Tambe *et al* [5] and Noborisaka *et al* [6] whose facets are (110) families of planes. The (112) facets have a larger number of surface dangling bonds with respect to the (110) facets that tend to reconstruct (Ga-Ga and As-As dimers) [7]. This may lower the surface energy of (112) facets less than that of (110) facets.

High-resolution TEM (HRTEM) images (not shown) of sample A, B and C indicate that all samples have pure zinc blende structures, and no stacking faults from bottom to top.
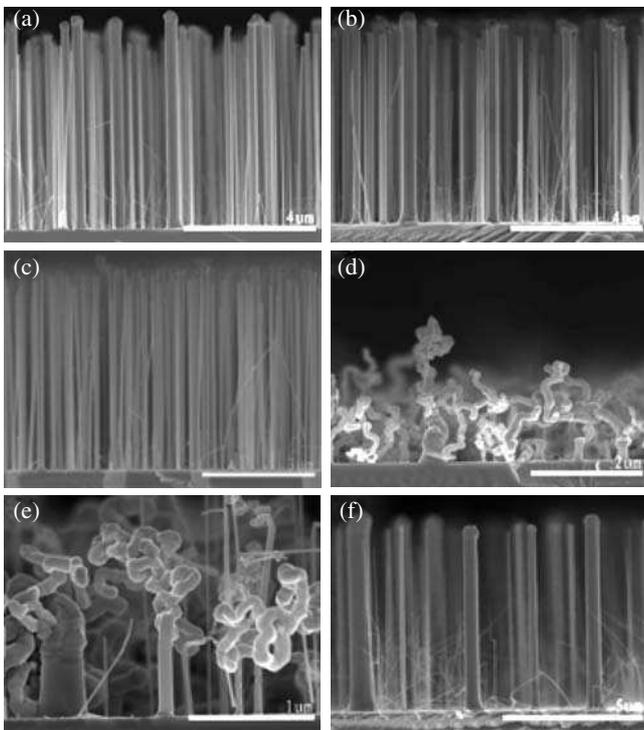
Fig. 1. Cross-sectional SEM images of (a) Sample A; (b) Sample B; (c) Sample C; (d) Sample D; (e) Sample E; (f) Sample F.

Fluctuations in the composition of would result in stacking faults or twins in the NW due to the change of tension and supersaturation in droplets. However, NWs' growth conditions such as the high growth rate and the relatively high V/III ratio may all contribute to the reducing of planar defects such as stacking faults and twins in the NWs [8]. Moreover, in our case, the number of Si atoms dissolved in droplets is too small to affect the crystallographic quality of NWs.

3. Conclusions

In summary, n-doped and p-doped GaAs nanowires were grown on GaAs (111) B substrate by means of VLS mechanism in a MOCVD system, respectively. From SEM figures, we can find that all n-type doping NWs are vertical to the substrate and no lateral growth occurs. The growth rate is proportional the flux rates of dopant SiH_4. Larger SiH_4 flux rate results in larger growth rate of NWs. The contribution from adatom diffusion can be negligible and almost all contribution comes from catalytic pyrolysis of the precursors impinging on droplets. For p-type doing, in high II/III ratio range, there exists a critical length, beyond which the kinking takes place. From TEM images, pure zinc blende structures without any stacking faults from bottom to top for all n-doped samples were achieved.

References

[1] F. Patolsky *et al*, *Science* **313**, 1100 (2006).

[2] R.S. Wagner *et al*, *Appl. Phys. Lett.* **4**, 89 (1964).
[3] M. Moewe *et al*, *Appl. Phys. Lett.* **93**, 023116 (2008).
[4] B.A. Wacaser *et al*, *J. Cryst. Growth* **287**, 504 (2006).
[5] M.J. Tambe *et al*, *Appl. Phys. Lett.* **93**, 151917 (2008).
[6] J. Noborisaka *et al*, *Appl. Phys. Lett.* **87**, 093109 (2005).
[7] R. Magri *et al*, *Phys. Status Solidi C* **7**, 374 (2010).
[8] H.J. Joyce *et al*, *Nano Lett.* **7**, 921 (2007).

Unconventional semiconductor superlattices — inorganic-organic hybrid nanostructures — with unusual electronic, optical and thermal properties

Yong Zhang

Department of Electrical and Computer Engineering, Energy Production and Infrastructure Center,
Optoelectronics Center, University of North Carolina at Charlotte, Charlotte, NC 28223, USA

Abstract. N-doped and p-doped GaAs nanowires (NWs) are grown on GaAs (111) B substrate by means of
vapor-liquid-solid (VLS) mechanism in a metalorganic chemical vapor deposition (MOCVD) system. It is found that for
n-type doping NWs growth rate is proportional the flux rates of dopant and the structure is pure zinc blende without any
stacking faults. For p-type doing, in high II/III ratio range, there exists a critical length, beyond which the kinking takes
place.

Superlattice, proposed by Esaki and Tsu in 1970 [1], has been a major force in providing man-made solids with unique properties that are not readily available in nature. Since the superlattice research was launched, the concept of the superlattice has been extended far beyond the originally proposed materials and structures. Taking this concept to the extreme in terms of the layer thickness, one has ultra-thin superlattices, such as $(GaAs)_n/(AlAs)_m$ with $n(m) = 1-4$, where n and m stand for the number of monolayers. The material properties of such superlattices are shown to be very different from either GaAs or AlAs [2], although, despite many decades of effort, it remains a great challenge to produce a superlattice with abrupt interfaces (i.e., without inter-diffusion) [3]. Furthermore, the chemical bonding at the interface of a typical semiconductor superlattice remains more or less the same as that in a bulk semiconductor. An unconventional superlattice with drastically different chemical bonding and thinnest possible layer thickness, a graphene/(2-D Si) superlattice, has recently been proposed [4], but not yet been realized.
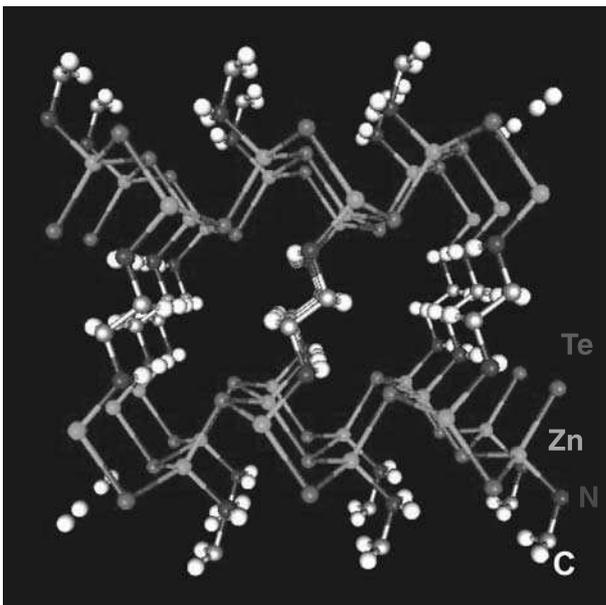
Fig. 1. Atomic structure of an inorganic-organic hybrid superlattice, β-ZnTe/(en)$_{0.5}$, determined by X-ray diffraction. H atoms are omitted in the plot for clarity.
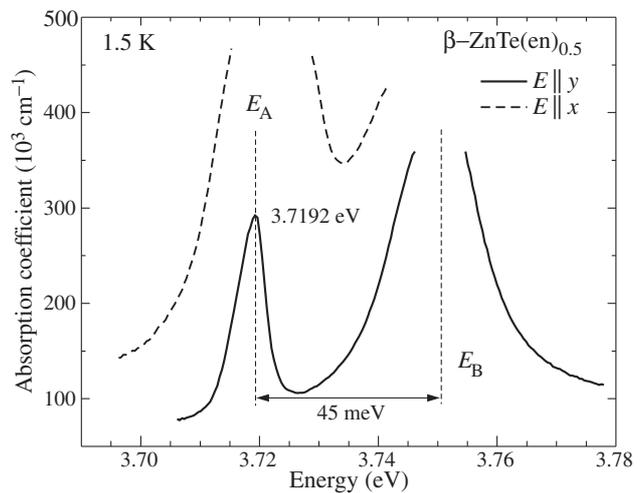
Fig. 2. Low temperature absorption spectra of β-ZnTe(en)$_{0.5}$ with polarizations perpendicular to the superlattice axis.
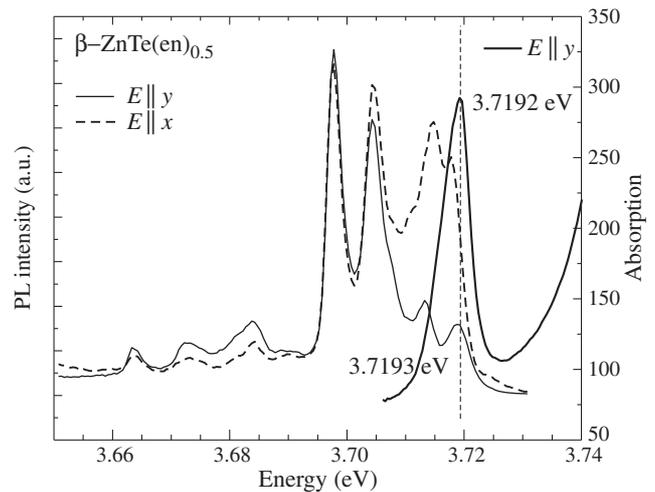
Fig. 3. Low temperature PL spectra of β-ZnTe(en)$_{0.5}$ with polarizations perpendicular to the superlattice axis.

In this talk, we will report the research effort on another unconventional type of superlattice, namely an inorganic-organic hybrid superlattice that also has very short period and atypical chemical bonding, and has been successfully synthesized and well characterized structurally [5,6]. Shown in Fig. 1 is the
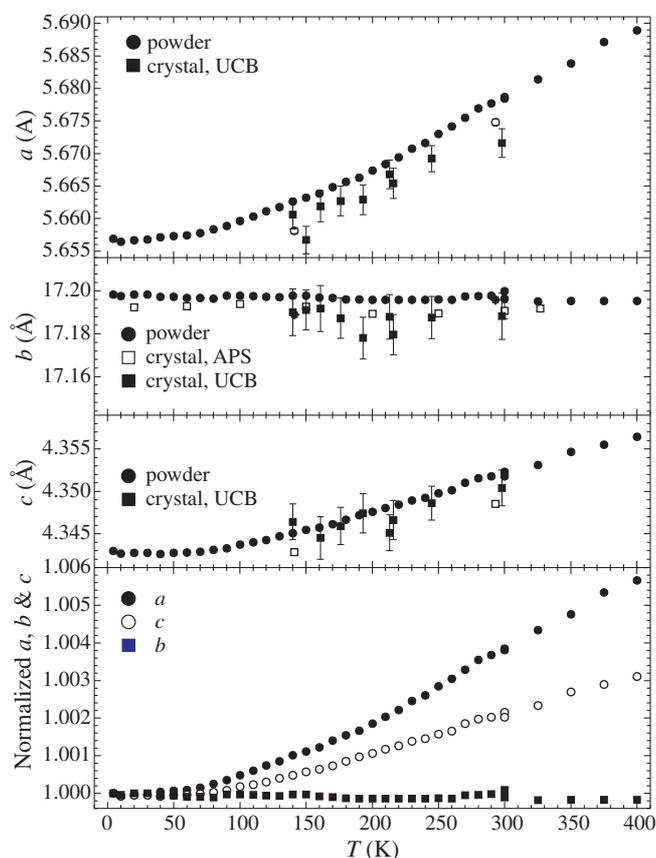
Fig. 4. The temperature dependence of the lattice constants, a, b, and c for ZnTe(en)$_{0.5}$, measured on both powder and single-crystal samples and on different x-ray diffraction systems.

atomic structure of a hybrid superlattice, ZnTe(en)$_{0.5}$, based on ZnTe and ethylenediamine (en = C$_2$N$_2$H$_8$). It is a prototype of a large group of hybrid superlattices that share the similar structure of II–VI(Mo)$_{0.5}$, i.e., thin II–VI slabs interconnected by small organic molecules. They have obtained by using a low cost chemical synthesis method [6]. Specifically, for ZnTe(en)$_{0.5}$, two mono-layer thick (110) ZnTe slabs are interconnected by en molecules, with the period along the superlattice direction being only 17.2 Å.

Such a hybrid superlattice has been shown to exhibit a number of unique aspects compared to the conventional inorganic semiconductor superlattice: for instance, (i) extremely high degree of structural perfectness (e.g., Raman width <1 cm^{-1} and XRD width <0.01 degree) [7,8]; (ii) drastically different chemical bonding situation from that of the inorganic component (e.g., the inorganic anions is only three- instead of four-fold coordinated) [6]; (iii) strongly enhanced inter-band optical absorption [7]; (iv) very large bandgap tuning [6,9]; (v) zero thermal expansion along the superlattice stacking direction and novel way of tuning thermal expansion [8,10]. Fig. 2 shows the low temperature (1.5 K) absorption spectra for two non-equivalent polarizations perpendicular to the superlattice axis. It show an excitonic absorption peak at 3.7192 eV, a 1.325 eV blue shift from that of ZnTe (2.394 eV); and strongly enhanced absorption, $\sim 3 \times 10^5$ cm^{-1} for the y polarization and $\sim 10^6$ cm^{-1} (estimated) for the x-polarization. Fig. 3 shows the low temperature PL spectra in two in-plane polarizations. For the y-polarization, the PL peak (3.7193 eV) is found at nearly the identical position of the excitonic absorption peak,

indicating the exciton-polariton nature of the emission. This is the very first unambiguous observation of the exciton-polariton emission in an inorganic-organic hybrid crystal [7].

The unique combination of the inorganic and organic leads to another interesting property, zero-thermal expansion observed along the superlattice axis in ZnTe(en)$_{0.5}$, because of the delicate compensation of the thermal expansion of the inorganic and organic components [8]. Fig. 4 shows the thermal expansion of the hybrid superlattice along the three symmetry axes. The thermal expansion coefficient for the superlattice axis b is extremely small: $|\alpha| < 4.3 \times 10^{-7}$ K^{-1} in a broader temperature range of 4–400 K. This finding provides a new mechanism for designing materials in a nanoscopic scale with desirable thermal expansion properties, from negative to positive thermal expansion [8,10].

References

[1] L. Esaki, and R. Tsu, *IBM Res. Dev.* **14**, 61 (1970).
[2] W.K. Ge *et al*, *Journal of Luminescence* **59**, 163 (1994).
[3] J.H. Li *et al*, *Physical Review Letters* **91**, 106103 (2003).
[4] Y. Zhang, and R. Tsu, *Nanoscale Research Letters* **5**, 805 (2010).
[5] X.Y. Huang, J. Li, and H.X. Fu, *Journal of the American Chemical Society* **122**, 8789 (2000).
[6] X.Y. Huang *et al*, *Journal of the American Chemical Society* **125**, 7049 (2003).
[7] Y. Zhang *et al*, *Physical Review Letters* **96**, 026405 (2006).
[8] Y. Zhang *et al*, *Physical Review Letters* **99**, 215901 (2007).
[9] B. Fluegel *et al*, *Physical Review B* **70**, 205308 (2004).
[10] J. Li *et al*, *Journal of the American Chemical Society* **129**, 14140 (2007).

New electromagnetic metamaterials based on precise metal-semiconductor shells

E. V. Naumova[1], *V. Ya. Prinz*[1], S. V. Golod[1], V. A. Seleznev[1] and V. V. Kubarev[2]

[1] Institute of Semiconductor Physics, SB RAS, Lavrentieva av., 13, Novosibirsk 630090, Russia
[2] Institute of Nuclear Physics, SB RAS, Lavrentieva av., 11, Novosibirsk 630090, Russia

Electromagnetic metamaterials are artificial materials composed of resonant elements whose interaction with electromagnetic radiation provides for extraordinary electromagnetic properties of such materials not found in their natural counterparts. Electromagnetic metamaterials offer much promise in many important applications, ranging from lenses with subwavelength focusing to cloaking. Metamaterials for terahertz (THz) range are especially important, because this range is missing devices for handling radiation. THz metamaterials will find application in security screening, medical imaging, nondestructive diagnostics, spectroscopy, communication technologies etc. The state-of-the-art achievements in the field of THz metamaterials composed of flat elements were reviewed in [1]. In the present study, six novel THz metamaterials with chiral, magnetic and bianizotropic properties, including flexible metamateirials and metamaterial-based systems, were developed. During development of the metamaterials, a key problem in the field of interest was solved, namely, passage from flat to three-dimensional precise elements was achieved, the latter elements offering a broader scope of opportunities in handling radiation in comparison with flat elements. In solving the problem, we used the previously developed approach for forming 3D nanoshells [2], which proved to be highly efficient in the design of many useful functional devices in Russia and abroad, from tubular lasers [3] to sensors and nanoscale instruments for biological and medical applications [2]. We have designed and fabricated two-dimensional arrays of highly-ordered, precise 3D resonant elements that could not be prepared by other presently known methods. Our first developments in the field of THz metamaterials composed of 3D helical elements were previously described in [4]. In the present study, electromagnetic properties of three of the six created metamaterials were thoroughly examined in the THz region using a Bruker Fourier-spectrometer (model IFS-66v) and the Novosibirsk free electron laser. The study showed that precise chiral materials were capable of rotating linearly polarized radiation through giant angles amounting to 35 degrees for a 30-μm thick metamaterial. Ellipticity and transmission spectra of the metamaterials in THz range have been measured. A specific feature exhibited by such spectra was sharp resonances, allowing smooth tuning of electromagnetic properties of fabricated systems through variation of substrate characteristics. A 0.5-% change in frequency or dielectric permittivity was shown capable of providing a 15-deg change of polarization angles. An original system for handling THz radiation using modulation of substrate properties was developed. This system forms a basis for future development of various smart systems and metamaterials with improved properties. Several important applications of developed metamaterials, and also physical models to describe the experimental data obtained for them, are outlined. Imprint lithography was used to demonstrate scalability of fabricated metamaterial elements.

References

[1] Hu Tao, W.J. Padilla, Xin Zhang, and R.D. Averitt, *IEEE J. of Selected Topics in Quantum Electronics* (2010).
[2] V.Ya. Prinz, V.A. Seleznev, A.K. Gutakovsky, A.V. Chehovskiy, V.V. Preobrazenskii, M.A. Putyato and T.A. Gavrilova, *Physica E* **6**, 828 (2000).
[3] V.Ya. Prinz, *Microelectron. Eng.* **69**, 466 (2003).
[4] V.Ya. Prinz, V.A. Seleznev, A.V. Prinz and A. Kopylov, *Sci. Technol. Adv. Mater. Topical Review* **10**, 034502 (2009).
[5] D. Heitman (Editor), *Quantum Materials*, Springer Verlag, Berlin, Heidelberg (2010).
[6] E.V. Naumova and V.Ya. Prinz, Russian Patent No. 2317942 (2008).
[7] E.V. Naumova, V.Ya. Prinz, V.A. Seleznev, S.V. Golod, R.A. Soots, V.V. Kubarev, B.A. Knyazev, G.N. Kulipanov, N.A. Vinokurov, *First International Congress on Advanced Electromagnetic Materials in Microwaves and Optics*, Rome, Italy, 74 (2007).
[8] E.V. Naumova, V.Ya. Prinz, S.V. Golod, V.A. Seleznev, V.V. Kubarev, *J. Opt. A* **11**, 074010 (2009).

Novel graphene — N-methylpyrrolidone monolayer hybrid material with tunable electronic property

I. A. Kotin[1,2], I. V. Antonova[2], R. A. Soots[2], V. A. Volodin[2,3] and V. Ya. Prinz[2]

[1] Novosibirsk State Technical University, Novosibirsk, 630092, Russia
[2] A.V. Rzhanov Institute of Semiconductor Physics, SB RAS, Lavrentjeva 13, 630090 Novosibirsk, Russia
[3] Center of Science and Education, Novosibirsk State University, Novosibirsk, 630090, Russia

Abstract. Novel technology for fabrication of hybrid structures by means of intercalation of N-methylpyrrolidone into a few-layered graphene and with use of annealing in the range $125-250\,°C$ as technological step was developed. Fabrication temperature was found to strongly determine combination of electronic properties of this hybrid material: opening of the band gap, high resistivity, relatively high mobility and sp^2 or sp^3 hybridization of carbon atoms are attributed to our hybrid material created at different temperatures.

Introduction

Chemical functionalization of graphene (a few-layered graphene) becomes now a focus of special interest for creation of complementary materials with wide spectrum of electronic properties [1]. The main motivation of this studies are modification of electronic properties via opening the energy band gap in the electron spectrum of single and few-layered graphene, the functionalization of graphene edges, decoration (passivation) of the defects. This approach can also be used as a tool to create graphene nanostructures of given shape and other applications. In conventional materials, the band gap is fixed by their crystalline structure, preventing such band gap control. A tunable band gap would be highly desirable because it would allow great flexibility in design and devices optimization. In present study we have used intercalation of N-methylpyrrolidone (NMP) into a few-layered graphene with the aim to create a new graphene-based material with variable properties in controllable manner. Such approach as intercalation provides a pure and two-side functionalization of graphene. A choose of intercalation agent is based on well-known property of the NMP to penetrate between every graphene layers and a wide spectrum of NMP applications in modern nanotechnology. As a result, we have created a novel multilayered hybrid material with tunable electronic properties.

1. Experimental details

Fabrication process of the hybrid structures includes the follows technological steps: (1) An electrostatic exfoliation of the few-layered graphene (FLG) films from highly oriented pyrolytic graphite (HOPG) and transfer it on the 300 nm SiO_2/Si substrate. Then we have obtained the few-layered graphene flakes with sizes up to $50 \times 100\ \mu m$ and thickness $\sim 2-4$ nm. (2) An intercalation of the NMP (C_5H_9NO, see Fig. 1c) into graphene flakes. (3) Annealing of the intercalated structures at temperature in the range of $125-250\,°C$ was the final operation which creates the hybrid structures. Fig. 1 presents the schematic diagrams of created structures, optical micrograph one of our structures and schematic image of NMP used for graphene functionalization.

2. Results and discussion

Strong increase in resistivity (in 10^5-10^7 times) was revealed for hybrid material in comparison with pristine FLG (Fig. 2a).

Resistivity of hybrid material as a function of the temperature used for structure fabrication is given in the Figure 1d. Increase in the NMP intercalation time leads to slight increase in resistivity of hybrid material (Fig. 2a,b). Strong non-monotonic dependence of resistivity and other properties of hybrid structures on the fabrication temperature caused by including of a special temperature of $\sim 200\,°C$ (boiling point of NMP) in interval of temperature used. Hybrid structures created at $200\,°C$ have properties similar to the pristine FLG flakes due to NMP evaporation from the interlayer spaces. Hybrid structures created in temperature ranges of $T < 200\,°C$ and $T > 200\,°C$ was found to demonstrate different properties. The first type of hybrid structures created at the temperatures of $125-175\,°C$ have high resistivity ($\sim 10^2-10^3\ \Omega$ cm), p-type conductivity, a strong temperature dependence of resistivity in the range of $77-300$ K. The band gap $\sim 3-3.5$ eV were revealed by a room temperature scanning tunneling spectroscopy and by current-voltage measurements in transistor regime for structures created at temperature of $150\,°C$. Relatively high carrier mobility were extracted for this structure ($1360\ cm^2$/V s for holes and $3600\ cm^2$/V s for electrons) from I-V characteristics measured transistor configuration with use of the substrate as a gate electrode. We have presumed for structures created at $T < 200\,°C$ that bonds between NMP and graphene are formed through oxygen atoms. The second type of hybrid structures and graphene — NMP interaction corresponds to $T > 200\,°C$ and distinguishes by appearance of the sp^3 hybridization of carbon atoms typically observed in the case of graphane formation. Fig. 1d shows the Raman spectra of hybrid structures created at different temperatures. According [2] the development of sharp D peak, appearance of a peaks at $\sim 1620\ cm^{-1}$, called D′, and around $2950\ cm^{-1}$, combination mode (D+D′), are attributed to interruptions of the π electron delocalisation consequent to the formation of C–H sp^3 bonds. In our case this process can be caused by NMP polymerization or polycondensation with releasing of hydrogen atoms. The band gap ($\sim 3.5-4$ eV) is revealed for structures created at $250\,°C$ (see, Fig. 1e).

3. Conclusions

New technology for fabrication of hybrid structures from the few-layered graphene and N-methylpyrrolidone monolayers with using of annealing in the range of $125-250\,°C$ as techno-
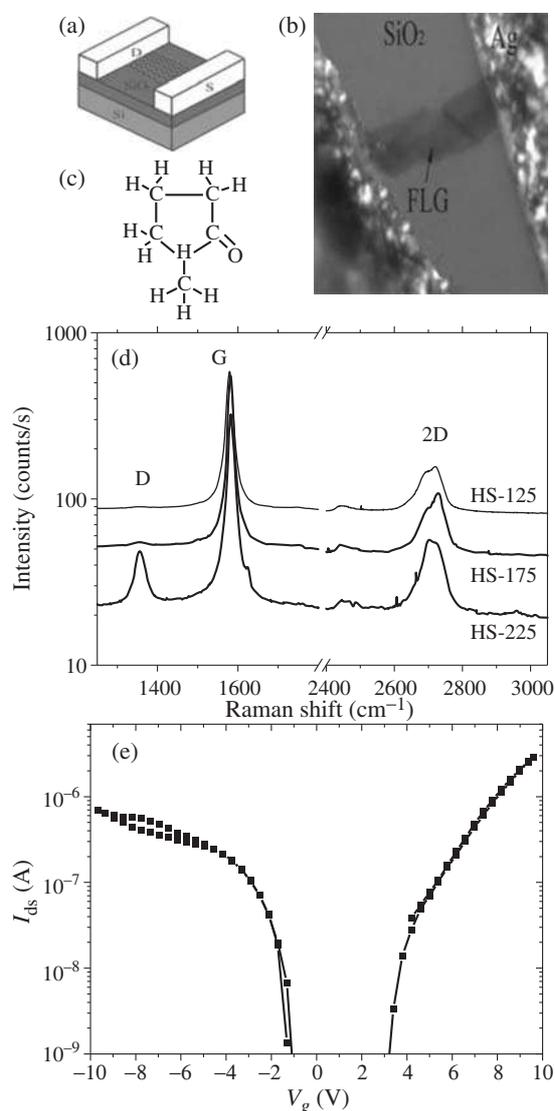
Fig. 1. (a) Schematic diagrams and (b) the optical micrograph one of our structures on SiO$_2$/Si substrate with two contacts. Such structures can be measured in a two terminated configuration and in a transistor one with use of the substrate as a gate electrode. (c) Schematic image of N-methylpyrrolidone, NMP, used for a few-layered graphene functionalization. (d) Raman spectra of hybrid structures created at different temperatures. Spectra are shifted in vertical direction. (e) Drain current at $V_{ds} = 150$ mV as a function of the gate voltage V_g for structure created at 250 °C.

logical step was developed. Opening of the band gap, strong and non-monotonic dependence of resistivity (up to 10^7 times) on the fabrication temperature, relatively high mobility (up to 3600 cm^2/V s), and sp^2 or sp^3 hybridization of carbon atoms were revealed for hybrid material. Combination of the properties is found to determine by temperature used for structure fabrication.

Acknowledgements

References

[1] M.J. Allen, V.C. Tung, R.B. Kaner, Honeycomb Carbon: A review of Graphene, *Chem. Rev.* **110** (1), 132 (2010).
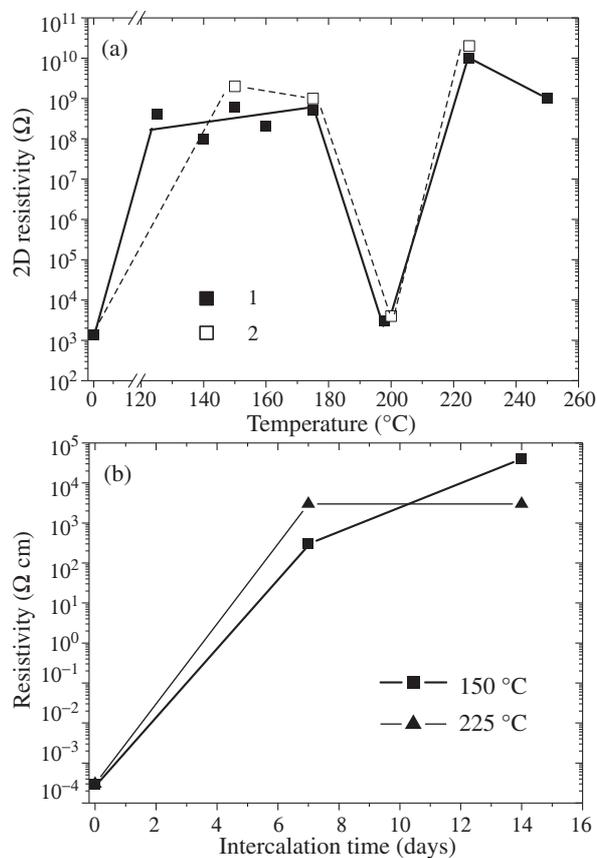
Fig. 2. (a) 2D resistivity (determined as a resistivity divided on the film thickness) as a function of a temperature used for structure fabrication. NMP intercalation time was 7 (1) and 14 (2) days. (b) Resistivity as a function of NMP intercalation time for structures created at 150 and 225 °C.

[2] D.C. Elias, R.R. Nair, T.M.G. Mohiuddin, S.V. Morozov *et al*, *Science* **323**, 610 (2009).

Elastic stress relaxation in nanostructures and its role in monolithic integration of III–V semiconductors on silicon and sapphire substrates

V. G. Dubrovskii

St Petersburg Academic University, St Petersburg, Russia

Abstract. Due to efficient relaxation of elastic stress on free sidewalls, the use of laterally confined nanostructures such as quantum dots (QDs), nanowires (NWs) and nanoneedles (NNs) enables a radical increase of critical thickness for dislocation-free growth in lattice mismatched material systems. This is of paramount importance for monolithic integration of dissimilar semiconductor materials, in particular, of optically active III–V semiconductors on Si. In this talk, we review some recent achievements in fabrication of coherent III–V nanostructures on silicon. We then discuss theoretical models of elastic strain relaxation in semiconductor nanostructures of different geometries, the critical dimensions for coherent epitaxial growth of those nanostructures on lattice mismatched substrates and present our newest results regarding the synthesis and physical properties of III–V QDs, NWs and NNs on foreign substrates including Si and sapphire.

Lattice mismatch persists as one of the most challenging bottlenecks for heterogeneous integration of dissimilar semiconductor materials. Electrical and optical properties of thin films grown on a foreign substrate are strongly impeded by high density misfit dislocations. QD nanoheterostructures is one of the well established methods to overcome the lattice mismatch issue. As was demonstrated in Ref. [1] in the case of InAs/GaAs(100) and further explored in other material systems, the ensembles of strained 3D crystal islands form spontaneously during the heteroepitaxy on a lattice mismatched substrate with no preliminary surface treatment. The small size of such islands and the presence of free lateral surfaces enable a coherent growth within a certain thickness interval prior to the onset of dislocations. The dominant driving force of coherent islanding is the relaxation of elastic stress: the islands are formed because the elastic energy in a 3D island is smaller than in a 2D wetting layer.

As follows from theoretical calculations of Ref. [2], the critical thickness increases infinitely when the lateral dimension is decreased to a certain threshold value. Coherent growth can be therefore realized in the NW geometry, with a small footprint
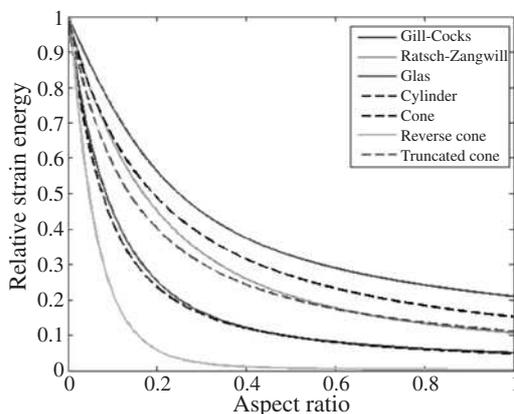
Fig. 2. Average experimental (squares) and theoretical dependences of preferred aspect ratio on the elastic energy, fitted by theoretical approximation of Ref. [8], the insert showing the saddle point of formation enthalpy.

being dictated by a metal catalyst particle assisting the NW growth in a bottom-up manner via the vapor-liquidsolid (VLS) mechanism [3]. Indeed, the Au-assisted metal organic chemical vapor deposition (MOCVD) [4] and molecular beam epitaxy (MBE) [5] have recently enabled the fabrication of coherent III–V NWs on the Si(111) substrate, with critical diameter of only 24–26 nm for 11.6% lattice mismatched InAs/Si(111) system. Another important example is given in Ref. [6], where catalyst-free, single crystalline wurtzite (WZ) GaAs NNs with 6–90 hexagonal pyramid shape and an ultra-sharp 2–4 nm tip were obtained by MOCVD on roughened Si substrates. Later on, similar GaAs NNs were grown on sapphire substrates with the extreme lattice mismatch of 46%. In our talk, we will review some of the abovementioned achievements.

We then present a theoretical model for the elastic energy relaxation in coherent strained nanostructures of different isotropic geometries [7]. In particular, a general analytical expression for the stress field in a 2D symmetrical geometry is presented, which, unlike previous results, is not restricted by the small aspect ratio or particular geometry. It is shown that, at large enough aspect ratio, the relaxation of both vertical and radial displacement fields with the distance from the substrate

Fig. 1. Elastic relaxations in different geometries (dashed lines), compared to the Glas formula [3] for the cylinder, the Ratsch–Zangwill formula for the rectangular QD and the Gill–Cocks formula for the full cone, all calculated for cubic materials.

(a)

(b)   (c)
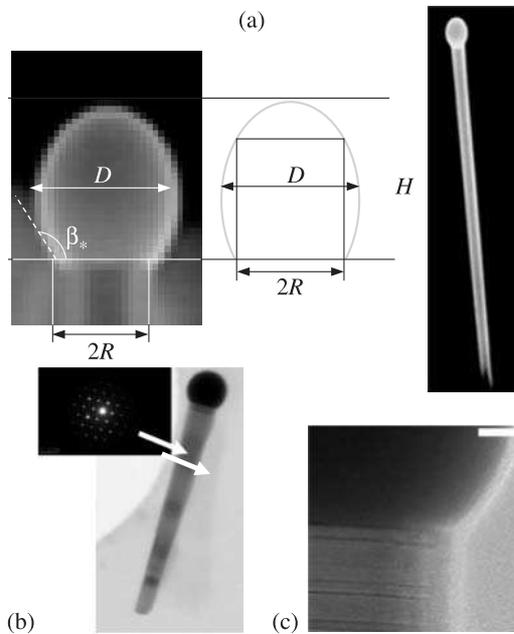
Fig. 3. Experimental and model droplet geometries in the novel VLS mode with the real NW diameter of 100 nm (a); TEM data showing absence of WZ phase in GaAs NWs on Si(111) inside the NW body (b) as well as at the top (c).

is exponential. Exponential approximation allows us to find analytical expressions for the stress and strain field. The cases of rigid and elastic substrates are considered simultaneously. By minimizing the total energy, we obtain the strain energy density as a function of vertical and radial coordinates. The end result is compared to the known analytical approximations and finite element calculations. We present simple analytical expression for the elastic relaxation where the fitting coefficient depends on the nanostructure geometry. Our data indicate that the elastic energy is highly depended on the aspect ratio and the island shape, with the relaxation becoming faster as the contact angle of island facets increases (Fig. 1). The calculations of critical thickness for the onset of plastic deformation in NWs, obtained with the abovementioned results for the elastic energy, are also discussed.

Next, we consider the formation enthalpy of a coherent strained 3D island as a function of two independent variables, the base dimension and the aspect ratio [8]. It is shown that the minimum nucleation barrier relates to a saddle point of formation enthalpy. The energetically preferred aspect ratio is obtained as a function of the lattice mismatch, material constants and supersaturation. The preferred aspect ratio increases with the lattice mismatch from modest values typical for QDs at 4–12% mismatch to very large values of the order of ten at 46% mismatch, corresponding to the case of GaAs NNs on sapphire (Fig. 2). It is shown that those NNs should adopt hexagonal wurtzite phase. Overall, the stress-driven nucleation of highly anisotropic islands offers a new growth mechanism for the fabrication of catalyst-free NWs and NNs, in particular, GaAs NNs on sapphire and GaN NWs on Si.

Finally, we present our newest experimental and theoretical results regarding the controlled synthesis of self-catalyzed,

pure zincblende (ZB) GaAs NWs on Si(111) substrates covered by native oxide [9]. Different surface preparation techniques enabling coherent growth of GaAs NWs on Si are discussed. We then briefly describe a new mode of the VLS NW growth with the droplet wetting the sidewalls and surrounding the nanowire rather than resting on its top. It is shown theoretically that such unusual configuration happens when the growth is catalyzed by a lower surface energy metal. Theoretical predictions are compared to the experimental data on the Ga-catalyzed growth of GaAs NWs by MBE on Si substrates. In particular, it is demonstrated that the experimentally observed droplet shape is indeed nonspherical (Fig. 3a). The new VLS mode has a major impact on the crystal structure of GaAs NWs, helping to avoid the uncontrolled ZB-WZ polytylism under optimized growth conditions. Since the triple phase line nucleation is suppressed on surface energetic grounds, all our NWs have pure ZB structure along the entire length, as demonstrated by the structural studies of our GaAs nanowires (Figs. 3b and c).

References

[1] L. Goldstein *et al*, *Appl. Phys. Lett.* **47**, 1099 (1985).
[2] F. Glas, *Phys. Rev. B* **74**, 121302 (2006).
[3] R.S. Wagner, W.C. Ellis, *Appl. Phys. Lett.* **4**, 89 (1964).
[4] L.C. Chuang *et al*, *Appl. Phys. Lett.* **92**, 013121 (2008).
[5] G.E. Cirlin *et al*, *Phys. Stat. Sol. RRL* **3**, 112 (2009).
[6] M. Moewe *et al*, *Appl. Phys. Lett.* **93**, 023116 (2008).
[7] X. Zhang *et al*, *J. Appl. Phys.*, submitted.
[8] V.G. Dubrovskii *et al*, *Cryst. Growth & Design* **10**, 3949 (2010).
[9] G.E. Cirlin *et al*, *Phys. Rev. B* **82**, 035302 (2010).

New mode of pure zinc blende nanowire growth caused by the catalyst wetting

N. V. Sibirev[1], G. E. Cirlin[1−4], Yu. B. Samsonenko[1−3], F. Jabeen[4], A. D. Bouravleuv[1,2], J. C. Harmand[4], M. V. Nazarenko[1], A. I. Khrebtov[1] and V. G. Dubrovskii[1,2]

[1] St Petersburg Academic University, St Petersburg, Russia
[2] Ioffe Physical-Technical Institute, St Petersburg, Russia
[3] Institute for Analytical Instrumentation RAS, Rizhsky 26, 190103 St Petersburg, Russia
[4] CNRS-LPN, Route de Nozay, 91460 Marcoussis, France

Abstract. We report on the new mode of the self-catalyzed nanowire growth with the droplet wetting the sidewalls and surrounding the nanowire rather than resting on its top. It is shown theoretically that such unusual configuration happens when the growth is catalyzed by a lower surface energy metal. We have shown that the nanowires are single crystals having the zincblende structure along their length apart from a thin wurtzite region near the tip. We attribute the observed phase purity to the sidewalls wetting by the catalyst. A model of a non-spherical elongated droplet shape in the wetting case is developed. Theoretical predictions are compared to the experimental data on the Ga-catalyzed growth of GaAs nanowires by molecular beam epitaxy. In particular, it is demonstrated that the experimentally observed droplet shape is indeed non-spherical. These results can provide a distinct method for the fabrication of chemically pure and stacking-fault-free zincblende nanowires.

Semiconductor Nanowires (NWs) have recently drawn much attention due to their importance for nanoscale electronics, photonics and sensing [1]. NWs are usually fabricated via the vapor-liquid-solid (VLS) mechanism [2,3], using modern epitaxy techniques such as metalorganic chemical vapor deposition(MOCVD) [1,2] or molecular beam epitaxy (MBE) [4]. The key factor underlying the VLS mechanism is the catalytic effect of a liquid metal particle assisting the NW growth from a supersaturated liquid alloy [4,5]. Gold is the most commonly used among other metal catalysts [1–3,5]. However, Au-catalyzed VLS NWs may suffer from several drawbacks such as the unwanted Au contamination [6].

During the VLS growth, two-dimensional (2D) NW monolayers (MLs) nucleate and extend laterally. Growth of small enough NWs is mononuclear [3,7]. There is much experimental evidence that, in the Au-catalyzed growth, the droplet wets the growth front but not the sidewalls [8]. The triple phase line (TPL) separating the vapor, liquid and solid phases is therefore shifted upwards upon the completion of each ML. Nebol'sin and Shchetinin [9] formulated an inequality for the surface energies under which the TPL position at the NW top is stable and, consequently, the standard VLS growth occurs.

$$\gamma_{\mathrm{SV}} < \gamma_{\mathrm{LV}} \sin\beta + \gamma_{\mathrm{SL}} . \tag{1}$$

Here γ_{SV}, γ_{LV} and γ_{SL} are the surface energies of solid-vapor, liquid-vapor and solid-liquid interface correspondingly, β is contact angle. Later, Glas and co-authors [3,10] introduced a concept of the TPL nucleation and presented an inequality for the surface energies under which 2D islands emerge at the TPL rather than at the liquid-solid interface. Glas and co-authors [10] also showed that a lower surface energy of wurtzite(WZ) NW sidewalls could lead the WZ formation instead of cubic zinc blende(ZB) crystal phase which is typical for bulk GaAs. They also show that the formation of WZ structure requires two conditions: (i) the TPL nucleation to gain the surface energy and (ii) high enough supersaturation of liquid alloy to overcome the stacking fault(SF) [10,11]. This view has gained much support [12,13] and is now widely used for
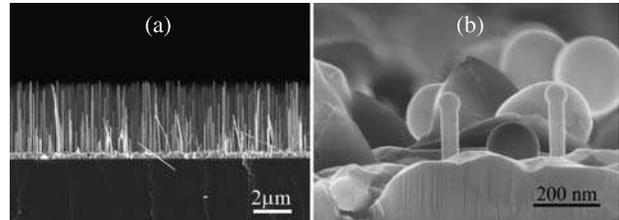
Fig. 1. SEM image of self-catalyzed GaAs NWs on Si(111) substrate grown at 610 °C (a) and 630 °C (b).

tuning the crystal phase of Au-catalyzed III-V NWs [3,13,14]. Therefore convenient NW growth leads the formation of WZ phase and SF.

Here we present the results which allow us to solve both of these problems: gold contamination and SF. This paper is devoted to self-catalyzed NW growth directly on Si(111) substrate by a special MBE procedure [4,15] and describes some distinctive features of this process. Here we present pure ZB NWs excluding the very tips just beneath the Ga droplet, where SF and WZ phase exist.

Our growth procedure and in situ diagnostics are as follows [15]: the GaAs NWs are grown by MBE using EP1203 setup directly on Si(111) substrates. Before the growth of NWs, the substrate temperature is increased to the desired in the range 560–630 °C [5,15,16] and kept constant during the openings in the native oxide layer growth run. After the formation of openings, the Ga flux is supplied to the surface for 5 s while the As shutter is closed. This initiates the formation of Ga droplets in the openings. When the As flux is switched on, the NW growth is started after incubation time. The examples of obtained GaAs NWs are presented in Fig.1.

Our data clearly show the presence of a Ga droplet on top of most NWs. We therefore propose the following growth mechanism: initial droplets are formed in the openings and consist of pure liquid Ga. When the As deposition is started, the growth species are supplied to the droplet by direct impingement and by surface diffusion. Rather than being a chemical catalyst as in
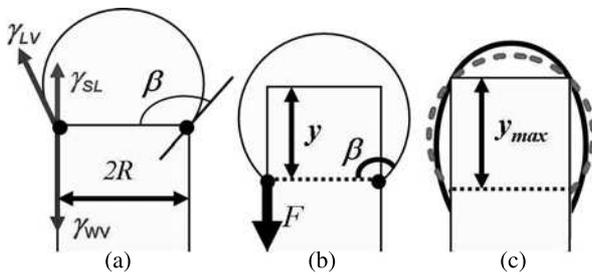
Fig. 2. Standard VLS growth involving surface energies SEM (a); VLS growth in the wetting case (b); Geometry of elongated droplet with height more than diameter — solid line and spherical; shape transformation of Ga droplet (c).

the MOCVD case, the droplet acts as a material collector [12]. Since stoichiometric GaAs cannot be formed in the liquid volume because of its low As content, Ga and As are transferred through the droplet to the solid surface initially Si and then GaAs, where a supersaturated liquid crystallizes in the VLS fashion via 2D nucleation [10,12,13]. After the steadystate growth mode is achieved, the droplet size and shape remains constant due to dynamic balance between the GaAs arrival to the droplet and the GaAs sink at the liquid-solid interface.

The standard VLS growth in the non-wetting case is shown schematically in Fig. 2a. When the TPL is randomly shifted downwards, the vertical restoring force $F = \gamma_{LV} \sin\beta + \gamma_{SL} - \gamma_{SV}$ arises. The contact angle could be obtained from the balance of horizontal forces at the TPL [14,16]:

$$\gamma_{SL} < -\gamma_{LV} \cos\beta . \tag{2}$$

If inequality (2) is not fulfilled, than droplet will be disrupted. For gold catalyst both conditions (1) and (2) are satisfied. However, liquid gallium has less surface energy than gold and it is become impossible to satisfy both of these conditions.

Let us now consider what happens if the condition (1) is unsatisfied. In this case, whenever the TPL moves slightly downwards, the surface force is also directed downwards and tends to increase the part of NW wetted by the liquid. Under the constraint of fixed liquid volume Ω and radius R, the penetration of NW cylinder into the droplet leads to the increase of contact angle β. As β increases, the vertical force $F = \gamma_{LV} \sin\beta + \gamma_{SL} - \gamma_{SV}$ can only increase. Therefore, the droplet will continue sliding down until the cylinder hits the droplet surface, see Fig. 2b.

When droplet reaches bottom position, as shown in Fig. 2c, the surface energy force continues stretching down the droplet. This force gives rise to further evolution of system morphology. The shape of the droplet became elongated. The shape of the droplet corresponds to the minimum of surface energy of the system droplet-nanowire. To find the new shape of droplet [3] we assume that the shape droplet surface is given by a Figure of rotation around the nanowire axis $r^2 = f(z)^2$. For simplicity we also assume that $Pf(z) - rP \ll r$. In this case the parabola is a good approximation for description of the droplet lateral sides the top of the drop remaining spherical. This consideration is confirmed by SEM images of GaAs NWs, which is presented in Figure 3.

In conclusion, we have developed kinetic model of the NW growth with the droplet wetting the sidewalls. We have given possible explanation of suppression of SF formation in self-
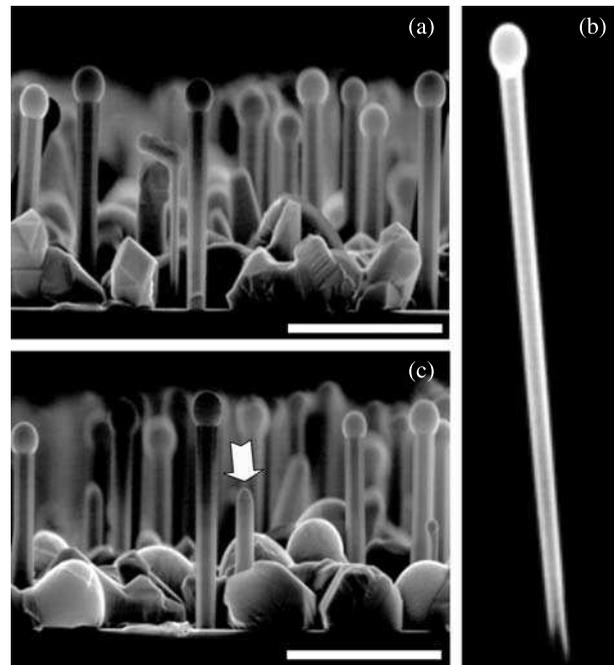
Fig. 3. Plan view SEM images of GaAs NWs grown after 15 min of growth (a) and (b), showing elongated droplet shape; scale bar represents 500 nm. Arrow in Figure (b) points at the NW having lost a part of the droplet. Figure (c) shows the NW extending towards the top.

catalyzed NW. We have obtained the shape of the droplet on the tip of NW.

References

[1] P.J. Pauzauskie *et al*, *Materials Today* **9(10)**, 36 (2006).
[2] W. Lu, C.M. Lieber, *Nature Materials* **6**, 841 (2007).
[3] V.G. Dubrovskii *et al*, *Nano Letters in print* (2011).
[4] Yu.B. Samsonenko *et al*, *Semiconductors* **45(4)**, 441 (2011).
[5] R.S. Wagner *et al*, *Appl. Phys. Lett.* **69**, 440 (1964).
[6] J.B. Hannon *et al*, *Nature* **69**, 440 (2006).
[7] V.G. Dubrovskii, N.V. Sibirev, *Phys. Rev. E* **70**, 19604 (2004).
[8] F.M. Ross *et al*, *Phys. Rev. Lett.* **95**, 146104 (2005).
[9] V.A. Nebol'sin, A.A. Shchetinin, *Inorganic Materials* **39**, 899 (2003).
[10] F. Glas *et al*, *Phys. Rev. Lett.* **99**, 146101 (2007).
[11] V.G. Dubrovskii, N.V. Sibirev, *Phys. Rev. B* **77**, 035414 (2008).
[12] V.G. Dubrovskii *et al*, *Phys. Rev. B* **78**, 235301 (2008).
[13] J. Johansson *et al*, *Cryst. Growth and Design* **9**, 766 (2009).
[14] H.J. Joyce *et al*, *Nano Letters* **10**, 908 (2006).
[15] G.E. Cirlin *et al*, *Phys. Rev. B* **82**, 035302 (2010).
[16] N. Wang *et al*, *Mater. Sci. Eng. R.* **60**, 1 (2008).

Strained $A^{II}B^{VI}$ nanostructures as active media for visible range ring resonator microlasers

S. V. Alyshev[1], A. O. Zabezhaylov[1] V. I. Kozlovsky[2] and E. M. Dianov[1]

[1] Fiber Optics Research Center, RAS, Moscow, Russia
[2] P.N. Lebedev Physical Institute, RAS, 53 Leninsky pr., 119991 Moscow, Russia

Abstract. Nanostructures consisted of GaAs and ZnSe buffer layers, sacrificial layer of MgS, and strained ZnSe/ZnSSe bilayer with CdS (ZnCdSe) quantum well incorporated were proposed as an active media for visible range micro lasers with a ring resonator. Proposed structures were grown by molecular-beam epitaxy and investigated by cathodoluminescence. Good luminescence properties were demonstrated. From strained nanostructures three dimensional nanoobjectcs were made by selective etching technique. Scanning electron microscope investigation has shown that the shape of three dimensional nanoobjects is close to the ring resonator one.

Introduction

Incorporation of quantum dots (QDs) or quantum wells (QWs) in high Q optical microcavities leads to microlasers with potentially ultralow or near-zero threshold. Such devises have good temperature stability and can operate at ultrahigh frequency providing the basic building blocks for chip-level optical communications.

In this regard, remarkable progress has been made in photonic crystal and microdisk lasers, however most of these devises operate under low temperature and/or pulsed mode [1,2].

Recently, a new type of microcavities was proposed. These microcavities are formed using rolled-up micro- and nanotubes (so-called ring microresonators). The key role was played here by a new technique of fabrication of three dimensional (3D) objects from strained epitaxially grown semiconductor structures [3,4,5].

The significant achievements have been made in development of lasers based on the ring microresonators. Nevertheless, the main effort was focused on producing near infra-red devises based on $A^{III}B^V$ or SiO_x/Si materials [6].

To apply this conception to $A^{II}B^{VI}$ materials, which are able to emit the light in the visible range we propose semiconductor nanostructures represented in Fig. 1. The structures consist of GaAs and ZnSe buffer layers, a sacrificial MgS layer, and strained ZnSe/ZnSSe bilayer. A CdS QW was incorporated into the structure emitting at 540 nm (green) while a ZnCdSe QW was incorporated into the structure emitting at 460 nm (blue).
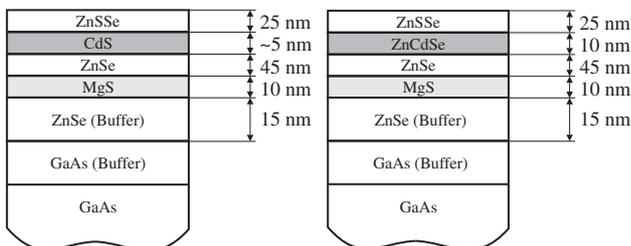
Fig. 1. Proposed $A^{II}B^{VI}$ nanostructures with strained $ZnS_{0.33}Se_{0.67}$/ZnSe bilayer and CdS (ZnCdSe) QW.
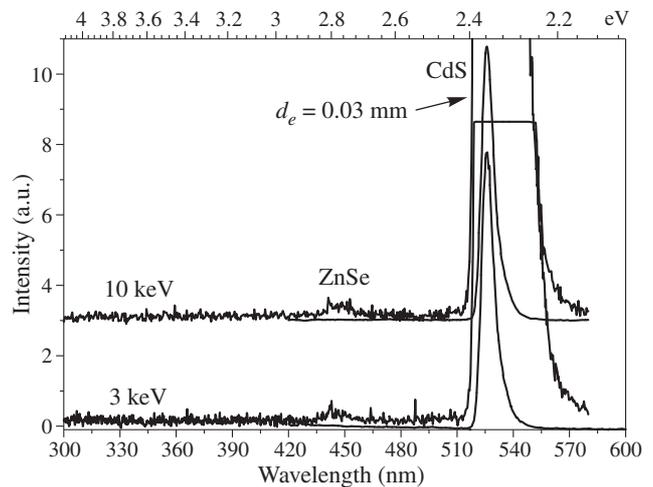
Fig. 2. LT CL spectrum of the structure with the CdS QW at $T = 18$ K, $E_e = 3$ and 10 keV, $d_e = 0.03$ and 1 mm.
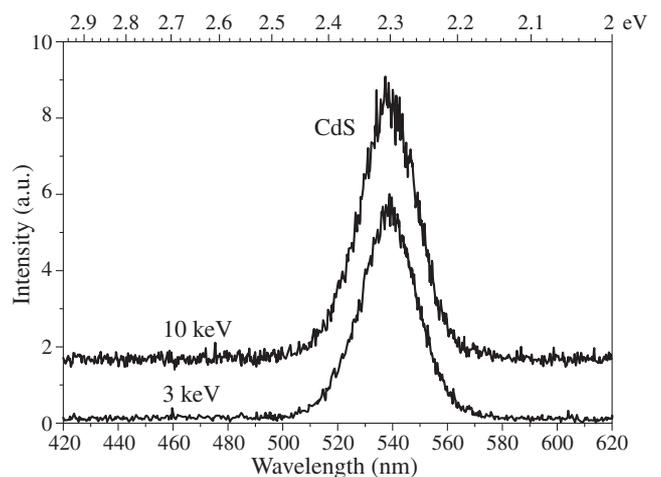
Fig. 3. RT CL of the structure with the CdS QW at $E_e = 3$ and 10 keV, $d_e = 1$ mm.

1. Experimental

All structures were grown by Molecular-Beam Epitaxy (MBE) on GaAs substrates misoriented by $10°$ from (100) to (111)Ga. Growth runs were accomplished on a TSNA 18 MBE machine with solid Zn, ZnS, CdS, Mg, Se and Cd sources. The substrate temperature during growth was 250 °C. The cathodolumines-
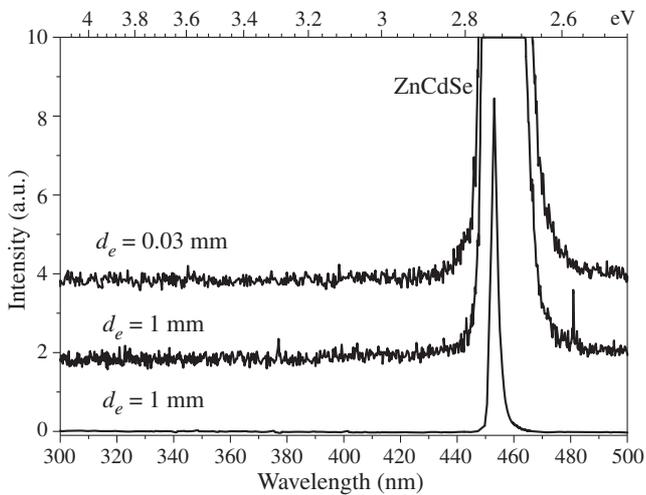
Fig. 4. LT CL spectrum of the structure with the ZnCdSe QW at $T = 23$ K, $E_e = 10$ keV and $d_e = 0.03$ and 1 mm.
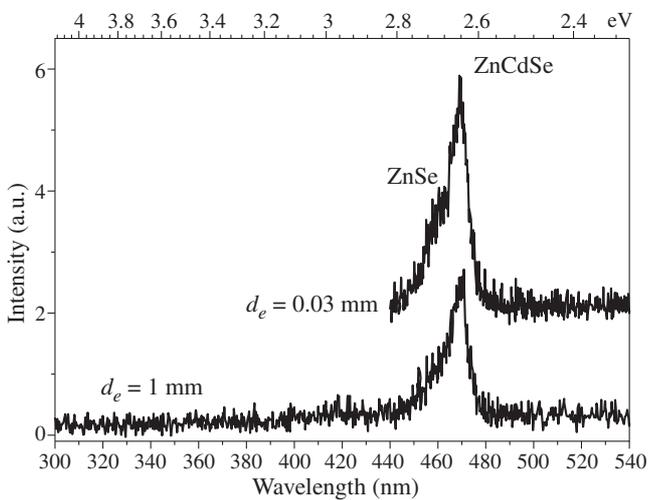
Fig. 5. RT CL of the structure with the ZnCdSe QW at $E_e = 10$ keV and $d_e = 0.03$ and 1 mm.

cence (CL) spectra were recorded at $T \sim 20$ K (LT) and 300 K (RT), electron energy $E_e = 3$, 10 keV, current $I_e = 1$ μA and electron beam diameter $d_e = 0.03$ and 1 mm. To form the 3D objects the surface of the samples were scratched and the sacrificial layer was etched away with HCl:H_2O solution. Scanning Electron Microscope (SEM) images were made using JSM5910LV (JEOL Serving Advance Technology) microscope at electron energy 20 keV.

2.   Results and discussion

Low temperature CL spectra and CL spectra at room temperature for structures with CdS QW are presented in Figs. 2 and 3 respectively. The same spectra for structures with ZnCdSe QW are presented in Figs. 4 and 5. One can see that even at low temperature there are no lines except ones from the QWs. Therefore it is possible to conclude that the structures provide reliable carrier transport and confinement. SEM images of formed 3D objects are presented in Fig. 6. In the upper scan, scratches and a film rolled-up from scratches are clearly seen. It should be mentioned that although the lithography technique was not applied the shape of 3D objects formed is close to the targeted result.
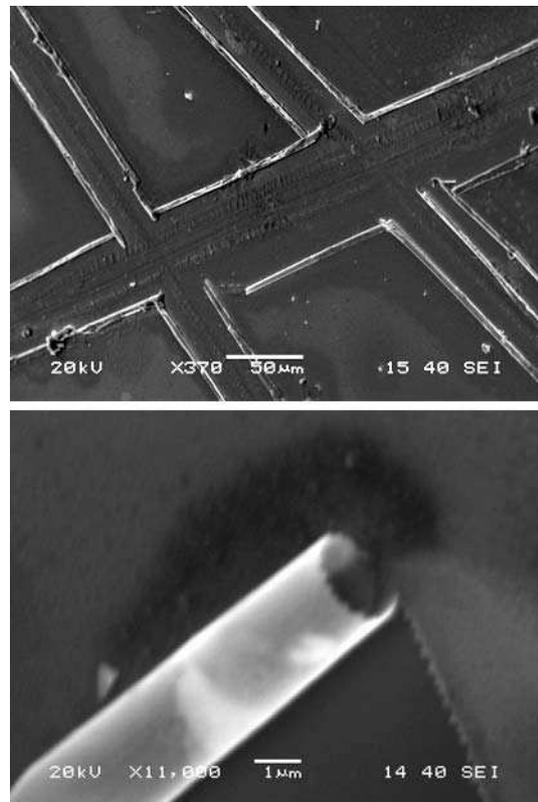
Fig. 6. SEM images of the formed 3D objects. In the upper scan, scratches and a film rolled-up from scratches are clearly seen. The lower scan show the enlarged edge of the rolled-up film.

3.   Conclusion

In summary, we have proposed strained semiconductor nanostructures as an active media for ring microresonator lasers operating in visible range. These nanostructures have been grown by MBE and characterized by LT and RT CL. The CL spectra demonstrate good optical quality of the structures grown. From strained nanostructures the 3D objects have been made and investigated by SEM. The SEM images evidence that shape of the formed 3D objects is close to the ring resonator one.

References

[1] Q. Song *et al*, *Appl. Phys. Lett.* **94**, 06110 (2009).
[2] S. Chakravarty *et al*, *IEEE Photon. Technol. Lett.* **18**, 2665 (2006).
[3] V.Y. Prinz *et al*, *Nanotechnology* **13**, 231 (2002).
[4] V.Y. Prinz *et al*, *Physica E* **6**, 828 (2000).
[5] S.V. Alyshev *et al*, *Semiconductors* **44**, 72 (2010).
[6] L. Feng *et al*, *Optics Express* **17**, 19933 (2009).

Luminescent nanostructures formed in stoichiometric SiO$_2$ layers by irradiation with 700 MeV Bi ions

G. A. Kachurin[1], S. G. Cherkova[1], D. V. Marin[1,2], V. G. Kesler[1], V. A. Volodin[1,2] and V. A. Skuratov[3]

[1] A.V. Rzhanov Institute of Semiconductor Physics, SB RAS, Lavrentjeva 13, 630090 Novosibirsk, Russia
[2] Novosibirsk State University, Pirogov str. 2, 630090 Novosibirsk, Russia
[3] Joint Institute for Nuclear Research, 141980 Dubna, Russia

Studies of Si nanostructures are currently an area of intense investigations. The ongoing drive for smaller Si device dimensions coupled with the discovery of strong luminescence from quantum-size Si nanocrystals stimulates research into the processes of Si nanostructures formation and modification. The nanocrystals have been conventionally fabricated by high temperature annealing of Si-enriched silica. It is tempting to find the way to preparation of the light sources in the widely used thermally grown stoichiometric SiO$_2$ layers. We have made an attempt to form the luminescent Si nanostructures in stoichiometric SiO$_2$ layers by disproportionation of the material in tracks of swift heavy ions. In such several nm in diameter tracks for the time of $10^{-13}-10^{-11}$ s occur the excited carrier concentrations more than 10^{22} cm^{-3}, temperatures up to 5000 K and high pressures. 320 nm-thick SiO$_2$ layers were thermally grown on the Si substrates. The layers were irradiated with 700 MeV Bi ions (ionization losses ~24 keV/nm, 99.73% of the total ones) to the doses of $3 \times 10^{12}-10^{13}$ cm^{-2}. Photoluminescence (PL), optical absorption, Raman and XPS spectroscopies were used for the characterizations. Optical and XPS

Fig. 2. XPS spectra of the layers before (solid line) and after Bi bombardment to the dose of 10^{13} cm^{-2} (dashed line). Thin lines — deconvolution of the dashed line into the components with the maxima: 103.6 eV (Si-4O), 102.4 eV (1Si-Si-3O), 99.8 eV (Si-4Si).

measurements have shown the stoichiometric composition of the as-grown SiO$_2$ layers. The PL band centered at ~600 nm appeared after the ion bombardment (Fig. 1). Its intensity grew with the dose, saturating between the doses of 3×10^{12} cm^{-2} and 5×10^{12} cm^{-2}. When passivated by annealing at 500 °C for 30 minutes in forming gas (6% H2 + 94% Ar), the maximum of the PL intensity increased for 5 times. The XPS spectra demonstrated after irradiation a decrease in number of Si-O$_4$ bonds in favour of Si-coordinated Si atoms (Fig. 2). Optical absorption in the region of $950-1150$ cm^{-1} evidenced scission of the Si-O bonds, and in the Raman spectra the band at ~480 cm^{-1}, typical of scattering on Si-Si bonds in amorphous Si, was seen after the ion dose as low as 3×10^{-12} cm^{-2}. The results obtained are interpreted as the formation of the light-emitting Si nanostructures in the tracks of swift heavy ions. The nanostructures are believed to be responcible for the PL band at ~600 nm, their production cross-section is assessed from the ion dose dependence and is found to be about 10 nm. The mechanism of the oxide reduction via disproportionation of the chemical composition, including Knotek–Feibelman process and desertion of oxigen atoms out of the tracks, is considered.

Acknowledgements

Fig. 1. PL spectra of SiO$_2$ layers before (solid line) and after Bi bombardment to the doses of 3×10^{12} cm^{-2} (circles) and 5×10^{12} cm^{-2} (triangles). Samples passivated.

Monte Carlo simulation of Ge–Si nanowire radial heterostructure formation

A. G. Nastovjak, I. G. Neizvestny and N. L. Shwartz

A.V. Rzhanov Institute of Semiconductor Physics, SB RAS, Lavrentjeva 13, 630090 Novosibirsk, Russia

Abstract. Formation of Ge–Si radial heterostructures in nanowires (NW) during CVD process was analyzed using Monte Carlo simulation. Effect of precursor type, flux intensity and temperature on axial to radial heterogrowth transition was investigated. Different ways to create core-shell NW structure were considered: proper choice of growth conditions or introduction of additional chemical species. These species can work as surfactants decreasing adatom diffusion length, or decrease activation energy of precursor dissociation, or initiate solidification of catalyst drop that prevents axial growth.

Introduction

Semiconductor nanowires with heterojunctions (HJ) have great potentials in future electronics, optoelectronics and medicine. It is possible to form axial and radial junctions in nanowires on the base of different materials [1]. Peculiarities of axial Ge–Si HJ formation were investigated earlier [2]. Increasing interest to Ge–Si nanowire structures with heterojunctions is due to their compatibility with conventional CMOS technology. Radial heterostructures are the base for unique devices, such as nanowire FETs with promising device performance [3,4]. There are several experimental works demonstrating radial core-shell Ge–Si heterostructure formation, with radial shell growth turned on by variation of temperature, gas composition and pressure [5–7]. Usually such structures are formed as follows: Ge core grown via vapor-liquid-solid (VLS) mechanism is covered with uniform Si shell. In spite of progress in core-shell structure formation the exact limitations of such growth have not been fully understood. In this work atomic-scaled analysis of Ge–Si core-shell NW growth was carried out using lattice Monte Carlo model. Effect of precursor type, flux intensity and temperature on transition from axial to radial heterogrowth was investigated.

1. Monte Carlo model and simulation results

Simulation of radial Si–Ge heterojunction formation in NW was carried out using the software that has been developed to investigate axial heterostructure growth [2]. In [2] VLS mechanism of NW growth was realized. Similar to axial HJ formation for radial heterojunction growth seven-component system was considered: substrate and wire material (Si); wire material (Ge); catalyst (Au); Si- and Ge-containing precursors (P_{Si} and P_{Ge}); liquid semiconductor materials dissolved in catalyst drop (Si_{liq} and Ge_{liq}). Input parameters of the model are initial substrate (composition, orientation, morphology), energy of covalent bonds E_{i-j} (i, j — matter sorts), activation energies of chemical reactions (E_r) and desorption (E_{sub}), temperature T (K), flux intensity F (ML/s). When choosing values of model energy parameters we take into account that interaction energies of semiconductor and catalyst (E_{Au-Si}, E_{Au-Ge}) should be lower than interaction energy E_{Si-Si}, E_{Ge-Ge} and E_{Au-Au} to provide the weak wetting between Si–Au and Ge–Au. The relationship $E_{Ge-Ge} < E_{Si-Si} < E_{Si-Ge}$ was chosen for Si–Ge interaction on the base of the literature data [8–11]. Simulation was carried out using following energies of covalent bonds: $E_{Si-Si} = 1$ eV, $E_{Si-Ge} = 1.2$ eV, $E_{Ge-Ge} = 0.95$ eV,
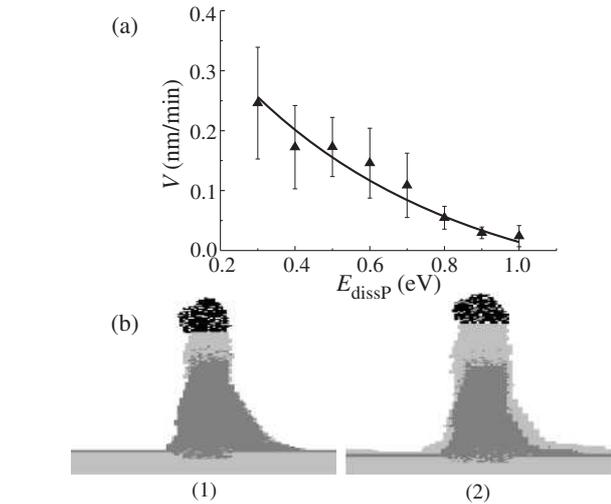
Fig. 1. a) Radial growth rate of silicon shell versus activation energy of precursor dissociation $E_{diss\,P}$ at $T = 800$ K; b) cross-sections of Ge–Si core-shell NW for $E_{diss\,P} = 1.0$ eV (1) and 0.3 eV (2); $\tau = 100$ s. Si(s) is marked in light-gray, Ge(s) — in dark-gray, Au — in black and Si_{liq}, Ge_{liq} — in white color.

$E_{Au-Si} = E_{Au-Ge} = 0.6$ eV, $E_{Au-Au} = 1$ eV. As the first step on Si(111) substrate activated by Au drop Ge containing precursors were deposited. So Ge core growth via VLS mechanism was simulated. The next step was Si shell formation. Simple precursor switching from P_{Ge} to P_{Si} does not result in silicon shell growth. Instead axial NW elongation occurs. Such phenomenon was observed experimentally too [12]. We considered several ways to stimulate radial growth: introducing additional species in the system leading to alteration of silicon precursor dissociation rate (1) or to solidification of catalyst drop and preventing VLS growth (2).

Effect of precursor dissociation activation energy $E_{diss\,P}$ on radial growth rate V was analyzed. Fig. 1a demonstrates this dependence: radial growth rate increases with $E_{diss\,P}$ decreasing. In Fig. 1b cross-sections of model Ge–Si core-shell structure are shown for two $E_{diss\,P}$ values: 1 and 0.3 eV. Images (1) and (2) correspond to the same deposition time τ of silicon precursor. At high $E_{diss\,P}$ axial growth dominates and at low $E_{diss\,P}$ silicon shell formation is clearly seen. Experimentally radial shell growth was "turned-on" by the addition of diborane, which serves to lower the decomposition temperature of silane [6,13].

Introduction of additional chemical component can influ-
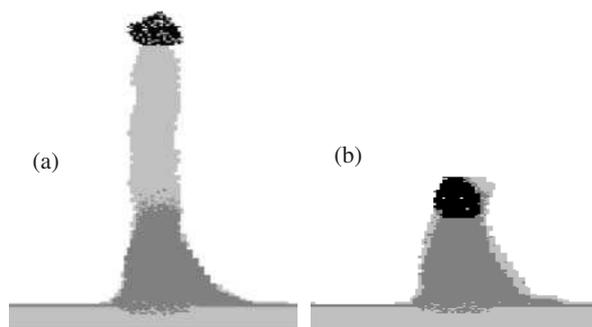
Fig. 2. Cross-sections of Ge–Si core-shell NW for two E_r values: 2.7 eV (a) and 5.0 eV (b); $T = 800$ K, $\tau = 500$ s. Si(s) is marked in light-gray, Ge(s) — in dark-gray, Au — in black and Si_{liq}, Ge_{liq} — in white color.

ence not only on precursor dissociation rate but also on catalyst drop properties. We consider effect of catalyst drop solidification on the process of Si-shell formation. In this case instead of VLS mechanism vapor-solid-solid (VSS) growth mechanism takes place and axial growth rate dramatically decreases. Dissolution rate of silicon in catalyst drop in the model was determined by activation energy E_r of reaction $Si(s) + Au \rightarrow Si(liq) + Au$. Fig. 2 demonstrates influence of E_r value on the silicon shell thickness. Value $E_r = 2.7$ eV corresponds to VLS growth mechanism when axial heterojunction is formed. P_{Si} deposition leads to silicon fragment of NW growth, with Si shell thickness being negligible. For $E_r = 5$ eV silicon is practically insoluble in catalyst drop and VSS growth starts. In this case, precursor dissociation results in the increase of silicon atom concentration on NW wall surface initiating Si shell formation. Moreover some impurities being surfactants can decrease Si adatom diffusion length and so provoke shell growth. There is some other way to create silicon shell. Growth temperature increase stimulates uncatalysed precursor decomposition leading to shell formation when right choosing precursor flux. So for given precursor type one should choose proper range of temperatures and flux intensities to grow the shell.

2. Summary

In this work atomic-scaled analysis of Ge–Si core-shell NW growth was carried out using lattice Monte Carlo model. It was demonstrated that radial growth can be stimulated by adding chemical species that decrease activation energy of precursor dissociation. Dependence of radial growth rate on activation energy of precursor dissociation was obtained. Impurities can provoke catalyst drop solidification resulting in transition from VLS to VSS growth mechanism or decrease silicon adatom diffusion length leading to shell formation.

References

[1] O. Hayden, R. Agarwal, W. Lu, *Nano Today* **3** 5–6, 12 (2008).

[2] A.G. Nastovjak, I.G. Neizvestny, N.L. Shwartz, *Proc. of 18th International Symposium "Nanostructures: Physics and Technology"*, St Petersburg, Russia, June 21–26, 2010, 179 (2010).

[3] G. Liang, J. Xiang, N. Kharche, G. Klimeck, Ch. M. Lieber, M. Lundstrom, *Nano Lett.* **7** 3, 642 (2007).

[4] J. Xiang, W. Lu, Y. Hu, Y. Wu, H. Yan, Ch.M. Lieber, *Nature* **441**, 489 (2006).

[5] K.M. Varahramyan, D. Ferrer, E. Tutuc, S.K. Banerjee, *Appl. Phys. Lett.* **95** 3, 033101 (2009).

[6] L.J. Lauhon, M.S. Gudiksen, D. Wang, Ch.M. Lieber, *Nature* **420**, 57 (2002).

[7] I.A. Goldthorpe, A.F. Marshall, P.C. McIntyre, *Nano Lett.* **8** 11, 4081 (2008).

[8] B. Voigtländer, *Surf. Science Rep.* **43**, 127 (2001).

[9] V. Cherepanov, B. Voigtländer, *Phys. Rev. B* **69**, 125331 (2004).

[10] A.V. Zverev, I.G. Neizvestny, I.A. Reizvikh *et al*, *Semiconductors* **39** 8, 967 (2005).

[11] T.B. Massalski, H. Okamoto, P.R. Subramanian, L. Kacprzak, *Binary Alloy Phase Diagrams* (ASM International: Material Park, OH), 1990.

[12] M.J. Tambe, S.K. Lim, M.J. Smith, L.F. Allard, S. Gradecak, *Appl. Phys. Lett.* **93**, 151917 (2008).

[13] D. Briand, M. Sarret, K. Kis-Sion, T. Mohammed-Brahim, P. Duverneuil, *Semicond. Sci. Technol.* **14**, 173 (1999).

Numerical study of fluctuation-induced effects during first-order phase transitions

M. V. Nazarenko[1], N. V. Sibirev[1], S. M. Suturin[2] and V. G. Dubrovskii[1,2]

[1] St Petersburg Academic University, St Petersburg, Russia
[2] Ioffe Physical-Technical Institute, St Petersburg, Russia

Abstract. The continuum Zeldovich equation of the second order that accounts for fluctuation effects is solved numerically using implicit method. The solution covers both the nucleation stage and the growth stage. Different power-law growth laws and dimensions of the embryos are considered. The results obtained are compared with the analytical model developed earlier. It is shown that the average embryo size and the supersaturation at the growth stage are consistent with the analytical expressions, but the dispersion of the embryo distribution increases faster than predicted by the analytical model. Theoretical results are illustrated by AFM images of Co quantum dots (QD) on $CaF_2(111)$ surface.

Introduction

The first-order phase transitions are common occurrences observed in nature and exploited in many engineering techniques. Considering epitaxial nanotechnology, first-order phase transitions result in growth of different nanostructures such as thin films, quantum dots (QD), nanowires, etc [1,2]. Classical nucleation-condensation theory is based on the Zeldovich equation in partial derivatives of the second order for the distribution of embryos over sizes. This equation is obtained as a continuous approximation of finite-difference master equations in the monomer limit, where the growth-evaporation rates are related via the detailed balance with the known minimum work of embryo formation. This work deals with numerical solutions of this equation for different systems and then comparison of these numerical result with analytical asymptotic expressions, obtained earlier in Ref. [3].

1. System of equations

Let $n(i, t)$ be the distribution function for embryos over size, i is the count of monomers in the embryo, t is the time and ∂_i, ∂_t are the corresponding partial derivatives, then the Zeldovich equation can be written as [4]:

$$\partial_t n(i, t) = -\partial_t \left[A(i)n(i, t) - B(i)n(i, t) \right].$$

Here $A(i)$ describes the regular growth and $A(i)$ — fluctuation effects. Using $F(i)$ — the corresponding minimum work of formation and W_i^+ — the corresponding growth rate we can write [1,5]

$$
\begin{aligned}
A(i) &= W_i^+ \left[1 - \exp\left(dF(i)/di \right) \right], \\
B(i) &+ \frac{1}{2} W_i^+ \left[1 + \exp\left(dF(i)/di \right) \right].
\end{aligned}
$$

We assume that $F(i) = a(i^{(d-1)/d} - 1) - \ln(\zeta + 1)(i - 1)$, where a is the dimensionless surface energy, d is dimension of the embryo, $\zeta = n(1, t)/n_{eq} - 1$ is the supersaturation and n_{eq} is the monomer equilibrium concentration. As for W_i^+, we consider power-law dependence: $W_i^+ = \frac{\zeta+1}{\tau} mi^{(m-1)/m}$, where τ is the characteristic growth time and m is the growth index. Invariant size ρ (the regular growth rate in terms of ρ is ρ-independent) is then equal to $\rho = i^{1/m}$. Some data for d and m in different systems in diffusion (DR) and ballistic (BR) regimes of growth is presentment in the Table 1 (cf. Ref. [4]).

Let i_c and ρ_c be the critical embryo size and radius. We then define U as

$$U \equiv \left(\frac{i_c}{i} \right)^{1/d} \equiv \left(\frac{\rho_c}{\rho} \right) = \frac{(d - 1)a}{d \ln(\zeta + 1)} \frac{1}{\rho^{m/d}},$$

so U account for near-critical region and allows us to consider Ostwald ripening.

Following [4] we assume $(1 - U)\ln(\zeta + 1) \ll 1$, then $g(\rho, t) = m\rho^{m-1}n(i, t)$ — the distribution function in terms of invariant size — obeys the following equation:

$$
\begin{aligned}
\frac{\partial g(\rho, t)}{\partial t} = &-\frac{\partial}{\partial \rho} \left[\frac{\zeta(1 - U)}{\tau} g(\rho, t) \right. \\
&\left. -\frac{[2 + \zeta(1 + U)]}{2\tau} \frac{\partial}{\partial \rho} \left(\frac{g(\rho, t)}{m\rho^{m-1}} \right) \right]. \quad (1)
\end{aligned}
$$

The material balance equation can be written as

$$\Phi = \zeta + G, \quad (2)$$

here $\Phi = t/t_\infty$ is the ideal supersaturation,

$$G = \frac{1}{n_{eq}} \int_2^\infty d\rho \rho^m g(\rho, t)$$

is the amount of material in all the embryos, t_∞ is the characteristic time of the material flux into the system. As for boundary

Table 1. Embryo dimensions and growth indexes for different material systems.

Material system	d	m
Growth of 2D embryos from 2D adatoms, DR	2	1
Growth of 2D embryos from 2D adatoms, BR	2	2
Growth of 3D embryos from 2D adatoms, DR	3	1
Growth of 3D drops from vapor, DR	3	3/2
Growth of 3D embryos from 2D adatoms, BR (Stranski–Krastanow growth of QD)	3	3/2
Growth of 3D drops from vapor, BR	3	3
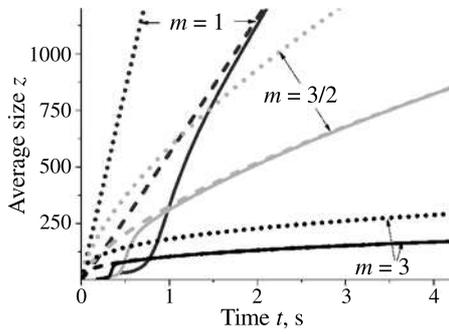
Fig. 1. The average size z against time t for $d = 3$ and different m. Dark gray — $m = 1$, light gray — $m = 3/2$, black — $m = 3$. Dotted lines correspond to analytical asymptotic expressions, solid lines — numeric results, dashed — numeric asymptotics.
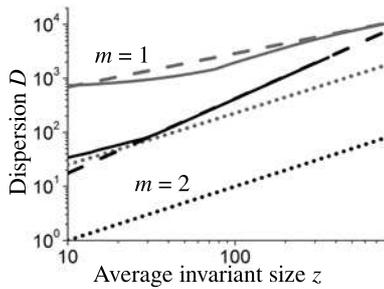
Fig. 2. The dispersion of supercritical embryos D againt the average invariant size z for $d = 2$ and different m. Gray — $m = 1$, black — $m = 2$. Dotted lines correspond to analytical asymptotic expressions, solid lines — numeric results, dashed — numeric asymptotics.

conditions, we assume that the distribution function goes to zero as ρ goes to ∞ faster than power-law, so

$$\lim_{\rho \to \infty} g(\rho, t)\rho^k = 0, \qquad \forall k \in \mathrm{N}. \qquad (3)$$

On the other hand, distribution of sub-critical embryos must be quasi-stationary:

$$n(i, t) = I(\zeta) \exp\left(-F(i)\right) \int_i^{+\infty} \frac{\mathrm{d}j}{W_j^+} \exp\left(F(j)\right), \qquad (4)$$

where I is the nucleation rate (cf. Ref. [5]).

2. Numeric results and analytic predictions

Equations (1)–(4) were solved using implicit grid method and variable time step (cf. Ref. [6]). During the nucleation stage the time step Δt was adjusted so as $I\delta \approx$ const, afterward Δt was constant. As for system parameters, the following values were
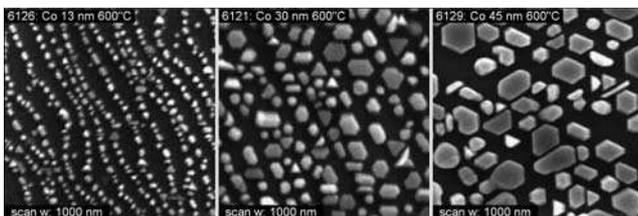
Fig. 3. Co QD on CaF$_2$(111) surface at 13, 30 and 45 nm of Co exposition.

Table 2. Numerical results and analytic predictions.

m	d	Determination	z	$D(z)$
1	2	numeric	$240t^{1.01}$	$166z^{0.62}$
		analytic	$575t$	$2.16z + 1.16z^{0.5}$
2	2	numeric	$64t^{0.506}$	$0.73z^{1.38}$
		analytic	$80t^{0.5}$	$0.1z$
1	3	numeric	$560t^{1.05}$	$1970z^{0.434}$
		analytic	$1060t$	$1.4z + 0.4z^{1/3}$
3/2	3	numeric	$325t^{0.67}$	$200z^{0.57}$
		analytic	$587t^{2/3}$	$0.047z + 1.4z^{0.5}$
3	3	numeric	$103t^{0.35}$	$0.33z^{1.6}$
		analytic	$181t^{1/3}$	Ostwald ripening

used: $n_{\mathrm{eq}} = 4.38 \times 10^{16}$, $a = 7.75$, $t_\infty = 0.06$ s, $\tau = 0.003$ s for all the systems considered. Some of the obtained results are presented on Figures 1 and 2.

The numerical results obtained were compared with earlier analytical predictions from Ref. [3], which considered asymptotic expressions for the average invariant embryo size z as a function of time t and the dispersion D as functions of z. The results of comparison are presented in Table 2.

3. Effects of spectrum spreading on QD arrays

As seen from Table 1 Stranski–Krastanow QD formation corresponds to $d = 3$, $m = 3/2$. where both analytical predictions and numerical results show spectrum spreading should be noticeable. Figure 3 shows evolution of Co QD array on CaF$_2$(111) surface. As can be seen from Fig. 3, spectrum spreading is indeed present. This show a possibility for a kinetically controlled engineering of QD array with the desired properties for different applications.

References

[1] D. Kashchiev, *Nucleation: Basic Theory with Applications*, (Oxford: Butterworth Heinemann), 2000.
[2] V.G. Dubrovskii, *Phys. Stat. Sol. (b)* **171**, 345 (1992).
[3] V.G. Dubrovskii, and M.V. Nazarenko *J. Chem. Phys.* **132**, 114508 (2010).
[4] V.G. Dubrovskii, *J. Chem. Phys.* **131**, 164514 (2009).
[5] V.G. Dubrovskii, and M.V. Nazarenko *J. Chem. Phys.* **132**, 114507 (2010).
[6] N.V. Sibirev, M.V. Nazarenko, and V.G. Dubrovskii *Tech. Phys. Lett.*, to be published.

Ge nanoclusters grown on Ge_xSi_{1-x} layer

A. I. Nikiforov, V. A. Timofeev, S. A. Teys, A. K. Gutakovsky and O. P. Pchelyakov

A.V. Rzhanov Institute of Semiconductor Physics, SB RAS, Lavrentjeva 13, 630090 Novosibirsk, Russia

Abstract. Critical thicknesses of the layers, when 2D to 3D growth and morphological hut–dome cluster transitions occur, were measured. The observed decrease in the critical thicknesses of 2D–3D and hut–dome transitions against the growth on the pure Si(100) surface results from accumulation of elastic strains with increasing Ge percentage or thickness of the GeSi solid solution. Dependence of the density and size of Ge nanoclusters on the solid solution composition is determined. The presence of a thin strained layer of the GeSi solid solution not only causes changes in the critical thicknesses of the transitions but also affects properties of the germanium nanocluster array.

The silicon structures with germanium quantum dots are of practical interest for optoelectronics due to their potential covering the regions from IR through the wavelengths used in fiber-optic communications. Reflection high-energy electron diffraction (RHEED) is the most used technique in MBE. This technique enabled oscillations of the in-plane lattice constant to be detected for the Ge film growing according to the 2D mechanism on the silicon surface [1]. There are available numerous papers that report studies of early stages of Ge growth on the Si(100) surface but only few data on the influence of Ge_xSi_{1-x} layer on the wetting layer thickness and "hut"–"dome" transition [2,3].

A Katun-C MBE installation equipped with two electron beam evaporators for Si and Ge was used for synthesis. As the deposited layer increases in thickness, elastic strains induced by mismatching of the Si and Ge lattice constants also increase. Starting with some critical thickness, from two-dimensional to three-dimensional growth mechanism (2D–3D) and from "hut"-clusters to "dome"-clusters (hut–dome) transitions is observed, a part of strains being relaxed that is energetically favorable due to a decrease in the free energy of the system. Thus, identifying the moment of 2D–3D and "hut"–"dome" transitions at various thickness of Ge_xSi_{1-x} layer at 500 °C allowed the 2D–3D and "hut"–"dome" transitions thickness of Ge film to be determined as a function of Ge_xSi_{1-x} thickness for different Ge content in Ge_xSi_{1-x} layers (Fig. 1) and the 2D–3D transitions thickness of Ge_xSi_{1-x} layer as a function of Ge content in Ge_xSi_{1-x} layers (Fig. 2).
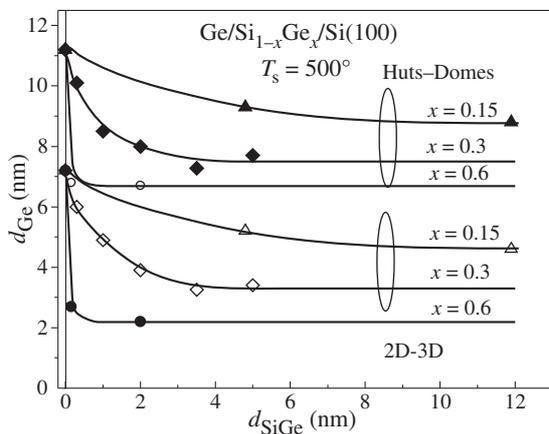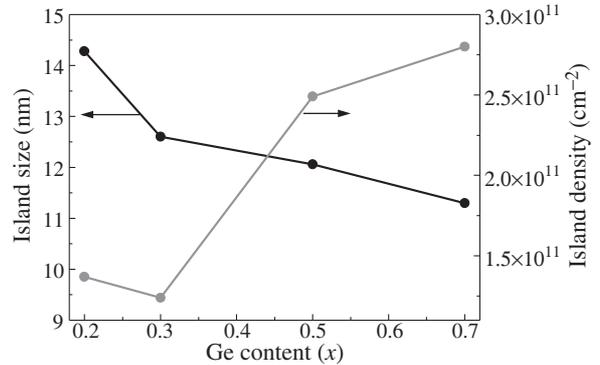
Fig. 2. Size and density of Ge nanoclusters on Ge_xSi_{1-x} as a function of Ge_xSi_{1-x} thickness.

The critical transition thicknesses are observed to decrease to reach saturation as the solid solution layer thickens or its content increases. The observed decrease in thicknesses is accounted for by strengthening the strain deformation in the solid solution layer.

The presence of a thin strained layer of the GeSi solid solution not only causes changes in the critical thicknesses of the transitions but also affects properties of the germanium nanocluster array. STM technique was used to analyze morphological changes in the surface of $Ge/Ge_xSi_{1-x}/Si$ systems with different Ge percentage in the solid solution layer. In Fig. 2, dependence of the size and density of Ge islands on Ge_xSi_{1-x} solid solution surface is resulted.

A STM image in Fig. 3 shows the surface morphology of the 2.3 nm thick Ge film over the underlying layer of $Ge_{0.5}Si_{0.5}$ solid solution. There are only observed islands in the form of "hut"-clusters on the surface, their shape and size being characteristic of Ge islands on the Si(100) surface. Therefore, it is reasonable to suppose similar mechanism of their formation, while the strained layer of the solid solution is the main factor affecting the critical thicknesses of the morphological transitions. The influence of the solid solution composition on properties of the array of Ge islands was determined by plotting the dependence of island density and size on the Ge content in the range from 10 to 20% (Fig. 3). The uncertain choice the solid solution thickness due to difficulties in identifying the 2D–3D transition made it impossible to obtain relevant data on smaller Ge contents (Fig. 1). The islands decrease in size and increase in density with an increase in the Ge content in the solid solution layer. Understanding the reasons for this kind of dependence needs more detailed studies. Crystal

Fig. 1. Critical thicknesses of Ge film for 2D–3D and "hut"–"dome" transitions as a function of Ge_xSi_{1-x} thickness and Ge content in Ge_xSi_{1-x} layers.
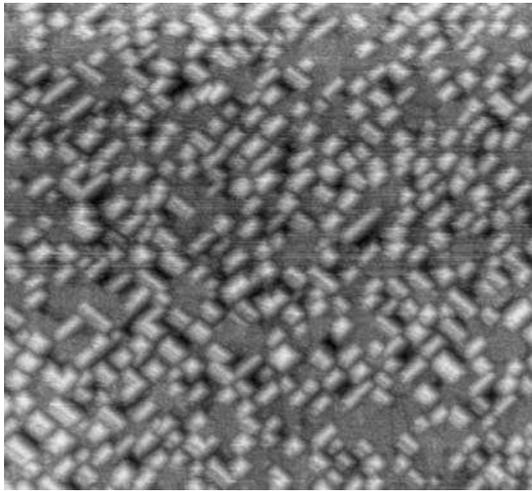
Fig. 3. STM image (400×400 nm^2) of Ge hut-clusters on a Ge$_x$Si$_{1-x}$ layer ($x = 0.5$, $d_{\text{GeSi}} = 1$ nm).
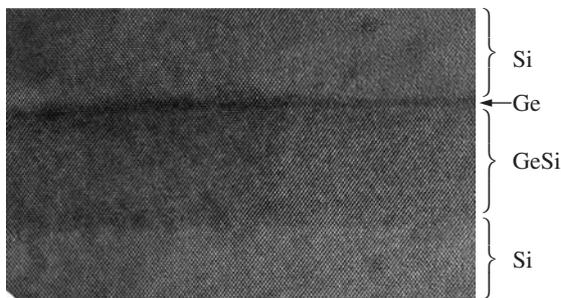
Fig. 4. Fragment of the high-resolution TEM image of Ge quantum dots on the Ge$_{0.4}$Si$_{0.6}$ 15 nm thick.

structure of Ge/Ge$_x$Si$_{1-x}$/Si heterolayers with quantum dots was analyzed using cross section high resolution TEM. Figure 4 shows such a TEM image. Layers of germanium, solid solution and silicon are rather different in contrast to allow them to be inspected individually. Neither of the layers contains any defects. Hence, the structure is elastically strained, plastic relaxation does not occur, and the germanium islands are of the characteristic "hut"-cluster shape.

Thus, the critical thickness of 2D–3D transition was determined as a function of composition during the growth of solid solution Ge$_x$Si$_{1-x}$. Non-relaxed atomically smooth GeSi layers were used as an initial surface to fabricate Ge nanoislands. The influence of germanium content in the solid solution on properties of the island array was studied. Based on the results obtained, it becomes possible to obtain dislocation-free strained heterostructures Ge$_x$Si$_{1-x}$ which contain germanium quantum dots in quantum wells formed by layers of GeSi solid solution.

References

[1] A.I. Nikiforov, V.A. Cherepanov, O.P. Pchelyakov, *Mat. Sci. Engineering B* **89**, 180 (2002).
[2] N.V. Vostokov *et al*, *Physics of the Solid State* **47**, 26 (2005).
[3] Zhensheng Tao *et al*, *Appl. Surf. Sci.* **255**, 3548 (2009).

Synthesis of silver nanoparticles by laser ablation in liquid

A. E. Tyurnina, V. Ya. Shur, D. K. Kuznetsov, E. A. Mingaliev and R. V. Kozin

Ural State University, Ekaterinburg, Russia

Abstract. The stable suspension with silver nanoparticles were produced by irradiation with a 1064-nm laser of Ag target drown in deionized water. The dependence of the nanoparticle sizes and suspension stability on the energy density, ablation time and condition of the target surface were studied. The appropriate experimental conditions allow to produce the particles with a typical size of 5 ± 2 nm. The spectral position of the plasmon resonance maximum and size distribution function measured by dynamic light scattering were used for characterization of nanoparticles. It was shown experimentally that increasing of the laser irradiation time and decreasing of the laser fluence lead to decrease of the nanoparticle size.

Introduction

The size dependence of the properties of silver nanoparticles opens their wide application in microelectronics, optics, catalysis, and medicine [1,2]. Among physical methods of the laser ablation of metals in vacuum or liquid is the most effective method of synthesis of the metal nanoparticles. In the last decade, the pulse laser ablation in liquids has proven to be a unique and efficient technique for generation and fragmentation of nanoparticles. Wide variety in nanoparticle material and used liquids leads to unlimited variety of colloid solution (suspensions) which can be produced by laser within a few minutes [1–3]. The laser ablation in liquid possesses such advantages as high purity and stability of colloidal solutions, due to production of charged nanoparticles and relative simplicity of the procedure [4].

The narrow distribution function of nanoparticle sizes can be achieved as a result of their multiply evaporation and condensation due to coming back into a laser beam during collective motion in the close liquid volume and sufficient absorption of the laser radiation. Laser ablation method allows to produce nanoparticles with given size and shape by choosing the proper laser wavelength, fluence, pulse duration, ablation time, mixing conditions and light focusing. The mechanisms of the influence of these factors are still not clear [4–6]. The main target of a laser ablation method is the synthesis of the stable suspensions of nanoparticles with narrow size distribution.

1. Experimental

The silver target was irradiated by a pulse Nd:YAG fiber laser system Fmark-20 RL. The laser beam was focused by a lens ($F = 254$ mm) on the surface of a silver target (purity 99.99%,
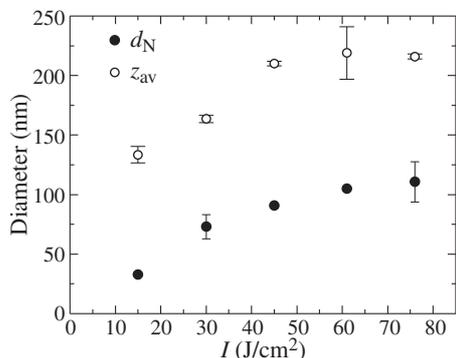
Fig. 1. Dependence of average hydrodynamic diameter (z_{av}) and mean diameter (d_N) on laser fluence for laser ablation during 60 s.
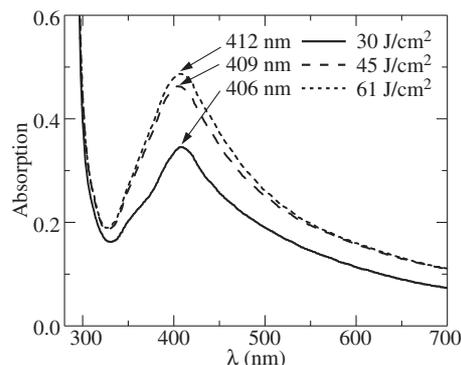
Fig. 2. Absorption spectra of silver colloidal solutions produced by 60 s laser ablation for different fluences.

thickness about 1 mm) placed on the bottom of glass vessel with 4 ml of pure deionized water. The thickness of water layer above the target was about 5 mm. The target was cleaned by deionized water in an ultrasonic bath before laser ablation.

The used laser fluence ranged from 15 to 80 J/cm² with laser spot diameter at the target surface about 40 μm.

The duration of the ablation experiments ranged from 1 to 60 min. The scanning by a laser beam was carried out on the surface of a target along the area about 5×5 mm² with velocity about 270 mm/s.

The sizes of nanoparticles were measured by dynamic light scattering using Zetasizer Nano-ZS, Malvern Instruments, UK. The average size of nanoparticles has been estimated also from absorption spectrum of the colloidal solution measured in a spectral range from 300 to 700 nm using a spectrophotometer Helios Alpha, TermoSpectronic, USA.

2. Influence of laser fluence

We have measured the monomodal size distribution function of the nanoparticles with polydispersity below 0.3. The dependence of the average hydrodynamic diameter z_{av} and corresponding mean diameter (d_N) (the position of a peak of the number-weighted distribution function) on laser fluence for laser ablation during 60 s was carried out (Fig. 1).

The measurements of the absorption spectra of the colloidal solution (Fig. 2) allow to reveal the absorbance resonance around 400 nm which typical for surface plasmon resonance (SPR) of Ag nanoparticles. The existence of the single SPR peak maintains that the shape of the synthesized nanoparticles is close to spherical [7].

The revealed decrease in the wavelength corresponding to
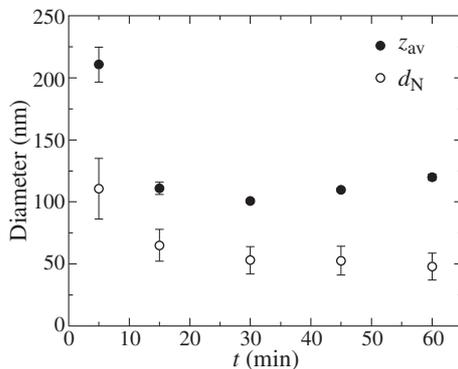
Fig. 3. Dependence of average hydrodynamic diameter (z_{av}) and mean diameter (d_N) of silver nanoparticles on laser ablation time for laser fluence 30 J/cm^2.

Fig. 4. Absorption spectra of silver colloidal solution produced at laser fluence 30 J/cm^2 for different laser ablation time.

SPR maximum with decreasing of the laser fluence can be attributed to formation of silver nanoparticles with smaller sizes [5].

The mechanism of nanoparticle formation during laser ablation represents not only nucleation and growth of particles in a dense plasma cloud, but also ejection of metal drops or solid fragments from the target ("explosive boiling") [5]. This is the reason to increase the agglomeration probability with increase of the laser fluence as it increase the melting depth of on the target surface and amount of target material simultaneously appeared in liquid. As a result the smallest and the most homogeneous nanoparticles have been produced at low laser fluence however decrease of ablation efficiency with reduction of laser fluence imposes restriction on nanoparticle synthesis at low laser energy.

3. Influence of laser ablation time

The dependence of the efficiency of ablation and concentration of colloid solution on ablation time the synthesis of nanoparticles has been studied at laser fluence 30 J/cm^2 in the time range from 5 up to 60 min.

The obtained dependence of the sizes of nanoparticles z_{av} and d_N on laser ablation time (Fig. 3) demonstrates essential decrease of both sizes during first 30 minutes. It is natural to attribute this effect to fragmentation of nanoparticles in colloid solution due to absorption of laser irradiation and ablation of target by laser beam scattered by nanoparticles ("screening effect"). The absence of further decreasing of sizes for longer ablation is caused by decreasing efficiency of fragmentation at 1064 nm for nanoparticles with diameter below 50 nm.

The decrease in the wavelength corresponding to SPR maximum with increasing of the ablation time was found for time below 30 min only without any measured change for longer ablation time (Fig. 4). This fact agrees with the earlier discussed result.

The colloid solutions produced at laser fluence 30 J/cm^2 and ablation time ranged from 15 to 60 min are very stable. The measured mean value of zeta potential is above 35 mV. Which is typical for the stable colloidal solutions [4].

4. Influence of surface state

The dependence of the nanoparticle sizes on the parameters of the target surface has been studied by comparison of the
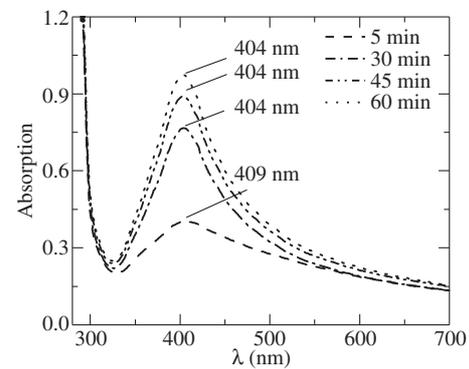
nanoparticles produced at the subsequent scanning of the target by the laser beam. It was shown that the proper preparation of the target surface after several scanning cycles allows to produce the spherical silver nanoparticles with average diameter extracted from of the number-weighted distribution function equal to 5 ± 2 nm.

The obtained results open up the possibilities for synthesis of colloid solution of spherical silver nanoparticles with needed sizes using ablation by pulsed 1064 nm laser.

References

[1] H. Fujiwara *et al*, *J. Phys. Chem. B* **103**, 2589 (1999).
[2] J.H. Hodak *et al*, *J. Phys. Chem.* **104**, 11708 (2000).
[3] Y.H. Yeh *et al*, *Chem. Lett.*, 1183 (1998).
[4] S. Barcikowski *et al*, *J. Nanopart. Res.* **11**, 1883 (2009).
[5] A. Pyatenko *et al*, *Silver nanoparticles*, (India, D.P. Perez) 334 (2010).
[6] N.V. Tarasenko *et al*, *Appl. Serf. Sci.* **252**, 4439 (2006).
[7] S. Link *et al*, *J. Phys. Chem. B* **104**, 6152 (2000).

Laser-assistant and furnace annealing crystallization of silicon-rich nitride based and Si–SiO$_2$ multilayer nanostructures

V. A. Volodin[1,2], K. O. Bugaev[1,2], D. V. Marin[1,2], A. A. Zelenina[2], D. V. Nesterov[2], A. Kh. Antonenko[1,2], G. N. Kamaev[1,2], S. A. Kochubei[1], A. G. Cherkov[1], A. K. Gutakovsky[1], L. I. Fedina[1], M. A. Neklyudova[1,2], A. V. Latyshev[1,2] and A. Misiuk[3]

[1] Institute of Semiconductor Physics, SB RAS, Lavrentieva av., 13, Novosibirsk 630090, Russia
[2] Novosibirsk State University, Pirogov str. 2, 630090 Novosibirsk, Russia
[3] Institute of Electron Technology, Al. Lotnikov 46, 02-668 Warsaw, Poland

Abstract. Furnace and pulse laser treatments were applied for crystallization of amorphous nanoclusters in silicon-rich nitride films, Si-SiO$_2$ multilayer nanostructures and a-Si:H films. The as-deposited and annealed structures were studied using optical methods and electron microscopy techniques. The influence of hydrogen on crystallization and formation of Si nanoclusters was studied. Regimes of crystallization of amorphous Si nanoclusters and nanolayers were found. This approach is applicable for the creation of dielectric films with semiconductor nanoclusters and silicon nanostructured films on non-refractory substrates.

The constant interest to amorphous, nano- and microcrystalline silicon films on non-refractory inexpensive substrates and their crystallization is stimulated by demands of giant microelectronics. For example, the enlargement of sizes of flat panel displays with active thin film transistor matrix can be described as "reverse Moor's low" [1]. Dielectric films with amorphous or crystalline Si clusters show promise as a material for optoelectronic and flash-memory applications [2]. Ultrathin Si-SiO$_2$ multilayer nanostructures with tunnelling barrier have perspectives in novel solar cell devices with enhanced efficiency [3]. Modern technique of deposition allows the production of dielectric films on substrates with temperature of plasticity as low as 100 °C. The problem of formation of amorphous Si nanoclusters, nanolayers and its crystallization is a topic of current research. The laser pulse crystallization has advantages in comparison with long time high temperature furnace annealing [4,5]. The present work is devoted to the development of furnace and laser assisted crystallization of amorphous Si based nanostructures.

The silicon reach nitride (SRN) films were deposited using low frequency (55 kHz) plasma enhanced chemical vapour deposition (LF-PECVD) technique. The stoichiometric parameter x in the SiN$_x$:H films was varied from 0.6 to 1.3 using various ratios of SiH$_4$ and NH$_3$ gases in the reactor during deposition. Ultrathin Si-SiO$_2$ multilayer nanostructures, which
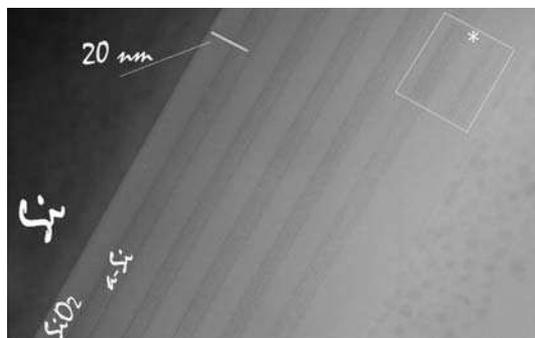
Fig. 1. HRTEM image of an as-deposited a-Si-SiO$_2$ multilayer nanostructure.
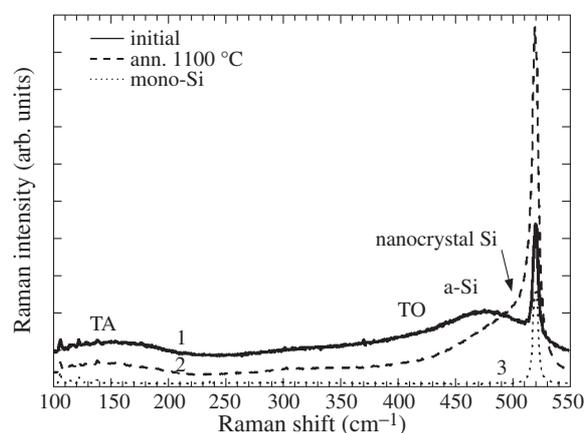
Fig. 2. Raman spectra of an as-deposited Si-SiO$_2$ multilayer nanostructure and after furnace annealing (1100 °C, 30 min).

consist of alternating layers of a-Si:H and SiO$_2$, were deposited on n-type (100) Si substrate with a resistivity of 4.5 Ω cm and on glass substrates. The experimental setup with source of wide aperture and high-density inductively coupled RF plasma (13.56 MHz) was used. Prior to the deposition of a-Si:H, a SiO$_2$ layer was deposited by plasma oxidation (gas flow into the reactor 60 sccm, RF power 300 W, substrate temperature 150 °C). Subsequently, a-Si:H layer with thickness of 200 Å was deposited. Afterwards the part of amorphous silicon layer was processed by plasma enhanced oxidation, so that the thickness of the remainder of the a-Si:H after that was about 70 Å. These alternative procedures (thin-film depositions and plasma enhanced oxidation) are repeated as many times as the planned periods. Thus, a structure containing 6 layers of a-Si:H with thickness of 70 Å, inserted between the layers of SiO$_2$ with thickness 130 Å (Fig. 1) has been created.

Excimer XeCl laser with wavelength of 308 nm and pulse duration of 25 ns and triple harmonic of YAG:Nd laser ($\lambda = 335$ nm, pulse duration of 10 ns) were used for laser treatments of the as-deposited films. Some films were annealed at temperatures $1100-1130$ °C at atmosphere pressure (10^5 Pa) and under pressure 1.1 GPa. High resolution transmission electron microscopy (HRTEM) and Raman spectroscopy technique was
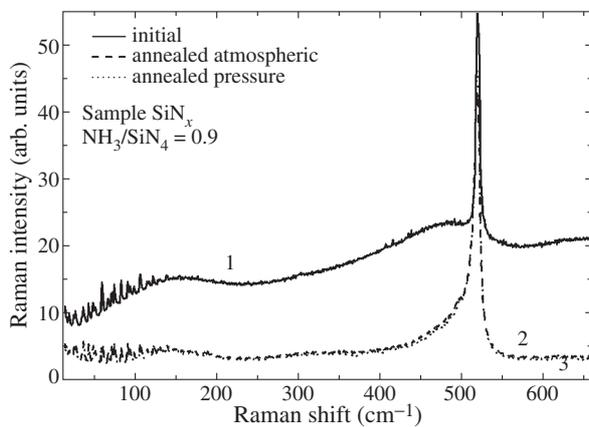
Fig. 3. Raman spectra of as-deposited and annealed SRN film on Si substrates.
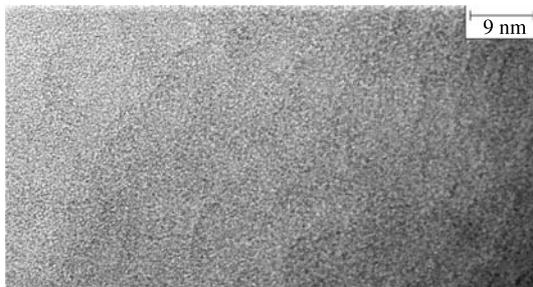
Fig. 4. HRTEM image of SRN $SiN_{0.7-0.9}$ film after annealing at temperature 1130 °C at under pressure 1.1 GPa.

used to identify the structure (amorphous or crystalline) of the Si nanoclusters in the films. Raman spectra were recorded in the back-scattering geometry and the 514.5 nm Ar^+ laser line was used as a source. Triple spectrometer (T64000 Horiba Jobin Yvon) with a micro-Raman setup was used. For some samples the photoluminescence (PL) and IR-spectroscopy were studied.

From Raman spectrum of an as-deposited a-Si-SiO$_2$ multilayer nanostructure (Fig. 2) one can see only broad amorphous peaks at 480 cm^{-1} (transverse optical — TO) and at 150 cm^{-1} (transverse acoustical — TA). The thermal annealing leads to crystallization of amorphous Si layers — one can see "shoulder" from nanocrystalline Si (curve 2). The position and the width of the Raman peaks strongly depend on size of the nanocrystals.

According to Raman scattering data SRN films with relatively high concentration of additional silicon contained amorphous Si clusters whose density increased with the concentration of the additional silicon [5]. One can see from Figure 3 that as-deposited SRN film with stoichiometry $SiN_{0.7-0.9}$ contains only amorphous Si nanoclusters. Narrow peak at 520 cm^{-1} from monocrystalline Si substrate is observed (the films are semitransparent). Furnace annealing (1130 °C, 5 hrs) leads to crystallization of a-Si nanoclusters — one can see "nanocrystalline" shoulder close to peak from monocrystalline Si substrate. No visible difference in Raman spectra of the SRN films annealed at atmospheric pressure and under pressure 1.1 GPa were observed. But dramatic differences in PL spectra of SRN films annealed under high pressure and without pressure were observed. Supposedly, pressure acts on defects (recombination centres) in SRN. According to IR spectra, in nearly stoichiometric SRN films, amorphous silicon nitride has crystallized
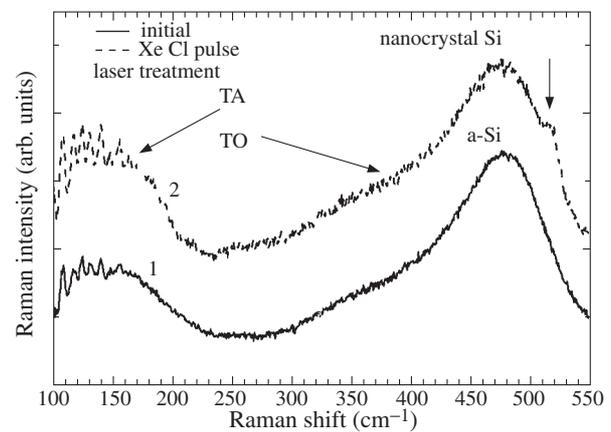
Fig. 5. Raman spectra of as-deposited a-Si-SiO$_2$ multilayer nanostructure and after excimer laser annealing.

under furnace annealing.

According to position of "nanocrystalline" Raman peak (518 cm^{-1}) the size of nanocrystals should be 6–7 nm. The HRTEM data confirm this conclusion (see Figure 4).

But, furnace annealing can be applied only for the case of very refractory substrates (fused silica or mono-crystal silicon). To crystallize amorphous silicon hydrogenated films, amorphous nanoclusters in SRN films and Si-SiO$_2$ multilayer nanostructures on cheap non-refractory glasses the pulse laser treatments were used. In the case of a-Si hydrogenated films for both XeCl and triple harmonic of YAG:Nd lasers the laser fluences needed for film crystallization were found. The laser fluences depend on hydrogen concentration. But, for multilayer a-Si-SiO$_2$ nanostructures, the threshold for crystallization was very close to threshold of laser ablation. As one can see from Figure 5, using one-step pulse laser treatments one can get only partial crystallization.

Presumably, it is due to high hydrogen concentration in these as-deposited films. From Raman spectra as-deposited multilayer nanostructure contain mostly Si-H$_2$ bonds, because the position of Si-H$_2$ peak is about 2100 cm^{-1}. Frequency of Si-H peak is about 2000 cm^{-1}. According to our estimates, atomic concentration of hydrogen reach up to 40%, and this is enough for blistering (and film breakaway) during pulse laser treatments. After laser treatments with fluence lower than ablation threshold, the most part of hydrogen abandon the film. So, multi-step laser treatments should be applied for full crystallization of such films.

References

[1] M.S. Shur *et al*, *10th International Symposium "Nanostructures: Physics and Technology"* St Petersburg, 2002.
[2] Nae-Man Park *et al*, *Phys. Rev. Lett*, **86**, 1355 (2001).
[3] R.A. Puglisi *et al*, *J. Appl. Phys.* **108**, 023701 (2010).
[4] V.A. Volodin *et al*, *Appl. Phys. Lett.* **73**, 1212 (1998).
[5] V.A. Volodin *et al*, *18h International Symposium "Nanostructures: Physics and Technology"* St Petersburg, 2010.

Nanoislands nucleation on vicinal substrate

Xu Zhang[1,2], V. G. Dubrovskii[1,3], N. V. Sibirev[1] and Xiaomin Ren[2]

[1] St Petersburg Academic University, St Petersburg, Russia
[2] Key Laboratory of Information Photonics and Optical Communications (Beijing University of Posts and Telecommunications), Ministry of Education, #10 Xitucheng Road, Haidian District, Beijing 100876, China
[3] Ioffe Physical-Technical Institute, St Petersburg, Russia

Abstract. An analytic stress-driven nucleation model of nanoislands grow on mismatched vicinal substrate is proposed. This model is only applied to the initial stage of nucleation. It is demonstrated that the formation enthalpy of nanowires (NWs) and nanoneedles (NNs) is function of three independent variables, the base radius, aspect ratio and miscut angle of vicinal surface. The theoretical analysis shows the minimum nucleation barrier of nanoislands which relates to a saddle point of formation enthalpy is lower on vicinal substrate than on flat substrate.

Introduction

The nucleation and growth of strained NWs and NNs on lattice-mismatched vicinal substrate have attracted great interest recently because the phenomenon is not only of fundamental interest but also has significant technological application. The NWs and NNs are often grown via the vapor-liquid-solid (VLS) mechanism activated by the drop of a metal catalyst. The nucleation process takes place at the interface of catalyst droplet and solid atomic III–V bilayers. Nucleation occurs because the liquid supersaturated in group III and group V elements.

In this letter, we consider a self-consistent model of stress-driven growth of coherent 3D islands in lattice mismatched systems at the initial nucleation stage. Theoretical analysis shows that the step effect of vicinal substrate has tremendous influence on the nucleation enthalpy of nanostructure. It is demonstrated that the formation enthalpy is function of three independent variables, the base radius, aspect ratio and miscut angle of vicinal surface. The result of our proposed model demonstrated that nucleation barrier of NWs and NNs on vicinal substrate is lower than that of flat substrate. So, it is much easier for island nucleation on vicinal substrate.

1. Theoretical model

The model geometries used below in this paper are shown in Fig. 1: we consider a cylinder (a) and pyramidal islands with a regular hexagonal cross-sections (b). The sidewalls of pyramidal islands are made up of vertical facets of elementary length dl, separated by the horizontal monoatomic steps of height dr. The steps are arranged regularly so that $dl/dr = L/R = 2\beta$, where L is the length, R is the base dimension and $\beta \equiv L/2R$ is the aspect ratio. The cylinder and hexagonal prism are typical model geometries for straight NWs [1], the hexagonal pyramid with stepwise sidewalls is the experimentally observed NN geometry [2].

From the nucleation theory [3,4], the formation enthalpy of a 3D island can be written down as

$$\Delta G^{3D}(R, \beta, \theta_m) = -\frac{\Delta\mu(\beta)}{\Omega}C_1 R^3\beta + \gamma_F C_2 R^2\beta + \Delta\gamma C_3 R^2 \quad (1)$$

with $C_1 = \sqrt{3}, 2\pi$; $C_2 = 6, 4\pi$; $C_3 = 3\sqrt{3}/2, \pi$ for hexagonal NN and cylindrical NW respectively, $\Delta\mu$ is the difference of chemical potentials between the vapor (or the adatom) phase and the island per atom pair, Ω is the elementary volume in the solid phase, γ_F is the surface energy of lateral facets (formed due to the nucleation), $\Delta\gamma \equiv \gamma_W - \gamma_S$, γ_W is the surface energy
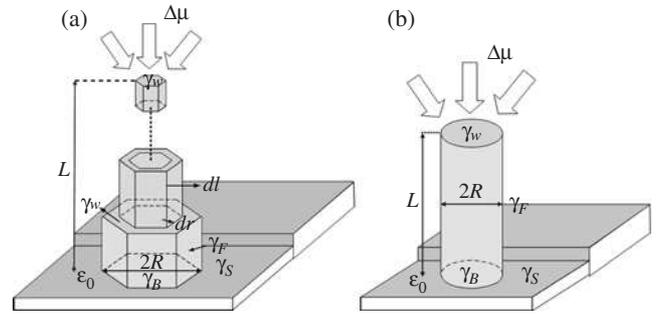
Fig. 1. Model of NW and NN geometries.

of top facet (formed due to the nucleation) and γ_S is the surface energy of the vicinal wetting layer, and the interfacial energy does not take into consideration. The first term in Eq. (1) gives the decrease in chemical potential due to the vapor-solid phase transition, the second term describes an energetically formation of sidewalls and the third term stands for the change in the in-plane surface energy caused by the island formation. The average surface energy of a vicinal surface with miscut θ_m (assuming noninteracting steps) is [5]

$$\gamma_S = \gamma_0 \cos(\theta_m) + \eta \sin(\theta_m) , \quad (2)$$

where γ_0 is the surface energy of flat substrate, η is the step formation energy per unit height, it can be defined as a function of the angle of low-energy facets θ_f. For the island facet to be the first low-energy facet to appear beyond the flat surface, in our case $\theta_f = 90°$, we use this value, giving $\eta = [\gamma_0 - \gamma_0 \cos(\theta_f)]\csc(\theta_f)$ and $\gamma_F = \gamma_W = \gamma_0(1-\alpha)$ [6];

α defines surface energy anisotropy, in our paper, the surface energy is considered to be isotropic ($\alpha = 0$). The vapor-solid difference of chemical potentials in a lattice mismatched material system is given by $\Delta\mu(\beta) = \Delta\mu_0 - w(\beta)$. The elastic energy is presented in the form $w(\beta) = w_{2D}z(\beta)$, where $z(\beta)$ is the elastic energy relaxation. The quantity $w_{2D} = (E\Omega\varepsilon_0^2)/(1-\upsilon)$ is the elastic energy per atom in a uniformly strained 2D layer with E as the Young's modulus, υ as the Poisson's ratio and ε_0 as the mismatch parameter. Plastic relaxation via the formation of misfit dislocations is neglected at the initial nucleation stage, because the dislocated islands most probably will not grow epitaxially. The simplest formula for $z(\beta)$ can be chosen in the form [7]

$$z(\beta) = 1/(1 + \beta/\beta_0) . \quad (3)$$
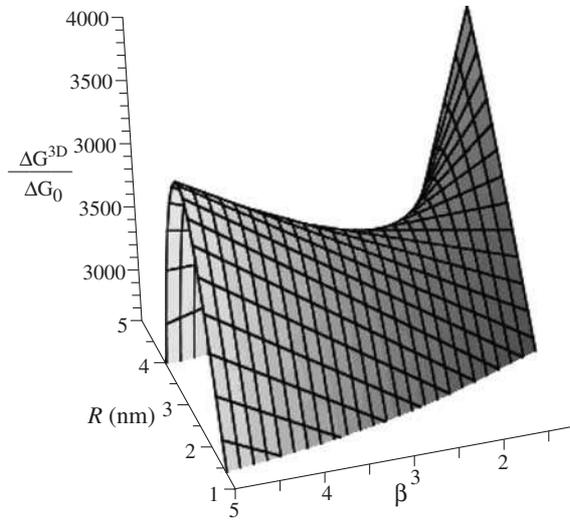
Fig. 2. The formation enthalpy of NWs on vicinal substrate with miscut angle equals $3°$, $a = -0.013$, $b = 0.045$, $c = 0.32$, $\varepsilon_0 = 0.2$, the above parameters correspond to GaN NWs growth on silicon substrate.
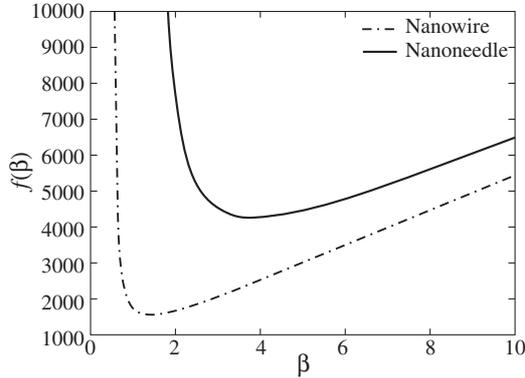
Fig. 3. Function $f(\beta)$ describes the preferred aspect ratio with approximation given by Eq. (3) for NWs and NNs respectively.

2.   Results and discussion

Obviously, elastic relaxation given by Eq. (3) is reduced to $z(\beta) = 1/(\beta/\beta_0)$ with $\beta_0 < 0.2$ for both cylinder and pyramidal islands, which is much lower than the aspect ratios of interest. The free enthalpy given by Eq. (1) always has a β-dependent maximum $\Delta G_*^{3D}(\beta, \theta_m)$ in R. The β-dependent maximum of ΔG_*^{3D} can be put in the form

$$\Delta G_*^{3D}(\beta, \theta_m) = \Delta G_0 f(\beta), \quad f(\beta) = \frac{(\beta + a)^3}{[b\beta - c\beta_0]^2}, \quad (4)$$

where $\Delta G_0 = \gamma_0 C_2 h^2/27$ (with h as the height of a monolayer) is a material related constant. The Eq. (4) contains three important parameters:

$$a = \frac{C_3}{C_2}[1 - \cos(\theta_m) - \sin(\theta_m)], \ b = \frac{C_1}{2C_2}\frac{h\Delta\mu_0}{\Omega\gamma_0}, \ c = \frac{C_1}{2C_2}\frac{hw_{2D}}{\Omega\gamma_0}. \quad (5)$$

The coefficient a is always negative for small miscut angle, the supersaturation coefficient b stands for the chemical potential of vapor phase with respect to the solid state, the coefficient c describes the normalized elastic energy of two dimension. The condition for $3D$ nucleation to occur is given by inequality $b > cz(\beta)$, which means the vapor supersaturation must be larger than the elastic energy in the island with aspect ratio β. The maximum radius is reached at

$$R_*(\beta, \theta_m) = \frac{2C_2\Omega\gamma_0}{3C_1}\frac{(\beta + a)}{\beta[\Delta\mu_0 - w_{2D}z(\beta)]}. \quad (6)$$

It is the critical radius at which the $3D$ nucleation enthalpy reaches its maximum given by Eq. (1). Then, the minimum aspect ratio is obtained from the equation $\beta = h/2R_*(\beta, \theta_m)$, so the minimum aspect ratio is expressed as $\beta_{\min}^{3D} = \frac{3}{2}(b - c) - a$. Since ΔG^{3D} has a maximum in R at $\Delta\mu(\beta) > 0$, the variable R is thermodynamically unstable and the supercritical embryos will grow infinitely. The nucleation barrier is now determined by the minimum of $\Delta G_*^{3D}(\beta, \theta_m)$ at a certain β_* relating to the saddle point of formation enthalpy $\Delta G_{\min}^{3D}(\theta_m)$, as demonstrated in Fig. 2. The preferred aspect ratio and the nucleation barrier at the saddle point are now found by minimizing Eq. (4) in β.

$$\Delta G_{\min}^{3D}(\theta_m) = \frac{C_2^2\Omega^2\gamma_0^3\{C_3\Delta\mu_0[1-\cos(\theta_m)-\sin(\theta_m)]+C_2\beta_0 w_{2D}\}}{C_1^2\Delta\mu_0^3}. \quad (7)$$

The simplest approximation for the elastic relaxation given by Eq. (3) provides an excellent fit to the analytical formula with β_0 equals 1/15 and 2/11 for NWs and NNs respectively [8]. We substitute equation Eq. (3) into $f(\beta)$ of Eq. (4), the behaviors of function $f(\beta)$, relating to different aspect ratios of emerging islands, shown in Fig. 3. The minimum value of aspect ratio for nanoneedles is larger than that of nanowires. In our case, the strain-driven catalyst-free growth of NWs (GaN NWs growth on silicon substrate) with highly mismatched systems requires the elastic energy contribution is much greater than the chemical energy $\Delta\mu_0$, thus coefficient $b \gg c$.

It is observed that there is a minimum value of energy barrier for island nucleation at flat substrate. The barrier arises because, for zero miscut, island formation raises the total surface energy. But at finite miscut, the surface energy of NW or NN may be less than or equal to that of the vicinal wetting layer it covers, so there is decreased surface energy cost and the nucleation barrier is eliminated or dramatically reduced. Form the formula (7) we can deduce that, compare to the nucleation barrier of flat substrate $\Delta G_{\min}^{Flat} = (C_2^3\Omega^2\gamma_0^3\beta_0 w_{2D})/(C_1^2\Delta\mu_0^3)$, the nucleation barrier of vicinal substrate is reduced. So, it is much easier for island nucleation on vicinal substrate.

References

[1] L.C. Chuang, M. Moewe, S. Crankshaw, and C. Chang-Hasnain, *Appl. Phys. Lett.* **92**, 013121 (2008).

[2] Michael Moewe, Linus C. Chuang, Shanna Crankshaw, Chris Chase *et al*, *Appl. Phys. Lett.* **93**, 023116 (2008).

[3] A.V. Osipov, F. Schmitt, S.A. Kukushkin and P. Hess, *Appl. Surf. Sci.* **188**, 156 (2002).

[4] I.N. Markov, *Crystal Growth for Beginners* (World Scientific, Singapore, 2003).

[5] B.J. Spencer, J. Tersoff, *Appl. Phys. Lett.* **96**, 073114 (2010).

[6] Hao Hu, H.J. Gao, and Feng Liu, *Phys. Rev. Lett.* **101**, 216102 (2008).

[7] V.G. Dubrovskii, N.V. Sibirev, X. Zhang and R.A. Suris, *Cryst. Growth Des.* **10**, 3949 (2010).

[8] Xu. Zhang, N.V. Sibirev, V.G. Dubrovskii, Xiaomin Ren, submitted to *J. Appl. Phys.*

Spin dynamics at the Fe/semiconductor interfaces and spin pumping transport studies using spin pumping in magnetic heterostructures

B. Heinrich

Department of Physics, Simon Fraser University, Burnaby, BC, Canada

GaAs/nFe/20Au(001) structures were deposited at room temperature (RT) using Molecular Beam Epitaxy (MBE), with number of Fe atomic layers (AL), $n = 5, 8, 7, 8, 10, 12, 14, 16, 20$, and 30. In-plane Ferromagnetic Resonance (FMR) (magnetization in the film surface) measurements from 9 to 72 GHz, allowed one to investigate the intrinsic and extrinsic contributions to magnetic damping. The FMR measurements were interpreted by LLG equations of motion. In this presentation, we report studies on thickness dependent magnetic damping in GaAs/Fe(001) in the ultrathin limit $n < 12$. The increase in ΔH for the films thinner than 12 AL is caused by the intrinsic Gilbert damping at the GaAs/Fe(001) interface. The Fe films with $n < 20$ show a linear dependence of ΔH on the microwave frequency f from 9 to 72 GHz. The thickness dependence of Gilbert damping parameter $G(d)$ (in s^{-1}) is well described by constant and linear terms $G_0 \times G_{int}/d$. The constant term $G_0 = 0.75 \times 10^8$ s^{-1} is close to that expected for the bulk Fe. The term proportional to $1/d$ is a typical interface contribution and it will be shown that is caused by noise in spin orbit interaction due to interface alloying of Fe and GaAs.

Spin transport in crystalline Au and Ag layers was investigated using magnetic single Ag,Au/Fe(001) and double layer Fe/Ag,Au/Fe(00) structures prepared by MBE on 2×6 GaAs (001) reconstructed templates. Pure spin currents were injected at the Ag,Au/Fe interface into the Ag and Au spacers by using rf spin pumping effect For the magnetic single Au,Ag/Fe/GaAs(001) layer structures the spin pumping introduces a non-local interface Gilbert damping. This contribution increases with the normal metal (NM) spacer thickness and eventually saturates when its thickness is larger that the spin diffusion length in NM. In magnetic double Fe/Au,Ag/Fe/GaAs (001) layers both spin-pumping and spin-sink effects are present. The magnetic damping was investigated by Ferromagnetic Resonance (FMR) from 10 to 74 GHz. The data analysis were carried out using Kirchhoff's laws of spintronics. The Ag ($n = 20, 100, 300, 500$, and 1500) and Au ($n = 20, 80, 150, 200, 250, 300, 1500$) spacers with the n atomic layers allowed one to investigate nonlocal spin transport from ballistic to spin-diffusion limit. The sheet conductance measurements allowed one to determine the role of electron momentum interface diffuse scattering and estimate an effective momentum relaxation time in the Ag and Au spacers. The measured data were interpreted using pure ballistic and spin diffusion theory which includes electron momentum and spin flip scattering. The results from FMR measurements allowed one to determine the electron momentum and spin flip relaxation times and the corresponding spin diffusion lengths in the Ag and Au spacers. The spin transport measurements were carried out from RT to He crogenic temperatures. This allowed one to investigate the spin flip scattering by phonons covering the full range of phonon q wave-vector spectra.

The spin-sink at the Fe/Ag interface was employed to detect directly the propagation of spin currents across the Ag spacers. The bottom Fe layer grown at the Fe/GaAs(001) interface was employed as a spin pump. The spin current generated in the Ag spacer was detected by the dynamic response of the top Fe layer using a ps and submicron resolved magneto-optical Kerr effect (TRMOKE).

Plasmonic nanowires as the tools for near-field magneto-optics and scanning microscopy: theory

V. A. Kosobukin

Ioffe Physical-Technical Institute, St Petersburg, Russia

Abstract. A theory is developed for near-field magneto-optics and microscopy with a linear probe scanning the near-surface region of a nanostructure. A cylinder nanowire supporting surface plasmons is considered as the probe. Near-field polar and longitudinal magneto-optical Kerr effects are investigated in scattering of light from a the nanowire and a magnetization nanodomain. Dependence of the near-field magneto-optical response on the probe-domain distance is analyzed, and the microscopy resolution is estimated.

Introduction

Problems of nanophotonics are topical for the near-field magneto-optical sudy of new magnetic nanocomposites and the related microscopy. Noble-metal inclusions supporting local plasmons are needful for enhancing the magneto-optical optical effects. This kind of ideas has been particularly realized in a near-field magneto-optical microscope operated with a noble-meal nanoparticle [1,2].

In this work, a theory is developed for near-field optics, magneto-optics and the related scanning microscopy with a linear plasmonic nanoprobe. Near-field polar and longitudinal magneto-optical Kerr effects in scattering of polarized light are treated. Features of the near-field images are analyzed in scanning the sample surface with a linear probe, and the microscopy resolution power is deduced.

1. Model and basic consideration

A scheme for apertureless nanooptics is shown in Fig. 1. A linear probe is placed near and above the interface between media whose permittivities are ε_1 and ε_2. The latter is related to a sample whose magnetization is laterally non-uniform on the nanometer scale. The probe is thought of as a noble-metal nanowire supporting long-lived local (surface) plasmons. The near-field magneto-optical Kerr effects in plasmon-assisted scattering of light from a nanowire are treated for polar and longitudinal magnetizations. The magnetization-linear magneto-optical scatterings are classified in terms of TM (p-polarized) and TE (s-polarized) waves. In varying the lateral distance between the probe and nanosized magnetic domain, the problem of scanning near-field microscopy in scattering mode is analyzed. The p-polarized wave (with the frequency ω)

$$\mathbf{E}_p^{\text{inc}}(\boldsymbol{\rho}, \omega) = \mathbf{e}_p E_p^{\text{inc}}(Q, \omega) \exp\left[i\left(Qx + \sqrt{\varepsilon_1 k_0^2 - Q^2}\, z\right)\right] \quad (1)$$

is incident onto the sample surface at an angle θ to excite the near-field of the linear nanoprobe placed nearby. In Eq. (1), $\boldsymbol{\rho} = (x, z)$, $\mathbf{e}_p = \mathbf{e}_x \cos\theta - \mathbf{e}_z \sin\theta$ is the wave polarization vector, $Q = q \sin\theta$, $q = \sqrt{\varepsilon_1}\, k_0$, $k_0 = \omega/c$. The local dielectric polarization $\mathbf{P}^{\text{I}} + \mathbf{P}^{\text{II}}$ is induced by the wave (1) in the probed region, and the response is detected in the far-field radiation.

Self-consistent polarization of the complex "probe+image charges" in response to the unperturbed field $\mathbf{E}^0(\boldsymbol{\rho})$ is

$$P_\alpha^{\text{I}}(\boldsymbol{\rho}, \omega) = \chi^{(\alpha)}(\omega)\delta\left(\boldsymbol{\rho} - \boldsymbol{\rho}_0\right) E_\alpha^0(\boldsymbol{\rho}_0, \omega). \quad (2)$$

Here, $\boldsymbol{\rho}_0 = (x_0, z_0)$ stands for the location of probe axis in the incidence plane xz. In what follows, the probing nanowire
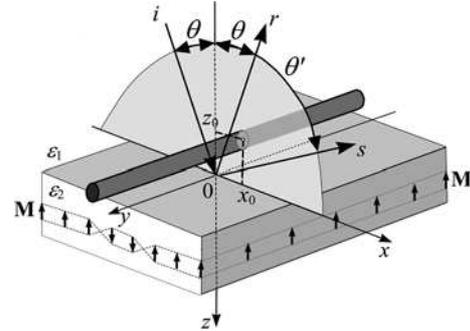
Fig. 1. Scheme for polar near-field magneto-optical Kerr effect.

is considered as an infinite circular cylinder of subwavelength radius $a \ll 1/k_0$. The transverse components of the diagonal effective polarizability tensor per a unit cylinder length are

$$\chi^{(\alpha)} = \frac{a^2}{2}\left(\frac{\varepsilon + \varepsilon_1}{\varepsilon - \varepsilon_1} - \frac{a^2}{4\,|z_0|^2}\frac{\varepsilon_2 - \varepsilon_1}{\varepsilon_1\,(\varepsilon_2 + \varepsilon_1)}\right)^{-1}, \quad (3)$$

where ε is the permittivity of nanowire material. Eq. (3) takes into account the image-charge effect depending on the distance $|z_0|$ between the probe and interface $\varepsilon_1/\varepsilon_2$. The poles of $\chi^{(\alpha)}(\omega)$ define the frequencies of local plasmons of a near-surface cylinder. If $a/|z_0| \ll 1$, Eq. (3) provides the diagonal polarizability components χ^0 of a single cylinder.

The polarization

$$P_\alpha^{\text{II}}(\boldsymbol{\rho}) = \frac{i\varepsilon_{\text{B}}}{4\pi}\, f_\parallel(x) f_\perp(z) \sum_\beta \left(\delta_{\alpha x}\delta_{\beta y} - \delta_{\alpha y}\delta_{\beta x}\right) E_\beta(\boldsymbol{\rho}) \quad (4)$$

with a complex magneto-optical parameter $\varepsilon_{\text{B}}(\omega)$ is related to a non-uniform polar magnetization $\mathbf{M}(\boldsymbol{\rho}) = M f_\parallel(x) f_\perp(z)\mathbf{e}_z$. Its distributions along and across the sample surface are $f_\parallel(x)$ and $f_\perp(z)$, respectively. In scanning mode, i.e. in varying the lateral distance $|x_0|$ between the probe and the magnetization nanodomain (Fig. 1), polarization-sensitive contrast induced by the domain can be observed in scattered light.

Using the electrodynamic Green function technique, the resonant response (2) of the "probe+image" complex is treated self-consistently within multiple-scattering approximation [2,3]. When p-polarized wave (1) is scattered due to the polarizations (2) and (4), the wavevector of radiation is in the scattering plane coinciding with the incidence plane. Taking into account Eqs. (2) and (4) one obtains the radiation field

$$\mathbf{E}(\boldsymbol{\rho}, \omega) - \mathbf{E}_p^{\text{inc}}(\boldsymbol{\rho}, \omega) = \sum_{n=0} \mathbf{E}^{(n)}(\boldsymbol{\rho}, \omega) \quad (5)$$

at the far-field point $\boldsymbol{\rho} = (x, z)$, $q\rho \gg 1$. In Eq. (5), the fields $\mathbf{E}^{(0)}$ and $\mathbf{E}^{(1)}$ correspond to conventional specular reflection and magneto-optical Kerr effect in the absence of a probe ($\mathbf{P}^{\text{I}} =$
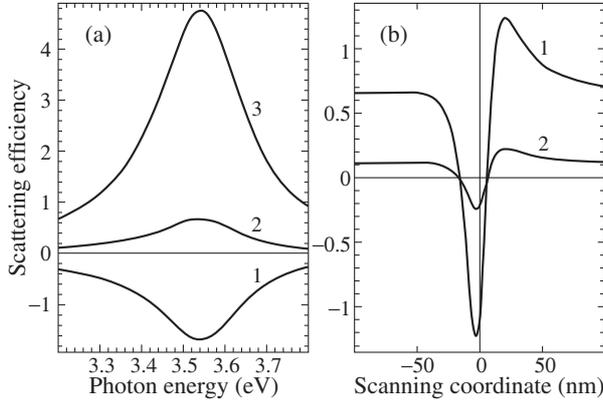
Fig. 2. (a) Spectra of $\delta S_M/(k_0^4 a^3 l)$ (1), $\overline{S}_M/(k_0^4 a^3 l)$ (2) and $S_0/(k_0 a)^3$ (3) at $x_0 = 0$. (b) $(\delta S_M + \overline{S}_M)/(k_0^4 a^3 l)$ depending on the scanning coordinate x_0 at photon energies 3.55 eV (1) and 3.2 eV (2). Calculated for Ag cylinder and Au sample with Co layer ($l = z_1 = 2$ nm) at $\theta = \theta' = 30°$, $\varepsilon_1 = 2$, $\Omega = 45°$, $a = 4.5$ nm, $|z_0| = 5$ nm, $w = 10$ nm.

0). The terms with $n \geq 2$ represent the probe-induced scattered fields

$$\frac{1}{E_p^{inc}} E_\alpha^{(n)}(\rho) = \sqrt{2\pi} i \frac{e^{iq\rho}}{\sqrt{q\rho}} F_\alpha^{(n)}\left(Q', Q; \rho_0\right)\cos\theta'. \quad (6)$$

The amplitudes $F_\alpha^{(n)}(Q', Q; \rho_0)$ stand for scatterings with the change $Q \to Q'$ of lateral wavevector component, where $Q' = q\sin\theta'$, $\sin\theta' = x/\rho$, $\cos\theta' = |z|/\rho$ (Fig. 1). Eq. (6) describes linearly polarized waves $\mathbf{E}_p' = \mathbf{E}^{(2)}$ and $\mathbf{E}_s' = \mathbf{E}^{(3)}$ with the polarization vectors $\mathbf{e}_p' = -(\mathbf{e}_x\cos\theta' + \mathbf{e}_z\sin\theta')$ and $\mathbf{e}_s' = \mathbf{e}_y$, and the wavevector $\mathbf{K}' = q(\mathbf{e}_x\sin\theta' - \mathbf{e}_z\cos\theta')$. The field corresponds to elastic scattering from the "probe+image" complex at $\mathbf{M} = 0$. The field $\mathbf{E}^{(2)}$ describes the probe-induced $p \to p$ scattering succeeded by magneto-optical $p \to s$ scattering. In this near-field process, the change $Q \to \kappa \to Q'$ of lateral wavevector component includes short-wavelength intermediate modes (evanescent waves with $\kappa \gg k_0$). In the presence of cylinder plasmons, the fields $\mathbf{E}^{(2)}$ and $\mathbf{E}^{(3)}$ are resonantly enhanced in $p \to p$ scatterings [3].

2. Results and discussion

Next, the efficiency of scattering is discussed for the wave (1). Consider the component of the scattered wave $\mathbf{E}_p' + \mathbf{E}_s'$ from Eq. (6) which is linearly polarized along the unit vector $\mathbf{e}_\Omega = \mathbf{e}_p'\cos\Omega + \mathbf{e}_s'\sin\Omega$ in the analyzer plane making an angle Ω with the scattering plane. The dimensionless cross-section $S = (2\pi L)^{-1} d\sigma/d\theta'$ for light scattering from the unit cylinder length L into the angle $d\theta'$ is proportional to the ratio of scattering intensity to incident flux. The magnetization-linear approximation for S is

$$S_0 + \overline{S}_M + \delta S_M = \frac{\rho}{2a|E_p^{inc}|^2}\left\{\left|E_p'\right|^2\cos^2\Omega + \mathrm{Re}\left[(E_p')^* E_s'\right]\sin 2\Omega\right\}. \quad (7)$$

Here, $E_p' = -E_x^{(2)}/\cos\theta'$ and $E_s' = E_y^{(3)}$ stand for p- and s-polarized waves (6), where $|\mathbf{E}_s'| \ll |\mathbf{E}_p'|$. For a cyrcular cylinder, $\chi^{(x)} = \chi^{(z)}$ in Eq. (3), therefore, $E_p' \sim \chi^{(x)}$ and $E_s' \sim \chi^{(x)}$. As a consequence, the scattering efficiency (7) is enhanced at the resonant frequences of $|\chi^{(x)}(\omega)|^2$.

If $\mathbf{M} = 0$, Eq. (7) with $E_s' = 0$ gives the only cross-section contribution S_0 of $p \to p$ scattering by a near-surface probe. If $\mathbf{M} \neq 0$, we assume that $f_\perp(z) = l\delta(z - z_1)$ [4] and

$$f_\parallel(x) = -1 + 2w^2/\left(x^2 + w^2\right) \quad (8)$$

in Eq. (4), i.e. $f_\parallel = \overline{f_\parallel} + \delta f_\parallel$. Here, $\overline{f_\parallel}$ is associated with laterally uniform and $\delta f_\parallel(x)$ with non-uniform contributions to polarization of an ultrathin magnetic layer of thickness l. Similar form is typical of the probed field $E_s' = \overline{E}_s' + \delta E_s'$ and efficiency $\overline{S}_M + \delta S_M$ of $p \to s$ scattering from Eq. (7).

In Eq. (7), the terms S_0 and $\overline{S}_M$ do not depend on x_0, for which reason of importance for near-field microscopy is $\delta S_M(x_0)$. With $\delta f_\parallel(x)$ from Eq. (8) and $\mathbf{M} \parallel \mathbf{e}_z$ one obtains

$$\delta S_M(x_0) = lw \sum_{\alpha=x,z} \mathrm{Re}\left[\left(F_x^{(2)}\right)^* U_\alpha\right] L_\alpha(x_0, w + |z_0| + z_1) \quad (9)$$

in quasi-static approximation (for the domain width w), where

$$L_\alpha(x, z) = \left(x^2 + z^2\right)^{-2}\left[\left(z^2 - x^2\right)\delta_{\alpha x} - 2xz\delta_{\alpha z}\right]. \quad (10)$$

It follows from Eqs. (9) and (10) that the magneto-optical contrast measured by a near-field microscope consists of even and odd contributions in x_0 excited via x- and z-components of the polarizability (3). The width $w + |z_0| + z_1$ of the two features entering Eq. (9) defines the size of the domain image in near-field microscopy.

The spectrum (7) was numerically calculated with Eq. (8) for Co layer with magnetization $\mathbf{M} \parallel \mathbf{e}_z$ and the optimum analyzer angle $\Omega = 45°$. Spectra of S_0 for $p \to p$ and $\overline{S}_M$, δS_M for $p \to s$ scatterings are shown in Fig. 2a for a fixed x_0, all being resonantly enhanced at the frequency of cylinder plasmon. Magneto-optical contribution $\delta S_M(x_0) + \overline{S}_M$ from Eq. (7) is presented in Fig. 2b depending on the scanning coordinate x_0. In microscopy, the term $\delta S_M(x_0)$ from Eqs. (9) describes x_0-dependent imaging contrast (10), appearing on the homogeneous "background" $\overline{S}_M$. Variation of the signal $\delta S_M(x_0) + \overline{S}_M$ is much larger at the plasmon resonance ($\hbar\omega = 3.55$ eV) than out of it (3.2 eV). The plasmonic enhancement is similar to that known for magneto-optical Kerr effects excited through surface plasmon-polaritons [4].

To summarize, polarization, angular and spectroscopic characteristics of the near-field magneto-optical scattering and scanning microscopy with a linear nanowire are shown to differ completely from their counterparts for a quasi-point particle [2]. When surface plasmons are excited in the nanoprobe, the contrast of a microscopy image is resonantly enhanced, which effect is useful to make the microscopy sensitivity higher. The predicted resonant enhancement of near-field magneto-optical Kerr effects can occur in magnetic nanocomposites with noble-metal inclusions supporting plasmons.

References

[1] T.J. Silva, S. Schultz, D. Weller. *Appl. Phys. Lett.* **65**, 658 (1994).
[2] V.A. Kosobukin. *Surf. Sci.* **406**, 32 (1998); *Proc. SPIE* **3791**, 93 (1999).
[3] V.A. Kosobukin. *Phys. Solid State* **51**, 400 (2009).
[4] V.I. Safarov, V.A. Kosobukin, C. Hermann, G. Lampel, J. Peretti, C. Marliere. *Phys. Rev. Lett.* **73**, 3584 (1994).

Spectral magnitooptics of nanocorrugated ferromagnetic films

M. V. Sapozhnikov[1], S. A. Gusev[1], V. V. Rogov[1], O. L. Ermolaeva[1], B. B. Troitskii[2] and L. V. Khokhlova[2]

[1] Institute for Physics of Microstructures RAS, Nizhny Novgorod, GSP-105, Russia
[2] G.A. Razuvaev Institute of Organometallic Chemistry, RAS, Nizhny Novgorod, Russia

Abstract. We report here on the optical and magnttooptical properties of nanostructured ferromagnetic films deposited on the top of PMMA colloidal crystal. Optical reflectance spectra and magnetooptical spectra were studied in the range of near UV, IR and visible light for *p*- and *s*-polarizations of the incident radiation. The resonant peculiarities were observed in the both spectra, their positions scaled with the PMMA sphere diameter and have dispersion with the incident light angle. In explanation of the above scenario the surface plasmon resonances should be considered.

The main aim of a rapidly developing optics of atificial nanostructures is a study of a possibility of optical effects management at the nanometer scale [1]. Despite the fact that the majority of works devoted to the structures based on noble metals, there is a significant increase in interest to the systems using magnetic materials. For example, the use of the magnetic materials allows to control the optical properties of nanocomposites by applying an external magnetic field [2]. Also the enhancement of magneto-rotation in a Co-Au magnetic composites was observed [3] and magneto-optical effects in magnetic periodic nanostructures were measured [4].

In our work we investigated the magnetooptical properties of ferromagnetic nanocorrugated films (Co and Ni) in the visible and near IR range of light. The optical investigations were followed by detailed studying of magnetic states in the system by magnetic force microscopy. The samples were prepared by magnetron deposition of the metal on the top of PMMA colloidal crystal. The morphology of the films was studied by electron and atomic force microscopy. It can be seen (Fig. 1) that the particles were packed into a dense hexagonal lattice, the period of the structures determined by a size of PMMA particles and lies within 100–500 nm. As the thickness of the deposited films (30 and 60 nm) was sufficiently less than the diameter of the particles, the film became corrugated in two dimensions.

The optical and magneto-optical spectra were measured with the use of a grating monochromator, a high pressure xenon lamp as the source and precision silicon photodiodes designed as detector for 200–1100 nm wavelength range. Spectra were measured separately for *s*-(TE) and *p*-(TM) polarizations for incidence angles from 20 to 60 (angle measured from normal) in the wavelength range 250–1000 nm. Magnetooptical spectra were measured in the geometry of the meridional Kerr effect, the difference of the polarization angles of the radiation re-
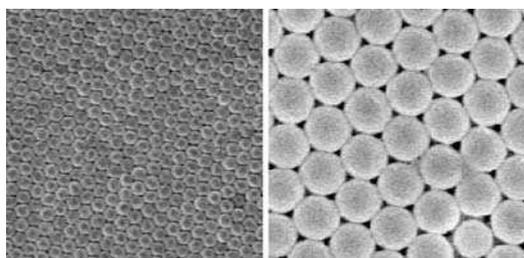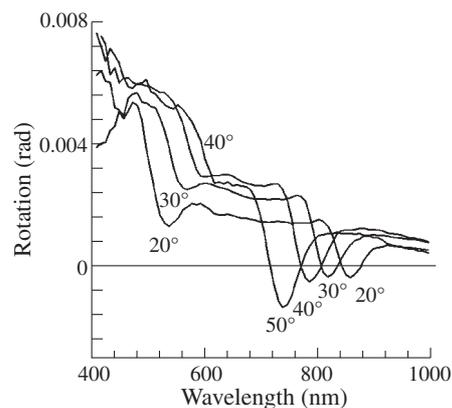
Fig. 2. Measured magnitoptical spectra of 30 nm thick nanocorrugated Co film (period is 370 nm) *p*-polarization of the incident light and for the angles of $20_{[}0]$, $30_{[}0]$, $40_{[}0]$ and $50_{[}0]$ of the light incidence. Thick line is the magnetooptical spectrum of the flat Co film.

flected from the structure of magnetized to saturation in two opposite directions were fixed. The usual shape of magnetooptical spectra are shown in Fig. 2. The following distinguished features were found. First, the magnetooptical spectra lost a monotonic character which is typical for a flat Co and Ni films and had two minima, let us define them as long-wave and short-wave minima. As for the long-wave minimum it blue-shifted with the increase of the angle of light incidence in the same manner for *s*- and *p*-polarization. On the contrary the short wave minimum red-shifted with the angle increase (Fig. 2). The positions of minima were scaled with the change in the period of the structure. The spectra peculiarities of nickel and cobalt nanocorrugated films were qualitatively the same. In the case of 30 nm structures the long-wavelength minima was more pronounced than shortwave especially for *p*-polarized light. When the thickness of nanostructured film increased up to 60 nm the short-wavelength minimum became more pronounced. It is important to note, that in certain cases the minima became so deep, that there was not just a decrease in optical rotation but the change of the rotation direction.

The measurements of the reflection spectra of nanocorrugated nickel films also showed the features missing in plane films spectra. It was found that: 1) reflectance spectra of nickel structures (Fig. 3), their dependence on the angle of incidence, polarization and structure period, were very similar to the reflectance spectra of the nanocorrugated cobalt films which had been studied previously [5]. 2) The resonant peculiarities in the reflectance spectra had asymmetrical shape and their positions

Fig. 1. SEM images of the nanocorrugated Ni film. The side of the frame is equal to 1.5 nm. The period is 125 nm for the structure at the left 370 nm for the one at the right.
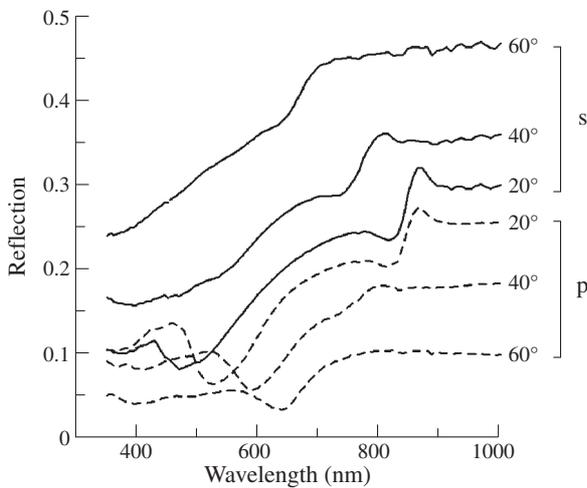
Fig. 3. Measured optical reflectance spectra of 30 nm thick nanocorrugated Ni film (particle size of initial PMMA colloidal crystal is 370 nm) for *s*- (solid line) and *p*-polarization (dashed line) of the incident light and for different angles of the light incidence.
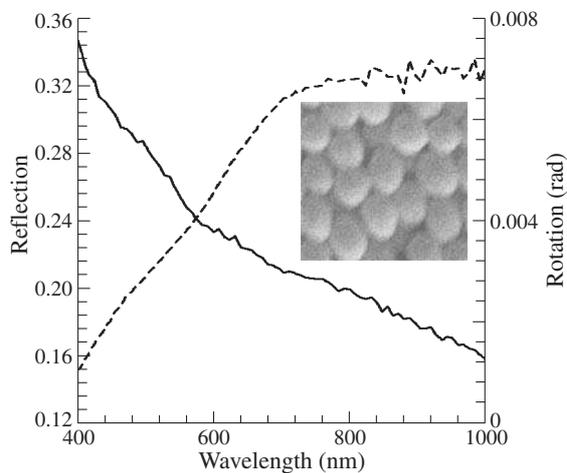
Fig. 4. Optical reflectance spectra (dashed line) and magnetooptical spectra (solid line) of 30 nm thick Co film deposited on the top of the irregular system of PMMA particles. Particle size is 355 nm, incident angle of the light is 40 degree. The SEM image of the irregular film is presented in the inset.

coincided with the positions of the magnetooptocal spectra peculiarities.

Qualitatively the shape of spectra can be explained in the following way. The angular dependence of the positions of the minima and their scaling with the period of the structure points on resonant excitation the propagating surface modes. In the case of two-dimensional structuring of the system they could be excited both by *s*- and *p*-polarized incident radiation and leaded to the resonances in the spectra. On the contrary in the case of the ferromagnetic film deposited on a disordered system of the colloidal particles, there was no any resonant peculiarities in the reflection or magnetooptical spectra (Fig. 4). Less long-wavelength minima in the magnetooptical spectra of 60 nm nanocorrugated films was correlated with a decrease in the deep of long-wavelength peculiarity in the reflectance spectra. It suggests that the long-wave minima associated with the excitation of plasmons on the inner boundary between the metal and dielectric, while the short wave minima is due to resonant excitations of the surface modes on the external surface.

The decrease (and particularly the change of the direction) of magnetooptic rotation was probably due to the opposite sign of the polarization rotation in surface modes.

References

[1] E. Ozbay, *Science* **331**, 189 (2006).
[2] G.A. Wurtz, W. Hendren, R. Pollard, R. Atkinson, L.Le Guyader, A. Kirilyuk, Th. Rasing, I.I. Smolyaninovand, A.V. Zayats F. Przybilla *et al*, *New Journal of Physics.* **10**, 105012 (2008).
[3] K. Yang, C. Clavero, J.R. Skuza, M. Varela, and R.A. Lukaszew, *J. Appl. Phys.* **107**, 103924 (2010).
[4] Z. Liu, L. Shi, Z. Shi, X.H. Liu, J. Zi, S.M. Zhou, S.J. Wei, J. Li, X. Zhang, Y.J. Xia, *Appl. Phys. Lett.* **95**, 032502 (2009).
[5] M.V. Sapozhnikov, S.A. Gusev, V.V. Rogov, O.L. Ermolaeva, B.B. Troitskii, L.V. Khokhlova, D.A. Smirnov, *Appl. Phys. Lett.* **96**, 122507 (2010).

Stress induced magnetic anisotropy in Finemet: its type, origin and relaxation

N. V. Ershov[1], N. V. Dmitrieva[1], Yu. P. Chernenkov[2], V. A. Lukshina[1], V. I. Fedorov[2] and A. P. Potapov[1]

[1] Institute of Metal Physics, Ural Branch of RAS, 620990 Ekaterinburg, Russia
[2] St Petersburg Nuclear Physics Institute, RAS, 188300 Gatchina, Russia

Abstract. A type of magnetic anisotropy induced in the Fe-Si-B-Nb-Cu alloys by annealing under tensile stress varies with the silicon content (C_{Si}). The longitudinal magnetic anisotropy, which is induced at low silicon concentrations, is replaced by the transverse one when C_{Si} becomes greater than 0.095. The atomic structure of nanocrystals in Fe-Si-B-Nb-Cu alloys subjected to the nanocrystallization annealing under tensile stress was investigated by X-ray diffraction in transmission geometry. It is shown that in the bcc nanocrystal lattice regardless of the silicon content there are the significant residual strains. Along the direction of the tensile load application, there is an increase in the interplanar distances and the decrease in the transverse direction. The strain is anisotropic: no distortions in the ⟨111⟩ directions are observed, and the distortions in the ⟨100⟩ directions are maximum and reach 1%. It is shown that the type of the magnetic anisotropy depends on the sign of the magnetoelastic coupling in nanocrystals, which, in turn, is determined by the contribution of the ordered phase Fe_3Si, characterized by a negative constant of magnetoelastic coupling. The residual strain relaxation after annealing at the nanocrystallization temperatures was also studied.

Introduction

Nanocrystalline Fe-Si-B-Nb-Cu alloys (Finemets) obtained by crystallization of amorphous ribbons quenched from the melt exhibit high soft magnetic properties: the permeability greater than 10^5, coercive force of about 0.5 A/m and the saturation magnetization exceeding 1 T [1]. In addition, their permeability can be purposefully controlled by inducing a magnetic anisotropy during annealing in a magnetic field [2,3] or in the field of tensile stress [4,5]. Magnetic anisotropy energy exceeding 5000 J/m^3 is attained by annealing under a tensile stress of 400–600 MPa. For the first time the effect of tensile load applied along the ribbon at nanocrystallization annealing was investigated in [4] and it was shown that after such treatment in a sample of the $Fe_{73.5}Si_{13.5}B_9Nb_3Cu_1$ alloy a state with the magnetic anisotropy of the "easy-plane" type is formed. The plane of the magnetic anisotropy is oriented perpendicularly to the direction of stretching. There's also the first time it was assumed that the transverse magnetic anisotropy is due to residual elastic strain in the lattice of nanocrystals having a negative constant of the magnetostriction.

It is known that the type of the magnetic anisotropy induced in the $Fe_{87-X}Si_XB_9Nb_3Cu_1$ alloy during tensile stress annealing (TSA) depends on the silicon content X [6]. If $X \leq 8$, in specimens after TSA the magnetic anisotropy of easy axis type is induced, whose axis is oriented along the tape (i.e. in the direction of load application during TSA). In the process of reversal magnetization along the tape axis, the permeability and the residual magnetization increase, coercive force decreases, the hysteresis loop becomes rectangular. If the concentration of silicon is equal to or greater than 11 at.%, then a transverse magnetic anisotropy of easy-plane type is formed after TSA. In this case, the permeability is constant over a wide range of magnetic fields (up to 10 kA/m), the magnetic hysteresis loop becomes inclined, and the magnetization is oriented predominantly in a plane transverse to the direction of load application during the annealing. If the formation of a state with magnetic anisotropy after annealing and cooling under a tensile load is associated with residual elastic stresses [4], a result of the so-called Villari effect, then the type of magnetic anisotropy can be explained by the nature of magnetoelastic coupling in the nanoparticles [6] mainly consisting of Fe-Si crystals having a bcc lattice.

1. Experimental

The studies were carried out using $Fe_{87-X}Si_XB_9Nb_3Cu_1$ alloy samples ($X = 0, 4, 6, 8, 9.5, 11, 13.5$) in the form of ribbons 20 μm thick and 1 mm wide obtained in the initial amorphous state by melt-spinning technique, where a molten metal alloy is ejected through an orifice onto a rotating copper wheel. The nanocrystallization annealing (NCA) and the stress annealing (TSA) under a tensile stress of 440 MPa were carried out in air at a temperature of 520 °C for 2 h (under these conditions, no secondary recrystallization still occurs and coercive force reveals no sharp changes in the annealing-temperature range of $510 - 570$ °C).

Atomic structure of the nanocrystalline alloy samples was studied by X-ray diffraction method in transmission geometry, which provides such measuring conditions that the scattering vector lies in the plane of the specimen. The samples in the form of a rectangular plate were prepared of ribbon fragments, which were glued to the thin narrow ring-like holder parallel to each other in several overlapping layers of thickness about 40 μm. Diffraction patterns of each the specimens were measured twice: with the scattering vector parallel and perpendicular to the axis of the ribbon.

From the position of the (hkl) diffraction peak, we estimated the corresponding interplanar distance in the lattice of nanocrystals of the $Fe_{1-x}Si_x$ phase. The difference of the positions of the (hkl) peak in the longitudinal and transverse scans demonstrates the strain of the nanocrystals in the [hkl] direction.

After TSA the hysteretic properties of the alloys vary depending on the silicon content and heat treatment conditions, and are directly related to their structural state [6]. The residual strains in the samples after relaxation annealing with duration

of 20 min – 10 h at temperatures of $500-600\ ^\circ$C were also measured by X-ray diffraction method.

2. Results and discussion

The X-ray diffraction patterns have the peaks with Miller indices such as (110), (200), (211), (220), (310), (222), (321), (400), (330), and further for the body-centered cubic (bcc) lattice of α-$Fe_{1-x}Si_x$. As the Fe_3Si phase unit cell parameter (the $D0_3$-type superstructure) is approximately twice as large as that of the bcc structure, in the available resolution of the diffractometer, the (hkl) bcc peaks in the X-ray diffraction patterns coincide with the $(2h, 2k, 2l)$ $D0_3$ peaks.

After TSA, in all specimens, in the direction of load application there is an increase in the interplanar distances; in the transverse direction they are reduced. In X-ray diffraction experiments, the strains are manifested in the fact that in the diffraction patterns the longitudinal scanning Bragg peaks are shifted to smaller angles with reference to their position in the pattern taken from the alloys annealed without stress (after NCA treatment). In the transverse scan, these peaks are shifted in the opposite direction. Such longitudinal tension and transverse compression of the nanocrystal lattice means that during the annealing under action of load the lattice is deformed, and the lattice distortions acquired are frozen. Most likely the deformations of nanocrystals recorded in the X-ray diffraction experiment are preserved at low temperatures due to the high rigidity of the amorphous matrix surrounding the nanoparticles.

The crystal lattice is deformed anisotropically, which does not depend on the silicon concentration X. The value of a relative shift for the observed peaks (hkl) correlates with the value of the angle between the scattering vector $[hkl]$ and one of the axes $\langle 111 \rangle$ which is the nearest to the scattering vector. The relative shift is maximum for (200) and (310), whereas no shift is observed for (222). It is quite natural to suppose that residual lattice strains in the nanocrystals embedded in an amorphous matrix are not isotropic and that the rigidity of a nanocrystal as a whole in different crystallographic directions is also anisotropic. The value of residual extension depends on the angle between the direction $[hkl]$ and the nearest axis $\langle 111 \rangle$, too: the greater this angle, the more the distortion.

In the [111] direction the distortions are minimum or absent, in the [100] they are maximum. Thus, the distortions have tetragonal character. At high silicon concentrations in the specimens there is a significant fraction of the ordered phase Fe_3Si ($D0_3$) (at $X = 11$, more than half of, and at $X = 13.5$, more than 80% Fe-Si solution volume) in whose lattice after TSA the similar anisotrpic distortions take place. If, after TSA at low concentrations of silicon, magnetic moments lie in the sample plane, but along the tape axis, which is determined from the shape of the magnetic hysteresis loop, then at $X \geq 11$, they change the orientation, namely, to belong to the transverse plane and come out of the plane of tape.

The above-said permits one to conclude that when $X \leq 8$ the longitudinal anisotropy is induced due to the tetragonal residual strains of the bcc lattice of the nanocrystals with a disordered α-FeSi phase, which demonstrates a positive magnetoelastic effect (longitudinal Villari effect). Then in the nanocrystals of the alloy with $X > 9.5$ the inducing of a transverse magnetic anisotropy is due to residual tetragonal lattice distortions of the phase Fe_3Si, of which a negative magnetoelastic coupling constant is typical (transverse Villari effect).

Thus, it is shown that the type (longitudinal or transverse) of magnetic anisotropy depends on the sign (positive or negative) of the magnetoelastic coupling constant in nanocrystals, whose sense is determined by the contribution of the ordered phase Fe_3Si (characteristic of a negative magnetostriction constant). A phenomenological model of the mechanism of the stress-related inducing of the longitudinal magnetic anisotropy at $X < 9$ and the transverse magnetic anisotropy at $X > 9$ as a result of tetragonal strains of Fe-Si nanocrystals in the alloys $Fe_{87-X}Si_XB_9Nb_3Cu$ is proposed.

The residual strains in the samples after relaxation annealing with duration of 20 min–10 h at temperatures of $500-600\ ^\circ$C were also measured by X-ray diffraction method in transmission geometry. The relative changes of interplanar spacings for planes of (200) and (310) types were compared with measurements of magnetic properties, in particular with the magnitude of decrement of the magnetic anisotropy constant. It is shown that after annealing at the nanocrystallization temperature of $500-540\ ^\circ$C, a decrease in the value of residual strain was observed, which is accompanied by the relaxation of the anisotropy of magnetic properties, which manifests itself in the reduction of transverse magnetic anisotropy constant, K_u. The relative change in the distance between (200) and (310) planes determined from the positions of the (200) and (310) peaks in the diffraction patterns recorded in the longitudinal and transverse scans linearly correlates with the magnitude of magnetic anisotropy constant.

A deviation from the linear correlation is observed only for samples, which were subjected to a prolonged annealing at $600\ ^\circ$C, which is 80 degrees above the temperature of nanocrystallization. In this case, the strains of the interplanar distances are practically zeroed within the error of X-ray diffraction measurements. At the same time the transverse magnetic anisotropy has a residual effect, which exceeds 10% the initial constant K_u. It is possible that the nonlinear character of the structure-property correlation is due to the peculiarities of the structural state of the finemet after annealing at $600\ ^\circ$C at which partial crystallization of the amorphous matrix starts and the changes in the structure of the nanoparticles can occur. But these processes require further study.

References

[1] Y. Yoshizawa *et al*, *J. Appl. Phys.* **64**, 6044 (1988).
[2] Y. Yoshizawa *et al*, *IEEE Transactions on Magnetics* **25**, 3324 (1989).
[3] G. Herzer, *J. Magn. Magn. Mater.* **112**, 258 (1992).
[4] A.A. Glazer *et al*, *Fiz. Met. Metalloved.* **12**, 56 (1991) in Russian.
[5] G. Herzer, *IEEE Transactions on Magnetics* **30**, 4800 (1994).
[6] V.V. Serikov *et al*, *Phys. Met. Metallogr.* **102**, 268 (2006).

Intra- and interlayer magnetic order in metallic nanostructures as seen with neutrons and x-rays

E. A. Kravtsov[1,2] and V. V. Ustinov[1]

[1] Institute of Metal Physics, Ural Branch of RAS, 620990 Ekaterinburg, Russia
[2] Ural Federal University, 620002 Ekaterinburg, Russia

Abstract. We discuss complementary application of modern neutron and synchrotron scattering methods to probe intra- and interlayer magnetic order in metallic multilayered nanostructures. We demonstrate that magnetic structure of ferromagnetic layers can be resolved by combining polarized neutron and resonant x-ray magnetic reflectometry, whereas antiferromagnetic layers can be probed by using high resolution neutron and anomalous x-ray diffraction.

Introduction

There has been great interest recently in metallic multilayered nanostructures composed of ferromagnetic and antiferromagnetic layers, which display a wide array of novel phenomena and acquire technological importance as potential elements of spintronic devices. In order to understand, and be able to tune properties of these artificial nanostructures, it is important to determine precisely (at subnanometer scale) intra- and interlayer magnetic structure, which are generally inhomogeneous in these structures. In the present report, we discuss complementary applications of modern neutron and synchrotron x-ray scattering methods to probe intra- and interlayer magnetic structure in these metallic nanostructures, which is the key to our understanding of novel physical phenomena.

1. Ferromagnetic nanostructures

Of the most powerful techniques to probe magnetization depth profiles in ferromagnetic multilayered nanostructures we note polarized neutron (PNR) and resonant x-ray magnetic reflectometry (RXMR). The main advantage of the PNR technique is its ability to directly probe atomic magnetic moments and provide information about the in-plane magnetic moment in absolute units. On the other hand, this technique is not element-specific and, due to low incoming neutron beam flux, has limited spatial resolution.

When applied in the hard x-ray regime, RXMR utilizes resonant enhancement for the x-ray magnetic scattering observed at K-edges of transition metals and L-edges of rare earths. RXMR provides both element-sensitivity and high spatial resolution due to the high flux of synchrotron radiation. However, when working with circularly polarized x-rays, it detects only one in-plane component of magnetic moment lying in the scattering plane. In addition, it is not always possible to probe all the elements in nanostructures and gain the complete information on the system.

A unified approach combining polarized neutron and resonant x-ray magnetic reflectometry allows one to determine magnetization profiles in ferromagnetic multilayered nanostructures. As we demonstrate for the case of Fe/Gd multilayers, complementary refinement of PNR and RXMR data makes it possible to resolve the element-specific & depth-dependent magnetization profiles in multilayers with unprecedented accuracy, including refinement of the inhomogeneous intralayer magnetic structure with near atomic resolution.
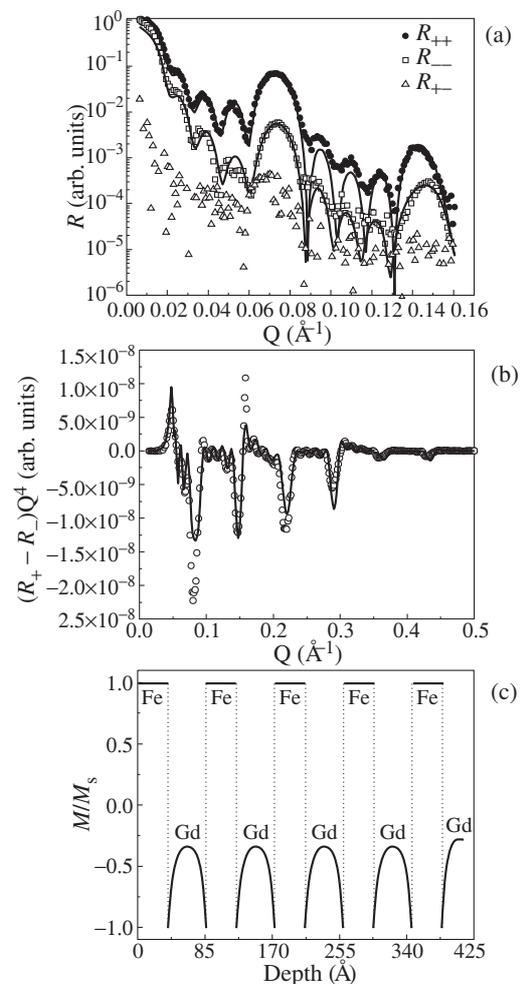
Fig. 1. (a) Experimental (points) and fitted (lines) PNR spectra from [Fe(35 Å)/Gd(50 Å)]$_5$ multilayer measured at $T = 140$ K, $H = 500$ Oe. (b) Experimental (circles) and fitted (line) RXMR spectra for measured at the Gd L_2-edge ($E = 7929$ eV) $T = 140$ K, $H = 500$ Oe. (c) Refined magnetization profile within the Fe/Gd heterostructure as revealed by the simultaneous refinement of PNR and RXMR spectra.

With our complementary approach, we have resolved element-specific complex magnetic structures in a [Fe(35 Å)/Gd(50 Å)]$_5$ heterostructure as a function of temperature and magnetic field by performing simultaneous self-consistent refinement of polarized neutron reflectometry and resonant x-ray magnetic reflectometry spectra [1]. The complementary use of the PNR
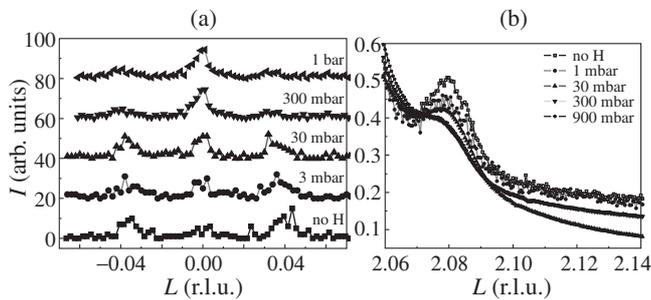
Fig. 2. Influence of the hydrogen pressure on the temperature dependence of the SDW and SW satellite peak intensities in $[Cr(500\,\text{Å})/V(14\,\text{Å})]_4$ multilayers as retrieved from scattering experiments with neutrons (a) and with synchrotron radiation (b).

and RXMR techniques has made it possible to determine changes in the value of magnetic moment as well as in-plane magnetization rotation in Fe/Gd heterostructures. In Figure 1 are shown the refined magnetization profiles together with PNR and RXMR spectra from the Fe/Gd heterostructure measured at $T = 140$ K, $H = 500$ Oe where within Gd layers there appears a magnetic state with inhomogeneous magnetization profiles. Gd magnetic moment was found to be enchased near Gd/Fe interfaces and decreased in the middle of Gd layers.

2. Antiferromagnetic nanostructures

Cr-based layered nanostructures are itinerant antiferromagnetic systems where low-temperature behavior is associated with the existence of spin-density waves (SDWs) incommensurate with the bcc lattice periodicity of Cr. The SDW in Cr-based systems coexists with a charge-density wave and a strain wave (SW) corresponding to periodic modulations of the charge density and the lattice spacing, respectively, with half the period of the SDW. Elastic strains, chemical impurities, dimensional and proximity effects from neighboring layers may cause the SDW to be commensurate with the Cr lattice periodicity.

Magnetic scattering of neutrons is directly sensitive to the magnetic state of Cr and, in principle, it is able to provide the very complete information on the SDW state in Cr films. The Cr magnetic moment modulation produces corresponding satellite reflections in the vicinity of forbidden Cr bcc Bragg reflections, which can be detected with neutron scattering. In the case of a commensurate SDW the neutron scattering reflections will be detected exactly at forbidden Bragg peaks. However, neutron scattering requires a significant amount of scattering material. In the case of thin films the intensity of the detected satellite reflections is often rather low and we cannot reach a good resolution in Q-space because of poor statistics. Synchrotron x-ray scattering is able to detect satellite reflections arising around fundamental Cr Bragg peaks due to strain waves. Although SW investigations do not reveal the SDW polarization, they have the advantage of a higher reciprocal-space resolution.

A complementary approach combining high-resolution neutron and anomalous x-ray diffraction allows one to resolve intralayer magnetic structure in antiferromagnetic layers with charge- and spin density waves. We apply this complementary approach to resolve spin-density wave state in Cr/V heterostructures and trace its evolution with temperature, magnetic field, and hydrogen uptake [2,3]. In our approach, we used neutron scattering results for a qualitative description of the

SDW behavior (magnetic phase diagram) and x-ray data to gain high resolution quantitative results. In Fig. 2 are shown neutron and synchrotron scattering results from [Cr(500 Å)/V(14 Å)]_4 multilayers, which provide direct experimental evidence that hydrogen uptake into adjacent vanadium layers can be used for fine tuning magnetic state in Cr layers, in particular, in order to switch between incommensurate and commensurate SDW states in a reversible way [3].

3. Conclusion

Summing up, the application of the complementary neutron and synchrotron x-ray scattering techniques is important for the determination intralayer magnetic structure in magnetic nanostructures. We stress the importance of such an approach, for it provides results that cannot be obtained by applying any of these techniques separately. Simultaneous application of two complementary techniques will be useful in the design of new spintronic devices.

References

[1] E. Kravtsov, D. Haskel, S.G.E. te Velthuis, J.S. Jiang, and B.J. Kirby, *Phys. Rev. B* **79**, 134438 (2009).

[2] E. Kravtsov, R. Brucas, B. Hjorvarsson, A. Hoser, A. Liebig, G.J. McIntyre, M.A. Milyaev *et al*, *Phys. Rev. B* **76**, 024421 (2007).

[3] E. Kravtsov, A. Nefedov, G. Nowak, K. Zhernenkov, H. Zabel, B. Hjorvarsson *et al*, *J. Phys.: Condens. Matter* **21**, 336004 (2009).

FeMn-based top spin valves with composite free layer

V. V. Ustinov, *M. A. Milyaev*, T. P. Krinitsina and L. I. Naumova

Institute of Metal Physics, Ural Branch of RAS, 620990 Ekaterinburg, Russia

Abstract. FeMn-based top spin valves with a composite free layer consisting of two ferromagnetic layers were prepared by high vacuum DC magnetron sputtering at room temperature. Magnetoresistance measured by the four-point probe method in CIP geometry reaches 9.4%. The maximum of magnetoresistive sensitivity was about 6.4%/Oe. The strong dependence of free layer hysteresis on the angle between applied magnetic field vector and the magnetic anisotropy axis in the film plane is revealed. The reduction of free layer hysteresis down to 0.1 Oe in the magnetic field range 10–20 Oe is demonstrated.

Introduction

Conventional spin valves consist of two ferromagnetic (FM) layers separated by a nonmagnetic spacer layer, one of FM layers being "pinned" by an antiferromagnetic layer. In the "top" spin-valve structure, the antiferromagnetic layer and the adjacent pinned FM layer are located in the upper part of the multilayer, whereas the "free" FM layer is disposed in the bottom part, on a buffer layer. The magnetization reversal of free and pinned layers occurs in different magnetic fields and is followed by magnetic hysteresis. To improve spin valve characteristics for various applications it's to reduce the low field hysteresis caused by the free layer magnetization reversal. One of the ways to decrease the low field hysteresis in antiferromagnetic FeMn-based spin valves is to make a composite free layer consisting of two FM layers, $Fe_{20}Ni_{80}/Co_{90}Fe_{10}$ [1–3]. In this bilayer, $Co_{90}Fe_{10}$ alloy has low magnetostriction and permalloy induces strong $\langle 111 \rangle$ texture in the $Co_{90}Fe_{10}$ layer, which results in the enhancement of the MR ratio. In this work the dependence of the low field hysteresis and GMR ratio of FeMn-based top spin valves with different Cu interlayer thicknesses and the $Fe_{20}Ni_{80}/Co_{90}Fe_{10}$ composite free layer on the angle between applied magnetic field vector and the magnetic anisotropy axis in the film plane have been studied.

1. Experimental

Samples of the composition $Si/Ta(50\,Å)/Fe_{20}Ni_{80}(20\,Å)/$ $Co_{90}Fe_{10}(55\,Å)/Cu(t_{Cu},Å)/Co_{90}Fe_{10}(55\,Å)/Fe_{50}Mn_{50}$ $(150\,Å)/Ta(20\,Å)$ with $t_{Cu} = 24\,Å$ (sample 1) or $t_{Cu} = 32\,Å$
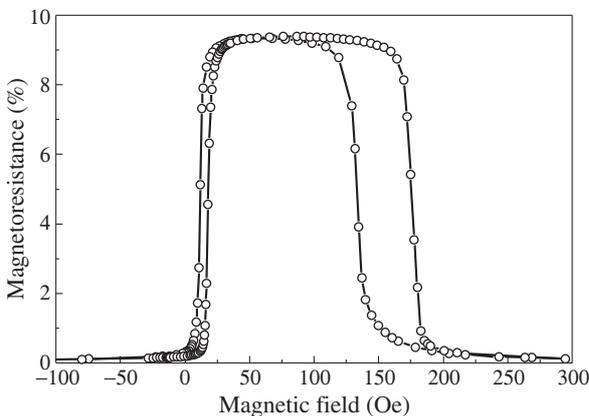
Fig. 1. Magnetoresistance curve for structure glass/ Ta(50 Å)/FeNi(20 Å)/CoFe(55 Å)/Cu(24 Å)/CoFe(55 Å)/FeMn (150 Å)/Ta(20 Å).
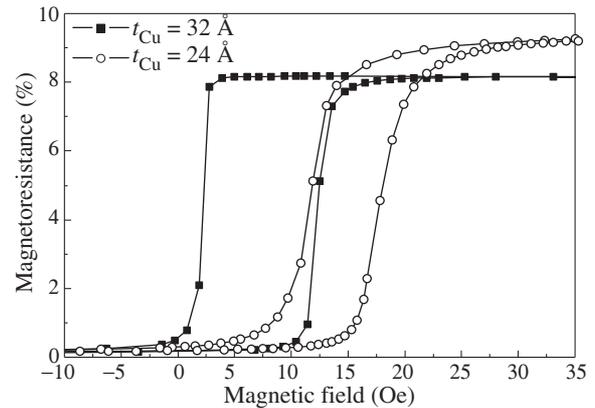
Fig. 2. Comparison of GMR and coersivity of free layer for structure Ta(50 Å)/FeNi(20 Å)/CoFe(55 Å)/Cu(t_{Cu}, Å)/CoFe(55 Å)/FeMn (150 Å)/Ta(20 Å) with 24 and 32 Å Cu layer thicknesses.

(sample 2) were prepared at room temperature on glass and naturally oxidated (100)Si substrates by DC magnetron sputtering in high purity argon under pressure of 0.1 Pa. The base pressure of residual gases in the deposition chamber was 10^{-7} Pa. Characterization of substrates was performed with a non-contact method of scanning interferometry using an optical profilometer. Typical roughness was rms $= 2-3$ Å and rms $= 5-7$ Å for glass and (100)Si substrates, respectively. Cu layer thicknesses $t_{Cu} = 24$ Å and $t_{Cu} = 32$ Å are chosen close to the second and third maximum of the interlayer exchange coupling in CoFe/Cu multilayers, respectively [4]. The multilayer deposition was performed in magnetic field of $H = 110$ Oe applied in the film plane. Magnetoresistance was measured by the four-point probe method in CIP geometry at room temperature. Crystallographic and microstructural information was obtained by transmission electron microscopy and X-ray diffraction.

2. Results

An evident (111) Bragg peak from fcc Cu and $Co_{90}Fe_{10}$ was detected by high-angle X-ray diffraction. The typical magnetic field dependence of magnetoresistance for exchange biased spin-valves is presented in Fig. 1. The maximal GMR ratios of 9.4% and 8.2% were detected for Cu layer thicknesses of $t_{Cu} = 24$ Å and $t_{Cu} = 32$ Å, respectively. The exchange-bias field of the pinned FM layer was $H_{eb} = 160$ Oe, that is a typical value for spin valves with FeMn antiferromagnetic layer. The shape of free layer magnetoresistive hysteresis loops is different for sample 1 and sample 2 (Fig. 2). Sample 2 has
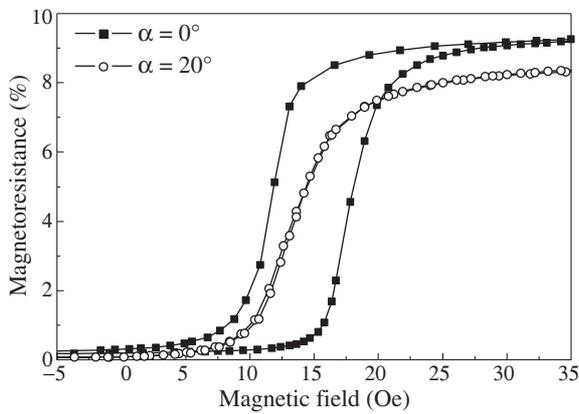
Fig. 3. The free layer hysteresis loops for the sample glass/Ta(50 Å)/FeNi(20 Å)/CoFe(55 Å)/Cu(24 Å)/CoFe(55 Å)/FeMn(150 Å)/Ta(20 Å) measured in geometry when magnetic field vector is applied along easy axis in the film plane ($\alpha = 0°$) and along direction deviated from easy axis in the film plane by the angle 20 degree ($\alpha = 20°$).

a rectangular-like shape of hysteresis loop and width about 10 Oe whereas the sample 1 with thinner Cu layer demonstrates a smooth field dependence of magnetoresistance with the hysteresis loop width at about 6 Oe. The maximal magnetoresistive sensitivity determined by the descending branch of the low field hysteresis loop was 6.4%/Oe for spin valve with $t_{Cu} = 32$ Å.

To reduce the free layer hysteresis down to 1 Oe in a similar spin valve structure, the special sample treatment has been used [5]. We propose an additional simple way how to reduce the free layer hysteresis. We found that the deviation of applied magnetic field vector in the film plane from easy axis crated in antiferromagnetic layer during multilayer deposition in external magnetic field leads to decrease of GMR ratio, magnetoresistive sensitivity, and low field hysteresis. It was established that the main hysteresis change occurs when the angle (α) between the applied magnetic field vector and the magnetic anisotropy axis is changed in the range of $\alpha = (0-20)$ degree. Fig. 3 demonstrates the 30 times decrease of the hysteresis loop width for the angle $\alpha = 20°$ in comparison with one for $\alpha = 0°$. At the same time the GMR ratio for the case of $\alpha = 20°$ still exceeds 8% and the sensitivity exceeds 1%/Oe. This kind of magnetic field dependence of magnetoresistance without hysteresis is of interest for GMR sensors, metrological tasks, and other applications in which the univocal correspondence between magnetic field value and electrical resistance of the sample is important. Physical reasons explaining the revealed reduction of free layer hysteresis still remain unclear. To understand why domain wall displacements in magnetic layers occurs without a pinning in case of $\alpha > 20°$ it is necessary to perform micromagnetic model calculations.

References

[1] H. Kanai, K. Yamada *et al*, *IEEE Transactions On Magnetics* **32**, 3368 (1996).

[2] S.Y. Yoon, D.H. Lee *et al*, *Sensor and Actuators A* **115**, 91 (2004).

[3] Y.S. Yu, K.S. Lee *et al*, *Electronic Materials Letter* **1**, 47 (2005).

[4] Y. Saito, S. Hashimoto *et al*, *IEEE Transactions On Magnetics* **28**, 2751 (1992).

[5] H.R. Liu, B.J. Qu *et al*, *Journal of Magnetism and Magnetic Materials* **267**, 386 (2003).

Experimental investigations of the change with magnetic flux of quantum number in superconducting ring

A. V. Burlakov, V. L. Gurtovoi, A. I. Ilin, *A. V. Nikulov* and V. A. Tulin

Institute of Microelectronics Technology, RAS, 142432 Chernogolovka, Moscow Region, Russia

Abstract. The magnetic dependencies of the critical current of aluminum ring with asymmetric link-up of current leads have been measured in order to clear up the essence of the paradoxical absence of the jump of the critical current at the quantum number change revealed before at the measurements of asymmetric superconducting ring. The measurements have shown that the experimental and theoretical dependencies agree in the region of magnetic field corresponding to integer numbers of the flux quantum and disagree at the half of the flux quantum. The jump is not observed as well as in the asymmetric rings.

Introduction

The discreteness of the spectrum of the permitted velocity $v = p/m$ states because of the Bohr's quantization $pr = n\hbar$ goes down with the radius r and mass m increase, in agreement with the Bohr's correspondence principle. Therefore the quantum phenomena, such as the persistent current of electrons, can be observed in nano-rings with $r > 300$ nm only at low temperature [1,2] even at microscopic mass $m = 9 \times 10^{-31}$ kg. Superconductivity is the exception thanks to the impossibility for Cooper pairs to change their quantum state n individually [3]. This exception gives us an opportunity for more detailed research of phenomena connected with the Bohr's quantization: a ring, in contrast to atom, can be made in different forms.

1. Periodical dependencies in magnetic field

We can observe the change of the quantum number n in magnetic field B thanks to a "huge" radius $r > 500$ nm of superconducting ring in comparison with atom orbit radius $r_B \approx 0.05$ nm. This change is observed because of the Aharonov–Bohm effect [1,4], i.e. the influence of the magnetic vector potential A of the canonical momentum $p = mv + qA$ of a particle with charge q. The momentum of a free particle is described with the gradient $p = \hbar\nabla\varphi$ of the phase φ of the wave function $\Psi = |\Psi| \exp i\varphi$, according to the quantum formalism. Because of the requirement that the complex wave function, describing a particle state, must be single-valued $\Psi = |\Psi| \exp i\varphi = |\Psi| \exp i(\varphi + n2\pi)$ at any point, the phase φ must change by integral n multiples of 2π following a complete turn along the path of integration, yielding $\oint_l dl\nabla\varphi = \oint_l dlp/\hbar = \oint_l dl(mv + qA)/\hbar = m\oint_l dlv/\hbar + 2\pi\Phi/\Phi_0 = n2\pi$. The integer number n of the permitted state with minimum energy $\propto v^2 \propto (n - \Phi/\Phi_0)^2$ should change with magnetic flux $\Phi = BS \approx B\pi r^2$ at $\Phi = (n + 0.5)\Phi_0$. The flux quantum $\Phi_0 = 2\pi\hbar/q$ equals ≈ 4140 T nm^2 for electron $q = e$ and ≈ 2070 T nm^2 for Cooper pair $q = 2e$. Consequently the n change can be observed in magnetic field $B > \Phi_0/\pi r^2 \approx 0.0026$ T in a superconducting ring with $r \approx 500$ nm and in the inaccessibly high magnetic fields $\Phi_0/\pi r_B^2 \approx 530000$ T for atom orbit with $r_B \approx 0.05$ nm.

The magnetic periodicity in different parameters, such as: resistance [4,5,6,7], magnetic susceptibility [8], critical current [9,10] and dc voltage [6,7,9] demonstrate unambiguously the n change with the magnetic flux $\Phi = BS$ inside ring: the resistance oscillations have minimum value at $\Phi = n\Phi_0$ and maximum value at $\Phi = (n + 0.5)\Phi_0$, in accordance with the theoretical relation $\Delta R \propto v^2 \propto (n - \Phi/\Phi_0)^2$; magnetic susceptibility and dc voltage change the sign at $\Phi = n\Phi_0$ and $\Phi = (n + 0.5)\Phi_0$, in accordance with the theoretical relation $M \propto V_p \propto \bar{v} \propto \overline{n - \Phi/\Phi_0}$; the critical current of symmetric ring have minimum value at $\Phi = (n + 0.5)\Phi_0$ and maximum value at $\Phi = (n + 0.5)\Phi_0$, in accordance with the relation $I_c = I_{c0} - 2I_p$, where $I_p = s2en_sv = I_{p,A}2(n - \Phi/\Phi_0)$ is the persistent current circulating in the ring clockwise or anticlockwise [9]. No jump, which could be connected with the jump of the permitted velocity $v \propto n - \Phi/\Phi_0$ and the persistent current, because of the n change at $\Phi = (n + 0.5)\Phi_0$ is observed at these measurements in accordance with the theory: the squared velocity $v^2 \propto (n - \Phi/\Phi_0)^2$ and the absolute value of the persistent current $|I_p| = I_{p,A}2|n - \Phi/\Phi_0|$ should not change with n change from n to $n + 1$ at $\Phi = (n + 0.5)\Phi_0$; the average velocity at $\bar{v} \propto \overline{n - \Phi/\Phi_0} = (-0.5 + 0.5)/2 = 0$ at $\Phi = (n + 0.5)\Phi_0$.

2. The jump absence at measurements of the critical current with different section of ring halves

The jump could be expected at measurement of the oscillations of the critical current of a superconducting ring with different section of ring halves $s_w > s_n$. The critical current measured in the one I_{c+} or other I_{c-} direction should be equal [9]

$$I_{c+}, I_{c-} = I_{c0} - I_{p,A}2\left|n - \frac{\Phi}{\Phi_0}\right|\left(1 + \frac{s_w}{s_n}\right), \qquad (1a)$$

when the external current I_{ext} measuring I_{c+}, I_{c-} is added with the persistent current I_p in the narrow ring half s_n and

$$I_{c+}, I_{c-} = I_{c0} - I_{p,A}2|n - \frac{\Phi}{\Phi_0}|\left(1 + \frac{s_n}{s_w}\right), \qquad (1b)$$

when the currents are added in the wide ring half s_w. The jump $\Delta I_c = I_{p,A}(s_w/s_n - s_n/s_w)$ should be observed because of the change of the persistent current direction with the n change at $\Phi = (n + 0.5)\Phi_0$. But the measurements [9,10,11] have revealed the absence of the expected jump in spite of the enough large amplitude $I_{p,A}$ of the persistent current and the relation $s_w/s_n \approx 2$. According to the universally recognised quantum formalism the anisotropy $I_{c,an}(\Phi/\Phi_0) = I_{c+}(\Phi/\Phi_0) - I_{c-}(\Phi/\Phi_0)$ of the critical current measured in the opposite directions should appear in the asymmetric ring $s_w/s_n > 1$ because of the change of the functions $I_{c+}(\Phi/\Phi_0)$, $I_{c-}(\Phi/\Phi_0)$ describing its magnetic dependencies, see Fig. 19 [9] and Fig. 3
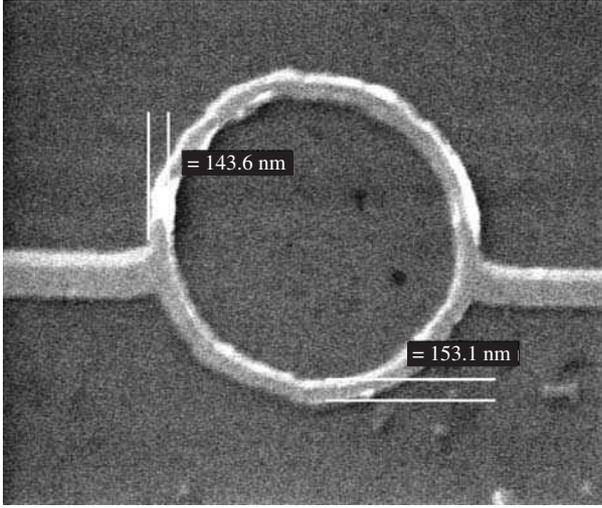
Fig. 1. The aluminum ring $r \approx 1\ \mu$m with asymmetric link-up of current leads, $l_{sh} \approx 0.7\pi r$, $l_{long} \approx 1.3\pi r$.

[11]. But it was found [10] that the anisotropy $I_{c,an}(\Phi/\Phi_0) = I_c(\Phi/\Phi_0 + \Delta\phi) - I_c(\Phi/\Phi_0 - \Delta\phi)$ appears because of the changes in the arguments $I_{c+}(\Phi/\Phi_0) \approx I_c(\Phi/\Phi_0 + \Delta\phi)$, $I_{c-}(\Phi/\Phi_0) \approx I_c(\Phi/\Phi_0 - \Delta\phi)$ of the functions rather than the functions themselves. The shift of the periodic dependencies of the critical current on the quarter of the flux quantum $\Delta\phi \approx 1/4$ [10] is very paradoxical phenomenon which can not be explained now as well as the absence of the I_{c+}, I_{c-} jump with the n change.

3. Measurements of the critical current of superconducting rings with asymmetric link-up of current leads

In order to clear up the essence of the second puzzle we have measured the magnetic dependencies of the critical current of aluminum ring with asymmetric link-up of current leads, Fig. 1. The critical current should determined with the transition into the resistive state only of the shot segment $l_{sh} \approx 0.35\,2\pi r$ at the relation of the persistent current amplitude and the critical current $I_{p,A}/I_{c0} < 0.25$ measured on the ring, Fig. 2, with the segment relation $l_{long}/l_{sh} \approx 0.65/0.35 \approx 1.8$. The critical current dependencies should describe with the relations

$$I_{c+} = I_{c0} - I_{p,A}\left(n - \frac{\Phi}{\Phi_0}\right), \tag{2a}$$

$$I_{c-} = I_{c0} + I_{p,A}\left(n - \frac{\Phi}{\Phi_0}\right), \tag{2b}$$

implying the jump $\Delta I_c = I_{p,A}$ at $\Phi = (n+0.5)\Phi_0$, Fig. 2. The measured dependencies $I_{c+}(\Phi/\Phi_0)$, $I_{c-}(\Phi/\Phi_0)$ correspond to the expected one (2) in the region near $\Phi = n\Phi_0$, Fig. 2. Nevertheless the jump, which must be because of the quantum number n change according to (2), is not observed, Fig. 2. The measured values of the critical current $I_{c+}(\Phi/\Phi_0)$, $I_{c-}(\Phi/\Phi_0)$ vary smoothly with magnetic flux value near $\Phi = (n+0.5)\Phi_0$, Fig. 2, in defiance of the quantum formalism predicting the I_c jump (2). The aspiration of Nature to avoid the jump surprises. It is puzzle that the experimental and theoretical dependencies agree near $\Phi \approx n\Phi_0$ and disagree near $\Phi \approx (n+0.5)\Phi_0$.
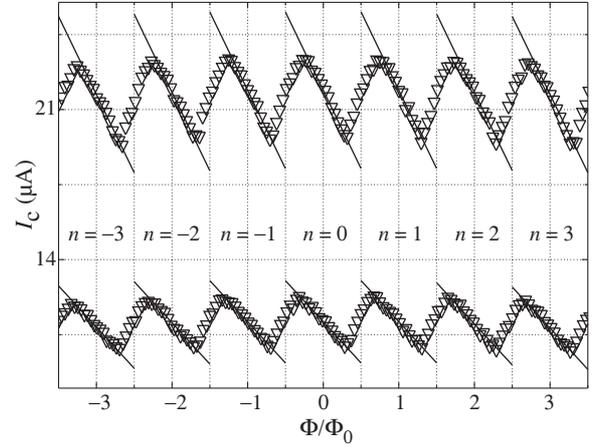
Fig. 2. The magnetic dependencies of the critical current $I_{c+}(\Phi/\Phi_0)$ of aluminum ring with asymmetric link-up of current leads measured at the temperature $T \approx 0.900T_c$; $T \approx 0.933T_c$; $T_c \approx 1.52$ K.

References

[1] A.C. Bleszynski-Jayich, W.E. Shanks, B. Peaudecerf, E. Ginossar, F. von Oppen, L. Glazman, J.G.E. Harris, *Science* **326**, 272 (2009).

[2] Hendrik Bluhm, Nicholas C. Koshnick, Julie A. Bert, Martin E. Huber, and Kathryn A. Moler, Persistent Currents in Normal Metal Rings, *Phys. Rev. Lett.* **102**, 136802 (2009).

[3] A.V. Nikulov, *AIP Conference Proceedings*, **1101** "Foundations of Probability and Physics-5" 134 (2009); arXiv: 0812.4118.

[4] V.L. Gurtovoi, A.V. Nikulov, and V.A. Tulin, *in Proceedings of 17th International Symposium "Nanostructures: Physics and Technology"* St Petersburg: Ioffe Institute, 87 (2009).

[5] W.A. Little and R.D. Parks, *Phys. Rev. Lett.* **9**, 9 (1962).

[6] A.A. Burlakov *et al*, *Pisma Zh. Eksp. Teor. Fiz.* **86**, 589 (2007); (*JETP Lett.* **86**, 517 (2007)); arXiv: 0805.1223.

[7] V.L. Gurtovoi *et al*, *Fizika Nizkikh Temperatur* **36**, 1209 (2010); arXiv: 1004.3914.

[8] N.C. Koshnick, H. Bluhm, M.E. Huber, K.A. Moler, Science **318** 1440 (2007).

[9] V.L. Gurtovoi *et al*, *Zh. Eksp. Teor. Fiz.* **132**, 1320 (2007); (*JETP* **105**, 1157 (2007)).

[10] V.L. Gurtovoi *et al*, *Zh. Eksp. Teor. Fiz.* **132**, 297 (2007); (*JETP* **105**, 262 (2007)).

[11] A. A. Burlakov, V.L. Gurtovoi, S.V. Dubonos, A.V. Nikulov, and V.A. Tulin, arXiv: cond-mat/0603005.

Magnetoelectric effect in oxide-based composite ferroelectric/ferromagnetic structrues

A. P. Nosov[1], V. I. Osotov[1], I. V. Gribov[1], N. A. Moskvina[1], M. V. Ronkin[1], V. G. Vasiliev[2], E. V. Vladimirova[2] and T. S. Karpova[2]

[1] Institute of Metal Physics, Ural Branch of RAS, 620990 Ekaterinburg, Russia
[2] Institute of Solid State Chemistry, Ural Branch of RAS, 620041 Ekaterinburg, Russia

Abstract. The magnetoelectric particulate composite magnetostrictive ferrite/ferroelectric structures were fabricated. Their structural, magnetic, and frequency dependent magnetoelectric properties were investigated. It is shown that such structures can be used in magnetic field sensing applications.

Introduction

Multiferroic magnetoelectric (ME) composite structures [1,2] made by combination of piezoelectric and magnetic substances together have drawn great interest in recent years due to their multifunctionality. In such structures the coupling interaction between piezoelectric and magnetic subsystems can produce at room temperature a ME response several orders of magnitude higher than that in the single phase ME materials so far available. The ME composites provide interesting opportunities for numerous potential applications such as magnetic and electric transducers, actuators, sensors of ac and dc magnetic fields. The ME effect in composite materials is known as a product tensor property which results from the cross interaction between different orderings of the two phases. This is a complicated electrical and magnetic phenomenon mediated by elastic interaction. The ME effect in composites is extrinsic and depends on microstructure and coupling interaction across magnetic-piezoelectric interfaces.

Complex oxides can have magnetostrictive or ferroelectric properties. Ferrites of various compositions can be used as a magnetostrictive component. Their advantage is in chemical stability, high values of Curie temperature and magnetostriction coefficient λ. Lead and barium titanates can be used as a ferroelectric component. The physical properties of oxide composite structures strongly depend on preparation conditions which can influence the value of the ME coefficient. We
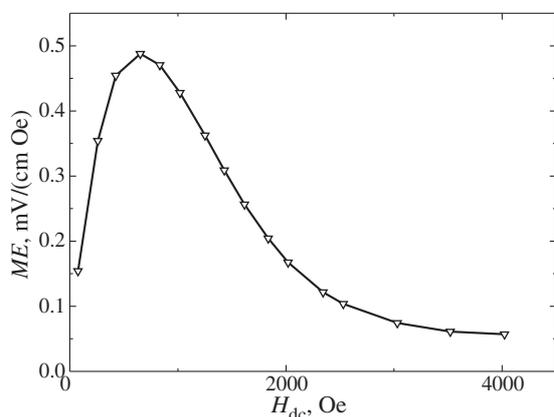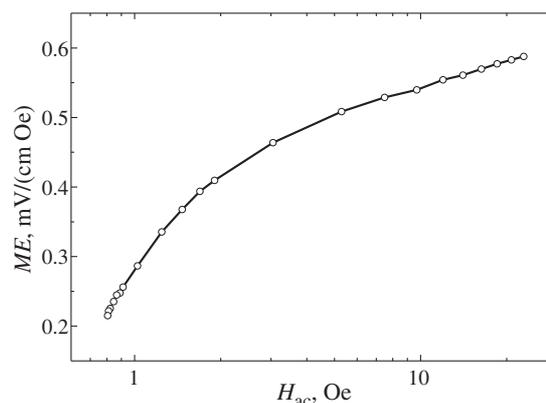
Fig. 2. The ac magnetic field dependence of the magnetoelectric coefficient. The $Ni_{0.8}Co_{0.1}Cu_{0.1}Fe_2O_4$/PZT composite. Frequency 140 Hz. $H_{dc} = 584$ Oe.

synthesized the iron- and nickel based ferrites, $BaTiO_3$-based ferroelectrics, composite structures, and investigated their ME properties.

1. Experimental

The $CoFe_2O_4$, $Ni_{0.8}Zn_{0.2}Fe_2O$ and $Ni_{0.8}Co_{0.1}Cu_{0.1}Fe_2O_4$ ferrites were synthesized using thermal treatment of oxalates, coprecipitated from the nitrate solutions. The metallic Fe, Cu, Zn, Ni, and $Co(NO_3)_3 \cdot 6H_2O$ were used as initial components. The precursors were thermally treated in air for 3 h. at 900–1000 °C. The phase composition was controlled by X-ray diffraction. The $BaTiO_3$-based materials were synthesized in similar way. For some compositions the commercially available PZT was used. The composite ME structures with various ratios of ferroelectric to magnetostrictive phases were obtained by pressing the initial powders and their thermal treatment in air or flowing oxygen for 3 h. at 1050 °C. Such temperature have benn chosen to avoid chemical reactions between the ferroelectric and magnetostrictive phases at higher temperatures. Silver paste was used for making electrodes for electrical contact.

Magnetoelectric properties were measured by application to the sample a small ac magnetic field with varying frequency f created by Helmholts coils and dc magnetic field H created by electromagnet. The dependence of ME coefficient on the value and frequency of the ac magnetic field and strength of the dc magnetic field were investigated.

Fig. 1. The dc magnetic field dependence of the magnetoelectric coefficient. The $Ni_{0.8}Co_{0.1}Cu_{0.1}Fe_2O_4$/PZT composite. Frequency 140 Hz.

Typical dc magnetic field dependence of the magnetoelectric coefficient recorded at the frequency of 140 Hz for the $Ni_{0.8}Co_{0.1}Cu_{0.1}Fe_2O_4$/PZT composite is shown in Fig. 1. The peak in the $ME(H)$ curve below 1 kOe is explained by the dc magnetic field dependence of λ and the fact that the $d\lambda/dH_{dc}$ dependence has maximum at $\sim$600 Oe.

Measurements of the orientation dependence of magneto-electric coefficient revealed almost 2.5 greater value of ME for the longitudinal orientation (H_{ac} parallel to H_{dc}) as compared to the transverse (H_{ac} perpendicular to H_{dc}) orientation due to the differences of the values of longitudinal and transverse components of magnetostriction.

Figure 2 illustrates the possibility of ac magnetic field sensing using ME composites under static magnetic field biasing of $H_{dc} = 584$ Oe. As is seen from Fig. 2. using such materials the sensors of magnetic field with sensitivity below 1 Oe can be made.

References

[1] M. Fiebig, *J. Phys. D* **38**, R123 (2005).
[2] C-W. Nan *et al*, *J. Appl. Phys.* **103**, 031101 (2008).

Observation of bright polariton solitons in strongly coupled semiconductor macrocavities

D. N. Krizhanovskii[1], M. Sich[1], R. Hartley[2], A. Gorbach[2], D. Skryabin[2], E. Cerda[3], K. Biermann[3], R. Hey[3], P. V. Santos[3] and M. S. Skolnick[1]

[1] Department of Physics and Astronomy, University of Sheffield, Sheffield S3 7RH, United Kingdom
[2] Department of Physics, University of Bath, Bath, BA2 7AY, United Kingdom
[3] Paul–Drude-Institut Berlin, Hausvogteiplatz 5-7, 10117 Berlin, Germany

Microcavity polaritons are two-dimensional composite bosons arising from strong exciton-photon coupling in a semiconductor microcavity. This system has been attracting much attention during the last 5–10 year. A number of phenomena due to polariton-polariton interactions have been observed such as polariton superfluidity [1], stimulated polariton-polariton scattering [2] and non-equilibrium polariton Bose–Einstein condensation (BEC) [3]. A characteristic property of interacting atom BECs is the existence of non-dispersive localised wavepackets — bright solitons, which are stabilised by attractive (repulsive) interactions for the case of positive (negative) effective mass. In the non-equilibrium systems, such as microcavity polaritons, the balance between net loss and gain is also critical for the soliton robustness. Here, for the first time we observe polariton bright solitons (predicted in Ref. [4]) due to the combination of the natural negative effective mass of the lower polariton (LP) branch at large k-vectors (Fig. 1 c)) and polariton-polariton repulsive interactions.

If the LP branch is driven resonantly by a blueshifted pump CW laser (Fig. 1c) the internal pump polariton field exhibits bistable behaviour (Fig. 1a) as a function of the pump k-vector ($\mathbf{k}_p$) at fixed laser energy. For a large pump spot (experimentally $\sim$70 μm), the soliton results from switching in *the bistable region* ($\mathbf{k}_p < 2.38$ μm^{-1}) from the lower to the upper state locally in a region of a few microns [4]. For $\mathbf{k}_p$ larger than the k-vector corresponding to the point of inflection of the LP dispersion, i.e. for the negative effective mass, the wavepacket of the switched on LP states is a soliton, which dispersion is suppressed by repulsive polariton-polariton interaction.

In our experiment, a ps pulsed probe beam focused to a small spot (7 μm) at position $x = -20$ μm triggers soliton formation (Fig. 1b). Soliton trace in the X direction (parallel to the direction of incidence of the pump) versus time is shown in Fig. 1b for $\mathbf{k}_{probe} = \mathbf{k}_p$. We found that the soliton width along X ($\sim$4.6 μm) and the soliton speed ($\sim$1.4 μm/ps) are independent of the probe size and probe k-vector. Fig. 1d shows the soliton dispersion in $E - k_x$ space, which is nearly linear and has a broad spectral and momentum distribution of $\sim$1.3 meV and 2 μm^{-1}, respectively. Soliton traces similar to that in Fig. 1b were obtained for probe spot size of 14 μm and for probe k-vector $\mathbf{k}_{probe} = 1/2\,\mathbf{k}_p$.

Essentially, the soliton emission does NOT arise from four-wave mixing (FWM) between the pump and the probe beams observed in Ref. [2], since the FWM signal is only expected at $\mathbf{k}_p$ due to phase matching. The probe just switches the system on to the upper pump bistable state locally, resulting in *self-organised* polariton-polariton scattering from the switched pump state into a continuum of LP states with k-vectors from 0 to $2\mathbf{k}_p$, which form a soliton. The soliton speed is given by the pump k-vector $\mathbf{k}_p$ and the soliton size is determined by the healing length $\xi = \sqrt{\hbar^2/(2|m_{eff}|E_{shift})} \sim 3-5$ μm by analogy with bright solitons in atom BEC. Here $m_{eff} < 0$ is polariton effective mass at $\mathbf{k}_p$, and $E_{shift} \sim 0.2$ meV is the pump blueshift with respect of the LP branch, defining the energy of polariton-polariton interactions in the localised wavepacket.

Finally, a second phase-locked probe beam was employed at a time delay after soliton initialisation. Although probe 2 beam only partially overlaps with the soliton in momentum and energy space, we are able to switch the soliton off when this beam is out of phase with the first probe pulse. This demonstrates ultrafast coherent control of polariton solitons, which have a potential to be used in fast ($>$100 GHz) polariton switches and logic gates [5].

Fig. 1. (a) Dependence of polariton PL emission as a function of pump k-vector at fixed pump energy showing bistable behaviour of the internal pump polariton field. (b) Soliton emission intensity versus position X and time. Probe arrives at time $t = 0$ at position $X = -20$ μm. (c) Schematic of the experiment. (d) Soliton dispersion in energy-momentum space $E(k_x)$ taken at 30 ps after the arrival of the probe beam.

References

[1] A. Amo, *Nature Physics* **5**, 805 (2009).
[2] A. Amo *et al*, *Nature* **457**, 291 (2009); A. Amo and D. Sanvitto, private communications.
[3] A.P.D. Love, D.N. Krizhanovskii *et al*, *Phys. Rev. Lett.* **101**, 067404 (2008).
[4] O.A. Egorov *et al*, *Phys. Rev. Lett.* **102**, 153904 (2009).
[5] T.C.H. Liew, A.V. Kavokin, and I.A. Shelykh *Phys. Rev. Lett.* **101**, 016402 (2008).

Whispering gallery modes of surface plasmon polaritons

A. A. Bogdanov[1,2,3] and *R. A. Suris*[1,2,3]

[1] Ioffe Physical-Technical Institute, St Petersburg, Russia
[2] St Petersburg State Polytechnic University, St Petersburg, Russia
[3] St Petersburg Academic University, St Petersburg, Russia

Abstract. In this work we analyze whispering gallery modes (WGMs) of surface plasmon polaritons (SPPs) on the surface of cylindrical microcavity. We show that by means of using SPPs, dimensions of the microcavity can be decreased up to subwavelength scales. Frequency dependence of Q-factor for considered microcavity has a resonance behavior. Appearance of the maximum is explained by the decrease of radiation losses and increase of free carrier absorption (FCA) with azimuthal wavenumber.

Introduction

Entire photonic integrated circuit includes passive, active and nonlinear elements [1]– [4]. Nowadays, one of the main problem of photonic integrated circuits is design of nonlinear optical elements [5]. Nonlinear optical effects in the solid state material rather week in comparison with nonlinear electrical effects. In order to reach considerable nonlinear optical effect, it is necessary to accumulate high optical power in microcavity with nonlinear core. Optical power accumulated in microcavity depends on the quality factor (Q-factor) of the resonator. The highest Q-factors, up to 10^{10} [6], are reached in the axial-symmetry resonators (cylindrical, toroidal, spherical) with whispering gallery modes (WGMs) [6]– [10].

Linear dimension of such resonators is rather big ($\sim 100\,\mu$m) in comparison with base elements of electrical integrated circuits (~ 10 nm). Decrease of resonator dimension results in exponential decay of Q-factor.

In this work we propose a solution of this problem by means of WGMs of surface plasmon polaritons (SPPs) [11].

1. Model

We use the simplest model of infinitely long metallic cylinder resonator with dielectric function $\varepsilon(\omega)$ (Fig. 1a). We suppose that the cylinder is surrounded by a vacuum. Dielectric function of the cylinder we describe within Drude-Lorentz approximation:

$$\varepsilon(\omega) = \varepsilon^\infty \left(1 - \frac{\Omega^2}{\omega(\omega + i\gamma)} \right). \qquad (1)$$

ϵ^∞ is a dielectric function of the material at $\omega \to \infty$, γ is inverse relaxation time that corresponds to free carrier absorption (FCA), Ω is plasma frequency of the material:

$$\Omega = \sqrt{\frac{4\pi n e^2}{m^* \epsilon^\infty}}. \qquad (2)$$

n_s is concentration of free electrons in the material, m^* is their effective mass.

We seek Maxwell's equations solution in the form of azimuthal wave. It means that electric and magnetic field, **E** and **H**, depend on azimuthal angle, ϕ, as $\exp(i\phi n)$ (m is an integer number), depend on the t as $\exp(-i\omega t)$ and does not depend on the z ($\frac{\partial}{\partial z} \equiv 0$). As a matter of fact, we consider the problem of cylindrical waveguide but suppose that propagation constant along z-axis is equal to zero ($k_z = 0$). In this case, Maxwell's
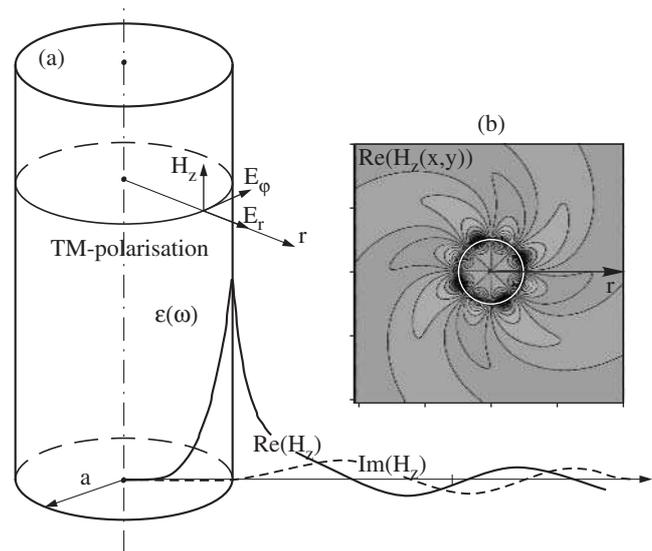
Fig. 1. (a) Model of axial-symmetry resonator: infinitely long cylinder with dielectric function $\varepsilon(\omega)$. Radius of the cylinder is a. (b) Pattern of magnetic lines of force for SPP WGM. Azimuthal wavenumber $m = 4$.

equations allow dividing of solutions into two types: TE and TM modes. We consider only TM-modes. Electric and magnetic field components for TM-mode are shown in Fig. 1a.

Q-factor of the resonator is defined as

$$Q = \frac{1}{2} \frac{\mathrm{Re}(\omega)}{\mathrm{Im}(\omega)}, \qquad (3)$$

where ω is the eigenfrequency depending on the azimuthal wavenumber, m.

2. Results and discussion

As an example, we consider gold cylinder ($\Omega = 9$ eV) of $0.2\,\mu$m radius. As a first step we ignore FCA ($\gamma = 0$). It means that optical losses occur due to radiation only. Field distribution for SPP WGM is shown at the Fig. 1a and pattern of magnetic lines of forces are shown in Fig. 1b. Dependence of real and imaginary parts of eigenfrequency, $\mathrm{Re}(\omega)$ and $\mathrm{Im}(\omega)$, on azimuthal wavenumber, m, for SPP WGM is shown in Fig. 2.

At high azimuthal wavenumber, eigenfrequency of SPP WGM tends to the frequency of surface plasmon ($\Omega/\sqrt{2}$) propagating along planar interface [11]. It is not by accident, because at high azimuthal wavenumber, wavelength of the SPP
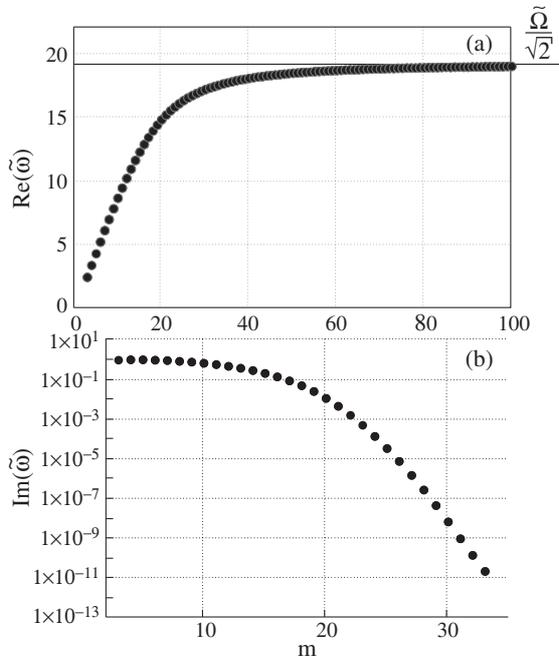
Fig. 2. (a) $\mathrm{Re}(\widetilde{\omega})$ versus m. (b) $\mathrm{Im}(\widetilde{\omega})$ versus m. Here we use dimensionless quantities: $\widetilde{\omega} = \omega \frac{a}{c}$. Cavity parameters are: $\Omega = 1.4 \times 10^{16}$ rad s^{-1}, $a = 0.2\,\mu$ m, $\gamma = 0$.

is much less than the radius of the cylinder and SPP behaves like in the plane geometry.

Radiation losses of eigenmode exponentially depend on the penetration depth of the field outside the resonator. Analysis of Maxwell's equations show that characteristic penetration depth of the field outside the resonator linearly decrease with azimuthal wavenumber, m. Therefore, radiation losses exponentially decrease with azimuthal wavenumber, m (Fig. 2b).

It is known that FCA for SPP propagating along planar interface increases at the frequencies close to the surface plasmon frequency [11]. Increase of FCA and decrease of radiation losses for SPP WGM result in appearance of the minimum in the dependence of $\mathrm{Im}(\omega)$ on the azimuthal wavenumber, m. In Fig. 3a we show dependence of $\mathrm{Im}(\omega)$ on m for the resonator considered above taking into account FCA. Minimum of the losses corresponds to $m = 16$. Frequency dependence of Q-factor on m for different inverse relaxation times is presented in Fig. 3b.

3. Conclusion

We have shown that by means of SPPs, dimensions of axial-symmetric resonators can be decreased up to subwavelength scales. Q-factor of the axial-symmetry cavities has resonance behavior depending on azimuthal wavenumber. Nature of this maximum is explained by the decreasing of radiation losses and increasing FCA with azimuthal wavenumber. Right choice of operation frequency can increase Q-factor of the resonator several times.
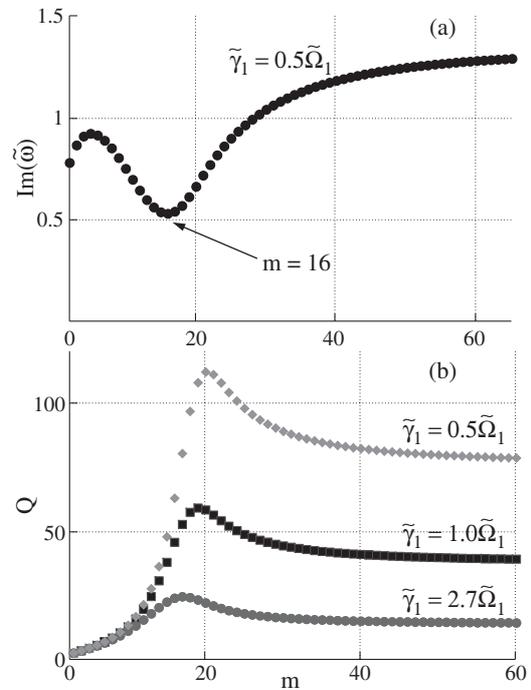
Fig. 3. (a) $\mathrm{Im}(\omega)$ versus m taking into account FCA in the resonator. (b) Q-factor versus m taking into account FCA in the resonator. Cavity parameters are: $\Omega = 1.4 \times 10^{16}$ rad s^{-1}, $a = 0.2\,\mu$m, $\gamma = 0.5\Omega$, $\gamma = 1.0\Omega$, $\gamma = 2.7\Omega$.

References

[1] S.E. Miller, *Bell Syst. Tech. J.* **48**, 2059 (1969).
[2] O. Wada, T. Sakurai and T. Nakagami, *IEEE J. Quant. Electron.* **QE-22**, 805 (1986).
[3] T.L. Koch and U. Koren, *IEEE J. Quant. Electron.* **QE-27**, 641 (1991).
[4] R. Nagarajan *et al*, *IEEE J. Sel. Top. in Quant. Electron.* **11**, 50 (2005).
[5] R.W. Boyd, *Nonlinear Optics* (San Diego: Academic Press) 2008, p. 640.
[6] K.J. Vahala, *Nature* **424**, 839 (2003).
[7] A.N. Oraevsky, *Quantum. Electron.* **32**, 377 (2002).
[8] V.S. Ilchenko, *IEEE J. Sel. Topics Quantum Electron.* **12**, 3 (2006).
[9] A.B. Matsko, *IEEE J. Sel. Topics Quantum Electron.* **12**, 3 (2006).
[10] V.S. Ilchenko , A.B. Matsko, *IEEE J. Sel. Topics Quantum Electron.* **12**, 15 (2006).
[11] J.M. Pitarke, V.M. Silkin, E.V. Chulkov, P.M. Echenique, *Rep. Prog. Phys.* **70**, 1 (2007).

Interaction of a point emitter with a gold Yagi–Uda nanoantenna array

S. V. Lobanov[1,2], T. Weiss[3,4], D. Dregely[4], H. Giessen[4], N. A. Gippius[1,3] and S. G. Tikhodeev[1,2]

[1] A.M. Prokhorov General Physics Institute, Moscow, Russia
[2] M.V. Lomonosov Moscow State University, Moscow, Russia
[3] LASMEA, University Blaise Pascal, 24 Avenue des Landais, F-63177 Aubière Cedex, France
[4] 4th Physics Institute, University of Stuttgart, Pfaffenwaldring 57, D-70550 Stuttgart, Germany

Abstract. We investigate numerically the light emission of a quantum dot (QD) from a periodic array of gold Yagi–Uda nanoantennas in the weak coupling limit. We show that the interaction of the QD (described as a point dipole) with the localized plasmon in the feed element of the antenna can lead to a very strong near-field enhancement of the dipole emission. The radiative intensity of the QD emission may exceed the radiative intensity of an equivalent dipole in free-space by a factor of hundred.

Optical nanoantennas which alow to control light emission from a single molecule or quantum dot have been in the focus of intensive investigations in the recent years [1–12].

Metal antennas are traditionally used for controlling the radiation pattern of electromagnetic wave emission in the radio and microwave frequency range. Though the electromagnetic properties of metals in the optical range differ significantly from that in the radio and microwave range, it seems to be reasonable to use the main concepts of radio antennas in the optical range as well. It has been suggested [2, 3, 5, 12] to construct a nanooptical antenna with elements that are arranged as in the radio Yagi–Uda antennas.

Yagi–Uda antenna consists usually of one or two reflectors, one feed element and several directors with appropriately selected scattering phases (reflector and director are slightly detuned inductively and capacitively). As it has been recently shown, the nanoantenna elements can be nanorods [3, 5, 12], core-shell [2] or spherical [11] nanoparticles. All elements scatter the light and the resulting interference forms a highly directed beam along the antenna axis. The size of the elements in such optical Yagi–Uda nanoantennas have to be smaller than the light emission wavelength in free-space. Such optical nanoantennas only work efficiently in narrow frequency domains, where the interaction of the emitter with light is resonantly enhanced because of the excitation of so-called localized plasmons [13, 14] in the nanoantenna elements.

Spontaneous emission is not an intrinsic atomic property, but it depends sensitively on the local density of photonic modes at certain frequencies in a microcavity [15, 16], or, equivalently, on the local electromagnetic field value at the position of the quantum emitter [4, 6, 10]. Using resonances, it is possible to increase the local electromagnetic field significantly, and, resultantly, to enhance and redirect the dipole emission. In the case of localized plasmon resonances, the collective excitation of electrons at the plasmon frequency leads to a considerably enhanced emission rate when the point dipole is located in the vicinity of metallic nanoparticles with the appropriate orientation of its dipole moment [5, 7, 9].

The exact description of photon radiation from the quantum emitter located in some metal-dielectric environment is very complicated. A convenient approximation is a model of an oscillating point dipole. It oscillates with constant frequency and magnitude fixed by the external source (so-called weak coupling limit). In other words, the emission of a current $\vec{j}(\vec{r}, t) = \vec{j}_0 \times \delta(\vec{r} - \vec{r}_0) \times e^{-i\omega t}$ inside an environment with spatially modulated permittivity has to be calculated. This system is now classical and can be described by Maxwell's equations.

The structure of interest is shown schematically in Fig. 1. It consists of a glass superstrate ($\varepsilon = 2.4$), a periodic array of optical Yagi–Uda nanoantennas ordered in a rectangular lattice, and a quartz substrate ($\varepsilon = 2.13$). The periods along the x- and y-axis are equal to 450 and 300 nm, respectively. Each antenna consists of three rectangular gold parallelepipeds of 30 nm height and 100 nm width. The lengths of the top (director), middle (feed), and bottom (reflector) elements are 220, 250 and 300 nm, respectively. They are located in glass and the vertical distance between them is equal to 100 nm. We assumed the gold permittivity to be described by the Drude formula with 2180 THz plasma frequency and 19.5 THz damping rate.

Our first goal is to calculate the directional pattern as well as the emission spectra in the direction normal to the antenna plane. It makes sense to normalize the computed emission intensity $P(\vartheta, \varphi)$, i. e., the Poynting vector of the dipole emission in the far field as a function of the spherical angles ϑ and ϕ, to the maximum intensity of the emission of a point dipole in free-space, which oscillates with the same magnitude and frequency. Thus, we can easily distinguish the enhancement of emission ($P > 1$) from the attenuation ($P < 1$) compared
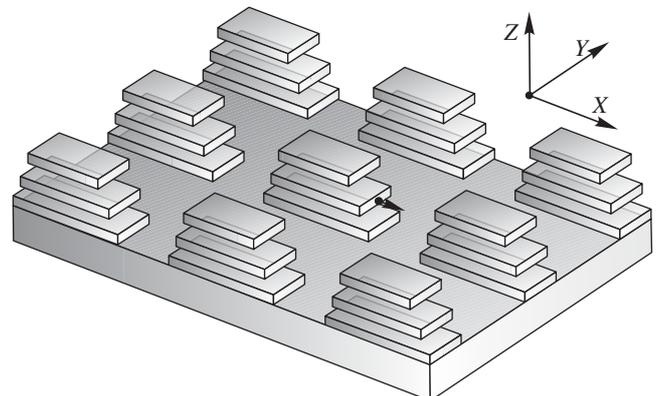
Fig. 1. Lateral view of a periodic array of optical Yagi–Uda nanoantennas with an x-oriented oscillating point dipole (black point with arrow) located at a horizontal distance of 5 nm from the feed element of one nanoantenna.
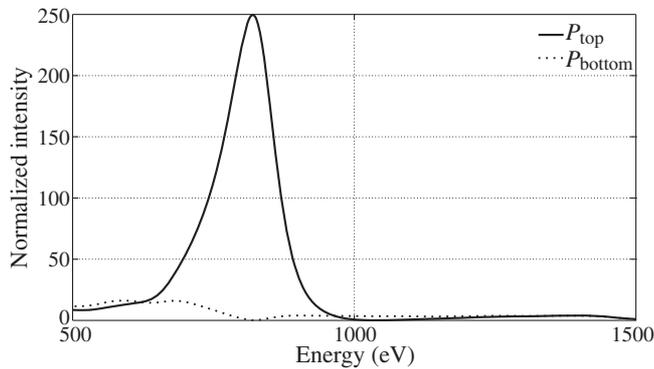
Fig. 2. Calculated spectra of the emission in top (solid curve) and bottom (dashed curve) directions of the oscillating point dipole (directed along x) coupled to the gold Yagi–Uda nanoantenna array.

to the dipole located in homogeneous vacuum.

The calculated emission spectra in top $(+z)$ and bottom $(-z)$ directions of the x-directed oscillating point dipole located inside the periodic array of gold Yagi–Uda nanoantennas are shown in Fig. 2. The dipole is placed on the horizontal symmetry axis along x-direction at a distance of 5 nm to the edge of the feed element (see in Fig. 1). Only one strong and narrow resonance occurs in the emission spectra in the top direction at the photon energy $\hbar\omega = 820$ meV ($\lambda = 1.5$ μm). Its magnitude is about 250 and the FWHM is 107 meV. The emission to the bottom direction is significantly smaller. It has even a minimum at the plasmon resonance.

Figure 3 depicts the calculated radiation pattern of emission $P(\vartheta, \varphi)\vec{e}_r$ at the resonant photon energy $\hbar\omega = 820$ meV (where $\vec{e}_r$ is the unit radial vector of a spherical coordinate system centered in the point dipole position). The calculated radiative part of the Purcell factor appears to be as high as 80, which indicates a very strong enhancement of the dipole emission by the feed element. In spite of only one director employed in our Yagi–Uda antenna, the emission in top direction appears to be highly directional.

Finally, we would like to mention that in the antenna array allows to control the emission directivity further, by using several emitting dipoles in different positions and controlling their phase difference of oscillations. Figure 3 shows the scaled by 1/2 2D polar diagrams of the emission of two synchronized dipoles, positioned at neighboring antennas of the array at distance $\vec{d}$, proportional to integer numbers of periods (see dotted and dashed lines in the left and central panels). The emission intensity of the synchronized pair of dipoles normalized to the maximum emission intensity of two non-synchronized dipoles is then simply $P_2(\vec{d}, \vartheta, \varphi) = P(\vartheta, \varphi)[1 + \cos(2\pi n(\vec{d} \times \vec{e}_r)/\lambda)]$, where $P(\vartheta, \varphi)$ is the directional pattern of a single dipole (solid line), and n is the refractive index of superstrate. Note that the polar diagrams P_2 of the synchronized dipoles demonstrate the effect of super-radiance: the Purcell factor of two synchronized closely positioned dipoles becomes twice larger than unsynchronized. It is seen also that it becomes possible to increase the directivity using two emitting dipoles.

To conclude, we show that the gold Yagi–Uda nanoantenna array enhances and simultaneously directs radiation of the oscillating point dipole. The dipole-nanoantenna enhancement depends very strongly on the oscillating frequency, dipole position, and orientation of its moment. It becomes possible to control the emission directivity further by using several syn-
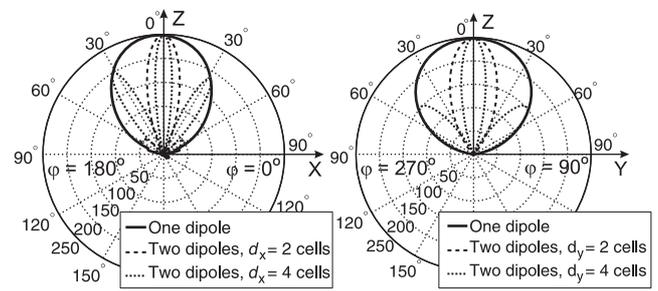
Fig. 3. Calculated 2D polar diagrams of far-field emission in xz (left panel) and yz (right panel) planes for the x-oriented oscillating point dipole coupled to the gold Yagi–Uda nanoantenna array at resonant photon energy ($\lambda = 1.5$ μm). Dashed lines show the scaled by a factor of 1/2 polar diagrams of $P_2(\vec{d}, \vartheta, \varphi)$, the emission of a pair of synchronized dipoles separated by distance $\vec{d}$ (see explanation in the text).

chronized emitting dipoles attached to different antennas in the array. This opens a way to manipulate an excited-state lifetime of a quantum emitter and to fabricate narrow beaming nanoscale antennas in the optical range.

References

[1] H. Gersen *et al*, *Phys. Rev. Lett.* **85**, 5312 (2000).
[2] J. Li *et al*, *Phys. Rev. B* **76**, 245403 (2007).
[3] H.F. Hofmann *et al*, *New J. Phys.* **9**, 217 (2007).
[4] S. Kühn *et al*, *Mol. Phys.* **106**, 893 (2008).
[5] T.H. Taminiau *et al*, *Opt. Express* **16**, 10858 (2008).
[6] A. Mohammadi *et al*, *New J. Phys.* **10**, 105015 (2008).
[7] G. Sun *et al*, *J. Opt. Soc. Am. B* **25**, 1748 (2008).
[8] G. Sun *et al*, *Appl. Phys. Lett.* **94**, 101103 (2009).
[9] A. Kinkhabwala *et al*, *Nat. Photon.* **3**, 654 (2009).
[10] R. Esteban *et al*, *Phys. Rev. Lett.* **104**, 026802 (2010).
[11] A.F. Koenderink, Nano Lett. **9**, 4228 (2009).
[12] T. Kosako *et al*, *Nat. Photon.* **4**, 312 (2010).
[13] W.L. Barnes *et al*, *Nature* **424**, 824 (2003).
[14] A. Polman, *Science* **322**, 868 (2008).
[15] E.M. Purcell, *Phys. Rev.* **69**, 681 (1946).
[16] G.W. Ford and W.O. Weber, *Phys. Rep.*

Elastic scattering of light in opaline photonic crystals under the multiple Bragg diffraction conditions

A. V. Sel'kin[1,2], *T. A. Ukleev*[1,2], *A. Yu. Men'shikova*[3] and *N. N. Shevchenko*[3]

[1] Ioffe Physical-Technical Institute, St Petersburg, Russia
[2] St Petersburg State University, St Petersburg, Russia
[3] Institute of Macromolecular Compounds, RAS, St Petersburg, Russia

Abstract. Optical spectra of light specularly and diffusively reflected by an opaline photonic crystal made up of polystyrene spheres have been studied. A resonant enhancement of the light scattering in the vicinity of photonic stop-band edges of the crystal is observed. A careful structural and optical characterization of the sample is performed through analyzing Bragg reflection spectra in the framework of the dynamical diffraction theory, and dispersion curves of electromagnetic modes are computed. A comparison is made between the dispersion curves and spectral positions of the light scattering peaks, which indicates a key role of photonic density-of-states in shaping the diffuse reflection spectra.

Introduction

Elastic scattering of electromagnetic waves appeared as diffusive reflection of light from a condensed matter is indicative of its random spatial inhomogeneity [1]. An investigation of the medium when analyzing angle and spectral characteristics of scattered light permits important extra information to be obtained about its disorder degree both in the bulk and on interfaces. In the case of spatially periodic systems like photonic crystals (PhCs) [2] the diffusive component of the reflected field arises due to the elastic scattering of light from the random inhomogeneity against the background of a regular diffractive component. In this work, new optical phenomena associated with resonant elastic scattering of light from opaline PhCs are studied. Geometrical and spectral characteristics of the scattering indicatrix are analyzed. The spectra of scattered light are compared with the Bragg reflection bands and dispersion curves of the electromagnetic modes of the PhC. We pay attention to spectral features of the scattering cross-section which result from a strong modification in photonic energy spectrum for the three-dimensional PhC possessing a high dielectric contrast.

1. Experimental

The opaline PhCs under study are the films (of about 5 μm in thickness) made up of monodisperse polystyrene spheres. The particles synthesized by styrene and methacrylic acid emulsifier-free emulsion copolymerization initiated by potassium persulfate have a spherical shape, uniform surface and particle size distribution less than 2%. The Bragg reflection and elastic light scattering spectra are measured in *s*-polarized light when incoming *s*-polarized radiation is incident on the lateral reflecting surface (111) of the PhC film. The plane of incidence coincided with the plane of scattering. The azimuth orientation of the sample was chosen for the plane of incidence be perpendicular to the oblique crystal planes (002) and (11$\bar{1}$). The sample was roughly oriented with a scanning electron microscope but it was more precisely positioned using measured Bragg reflection spectra under the multiple Bragg diffraction conditions [3]. Electron microscopy images allowed us to determine the mean distance, $a_{00} \approx 280$ nm, between neighboring particles placed in the lateral plane.

The spectral measurement results shown in Fig. 1 demon-
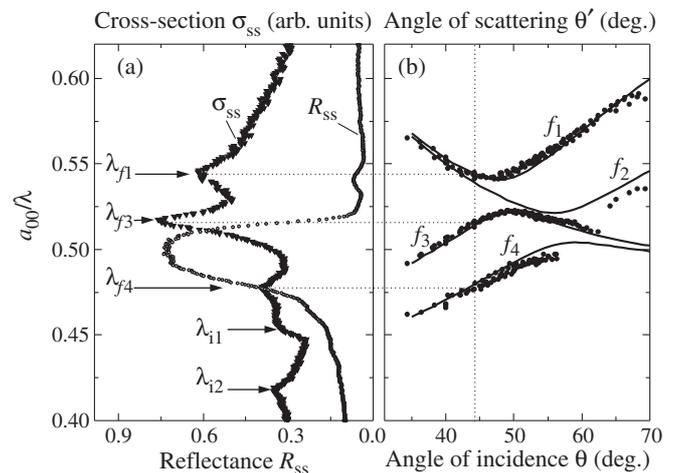
Fig. 1. (a) Spectra of *s*-polarized light specularly (R_{ss}) and diffusively (σ_{ss}) reflected by the opaline PhC made up of polystyrene spheres: R_{ss} for the incidence angle $\theta = 44°$, σ_{ss} for the incidence and scattering angles $\theta = 0°$ and $\theta' = 44°$, respectively; in the normalized frequency a_{00}/λ, a_{00} is the distance between neighboring spheres in the lateral plane, λ is the wavelength of light in vacuum. (b) Location of the scattering peaks in the σ_{ss}-spectra as a function of θ' at normal incidence of light (symbols — experiment, solid lines — theory).

strate more important features in the diffusive reflection spectrum. In Fig. 1a, the light scattering spectrum (the curve σ_{ss} for the angle of incidence $\theta = 0°$ and the angle of scattering $\theta' = 44°$), is compared with the specular Bragg reflection spectrum (at the angle of incidence $\theta = 44°$). It is worth noting that the maximum intensity of the diffusive scattering is three-four orders of magnitude less than that of the specular (Bragg) reflection.

The light scattering spectrum shows a rather rich structure. At least, five peaks (λ_{i1}, λ_{i2}, λ_{f1}, λ_{f3} and λ_{f4}) are present in the σ_{ss} spectrum. The dependencies of scattering peak positions on the scattering angle θ' at the fixed angle of incidence $\theta = 0°$ are shown in Fig. 1b by experimental dots on the corresponding curves f_1 to f_4. As to the peaks λ_{i1} and λ_{i2}, their spectral positions don't depend on the angle θ' if θ is fixed. A comparison between the spectra $\sigma_{ss}(\theta = 0°, \theta' = 44°)$ and $R_{ss}(\theta = 44°)$ shows that the scattering peaks appear on the

short- and long-wavelength edges of the main reflection band $R_{\text{ss}}(\theta = 44°)$, whereas the scattering peak λ_{f1} corresponds to the additional (in the short-wave range) peak in the R_{ss} spectrum. As this takes place, the spectral maxima λ_{i1} and λ_{i2} observed in the long-wave range of the entire spectrum arise on the Bragg reflection band edges for the normal incidence of light (the spectrum $R_{\text{ss}}(\theta = 0°)$ isn't depicted in Fig. 1).

Measuring in detail the angle dependencies of the $\sigma_{\text{ss}}(\theta, \theta')$ spectra, we found their high sensitivity to the values of θ and θ'. A strong correlation of the scattering peak positions with the band edges of the Bragg reflection is always observed. In Fig. 1b, the results of the measurements for the fixed angle of incidence $\theta = 0°$ and for different angles of scattering θ' are depicted by black circles. The vertical dashed line corresponds to the angle of scattering $\theta' = 44°$ used in measuring the σ_{ss} spectrum in Fig. 1a. The same line denotes the angle of incidence $\theta = 44°$ at which the Bragg reflection spectrum R_{ss} is recorded.

As can be seen from Fig. 1b, the scattering peak positions λ_{f1}, λ_{f3} and λ_{f4} as a function of the scattering angle θ' are given by smooth curves (respectively, f_1, f_3 and f_4) which form a well defined anti-crossing area (for f_1 and f_3 in the vicinity of the $\theta' \approx 48°$). The branch f_1 is measured experimentally in a rather wide range of angles $34° < \theta' < 70°$, whereas the experimental branches f_3 and f_4 are measurable only up to $\theta' \approx 63°$ and $\theta' \approx 57°$, respectively. At higher θ' values, the scattering peaks disappear on the continuous background of the diffusive reflection. On the other hand, the scattering spectrum manifests at $\theta' > 63°$ the weak peaks λ_{f2} (the f_2 branch) which also correlate with the long-wave edge of the Bragg reflection band.

2. Theoretical model and discussion

The fact that the positions of diffusive reflection peaks in the $\sigma_{\text{ss}}(\theta, \theta')$ spectra coincide with the edges of the specular Bragg reflection bands $R_{\text{ss}}(\theta)$ and $R_{\text{ss}}(\theta')$ allows us to make a conclusion about an important role of the photonic density of states spectrum for the spectral behavior of the elastic light scattering. Namely, the diffusive reflection peaks correspond to the photonic stop-band edges, where the density of such states reaches the maximum values.

In order to validate such conclusion, we carried out a careful structural and optical characterization of the PhC sample under study in the framework of the approach proposed earlier [3]. As a result, the values of the main geometrical and dielectric parameters have been found that give true energy positions of the Bragg reflection bands and describe qualitatively the reflectance contours both for *s*- and *p*-polarization of light. With the parameter values determined we calculated numerically the energy spectrum (dispersion curves) of the electromagnetic modes of the sample. It should be emphasized that the dispersion curves calculated are the same that used in computation of the Bragg reflection contours, i.e., they include the decaying stop-band modes which are of crucial importance in the presence of boundaries.

A comparison between the dispersion curves and spectral positions of the light scattering peaks did show that the cross-section is enhanced in the optical frequency domains where the mode group velocity V_{g} becomes anomalously low, i.e., the electromagnetic density of states drastically increases. In

Fig. 1b, the solid lines represent the computed positions of the singular points ($V_{\text{g}} = 0$) on the TE-mode dispersion curves as a function of the incidence angle θ. The complex multi-mode character of the photonic energy spectrum follows directly from including the multiple Bragg diffraction effects in the theoretical model under consideration [4]. The theoretical curves are seen to be well consistent with the experimental data (the symbols on the solid lines f_1 to f_4) confirming our deduction about the resonant enhancement of the elastic scattering of light in the vicinity of singularities in the energy spectrum of the PhC electromagnetic eigen-states. Note that the phenomenon of the resonant elastic scattering of light in spatially periodic medium has recently been demonstrated theoretically [5] with a planar Bragg structure (1D photonic crystal) possessing statistically rough interfaces.

3. Conclusion

In connection with the results presented in this work, it should be particularly emphasized that the theoretical and numerical analysis of the Bragg reflection spectra and dispersion relations for the PhC eigenmodes were carried out in the framework of the dynamical theory of light diffraction. Such an approach allowed us, without complicated and time consuming numerical modeling, on a basis of relatively simple analytical expressions, to gain more penetrating insight into physical mechanisms responsible for optical phenomena observed in PhCs including the novel effects of elastic scattering of light in PhCs under the multiple Bragg diffraction conditions.

References

[1] A. Ishimaru, *Wave Propagation and Scattering in Random Media, IEEE Press, Oxford University Press*, (IEEE Press, Oxford University Press) 574 (1997).

[2] J.D. Joannopoulos, S.G. Johnson, J.N. Winn, R.D. Meade, *Photonic Crystals: Molding the Flow of Light (2nd edition)*, (Princeton: Princeton University Press) 304 (2008).

[3] A.G. Bazhenova, A.V. Sel'kin, A.Yu. Men'shikova, and N.N. Shevchenko, *Physics of the Solid State* **49** 11, 2109 (2007).

[4] V.G. Fedotov, A.V. Sel'kin, A.Yu. Men'shikova, N.N. Shevchenko, and A.V. Yakimanskiy, *Proc. of 17th Int. Symp. "Nanostructures: Physics and Technology"* (Minsk, Belarus, 2009), 109 (2009).

[5] A.V. Sel'kin, V.A. Kosobukin, Yu.N. Lazareva, and A.K. Zharinov, *Proc. of 18th Int. Symp. "Nanostructures: Physics and Technology"* (St Petersburg, Russia, 2010), 312 (2010).

Opal-based photonic crystal heterostructures: Multiple Bragg diffraction effects

V. G. Fedotov

Faculty of Physics, St Petersburg State University, St Petersburg, Russia
Ioffe Physical-Technical Institute, St Petersburg, Russia

Abstract. New approach to the quantitative description and analysis of reflection and transmission spectra of photonic crystal heterostructures is suggested. The spectra of reflectance and transmittance are calculated using the dynamical diffraction theory generalized to the case of high dielectric contrast of a three-dimensional spatially periodic medium. Comparison of the calculated contours with the reflection contours of the semi-infinite photonic crystals and the energy spectra of electromagnetic eigenmodes is performed.

Introduction

Photonic crystal (PhC) structures (spatially periodic solid-state structures whose dielectric constant is modulated with spacing comparable to the light wavelength) are considered to be promising materials for optoelectronics and nanophotonics [1]. Such structures attract also much attention in up-to-date studies due to the fundamental scientific problems which come about in attempting to explain PhC mediated optical phenomena [2].

PhC heterostructures consisting of PhCs differing in dielectric (permittivity) or structural (lattice geometry) parameters could be used as prospective structures for designing light-manipulating devices in laser and telecommunication technologies such as effective waveguides and light traps [3].

In this paper, we show the results of theoretical studies of shaping mechanisms for reflection and transmission spectra of the PhC heterostructures based on thin films of three-dimensional (3D) PhCs. Here, we consider the heterostructures consisting of two PhC films with the symmetry of face-centered cubic opal lattice. The effects of the multiple Bragg diffraction (MBD) [4] due to three-dimensionality of the structure were taken into account. At the same time the interference effects that appear due to reflection of electromagnetic field eigenmodes inside the structure from external interfaces as well as from the heterointerface were considered.

1. Results

The reflection and transmission spectra are calculated using the dynamical multiple diffraction theory generalized to the case of high dielectric contrast of a 3D spatially periodic medium within the framework of three-band mixing approximation [5]. In such a case, simultaneous diffraction from two systems of crystal planes, (111) and (11$\bar{1}$), taking into account, with the (111) planes being parallel to the reflecting surface of the structure, and the (11$\bar{1}$) planes being non-parallel to the reflecting surface. Based on this approximation, an approach is proposed to the analysis of complex-shape contour of the Bragg reflection from a PhC heterostructure.

Typical values of structural and dielectric parameters of the opal-like PhCs fabricated from spherical polystyrene particles [6] were used for numerical calculations of the spectra. The permittivity of the spherical particles forming the structure $\varepsilon_a = 2.522$ and the permittivity of pores $\varepsilon_b = 1$. Particle diameter for the first of the films forming the heterostructure was chosen to be 300 nm and for the second of the films was chosen to be 375 nm. Calculations were performed for *s*- and *p*-polarized light at the incidence angle $\theta = 57°$ at which
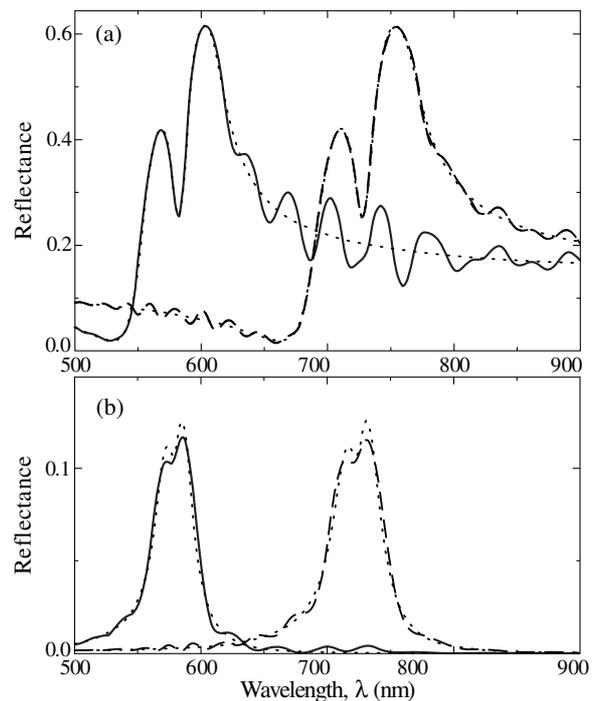
Fig. 1. Bragg reflection spectra of a photonic crystal heterostructure assembled from polystyrene spheres of 300 nm in diameter (20 monolayers) and 375 nm in diameter (20 monolayers). The incidence angle $\theta = 57°$ for *s*- (a) and *p*- (b) polarized light. The solid curve corresponds to reflection from the film assembled from spheres of 300 nm in diameter. The dashed curve corresponds to reflection from the film assembled from spheres of 375 nm in diameter. The dotted curves are the reflection spectra from semi-infinite photonic crystal structures assembled from spheres of appropriate diameter.

the MBD is most pronounced. Dissipative channels of energy losses and additional elastic scattering of light can be taken into account in the phenomenological manner by including an additional imaginary term $i\varepsilon_0''$ into the average permittivity of the PhC material. The imaginary part of the average permittivity is taken to be $\varepsilon_0'' = 0.05$. Thickness of the films forming the heterostructure were specified by the number of monolayers $N_{ml1} = N_{ml2} = 20$. It is worth noting that the shape of reflectance and transmittance contours substantially depends on the details of the boundary conditions at the external interfaces as well as at the internal heterointerface.

The calculated spectra of the Bragg reflection from a PhC
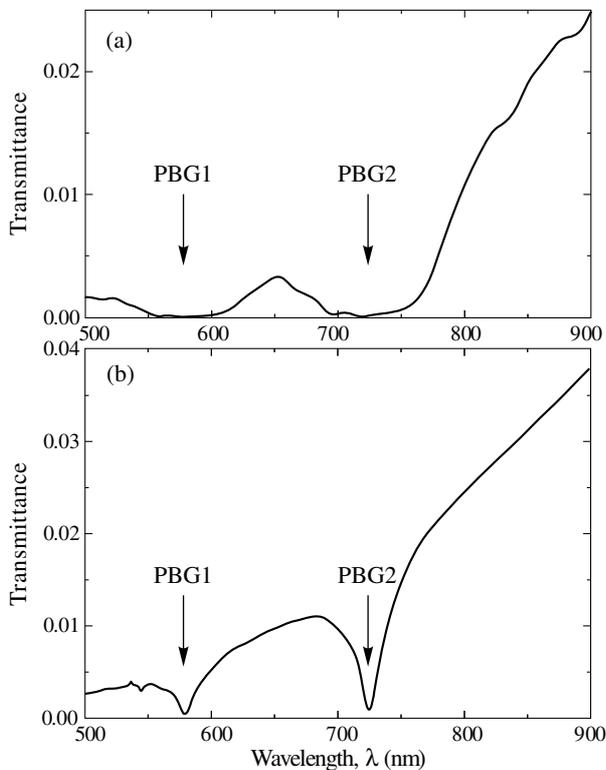
**Fig. 2.** Transmission spectra of a photonic crystal heterostructure assembled from polystyrene spheres of 300 nm in diameter (20 monolayers) and 375 nm in diameter (20 monolayers). The incidence angle $\theta = 57°$ for s- (a) and p- (b) polarized light. The solid curve corresponds to reflection from the film assembled from spheres of 300 nm in diameter. The dashed curve corresponds to reflection from the film assembled from spheres of 375 nm in diameter.

heterostructure are shown in Fig. 1 by solid and dashed curves. In this case, the solid curves correspond to reflection from the film consisting of spherical particles of 300 nm in diameter and the dashed curves correspond to reflection from the film consisting of spherical particles of 375 nm in diameter. The resonant features are expressed more weakly for *p*-polarized light which is associated with a smaller width of main photonic stop-band for the corresponding polarization compared with *s*-polarized light [6]. As we see, upon reflection, in both cases the spectra exhibit a peak with a dip caused by the diffraction of light from the $(11\bar{1})$ system of oblique crystal planes [4]. However, since the dielectric properties of the films are identical, the MBD conditions should take place for both PhC films at the same angle of incidence of light on the structure. Thus, two doublet structures (corresponding to the two parts of the heterostructure) should appear in the spectrum of the PhC heterostructure.

2. Discussion

The observed spectral features correspond to the position of the photonic band gap (PBG) of the film, at the side from where the light falls. This fact becomes clear from comparing the spectra of light reflection from PhC heterostructure with the spectra of light reflection from a semi-infinite PhC consisting of particles of the same diameter. The spectra of the Bragg reflection of light from a semi-infinite PhC formed by particles of the same diameter as the corresponding PhC films are shown in Fig. 1 by dotted curves.

The observed phenomenon explanation is as follows. When light is reflected from the considered PhC heterostructure, the extinction length (defined by the imaginary part of the mode wave vector) is much smaller than the structure thickness due to the effects of absorption and diffuse scattering. This leads to the fact that much less light reaches the far part of the heterostructure than the near part. As a result, the resonance associated with the PBG of far (with respect to the light source) PhC film exhibits in the reflection spectra is much weaker than the resonance associated with the PBG of the near film.

Distortion of the classical Fabry–Pérot interference pattern in the off-resonant region of the spectrum is due to the complex nature of the interference on the three interfaces (the outer surfaces of the PhC heterostructure and the internal heterointerface). Increasing of Fabry–Pérot oscillations intensity in the spectral range of PBG of the far (with respect to the light source) PhC film is as follows. The existence of PBG reduces the extinction length for the corresponding film in the resonant region. This results in raising of interference on the interfaces of the near PhC film.

Fig. 2 shows the transmission spectra of the PhC heterostructure. The figure shows that regardless from which side of the structure light falls there are two transmission bands corresponding to the PBGs of each PhC films forming the heterostructure in the transmission spectra (for both *s*- and *p*-polarized light).

In conclusion, this paper generalizes the previously proposed approach [5,7] to analyze the spectra of Bragg reflection from PhCs. The theory developed in this paper is also based on the numerical models of electromagnetic wave interaction with the PhC medium, which are relatively simple and do not require tedious numerical calculations. Reflection and transmission spectra of the PhC heterostructures are calculated. An analysis of features (directly related to the peculiarities of the dispersion relations of electromagnetic field eigenmodes in the films forming the heterostructure) manifested in such spectra is made.

References

[1] J.D. Joannopoulos, S.G. Johnson, J.N. Winn, and R.D. Meade, *Photonic Crystals. Molding the Flow of Light* (Princeton University Press, Princeton – Oxford, 2008).

[2] K. Sakoda, *Optical Properties of Photonic Crystals* (Springer, Berlin – Heidelberg – New York, 2005).

[3] E. Istrate and E.H. Sargent, *J. Opt. A: Pure Appl. Opt.* **4**, 242 (2002).

[4] H.M. van Driel and W.L. Vos, *Phys. Rev. B* **62**, 9872 (2000).

[5] V.G. Fedotov, A.V. Sel'kin, A.Yu. Men'shikova, N.N. Shevchenko, and A.V. Yakimanskiy, *Proc. of 17th Int. Symp. "Nanostructures: Physics and Technology"*, Minsk, Belarus, 2009, p. 109.

[6] A.G. Bazhenova, A.V. Sel'kin, A.Yu. Men'shikova, and N.N. Shevchenko, *Phys. Solid State* **49**, 2109 (2007).

[7] A.V. Sel'kin, *Proc. of 12th Int. Symp. "Nanostructures: Physics and Technology"*, St Petersburg, Russia, 2004, p. 111.

On dynamical diffraction theory in reflection and transmission spectroscopy of 3D photonic crystal films

V. G. Fedotov[1,2] and *A. V. Sel'kin*[2,1]

[1] Faculty of Physics, St Petersburg State University, St Petersburg, Russia
[2] Ioffe Physical-Technical Institute, St Petersburg, Russia

Abstract. A study is made of Bragg reflection and transmission spectra for three-dimensional opal-like photonic crystal slabs using numerical experiments. A comparison between the results of a full-wave electrodynamic simulation and an analytical three-band mixing model is performed. The analytical approximation based on ideas of dynamical diffraction theory is shown to describe correctly the complex shape of the Bragg reflection and transmission contours due to the three-dimensional character of diffraction. The striking interference pattern (interference "comb") predicted early in the framework of the simple analytical model is reproduced in detail with the full-wave numerical calculations.

Introduction

Photonic crystal (PhC) structures (spatially periodic solid-state structures whose dielectric constant is modulated with spacing comparable to the light wavelength) are considered to be promising materials for optoelectronics and nanophotonics [1]. Such structures attract also much attention in up-to-date studies due to the fundamental scientific problems which come about in attempting to explain PhC mediated optical phenomena [2].

Physics of PhCs is substantially based on the well-known electrodynamics equations. Methods for solving many practical problems relating to such systems are known [3]. However, as a rule, these recipes are of general character. They require tedious numerical calculations and do not provide clear understanding the mechanisms of light interaction with spatially confined PhC structures. Rather simple models permitting calculations and the analysis of real optical spectra (such as reflection and transmission) containing principal information about PhCs are not developed (or are not quite investigated) nowadays. In particular, dynamical aspects of a strong modification of the Bragg reflection spectra under the multiple Bragg diffraction (MBD) conditions (i.e., due to the resonant light scattering simultaneously by several systems of intercepted crystal planes) [4] remain not clear enough.

In this paper, we study Bragg reflection and transmission spectra formed by resonant light diffraction from a three-dimensional (3D) opal-like PhC using dynamical multiple diffraction theory as well as numerical experiment (full-wave electrodynamic simulation). Here, we justify applicability of the dynamical diffraction theory to PhCs possessing high dielectric contrast. Particular attention is paid to a new interference effects which are manifested for thin PhC films of high enough perfection.

1. Theoretical model

The eigenmode dispersion curves and zero-order diffraction (reflection and transmission) spectra are calculated using the dynamical multiple diffraction theory generalized to the case of high dielectric contrast of a 3D spatially periodic medium within the framework of three-band mixing approximation [5]. In such a case, only the terms corresponding to the $\mathbf{G}_{111}$ and $\mathbf{G}_{11\bar{1}}$ reciprocal lattice vectors survive in the dielectric function,

$$\varepsilon(\mathbf{r}) = \varepsilon_0 + \varepsilon_{111}e^{i\mathbf{G}_{111}\mathbf{r}} + \varepsilon_{11\bar{1}}e^{i\mathbf{G}_{11\bar{1}}\mathbf{r}} + \varepsilon_{111}^*e^{-i\mathbf{G}_{111}\mathbf{r}} + \varepsilon_{11\bar{1}}^*e^{-i\mathbf{G}_{11\bar{1}}\mathbf{r}},$$
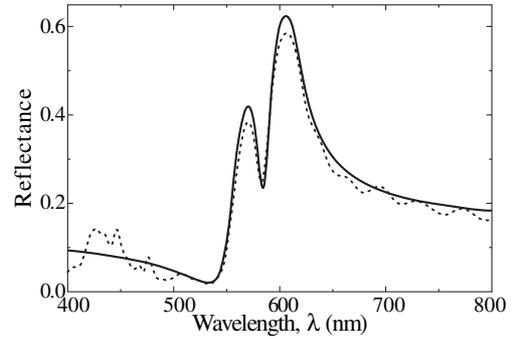
Fig. 1. Bragg reflection spectra of an opal-like photonic crystal (assembled from polystyrene spheres of 300 nm in diameter). The solid curve is calculated within the three-band mixing approximation (diffraction only from (111) and (11$\bar{1}$) crystal planes) for a semi-infinite photonic crystal. The dotted curve is the result of full-wave electrodynamics simulation (with a discretization of Maxwell's equations) for a photonic crystal film with the 21 monolayers thickness. The incidence angle $\theta = 57°$, the imaginary part of the average permittivity is taken to be $\varepsilon_0'' = 0.05$.

where $\varepsilon_0 = \varepsilon_a f + \varepsilon_b(1 - f)$ is the average permittivity of PhC assembled from the spheres of permittivity ε_a and pores with permittivity ε_b, f is the filling volume fraction of the spheres in PhC, and ε_{111} and $\varepsilon_{11\bar{1}}$ are the appropriate Fourier coefficients which characterize the spatial modulation of $\varepsilon(\mathbf{r})$ along the [111] and [11$\bar{1}$] directions, respectively.

Calculations of the spectra are performed with an account of the $\omega(\mathbf{K})$ dispersion relations for the electromagnetic modes excited inside PhC. Such relations are derived by placing a self-consistency condition on the superposed incident ($\mathbf{G} = 0$) and diffracted ($\mathbf{G} = \mathbf{G}_{111}, \mathbf{G}_{11\bar{1}}$) waves and are governed by the dispersion equation

$$\mathbf{K}^2 - k_0^2\varepsilon_0 = \frac{|\varepsilon_{111}|^2 k_0^4}{(\mathbf{K} - \mathbf{G}_{111})^2 - k_0^2\varepsilon_0} + \frac{|\varepsilon_{11\bar{1}}|^2 k_0^4}{(\mathbf{K} - \mathbf{G}_{11\bar{1}})^2 - k_0^2\varepsilon_0},$$

where $k_0 = \omega/c$ is the magnitude of the free-space wave vector, ω is the frequency, and c is the velocity of light in free space. The Maxwellian boundary conditions of continuity of tangential components for electric and magnetic fields are assumed to be held so that the fields in the surface plane are matched for each spatial Fourier component [2].

Full-wave electromagnetic simulations are carried out using a discretization of Maxwell's equations on a grid of spatial coordinates for the exact formulation of the problem [3]. The
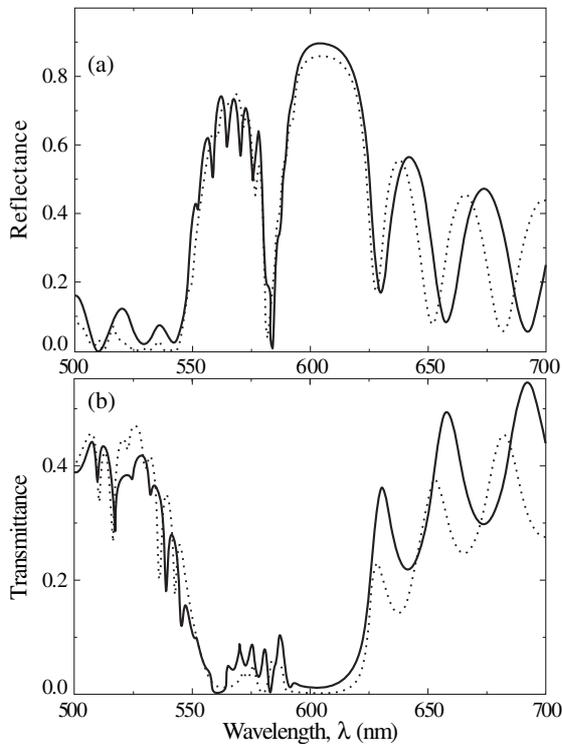
Fig. 2. Bragg reflection (a) and transmission (b) spectra of an opal-like photonic crystal film (assembled from polystyrene spheres of 300 nm in diameter) with the 21 monolayers thickness. The solid curve is calculated within the three-band mixing approximation (diffraction only from (111) and (11$\bar{1}$) crystal planes). The dotted curve is the result of full-wave electrodynamics simulation (with a discretization of Maxwell's equations). The incidence angle $\theta = 57°$, the imaginary part of the average permittivity is taken to be $\varepsilon_0'' = 0.01$.

periodic boundary conditions were applied for computational domain in the directions perpendicular to the [111] to consider infinite slab and the absorbing boundary conditions were applied in the [111] direction for the case of infinite open space.

Typical values of structural and dielectric parameters of the opal-like PhC fabricated from spherical polystyrene particles were used for numerical calculations of the spectra. Specifically, for polystyrene $\varepsilon_a = 2.522$ and for vacuum $\varepsilon_b = 1$. Calculations were performed for *s*-polarized light at the incidence angle $\theta = 57°$. Dissipative channels of energy losses and additional elastic scattering of light can be taken into account in the phenomenological manner by including an additional imaginary term $i\varepsilon_0''$ into the average permittivity of the PhC material.

2. Results and discussion

Comparison between the results of the full-wave electrodynamic simulation for a PhC film with the 21 monolayers thickness and those obtained in the three-band mixing approximation for a semi-infinite PhC is given in Fig. 1. This comparison shows that the more remarkable differences between the full-wave simulation and the analytical approximation used is only observed near the short-wave edge of the spectral range considered.

Physical reason of the results discussed is as follows. In the spectral range of interest, for the diameters of particles constituting PhC, no other peculiarities, except for those generated

by crystal planes (111) and (11$\bar{1}$), exist. Remarkable contribution to the energy spectrum in this spectral range is due to only (111) and (11$\bar{1}$) planes, as well. Thus, the three-band mixing approximation correctly describes the positions of spectral peculiarities (Bragg peak and dip in reflection) as well as the shape of the reflection contour.

The reflection and transmission spectra of PhC film possessing high enough structural perfection ($\varepsilon_0'' = 0.01$) is shown in Fig. 2. An additional short-periodic Fabry–Pérot-like interference structure (interference "comb") is seen in the resonant range of the spectra. This structure is due to the spatial quantization of additional low-group-velocity modes [6], and is clearly demonstrated by the results of the numerical experiment (full-wave simulation). Such extra structure disappears with increasing the imaginary part of permittivity, which corresponds usually to the deterioration of the PhC structural quality.

It is important to emphasize that relatively simple numerical models of electromagnetic wave interaction with the PhC medium allow for 3D character of light diffraction and permit correct description of the Bragg reflection contour doublet structure which appears due to the MBD effects. Our calculations justify the approach to the analysis and quantitative description of the Bragg reflection complex-shape contour suggested previously [5] and allows one to calculate in a simple analytical way the Bragg reflection spectra of opal-like PhCs.

In conclusion, comparison between the results of the full-wave electrodynamic simulation (using discretization of Maxwell's equations for the exact formulation of the problem) and those obtained within the three-band mixing approximation is performed. It is shown that this approximation, based on the dynamical diffraction theory, describes correctly the complex shape of the Bragg reflection contour associated with the 3D character of diffraction. The effect of the interference "comb" predicted previously for Bragg reflection and transmission spectra of thin opal-like PhC films is confirmed by the full-wave electrodynamic computations.

References

[1] J.D. Joannopoulos, S.G. Johnson, J.N. Winn, and R.D. Meade, *Photonic Crystals. Molding the Flow of Light* (Princeton University Press, Princeton–Oxford, 2008).

[2] K. Sakoda, *Optical Properties of Photonic Crystals* (Springer, Berlin–Heidelberg–New York, 2005).

[3] A. Bondeson, T. Rylander, P. Ingelström, *Computational Electromagnetics* (Springer, New York, 2005).

[4] S.L. Chang, *Multiple Diffraction of X-Rays in Crystals* (Springer, Berlin–Heidelberg–New York–Tokyo, 1984).

[5] V.G. Fedotov, A.V. Sel'kin, A.Yu. Men'shikova, N.N. Shevchenko, and A.V. Yakimanskiy, *Proc. of 17th Int. Symp. "Nanostructures: Physics and Technology"*, Minsk, Belarus, 2009, p. 109.

[6] V.G. Fedotov and A.V. Sel'kin, *Proc. of 18th Int. Symp. "Nanostructures: Physics and Technology"*, St Petersburg, Russia, 2010, p. 302.

Radiating gathering enhancement of X-ray waveguide-resonator

V. K. Egorov, E. V. Egorov

IMT RAS, 142432 Chernogolovka, Moscow District, Russia

Abstract. The problem of integral intensity increase of radiation beams formed by the planar X-ray waveguide-resonator (PXWR) is discussed. Original solution of the problem in form of the input skewed concentrator for PXWR is presented. This allowed to increase the device radiation gathering power on five times.

The basic features of the waveguide-resonance mechanism for X-ray radiation propagation managed to be understood in result of systematical researches of X-ray flux transportation efficiency showed by an air planar extended slit clearance (planar X-ray guide) formed by flat quartz plates (reflectors) in the conditions of the slit width variation [1]. The obtained data allowed to plot the experimental dependence of CuK$\alpha\beta$ flux integral intensity formed by such X-ray guide on width of its slit clearance. Similar measurements for X-ray beam former built on base of the double slit-cut system consisting of two vertical slit-cuts with distance between them equal to X-ray guide length were executed for comparison. Both experimentally received dependences are presented in Figure 1. X-ray beam formation by the double slit-cut system was executed for the slit width dimention interval 6-100 mm. The dependence is well approximated by linear function. The propagation of X-ray beam formed by any slit-cut systems is described by the mechanism of its free stream. Similar dependence for the quartz X-ray guide managed to be constructed for wider dimentional interval of 0.02–100 mm. This dependence has been described by three linear sections: 0–200 nm (a); 0.2–3 mm (b); 3–100 mm (c). The wide size interval (c) corresponds to well studied area of X-ray flux propagation on the superposition basis of the free stream mechanism and the multiple consecutive external total reflection on the surfaces forming the capillary channel. Approximation of the dependence characteristic for the capillary dimentional interval into the nanosize area shows an evident inconsistency of the mentioned mechanisms for an explanation of high flux transportation efficiency magnitude featuring for the planar X-ray guides with a slit clearance width $s < 3$ mm. This fact allowed to assume that the nanosize area is characterized by X-ray flux propagation mechanism differing from earlier known. There was offered to conside the area (b) as an interval of the changed propagation mechanism. The new mechanism has received the name of a waveguide-resonance propagation of X-ray quasimonochromators radiation flux. The model of it managed to be constructed being based on the radiation fundamental parameter — its coherence length L ($L = \lambda_0^2/\Delta\lambda$), where λ_0 is average value of the radiation wavelength, $\Delta\lambda$ is degree of its monochromaticity). The phenomenon of X-ray beam total external reflection (TER) on the material interface is connected with formation of X-ray standing wave area [2]. The size of this area is defined by half of the radiation coherence length [1]. $L/2$ value for CuK$\alpha\beta$ radiation is equal to 196 nm. This magnitude is approximately coinciding with top border of the dimensional interval (a). On base of this correlation the conclusion has been drown that basic distinction between the multiple total reflection and the mechanism of waveguide-resonance stream is connected with presence or absence of mutual overlapping for local interference field areas of X-ray standing wave (Fig. 2). In condition of the waveguide-resonance mechanism realization ($s < L/2$) X-ray flux excites the uniform interference field of X-ray standing wave in whole volume of the extended slit clearance. This field allows to transport of X-ray radiation flux almost without attenuation. The device working in frame of this mechanism realization was called the planar X-ray waveguide-resonator (PXWR).

1. Specific features of PXWR

The PXWR captures a radiation flux in the angular interval corresponding to a double critical angle of the radiation TER for a reflector material. It forms X-ray beams with nanosize width. Owing to essential distinction of X-ray source focus projection width and the width of PXWR slit clearance, this device forms radiation beams with enhanced radiation density. Despite a little size of the waveguide-resonator slit clearance, its emergent beam is not accompanied by diffraction satellites. PXWR reduces intensity of the white radioactive component in energy spectrum of the emergent beam owing to the worst spatial coherence of this component. But PXWR of simplest design is characterized by is the rather big angular divergence of the emergent beam near $0.1-0.2°$. Besides, the PXWR

Fig. 1. Scheme for study of intensity spatial distribution in beams formed by planar waveguide, real distributions and dependences of the beam integral intensities formed by waveguide (1) and double slit-cut unit (2).
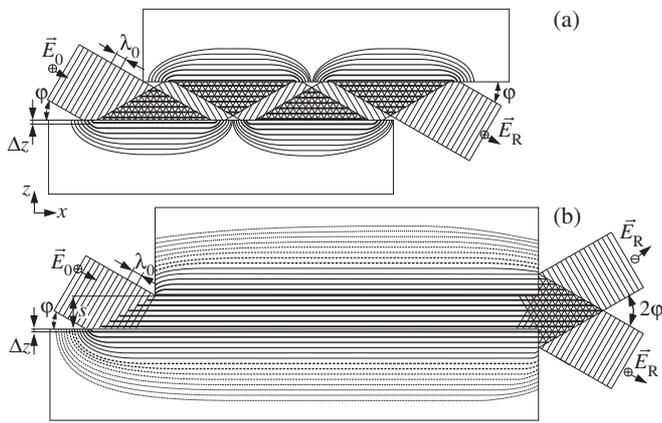
Fig. 2. Schemes of X-ray flux propagation through a planar extended slit clearance accordingly to the multiple total external reflection mechanism (a) and by the waveguide-resonance one (b).
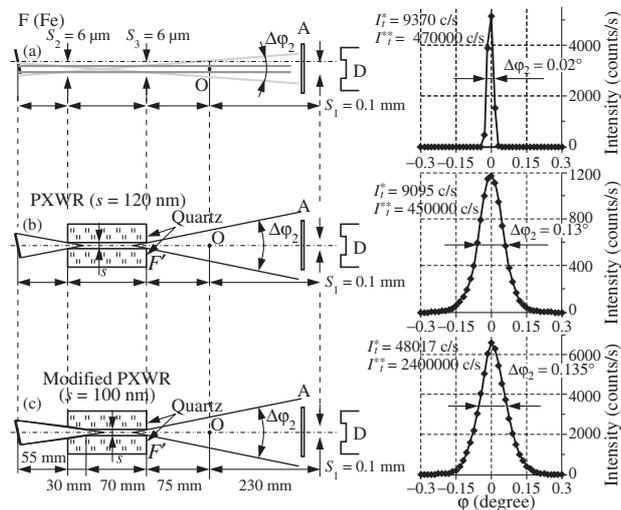
Fig. 3. Schemes for study of FeK$\alpha\beta$ spatial intensity distribution and respective distribution in beams formed by the double slit-cut system (a), the simple PXWR (b) and the modified waveguide-resonator (c).

forms X-ray beams conceding on the integral intensity parameter to beams formed by both the double slit-cut system and monocapillaries (Fig. 1). This work presents the attempt to raise PXWR radiation gathering power by modification of its design.

2. PXWR equipped by the skewed concentrator

As the PXWR is capable to capture into the extended slit clearance only small part of X-ray flux irradiated by X-ray tube, it shows up a quite obvious to increase of its radiating gathering power by rise of the radiating capture efficiency. The most rational method of this problem solution in the context of simplicity of its experimental realization to equip a simple PXWR by the total reflection input skewed concentrator. To bypass the aligning problems it was suggested to built of PXWR on base of specific construction reflectors. Third of its working surface was grinded away under the angle which was equal to half from magnitude of TER critical angle. Furthermore, titanium strips were deposited on the reflector edges. (Strips thickness defines the width of PXWR slit clearance.) The modified PXWR was configured from two upgraded reflectors, and, in result, we received the input mouth with the angular width which was not exceed TER critical angle magnitude for reflector material.
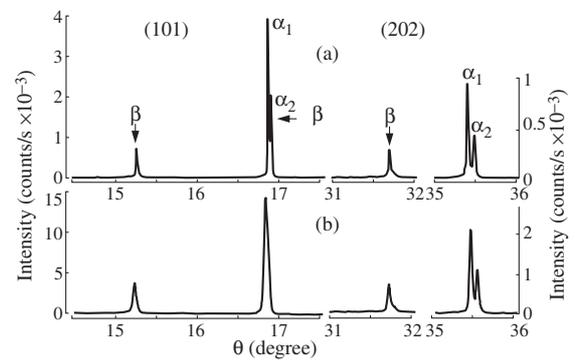
Fig. 4. Diffraction patterns fragments of the (101) SiO$_2$ single crystal obtained with FeK$\alpha\beta$ diffracted beams formed by the double slit-cut system (a) and the modified PXWR (b).

3. Testing of skewed concentrator efficiency

For the comparative analysis of X-ray beam parameters formed by modified PXWR it was executed study of intensity spatial distributions in FeK$\alpha\beta$ beam formed by PXWR with simplest construction ($s = 120$ nm), double slit-cut system completed by two slit-cuts ($S_1 = S_2 = 6$ mm) with distance between them corresponding to the PXWR lenght and modified waveguide-resonator. Measuring schemes and experimental diagrammes of intensity spatial distributions are presented in Figure 3. Measurements was executed in conditions of X-ray source BSW-24 (Fe) working regime $U = 20$ keV, $I = 10$ mA. Envelope form of distributions and its FWHM (full width at half maximum) for beams formed by simplest and modified PXWRs are practically identical. But the integral intensity of the modified waveguide-resonator emergent beam is higher on five times. The received result is below as the expected one, apparently, owing to the correct coordination absence between skewed concentrator and PXWR slit clearance. Comparison of FeK$\alpha\beta$ intensity distribution parameters in beams formed by the double slit-cut system and both PXWRs shows that the slit-cut unit has on its output X-ray beams with smaller angular divergence.

Besides intensity spatial distribution study in beams formed by the slit-cut unit and both PXWRs it was executed a comparative testing of the beams application possibilities for X-ray practical diffractometry. Figure 4 shows fragments of SiO$_2$ monocrystal diffraction patterns received in conditions of the beams diffraction formed by the slit-cut unit and the modified waveguide-resonator. In case of the PXWR application the diffraction peaks intensity is higher in comparison with the slit-cut unit using. But the slit-cut unit allows to achieve a better angular resolution. It is needed to remember that PXWR including into the diffractometer setup leads to destroy of the Bragg–Brentano focusing geometry owing to appearing of the virtual focus F' (Fig. 3). Optimal conditions of PXWR application for X-ray diffractometry demands the second PXWR including into the diffractometer registration brench.

4. Conclusion

The presented results show that the skewed concentrator including into the waveguide-resonator optical scheme increases its radiation gathering power, essentially.

References

[1] V.K. Egorov *et al*, *X-ray Spectrometry* **33**, 360 (2004).
[2] M. Medzyk *et al*, *Phys. Rev. Lett.* **62**, 1376 (1989).

The fundamental obscurity in quantum mechanics. Why it is needed to shout "wake up"

V. V. Aristov and A. V. Nikulov

Institute of Microelectronics Technology RAS, 142432 Chernogolovka, Moscow region, Russia

Abstract. The orthodox quantum mechanics can describe results of observation but not an objective reality. Misunderstanding of its positivistic essence results to numerous mistaken publications, in particular about a possibility of a real quantum computer.

Introduction

The inevitable transition from classical world to quantum world because of the progressive miniaturization of nanostructures has prompted such fundamentally new idea as quantum computing [1]. The widespread interest in this idea seems quite valid. The minimal sizes of nanostructures come nearer to atomic level and subsequent miniaturization will not be possible in the near future. Therefore exponential increase of calculating resources with number of quantum bits has provoked almost boundless enthusiasm. This exponential increase seems possible thanks to the principle of superposition of states, interpreted [2] as the cardinal positive principle of quantum mechanics. Feynman [3] proposed universal simulation, i.e. a purpose-built quantum system which could simulate the physical behaviour of any other, noting that the calculation complexity of quantum system increases exponentially with number n of its elements. A system of n elements ψ_i with two observable values $+1$ or -1 should describe by the superposition

$$
\begin{aligned}
\psi &= \gamma_1 \psi_1(+)\psi_2(+)\cdots\psi_i(+)\cdots\psi_n(+) + \cdots \\
&+ \gamma_2 \psi_1(-)\psi_2(+)\cdots\psi_i(+)\cdots\psi_n(+) + \cdots \\
&+ \gamma_j \psi_1(-)\psi_2(-)\cdots\psi_i(-)\cdots\psi_n(+) + \cdots \\
&+ \gamma_N \psi_1(-)\psi_2(-)\cdots\psi_i(-)\cdots\psi_n(-)
\end{aligned} \tag{1}
$$

with $N - 1 = 2^n - 1$ independent variables γ_j. Feynman gave arguments which suggested that quantum evolution of (1) could be used to compute certain problems more efficiently than any classical computer. Indeed, it seems possible to change $N = 2^n$ variables γ_j with help of an influence on a single element ψ_i of the quantum system (1). This feature is referred to as quantum parallelism and represents a huge parallelism because of the exponential dependence on n: only 1000 elements, quantum bits, seems to replace $2^{1000} = 10^{301}$ classical processors [1].

The universal simulation proposed by Feynman could not result in the idea of universal quantum computer, possibility of which was substantiated by Deutsch [4]. In the early 1990's several authors sought computational tasks which could be solved by a quantum computer more efficiently than any classical computer. Shor has described in 1994 [4] an algorithm which was not only efficient on a quantum computer, but also addressed a central problem in computer science: that of factorising large integers. Armed with Shor's algorithm, it now appears that such a fundamental significance is established, by the following argument: either nature does allow a device to be run with sufficient precision to perform Shor's algorithm for large integers (greater than, say, a googol, 10^{100}), or there are fundamental natural limits to precision in real systems. Both eventualities represent an important insight into the laws of nature.

1. Could quantum computer be possible as a real device?

The Shor's algorithm has provoked numerous publications [6–8] growing rapidly about quantum computing and colossal efforts applied to creation of a real quantum computer. Because of this enthusiasm only few experts venture to doubt in the reality of quantum computer. Nevertheless this doubt is very valid. There is important to note first of all that the substantiation by Deutsch the possibility of a real universal quantum computer must be connected with his belief in the "Many Universes Theory" of quantum physics [9]. According to this idea when a particle changes, it changes into all possible forms, across multiple universes. Deutsch proving the connection between the reality of the quantum computer and the existence of the parallel universes asks in his book [10] *those who is still declined to count, that there is only one universe: "When Shor's algorithm has factorized number, having involved about 10^{500} computing resources which can be seen where this number was factorized on multipliers? About 10^{80} atoms exist in whole seen universe, the number is insignificant small in comparison with 10^{500} ".*

The unreality of the quantum computer only in one universe can be understood from the fact that the exponential increase of the number $N - 1 = 2^n - 1$ of independent variables of the quantum register (1) with the number n of quantum bits can be possible only at the invalidity of the relation

$$
\psi_i = \alpha_i \psi_i(+) + \beta_i \psi_i(-), \qquad \alpha_i^2 + \beta_i^2 = 1 \tag{2}
$$

for the superposition of states of each quantum bit. The invalidity of (2) can not be real only in one universe logically: the quantum bit (2) has only two states $\psi_i(+)$, $\psi_i(-)$ and the sum of their probability α_i^2, β_i^2 must be equal unity. The relations $\alpha_i^2 + \beta_i^2 = 1$ for each quantum bit reduce the quantum register (1) to the classical one with $N \approx n$.

2. Irremediably conflict of the entanglement with realism

The invalidity of (2) at the entanglement or EPR correlation was revealed by the opponent [11,12] of the Copenhagen interpretation in order to prove the incompleteness of the quantum description of physical reality. The EPR paradox has demonstrated irremediably conflict of the superposition principle with local realism: the collapse of the superposition

$$
\psi_{\text{EPR}} = \alpha_{\text{EPR}} \psi_1(+)\psi_2(-) + \beta_{\text{EPR}} \psi_1(-)\psi_2(+) \tag{3}
$$

describing the EPR pair at observation of one particle 1

$$\psi_{\text{EPR}} = \psi_1(+)\psi_2(-) \qquad (4)$$

implies instantaneous change of the state of the other particle 2, irrespective of the distance between these particles. Schrodinger described the EPR correlation (3) as *entanglement of our knowledge* [12] because of this conflict. The identification of the state vector (1,2,3) with "knowledge of the system" by Heisenberg is defined in [13] as the fourth principal element of the Copenhagen interpretation. This information interpretation is enough natural because the collapse from (3) to (4) describes the change of our knowledge at observation. It eliminates simple non-locality problem *non-locality of the first kind* according to [13], which is at the description. The famous work by John Bell [14] has allowed to reveal the non-locality on a more deeper level, at observations. Interpretations become irrelevant because real observations are involved in this *non-locality of the second kind* [13].

The experimental evidences [15] of violation of the Bell's inequalities testify to the observation of the EPR correlation. But it is mistake to conclude that the EPR correlation can exist really because *it is a gross violation of relativistic causality* [16]. For Bell the violation of the Bell's inequality was *"the real problem with quantum theory: the apparently essential conflict between any sharp formulation and fundamental relativity"* [16]. This troubling conflict between the empirically verified predictions of quantum theory and the notion of local causality that is motivated by relativity theory is discussed by experts [17–20]. Some of they hope [17,18] that this conflict can be overcome at the cost of renunciation of realism and determinism, whereas the other one [19,20] state that even this can not be possible. Mermin confessed in 2001 [21]: *"Until quite recently I was entirely on Bell's side on the matter of knowledge-information. But then I fell into bad company. I started hanging out with the quantum computation crowd, for many of whom quantum mechanics is self-evidently and unproblematically all about information"*. Because of his associations with quantum computer scientists he has *"come to feel that 'Information about what?' is a fundamentally metaphysical question that ought not to distract tough-minded physicists"* [21]. Ghirardi, calling in question this point of view, reminds [22] that Bell *"refused to consider such a position unless [23], in advance, one would have answered to two basic (for him) questions: whose information?, and: information about what?"* This controversy by the experts testifies that the EPR correlation, and consequently quantum computer, can not be real in the reality of single universe.

3. The principle of superposition and positivism

Thus, the EPR correlation and violation of the Bell's inequalities [15] testify rather to the fundamental obscurity in quantum mechanics than to a possibility of a real equipment. Ironically, numerous authors [1,6–8] are sure that this unreal principle introduced by the opponent [11,12] of the Copenhagen interpretation can be a basis of a real device, quantum computer. This mass delusion could be possible because of blind admiration on the progress of physics and engineering of the XX century developed thanks to quantum mechanics. But as Bell noted [16] *"This progress is made in spite of the fundamental obscurity in quantum mechanics. Our theorists stride through*

that obscurity unimpeded... sleepwalking?" He said [16]: *"The progress so made is immensely impressive. If it is made by sleepwalkers, is it wise to shout 'wake up'? I am not sure that it is. So I speak now in a very low voice"*. The authors [1,6–8] and others do not understand that superposition of state can not be real and that this principle can be valid only in the limits of the positivism point of view, according to which quantum mechanics can describe only phenomena but no a reality. The numerous mistaken publications, possible because of this lack of understanding of the fundamental obscurity connected with the positivistic essence of quantum mechanics, compel to shout "wake up".

References

[1] A. Steane, *Rept. Prog. Phys.* **61**, 117 (1998).

[2] L.D. Landau and E.M. Lifshitz, *Quantum Mechanics: Non-Relativistic Theory*. Volume 3, Third Edition, Elsevier Science, Oxford, 1977.

[3] R.P. Feynman, *Int. J. Theor. Phys.* **21** 467 (1982).

[4] D. Deutsch, *Proc. Roy. Soc. Lond. A* **400**, 97 (1985).

[5] P.W. Shor, in Proc. 35th Annual Symp. on Foundations of Computer Science, Santa Fe, IEEE Computer Society Press (1994); E- print: quantph/ 9508027.

[6] M.A. Nielsen, and I.L. Chuang, *Quantum Computation and Quantum Information*. Cambridge University Press, 2000.

[7] D. Bouwmeester, A. Ekert, and A. Zeilinger (Eds.), *The Physics of Quantum Information. Quantum Cryptography. Quantum Teleportation. Quantum Computation.* Springer, Berlin, Heidelberg, 2000.

[8] T.D. Ladd, F. Jelezko, R. Laflamme, Y. Nakamura *et al*, *Nature* **464**, 45 (2010).

[9] Q. Norton, The Father of Quantum Computing. http://www.wired.com/science/discoveries/news/2007/02/72734.

[10] D. Deutsch, *The Fabric of Reality*. The Penguin Press, 1997.

[11] A. Einstein, B. Podolsky, and N. Rosen, *Phys. Rev.* **47**, 777 (1935).

[12] E. Schrodinger, *Naturwissenschaften* **23**, 807 (1935); *Proc. Cambridge Phil. Soc.* **31**, 555 (1935).

[13] J.G. Cramer, *Rev. Mod. Phys.* **58**, 647 (1986).

[14] J.S. Bell, *Physics* **1**, 195 (1964).

[15] A. Aspect *et al*, *Phys. Rev. Lett.* **47** 460 (1981); **49**, 91 (1982); **49**, 1804 (1982).

[16] J.S. Bell, "Speakable and unspeakable in quantum mechanics. Collected papers on quantum philosophy", Cambridge University Press, Cambridge, 1987, p. 169.

[17] N.D. Mermin, *Am. J. Phys.* **66(9)**, 753 (1998); arXiv: quant-ph/9801057.

[18] A. Zeilinger, *Nature* **438**, 743 (2005).

[19] T. Norsen, *Found. Phys.* **39**, 273 (2009).

[20] GianCarlo Ghirardi, *Found. Phys.* **40**, 1379 (2010).

[21] N.D. Mermin, in *Quantum (Un)speakables: Essays in Commemoration of John S. Bell*. Eds. Reinhold Bertlmann and Anton Zeilinger, Springer Verlag, 2002; arXiv: quant-ph/0107151.

[22] Giancarlo Ghirardi, *Found. Phys.* **38**, 1011 (2008).

[23] J.S. Bell, *Physics World*, **3**, 33 (1990).

Towards advanced capacitive nanostructures for deep-sub-voltage carbon nanoelectronics and self-powered microsystems

A. L. Despotuli, A. V. Andreeva and V. V. Aristov
Institute of Microelectronics Technology and High Purity Materials, RAS, 142432 Chernogolovka, Russia

Abstract. For ranking a high-tech object to a class "advanced", both the object and scope of its potential application should be defined in terms of utmost criteria. The elaboration of required criteria for important group of objects might initiate the change of standard for presentation of high-tech objects and speed up the technological progress. The ultimate physical limit approach is applied to the case of electrode nanostructures of double electric layer supercapacitors (SCs) required for the development of deep-sub-voltage nanoelectronics and microsystems. This work is the first research in the area of hetero-integration of future carbon nanoelectronics and nanoionics.

Introduction

The term "deep-sub-voltage (DSV) nanoelectronics" was proposed as a general notion for integrated circuits (ICs) operating near the theoretical limit of energy consumption ϵ per 1 bit processing [1]. Modern ICs are already the sub-voltage ones. The need in micrometer-sized capacitors with the high density of capacitance (surface δ_C, volume ρ_C) increases steadily with each new nanoelectronics technological node which again decreases the power supply voltage (V_{dd}) of ICs [1]. Other trend synergistic with scaling is a rapid development of microsystems technologies. A third trend, concomitant of scaling, is more and more wide using of new types of nanostructures, nanomaterials and compounds. All three trends collide in extremely scaled autonomous microsystems, for example, in biomedical applications [2]. Nanomorphic Cell [2] represents the ultimate potential of miniaturization technologies, i.e. based on the fundamental scaling limits for energy sources, sensors, computation and communication subsystems. The realization of these promising micro(nano)systems and self-powered sensor networks requires extensive researches from device to architecture level. We foresee the appearance of devices for energy and charge storage in the DSV-regime. In response to this challenge, the development of new class of all-solid state impulse micron-sized supercapacitors (nanoionic supercapacitors) was initiated in IMT RAS [3]. These SCs are based on advanced superionic conductors (AdSIC) — materials with crystalline arrangement close to optimal for unipolar fast ion transport. Advanced carbon nanostructures are commonly considered as a feasible future of nanoelectronics beyond 22-nm technology node (2016), therefore micron-sized on-chip SCs [1] on the basis of cabon materials and AdSICs may be well compatible with microelectronics technologies.

The possibilities of development of the on-chip DSV SCs are considered below. The ultimate physical limit approach was applied to such characteristics of SC-electrode nanostructures as the surface densities of charge (δ_Q), current (δ_I), electrostatic (δ_C) and quantum capacitances (δ_{qC}), volume densities of energy (ρ_E) and power (ρ_W), maximum operational frequency of functional nanostructure (f_{max}), voltage of electrochemical decomposition (V_{dec}) of ionic conductor/electronic conductor (EC) heterojunction, and crystal potential relief depth (η) in an ionic conductor. The work gives an affirmative answer on the question: "Is there a reserve for significant rise of key characteristics of carbon based SCs suited for on-chip useing?"

1. Nanoionics

There are special problems with miniaturization of energy (power) sources. For example, in capacitors the breakdown electric field F_{max}, dielectric constant k, and surface δ_C (volume ρ_C) capacity density relate to V_{dd} [1] as:

$$V_{max} = F_{max} \left(k\epsilon_0/\rho_C\right)^{1/2} = \left(F_{max}k\epsilon_0\right)/\delta_C > \simeq V_{dd} . \quad (1)$$

where $\epsilon_0 = 8.85 \times 10^{-12}$ F/m. In capacitors of conventional design the values of δ_C and ρ_C cannot be more increased in the sub-voltage region V_{dd} because of an exponential growth of tunnel current leakage through a dielectric layer less than $d = V_{max}/F_{max} \sim 1-1.5$ nm thick. All solid state ion-conducting nanostructures and devices can bring much benefits to the area of energy (power) storage (generation). Therefore they will play an important role in nanoelectronics and nanosystems [3]. Nanoionic devices were first proposed in 1992: "The results obtained show that it is possible to form arrays of electrochemical devices with single elements $\sim$10 nm in size in the films" [4], and now electrochemical ionic memory is in the scope of interest of ITRS-2009 (see Emerging Research Devices). Future nanoelectronics will use DSV-sources and nanoionic supercapacitors [1] which are now in the scope of SAMSUNG's interest (see SAIT Global Research Outreach Program 2010).

2. Future deep-sub-voltage carbon nanoelectronics

Nanoelectronics looks beyond the horizon of conventional ICs (post-silicon electronics), where the molecular or carbon electronics (nanotubes and graphene-based nanostructures) may be predominant. Future digital nanoelectronics will be the DSV ones [1]. There is potential to produce wafer-scale graphene films with full planar processing for devices. It promises high compatibility with CMOS processes, and it is a significant advantage over carbon nanotubes [5]. Last years graphene nanoribbon tunnel field-effect transistors and bilayer graphene tunnel field-effect transistors were proposed for ultra-low-power circuit design [6,7]. These tunnel nanodevices can switch

from on to off with only 0.1 V ($\approx V_{dd}$). In the DSV-nanoelectronics the supply voltage is lowered to the thermal noise level [8]. It will require special on-chip capacitors for a blanking of various noises [1].

3. Energy harvesting in deep-sub-voltage regime

The autonomous devices harvesting energy from environment for maintenance of own long term activities are of critical importance for sensing, defense, medical implants, and mobile personal electronics. Commonly encountered challenge of energy harvesting may be called the low power density (ρ_W) of environmental sources (heat flow, mechanical vibration and radio-frequency electromagnetic waves). Therefore, a power unit of autonomous micro- and nanosystems will generate small values of ρ_W

$$F \times \delta_I = \rho_W \,, \qquad (2)$$

where F is the strength of electric field and δ_I is the density of current. Let us consider a hypothetic nanosystem that uses a power unit on the base of carbon nanotube (NT). As NTs can provide a large δ_I ($\sim 10^7$ A/cm^2, then the value F may be small. It means the power units of nanosystem will operate in a DSV-regime, as the characteristic size of nanosystem (L) is also small ($F \times L \sim V_{dd}$). The example: the multifunctional nanodevices for energy harvesting in uniconventional spectral ranges for both military and commercial applications [9]. This novel device technology based on nanowire antennas and very high speed rectifiers may be used for converting of infrared and THz electromagnetic radiation into DC power. Nanoscale energy harvesting with an array of vertically aligned zinc oxide (ZnO) nanoribbons can generate the electricity from elastic deformations induced by sliding friction or mechanical vibration with the power $\rho_W \sim 10$ nW/mm^3 [10]. A peak power above $2~\mu$W/mm^3 [11] was achieved. The generated energy [9–11] should be stored in the pulsed DSV SCs.

4. The main items of report

(i) Voltage of electrochemical decomposition of capacitive AdSIC/EC heterojunctions [12]; (ii) Relation between k and η for AdSIC/EC heterojunctions [13]; (iii) Interface design methods [13]; (iv) Large current on the non-Faraday imperfect AdSIC/EC heterojunctions; (v) Magnitude of $\rho_W \times \rho_E$ as indicator of SC-technology level [13]; (vi) Quantum capacitance of advanced carbon electrode nanostructures [13].

5. Summary

For the revealing of new possibilities in the area of creation of advanced carbon-based supercapacitors (SCs) the ultimate physical limit approach was applied to a set of characteristics. In this work: (1) new notion, namely the voltage of electrochemical decomposition of the ionic conductor/EC heterojunction V_{dec} was introduced and the ultimate limit criterion $V_{dec} \times \delta_C < 150$ V μF/cm^2 was revealed; (2) new nanoionic relation $\delta_C \propto 1/\eta$ for the advanced superionic conductor/EC heterojunctions was defined; (3) inevitability of using of interface design methods and effects of self-organization for the creation of advanced heterojunctions with the double electric layer (DEL) capacitance $\delta_C \sim 100~\mu$F/cm^2 and $f_{max} \sim 10^8 - 10^9$ Hz was emphasized; (4) low current density δ_I of

functional heterojunctions in non-Faraday DEL-SCs as compared with typical exchange-current densities for $M^+ + e \rightleftharpoons M$ (300 K) Faraday reactions in liquid electrolyte/M-metal electrode systems (300 K) was pointed out as a large reserve to increase the ρ_E and ρ_W densities in DEL-SCs. The criterion for the SC-transition into regime of external strong influences $\delta_I \cdot > \sim 0.01\delta_{Qmax}\nu_0 \exp(-\eta/k_B T)$ was introduced. It was shown that in a such regime the non-equilibrium values of the DEL-capacity density δ_C at imperfect AdSIC/EC heterojunctions depend on the current density δ_I, the depth of potential relief $\eta(x)$, the temperature T, and the time t; (5) criterion $\approx 10^9$ J^2/s kg$^2 \cdot < \rho_E \times \rho_W \cdot \ll \sim 10^{24}$ J^2/s kg^2 suited for ranking SCs as advanced devices was proposed; (6) small values δ_{qC} (about 10–20 μF/cm^2) in the pristine graphene and 1D carbon nanomaterials were recognized as the main obstacle for improving DEL-SCs, and the condition $\delta_{qC} \approx 5\delta_C$ was proposed as the criterion for ranking carbon nanostructures to an advanced class; (7) uniform metal-covered carbon nanotubes, bundles of metal SWCNTs, and graphene sheets with high concentrations of dopants and extended defects were proposed for the creation of advanced carbon electrode nanostructures and SCs with $\delta_{qC} \approx 5\delta_C \sim 500~\mu$F/cm^2 and $\rho_E \times \rho_W \cdot > \sim 10^9$ J^2/s kg^2.

References

[1] A.L. Despotuli and A.V. Andreeva, *Int. J. Nanosci.* **8**, 389 (2009).

[2] V.V. Zhirnov and R.C. Cavin, *Microsystems for Bioelectronics: the Nanomorphic Cell*, (Oxford: William Andrew) 204, 2010.

[3] A.L. Despotuli, A.V. Andreeva and B. Rambabu, *Ionics* **11**, 306 (2005).

[4] A.L. Despotuli, and V.I. Nikolaichik, *Solid State Ionics* **60**, 275 (1993).

[5] X. Yang, J. Chauhan, J. Guo and K. Mohanram, *Proc. of CLSVLSI 10 (Providence, Rhode Island, USA, 2010).*

[6] Q. Zhang, T. Fang, H. Xing, A. Seabaugh and J. Debdeep, *IEEE Electron Device Lett.* **X**, X (2008).

[7] G. Fiori and G. Iannaccone, *IEEE Electron Device Lett.* **30**, 1096 (2009).

[8] B. Marr, J. George, B. Degnan, D.V. Anderson and P. Hasler, *VLSI Design* **2010**, ID460312 (2010).

[9] O. Imafidon, S. Georgakopoulos, P.K. Vabbina and N. Pala, *Proc. Micro- and Nanotechnology Sensors, Systems, and Applications II (Orlando, Florida, USA, 2010)*, SPIE, 76792L, 2010.

[10] C. Majidi, M. Haataja and D.J. Srolovitz, *Smat. Mater. Struct.* **19**, 055027 (2010).

[11] S. Xu, Y. Qin, C. Xu, Y. Wei, R. Yang and Z.L. Wang, *Nature Nanotech.* **5**, 366 (2010).

[12] A.L. Despotuli and A.V. Andreeva, *Nanotechnologies in Russia* **5**, 506 (2010).

[13] A.L. Despotuli and A.V. Andreeva, *Nanosc. Nanotechnol. Lett.* **3**, 119 (2011).

Piezoelectric effect in GaAs nanowires

I. P. Soshnikov[1,2], D. E. Afanas'ev[3], V. A. Petrov[1], G. E. Cirlin[1,2,3,4], A. D. Bouravleuv[1,2],
Yu. B. Samsonenko[1,2,4], A. I. Khrebtov[2], E. M. Tanklevskaya[2] and I. A. Seleznev[5]

[1] St Petersburg Academic University, St Petersburg, Russia
[2] Ioffe Physical-Technical Institute, St Petersburg, Russia
[3] Physical Faculty, St Petersburg State University, Ulyanovskaya 3, Petrodvorets, St Petersburg 198504, Russia
[4] Institute for Analytical Instrumentation RAS, Rizhsky 26, St Petersburg 190103, Russia
[5] Oceanpribor corp. Chkalovskii pr., 46., St Peterburg 197376, Russia

In the previous studies (e.g., [1]) it was found that nanowires (NWs) arrays of III–V materials in most cases were growing in hexagonal phases (wurtzite, polytypes) instead of bulk III–V materials growing in cubic phase. It is known that the piezoelectric properties of II–VI compounds [2,3] depend on their crystal phase. Therefore, it seems that the changing of the crystal phase of III–V materials from zinc blende to wurtzite can also change their piezoelectric properties.

Here we report on the experimental study of the samples with GaAs nanowires.

GaAs NWs were grown by molecular beam epitaxy (MBE) on the n-type GaAs (111)B substrates. NWs obtained have diameters close to 25 nm, the lengths from 1000 up to 2500 nm and the surface density about 10^8 cm^{-2}. After the growth, the samples were covered by the PMMA surface layer. Then the top GeNiAu contact was plated (Fig. 1).
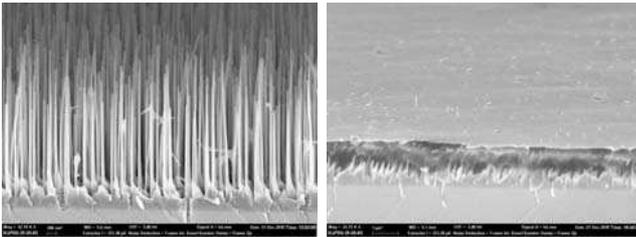
Fig. 1. The cross-sectional scanning electron microscopy images of sample before and after deposition of PMMA and contact layers.
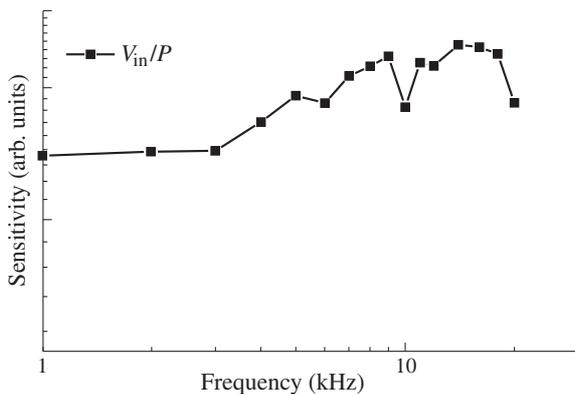
Fig. 2. Gain-frequency characteristic of the voltage, generated by the acoustic field excited under 65 dB.

The piezoelectric effect induced by acoustic waves with the sound pressure level below 65 dB was measured using a special instruments. It was shown that the generated voltage is dependent on the frequency of the acoustic wave in the range from 0.5 to 20 kHz (Fig. 2). The voltage reaches the value 1–2 mV at the 65 dB magnitude and 1 kHz frequency that corresponds to the sensitivity about ∼1 mV/Pa.

The estimation of piezoelectric modulus gives the value of $d_{33} \sim 26$ pCl/N that is significantly higher than the values for the bulk GaAs: $d_{33} = 0$, $d_{14} = 2.7$ pCl/N [3]. This difference can be explained by the presence of the hexagonal phases in NWs and also as a result of the strain introduced by the contact layer [2].

References

[1] I.P. Soshnikov *et al*, *Phys. Solid State* **47**, 2213-8 (2005).
[2] K. Huebner, *Phys. Status Solidi (b)* **57**, 627 (1973).
[3] Landolt-Börnstein, *Group III Condensed Matter Numerical Data and Functional Relationships* in Science and Technology v. 41B: II–VI and I–VII Compounds; Semi-magnetic Compounds Ed. O. Madelung, U. Rössler, M. Schulz.

Three-axis Hall sensor based on strained modulation doped semiconductor shells

A. B. Vorob'ev, *A. V. Chesnitsky*, E. V. Ilyushina, A. I. Toropov and V. Ya. Prinz

Institute of Semiconductor Physics, 630090 Novosibirsk, Russia

Abstract. An integrated three-axis Hall sensor is fabricated using strain-induced microstructuring. Three-axis measurements of magnetic field are demonstrated. The sensitivity of the sensor exceeds 10^3 Ω/T at 300 K.

Increasing device integration requires decreasing sensor sizes and transition from one-axis sensors, that can measure projection of a vector quantity to one axis only, to two- and three-axis ones. Particularly, two- and three-axis magnetic field measurements are needed for the following applications: (1) contactless position detectors and transducers of angular movement and linear displacement, which are widely used in industry; (2) electronic compasses for navigation systems; (3) tracking of magnetic markers in living organisms for medical and biological studies; (4) probes for scanning Hall probes microscopy.

Up to now, three techniques for two-axis Hall measurements are developed. They are based on: (1) vertical Hall devices [1], (2) ferromagnetic concentrators, (3) array of planar Hall sensors. However, all these solutions have substantial disadvantages. Fabrication of vertical devices and ferromagnetic concentrators is incompatible with conventional planar technology; ferromagnetic concentrators and arrays of planar sensors are relatively large; finally, none of these methods allows measurements of all magnetic field vector projections at once, third magnetic field component is measured with an additional properly oriented planar Hall sensor [2]. Hence, a technique for fabrication of three-axis magnetic field sensors, compatible with conventional semiconductor technology, is needed.

Strain-induced, three-dimensional micro-and nanostructuring [3] allows us to fabricate conductive shells with a few Hall sensors having different preset spatial orientations. Experimentally, fabrication of the cylindrical shell with two pairs of Hall probes and simultaneous measurements of the Hall voltages induced by the different local values of the normal-to-surface component of the magnetic-field vector were shown [4]. As an apparent cosequence of those experiments, an idea to fabricate magnetometer based on cylindrical shells supplied with a few pairs of Hall probes located along the periphery of the shell was proposed. Recently, an attempt to fabricate room-temperature three-axis Hall sensor using so-called "micro-origami" version [5] of the strain-induced microstructuring was made [6,7]. However, experimental results in Ref. 7 demonstrate only two-axis magnetic field measurements.

In the present work we report on fabrication of three-axis Hall sensor based on GaAs/InGaAs shells and demonstrate measurements of all three magnetic field vector components with the fabricated device. Active part of the sensor consists of two cylindrical shells with curvature radii of about 10 μm, oriented so that generatrices of cylindrical surfaces are mutually perpendicular. 13-nm-thick GaAs quantum well cladded with δ-doped AlGaAs barriers is embedded in the walls of shells and contains electron gas with the sheet density of about 10^{12} cm^{-2}. The walls of the shells were lithographically patterned to define Hall bars. Figure 1 illustrates fabrication of
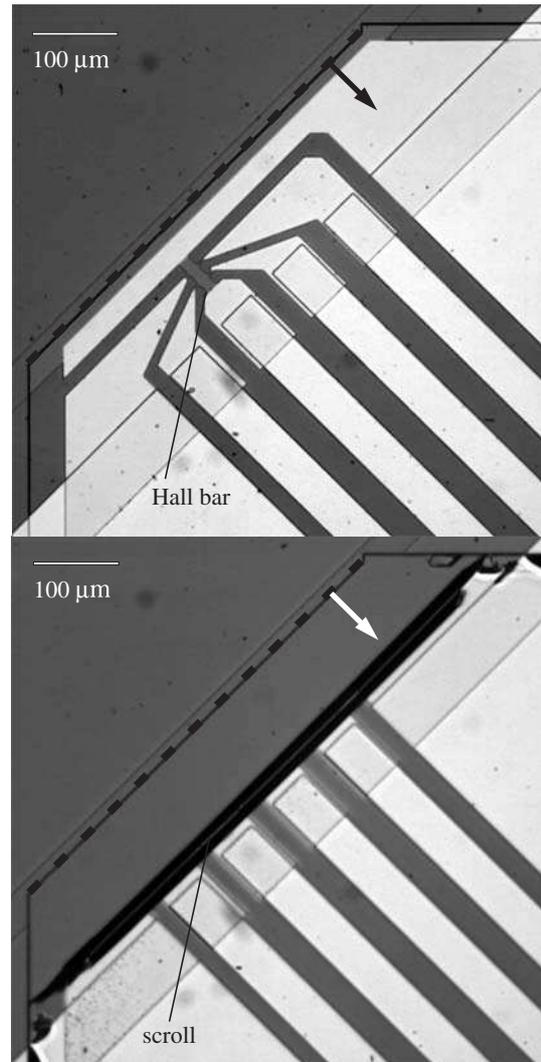
Fig. 1. Photographs (plan view) of initial flat lithographically patterned Hall bar (top image) and cylindrical shell (scroll) containing the same Hall bar after rolling process (bottom image). The arrow shows rolling direction, the dashed line shows the starting edge for rolling process.

contacted cylindrical shell. The curvature radius of the shell and the distance between pairs of Hall probes are chosen in such a way to provide measurements of Hall voltages induced by mutually orthogonal components of the magnetic-field vector. The relative sensitivity of the fabricated sensor exceeds 1000 Ω/T at room temperature.

Active part of the three-axis Hall sensor, in principle, is scalable down to ∼100 nm in size. The proposed technique of three-axis sensor fabrication is fully compatible with the conventional semiconductor planar technology. Particularly, it implies an opportunity to integrate the three-axis sensor itself with signal conditioning circuitry in one chip.

References

[1] R.S. Popovic, *IEEE Electron Device Lett.* 357 (1984).
[2] R.S. Popovic *et al*, *IEEE Trans. Instrum. Measurement* **56**, 1396 (2007).
[3] V.Ya. Prinz *et al*, *Physica E* **6**, 828 (2000).
[4] A.B. Vorob'ev *et al*, *Phys. Rev. B* **75**, 205309 (2007).
[5] P.O. Vaccaro *et al*, *Appl. Phys. Lett.* **78**, 2852 (2001).
[6] J. Sileo *et al*, *Microelectron. Eng.* **87**, 1217 (2010).
[7] M.T. Todaro *et al*, *J. Micromech. Microeng.* **20**, 105013 (2010).

Electrodynamics of magnetophotonic crystals: opal-matrix with metallic and ferrite nanoparticles embedded

V. V. Ustinov and *A. B. Rinkevich*

Institute of Metal Physics, Ural Branch of RAS, 620990 Ekaterinburg, Russia

Abstract. Photonic crystals become a fashionable object of investigation on microwaves and the interest is caused both extraordinary electrodynamic effects and possible applications. Interaction of high-frequency electromagnetic waves with magnetophotonic crystals which are regarded as metamaterials represents an area of investigation most perspective at present. Magnetic state of a nanocomposite is a factor defining its microwave properties in magnetic field and partially the resonance phenomena. ENZ-materials constitutes a special group of metamaterials which have a near zero dielectric constant. A supercoupling effect represents one of most striking example of anomalous wave propagation in these media.

Microwave resonant phenomena are studied in this paper for the nanocomposite containing nanoparticles of metallic cobalt or ferrite-spinels embedded into the dielectric matrix that is a latticed package of submicron SiO_2 spheres. Magnetic resonance is studied in the nanocomposites and its action on the reflection and transmission coefficients. The presence of the magnetic antiresonance is established and the necessary conditions of its appearance are ascertained. It has been shown that electromagnetic properties of this metamaterial are quite different on macro- and submicron scales.

Opal matrices with the diameter of submicron SiO_2 spheres about 250 nm were used as packages for preparation the samples. The nanocomposites with the particles of cobalt or ferrite-spinels embedded were obtained with the impregnation method with the posterior thermal treatment. The structure of the nanocomposite is shown in Fig. 1. The particles of the phases embedded have the irregular shape and the sizes from 10 to 80 nm. The volume concentration of the introduced substance is from 5 to 15%.

The magnetic measurements were carried out at room temperature. In the fields up to 50 kOe the magnetization curve is close to a straight line without any sign of saturation. The microwave measurements are carried out in frequency diapason from 26 to 38 GHz. The sample was placed into the waveguide as shown in Fig. 2.

The algorithm was worked out permissive to select the values of the effective parameters of the material studied. From the calculation we have got both real and imaginary parts of
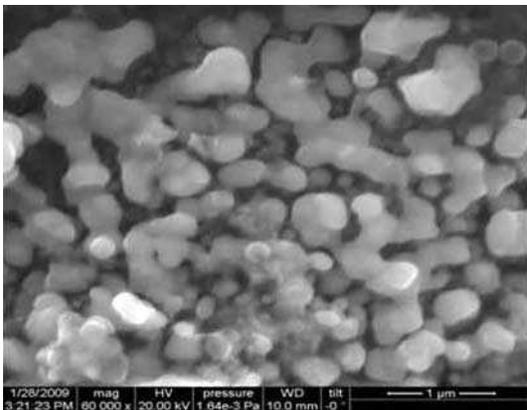
Fig. 1. Electron microscopic study of the nanocomposite with Co embedded structure: magnification ×60000, voltage 20 kV.
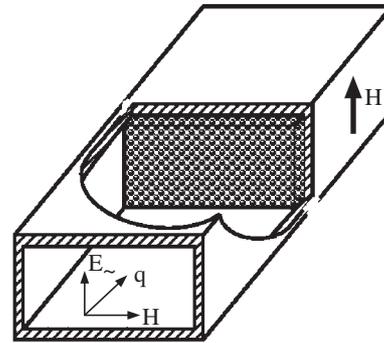
Fig. 2. Scheme of the sample displacement in the waveguide.

the dielectric permittivity of the nanocomposite.

The magnetic field dependence of transmission coefficients measured for the nanocomposite with Co particles at several frequencies is shown in Fig. 3. The minimums actually present both in reflection and in transmission. The field corresponding to the minimum increases when frequency rises as expected for the resonance belonging to the uniform branch. The magnitude of resonance also increases with frequency. The presence of magnetic resonance confirms the fact that the ferromagnetic cobalt presents in the nanocomposite. An additional maximum is seen in Fig. 3 besides the minimum. This maximum occurs in the fields ≈4 kOe that is less than the resonance field. In this region the increase takes place in the reflection and transmission coefficients, therefore, decrease of absorption is realized i.e. magnetic antiresonance. From the fields of magnetic resonance and antiresonance the spectra have been reconstructed. It is important that magnetic antiresonance occurs in the 3D-nanocomposite media with both metallic and dielectric particles.

Let us examine is a sign of the refraction coefficient either positive or negative for the nanocomposite studied? The complex refraction coefficient is defined by the relation $n = n' - in''$, where n' is the refraction coefficient and n'' is the absorption coefficient. The analysis shows that the spatial distributions of the refraction coefficient are absolutely different at macro- and submicron scales. The dependences shown in Fig. 4 represent the results of the calculation for the nanocomposite with Co particles. It is evident that the macroscopic refraction coefficient has no peculiarities, namely its real part always positive and much exceeds the imaginary part. The resonant variations of the macroscopic refraction coefficient
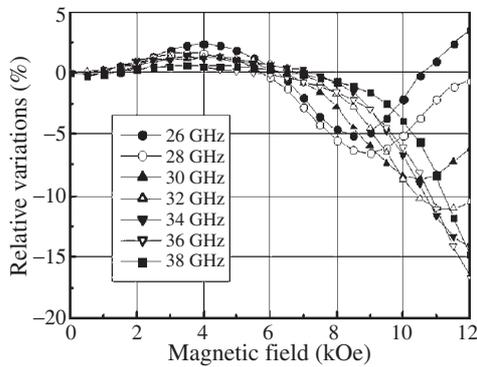
Fig. 3. Magnetic field dependency of the reflection coefficient module.
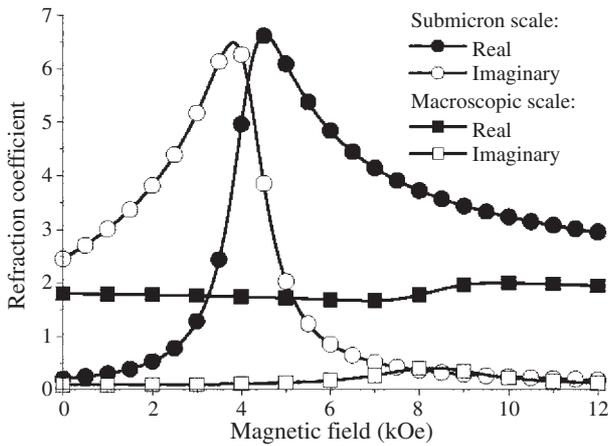
Fig. 4. Magnetic field dependency of the refractive n' and absorption n'' indices of the nanocomposite for $f = 26$ GHz.

are low. The refraction coefficient on the submicron scale is very spatially heterogeneous. The real part of the refraction coefficient even in this case is found to be positive, and the nanocomposite is not a double left handed media. It should be noted that in low DC fields at the submicron scale the refraction coefficient is low, $n' \ll 1$. One could believe that this low value of the refraction coefficient gives an argument to suppose the nanocomposite studied as a media that on the submicron scale looks like the ENZ-media. The examination of the phase velocity however reveals the essential difference because the fact that the phase velocity contains both real and imaginary parts. Therefore the electromagnetic properties of the studied nanocomposite differ markedly from the ENZ-media.

Acknowledgements

Screening of plasmons in a two-dimensional electron system by lateral gates

V. V. Popov and O. V. Polischuk

Kotelnikov Institute of Radio Engineering and Electronics (Saratov Branch) RAS, 410019 Saratov, Russia

Abstract. We show theoretically that screening of the plasmons in a two-dimensional system (2DES) by lateral gates (or by lateral contacts) increases with increasing the plasmon wavevector as opposed to conventional screening of the plasmons in 2DES by a topside gate. This finding can explain recent results on experimental observation of the plasmon resonances in 2DES with lateral gates.

In an infinite homogeneous two-dimensional electron system (2DES), the plasmon spectrum is [1]

$$\omega = \sqrt{\frac{2\pi e^2 N q}{m^* \bar{\epsilon}}} , \qquad (1)$$

where ω and q are the plasmon frequency and wavevector, respectively, N is the sheet electron density in 2DES, e and m^* are the electron charge and effective mass, respectively, and $\bar{\epsilon}$ is the effective dielectric function, which describes the screening of plasmons by surrounding dielectric media and conductive sheets. If 2DES is placed on the surface of a substrate having the dielectric constant ϵ_s then $\bar{\epsilon} = (1 + \epsilon_s)/2$. In this case, the plasmon frequency $\omega \equiv \omega_0$ is proportional to the square root of the plasmon wavevector. If the 2DES is located on the surface of a substrate having the dielectric constant ϵ_s and covered by a barrier layer having the dielectric constant ϵ_b and thickness d, the effective dielectric function is

$$\bar{\epsilon} = \frac{1}{2} \left[\epsilon_s + \epsilon_b \frac{1 + \epsilon_b \tanh(qd)}{\epsilon_b + \tanh(qd)} \right] . \qquad (2)$$

[For sufficiently thick barrier layer so that $qd \gg 1$, Eq. (2) yields $\bar{\epsilon} = (\epsilon_s + \epsilon_b)/2$.] Finally, if the barrier layer is covered by a perfectly conductive plane (the gate plane), the effective dielectric function is

$$\bar{\epsilon} = \frac{1}{2} \left[\epsilon_s + \epsilon_b \coth(qd) \right] . \qquad (3)$$

For a small separation between the gate plane and 2DES so that $qd \ll 1$, the approximation $\coth(qd) \approx 1/qd$ is valid and, hence, the plasmon spectrum given by Eq. (1) with the effective dielectric function Eq. (3) exhibits a linear dispersion

$$\omega \equiv \bar{\omega} = q \sqrt{\frac{4\pi e^2 N d}{m^* \epsilon_b}} . \qquad (4)$$

In diode and transistor structures with confined 2DES channels, the plasmons in 2DES are also screened by the side (source and drain) metal contacts. Theoretical studies performed both in the electrostatic [2,3] and electromagnetic [4–6] approaches demonstrated that the screening by the side contacts leads to softening of the plasmon modes in 2DES. It was concluded in [5] that the electromagnetic effects can be very important in considering plasmon modes in a slot diode with 2DES channel even for a short channel when the plasma oscillations in 2DES
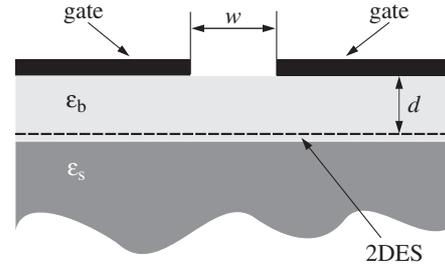
Fig. 1. Schematic of the 2DES structure with lateral gates. External electromagnetic wave with polarization of the electric field across the gate slit is incident from the top.

without side metal contacts can be described in quasistatic approximation.

In this paper, we calculate the frequencies of the plasmon resonances in 2DES with lateral metal gates (see Fig. 1) in a self-consistent electromagnetic approach similar to that elaborated in [6] for the transistor structure with a topside gate. In the structure under consideration, the resonant cavity for plasmons in 2DES is formed by the edges of metal lateral gates separated from each other by distance w. We normalize the frequency of the plasmon resonance in 2DES with lateral metal gates by comparing it with the plasmon frequency ω_0 in ungated 2DES, which are given by Eq. (1) with the effective dielectric function $\bar{\epsilon} = (1 + \epsilon_s)/2$, assuming the plasmon wavevector to be $q = 2.2/w$ with w being the separation between the lateral gates. This effective plasmon wavevector describes the fundamental plasmon mode in ungated 2DES strip [7].

Figure 2 shows the ratio between frequency ω_0 and the calculated frequency of the fundamental plasmon resonance in the 2DES with lateral gates (open square symbols) as a function of the effective plasmon wavevector $q = 2.2/w$. It is seen from Fig. 2 that the plasmon frequency in the 2DES with lateral gates exhibits non-square-root dependence on the plasmon wavevector. This fact can be explained by the following. In our model we assume the lateral gates to be infinite semi-planes split by a gap of width w. However, only the edge regions of the lateral gates, each with the length of about a quarter of the electromagnetic wave $\lambda/4$, participate in screening the plasmons in 2DES under the gate slit. Then the strength of the screening can be quantitatively described by the screening parameter $\lambda/(4w) \equiv \pi c/(2w\omega)$, which defines a distributed capacitance between the lateral gate semi-planes [8]. The frequency of the plasmon resonance in 2DES under the gate slit increases with decreasing the length of the plasmonic cavity roughly proportional to $\sqrt{1/w}$. Therefore, the screening pa-
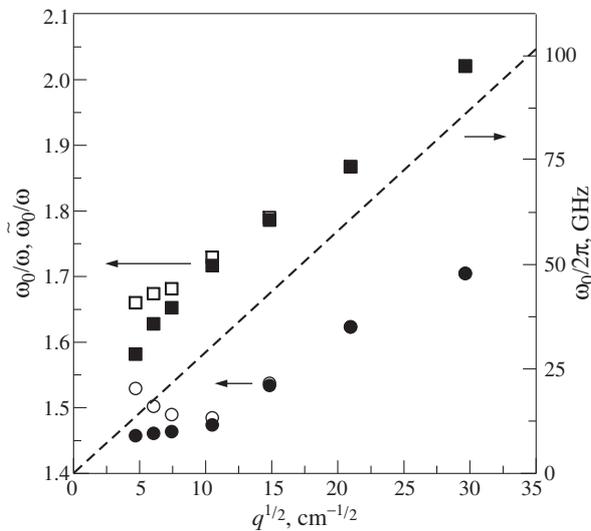
Fig. 2. Softening factor for the fundamental plasmon mode in 2DES with lateral gates as a function of the square-root of the plasmon wave vector $q = 2.2/w$ (squares). The same for the slot diode with 2DES channel (circles). Different points correspond to different channel length, w (from left to right in millimeters): 1, 0.6, 0.4, 0.2, 0.1, 0.05, 0.025. Parameters of the structure are $N = 1 \times 10^{11}$ cm^{-2}, $d = 0.6$ μm, $\epsilon_b = \epsilon_s = 12.8$, $m^* = 0.069 m_0$ where m_0 is the free electron mass. Electrostatic results, ω_0/ω, are shown by open symbols while the electromagnetic ones, $\tilde{\omega}_0/\omega$, are shown by filled symbols. Dispersion $\omega_0(q^{1/2})$ of the ungated plasmons is shown by dashed line as a reference.

rameter also increases as $\sqrt{1/w}$ with decreasing the length of the plasmon cavity (i.e., with increasing the plasmon wavevector). As a result, the plasmon frequency ω in the 2DES with lateral gates becomes stronger redshifted from the frequency of the ungated plasmons ω_0 so that the ratio ω_0/ω increases (i.e., the plasma oscillations become "softer"). In fact, the softening factor ω_0/ω itself can be considered as another screening parameter: one has a greater ratio ω_0/ω for stronger screening. Similar dependence is shown by open circle symbols in Fig. 2 for a slot diode with 2DES channel (i.e., for $d = 0$) [4] though with a weaker screening effect. The screening in the 2DES with lateral gates (for $d \neq 0$) is stronger than that in a slot diode with 2DES channel because there are additional gate-to-channel capacitances in the structure with $d \neq 0$. It is worth noting that the behavior of screening the plasmons in 2DES with lateral gates is quite different from that in 2DES with a topside gate contact described by Eq. (4). The screening by the topside gate decreases as $\omega_0/\bar{\omega} \propto \sqrt{w}$ [for greater d, this dependence will be modified subject to Eq. (3)], where w is the topside gate length, while the screening by lateral gates increases with decreasing the plasmon cavity length. The screening by the topside gate can be interpreted as an electrostatic effect of the gate-to-channel capacitance, which is directly proportional to the topside gate length. However, a purely electromagnetic parameter (the electromagnetic wavelength at the plasmon resonance frequency) controls the screening of the plasma oscillations in the 2DES with lateral gates even for short 2DES channels with $4w/\lambda \ll 1$.

A square-root dependence of the ungated plasmon frequency on the plasmon wavevector will be also distorted if 2DES is covered by the barrier layer of finite thickness with no gate contact at all [see Eq. (2)]. However, this would be a subtle effect since a barrier layer is, typically, much thinner than the plasmon wavelength.

For small plasmon wavevectors, the electromagnetic retardation effects in ungated 2DES can be important [6]. We also normalized the calculated plasmon resonance frequencies in the structures with lateral screening comparing it with the ungated plasmon frequency $\tilde{\omega}_0$ calculated accounting for electromagnetic correction (filled symbols in Fig. 2). We calculated the frequency $\omega = \tilde{\omega}_0$ by solving the dispersion equation for the plasmon-polaritons in ungated 2DES

$$\frac{k_0}{\sqrt{q^2 - k_0^2}} + \frac{\epsilon_s k_0}{\sqrt{q^2 - k_0^2 \epsilon_s}} = \frac{4\pi}{c} \frac{e^2 N}{m^* \omega}, \qquad (5)$$

where $k_0 = \omega/c$ with c being the speed of light. [Equation (5) coincides with Eq. (1) in the limit $c \to \infty$ for $\bar{\epsilon} = (1 + \epsilon_s)/2$]. Comparison between $\tilde{\omega}_0/\omega$ and ω_0/ω data in Fig. 2 shows that electromagnetic correction to the plasmon frequency in ungated 2DES is important only for small plasmon wavevectors (smaller than 100 cm^{-1}). However, the electromagnetic parameter (the electromagnetic wavelength at the plasmon resonance frequency) strongly affects the screening of plasmons in 2DES with lateral gates (lateral contacts) in a much broader range of the plasmon wavevectors.

Non-square-root dependence of the plasmon resonance frequency on the plasmon wavevector was observed recently [9] in 2DES discs of sub-mm diameter with lateral gate electrodes in gigahertz frequency range. The experimental observations reported in [9] can be interpreted based on the results of this study by enhancement of the plasmon screening by lateral gate in 2DES discs of smaller diameter.

References

[1] A. V. Chaplik, *Surf. Sci. Reports* **5**, 289 (1985).
[2] V. Ryzhii *et al*, *J. Appl. Phys.* **98**, 7625 (2004).
[3] A. Satou *et al*, *J. Appl. Phys.* **98**, 034502 (2005).
[4] V.V. Popov *et al*, *Fiz. Tekh. Poluprovodn.* (St Petersburg) **39** (1), 157 (2005); [*Semiconductors* **39**, 142 (2005)].
[5] S.A. Mikhailov and N.A. Savostianova, *Phys. Rev. B* **74**, 045325 (2006).
[6] V.V. Popov *et al*, *J. Appl. Phys.* **104**, 024508 (2008).
[7] S.A. Mikhailov and N.A. Savostianova, *Phys. Rev. B* **71**, 035320 (2005).
[8] J.S. Wei, *J. Quantum. Electron.* **13**, 152 (1977).
[9] S.I. Gubarev *et al*, *Pis'ma Zh. Eksp. Teor. Fiz.* **90**, 588 (2009) [*JETP Lett.* **90**, 539 (2009)].

Wide spectral observation of the magnetorefractive effect in the nanoscale La$_{0.7}$Ca$_{0.3}$MnO$_3$ thin-films

A. V. Telegin and Yu. P. Sukhorukov

Institute of Metal Physics, Ural Branch of RAS, 620990 Ekaterinburg, Russia

Abstract. Complex investigations of the optical and magneto-optical properties of La$_{0.7}$Ca$_{0.3}$MnO$_3$ epitaxial films indicated that magnetorefractive effect in manganite in the IR region can reach giant values up to 20%. In the middle infrared region the resonance-like magnetorefractive effect has been observed. The change a sign of MRE and reducing the magnitude of effect in the visible range was detected. The different nature of MRE in manganites in middle infrared range and visible one was discussed. A model based on the theory of the magnetorefractive effect has been proposed to qualitatively explain the observed features.

Introduction

Magnetorefractive effect (MRE) is a magnetic-field-induced change in reflectivity and transmission of electromagnetic waves in magnetic materials. According to the MRE theory effect may appears due to the influence of magnetic field on electronic band structure, parameters of interband or intraband optical transitions, and due to the magnetoresistance [1,2]. MRE can be used for contactless measurements of magnetoresistance, in magnetic sensors, modulators of light and so on [3,4]. The study of frequency dependencies of MRE in reflection and transmission modes is a new upcoming method of spectroscopy of magnetic materials. In this report, we present experimental results on MRE in La$_{0.7}$Ca$_{0.3}$MnO$_3$ films possessed the colossal magnetoresistance effect at the Curie temperature.

1. Experimental

The nanoscale epitaxial La$_{0.7}$Ca$_{0.3}$MnO$_3$ film with different thickness were grown on LaAlO$_3$ substrate by a method of chemical deposition from the vapor of metalloorganic compounds (MOCVD). The magnetoreflection spectra of samples were investigated for unpolarized light in the visible and mid-IR range (from 0.4 to 27 μm) at the normal light incident in the magnetic field up to 1.1 T applied in-plane to the sample surface (Fig. 1). The magnetotransmission spectra were investigated in the spectral range from 0.8 to 22 μm at magnetic field up to 0.8 T applied out off-plane to the sample surface. All spectral dependencies were measured at the Curie temperature of samples (T_C about 255 K). Optical and electrical properties, as well as magneto-optical Kerr effect and magnetoresistance were also studied for the same samples. In the middle IR spectral range MRE and colossal magnetoresistance have a similar temperature and field behavior and reach their maxima near the Curie temperature (Figs. 1,2).

It was shown the MRE on magnetoreflection and magnetotransmission modes is an optical response to the colossal magnetoresistance in manganites [2,5,6]. Magnitude of the negative magnetotransmission effect in La$_{0.7}$Ca$_{0.3}$MnO$_3$ film can reach a few orders microm. The so-called optical amplification of the MRE for the films in comparison with that for the crystals was obtained, which is connected with the additional contribution of light reflected from the substrate and perhaps with optical interference process. The spectrum of magnetoreflection showed the presence of a resonance-like contribution (~20%) to the effect. If the origin of background positive
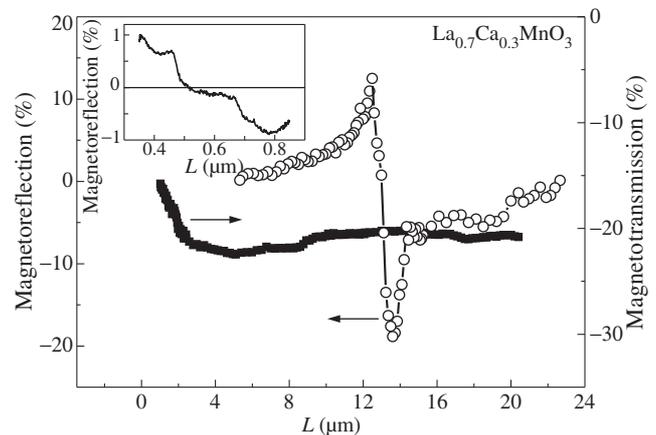
Fig. 1. The spectra of magnetoreflection (open symbols) and magnetotransmission (dark symbols) of La$_{0.7}$Ca$_{0.3}$MnO$_3$ film ($d = 50$ nm) in the magnetic field 0.3 and 0.8 T accordingly at $T = 255$ K. On inset — the magnetoreflection of film in the visible range in the field 1.1 T.

magnetoreflection (~5%) connects with the changing of ratio between localized and de-localized charge carriers in the magnetic field applied near T_C, then the nature of resonance-like contribution could be explained by change of the frequency of minimum in reflection spectra of films (about 13 μm) under the same conditions [5]. The resonance-like effect have not been observed in the magnetotransmission spectra of films. In comparison with IR region in the visible one there was detected no strict correlation between MRE and colossal magnetoresistance in the manganite films (inset on Fig. 2).

For example, there is a change of sign of magnetoreflection (inset on Fig. 1) missing in the magnetotransmission spectum and connected with addinional contribution to MRE of different nature. The magnitude of the MRE is also many times less in comparison with that in the IR-region. The feature can be related with the alteration of the optical density in the region of interband transitions and shifting of fundamental absorption bands under external magnetic field applied. It was shown, the spectra of the MRE of La$_{0.7}$Ca$_{0.3}$MnO$_3$ films in the visible spectral range are similar to the spectra of optical density in the region of interband electron transitions. The observed features of spectral and temperature dependences of MRE in magnetoreflection and magnetotransmission modes in samples are in
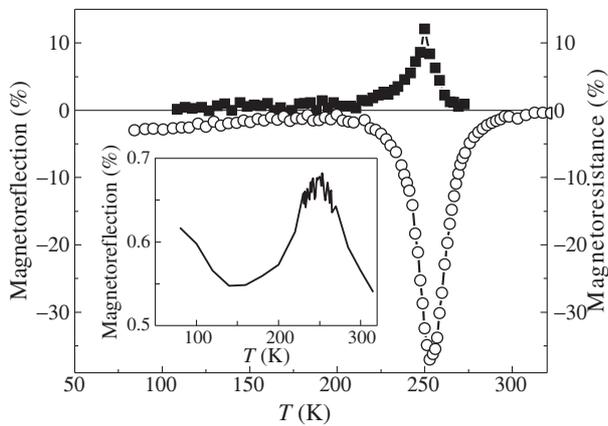
Fig. 2. The temperature dependences of magnetoresistance (open symbols) and magnetoreflection (dark symbols) at 12 μm in La$_{0.7}$Ca$_{0.3}$MnO$_3$ film ($d = 50$ nm) at the magnetic field 0.8 and 0.3 T accordingly. On inset — the temperature dependence of magnetoreflection of film at 0.4 μm in the field 1.1 T.

a qualitative agreement with the developed theory of MRE [1]. We proposed a modified theory of MRE in manganites taking into account inherent magnetic phase separation [2]. To analysis the magnitude of the MRE for different materials a new specific unit of the magnetotransmission and magnetoreflection effects in manganites — %/kOe — was used. Finally, the giant MRE in magnetoreflection and magnetotransmission modes in the wide spectral range may open new ways to use manganite films for creation of different optoelectronic devices [7,8].

References

[1] A.B. Granovsky *et al*, *J. Communication Technology and Electronics* **52**, 1071 (2007).
[2] Yu.P. Sukhorukov *et al*, *JETP* **111**, 360 (2010).
[3] E.A. Ganshina *et al*, *JMMM* **300**, 62 (2006).
[4] Yu.P. Sukhorukov *et al*, *RF Patent*, Byull. Izobret. **4** No. 2346315 (2009).
[5] A.B. Granovsky *et al*, *JETP* **112**, 77 (2011).
[6] Yu.P. Sukhorukov *et al*, *Request for RF Patent* **X**, 060085 (2010).
[7] Yu.P. Sukhorukov *et al*, *Phys. Rev. B* **37**, 4137 (1988).
[8] O.Yu. Gorbenko *et al*, *Physics of metals and metallography* **104**, 556 (2007).

Bloch oscillations and Terahertz electroluminescence of natural SiC superlattice

V. I. Sankin, A. V. Andrianov, A. O. Zakhar'in and A. G. Petrov

Ioffe Physical-Technical Institute, St Petersburg, Russia

Abstract. We report on efficient terahertz emission from high electric field biased SiC structures with natural superlattice at liquid helium temperatures. The emission spectrum demonstrates a single line, the maximum of which shifts linearly with increase in bias field. We attribute this emission to steady-state Bloch oscillations of electrons in SiC natural superlattice.

Introduction

The possibility of oscillating motion of electrons in crystals at high field bias has attracted great interest since it was predicted [1, 2]. The Bloch oscillations (BO) with frequency $\nu = eFa/h$, where e, h and a are the electron charge, the Plank constant and the crystal lattice period respectively, originate due to the acceleration of electrons in electric field and Bragg reflection of them at the Brillouin zone boundary. The BO in artificial supperlattices were found in experiments with the technique of degenerated four-wave-mixing [3–6] and the direct measurements of very small THz emission [7–9] using the coherent excitation by pulsed 100 fs laser. Thus, structures which need pulsed optical excitation for operation are unlikely to yield useful devices [9].

Thereat electron transport studies on the SiC structures with the natural superlattices [10,11,12] have demonstrated the pronounced NDC effects caused by the Wannier–Stark localization phenomenon. These results also hold out well-grounded hope to get THz emission due to the Bloch oscillations in SiC NSL. This work reports on new demonstration of WSL process namely, the first experimental observation of THz electroluminescence (1.5–2 THz spectral range) from SiC structures with the natural superlattice.

1. Results and discussion

The samples studied in this work were unipolar 6H-SiC $n^+ - n^- - n^+$ diode structures which are performed of 6H-SiC NSL with parameters: period $d = 7.5$ Å, superpotential $b \approx 1$ Å, $U \approx 1.5$ eV. The n^- epitaxial layer (the base of the diode) was grown by the sublimation on-axis method on Lely substrate, which had $N_d - N_a \approx 2 \times 10^{18}$ cm^{-3} and 200 μ thickness. The base had the donor concentration of $10^{15} < N_d - N_a < 10^{16}$ cm^{-3} and thickness of $2 - 4$ μ. The top n^+ — layer with $N_d - N_a \approx 10^{20}$ cm^{-3} was fabricated on the n^- epitaxial layer by ion implantation of nitrogen with subsequent annealing. Finally, the mesa-structures were made by dry etching after photolithography procedure. These diode structures were used for investigations of the terahertz emission at liquid He temperatures.

The sample under test was fed with the train of 8 pulses; each pulse in the train was 1 μs long with 950 μs time interval. The spectral measurements were performed with a spectral resolution of 0.6 meV using a Fourier spectrometer operating in the step-scan mode.

The intensive THz signal was detected at bias voltages exceeding 190–195 V. The existence of such threshold voltage for the THz emission can be explained by impurity breakdown
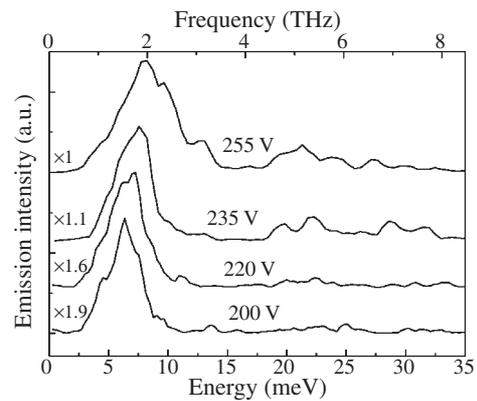
Fig. 1. Spectra of the THz emission from the SiC mesa structure at several bias voltages. $T \approx 7$ K. Spectra are corrected on the spectral response of the measurement system, normalized on the emission maximum and vertically shifted for clarity. The scaling factors are shown in the graph.

in the top heavily doped n^+ — SiC layer required for injection of electrons into NSL. We found that the spectrally integrated THz emission peak power is about 10 μW at 46.2 W of peak pumping power (0.21 A, 220 V). The corresponding external quantum efficiency of the THz emission is about 0.01 THz photons/electron. Fig. 1 demonstrates a set of THz electroluminescence spectra measured at different amplitudes of the bias voltage. As is seen the THz emission spectrum consists of practically single line, the maximum of which shifts to higher frequencies with an increase in bias voltage as predicted the theory [1, 2]. It is possible to see from Fig. 1, that the shift of the THz emission maximum versus the bias voltage can be well approximated by linear law.

To summarize, the THz emission due to electron Bloch oscillations in steady-state regime has been observed for the first time. The experiments were performed on SiC structures with natural superlattice under electrical pumping. The discovered intensive THz electroluminescence with the variable frequency can find practical applications for electrically tunable THz emitters. The considerable variation of the emission frequency from 0.3 to 3 THz can be attained by a choice of SiC polytype with appropriate parameters of the superlattice: the greatest frequency of the emission can be achieved with 4H-SiC, but for the least emission frequency any polytype can chosen from the row of 15R-SiC, 21R-SiC, 27R-SiC, 33R-SiC and so on.

References

[1] F. Bloch, *Z. Phys.* **52**, 555 (1928).

[2] C. Zener, *Proc. R. Soc. London Ser. A* **145**, 523 (1934).

[3] J. Feldman, K. Leo, D.A.B. Miller *et al*, *Phys. Rev. B* **46**, 7252 (1992).

[4] K. Leo, P. Haring Boilvar, E. Bruggeman *et al*, *Solid State Commun.* **84**, 943 (1992).

[5] G.C. Cho *et al*, *Phys. Rev. B* **54**, 4420 (1996).

[6] V.G. Lyssenko *et al*, *Phys. Rev. Lett.* **79**, 301 (1997).

[7] C. Washke *et al*, *Phys. Rev. Lett.* **70**, 3319 (1993)

[8] Y. Shimada *et al*, *Phys. Rev. Lett.* **90**, 046806 (2003).

[9] K. Leo, *Semicond. Sci. Technol.* **13**, 249, (1998).

[10] V.I. Sankin and I.A. Stolichnov, *Superlattices and Microstruct.* **23**, 999 (1998).

[11] V.I. Sankin and I.A. Stolichnov, *JETP Lett.* **64**, 105 (1996).

[12] V.I. Sankin *Fizika i Tekhnika Poluprovodnikov* **36**, 769 (2002); [*Semiconductors* **36**, 717 (2002)].

Amplification of far-infrared and THz pulses due to optical pulse conversion in semiconductor nanoheterostructures

V. A. Kukushkin

Institute of Applied Physics, RAS, Nizhny Novgorod, Russia

Abstract. A method of far-infrared or THz pulse amplification via the conversion of a simultaneously propagating pump optical pulse in semiconductor nanoheterostructures with quantum wells is suggested. It is based on the optical pulse creating transient population inversion at a long-wavelength intersubband transition in a three-level scheme involving conduction and valence band subbands. Calculations show that for the peak power of a 2–3-picoseconds pump optical pulse of 60 W the present scheme with optimized parameters is able to provide a more than 2.5-times increase of the peak power of a probe far-infrared pulse with a carrier wavelength $\simeq 60~\mu$m.

Introduction

Amplification and generation of far-infrared (far-IR) and THz electromagnetic radiation is an important problem of modern laser physics due to the continuous growth of its employment both in fundamental research and various applications including medicine, telecommunication technologies, nondestructive imaging and diagnostics of different materials and natural media, molecular spectroscopy, security systems, etc. Among the most promising sources of radiation in this frequency range are semiconductor nanoheterostructure-based devices. One of them is a quantum cascade laser (QCL) [1] utilizing transitions between subbands of dimensional quantization arising in the conduction bands of nanoheterostructures with quantum wells (QWs). QCLs proved to be very efficient in the mid-IR range where they are capable of room temperature operation with a power of order 100 W (in peak) in the pulsed regime and several watts in the c.w. mode [2]. However, their advance on the far-IR and THz region (which began in 2002 when a QCL operating at 4.4 THz was demonstrated [3]) encounters many problems [4,5]. They are mainly connected with large free-carrier absorption of the far-IR and THz field in superlattice minibands, created in these devices to provide electron transport in the orthogonal to the QW plane direction, and the difficulty to maintain a stationary inversion between close subbands with a small upper subband lifetime. In result, far-IR and THz QCLs work under cryogenic cooling only, and, even in the pulsed mode, their peak output powers do not exceed several hundreds of milliwatts [6].

Therefore, there is a considerable interest to alternative ways of far-IR or THz radiation amplification and generation in QW nanoheterostructures. One of them consists in the creation of not a stationary but a transient inversion at a laser transition between two conduction band subbands for a time less than the upper subband lifetime. This allows to avoid problems of the stationary inversion maintenance between close subbands with a small upper subband lifetime characteristic of QCLs. The transient inversion can be created in a three-level scheme involving, in addition to the two conduction band subbands (numbered 2 and 3), a third subband 1 lying in the valence band (Fig. 1a).

Applying to this scheme a powerful optical pulse with a duration less than the subband 3 lifetime and a carrier frequency ω_1 equal to that of transition $1 \leftrightarrow 3$ results in a transient equilibration of the subband 1 and 3 populations. Taking into ac-
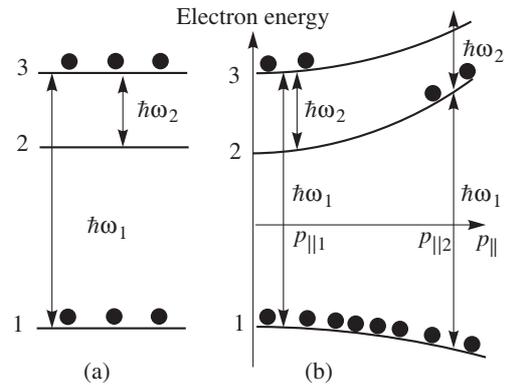
Fig. 1. Electron energies at some absolute value of the electron quasimomentum in the QW plane $p_{\|1}$ (a) and their dependence on $p_\|$ (b). Filled circles denote electrons.

count that the equilibrium population of subband 2 in undoped structures being considered is negligibly small, this leads to the creation of a transient inversion on transition $2 \leftrightarrow 3$. Therefore, if a probe far-IR or THz pulse has a carrier frequency ω_2 coinciding with the transition $2 \leftrightarrow 3$ frequency and a duration equal to that of the pump pulse and propagates simultaneously with the latter, its amplification becomes possible.

Employing not injection but optical pumping, this method has another important advantage over QCLs as it does not require to provide electron transport in the orthogonal to the QW plane direction. So, it allows to isolate QWs from each other (by means of high and thick enough barriers) and avoid the formation of superlattice minibands. This results in a significantly lower free-carrier absorption of the far-IR and THz pulses in comparison with that in QCLs.

The present method is analogous to that employed in lasers with a synchronized pump which have been realized on dyes [7], dye centers in alkali-halogen crystals [8] and optical fibres [9] (please see the overview of these and other works on these subject in [10]). Its application to QW nanohetrostructures encounters the following difficulty. The electron energy in each QW subband is a function of the absolute value (in the isotropic approximation) of the electron quasimomentum in the QW plane $p_\|$ (Fig. 1b). If the pump optical pulse is resonant with transition $1 \leftrightarrow 3$ at some $p_{\|1}$, it is inevitably resonant with transition $1 \leftrightarrow 2$ at some $p_{\|2} > p_{\|1}$ as well. So, it populates not only subband 3 (near $p_\| = p_{\|1}$), but also subband 2 (near $p_\| = p_{\|2}$) so that inversion near $p_{\|1}$ and anti-

inversion near $p_{\|2}$ on transition $2 \leftrightarrow 3$ arise. Therefore, if the frequency of transition $2 \leftrightarrow 3$ were not dependent on $p_\|$ (i.e., subbands 3 and 2 were parallel), the amplification of a probe far-IR or THz pulse with a carrier frequency ω_2 equal to that of transition $2 \leftrightarrow 3$ at $p_{\|1}$ would be compensated with its absorption near $p_{\|2}$ and the present scheme could not work. But actually subbands 3 and 2 are not exactly parallel because the effective mass characterizing the electron in-plane quasifree motion in the 3rd subband is slightly higher than that in the 2nd subband. This effect is caused by corrections to the parabolic dependence of the electron energy on its quasimomentum in the conduction band of bulk semiconductors [11]. The aim of the present report is to show that this non-parallelity of conduction band subbands in QWs, though being rather small, is sufficient to make transition $2 \leftrightarrow 3$ frequency at $p_{\|2}$ smaller than ω_2 by an amount larger than a transition $2 \leftrightarrow 3$ linewidth. This makes the probe far-IR or THz pulse absorption at transition $2 \leftrightarrow 3$ near $p_{\|2}$ non-resonant and let it be overcome by the amplification near $p_{\|1}$.

1. Estimates of the far-IR or THz pulse amplification coefficient

As the basis for the QW structure fabrication let us orient to the AlGaAs heterosystem. Then, let us consider a sequence of asymmetric (i.e. having different left and right barrier heights and thicknesses) QWs in which both the $1 \leftrightarrow 3$ and $2 \leftrightarrow 3$ transitions are dipole allowed and have transition matrix elements of order 0.3 and 3 nm respectively. To provide the optical pump and amplified far-IR or THz pulses confinement, this QW system has to be incorporated in a waveguide. For the optical field it can be a usual dielectric waveguide formed by a thin core layer and two symmetric cladding layers which have a larger Al content (and, therefore, a smaller refraction index) than the core one. The far-IR or THz field confinement can be achieved by employing a single-plasmon waveguide widely used in THz CQLs [4]. It is formed by a thin metallic (e.g. Au) layer deposited on the structure surface and a thin highly doped semiconductor layer placed between the structure and substrate. Being sufficiently far from the core layer, these layers have a small overlap with the optical field and therefore do not increase significantly its absorption coefficient. The QW sequence is equally divided into two active regions placed in cladding layers symmetrically with respect to the core layer.

The pump optical pulse is supposed to have a carrier wavelength $\lambda_1 \simeq 0.8\,\mu$m (in vacuum) and propagate in such a combined waveguide in the form of a TE mode. The far-IR or THz pulse should propagates in it as a TM mode which provides its interaction with transition $2 \leftrightarrow 3$. For the two pulse to coincide in space during their propagation through the structure, they are to have equal group velocities. For the given λ_1 this condition can be fulfilled for various far-IR or THz pulse carrier wavelengths λ_2 by adjusting the waveguide parameters. To be concrete let us make the following estimates for $\lambda_2 \simeq 60\,\mu$m (in vacuum). In such a case the $2 \leftrightarrow 3$ transition frequency, which has to be equal to that of the far-IR or THz pulse, is significantly smaller than the AlGaAs longitudinal optical (LO) phonon frequency. So, at sufficiently low (e.g. liquid nitrogen) temperatures and small $p_{\|1}$ when both the thermal energy and $p_{\|1}^2/(2m_3)$ (where m_3 is the effective electron mass in the 3rd subband) are much smaller than the LO phonon energy, the 3rd
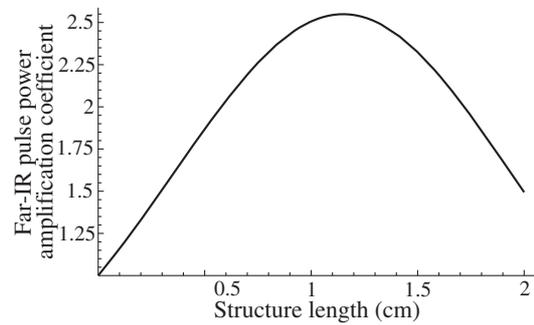

Fig. 2. The far-IR pulse amplification coefficient as a function of the structure length.

subband lifetime can be of order several ps and is determined by electron scattering on acoustic phonons, impurities and interface defects. So, for $\lambda_2 \simeq 60\,\mu$m the amplified far-IR pulses can be as long as 2–3 ps. For a pump optical pulse with the same duration and a peak power of 60 W in the case of the active regions consisting of 50 QWs each calculations show that the far-IR pulse amplification coefficient reaches its maximal value of 2.5 (in power) for the structure length of order 1 cm (Fig. 2).

Its decrease for longer structures is connected with the pump optical pulse extinction due to its absorption at transition $1 \leftrightarrow 3$. The further increase of the far-IR pulse power by this method can be achieved by placing several such structures at some distance one after another and introducing into each structure a new pump optical pulse at the moment when it is reached by the amplified far-IR one. Employing such a cascade scheme allows to obtain the resulting far-IR pulse amplification coefficient of order $2.5 \times$ the number of the structures involved.

References

[1] J. Faist *et al*, *Science* **264**, 553 (1994).
[2] S. Slivken *et al*, *Proc. of SPIE* **7608**, 76080B (2010).
[3] R. Kohler *et al*, *Nature* **417**, 156 (2002).
[4] B.S. Williams, *Nature Photonics* **1**, 517 (2007).
[5] G. Scalari *et al*, *Laser & Photon. Rev.* **3**, 45 (2009).
[6] B.S. Williams *et al*, *Electron. Lett.* **42**, 89 (2006).
[7] V.A. Nekhaenko *et al*, *Quant. Electron.* **16**, 299 (1986).
[8] T.T. Basiev *et al*, in *Proceedings of the IVth All-Russian Conference "Tunable lasers"*, Novosibirsk, December 6–9, 1983, p. 399 (1984) (in Russian).
[9] V. A. Arkhangelsaya *et al*, *Quant. Electron.* **10**, 657 (1980).
[10] S. A. Akhmanov *et al*, *Optics of Femtosecond Laser Pulses* (Melville, N. Y.: American Institute of Physics, 1991).
[11] U. Ekenberg, *Phys. Rev. B* **40**, 7714 (1989).

Application of mid-infrared LEDs and wideband photodiodes (1.6–2.4 μm) for detection of water in oil

Yu. P. Yakovlev, N. D. Stoyanov, S. S. Molchanov and K. V. Kalinina

Ioffe Physical-Technical Institute, St Petersburg, Russia

We propose a novel technique for measuring water in oil based on mid-infrared (1.6–2.4 μm) light emitting diodes (LEDs) and wideband photodiode (1.2–2.4 μm).

For developing this technique we investigated absorption spectra of pure water, water-free oil, and cut oil with different water concentration using nine LEDs emitting at 1.6–2.4 μm spectral range [1] (Fig. 1). According to Fig. 1 water has a strong absorption bands in the range about 1.85–2.05 and 2.4–2.6 μm, oil — in the range about 1.65–1.87 and 2.24–2.47 μm. So, there is a region with a large difference in the absorption of infrared radiation between water and oil — from 1.6 to 2.5 μm. LED19 radiation (central wavelength 1.94 μm) is strongly absorbed by water, LED16 radiation (central wavelength 1.65 μm) — is absorbed by oil and slightly influenced by water. The difference in the absorption values of these two LEDs can be used to determine water concentration. But radiation propagation through water-oil emulsion is strongly influenced by scattering at water-oil drops interfaces, also it may depend on some other environmental effects. So, to compensate these effects at list one more emitter (reference) should be used. LED22 (maximum wavelength 2.20 μm) can be chosen for this purpose as its radiation is almost equally depends on water and oil presence. The optical cell for water in oil sensor was developed using three-element LED-matrix with maximum radiation intensities at 1.65 (oil detection), 1.94 (water detection) and 2.20 (reference signal) and wideband photodiode operating at 1.3–2.4 μm spectral range [2] (Fig. 2). We obtained the calibration curve that was the dependence of water concentration in cut-oil from the computed signal from three LEDs (Fig. 3). Based on this optical measurement technique the pilot sample of water in oil sensor providing on-line operation directly at oil-well was created. This sensor allows detection of water in oil in the range of water concentration

Fig. 2. (a) 3-element LED-matrix spectra and PD spectral response, (b) optical cell design.
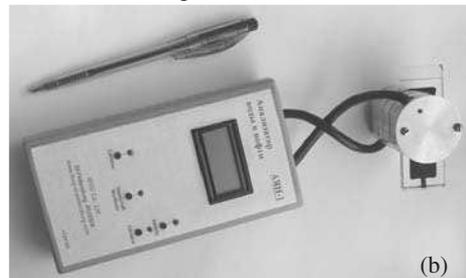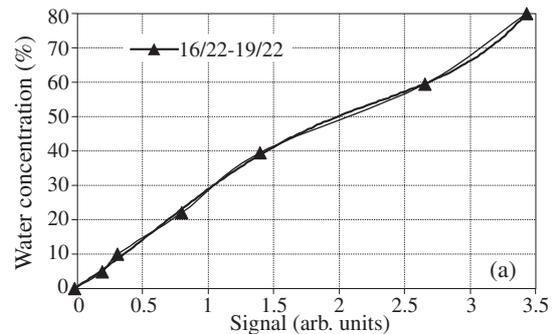
Fig. 3. (a) Calibration curve, (b) portable optical water in oil sensor.

0–80% with an error 2–3%.

Fig. 1. (a) Absorbance of mid-IR radiation by 100% water, (b) absorbance of mid-IR radiation by 100% oil ("devon" type).

## References

[1] N.D. Stoyanov, B.E. Zhurtanov ... and Yu.P. Yakovlev, *Semiconductors* **37**, 996 (2003).
[2] I.A. Andreev, N.D. Il'inskaya ... and Yu.P. Yakovlev, *Semiconductors* **37**, 974 (2003).

Midinfrared absorption spectra of nanostructured copper oxides Cu_2O and CuO

B. A. Gizhevskii[1], E. V. Mostovshchikova[1], N. N. Loshkareva[1], V. R. Galakhov[1], S. V. Naumov[1], N. A. Ovechkina[1], N.V. Kostromitina[1] and A. Buling[2]

[1] Institute of Metal Physics, Ural Branch of RAS, 620990 Ekaterinburg, Russia
[2] FB Physik, University of Osnabrück, Barbarastrasse 7, D-49069 Osnabrück, Germany

Abstract. High-density Cu_2O and CuO nanoceramics were prepared from oxide powders by high pressure torsion method. Optical absorption spectra of Cu_2O and CuO have been studied in the middle infrared range. We found the influence of annealing in vacuum and air on the optical properties of nanostructured copper oxides.

Introduction

Nanomaterials based on copper oxides are interesting both for fundamental physics and practical applications. Cuprous oxide Cu_2O is one of the best-studied classical wide-gap semiconductor. Cupric oxide CuO is a typical representative of strong correlated system, antiferromagnetic semiconductor and a basis of cuprate superconductors. It is a well-known quantum size effect on optical properties of nanostructured Cu_2O: the fundamental absorption edge E_g increases as the crystallite size decreases up to nanoscale, i.e. blue shift of the edge takes place. In the case of nano-CuO E_g demonstrates a red shift in the nanostate [1]. There is very poor information about optical properties of nanostructured Cu_2O and CuO in the infrared range. Middle infrared spectra may supply interesting data about specific defects, impurities and phonon bands of nanostructured oxide materials.

1. Experiment and sample preparation

In the present work, we studied optical absorption spectra of Cu_2O and CuO nanoceramics in the range of 0.08–1.2 eV and compared the midinfrared spectra of nanooxides with those of corresponding single crystals. Raman spectra were measured in the range 100–1400 cm^{-1} at room temperature. We also measured X-ray absorption spectra (XAS, measured at the
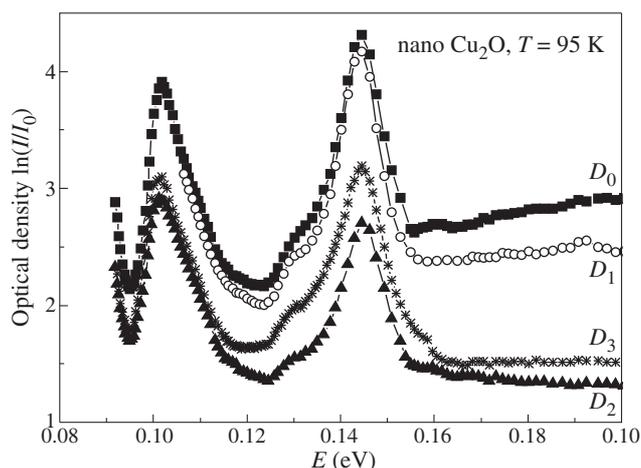
Fig. 2. Effect of temperature annealing on absorption spectra of nano Cu_2O.

Russian–German Beamline at BESSY) to determine changes in the valences states of copper ions and to clarify the phase composition of nanooxides. High-density Cu_2O and CuO nanoceramics were prepared from oxide powders by high pressure torsion method. The initial coarse-grain powder of corresponding oxide was placed between the anvils and pressed at pressure up to 10 GPa. Shear deformation was achieved by rotating one of the anvils with respect to the other one. The samples were characterized by X-ray diffraction (XRD), and a number of samples were examined using scanning tunnelling and scanning electron microscopy. The crystallite size (12–40 nm) and microdeformations were evaluated from broadening of X-ray diffraction lines. High density and quality of the nanoceramics allowed to obtain the optical spectra of good quality.

2. The infrared spectra of nano Cu_2O and CuO

The infrared spectra of nano-Cu_2O as well as of a Cu_2O single crystal display two intensive bands with a fine structure at 100 and 140 meV (Fig. 1). Interpretation of these bands is contradictory in literature: biphonons, multiphonons or localized phonon modes [2]. We revealed the features at 130 meV and for one of Cu_2O nanostructured samples the additional band at 160 meV which absent in the spectra of the single crystal. We note that the bands at 100 and 140 meV are clearly visible not only at low temperatures but at room temperature also. These bands have weak temperature dependence. Therefore, it is unlikely that they connected with biphonons. Our XRD data did
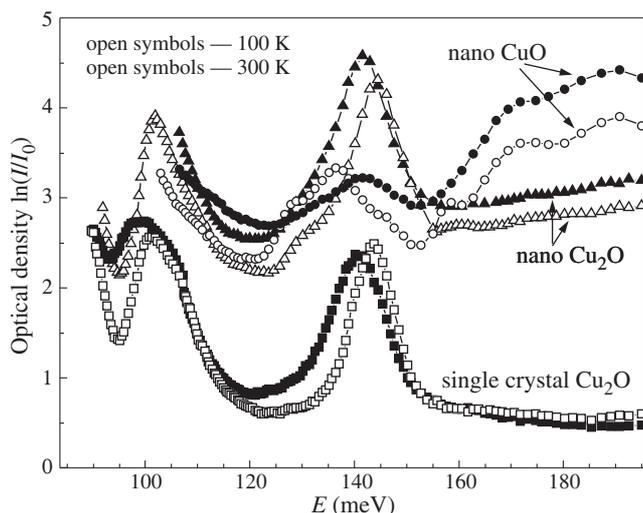
Fig. 1. Optical density spectra of nano CuO, nano Cu_2O and of a single crystal Cu_2O.
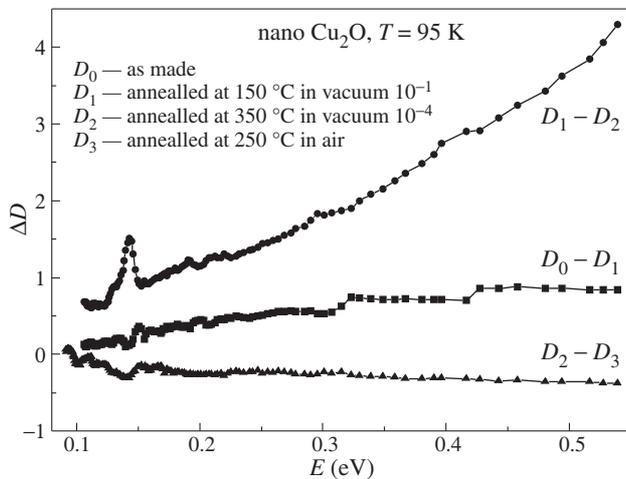
**Fig. 3.** Difference absorption spectra after annealing in vacuum (D_0–D_1, D_1–D_2) and in air (D_2–D_3).
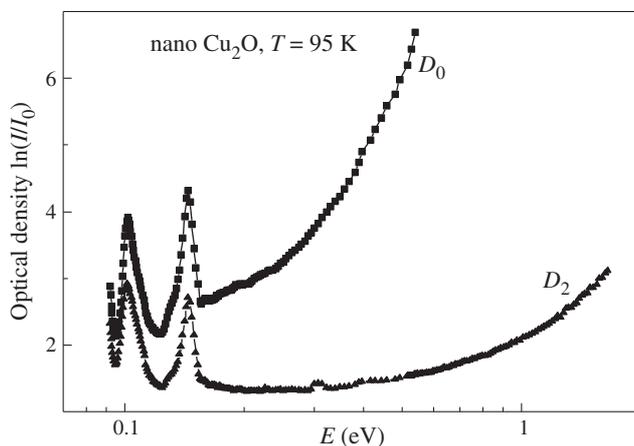

Fig. 4. Absorption spectra of nano Cu_2O before (D_0) and after annealing in vacuum (D_2).

not detect CuO or other excess phases in nano-Cu_2O. However, according to the XAS data all Cu_2O nanostructured samples contain high concentration of Cu^{+2} ions. The sample with the highest concentration of Cu^{+2} ions exhibits the most intense band at 140 meV. After annealing in vacuum which reduces the concentration of Cu^{+2} ions, intensity of this band decreases, but its energy position does not change (Fig. 2). We suppose that the band at 140 meV is formed due to presence Cu^{+2} ions or Cu-vacancies.

In the spectra of nano-CuO we observed the band at the same energy 140 meV with the similar shape to that of Cu_2O. According to our X-ray photoelectron spectral data, CuO nanoceramics contain up to 8–10 percent Cu^+ ions. Effect of temperature annealing in vacuum and in air on IR absorption spectra of nano-Cu_2O is well visible in Fig. 3 and Fig. 4.

Probably that these bands in the spectra of copper oxides are connected with presence of defects of nonstoichiometry such as vacancies and cations with different valency. Concentration of such kind defects in nanostructured samples considerably above, than in equilibrium crystals. Note that an anomaly of the temperature dependence of 140 meV-band intensity appears near T_N in the IR spectra of CuO. Besides the band at 140 meV in nano-CuO, we observed a broad band with the complex structure near 190 meV (Fig. 1). This wide band was observed

in the spectra of CuO single crystals and was explained by the transitions in $(CuO_4)^{5-}$ clusters [3] or in terms of phonon-assisted magnetic excitation [4].

Raman spectra of Cu_2O nanostructured samples demonstrate weak bands at 100 meV and in the range of 130–150 meV. These bands are widened in comparison with similar bands in single crystals. In Raman spectra of CuO the strong band is observed at 140 meV. The band at 100 meV, observed in IR spectra, is absent.

Nanostructered oxides are nonequilibrium materials with a considerable concentration of point and surface defects. The point defectiveness of nanostructured Cu_2O as well as CuO is determined by a noticeable deviation from stoichiometry and presence of high concentration of cations with different valence, which leads to peculiarity of physical properties, in particular, the optical spectra.

References

[1] B. A. Gizhevskii *et al*, *JETP. Phys. Lett.* **102**, 297 (2006).
[2] M. Jorger *et al*, *Phys. Rev. B* **71**, 235210 (2005) .
[3] A. S. Moskvin *et al*, *JETP* **78**, 518 (1994).
[4] S. H. Jung *et al*, *Phys. Rev. B* **80**, 140516(R) (2009).

Propagation of electromagnetic waves in 3D opal-based magnetic nanocomposites at microwave frequencies

G. S. Makeeva[1], O. A. Golovanov[1], *A. B. Rinkevich*[2] and M. Pardavi-Horvath[3]

[1] Penza State University, Penza, Russia
[2] Institute of Metal Physics, Ural Branch of RAS, 620990 Ekaterinburg, Russia
[3] George Washington University, Washington, USA

Abstract. The 3D magnetic nanocomposite, consisting of opal submicron sphere matrices with magnetic nanoparticles, shows interesting magnetic properties and unique microwave behavior [1] with potential applications for future magnetophotonic devices at GHz and THz frequencies. The electromagnetic properties of such nanocomposites can be tuned by external bias magnetic field. The propagation of electromagnetic waves (EMWs) in the 3D opal-based magnetic nanocomposites at microwave frequencies was investigated numerically using rigorous mathematical modeling based on solving Maxwell's equations with electrodynamic boundary conditions, complemented by the Landau–Lifshitz equation, including the exchange term [2].

The numerical approach is based on the decomposition onto autonomous blocks with Floquet channels (FAB) [2]. The domain of the 3D opal-based magnetic nanocomposite is divided into FABs (Fig. 1a) in the form of a rectangular parallelepipeds, containing the opal submicron spheres and magnetic nanoparticles, filling the octahedral and tetrahedral void regions (Fig. 1b), with virtual Floquet channels on bounds (input sections $S\alpha$).

Fig. 2. Real and imaginary parts of complex wave number Γ_0 of the fundamental mode of quasi-extraordinary EMW in 3D opal-based magnetic nanocomposites depending on transverse bias magnetic field $\mathbf{H}_0$ for magnetic nanoparticles of (a) — $NiFe_2O_4$; $4\pi M_s = 3.2$ kG; (b) — $Ni_{0.7}Zn_{0.3}Fe_2O_4$; $4\pi M_s = 5$ kG; SiO_2 opal submicron spheres $r = 125$ nm; $f = 9.375$ GHz; 1 — $Re\Gamma_0$; 2 — $Im\Gamma_0$.

The FAB descriptor (a multimode multi-channel scattering matrix S or conductivity matrix Y) is determined by solving the 3D diffraction boundary problem by using the Galerkin's projection method [2].

The electrodynamic analysis of propagation of EMWs in the 3D opal-based nanocomposites was performed by solving the characteristic equation [3] included the blocks of the FAB conductivity matrix Y, resulting from taking into account electrodynamic boundary conditions. That's why the simulation of propagation of EMWs in 3D periodic arrays of arbitrary shaped magnetic nanoelements in the opal nanosphere matrix is possible by using the developed α. Based on the method outlined above, the bias magnetic field dependence of the propagation constants for EMWs, propagating in the 3D magnetic opal nanocomposites was calculated.

Fig. 1. Division of the 3D magnetic opal into autonomous blocks: (a) 1 — region, filled by magnetic nanoparticles; 2 — SiO_2 submicron spheres; (b) autonomous block in the form of a rectangular parallelepiped with virtual Floquet channels: V_0 is the basic region; $V = V_1 \cup V_2 \cup V_3 \cup V_4$ are regions of dielectric submicron spheres; $V_0 - V$ is the region of magnetic nanoparticles; $0_\alpha z_\alpha$ ($\alpha = 1, 2, \ldots, 6$) are local coordinate systems on input sections $S\alpha$ (bounds).

The complex wave number Γ_0 of the fundamental mode of the quasi-extraordinary EMW was determined depending on the bias magnetic field $\mathbf{H}_0$ with the transverse orientation. The main results are shown in Figs. 2a,b. The radius of the SiO_2 submicron spheres was set $r = 125$ nm, $\varepsilon_r = 4.6 - i3 \times 10^{-4}$, $\mu_r = 1$; and for magnetic nanoparticles of either $NiFe_2O_4$ with $4\pi M_s = 3.12$ kG, or $Ni_{0.7}Zn_{0.3}Fe_2O_4$ with $4\pi M_s = 5$ kG ($\alpha = 6 \times 10^{-3}$, $\varepsilon_r = 9.5 - i0.3$).

As expected for a magnetic nanoparticle system, the peak of resonance absorption of quasi-extraordinary EMW (Fig. 2) does not coincide with the FMR frequency of the bulk continuum ferrite. The bias field dependence of the real part of the propagation constant shows the presence of a stop-band, strongly dependent on the magnetization.

The results of computing by using the method developed permit to analyze and optimize the electromagnetic properties of 3D opal-based magnetic nanocomposite materials. By changing the magnetization chemically, or through the filling factor of the magnetic component, or varying the configuration of the magnetic opal, significant changes in the propagation constants of the EMWs are expected.

References

[1] A. Rinkevich *et al*, *Technologia i konstruirovanie v electronnoi apparature*, 55 (2008) *(in Russian)*.
[2] O. A. Golovanov *et al*, *Radiotekhnika i Elektronika* **54**, 1421 (2009).
[3] G.S. Makeeva *et al*, *Radiotekhnika i Elektronika* **54**, 1455 (2009).

Magnetic antiresonance in 3D-nanocomposites with transition-metal nanoparticles

A. B. Rinkevich[1], *D. V. Perov*[1], *M. I. Samoylovich*[2], *S. M. Klesheva*[2] and *E. A. Kuznetsov*[3]

[1] Institute of Metal Physics, Ural Branch of RAS, 620990 Ekaterinburg, Russia
[2] Central Research Technological Institute "TECHNOMASH", 121108 Moscow, Russia
[3] Niznij Tagil State Socially-Pedagogical Academy, 622031 Nizhny Tagil, Russia

Abstract. Investigation and application of extraordinary electromagnetic properties of metamaterials and nanocomposites becomes one of the most promising topics in last years. The problem of interaction between electromagnetic wave and magnetic nanoparticles is of essential interest. Resonance phenomena in 3D opal-based nanocomposites are studied here through frequency and magnetic field dependences of the transmission and reflection coefficients measured in millimeter waveband. Observation of magnetic antiresonance phenomenon is reported in a 3D-nanocomposite based on opal packages with embedded metallic magnetic particles. The antiresonance is seen at microwave frequencies of the millimeter waveband and it results in distinct maximum of the reflection or transmission coefficient.

The opal matrix packages with sphere diameter of ∼250 nm were produced with transition metal Fe, Ni and Co nanoparticles in the inter-sphere voids. The inserted particles have polycrystalline structure and are irregular in shape, see Fig. 1. The typical size of the particles falls in the interval from 5 to 60 nm. The magnetization curves measured at room temperature is shown in Fig. 2. In the field interval used there is no sign of saturation and the magnetization curve looks as a straight line.

Microwave measurements have been carried out in the millimeter waveband in frequency range from 26 to 38 GHz. For measurements the sample was displaced inside a cross-section of the rectangular waveguide. External magnetic field **H** lies in the plane of the sample perpendicularly to the microwave magnetic field vector **H**∼. The relative variation of the transmission and reflection coefficient module in magnetic field is measured. External permanent magnetic field can essentially change the reflection and transmission coefficients of the 3D-nanocomposites studied. It is assumed that the main reason for these variations is magnetic resonance in magnetic particles. We demonstrate here another reason of strong microwave variations besides the magnetic resonance. Let us discuss the magnetic field dependence of reflection coefficient measured at different frequencies (Fig. 3).

The reflection coefficient at first increased and then decreased after a maximum, reaches a minimum caused by mag-
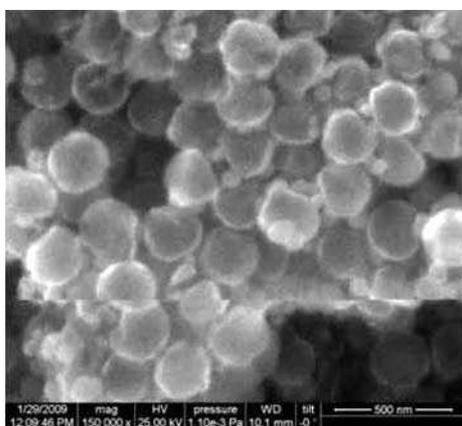
Fig. 1. Structure of 3D-nanocomposite with Co nanoparticles.
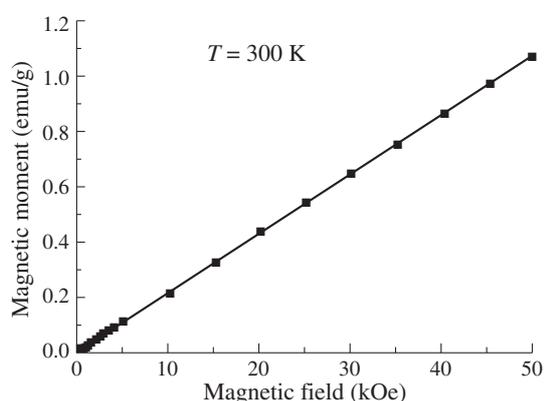
Fig. 2. Magnetization curve for 3D-nanocomposite with Co nanoparticles.
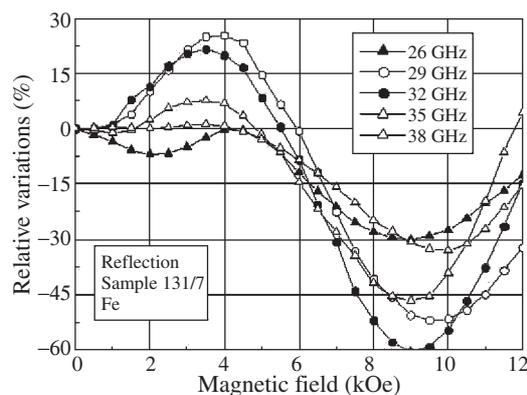
Fig. 3. Magnetic field dependences of reflection coefficient for the nanocomposite with Fe particles measured at different frequencies of millimeter waveband.

netic resonance and then increases again. The maximum is seen often in the transmission coefficient also, and therefore there is a minimum of absorbed power near the maximum, that is antiresonance. This picture is typical for magnetic resonance and the minimums of reflection and transmission coefficients observe because of great imaginary part of magnetic permeability. Certainly, the resonance line for the 3D-nanocomposite is very wide as long as the metallic particles are irregular in shape and randomly oriented. Consequently, the magnetization in
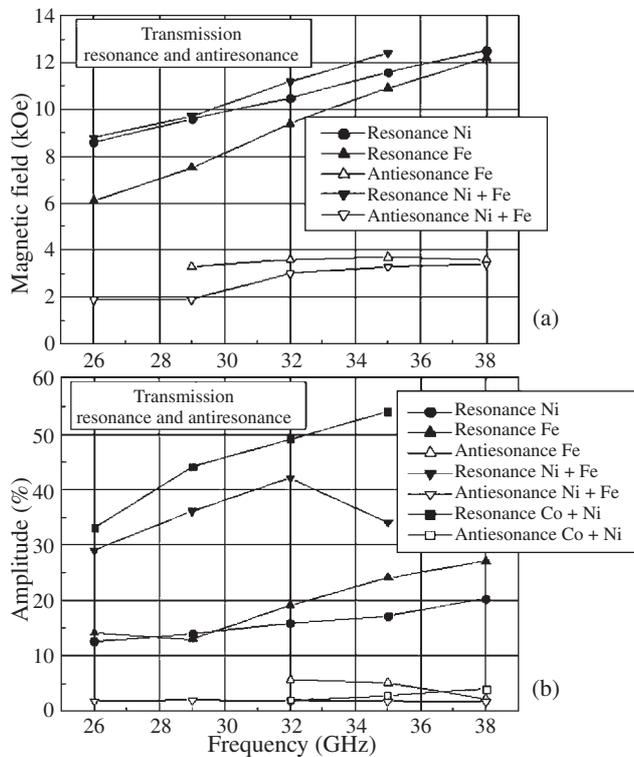
Fig. 4. Spectra of magnetic resonance and antiresonance (a) and frequency dependences of the magnitude of resonance and antiresonance for different nanocomposites (b).

different particles varies strongly from one to another.

From the fields of magnetic resonance and antiresonance the spectra were reconstructed, see Fig. 4a. Antiresonance is always seen in the fields less than the resonance field. The frequency dependences of resonance and antiresonance magnitude are shown in Fig. 4b for several nanocomposites. It is clearly seen that the resonance magnitude for the nanocomposites containing the particles of two transition metals much exceeds the magnitude for the nanocomposites with the particles of one metal. The results obtained and great variations of microwave parameters create suppositions for developing of magnetic field driven microwave devices based on magnetic resonance or antiresonance.

Acknowledgements

An electron-hole spectrum of Si/Ge structure with Ge quantum dots

A. B. Talochkin and I. B. Chistokhin

Institute of Semiconductor Physics, SB RAS, Lavrentieva av., 13, Novosibirsk 630090, Russia

Abstract. Spectra of the lateral photoconductivity of Si/Ge structures with Ge quantum dots (QDs) grown by means of a molecular beam epitaxy (MBE) are studied. The lines of optical transitions between hole levels of QDs and Si electron states are observed. This allows us to build up a detailed energy scheme of the Si/Ge structures with different QD sizes. It is shown that the hole levels of pseudomorphic Ge QDs are well described by a simplest "quantum box" model using the real sizes of Ge islands. It is established that the low energy edge of photosensitivity can be governed by varying the growth parameters of Si/Ge structures.

Introduction

The electron-hole spectrum of Si/Ge structures with Ge QDs grown by means of MBE was studied in numerous works during the last decade [1–3]. In the majority of experiments, the measured integrated spectra turn out to be merged into a wide spectral range, and hole levels intrinsic to an individual Ge QD did not display themselves. Such a behavior is caused by the influence of different non-uniformities, the main of which is related to the non-uniform strain relaxation in a Ge QD array [4]. We have recently found that this negative influence of non-uniformity can be eliminated in a Ge QD array grown pseudomorphically to a Si matrix at low temperature ($T_s \simeq 250$ °C) [4,5]. Besides, deviations in the growth conditions from the optimal ones which do not disturb essentially the QD array uniformity allow one to change QDs sizes and to observe the hole levels of an individual Ge QD [6].

In this work, we study spectra of the lateral photoconductivity (PC) of Si/Ge multilayer structures with Ge QDs grown by using MBE at different growth conditions which ensure the extreme high uniformity of obtained QD arrays.

1. Experimental

The studied multilayer Si/Ge structures with Ge QDs were grown by using "RIBER-Siva32" MBE installation. The Si (100) wafer n-doped (7.5 Ω cm) was used as a substrate. A 100 nm undoped Si buffer layer was first grown on a cleaned wafer at $T_s = 700$ °C. Then, the Ge layer with the effective thickness of 1.1 nm was grown at the substrate temperature of 250 °C. The grown Ge layer was coated with a 2 nm thick Si layer at the same temperature. Then, a 16 nm thick Si spacer was grown at temperature varying for different samples within the range of $450 < T_s < 600$ °C. The structure period that included the QD Ge layer and the 18 nm thick Si spacer was repeated 17 times. The schematic of the grown structure is shown in Fig. 1. Ohmic contacts were made by means of 0.1 mm — thick In layer deposition. PC spectra were measured in the range of 1.2–0.3 eV at $T = 78$ K using standard techniques. The electric circuit of the PC measurements is shown in Fig. 1. The strain and degree of its uniformity in the Ge QD arrays were examined using Raman scattering by optical phonons [5].

2. Photoconductivity of Si/Ge structures with Ge QDs

Fig. 2 shows the PC spectra of two samples (a) and (b). For the first one, $T_s = 450$ °C, and the QD arrays are pseudomorphic
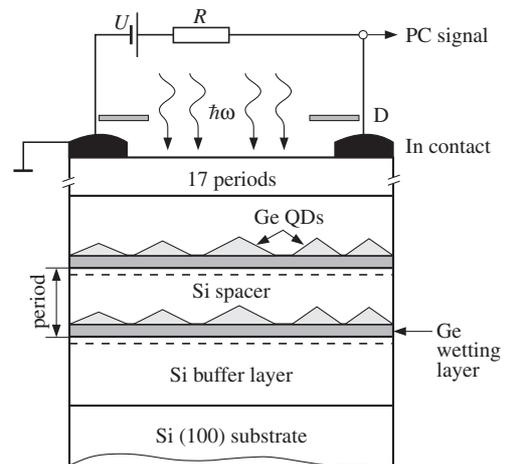
Fig. 1. Schematic of multilayer Si/Ge structure with Ge QDs, and electrical scheme for PC measurement.

to a Si matrix. The Si layers of the sample (b) were grown at $T_s = 500$ °C, which leads to a decrease in the QD strain value by 20 percent and to an increase in their sizes. The PC spectra of both the samples reveal photoresponse at light energy lower than the Si fundamental band gap (E_g^{Si}), which was observed in numerous studies previously and related to the optical transitions between the QD hole levels and the Si electron states. In our case, the sets of peaks marked in Fig. 2 by small arrows are observed, and the structure of the spectra is nearly identical for both the samples. The observed spectra consist of the three doublets, and the low-energy ones are denoted by A and B. They are related to the electron levels appearing in the Si band bending region near Si/Ge interfaces. As the result of influence of the strains penetrating from Ge QDs into Si the Si electron state (Δ_1) is split into two levels (A and B), the spatial positions of which are shown in Fig. 1 with dashed lines. In our case, the lateral conductivity channel through these levels is formed due to high uniformity of QD arrays in studied Si/Ge structures.

Application of a simplest "quantum box" (QB) model with infinite walls allows us to clear up the main features of the observed PC spectra. The energy shift of a particle appearing due to quantization of its spectrum is determined by well known equation:

$$\Delta E_{(nmk)} = \frac{\pi^2 \hbar^2}{2m^*} \left(\frac{n^2}{h^2} + \frac{m^2}{a^2} + \frac{k^2}{a^2} \right), \qquad (1)$$
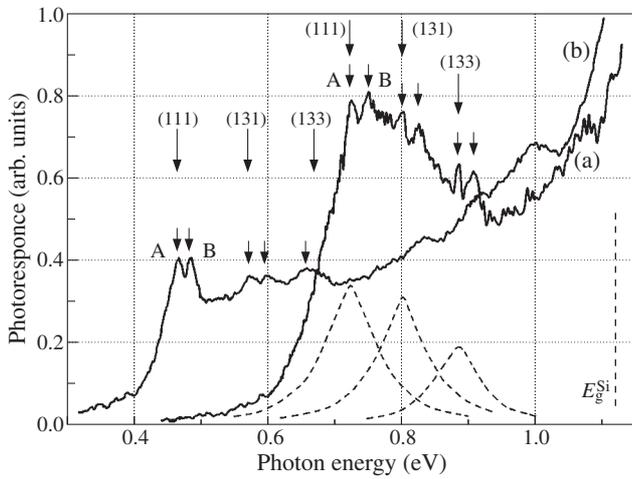
Fig. 2. Spectra of lateral PC of the two samples (a) and (b) of multilayer Si/Ge structure with Ge QDs measured at $T = 78$ K. Sample (a) contains Ge QD arrays pseudomorphic to Si matrix, and those of the sample (b) are partially relaxed due to Si-Ge interdiffusion. Small arrows indicate the observed peak positions, and the large ones show the optical transition energies calculated using the QB model. The Gaussian curves shown by dashed lines were obtained by decomposing the contour (a) into the components.

where n, and (m, k) are the quantum numbers for the growth axis and the growth plane, respectively, h and a are the height and the lateral size of a parallelepiped approximating the QD shape. Eq. (1) shows that the low-energy edge of the spectra is determined by the quantization energy of the ground hole state $\Delta E_{(111)}$. These values are 0.44 eV and 0.12 eV for the samples (a) and (b), respectively, and determined by the QD height h. For the sample (a) $h \approx 1.75$ nm, which well corresponds to the real Ge island height. For the sample (b) $h \approx 3.5$ nm due to intermixing of the components in a growth process. In turn, the observed distance between the doublets is determined by the QD size in the growth plane, which are 11 and 10 nm for the samples (a) and (b), respectively. The QD hole level energies calculated by means of the used model for the QD sizes determined above are shown in Fig. 2 by large arrows with indication of the set of quantum numbers of the corresponding hole states. One can see that the experimental results are in good agreement with the calculations.

3. The electron-hole spectrum of Si/Ge structure with Ge QDs

The simple analysis presented above allows us to build up the detailed energy scheme of the QD hole levels and the optical transitions of Si/Ge structures with Ge QDs depending on the QD sizes. These schemes determined for the samples (a) and (b) are shown in Fig. 3. The hole levels, the optical transitions between which and the Si states (A and B) (vertical arrows in Fig. 3) contribute to PC, are shown by solid lines. The hole levels with even quantum numbers for the directions of the growth plane ((121), (122) etc.) are indicated in Fig. 3 with dashed lines. The optical transitions between these levels and the Si electron sates are forbidden due to symmetry of envelope wave functions [6]. As a result, they do not appear in the PC spectra. Thus, the used model describes correctly the number of peaks observed in the PC spectra of Si/Ge structures with Ge QDs.
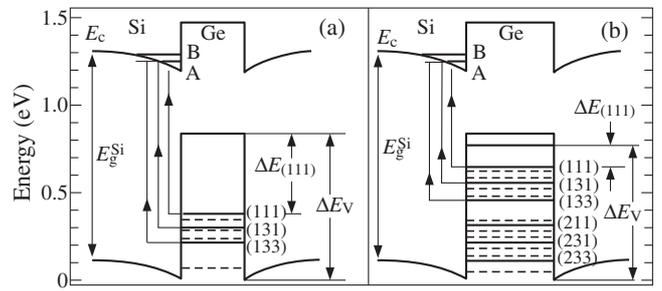
Fig. 3. Band diagrams of the Si/Ge structure with Ge QDs obtained for the two samples (a) and (b). Solid and dashed lines indicate the positions of the QD hole levels calculated using the QB model, and the solid ones (A and B) show the Si electron states. The vertical arrows indicate the allowed optical transitions between the QD hole states and the level A.

We note that decomposition of the observed PC contour of the sample (a) into Gaussian components is shown in Fig. 2 by dashed lines. They have the sufficiently large half-width $\delta E \approx 0.1$ eV determined by dispersion of QD height due to the strong dependence of level energy on QD height (Eq. (1)) because Ge QDs have the same strain state, and the strain dispersion is absent. From Eq. (1), we find that the determined line half-width corresponds to the relative dispersion of QD height $(\delta h / h) \approx 0.1$. This value quite well agrees with the results of statistical analysis of Ge QD arrays [7,8], and indicates that the uniformity of QD sizes in our structures is sufficiently high.

In conclusion, high uniformity of Ge QD arrays, which is ensured in the rather narrow range of growth conditions, allows us to observe the hole levels of an individual QD in the PC spectra of multilayer Si/Ge structure with Ge QDs. The simplest "quantum box" model describes well the QD hole levels, their number observed in PC spectra, and also explains their shape.

References

[1] K. Brunner, *Rep. Prog. Phys.* **65**, 27 (2002).
[2] D. J. Paul, *Semicond. Sci. Technol.* **19**, R75 (2004).
[3] J.-M. Baribeau, X. Wu, N.L. Rowell and D.J. Lockwood, *J. Phys.: Condens. Matter* **18**, R139 (2006).
[4] A.B. Talochkin, V.A. Markov and V.I. Mashanov, *Appl. Phys. Lett.* **91**, 093127 (2007).
[5] A.B. Talochkin and A.G. Cherkov, *Nanotechnology* **20**, 345702 (2009).
[6] A.B. Talochkin, I.B. Chistokhin and V.A. Markov, *Nanotechnology* **20**, 175401 (2009).
[7] Z. Jian, H. Zhu, F. Lu, J. Qin, D. Huang, X. Wang *et al*, *Thin Sol. Films* **321**, 60 (1998).
[8] M. Kastner and B. Voigtlander, *Phys. Rev. Lett.* **82**, 2745 (1999).

The possibility of direct band Ge and Ge/InGaAs quantum wells in GaAs

A. A. Dubinov and V. Ya. Aleshkin

Institute for Physics of Microstructures, RAS, 603950 Nizhny Novgorod, Russia

Abstract. A Ge quantum well (QW) of sufficiently small thickness (<2 nm) in GaAs becomes a direct-band structure. The maximum wavelength corresponding to the absorption edge of a Ge direct-band QW is shorter than 1.2 μm. In a direct-band combined Ge/In$_{0.35}$Ga$_{0.65}$As QW the maximum wavelength corresponding to the absorption edge exceeds 1.5 μm. Calculations of the surface conductivity of such QWs have demonstrated a possibility for using these systems as active medium in semiconductor lasers.

Introduction

In recent years, semiconductor lasers emitting at 1.3 and 1.5 μm have been required in telecommunication because in this range quartz waveguides ensure minimum dispersion and absorption of radiation.

This work deals with investigation into another possibility to produce effective lasing in the $1.3-1.5$ μm wavelength range, using GaAs-based structures with Ge and combined Ge/InGaAs QWs. The lattice constants of Ge and GaAs are close, which is promising of attainability of practically perfect Ge/GaAs heterojunctions. The technology for growing strained QWs of InGaAs on GaAs is fairly well developed and the lasers on their basis have long been a commercial product.

Ge is an indirect semiconductor. The lower valley in the conduction band is the L-valley, and the top of the valence band is located in the Γ-point of the Brillouin zone. The difference between the edges of the L- and Γ-valleys in the conduction band is only 140 meV [1], and the direct optical transition corresponds to a 1.55 μm wavelength at room temperature. At present there is no unanimity of opinion in the physical community as to the value of the conduction and valence bands offsets for a Ge/GaAs heterojunction. It is possibly connected with the surface states at the heterojunction between the non-polar and polar materials (Ge and GaAs), and with large doping levels in the regions around the heterojunction, which causes the band offset value at the Ge/GaAs heterojunction to depend on the heterostructure growth regime [2].

We show in this paper that for relatively small thickness values of Ge QW in GaAs there is a possibility that the lowest subband of the conduction band even in a single QW is the Γ-subband. Indeed, in narrow QWs the lowest subband edge tends to the energy edge of the corresponding valley in the conduction band in the barriers (GaAs). Since the lower conduction band valley is the Γ-valley in GaAs and the superposed L-valley is about 300 meV apart from the Γ-valley [1], the lower level of the L-valley in a narrow Ge QW is higher than that of the Γ-valley. In a structure with Ge and InGaAs layers the layer thicknesses and the In content can be chosen such that the conduction band bottom in the combined QW will be in the Γ-valley of InGaAs and the valence band top will be in the Ge layer. The energy of the electron radiative transitions from the InGaAs conduction band to the Ge valence band in such QWs will be in the $1.3-1.5$ μm wavelength range. These radiative transitions are direct in the momentum space (the Ge valence band top and the InGaAs conduction band bottom are in the Γ-valley), but indirect in the coordinate space. Due to a
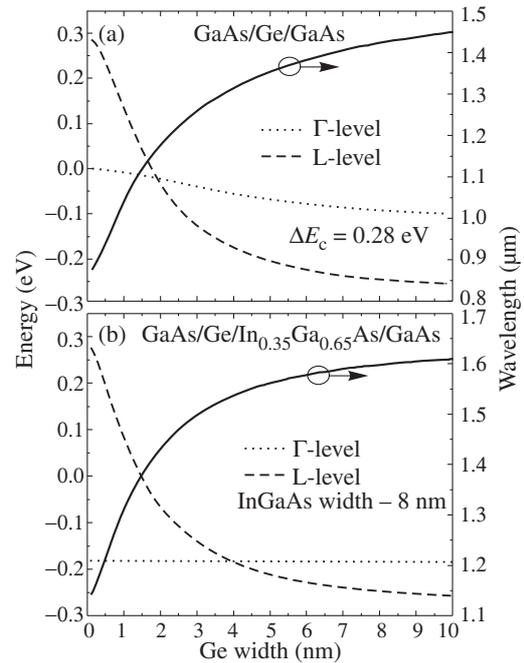
Fig. 1. The ground state of the Γ- , L-valleys energies and the wavelength of radiation corresponding to the edge of direct-band transitions versus Ge layer thickness in GaAs/Ge/GaAs (a) and GaAs/InGaAs/Ge/GaAs (b) heterostructures.

small electron mass in the Γ-valley of Ge (0.04 of a free electron mass) and a small value of band offset of the Γ-valley in the Ge/InGaAs heterojunction, the electrons of the lower subband bottom in the conduction band deeply penetrate in the Ge layer, causing a fairly large overlap of the conduction and valence bands wave functions. Therefore, the probability of interband radiative recombination in such combined QWs will be high enough to ensure that they provide an active medium for lasing.

1. Electron spectrum in Ge and Ge/InGaAs QWs

To take into account the effects of nonparabolicity of the electron spectra in Γ-valley, the Γ-valley states were calculated in the Kane model, including the spin-split off band and strain effects arising due to the difference of the lattice constants in GaAs, Ge and InGaAs. Since the nonparabolic effects are weak for the states of the heavy hole band and the electron spectrum of the L-valley, these states were calculated using the effective mass approximation. As mentioned above, although

the GaAs/Ge heterojunction has been investigated for nearly half a century now, the band offsets measurements in different structures markedly differ. Therefore, we used three different values for the conduction band offsets ΔE_c: 0.28 eV [3], 0.33 eV [2] and −0.025 eV (in the latter case the GaAs/Ge heterojunction is the type-II heterojunction) [2]. ΔE_c denotes the band offset between the bottoms of the L-valley of Ge and the Γ-valley of GaAs. Calculated dependences of the lowest energy levels in the L- and Γ-valleys of GaAs/Ge heterostructure on the Ge layer thickness are shown in Fig. 1a. The energy reference point is the conduction band bottom in GaAs. In this figure we also present the dependence of the radiation wavelength corresponding to transitions from the conduction band bottom in the Γ-valley to the valence band top, on thickness of the Ge layer. For the cases $\Delta E_c = 0.28$ and 0.33 eV the Ge QW can be direct for thicknesses under 2 nm. As mentioned above, the reason for this effect is that the L-valley lies higher than the Γ-valley in GaAs. In relatively narrow QWs the lowest energy level approaches the bottom of the corresponding valleys in the barriers. This effect is responsible for the direct band structure in a Ge QW. For type-II heterojunction the structure is direct-band for any thickness of the Ge layer because the conduction band bottom lies in the Γ-valley of GaAs. The calculations were made for the material parameters at room temperature. It is also seen from the figure that the radiation wavelength from the direct-band Ge QW is smaller than 1.15 μm for the $\Delta E_c = 0.28$ eV and smaller than 1.11 μm for the $\Delta E_c = 0.33$ eV. For the type-II heterojunction the radiation wavelength may exceed 1.15 μm in QWs with a thickness under 10 nm.

The real part of the Ge QW interband conductivity was calculated on the assumption that all of the conduction band states are empty and all of the valence band states are filled by electrons:

$$\text{Re} \left(\sigma(\omega) \right) = e^2 \frac{|p_{if}^x|^2 m^*}{\hbar^2 m_0^2 \omega} \theta \left(\hbar\omega - E_g \right) . \qquad (1)$$

In equation (1) e is the electron charge, p_{if}^x is the matrix element of the momentum x-component, m_0 is the free electron mass, $m^* = m_c m_h / (m_c + m_h)$ is the optical effective mass, m_c, m_h are the electron and hole masses in a QW, E_g is the energy gap between the conduction and valence subbands. Note that in the case of population inversion, when the corresponding states in the conduction band are filled and in the valence band empty, the conductivity (1) changes sign.

Now consider a GaAs/Ge/In$_x$Ga$_{1-x}$As/GaAs heterostructure with a combined QW. Further we will assume $x = 0.35$ because this value is close to maximum for such QWs. For the case $\Delta E_c = 0.28$ eV at the GaAs/Ge heterojunction the Γ-valley bottom of In$_{0.35}$Ga$_{0.65}$As lies by about 40 meV lower than that in Ge, and the L-valley bottom in In$_{0.35}$Ga$_{0.65}$As is by 65 meV higher than in GaAs. So it is clear that for relatively narrow Ge layers the lowest level of the conduction band is the Γ-valley level with the wave function maximum in the In$_{0.35}$Ga$_{0.65}$As layer. The wave function maximum of the ground hole level is located in the Ge layer. Fig. 1b illustrates the position of the lowest level in a QW for the L- and Γ-valleys of GaAs/Ge/In$_{0.35}$Ga$_{0.65}$As/GaAs heterostructure, depending on Ge layer thickness. The thickness of the In$_{0.35}$Ga$_{0.65}$As QW is 8 nm (which is close to the critical value). Note that a

laser with an 8 nm wide In$_{0.35}$Ga$_{0.65}$As QW in GaAs generates light at the wavelength of 1.13 μm at room temperature [4]. One can see from the figure that the energy of the lowest level in the Γ-valley is practically independent of Ge layer width. The reason for this is that the wave function of this state is localized in the In$_{0.35}$Ga$_{0.65}$As layer mainly. For the Ge layer thickness values less than 4 nm the lowest level is the Γ-level. As seen from Fig. 1b, the interband transitions correspond to the wavelengths in the 1.5 μm range. Since Ge layer is a deeper QW for the holes than In$_{0.35}$Ga$_{0.65}$As layer, the wave function of the holes ground state is situated in the Ge layer mainly. So, the radiative transitions in such heterostructures are indirect in the coordinate space. The real part of the QW interband conductivity for a GaAs/Ge/In$_{0.35}$Ga$_{0.65}$As/GaAs heterostructure has a 5.6 times less conductivity than a heterostructure with a 10 nm In$_{0.2}$Ga$_{0.8}$As simple QW. As mentioned above, the reason for such a decrease in conductivity is different localizations of electrons and holes in the coordinate space. However, despite this fact, a combined Ge/In$_{0.2}$Ga$_{0.8}$As QW can be successfully used for generation of 1.5 μm radiation in GaAs-based heterostructures.

2. Conclusions

The possibility of creation of the direct band Ge and Ge/InGaAs QWs in GaAs is shown for small Ge QW thickness. Such QWs can emit efficiently the radiation in the 1.3−1.5 μm wavelength range and can be used in laser diodes.

References

[1] O. Madelung, *Semiconductors: Data Handbook*, (New York: Academic Press, 1998).
[2] M. Dahmen, U. Rau *et al*, *Appl. Phys. Lett.* **62**, 261 (1993).
[3] M.S. Unlu, S. Strite *et al*, *Appl. Phys. Lett.* **56**, 842 (1989).
[4] B.N. Zvonkov *et al*, *Appl. Phys. Lett.* **92**, 021122 (2008).

Energy structure of novel GaSb/GaP quantum dots system

D. S. Abramkin, M. A. Putyato and T. S. Shamirzaev

A.V. Rzhanov Institute of Semiconductor Physics, SB RAS, Lavrentjeva 13, 630090 Novosibirsk, Russia

Abstract. The energy structure of GaSb/GaP quantum dots (QDs) formed on mismatched GaAs substrate has been investigated by photoluminescence. In spite of significant lattice mismatch between GaSb and GaP (11.8%) the GaSb/GaP QDs are formed in Stranski–Krastanov growth mode with formation of the wetting layer. The intensive photoluminescence connected with exciton recombination in wetting layer and QDs evidences the high quality of the structures with the QDs. The band alignment of GaSb/GaP QDs is shown to be type I with the lowest conduction band states at the indirect X_{XY} minima of the GaSb conduction band.

Introduction

Structures with self-assembled quantum dots (QDs) attract investigators due to potential application to production of light-emitting devices [1]. To date the majority of the studies reported so far have concentrated on QDs in GaAs matrix, emitting in the near infrared spectral region, for example In(Ga)As/GaAs and InP/GaAs QDs, while the QDs emitting in visible spectral region based on others III–V compound semiconductors have received much less attention. Nevertheless, the high-performance semiconductor devices emitting in the visible wavelength range is still actual. The use of GaP, which has a larger band gap than GaAs, as a matrix for QDs fabrication has further potential advantages allowing better flexibility in varying the emission wavelength. Additionally, structures on GaP could take advantage of well-developed Al free light-emitting diode technology. In this report, we present the results of a first study of the energy spectrum of the novel self-assembled GaSb QDs formed in GaP matrix.

1. Experimental

Structure with the QDs (A) was grown on the mismatched (001) GaAs substrate by molecular beam epitaxy. The GaP layer with a thickness of 1 μm was grown on the substrate at temperature $T = 580\,°C$. The introduction of misfit dislocations leads to full relaxation of strain in this layer. Then the temperature decreases down to 450 °C and 2 monolayers of GaSb were deposited on GaP surface. The transition from 2D to 3D growth mode, which was registered by reflection of high energy electron diffraction, allows us to conclude that QDs are formed in Stranski–Krastanov growth mode with formation of wetting layer (WL). Further GaP cap layer with thickness of 50 nm was grown above at the same temperature. A test structure (B) without QDs was grown under similar conditions. Steady-state photoluminescence (PL) was excited by a He-Cd laser ($h\nu = 3.81$ eV) with excitation power density (P) varied in the range of 0.1–25 W/cm^2. Time-resolved PL was excited by N$_2$ laser ($h\nu = 3.68$ eV) with pulse duration 7 ns and peak excitation power density 400 W/cm^2.

2. Photoluminescence of GaSb/GaP QDs

The steady state PL spectra of the structures A and B measured at 5 K are presented in Fig. 1a. A PL band connected with donor-acceptor recombination in GaP presents in the spectrum of the structure B [2]. Additional intensive bands marked as WL and QD appear in the spectrum of the structure A. The intensive PL evidences the high quality of the structure GaSb/GaP
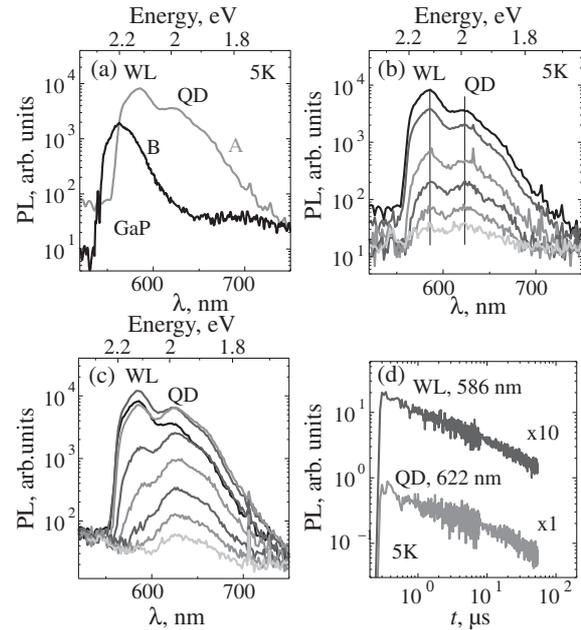
Fig. 1. (a) PL spectra of the structures A and B; (b) PL spectra of the structure A measured at the excitation power density P (from top to down), W/cm^2: 25, 8.72, 3.3, 1.15, 0.57, 0.23; (c) PL spectra of the structure A measured at the temperatures, K: 5, 15, 30, 40, 50, 60, 70, 80; (d) PL kinetic of the WL and QD bands.

grown on the mismatched GaAs substrate. Spectra of the structure A measured at various excitation densities are presented in Fig. 1b. The relative intensity of the WL band increases with increase in P. Authors of Ref. 3 demonstrate that saturation of intensity of PL band related to exciton recombination in QDs and increase in relative intensity of PL band related to exciton recombination in wetting layer with increase in P occur in structures with self-assembled QDs due to filling of the QDs with carriers. Following Ref. 3 we identify the QD and WL bands as connected with recombination of excitons in the GaSb/GaP QDs and wetting layer, respectively. The temperature dependence of the PL spectra of the structure A presented in Fig. 1c confirms our interpretation. Indeed, the intensity of the WL band quenches faster with temperature increase then the intensity of the QD band as a result of stronger localization of exciton in the QDs. In order to reveal, which type of band alignment is realized in the QDs and wetting layer we analyze the energy position of both QD and WL bands as a function of P. As it is shown in Fig. 1b, the position of both WL and QD bands do not shift with increase in P. Since position of a
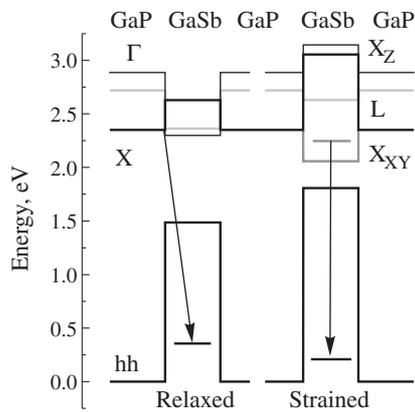
Fig. 2. Calculated band alignment of the completely relaxed (left) and strained (right) GaSb/GaP QWs.

band in PL spectra of any heterostructure of type II demonstrates strong blueshift with increase in P [4], we conclude that both GaSb/GaP QDs and wetting layer have band alignment of type I.

### 3. Enegry structure of GaSb/GaP QDs

The PL decay of the WL and QD bands after excitation by N_2 laser pulse are presented in Fig. 1d. One can see that the bands demonstrate very long decay of the PL lied in tens microsecond region of time. Observed PL decay times for both PL bands are too long for the QDs and wetting layer with a direct band gap structure. Therefore, we conclude, that the ground electron state of the QDs as well as wetting layer belongs to an indirect valley of the GaSb conduction band. In order to clarify, to which valley of the GaSb conduction band belonged the ground electron state in the wetting layer and QDs we calculate band alignment of a model structure — thin GaSb quantum well (QW) in GaP matrix. The calculation takes place in the framework of the model presented in Ref. 5. Since significant lattice mismatch of GaSb and GaP (11.8%) can lead to strain relaxation in the structure, we calculate two extreme cases: the strained GaSb layer and completely relaxed GaSb layer. The result of the calculation is presented in Fig. 2. One can see that the band alignment of type II is realized in the case of completely relaxed QW, while the strained QW demonstrates band alignment of type I with electron state belonged to X_{XY} valley of GaSb conduction band. It is easy to demonstrate that the band alignment of type I is conserved in the case of partial (down to 50%) relaxation of the strain. Therefore, the strain relaxation of the QDs in our GaSb/GaP heterostructure does not exceed 50%.

Acknowledgements

References

[1] D. Bimberg, M. Grundmann, N.N. Ledentsov, *Quantum Dot Heterostructures*, (New York: Wiley), (1999).

[2] R.Z. Bachrach, *Journal of Electronic Materials* **3**, 645 (1987).
[3] J.W. Tomm, T. Elsaesser *et al*, *Phys. Rev. B* **67**, 045326 (2003).
[4] N.N. Ledentsov *et al*, *Phys. Rev. B* **52**, 14058 (1995).
[5] C.G. Van de Walle, *Phys. Rev. B* **39**, 1871 (1989).

Effect of gamma irradiation on optical absorption and photoluminescence in borosilicate glasses doped with CdS-CdSe nanoparticles

V. Chernov, J. Argüelles-Campoy, T. Piters, R. Meléndrez and M. Barboza-Flores

Departamento de Investigación en Física, Universidad de Sonora, A.P. 5-088. Hermosillo, Sonora 83190, México

Abstract. The behavior of optical absorption (OA) and photoluminescence (PL) in gamma (^{60}Co) irradiated borosilicate glasses doped with CdSSe nanoparticles has been studied. From the results obtained follows that gamma radiation destroys OA bands caused by the embedded nanoparticles. Storage at environmental temperature leads to partial restoration of these bands. The PL intensity increases significantly in the energy region between 1.7 and 2.2 eV under gamma irradiation. The observed behavior of OA and PL can be attributed to the ionization of the nanoparticles that give a possibility to use these glasses in nanodosimety.

Introduction

The primary goal of ionizing radiation dosimetry is a measurement by some detector macro- and/or microcharacteristics of ionizing radiation with the purpose to determine an effect of this radiation on biological objects. The development of nanodosimetry is based on the concept that DNA clustered damage in regions having dimensions of the order of 10 nm plays a major role in the biological effectiveness of ionizing radiation [1,2]. The size of nanoparticles is comparable to the sizes of radiation-sensitive structures of biological objects. Therefore, the separate nanoparticles embedded in dielectric media seem to be ideal objects for register and quantify energy depositions in the nanometer volumes that can be explored for development of an effective nanodosemeter [2,3]. Optical and luminescent properties of embedded nanoparticles strongly depend on their structure, the size and an environment [4] that gives a broad opportunity for searching for radiation induced effects suitable for studying absorbed ionizing radiation energy in the nanometer volumes and for simulation of the radiating yield of biological objects.

Since the pioneering publication of G. Bret and F. Gires [5], CdSSe-doped borosilicate glasses have been actively investigated. Many experimental and theoretical works were carried out for effect of preparation conditions and external factors such as temperature, pressure, electric field, and illumination by intense light. The effect of ionizing radiation on the glasses with the embedded CdSSe nanoparticles was investigated insufficiently up to now. There are several works, in which optical absorption (OA) in X-ray and high-energy electron irradiated CdSSe doped borosilicate glasses were presented (see [6] and references there in). It was shown that irradiation results in an apparent blue shift of the absorption edge and smearing out of the confinement-related absorption maxima. This was explained by charge transfer from the nanoparticles to some traps formed in the host matrix under irradiation. From the other hand, the radiation-induced absorption increment was found in CdS doped borosilicate glasses [7]. The glasses irradiated with UV light or X-rays exhibit pronounced thermoluminescence (TL) [8,9] above room temperature. However, relation between OA and TL remains unclear. The effect of ionizing radiation on photoluminescence (PL) of CdSSe doped borosilicate glasses is presented in [9], where the decrease of the

PL intensity after 10-MeV electron beam irradiation has been found.

In this work we present the behavior of OA and PL in gamma irradiated borosilicate glasses doped with CdS-CdSe nanoparticles. The TL and optically stimulated luminescence of these glasses were investigated by us earlier [10]. The main aim of this study consists in the search for radiation-induced properties, which will depend on distribution of deposited ionizing radiation energy in nanosized volumes.

1. Experimental

The investigated samples were sliced from commercially available OG530, OG570, RG630 and RG665 Schott glass filters, where the numbers indicate the cut-off wavelengths of the different glasses. The filter glasses consist of CdS_xSe_{1-x} nanocrystallites embedded in a borosilicate glass matrix, where the sulphur content x as well as the nanoparticle size determine the cut-off wavelengths of the filters. The volume fraction of the nanoparticles in the matrix and their average size are about 1% and few nanometers, respectively.
Gamma irradiation (14400 Ci ^{60}Co gamma source, 200 Gy/min dose rate) was performed with a MDS Nordion research irradiator Gammacell 220 Excel. A Perkin–Elmer Lambda-19 UVV is spectrophotometer and a Jobin–Yvon Fluorolog-3 fluorometer were used for OA and PL measurements.

2. Results

Fig. 1 shows the energy dependences of the absorption coefficients of the OG530 and RG665 glass samples. The coefficients were extracted from the OA spectra of the thin (0.2 mm) samples. The other glasses exhibit the similar behavior of the absorption coefficients with irradiation and the post irradiation storage. The interband absorption of the borosilicate glass matrix itself is started at about 4 eV, therefore the absorption at lower photon energies is caused by the embedded nanoparticles. This absorption is well investigated now and attributed mainly to the exciton absorption in the semiconductor nanoparticles in a wide band glass matrix, which can be represented as three dimensionally confined quantum wells. The spectral position and shape of the exciton absorption bands are closely related to those one of bulk semiconductors, but depends strongly on the nanoparticle size. The absorption spec-
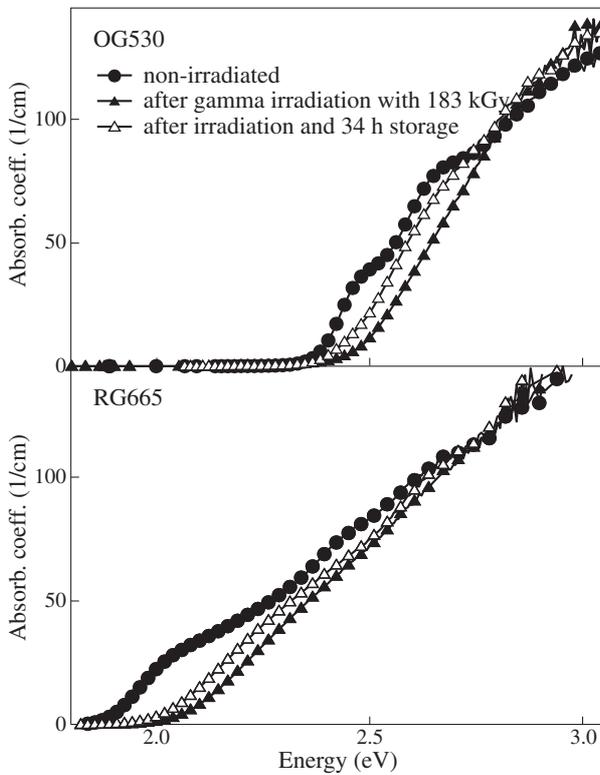
Fig. 1. Absorption coefficients of non-irradiated (points) and gamma irradiated (triangles) OG530 and RG665 Schott glass filters. The thickness of the samples is 0.2 mm.

tra of the thick (1.4 mm) samples exhibit only the exponential absorption edges at 2.4, 2.2, 2.0 and 1.9 eV for the OG530, OG570, RG630 and RG665 filters, respectively. In the spectra of thin (0.2 mm) samples the additional maxima at the absorption edges, related to the quantum-size effects, are observed.

After gamma irradiation with 180 kGy these maxima disappear almost completely blue-shifting the absorption edge by about of 0.1 eV. The observed behavior of the OA under gamma irradiation can be attributed to the ionization of the nanoparticles due to electron transfer to existing or radiation-created electron traps in the glass matrix [6].

Fig. 2 shows PL spectra of the OG570 glass sample. The other glasses exhibit the similar PL behavior. The PL consist of several overlapped band attributed to the embedded nanoparticles. The PL of embedded nanoparticles is usually classified into three types [4]. The first one (direct recombination PL) is the direct electron-hole recombination at the absorption edge, the second (surface state recombination PL) corresponds to shallow trap states near the band edge, and the third (deep trap PL) to deep traps far below the edge. The deep trap PL is the red-shifted emission and spectrally resolved from the band edge emission. Preliminary measurements have shown that all three types of PL are observed in the investigated samples. The deep trap PL is most pronounced and consists of two bands with maxima at about 1.5 and 1.8 eV, those positions depends weekly on the samples composition. The direct and surface state recombination PL are also visible but an additional study is needed for their identification. Gamma irradiation with 10 kGy leads to pronounced changes in PL spectra. The PL intensity increases significantly in the energy region between 1.9 and 2.3 eV that corresponds to the increasing of direct and surface state recombination PL. The observed enhancement of
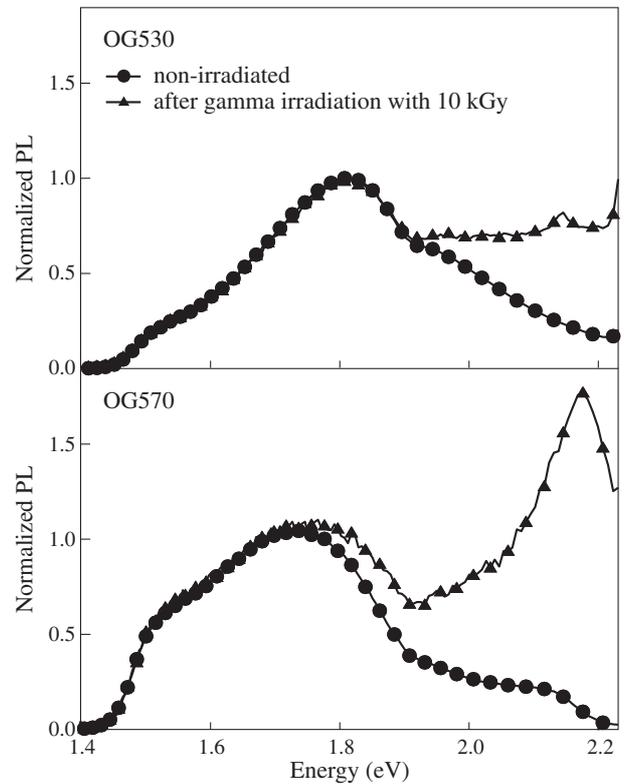
Fig. 2. PL of OG530 and OG570 Schott glass filters measured before and after gamma irradiation with 10 kGy. The wavelength of excitation light is 530 nm. The PL intensities were normalized on the low energy part of spectra.

PL can be caused by the decrease of nonradiative recombination due to effect of gamma radiation on the nanoparticle glass matrix interface. The deep trap PL is not practically changed after irradiation.

References

[1] K.M. Prise *et al*, *Radiat Res.* **156**, 572 (2001).
[2] R.W. Schulte *et al*, *Z. Med. Phys.*, **18**, 286 (2008).
[3] V. Chernov *et al*, *Proc. 10th SCINT* Korea, 71 (2009).
[4] W. Chen, In: *Handbook of Nanostructured Materials and Nanotechnology*, USA **4**, 325 (2000).
[5] G. Bret and F. Gires., *Appl. Phys. Let.* **4**, 175 (1979).
[6] Yu.M. Azhniuk *et al*, *J. Appl. Phys.* **107**, 113528 (2010).
[7] T. Miyoshi *et al*, *J. Mater. Sci.* **43**, 203 (2008).
[8] T. Miyoshi *et al*, *Jpn. J. Appl. Phys.* **40**, 2327 (2001).
[9] Yu.M. Azhniuk *et al*, *Physica E* **17**, 518 (2003).
[10] V. Chernov *et al*, *Proc. 16th Intern. Conf. "Nanostructures: Physics and Technology"* Russia, 2008.

Temperature dependence of luminescence in multilayer InAs/InAs heterostructures

B. S. Kulinkin[1], V. G. Davydov[2] and *V. A. Gaisin*[2]

[1] St Petersburg State Medical University, 6/8 Leo Tolstoy st., St Petersburg 197022, Russia
[2] Physical Faculty, St Petersburg State University, Ulyanovskaya ul. 1, Petrodvorets, St Petersburg, 198504, Russia

Abstract. Energy structure of InAs self-assembled quantum dots (QDs) embedded in AlAs has been studied. Photoluminescence spectrum of the QDs manifests itself superposition of a low-energy and several high-energy luminescence bands related to carries recombination in QDs of different size.

Introduction

Self-assembly of semiconductor quantum dot heterostructures with strong three-dimensional confinement is currently considered for fabrication of novel devices [1]. Earlier we have investigated photoluminescence spectra of heterostructures containing ten layers of InAs/GaAs quantum dots located on a (100) surface GaAs. Measurements were done in a wide temperature interval of 80–300 K with application of hydrostatic pressure ($P = 0-16$ kbar) [2].

The PL spectrum at $P = 0$ and $T = 77$ K consists of a wide slightly structured band in the region of 900–1300 meV. The PL band was decomposed into four components, of which one (L4) is associated with stacks of QDs and three others (L1, L2, L3) are associated with large size QD (AQD) in contact with wetting layer (CQD). The sizes of all QDs increase monotonically along the direction of growth axis with layer number.

For investigated QDs the baric coefficient (BC) have been measured. Baric dependencies of the energy structure for InAs quantum dots in the GaAs matrix are calculated in the framework of the deformation potential model. The assumed absence of interaction between QDs having the spherical shape and uniform size enabled to identify the dependence between baric coefficient and radiative transition energy in a quantum dot. The numerous calculations are in good agreement with measured dependence of BC on sizes of QD in the range of the sizes of 10–200 nm. The possible reasons of quantitative discrepancies of the theory and experiment were discussed.

The system of InAs QD's embedded in an AlAs matrix is very close to the system of InAs/GaAs QD's from the point of view of the Stranskii–Krastanov growth mode, since AlAs has practically the same lattice constant as GaAs. However, their optical characteristics strongly differ (long non-exponential PL decays have been observed in InAs/AlAs whereas luminescence of InAs/GaAs dots decays uniformly and fast, in the sub nanosecond range) [3].

In this work results of the further researches of heterostructures are presented.

1. Experimental

The samples of InAs QDs in an AlAs matrix studied in this work were grown by molecular beam epitaxy in a Riber-32P system. The samples consisted of five layer of the QDs sandwiched between two 25 nm thick layers of AlAs grown on top of a 200 nm buffer GaAs layer. The nominal amount of deposited InAs was equal to 2.5 monolayers. A 20 nm GaAs cap layer was grown on top of the sandwich in order to prevent oxidation of AlAs. The PL was excited by a He-Cd laser.

2. Results and discussion

In this paper, we investigate the temperature behavior of the QD PL spectra. PL spectrum of InAs/AlAs QDs was measured at 5 K. The spectrum contains four bands referenced here as L1–L4 (in the order of wavelength). The PL bands were decomposed into several components. The best agreement with experiment has been obtained under approximation of the bands by Gaussians with various intensities, half widths and positions of maxima. For description of the temperature behavior of integral intensities of the components, an Arrenius law,

$$\frac{I}{I_0} = \frac{1}{1 + Ce^{\frac{E_a}{kT}}} \, ,$$

has been used, where constant C and, activation energy E_a are fitting parameters. It was found that temperature dependences of a luminescence of QD InAs embedded in AlAs and GaAs heterostructures are similar. Using this temperature dependency, an energy level schema of the QDs was constructed and compared to the theoretical calculations.

Acknowledgements

References

[1] D. Bimberg, M. Grundmann *et al*, *Quantum Dot Heterostructures* Wiley, New York (1999).
[2] B.V. Novikov, G.G. Zegrya, R.M. Peleshchaky, O.O. Dankivy *et al*, *Semiconductors* **42** (9), 1076 (2008).
[3] T.S. Shamirzaev *et al*, *Physica E* **20**, 282 (2004).

The observation of direct band photoluminescence from Ge/GaAs heterostructures with Ge quantum well

A. A. Dubinov[1], *V. Ya. Aleshkin*[1], *K. E. Kudryavtsev*[1], *A. N. Yablonskiy*[1] and *B. N. Zvonkov*[2]

[1] Institute for Physics of Microstructures, RAS, 603950 Nizhny Novgorod, Russia
[2] Research Physical-Technical Institute of the Nizhny Novgorod State University, 603950 Nizhny Novgorod, Russia

Abstract. A GaAs/Ge/GaAs heterostructures with Ge quantum well were grown by metal-organic chemical vapor deposition epitaxy on GaAs substrates. Sufficiently intensive peak of photoluminescence at wavelength 1.5 μm was observed in all structures. This peak corresponds to the direct band optical transition in Ge.

Introduction

In recent years, semiconductor lasers emitting at 1.3 and 1.5 μm have been required in telecommunication because in this range quartz waveguides ensure minimum dispersion and absorption of radiation. However, the only commercially available lasers operating at these wavelengths are InGaAsP-based quantum well lasers on InP substrates [1]. Cheaper GaAs substrates and conventionally grown InGaAs quantum wells cannot be used for lasing in this spectral region due to a large mismatch of the lattice constants for GaAs and the InGaAs solid solution with a high In content.

This work deals with investigation into possibility to produce effective lasing in the 1.5 μm wavelength range, using GaAs-based structures with Ge direct band quantum wells. The lattice constants of Ge and GaAs are close, which is promising of attainability of practically perfect Ge/GaAs heterojunctions. Germanium is an indirect semiconductor. The lowest valley in the conduction band is the L-valley, and the top of the valence band is located in the Γ-point of the Brillouin zone. The difference between the edges of the L- and Γ-valleys in the conduction band is only 140 meV [2], and the direct optical transition corresponds to a 1.55 μm wavelength at room temperature. This energy difference between the L- and Γ-valleys can be compensated by the tensile strain of the Ge layer (but direct band transition wavelength increases) and/or sufficiently high donor impurity doping (more than 10^{20} cm^{-3}) of the Ge layer. So the Fermi level will be in the Γ-valley. The direct radiative electron transitions (direct in the momentum space) under sufficiently high pumping at room temperature will dominate indirect transitions from the L-valley due to a low probability of the latter. Note also that the use of this effect in bulk tensile strained Ge as an active matter recently led to creation of an optically pumped 1.6 μm — laser that was grown on a silicon substrate [3].

1. Experimental

The Ge/GaAs heterostructures were grown by metal-organic chemical vapor deposition epitaxy on GaAs substrates. High doped Ge layers were deposited by laser evaporation. The structures with five Ge quantum well widths (4, 8, 10, 16, 30 nm) were grown at three different temperatures (550, 590, 650 °C). Ge quantum wells were overgrown by 100–300 nm GaAs.

The photoluminescence (PL) from these structures was investigated with using the parametric oscillator MOPO-SL ("Spe-
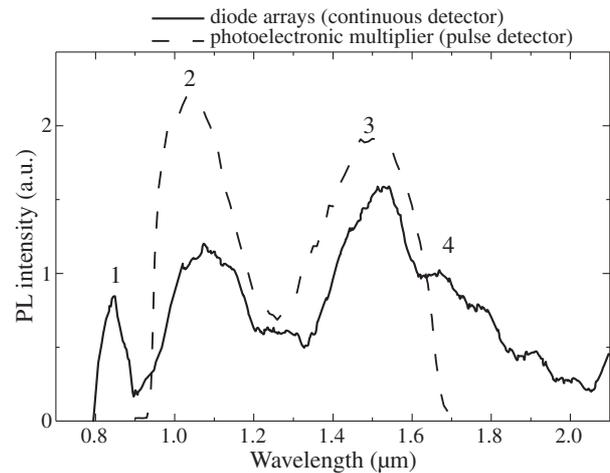

Fig. 1. Photoluminescence spectra of a GaAs/Ge/GaAs heterostructure with thickness of Ge quantum well 30 nm. A structure was grown at 550 °C.

ctra-Physics", the radiation pulse duration 10 ns) for pumping at temperatures 77 and 300 K. As radiation-measuring instruments we used diode arrays (diapason 0.62–2.2 μm) and photoelectronic multiplier (diapason 0.93–1.7 μm).

Sufficiently intensive peak of photoluminescence at wavelength 1.5 μm (line 3 in Fig. 1) was observed in all structures. This peak corresponds to the direct band optical transition in Ge. Moreover, intensive peaks at wavelengths 0.83 μm (corresponded to the direct band optical transition in GaAs, line 1) and 1.1 μm (corresponded to optical transition in defects of GaAs, line 2) and weak peak at wavelength 1.7 μm (corresponded to the indirect band optical transition in Ge, line 4) were observed in these structures too. The largest PL intensity of the peak at 1.5 μm was detected from samples with Ge quantum well width 4 nm and grown at 650 °C. The reason for this effect that the structures, which were grown at the highest temperature and with the narrowest Ge quantum well, are more perfect. Moreover, the difference between electron energy of the L- and Γ-subbands decreases at a decrease of Ge quantum well width. So the intensity of the direct band optical transitions in the momentum space grows. The presence in the photoluminescence spectra of the structures lines associated with defects in GaAs, which arise due to the growth of GaAs on Ge layer, indicating the imperfection of these structures.

In future, the improvement of the growth methods for the Ge/GaAs heterostructures will lead to the possibility of the

observation of stimulated radiation at wavelength 1.5 μm from these structures.

References

[1] S.J. Caracci *et al*, *J. Appl. Phys.* **75**, 2706 (1994).
[2] O. Madelung, *Semiconductors: Data Handbook*, (New York: Academic Press, 1998).
[3] J. Liu, X. Sun *et al*, *Opt. Lett.* **35**, 679 (2010).

Optical properties of CdSe, CdS, CdSeS spherical nanocrystals in a fluorophosphates matrix

B. S. Kulinkin[1], V. G. Davydov[2] and *V. A. Gaisin*[2]

[1] St Petersburg State Medical University, 6/8 Leo Tolstoy st., St Petersburg 197022, Russia
[2] Physical Faculty, St Petersburg State University, Ulyanovskaya ul. 1, Petrodvorets, St Petersburg, 198504, Russia

Abstract. Absorption spectra of the CdS, CdSe and CdTe nanocrystals of different size was studied. Previously found in CdSeS systems coinsidence of splitting between two spectral lines with the spin-orbital splitting of the valence band was also observed in CdSe and CdTe. Physical reasons of such a coinsidence are discussed.

Earlier the absorption of sulfoselenide solid-solution nanocrystals has been studied. Nanocrystals of cadmium sulfoselenide were grown within a volume of P_2O_5–Na_2O–ZnO–AlF_3 glass-forming system where CdS and CdSe were added. An analysis of the composition of the glasses thus produced, made with an electron-beam microprobe. Differential absorption spectra of the mixed semiconductor samples were studied at the $T = 300$ and 77 K in the 380–620 nm spectral region (see Fig. 1). Near to edge of fundamental absorption were observed oscillations. The oscillations are associated with transitions between the hole and electron quantum confined levels.

It was found that the energy difference ΔE_i between lines corresponding to transition to the conduction band from the first level of dimensional quantization and one of the higher levels of dimensional quantization in the range of structures $0 < x < 0.4$ coincides with the value of spin-orbital splitting E_{SO} of bulk crystals of the same structure. The observed effect has been directly confirmed by the calculations performed for $x = 0.3$ within the limits of model, developed in work [1]. This effect can be explained by the anticrossing of levels of dimensional quantization of light and heavy holes with similar levels of dimensional quantization of spin-orbital split valence zone.

In the present work we have obtained following results:

1. dependence of absorption spectra of CdSe, CdS and CdTe samples on the sizes of microcrystals. In case of CdSe and CdTe microcrystals the previously observed effect of coincidence between ΔE_i and E_{SO} is present. However, CdS microcrystals didn't exhibit this effect.

2. The analysis of numerical calculations of the absorption spectra of microcrystals of mixed composition $CdSe_{0.7}S_{0.3}$ and similar calculations for CdSe microcrystals [2] was carried out. Two possible models leading to occurrence of this effect are considered:

— coincidence between energy transitions from level of dimensional quantization of the bottom valence band of light holes to the first level of dimensional quantization of conductivity band and similar transitions from spin-orbital band, or

— changing of band structure of a bulk material owing to crossing of a band of light holes with spin orbital valence band.

Necessary and sufficient conditions for observation of above-mentioned effect are revealed:
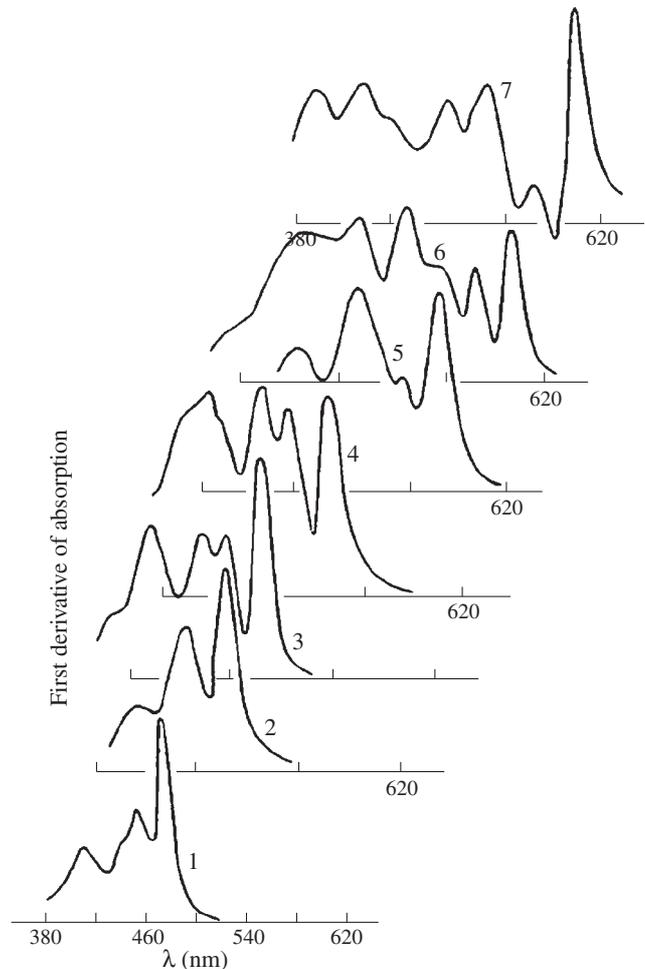
Fig. 1. Wavelength-modulated light transmission spectra of CdS_xSe_{1-x} nanocrystals in fluorophosphates glassy matrices at $T = 77$ K.

label	1	2	3	4	5	6	7
x	1	0.9	0.76	0.6	0.4	0.2	0

— the larger value of effective mass of holes in spin-orbital band in comparison with mass of light holes in valence band, and

— coincidence between energy levels of light and heavy holes at top of a valence band.

It is shown that one of the possible reasons leading to absence of effect in case of microcrystals of mixed structures with $x > 0.4$ is that they have wurzite structure.
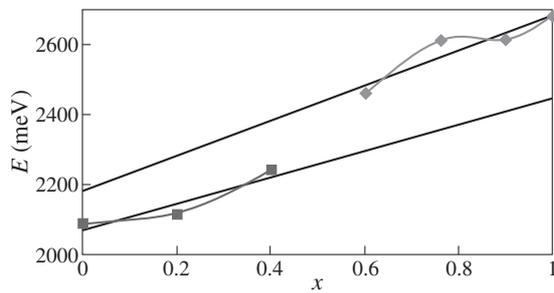
Fig. 2. Dependence of energy of the basic line on the structure chemical composition.
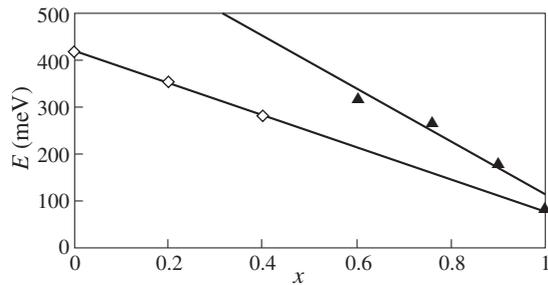
Fig. 3. Dependence of energy of the spin-orbital splitting on the structure chemical composition.

3. Decomposition of previously obtained spectra is made. Dependences of energy of the basic line and magnitude of spin-orbital splitting on the structure-composition are measured. Change of slope (see Figs. 2,3) of such linear dependences at about $x \approx 0.4\ldots0.5$ confirms transition from hexagonal to cubic structure.

References

[1] A.I. Ekimov *et al*, *J. Opt. Soc. Am. B.* **10**, 100 (1993).
[2] V.A. Gaisin, S.V. Karpov, E.V. Kolobkova, B.V. Novikov *et al*, *Phys. of the Solid State* **41**, 1378 (1999).

GaAs quantum dots embedded into the AlGaAs nanowires

V. N. Kats[1], *V. P. Kochereshko*[1], *A. V. Platonov*[1], *G. E. Cirlin*[1,2], *A. D. Bouravleuv*[1,2],
Yu. B. Samsonenko[1,2], L. Besombes[3] and H. Mariette[3]

[1] Ioffe Physical-Technical Institute, St Petersburg, Russia
[2] St Petersburg Academic University, St Petersburg, Russia
[3] CEA-CNRS group "Nanophysique et Semiconducteurs", CEA, INAC, SP2M, and Institut Nèel,
17 rue des Martyrs, F-38054 Grenoble, France

Abstract. Photoluminescence characterization of GaAs quantum dots embedded into AlGaAs nano-wires has been performed. Time integrated and time resolved photoluminescence measurements from both an array and a single quantum dot/nano-wire are reported. The influence of the diameter size distribution is evidenced by the optical spectroscopy.

We report on the photoluminescence (PL) study of the quasi-one-dimensional semiconductor structures — cylindrical nano-wires (NW) based on the AlGaAs compounds. The NW's diameter was aout 20–50 nm and their length was about 0.5–1 μm length. The samples were grown by MBE on GaAs (111)B semi-insulating substrates. We have studied the samples that contain one or several quantum dots inside each wire. These dots were GaAs discs of 2 nm in thickness and of 20–50 nm in diameter. We have investigated single NW's and NW ensembles.

A systematic photoluminescence study was performed on the samples at low temperature and various optical excitation densities in magnetic fields up to 11 T.

Inset on the Fig. 1a shows an STM image of the sample grown at "high" temperature (580 °C). It can be seen that the nano-wires are strongly inhomogeneous in diameter and position on the substrate.

The diameter ranges between 100 and 500 Å, and even varies along a given wire. Most of the wires are perpendicular to the substrate, but some of them are lying horizontally, revealing also the orientations inhomogeneity and some of them are cut from the substrate at all. It is clear that this sample is strongly inhomogeneous.

Photoluminescence spectrum from this type of the samples is shown on the Figure 1a. The spectrum is very broad and spreads from 1.65 to 1.95 eV without any reproducible structure. This emission band is a mixture of recombination coming from NWs and QDs embedded into them, without any possibility to separate both contributions.

Instead, for the samples grown at lower temperature (560 °C), a much better homogeneity is obtained for the both diameter and length of the NWs (see inset on the Fig. 2b. For example, we can estimate from this figure that the distribution of the NW diameters does not exceed 15%. Additionally, the diameter does not vary along the wire.

The PL spectrum taken from this structure at temperature of 10 K is represented on the Fig. 2b by solid line. Two intense lines at the energies 1.73 and 1.87 eV are dominated in the spectrum. These lines are attributed to the carrier recombination in the quantum dots and nanowires, respectively.

Indeed, the nano-wire material $Al_xGa_{1-x}As$, $x \approx 0.25-0.30$ has bandgap $E_g^{AlGaAs} = 1.8-1.9$ eV, and the bandgap of the quantum dot material is $E_g^{GaAs} = 1.519$ eV at helium temperatures. Consequently, the PL line from the quantum dots may have the energy from $E_g = 1.519$ eV, in the very large dots
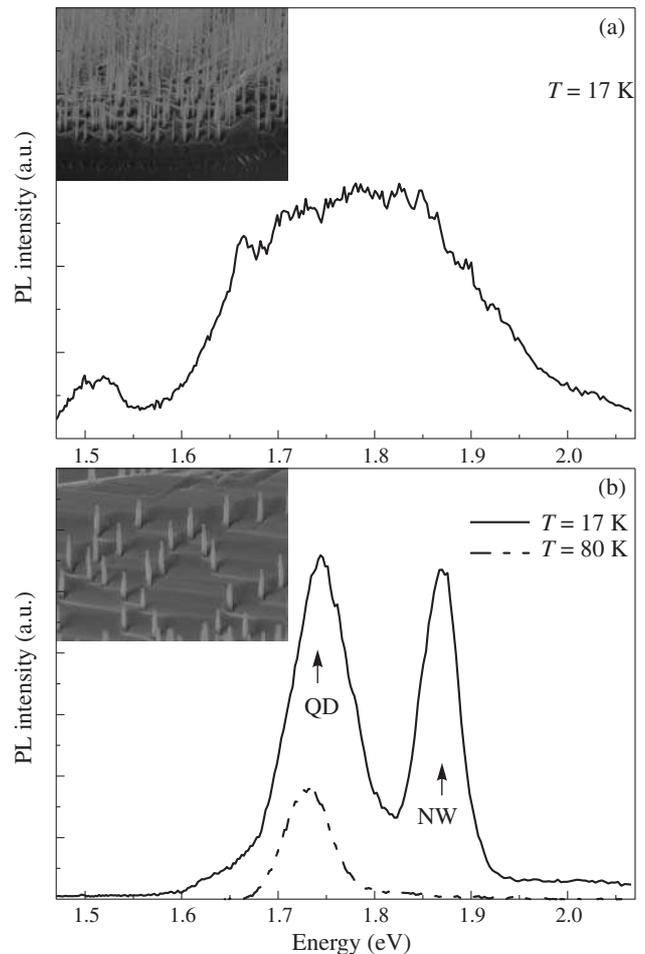
Fig. 1. a) Photoluminescence spectrum taken from the "high temperature" sample. Inset: TEM image of the given sample. b) Photoluminescence spectra taken from the "low temperature" sample. Inset: TEM image of the given sample.

up to $E_g^{AlGaAs} = 1.8$ eV, in the very small ones. From the other hand the PL line of NW can not be lower in energy than the $Al_{0.25}Ga_{0.75}As$ bandgap, i.e. below $E_g^{AlGaAs} = 1.8$ eV. By contrast with the results shown on Figure 1a, the width of these PL lines reveals a much narrower distribution of NW diameters.

The difference in the nature of these two lines shown in Figure 2b is confirmed by the temperature dependence of the emission spectrum. The PL spectrum taken at 77 K is presented on the Fig. 2b by the dashed line. The PL emission from
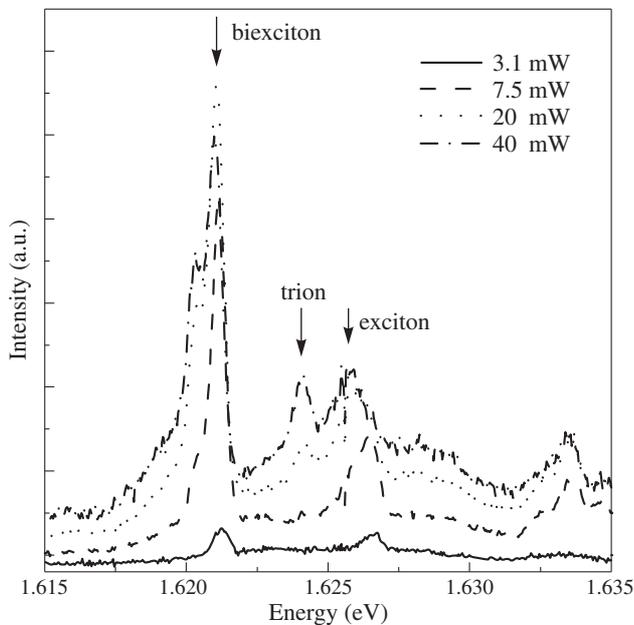
**Fig. 2.** Photoluminescence spectra taken from a single quantum dot at different optical excitations.

the nano-wire range completely disappears by the temperature increase, whereas the QD line drops down by only a factor of three. This is an evidence of the strong localization of the carriers that contribute to the QD line emission. On the other hand the carriers in the NW may diffuse along the wire and can be captured by the QD, the later explains the NW line vanishing.

Comparing the results shown in Figs. 1a,b we can conclude that it is possible to obtain a homogenous distribution of NW diameters by adjusting the growth conditions.

We performed also the optical study on a single QD. For this purpose a strongly increased image of the sample surface was projected into the slit of the spectrometer. As a result, only the signal coming from a very small number of NWs is collected. The spatial resolution of the objective was $\propto$ 1.5 μm, and the average distance between nano-wires was about $\propto$ 0.8 μm. Consequently the photodetector can collect a signal coming from one or several nano-wires contained quantum dots.

Figure 2 shows a set of PL spectra taken from a single QD at different levels of optical excitation. The emission spectrum shown on Fig. 2, corresponds to a NW having a diameter of about 500 Å, which is a little bigger than the one of the sample presented in Figure 1.

The line of the exciton ground state in the qiven QD was observed on the energy of 1.626 eV at low excitation levels. The biexciton line was observed at 1.621 eV. At high excitation levels the PL line from the ground state is saturated and the biexciton line starts to dominate. In this structure a line of trion at 1.624 eV was also observed.

The magnetic fields measurement shown that the Zeeman splitting corresponds to the g-factor $\sim$1.0 for all lines in these structures.

The decay time for ground sate was found to be 5 ns. This is typical value for the decay time of the exciton recombination in self-assembled (Stranski–Krastanov) quantum dots.

The full width at half maximum (FWHM) of the emission line of a single quantum dot was found to be of 0.5 meV. This is little bit bigger than can be expected for a single QD. Such linewidth is not lifetime limited; it implies instead that the linewidth is not an intrinsic property of genuine quantum dots, but a consequence of their local environment, which can be explained by fluctuating Stark shift caused by photo-excited charged carriers. Such results were already reported in Ref. 1 for the lattice matched quantum dots like GaAs/AlGaAs by using a droplet epitaxy method.

As it follows from the theoretical estimations the biexciton binding energy in such QDs can reach 10 meV. In several samples (not in all) of a kind we could observe a trion line. The intensity of the trion line increases by increasing the optical excitation and saturates on the same level as the exciton line. The biexciton line saturates at high optical excitation on the level, which is two times higher then the maximal amplitude of the exciton line.

1. Conclusion

Photoluminescence spectra from a QD embedded into NW have been measured. It has been demonstrated that by adjusting growth procedure one can obtain a homogenous distribution for the QD/NW sizes. Micro-PL spectroscopy reveals the carriers recombination in a single QD. Ground and excited exciton states are observed in these spectra. At high optical excitation line of biexciton reveals in the spectra.

References

[1] K. Kuroda, T. Kuroda, K. Sakoda, G. Kido, and N. Koguchi, *J. Lumin.* **789**, 122 (2007).

Two-photon absorption of excitons in semiconducting quantum dots

V. Dneprovskii[1], *M. Kozlova*[1], A. Smirnov[1], E. Zhukov[1] and T. Wumaier[2]

[1] Physics Faculty of M.V. Lomonosov Moscow State University, 119991 Moscow, Russia
[2] Xinjiang Technical Institute of Physics and Chemistry, CAS, China

Abstract. The proposed method of nonlinear absorption investigation utilizing the measured traces of luminescence (the dependences of colloidal CdSe/ZnS quantum dots' luminescence intensity upon distance) in the case of two-photon resonant excitation of excitons by powerful picosecond laser pulses has allowed us to define the values of two-photon absorption coefficients, to reveal the influence of nonradiative Auger recombination, and to realize the limiting effect — invariable transmitted intensity of laser pulses at input intensities exceeding limiting threshold.

Different methods may be utilized to measure nonlinear absorption of semiconducting quantum dots (QDs) in the case of two-photon excitation by powerful laser pulses. Two of them were applied in this paper

1. Most often applied one is to measure the dependence of transmitted intensity upon input pulse intensity. In the case of negligibly small linear absorption the change of intensity $dS/dz = -\beta S^2$, where β is the coefficient of two-photon absorption. Thus the measured dependence of transmitted intensity S_T upon input intensity S_0 allows us to calculate β using the expression

$$\frac{S_0}{S_T} = 1 + \beta z S_0 . \tag{1}$$

2. In the case of two-photon absorption of excitons in semiconducting QDs the measuring of the dependence of luminescence intensity upon distance z (trace of luminescence) is a convenient way to investigate two-photon absorption. This method was utilized for the first time in [1] to investigate the effect of self-induced transparency in the case of two-photon excitation of semiconductors. At moderate intensities of excitation when less than one electron-hole pair (less than one exciton) is excited in a single QD and nonradiative Auger recombination [2,3] is suppressed the intensity of luminescence $I(z)$ is proportional to the number of absorbed photons (absorbed energy) in the layer Δz:

$$I(z) \approx \tau \left[S(z) - S(z + \Delta z) \right] , \tag{2}$$

τ is laser pulse duration. Thus, in the case when $\Delta z \to 0$

$$I(z) \approx \tau \frac{\beta \Delta z S_0^2}{1 + 2\beta z S_0 + (\beta z S_0)^2} . \tag{3}$$

The measured ratio of the intensities of luminescence at distance z_2 to that at distance z_1

$$\frac{I(z_2)}{I(z_1)} = \frac{1 + 2\beta S_0 z_1 + (\beta z_1 S_0)^2}{1 + 2\beta S_0 z_2 + (\beta z_2 S_0)^2} \tag{4}$$

allows to determine βS_0 and β in the case of known S_0.

Two-photon absorption of colloidal solution of highly luminescent Green 545 CdSe spherical core capped with epitaxial ZnS shell and surface hydrophobic layer QDs was measured. To achieve the resonant two-photon excitation of the basic exciton optical transition by 30-picosecond pulses of mode-locked Nd:YAG laser QDs of appropriate size (radius 2.6 ± 0.4 nm)
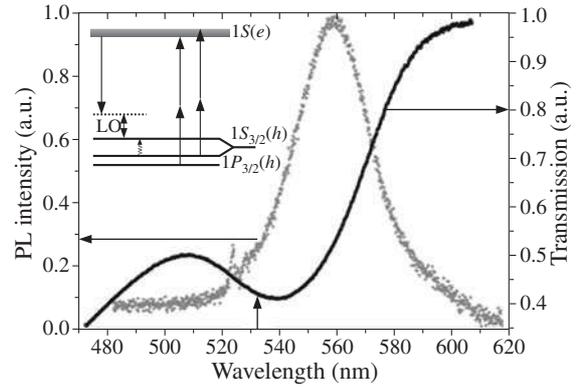

Fig. 1. The transmission and photoluminescence spectra of colloidal CdSe/ZnS quantum dots. The wavelength of two-photon excitation is shown by arrow. The transitions are shown schematically in insert.

were chosen using the measured transmission and photoluminescence excitation [4] spectra. The transmission and luminescence spectra (the latter at two-photon excitation) are shown in Fig. 1 for colloidal solution of the chosen QDs. The Stokes shift of the luminescence spectrum maximum relatively to the transmission minimum arises in CdSe QDs because of crystal field in hexagonal lattice, weak deviation from the spherical shape, electron-hole exchange interaction [5–7]. Thus LO-phonon assisted luminescence arises due to two-photon resonant excitation of excitons in CdSe/ZnS QDs (optical transition $1S_{3/2}(h) - 1S(e)$ and $1P_{3/2}(h) - 1S(e)$ that is allowed only for two-photon process).

The analyzed luminescence traces excited by two-photon absorption of the Nd:YAG mode-locked laser train of pulses in 1 cm cell filled by colloidal solution of CdSe/ZnS QDs with 10^{17} cm^{-3} density are shown in Fig. 2. The measured duration of a single pulse in the train using Hamamatsu C979 streak camera (30 ps) did not vary at least for the first part of the train. The total energy of the train was defined utilizing pulse energy measuring device Ophir PE25 and the distribution of the total energy among individual pulses was defined from the oscillograms of the train obtained with 1 ns time resolution. In this case the amplitude of individual 30-picosecond pulse (Fig. 4) is proportional to its energy. Special photo camera was utilized to photograph the trace of luminescence from the lateral side of the sell with QDs. To exclude the radial intensity distribution of the exiting laser beam (it has the Gaussian distribution) the dependence of luminescence intensity upon distance was measured only for the central part of the trace.

Fig. 3. The dependence of photoluminescence intensity of CdSe/ZnS quantum dots upon the pumping intensity in the case of one-photon excitation by 100 fs laser pulses.
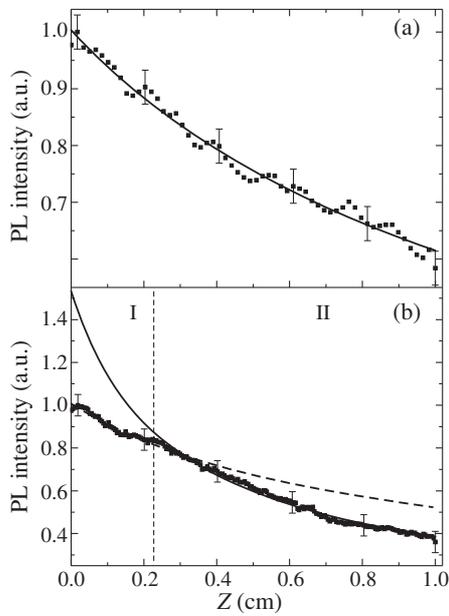
Fig. 2. The measured decreasing of CdSe/ZnS quantum dots' photoluminescence intensity along the trace and the calculated dependences for different total energies of the train of pulses $W = 1.7$ mJ (a) and $W = 3.5$ mJ (b).

In Fig. 2(a) the measured decreasing of luminescence intensity along the trace $I(z)$ is shown for the total pumping energy of the train of pulses $W = 1.7$ mJ with the calculated (equations (3) and (4) were utilized) longitudinal distribution of the luminescence intensity. The contribution of all laser pulses of the train in luminescence was taken into account. The calculated longitudinal decreasing of luminescence intensity with $\beta = (0.23 \pm 0.02)$ cm/GW is in good agreement with that measured.

The measured intensity of luminescence $I(z)$ shown in Fig. 2(b) was obtained at higher total energy $W = 3.5$ mJ. It is impossible to describe experimental result applying equations (3), (4) for any value of β. We suppose that the initial part (part I) of luminescence trace separated by vertical dashed line in Fig. 2(b) is characterized by competition of radiative and nonradiative Auger recombination. The calculated dependence for the separated part I is shown by dashed line. The estimated value of absorbed photons' density is enough for excitation of more than one electron-hole pair (exciton) per single QD and thus to effective Auger recombination in QDs of small radius accompanied by decreasing of intensity of luminescence. The application of equations (3), (4) for part II in Fig. 2(b) of the trace of luminescence allowed to determine coefficient of two-photon absorption: $\beta = (0.23 \pm 0.02)$ cm/GW.

Additional experiment confirms the suggested division of the trace of luminescence in two parts in Fig. 2(b). The measured dependence of the intensity of CdSe/ZnS QDs' luminescence on the pumping intensity in the case of one-photon excitation by 100 fs laser pulses (Fig. 3) showed that for moderate intensities (the estimated density of excited electrons corresponded to excitation of not more than one electron in single QD) it is linear. For high excitation (more than one electron in a single QD) it becomes nonlinear, and we suppose that Auger process is responsible for this nonlinear part of the dependence of intensity of luminescence upon exciting intensity of 100 fs pulses.
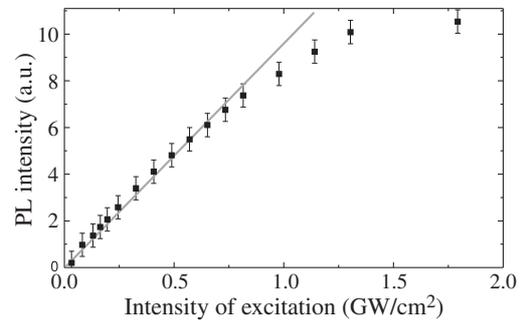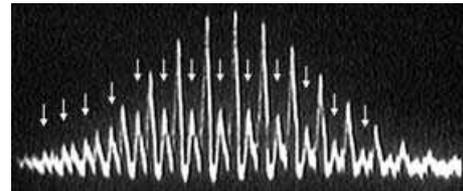
Fig. 4. The oscillogram of transmitted through the cell with colloidal CdSe/ZnS quantum dots pulses (pointed by arrows) and pumping pulses.

At high exciting intensities S_0 when $\beta S_0 \gg 1$ the limiting effect may arise — constant (independent of S_0) transmitted intensity $S_T = \frac{1}{\beta z}$. In order to discover the limiting effect we excited colloidal CdSe/ZnS QDs of higher (10^{18} cm^{-3}) density for which the measured coefficient of two-photon absorption $\beta = (0.8 \pm 0.2)$ cm/GW. The limiting effect in the case of resonant two-photon excitation of excitons in CdSe/ZnS QDs was obtained. It is confirmed by oscillogram (Fig. 4) of the train of transmitted and input laser pulses. To compare the train of input and output pulses a special optical 3 ns delay line was utilized. The limiting effect for the most powerful input pulses is manifested in invariable amplitudes of transmitted pulses.

Acknowledgements

References

[1] D. Gruev, V. Dneprovskii, E. Silina, *Quantum Electronics (Russian edition)* **2**, 2350 (1975).

[2] V. Dneprovskii, A. Efros, A. Ekimov, V. Klimov, I. Kudriavtsev, M. Novikov, *Solid State Commun.* **74**, 555 (1990).

[3] D. Chepic, A. Efros, A. Ekimov, M. Ivanov, V. Kharchenko and I. Kudriavtsev, *J. Lumin.* **47**, 113 (1990).

[4] V.S. Dneprovskii, E.A. Zhukov, M.V. Kozlova, T. Wumaier, Dau Sy Hieu, M.V. Artem'ev, *Physics of Solid State* **52**, 1941 (2010).

[5] A.L. Efros, *Phys. Rev. B: Condens. Matter* **46**, 7448 (1992).

[6] A.L. Efros and A. Rodina, *Phys. Rev. B: Condens. Matter* **47**, 10005 (1993).

[7] M. Nirmal, D. Norris, M. Kuno, M. Bawendy, A.L. Efros, and M. Rosen, *Phys. Rev. Lett.* **75**, 3728 (1995).

Photoelectric properties of InAs/AlAs heterostructures

B. S. Kulinkin[1], V. G. Davydov [2] and V. A. Gaisin[2]

[1] St Petersburg State Medical University, 6/8 Leo Tolstoy st., St Petersburg 197022, Russia
[2] Physical Faculty, St Petersburg State University, Ulyanovskaya ul. 1, Petrodvorets, St Petersburg, 198504, Russia

Abstract. Effect of an electric field applied along the growth direction of the structure on photoluminescence of multiplayer structure with InAs/AlAs QDs was studied. Bands relating to transitions at QDs of GaAs was observed in photoluminescence spectra at spectral region of 500–800 nm. An oscillation of photoluminescence intensity along the spectrum connected with Franz–Keldysh effect in cap GaAs layer was observed under electric field of 30 kV/cm.

Introduction

Systems of self-assembled InAs quantum dots (QD's) have been intensively studied in recent years due to their importance for fabrication micro- and optoelectronic devices [1]. The most investigated system with such QD's is system of InAs QD's embedded in GaAs and/or AlAs matrix. The system of InAs QD's embedded in AlAs matrix is very close to the system of InAs/GaAs QD's from the point of view of the Stranski–Krastanov growth mode, since AlAs has practically the same lattice constant as GaAs and both of them are more chemically stable than InAs. The system of InAs/AlAs QD's demonstrates millisecond recombination dynamics and strong no-monotonic shift of photoluminescence (PL) band with change in excitation power density — which is quite different from that of the InAs/GaAs QD's system. Recently in order to obtain additional information about structure of energy levels in heterostructure with InAs/AlAs QD's we have studied photoluminescence of this structure under electric field E applied along the growth direction.

1. Experimental

Structure with self-assembled InAs/AlAs QDs was grown by the molecular beam epitaxy on semi-insulating (001)-oriented GaAs substrates using a Riber-32P system. The structure (see Fig. 1) consists of five layers of InAs QDs separated by 8 nm thick AlAs spacer layers. The QD layers were deposited with a nominal amount of InAs of 2.5 monolayers (ML). A 20 nm GaAs cap layer was grown on top of the structure in order to prevent oxidation of AlAs.

In order to apply electric field (up to 0.30 kV/cm) the samples are pressed against quartz plate covered with transparent electrode of SnO_2. Backside of the sample was covered by silver grease to form the opposite contact. The radiation of a He-Cd laser (441.6 nm) was used to excite PL.
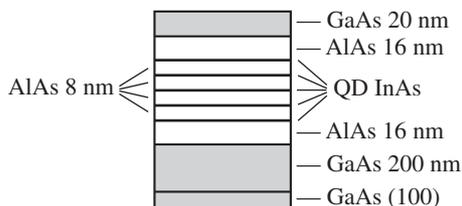


Fig. 1. Self-assembled InAs/AlAs QDs structure.
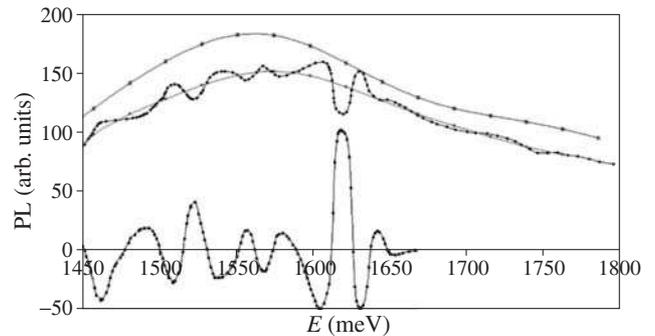
Fig. 2. PL spectra of InAs/AlAs QD's measured at 77 K without (1) and with (2) applying of E with strength of 30 kV/cm and their normalized difference (3).
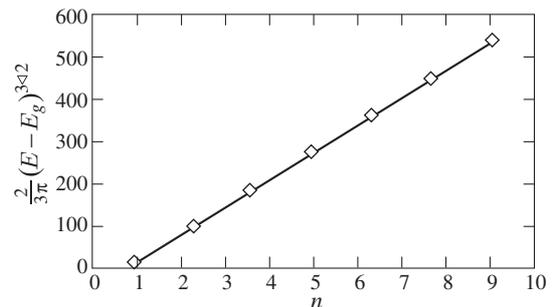

Fig. 3. Calculated energy positions of FK oscillation extrema $E_n - E_g$, where E_g is a bang gap of the GaAs and n is index number of the extremum, for E strength of 30 kV/cm.

2. Results and discussions

Photoluminescence spectra (PL) of the structure with QDs have been recorded at temperatures of 77 and 300 K and different strength of electric field (0–30 kV/cm) measured. The PL spectra consists of two adjacent broad bands related to transitions in QD_1 (1400–1700 meV) and QD_2 (1700–1800 meV), as seen in Fig. 2.

We subtract curve 1 form curve 2 and built differented spectrum depicted in Fig. 2 as curve 3. It has been established that electric field leads to the the PL quenching. Besides, application of the electric field leads to appearance of an oscillations of PL intensity along the spectrum. We suppose that the oscillations result from spectral modulation of light reflection in cap GaAs layer due to Franz–Keldysh (FK) effect [2]. In order to verify this supposition we have calculated absorption

caused by FK effect in layer of GaAs with thickness of 200 nm (which equals to the thickness of cap layer of our structure) and compare its extrema to the extrema of the curve 3 in Fig. 2. Calculated energy positions of FK oscillation extrema $E_n - E_g$, where E_g is the bang gap of GaAs and n is number of extremum, for E with strength of 30 kV/cm are demonstrated in Fig. 3.

The harmonic analysis is carried out. The contribution to a spectrum of light holes is found out and the dispersion electrooptical factor is defined.

References

[1] D. Bimberg, M. Grundmann, and N.N. Ledentsov *et al*, *Quantum Dot Heterostructures* (Wiley, New York), 1999.
[2] J. Hader, N. Linder, G.H. Dohler, *Phys. Rev. B* **55**, 6960 (1997).

Phase-sensitive dependence of the dark resonances in double tunneling-coupled quantum wells

K. A. Barantsev[1], *A. N. Litvinov*[1], B. G. Matisov[1], G. A. Kazakov[1] and Yu. V. Rozhdestvensky[2]

[1] St Petersburg State Polytechnical University, 195251 St Petersburg, Russia
[2] State University of Information Technologies, Mechanics and Optics, 197101 St Petersburg, Russia

Abstract. In the work the dark resonances have been investigated at by interaction of optical and infrared irradiation with tunneled-coupled quantum wells. The conditions of the formation of such resonances in this system were determined. The influence of laser field phases on dark resonances is studied.

Now an interest of researchers attract the coherent population trapping (CPT) effect which consist in arising of superposition quantum state (dark state) of low states of three-level Λ-system at interaction of such systems with laser fields [1]. The appearance of such dark state has been induced by induction of low-frequency coherence. In the result the excited medium under acting of laser irradiation change its characteristics. This fact allows to bring such name as "coherent medium". The changing of characteristics of optical dense medium and its influence on propagation of multi-frequency laser irradiation was called as effect of electromagnetically-induced transparency (EIT) [2].


(a)
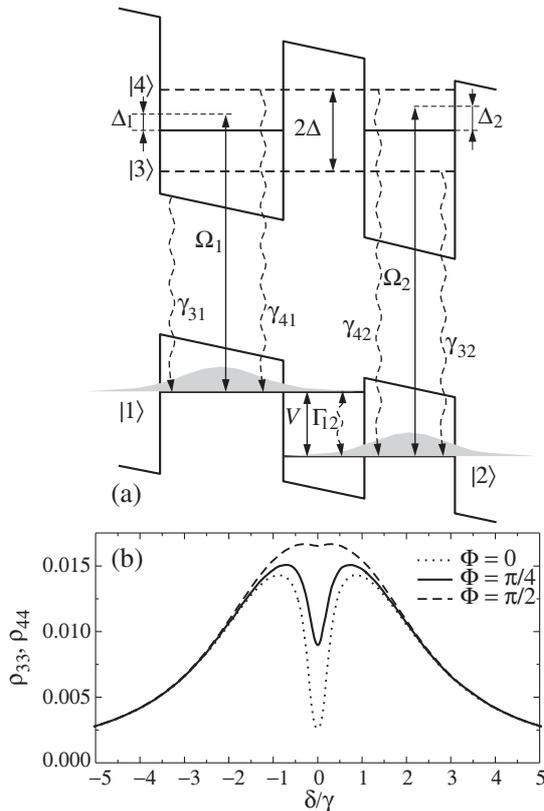
Fig. 1. (a) — The structure consisting of double tunneling-coupled quantum well. Here Δ_1, Δ_2 are laser detuning of optical fields, Ω_1 and Ω_2 are Rabi frequencies of optical fields and V is Rabi frequency of infrared field. (b) — The dependence of ρ_{33} and ρ_{44} on two-photon detuning for three means of the difference of phases Φ between excited fields. Hear $\Omega_1 = \Omega_2 = V = 0.25\gamma$, $\Delta = \gamma$.
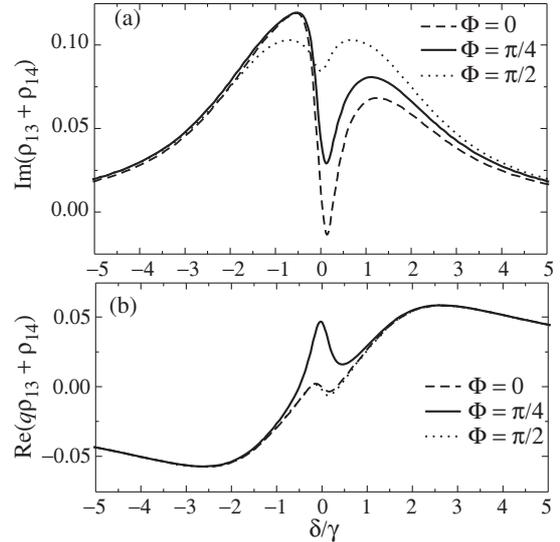

Fig. 2. The dependence of absorption coefficient $\mathrm{Im}(q\rho_{13} - \rho_{14})$ (a) and index of refraction $\mathrm{Re}(q\rho_{13} - \rho_{14})$ (b) of first laser field on two-photon detuning for other values of Φ. The values of parameters are $\Omega_1 = \Omega_2 = V = 0.25\gamma$, $\Delta = \gamma$, $q = \kappa = 1$.

The progress in the realization of element base for quantum computation on EIT resonance associated with realization of this effect in solids. In these materials semiconductors nanostructures the real (big) interest attract in particular double tunneling-coupled quantum wells [3]. The investigation of coherent effect coupled with quantum interference in such structures was performed in [4–7].

In the present paper the facility of control of dark resonance by third (coupling) field in double tunneling-coupled quantum wells (Fig. 1(a)) was considered. Such peculiarities of excitation allow to extend of facilities of control of dark resonance by phases of excited fields [8–10].

The numerical results of dependence of populations ρ_{33}, ρ_{44} on two-photon detuning δ for three values of atomic contour phase is presented on Fig. 1(b). From this one can see that at $\Phi = 0$ the dip and narrow resonance in spectrum of absorption is observed. This feature corresponds to the dark resonance. However when one increase Φ from 0 till $\pi/2$ the magnitude of dip is decrease and at $\pi/2$ the dark resonance vanish (the dip for ρ_{33} and ρ_{44} do not appear). This fact clearly demonstrates that the dark resonance can arise and vanish in dependence on value of phases of excited field.

The dependence of dispersion and absorption spectra of laser fields acting on transitions $|1\rangle \rightarrow |3\rangle(|4\rangle)$ for different

phase values is presented on Fig. 2(a) and 2(b). From shape of this dependence one can see that the resonance amplification in index of refraction in area of the dark resonance at $\Phi = \pi/4$ is observed. When $\Phi = \pi/4$ the dependence of index of refraction on two-photon detuning in changed radically.

Conclusions:

We considered the interaction of three laser fields (two optical fields and one coupling field having infra-red range), formed closed contour of excitation, with double tunneling-coupled quantum wells. It is established that in this system dark resonance can arise and vanish. For $\Phi = 0$ the amplitude of the dark state is maximal and for $\Phi = \pi/2$ the dark resonance is absence. It is found that the index of refraction for laser fields of optical range in area of dark resonance at $\Phi = \pi/4$ have different resonance peculiarities which vanish when the amplitude of coupled field increase.

References

[1] B.G. Agapyev, M.B. Gorniy, B.G. Matisov, Yu.V. Rozhdestvensky, *Usp. Fiz. Nauk* **163**, 1 (1993).

[2] S. Harris, *Physics Today* **50**, 36 (1997).

[3] A.N. Litvinov, D.K. Loginov, G.A. Kazakov, B.G. Matisov, *Proceedings of Nanostructures: Physics and Technology*, 106 (2010).

[4] L. Silvestri, F. Bassani, G. Czajkowski *et al*, *Eur. Phys. J. B* **27**, 89 (2002).

[5] L. Silvestri and G. Czajkowski, *Phys. stat. sol. c* **5**, 2412 (2008).

[6] W.X. Yang, J. Xu, and R.K. Lee, arXiv: 0803.1888v1.

[7] N. Cui, Y. Niu, and G. Gong, arXiv: 0912.4172v1.

[8] D.V. Kosachiov, B.G. Matisov, Yu.V. Rozhdestvensky, *J. Phys. B.* **25**, 2473 (1992).

[9] S. Kajari-Schored, G. Morigi, S. Franke-Arnold *et al*, *Phys. Rev. A* **75**, 013816 (2007).

[10] A. Joshi, *Phys. Rev. B* **79**, 115315 (2009).

Kinetic properties of InAs quantum dots grown on vicinal GaAs substrates

X. Liu[1,2], V. G. Dubrovskii[2], N. V. Sibirev[2] and X. Ren[1]

[1] Key Laboratory of Information Photonics and Optical Communications, Beijing University of Posts and Telecommunications, Beijing, China
[2] St Petersburg Academic University, St Petersburg, Russia

Abstract. InAs quantum dots grown on vicinal GaAs substrates exhibit different kinetics properties. In order to explore the mechanism within the vicinal quantum dots formation process, the distribution density of quasi-3D clusters in the metastable growth region is studied here. The ratio of certain sized quasi-3D cluster density between vicinal quantum dots and quantum dots grown on singular substrates is distinct, which indicate the total material density and nucleation rate differences.

Introduction

The vicinal GaAs substrates provide new possibilities to modulate the InAs quantum dots(QDs) performance by varying misorientation angles and buffer layer thicknesses *et al*. The position of InAs QDs can be well controlled adopting GaAs vicinal substrates [1,2]. The QDs nucleate predominately along the steps and there are rare QDs on the terraces below certain deposition thickness, which can be explained by the higher material density around the steps compared with the singular substrates [2,3]. The alignment of InAs QDs along the step edges favors the spatially ordering of multiple QDs layers [1,2]. In this way, the defects induced by nanolithography for QDs ordering can be avoided. It is also possible to obtain sharp emission from single vicinal QDs grown in the subcritical deposition region [4]. These advantages make the theoretical research of vicinal QDs formation mechanism attractive. Here, the analysis of the quasi-3D islands kinetics before SK transition is developed for further exploration. The assumption of predominately growing along the step edges of quasi-3D islands is adopted.

1. Theoretical models

1.1. Assumptions

In order to explain the differences between singular QDs and vicinal QDs, we compared the InAs material densities of the two cases. Several assumptions and simplifications are proposed for further analysis: (1) we consider the MBE case. The steps on the vicinal substrate are multiatomic and vertical after GaAs or AlGaAs buffer layer epitaxy prior to InAs deposition, which is the requisite for steps of high quality and for optoelectronics characterization. The buffer layer is not only technically important but also theoretically convenient, for we can ignore the influence of InAs adatoms from the upper terraces; (2) the analysis is based on the experimental observation that before QDs formation there exist quasi-3D multilayer InAs clusters [5]. The layer-by-layer growth mode interruption caused by the large lattice mismatch in the InAs/GaAs system is the reasonable explanation to this phenomenon. Following we will refer the quasi-3D clusters as *i*-sized clusters, and *i* is the number of In-As pairs(in the following, it could be referred as both "adatoms" and "monomers") in the cluster; (3) we consider the clusters formed by continuous In-As pair attachment; (4) the adatoms favorable nucleation sites are the step edges on the vicinal substrate for a lower energy barrier, and the collection of monomers from elsewhere (such as beam flux direct impingement) for a given cluster is ignored. Which is not the truth when the clusters even grow bigger, then the collection of monomers from the terrace cannot be ignored; (5) the methodology we adopted is the classical nucleation theory [6], which usually take the number *i* of the clusters as continuous variable and the nucleation course is stationary one whose rate is considered as constant one, i.e., we ignore the temperature and adatom density fluctuation before the clusters approaching the overcritical size to form QDs.

The above simplifications will be discussed after the comparison between singular QDs and vicinal QDs properties.

1.2. Theoretical methodology

The nucleation rate I is one of the most important parameter in classical nucleation theory, whose general definition is given as $I(t) = d\zeta(t)/dt$.

$$\zeta(t) = \int_{i^*}^{i_c} n(i,t)\,di\,,$$

i^* denotes the critical size in the course of phase transition from adatom to clusters (simplified as critical size below), while i_c denotes the critical size in the course of phase transition from clusters to QDs (simplified as overcritical size below). Besides, $n(i,t)$ is defined as the density of i-sized cluster at certain time t, in this way $\zeta(t)$ is the total density of the clusters before QDs formation. To simplify the modeling, we just consider the first course. Further, take the stationary nucleation case, I and n is independent of time t, so:

$$n(i) = n_e(i)\,\frac{1 - \mathrm{erf}\left[\beta\left(i - i^*\right)\right]}{1 - \mathrm{erf}\left[\beta\left(1 - i^*\right)\right]} \tag{1}$$

$n(i) \approx \frac{1}{2} n_e(i)\{1 - \mathrm{erf}[\beta(i - i^*)]\}$, provided that $\beta(i^* - 1) > 1$ here $n_e(i)$ is the equilibrium density, which is introduced for theoretical analysis in classical nucleation theory, erf is the error function and

$$n_e(i) = n_e^*(i)\exp\left[\beta^2\left(i - i^*\right)^2\right], \tag{2}$$

$$n_e^*(i) = n_0\exp\left(-F^*/k_B T\right) \tag{3}$$

is the equilibrium density of critical cluster density where F^* is the energy barrier for the formation of a i^*-sized cluster, k_B is
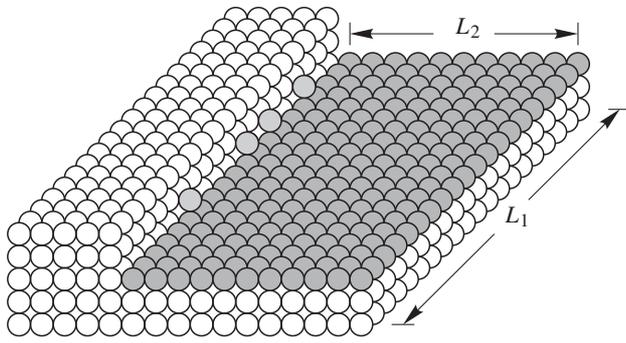
Fig. 1. Schematic diagram of InAs adatoms on the vicinal GaAs substrate. For simplicity, the InAs material on the upper terrace and step edge is not illustrated.
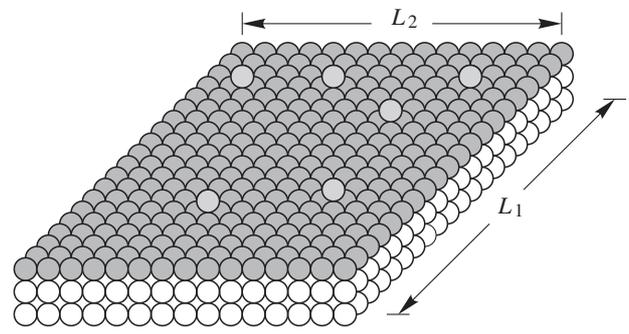
the Boltzmann constant and T is the temperature; the numerical factor $\beta > 0$ is given by

$$\beta = \left[-F'' \left(i^* \right) / 2k_B T \right]^{1/2} . \quad (4)$$

whose similar form is called Zel'dovich factor.

1.3. Comparison between vicinal QDs and singular QDs

Vicinal i-sized clusters:

Based on the assumption that the adatoms condensation sites are the step edges on the vicinal substrate, which implies that $n_0(v) = n\,(\text{step})L_1/a_0$ (v means "vicinal") and $n\,(\text{step})$ is the step density on the vicinal substrate which can be controlled by varying misorientation angles and buffer layer thicknesses; L_1 is the step length and a_0 is the size of a In-As dimer, L_1/a_0 has a meaning of the total nucleation sites on a single step-terrace system.

Singular i-sized clusters:

Taking a same area as the terrace in the step-terrace system on the vicinal substrates, the nucleation sites on singular substrate is $L_1 \times L_2/a_0^2$ (L_2 is defined as the terrace width). So $n_0(s) = \frac{L_1 \times L_2/a_0^2}{L_1 \times L_2} = a_0^{-2}$ (s means "singular case").

For further simplification, we assume that vicinal and singular systems have the same value of the energy barrier to form a quasi-3D cluster nuclei. In this case, the nucleation sites density makes the major difference. In such way, we obtain the actual i-sized cluster density difference between vicinal substrate and singular one:

$$k = \frac{n(v)}{n(s)} = n\,(\text{step})\,a_0 L_1 . \quad (5)$$

The following analysis is straightforward: if we consider the material density $G = \int_{i^*}^{i_c} i\, n(i)\,di$ within the range of i^* and i_c, the difference between vicinal and singular cases is also the factor k. We introduce line step density as $n'\,(\text{step}) = n\,(\text{step})L_1$, taking $L_2 = 100$ nm and $a_0 = 0.5$ nm, the ratio k is calculated as 10^{-3}. So small a k implies that under the same material deposition, the quasi-3D clusters are much easier to approach the overcritical region to form QDs, which is verified by the experimental observation. Furthermore, the material density G and nucleation rate I of quasi-3D clusters on vicinal substrates are both about $1/k$ larger than the singular case.

Fig. 2. Schematic diagram of InAs adatoms on the singular GaAs substrate.

2. Discussion

From the calculations, we used some simplifications to obtain the vicinal QDs behaviors before QDs formation, and the simplifications need revisions. Besides, the similar modeling should be extended to the region of QDs formation which is of practical interests. The formation energetics of the quasi-3D InAs cluster nuclei should be calculated separately for different step orientations. More accurate depiction of quasi-3D clusters or attachment rate of monomers to QDs should be given.

References

[1] M. Kitamura *et al*, *Appl. Phys. Lett* **66**, 26 (1995).
[2] F. Poser *et al*, *J. Crystal Growth* **248**, 317 (2003).
[3] R. Leon *et al*, *Phys. Rev. Lett.* **78**, 4942 (1997).
[4] U. Perinetti *et al*, *Appl. Phys. Lett* **94**, 163114 (2009).
[5] F. Patella *et al*, *Phys. Rev. B* **67**, 205308 (2003).
[6] D. Kashchiev, *Nucleation: Basic Theory with Applications.* (Oxford: Butterworth Heinemann), (2000).

Indium dose dependence of carrier transfer in InAs/AlGaAs quantum dots system

A. A. Lyamkina[1,2], S. P. Moshchenko[2], D. S. Abramkin[2], D. V. Dmitriev[2], D. V. Gulyaev[2], T. S. Shamirzaev[2] and A. I. Toropov[2]

[1] Novosibirsk State University, Pirogov str. 2, 630090 Novosibirsk, Russia

[2] A.V. Rzhanov Institute of Semiconductor Physics, SB RAS, Lavrentjeva 13, 630090 Novosibirsk, Russia

Abstract. Indium dose dependence of carrier transfer in InAs/AlGaAs quantum dots is studied. Droplet to Stranski–Krastanov growth mode transition occurs in chosen growth conditions, that allows us to investigate growth mode dependence within the one sample. Temperature dependence of integral PL intensity was measured to study carrier transfer. It is shown that in Stranski–Krastanov mode non-radiative recombination centers with high density arise in the wetting layer, while in droplet mode the wetting layer is almost defect-free and thus carrier transfer is highly efficient.

Introduction

InAs/AlAs quantum dots (QDs) are pesrpective system to produce light-emitting devices for the visible spectral range. However, as it was shown in our recent work [1], there is problem to produce effective light-emitting devices based on InAs/AlAs QDs due to insufficient capture of charge carriers from wetting layer (WL) to the QDs. This problem is caused by high concentration of non-radiative recombination centers localized in the WL that capture charge carriers impeding their penetration into the QDs. In this work we investigated the In dose dependence i.e. influence of growth mode on carrier transfer from WL to QDs.

1. Experimental

The structures with InAs/AlGaAs QDs studied in this work were grown by MBE using a Riber32P system with valve arsenic source on semi-insulating (001) GaAs substrate. After removal of native oxide a 0.2 μm thick $Al_{0.9}Ga_{0.1}As$ buffer layer was grown. Simultaneously the quality of the surface was controlled by means of reflection high-energy electron diffraction and metal-enriched (5×2) surface reconstruction was clearly observed. To study In dependence the rotation was switched off during In deposition. Two monolayers of In were deposited to the $Al_{0.9}Ga_{0.1}As$ surface at 510 °C in the absence of arsenic flux and the array of initial In droplets formed. Then the sample was exposed to a beam equivalent pressure of 1.5×10^{-5} Torr of As_4 and InAs quantum dots crystallized. The growth was interrupted for 60 s after In source had been closed and then the QDs were capped with 25 nm of $Al_{0.9}Ga_{0.1}As$.

2. Carrier transfer

To investigate the capture of carries from the WL to QDs, the temperature dependence of integral intensity of the WL and QD bands of PL spectrum was measured (Fig. 1). For low In dose intensity of the QD band increases and intensity of the WL band decreases simultaneously. It evidences that nonequilibrium carriers, delocalized in the WL with a temperature increase, are captured in QDs mainly and don't recombine in non-radiative way as in Stranski–Krastanov (SK) grown samples [1]. Then, over critical In amount QD band intensity doesn't not increase with temperature increase and carrier transfer from WL to QDs is impaired.
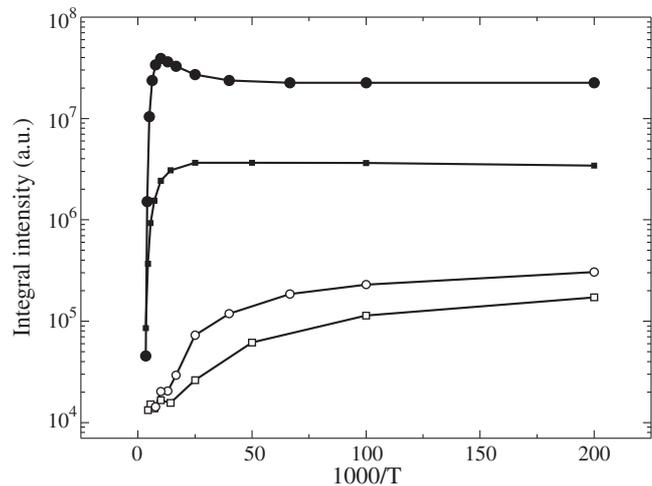

Fig. 1. Integral intensities for QD and WL bands: circles — under-critical indium dose, squares — overcritical dose. Filled and open symbols denote QD and WL bands correspondingly.

Such behaviour can be treated within the framework of droplet to SK transition, that takes place over critical In dose [2]. Elastic relaxation in SK mode can create defects (worked as nonradiative centers) in a WL/lower layer interface. Otherwise, in the droplet epitaxy a conversion of a In droplet to InAs QD is arsenic-driven and soft. Thus, in droplet epitaxy mode WL/lower layer interface doesn't change and it can be saved defect-free. Therefore, we assume that in droplet mode the density of non-radiative recombination centers in the WL is lower, than in Stranski–Krastanov one and, thereby carrier transfer is more efficient.

References

[1] T.S. Shamirzaev, D.S. Abramkin, A.V. Nenashev, K.S. Zhuravlev, F. Trojanek, B. Dzurnak and P. Maly, *Nanotechnology* **21**, 155703 (2010).

[2] A.A. Lyamkina, Yu.G. Galitsyn, D.V. Dmitriev, V.A. Haisler, S.P. Moshchenko and A.I. Toropov, *Proc. of Symposium Nanostructures: Physics and technology (Minsk, 2009)*, Ioffe Institute, p. 144, 2009.

Investigation of photoexcited carriers lifetime in narrow-gap Hg$_y$Cd$_{1-y}$Te/Cd$_{1-x}$Hg$_x$Te QW heterostructures by means of terahertz pump-probe technique

S. V. Morozov[1], V. I. Gavrilenko[1], A. V. Antonov[1], V. V. Rumyantsev[1], A. A. Dubinov[1], O. Drachenko[2], S. Winnerl[2], H. Schneider[2] and M. Helm[2]

[1] Institute for Physics of Microstructures, RAS, 603950 Nizhny Novgorod, Russia
[2] Forschungszentrum Dresden–Rossendorf Institute of Ion Beam Physics and Materials Research, Dresden, D-01314, Bautzner Landstraße, 400

Abstract. In work was the THz pump-probe studies of photoexcited carrier lifetime in narrow-gap Hg$_y$Cd$_{1-y}$Te/Cd$_{1-x}$Hg$_x$Te QW heterostructures with graphene-like energy-momentum using the free electron laser facilities.

Introduction

HgCdTe (MCT) photodetectors are widely used in mid IR range (see, for example [1]). HgTe is known to be a gap-less semiconductor with inverted band structure (or negative band gap), i.e. Γ8 point in the centre of Brillouin zone is over Γ6 one in contrast to "normal" semiconductors. Due to this remarkable property a band gap can be engineered from 0 up to 1.6 eV in MCT solid solutions or in HgTe/CdTe based heterostructures. However it is a problem to advance MCT detectors to THz range because the content fluctuations in solid solution smear the valence and conduction band edges. Using of MBE grown high quality HgTe/CdTe based QWs/superlattices (SL) seems to be a solution to overcome this problem.

Schulman and McGill suggested for the first time to employ HgTe/CdTe SLs for the photodetectors as a material with variable by changing the QW layer thickness band gap [2]. However up to now studies into THz photoresponse in HdTe/CdTe QW heterostructures have been carried out on the samples with 2D electron gas only where the effect results from the intrabans radiation absorption [3–6]. MBE allows the controllable growth of SL and Hg$_x$Cd$_{1-x}$Te QWs with high homogeneity under in situ ellipsometric control of layer thickness and content [6]. High quality HgTe/CdHgTe QWs with 2D electron gas has been demonstrated, the mobility being as high as $(5-6) \times 10^5$ cm^2/V s [7]. It is also worth mentioning that narrow gap MCT QW heterostructures possesses grapheme-like energy-momentum law. I.e. the energy-momentum relation both in the conduction and in the valence band nearby the 0 point is closed to the linear ones with the same slope while the effective mass tends to zero — Fig. 1.

In heterostructures with narrow (but finite) gap the effective mass at the band edge is also finite but very small. The smallness of the effective mass and hence of the density of states results in the low concentration of the thermally excited charge carriers. This peculiarity is useful for designing THz photodetectors operating at interband transitions. In MCT heterostructures with the inverted band structure the conduction band states are formed the *p*-type Bloch wavefunctions corresponding to Γ8 representation. For such states the effects of spin-orbit interactions are much larger than those for the states corresponding to Γ6 one. The latter results in giant spin splitting of the conduction band (in the absence of the magnetic
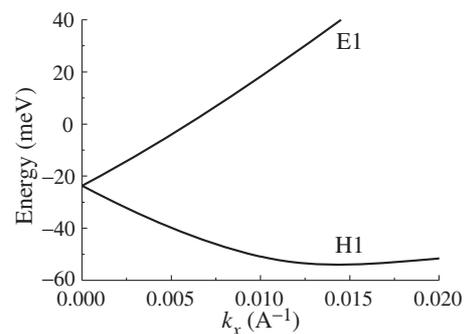

Fig. 1. Calculated energy spectrum in HgTe/CdTe (013) QW 70 Å wide. The electron and hole velocity near $k_x = 0$ is 5.6×10^7 cm/s.

field) in asymmetrical QWs that can be used for creating spintronic devices. To design both the lasers and the photodectors it nessessary to possess the information not only on the energy spectrum of the structures but on the carrier lifetimes as well. To the date the most informative and precise experimental tool to measure carrier lifetimes is optical pump-probe method. This method is based on the measurement of the transmission (or reflection) modulation as a function of the time delay between the excitation (pump) and the probing (probe) radiation pulses. Pump-probe technique allows directly measuring the interband recombination time at the carrier excitation with radiation quanta equal to the band gap.

1. Results and discussion

The sample to be investigated in the framework of this proposal were grown by MBE technique on semiinsulated GaAs(013) substrates and according to the calculations and preliminary measurements possess the normal (not inverted) band structure. The active part of structures were grown on relaxed CdTe buffer layer. In already studied heterostructure #1225_1 [8] the active part consists of the lower Cd$_y$Hg$_{1-y}$Te ($y \sim 0.6$) barrier of 30 nm thickness, Hg$_{1-x}$Cd$_x$Te ($x \sim 0.13$) QW 30 nm wide, a similar Cd$_y$Hg$_{1-y}$Te upper barrier and CdTe cap layer 40 nm in thickness. To date we have already performed preliminary THz pump-probe measurements using FELBE (pulse duration about 10 ps) with the structure #1225_1 for different excitation wavelengths and powers. Earlier preliminary measurements of THz photoconductivity spectra of this structure has been performed using Bruker Vertex 80v FT spectrometer at $T = 4.2$ K [8].
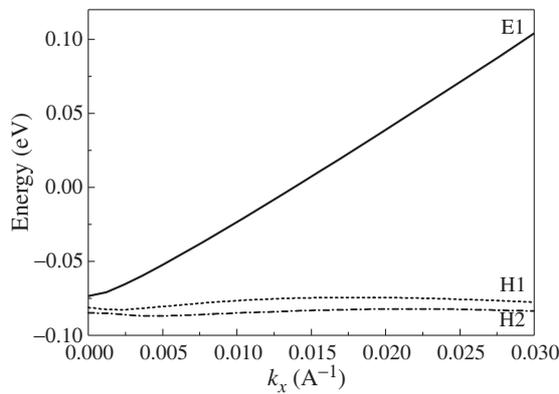
**Fig. 2.** Calculated energy spectrum in the heterostructure #1225_1 [8].
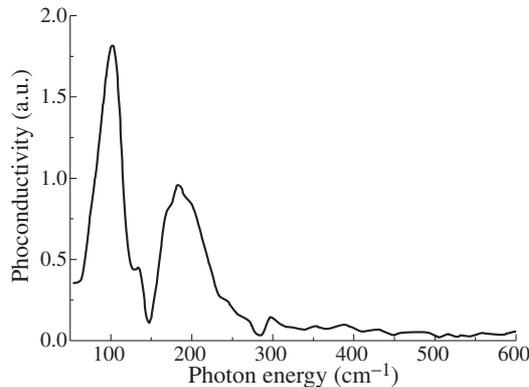
Fig. 3. Measured photoconductivity spectrum in the heterostructure #1225_1 at $T = 4.2$ K.

A broad photoconductivity band ranging from 60 to 300 cm^{-1} has been discovered (Fig. 3) resulted from the interband absorption in Hg$_{0.64}$Cd$_{0.36}$Te/Cd$_{0.86}$Hg$_{0.14}$Te QW with dips at 129 and 147 cm^{-1} owing to the absorption by optical phonons in upper CdHgTe barrier.

According to the calculated band structure (Fig. 2) and the measured photoconductivity spectrum (Fig. 3) the band gap at $k = 0$ is of 7.4 meV. The pump-probe measurements in this sample were carried out at the FELBE wavelength 88μm (energy quantum 14 meV), i.e. the electrons were excited far from the conduction band edge. By the "single-color" pump-probe technique it has been discovered that the transmission signal relaxation time increases with the pump power and is 10 ps at the power of 60 mW and about 50 ps at power of 100 to 200 mW.

At the low pump power the signal shape is gaussian while at higher power the exponential decay is clearly seen (Fig. 4). It seems that the gaussian form of the signal at power of 60 mW results repeat the form of the FELBE pulse while the characteristic times of the relaxation processes are shorter than 10 ps. Such fast relaxation seems to result mainly from the cooling of photoexcited holes by acoustical phonon emission, the hole scattering rate by acoustical phonons being estimated as 10^{11} s^{-1}. It is worth mentioning that the electron scattering rate by acoustical phonons is much less (it is estimated as $\sim 5 \times 10^9$ s^{-1}) because of the very small effective mass $0.003m_0$ [8] and significantly less deformational potential of -4.6 eV if compared with that in GaAs (~ -11 eV). At a higher pump power the valence band population increases that
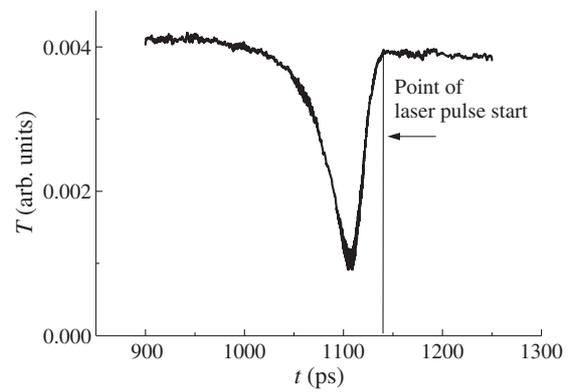

Fig. 4. Transmission signal versus time at the excitation wavelength 88 μm and power 150 mW for the heterostructure #1225_1 measured at $T = 4.2$ K.

restricts the intraband relaxation due to the Pauli exclusion principle.

References

[1] M.A. Kinch, *J. Electron. Mater.* **29**, 809 (2000).
[2] J.H. Schulman, N.C. McGill, *Appl. Phys. Lett.* **34**, 663 (1979).
[3] C. Stellmach, R. Bonk, Yu.B. Vasilyev *et al*, *Phys. Stat. Sol. (c)* **3**, 2510 (2006).
[4] F. Gouider, Y.B. Vasilyev, M. Bugar *et al*, *J. Low Temperature Physics* **159**, 184 (2010).
[5] S.N. Danilov, B. Wittmann, P. Olbrich *et al*, *J. Appl. Phys.* **105**, 013106 (2009).
[6] S. Dvoretsky, N. Mikhailov, Yu. Sidorov *et al*, *J. Electron. Mater.* **39**, 918 (2010).
[7] Z.D. Kvon, S.N. Danilov, N.N. Mikhailov *et al*, *Physica E* **40**, 1885 (2008).
[8] A.V. Ikonnikov, A.A. Lastovkin, K.E. Spirin *et al*, *JETP Letters*, **92(11)**, 837 (2010).

Features of Ge(Si)/Si(001) self-assembled island nucleation in multilayer structures

A. V. Novikov[1], D. V. Yurasov[1], M. V. Shaleev[1], N. D. Zakharov[2] and P. Werner[2]

[1] Institute for Physics of Microstructures, RAS, 603950 Nizhny Novgorod, Russia
[2] Max-Planck-Institut für Mikrostrukturphysik, Weinberg 2, 06120 Halle/Saale, Germany

Abstract. The formation of Ge wetting layer and nucleation of Ge(Si) self-assembled islands in multilayer structures were investigated experimentally. It was shown that the inhomogeneous strain fields produced by the buried islands cause a significant redistribution of the material of the Ge wetting layer in upper layers of multilayer structures. As a result of such redistribution of Ge atoms local unfacetted elevations ("hills") form on the wetting layer above the buried islands. It was observed that these hills are the preferable sites for the islands nucleation. The possibility to use the hills for local ordering of islands was demonstrated.

Introduction

It is well known that in the multilayer structures with self-assembled islands the vertical ordering of islands occurs if the spacer layers of host material are rather thin. Such ordering was observed for different strained heterosystems like Ge/Si and InAs/GaAs [1,2]. It was demonstrated [2,3] that the physical reason for the preferential island nucleation in the upper layers above the islands of underlying layers is the strain fields produced by the buried islands. It was supposed [2] that vertical ordering of islands is facilitated by the nonuniform distribution of the wetting layer material in the growth plane. Recently the direct experimental confirmations of this hypothesis for Si/Ge system were demonstrated [4]. Present work is devoted to the detailed investigations of features of wetting layer formation and specialities of the nucleation and growth of Ge(Si) self-assembled islands in multilayer structures.

1. Experimental

The SiGe structures under investigation were grown by solid source MBE on Si(001) substrates at growth temperatures $T_g = 600-700$ °C. The structures consisted of 2–3 layers of Ge(Si) self-assembled islands separated by 20 nm thick Si spacer layers. The amount of deposited Ge in the first layer was $d_{Ge} = h_{c1} + 3$ monolayers (ML) (1 ML ≈ 0.14 nm), where h_{c1} is the critical thickness of 2D growth of Ge film in the first layer ($h_{c1} = 4-5$ ML subject to growth temperature). The growth conditions of investigated samples are described in detail elsewhere [4]. Sample morphology was studied by an atomic force microscopy (AFM) using "NTEGRA Prima" NT-MDT microscope in the tapping mode. The transition point from the 2D to 3D growth mode was detected *in situ* by the reflection high energy electron diffraction (RHEED) technique. The using of RHEED gives the possibility for accurate determination of the critical thickness of 2D growth of Ge film (h_c) for each layer in multilayer structures. The transmission electron microscopy (TEM) studies were performed on Philips CM20 and JEM 4010 electron microscopes with acceleration biases of 200 and 400 kV, respectively.

2. Results and discussion

It was obtained that the uniform Ge wetting layer does *not* form in the upper layers of multilayer structures with Ge(Si) self-assembled islands (Fig. 1a) in contrast to the single-layer
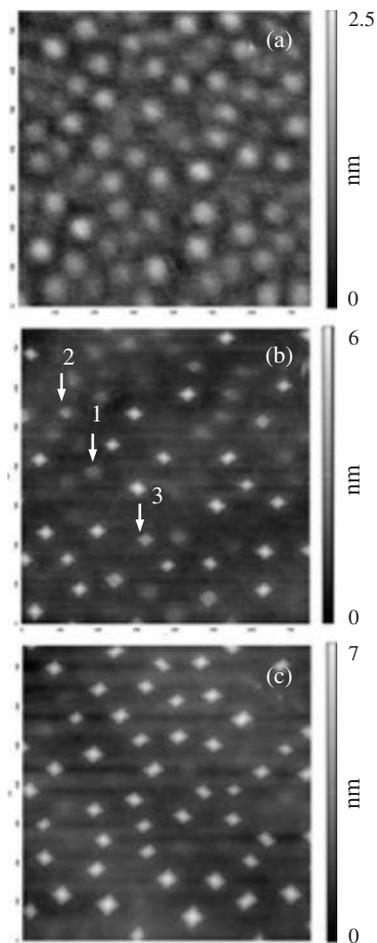

Fig. 1. AFM images of the upper layer of structures with 3 islands layer grown at $T_g = 600$ °C: (a) $d_{Ge} < h_c$, (b) $d_{Ge} \sim h_c$, (c) $d_{Ge} > h_c$. The size of AFM images is 0.75×0.75 μm. On the AFM scan (b) arrows indicate: hill (1), partially facetted hill (2) and T-pyramid (3).

structures. The strain fields produced by the buried Ge(Si) islands lead to the preferential diffusion of Ge adatoms to the tensile-strained regions of Si spacer located above buried islands. As a result the local unfacetted elevations (hills) with the surface density and lateral dimensions close to those of islands in underlying layer form already at the early stage of Ge wetting layer formation (Fig. 1a) [4]. According to the TEM
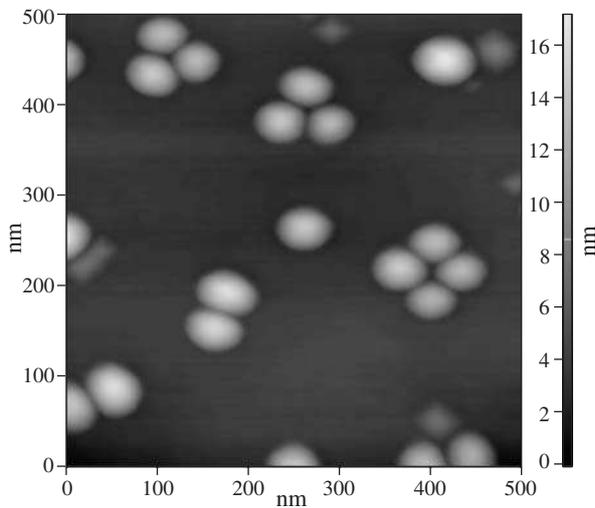
Fig. 2. AFM image of the second layer of multilayer structure with the different growth temperatures for the first (700 °C) and second (600 °C) island layers.

data these hills appear directly above the buried Ge(Si) islands. So the hills formation can be connected with the preferential diffusion of Ge adatoms to the tensile strained regions of Si spacer which are located above the buried islands. Due to the smaller lattice mismatch accumulation of Ge adatoms in the tensile strained regions of Si spacer is energetically favorable.

It was revealed that the Ge(Si) islands nucleation in the upper layers of multilayer structures differs from that in the single-layer ones. Particularly in multilayer structures it goes via the faceting of the hill's sides by the {105} planes and the gradual transformation of unfacetted hills to the truncated pyramids (T-pyramids) (Fig. 1b) [4], but not by the spontaneous nucleation of so-called "pre-pyramid" islands as in single-layer structures [5]. The T-pyramids turns into the "usual" pyramids with the increase of the amount of deposited Ge (Fig. 1c). At this point the typical "spotty" picture on the RHEED pattern forms manifestly.

As was reported earlier [6] the island formation in the upper layers of multilayer structures occurs at the smaller amount of deposited Ge in comparison with the single layer ones. However the height of the observed hills is greater than the critical thickness of 2D growth (h_c) in the single layer structures. This fact can be explained by the local tension of Si spacer layer in the regions above the islands and so the smaller lattice mismatch between Ge and substrate there. Because of the formation of the nonuniform Ge wetting layer in the multilayer structures with islands such parameter as "critical thickness of the 2D growth", which is widely used for description of the growth mode of strained layers can be used only as an integral parameter that does *not* reflect the real distribution of wetting layer material on the surface in upper layers of multilayer structures.

Investigations of multilayer structures in which the first and subsequent Ge(Si) island layers grown at different temperatures (hereinafter referred to as "temperature — asymmetric structures") revealed that lateral sizes of hills and islands in the multilayer structures are determined by different parameters. In particular, the lateral sizes of hills depend on the lateral sizes and surface density of the buried islands, whereas the lateral sizes of uncapped islands are defined basically by

the growth temperature. There are two different situations for "temperature-asymmetric structures".

1. If the growth temperature of the first island layer is lower than of the subsequent island layers ($T_g = 600$ and 700 °C, respectively in the present work) the sizes of islands in upper layers are larger than sizes of hills. But surface density of the islands in upper layers is determined by the density of hills which is close to density of buried islands grown at low temperature. As a result the surface density of islands in upper layers of such "temperature-asymmetric structures" is significantly higher than in the structures completely grown at high ($T_g = 700$ °C) temperature.

2. Otherwise, if the growth temperature of the first island layer is higher than of the subsequent island layers ($T_g = 700$ and 600 °C, respectively in the present work), the lateral sizes of hills are significantly larger than lateral sizes of islands which will form on these hills. It was demonstrated that several (2–4) closely packed small islands can be grown on the single large hill in such "temperature-asymmetric structures" (Fig. 2) which results in the appearance of the island clusters or so-called "quantum dot molecules" [7].

Acknowledgements

References

[1] A.A. Darhuber *et al*, *Phys. Rev. B* **55**, 15652 (1997).
[2] Q. Xie *et al*, *Phys. Rev. Lett.* **75**, 2542 (1995).
[3] J. Tersoff *et al*, *Phys. Rev. Lett.* **76**, 1675 (1996).
[4] D.V. Yurasov *et al*, *J. Crystal Growth* **313**, 12 (2010).
[5] A. Vailionis *et al*, *Phys. Rev. Lett.* **85**, 3672 (2000).
[6] O.G. Schmidt *et al*, *Phys. Rev. B* **61**, 13721 (2000).
[7] X. Deng and M. Krishnamurthy, *Phys. Rev. Lett.* **81**, 1473 (1998).

Temperature quenching of PL intensity in self-organized ZnTe/CdTe/ZnTe quantum dots

A. Reznitsky[1], A. Klochikhin[1,2] and *S. Permogorov*[1]

[1] Ioffe Physical-Technical Institute, St Petersburg, Russia
[2] B.P. Konstantinov Nuclear Physics Institute,188350, St Petersburg, Russia

Abstract. We have studied the temperature dependence of the photoluminescence (PL) intensity of nano-size heterostructures ZnTe/CdTe/ZnTe containing self-organized CdTe quantum dots (QD) in temperature range 5–250 K at different intensities of optical excitation. It has been found that the temperature quenching of PL intensity is governed by thermal activation of electrons and holes to the centers of nonradiative recombination. These two processes should be considered as independent which leads to the two-exponential character of the thermal decay curves. The character of temperature quenching of PL intensity strongly depends on the pumping power. The higher is the excitation power, the slower is the temperature decay of the PL intensity. We attribute the observed effect to the saturation of the centers of nonradiative recombination for electrons or holes in the barrier regions of heterostructures.

The understanding of the mechanisms of nonradiative recombination in quantum size heterostructures is very important for the construction of the optoelectronic devices. Although the heterostructures containing the quantum dots demonstrate better working parameters than those with quantum wells, the working characteristics of these structures are by far lower than the theoretical expectations. The main drawbacks are coming from the nonradiative recombination of carriers which strongly reduces the operation efficiency of devices at room and even liquid nitrogen temperatures.

In this work we have studied the PL spectra of MBE-grown CdTe/ZnTe structure containing five isolated QW's (A, B, C, D, and E) with progressively increasing CdTe content W_{CdTe} (1.8, 2.5, 4.3, 6.5, and 8.6 monolayers (ML)), separated by thick (60 nm) ZnTe barriers. The PL spectra of the sample at optical excitation above the ZnTe barrier are shown on Fig. 1a,b. The spectra contain three PL bands of comparable intensities corresponding to the radiative recombination of carriers in A, B, and C QW's. For QW's with higher Cd content W_{CdTe} (6.5 and 8.6 ML) the PL intensity is by more than 50 times lower than in A,B, and C QW's.

Transmission electron microscopy [1] has shown that only A, B, and C QW's in this structure are coherently strained whereas D and E QW's exhibit partial structure relaxation of the interfaces with formation of structural defects which are serving as the centers of nonradiative recombination (NR). The study of micro-PL spectra has shown that the distribution of CdTe across the QW planes is highly inhomogeneous which is evidenced by the presence of sharp resolution limited (<0.2 meV) emission lines (Fig. 1b). These lines corresponds to the PL of exciton states localized within the separate QD's formed via the self-organization processes during the growth [2].

The temperature dependence of the integrated PL intensity $I_{PL}(T)$ in the range 5–150 K for A, B and C QW's at excitation above the ZnTe barrier is shown in Fig. 2. For each band the measurements were carried out at two excitation densities (1 and 100 W/cm^2). Two characteristic features of our experimental results should be noted. First, the general dependence of the temperature quenching of the PL intensity for all three bands strongly depends on the density of optical excitation. Second, in all cases the curves of the temperature quenching
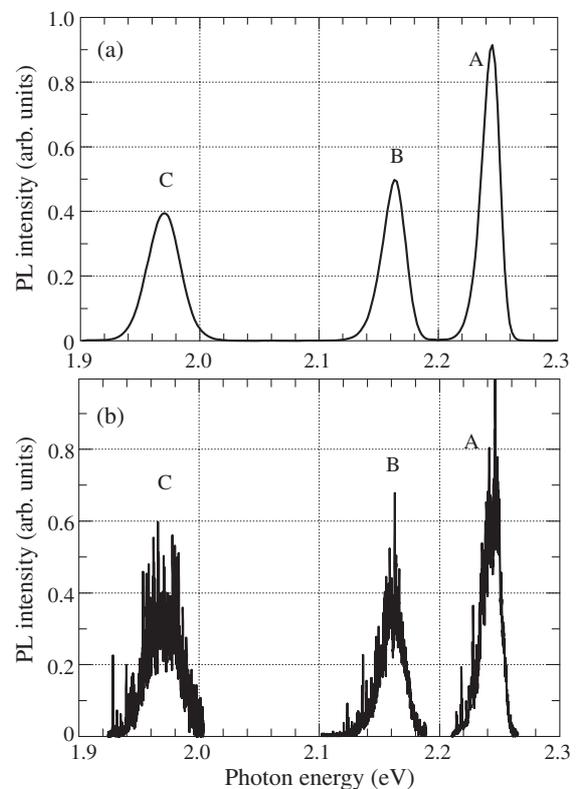

Fig. 1. (a) PL spectra of QW's from A, B, and C at $T = 2$ K and excitation by 441.6 nm line of He-Cd laser, (b) micro-PL spectra of QW's A, B, and C from the 0.5-μ-diameter spot at $T = 7$ K and excitation above ZnTe-barrier.

have complicated character.

At low excitation densities for every of three QW's two different temperature regions in the quenching of emission intensity are observed. Up to 50 K the decrease of the emission intensity is rather steep and above this temperature it becomes smoother. Most clear it is seen on the panel b of the Fig. 2 for B QW but can be also noticed for A and C QW's. Usually the temperature dependence of $I_{PL}(T)$ is assumed to arise due to the activation processes and can be described assuming the exponential relation $exp(-E_{ac}/kT)$ of population of radiative states in QD and nonradiative states in barrier which are separated by activation energy E_{ac}. The emitting states of localized
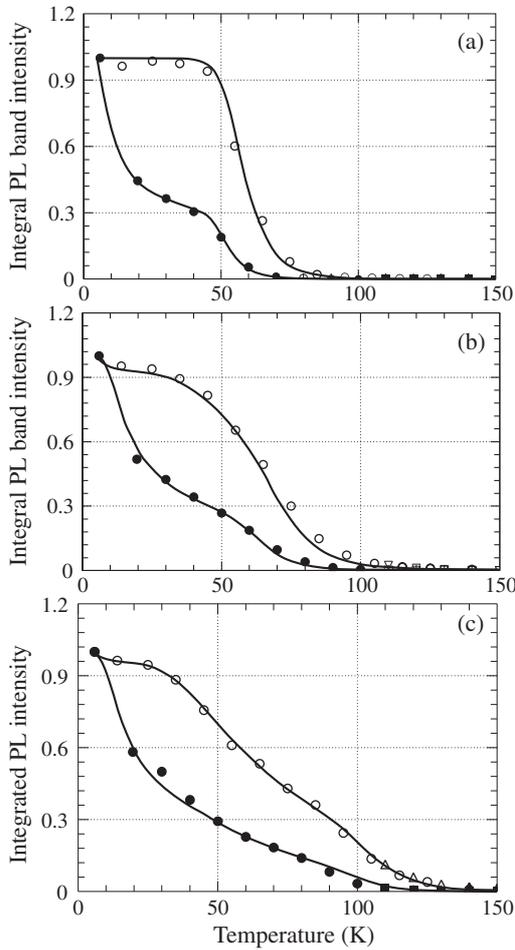
Fig. 2. Temperature dependence of the integrated PL intensity of three quantum wells formed by 1.8 (a), 2.5 (b), and 4.3 (c) ML of CdTe at two different excitation powers 1 (lower curves) and 100 (upper curves) W/cm^2. Symbols are experimental data, solid lines are the results of calculations.

excitons in QD's are formed by two carriers, electron and the hole. The nonradiative escape of every of them will lead to the destruction of the radiative state. So for the description of our experimental results we have used two-exponential function suggested by simple kinetic considerations which accounts for the separate nonradiative relaxation of the two kinds of carriers

$$\frac{I(T)}{I_0} = \frac{1}{1 + \alpha \exp\left(-E_1/kT\right) + \beta \exp\left(-E_2/kT\right)} . \quad (1)$$

Here $I(T)$ is a temperature dependent integrated PL intensity, I_0 is that at the lowest temperature, α and β are numerical parameters, and E_1 and E_2 are characteristic activation energies for thermal transitions from radiative to the nonradiative states for holes and electrons. The activation energies for the release of holes and electrons from the QD are expected to be quite different, since in ZnTe/CdTe/ZnTe heterostructures the band offset in the valence band is much smaller than that for the conduction band [3]. The activation energies for holes E_1 providing the best fit of the results were found to be $2.6 \rightarrow 3.0 \rightarrow 5.2$ meV for the A, B, C sequence of QW's in qualitative agreement with the increase of the well depth with the increase of the CdTe content. The value of activation energy for the electron release E_2 was found to be in the range 60 to 100 meV for all three QW's.

As it is seen from Fig. 2, the increase of the excitation density for all three QW's A, B, and C leads to the slowing of the temperature quenching of the PL intensity in the region of low temperatures. Most pronounced this effect is for the A QW. However, the same tendency can be also noticed in the results for two other QW's B and C. We suppose that the observed effect is caused by the saturation of NR centers of recombination at the increase of the excitation density. It can be assumed, that the concentration of NR centers increases with the increase of CdTe content in A, B, and C QW's. Also, the increase of nominal Cd content in the QW increases the density of QD's per unit area. The centers of NR recombination can be completely saturated for the A QW with the lowest density of QD's and presumably the lowest concentration of centers of NR recombination at temperatures below 50 K. The saturation is not complete for B and C QW's since at the same density of optical excitation the number of electron-hole pairs per one QD is decreasing in A, B, C sequence. Qualitatively these assumptions are in agreement with our fitting results, but the interpretation of the physical meaning of obtained parameter values needs further elaboration of the model.

Acknowledgements

References

[1] J. Cibert, Y. Gobil, Le Si Dang, S. Tatarenko, G. Feuillert, P.H. Jouneau, and K. Saminadayar, *Appl. Phys. Lett.* **56**, 292 (1990).

[2] L. Marsal, L. Besombes, F. Tinjod, K. Kheng, A. Wasiela, B. Gilles, J.-L. Rouviere and H. Mariette, *J. Appl. Phys.* **91**, 4936 (2002).

[3] P. Peyla, Y. Merle d'Aubigne, A. Wasiela, R. Romestain, H. Mariette, M.D. Sturge, N. Magnea, H. Tuffigo, *Phys. Rev. B* **46**, 1557 (1992).

Intraband photocurrent spectroscopy of self-assembled Ge quantum dots on strained Si$_{0.65}$Ge$_{0.35}$ layer

A. I. Yakimov, A. I. Nikiforov, V. A. Timofeev, *A. A. Bloshkin*, V. V. Kirienko and V. A. Dvurechenskii

A.V. Rzhanov Institute of Semiconductor Physics, SB RAS, Lavrentjeva 13, 630090 Novosibirsk, Russia

Abstract. We report on intraband photocurrent spectroscopy of Ge self-assembled quantum dots grown on strained Si$_{0.65}$Ge$_{0.35}$ layer. The *p*-type devices show broad spectral response ranging from 2 to 12 μm. By a comparison between photocurrent measurements and the hole energy level scheme, as deduced from six-band $\mathbf{k} \times \mathbf{p}$ calculations, the two main contributions to the photoresponse are identified. The absorption band between 2 and 4 μm is attributed to the bound-to-continuum transitions between the bound states of the quantum dots and the continuum states in the Si barrier. The photoresponse at longer wavelength (4–12 μm) is associated with hole transitions from the dots to the nearby Si$_{0.65}$Ge$_{0.35}$ layer.

Introduction

Intraband optical transitions in QDs have attracted a great deal of attention due to their potential applications in infrared detectors operating at normal incidence and displaying low dark current. Most of the demonstrations of quantum dot photodetectors were achieved with III–V heterostuctures. SiGe-based QD photodetectors represent another attractive type of the device due to its compatibility with standard Si readout circuitry. At present, the most highly developed technology for fabricating arrays of SiGe-based QDs utilizes strain-driven epitaxy of GeSi nanoclusters on Si(001) surface. A typical energy gap between the GeSi dot ground state and the Si valence band edge is about 300–400 meV and weakly depends on the growth conditions. With the increase in the growth temperature, the dots become larger, and the Ge content decreases. Since the energy level confined to a dot becomes deeper with increasing dot size and more shallow with decreasing Ge content, the hole binding energy changes slightly with the growth temperature. The photoresponse in the spectral range 3–4 μm was really observed by several groups [1–3] and attributed to the transitions from hole states bound in GeSi QDs to continuum states of Si matrix. There are only few works announcing the long-wavelength (8–12 μm) operation of detectors based on Ge/Si quantum dots [4,5]. Since the long-wavelength photoresponse in this system is originated from the bound-to-bound intraband transitions, it is unlikely to expect superior performance of such devices and one is obliged to seek another approach. In this paper we demonstrate that technologically important range between 8 and 12 μm can be reached by the use of self-assembled Ge QDs grown on strained Si$_{1-x}$Ge$_x$ layers. The concept of the device is similar to the dots-in-a-well detectors proposed for III–V nanostructures. The advantage of this structure is the ability to control the effective valence band offset at the Ge/Si$_{1-x}$Ge$_x$ interface and hence the operating wavelength by varying the composition x and thickness of only the underlying Si$_{1-x}$Ge$_x$ quantum well.

1. Device structure

Samples were grown by solid-source molecular-beam epitaxy on a Si substrate with a resistivity of 150 Ω cm. Before Ge QDs growth, a 15-nm-thick strained Si$_{0.65}$Ge$_{0.35}$ layer was deposited at a rate of 0.008 nm/s at 500 °C. Ge QDs form by self-assembling in the Stranski–Krastanov growth mode at 500 °C

by deposition of 0.4 nm Ge over the Si$_{0.65}$Ge$_{0.35}$ buffer layer. The active region of the devices is a five-layer stack, where each period consists of a Si$_{0.65}$Ge$_{0.35}$ buffer layer, Ge QD layer and a 100 nm Si barrier. The doping of the dots was achieved with a boron δ-doping layer inserted 10 nm below each Si$_{0.65}$Ge$_{0.35}$ quantum well, providing after spatial transfer approximately 6 holes per dot. For vertical photocurrent (PC) measurements, the active region is enclosed between two heavily boron-doped contact layers ($p = 5 \times 10^{18}$ cm^{-3}), where the bottom and top contact are 500 and 300 nm thick, respectively. For the lateral detector structure, no highly doped contact layers are needed. From scanning tunneling microscopy, we observe the Ge nanoclusters to have a shape of "hut" clusters bounded by {105} facets with a typical base length of 12 nm and an areal density of $\sim 1.5 \times 10^{11}$ cm^{-2}. Waveguide structures were prepared with a polished backside and polished 45° facets to enhance the absorption and to study the polarization dependence of the induced PC. The measurement system for spectral response consisted of a Vertex 70 FTIR specrometer operating in a step-scan mode.

2. Experimental results

Figure 1 shows the vertical PC measured at 95 K for *p*-polarized, *s*-polarized and unpolarized midinfrared excitation. The
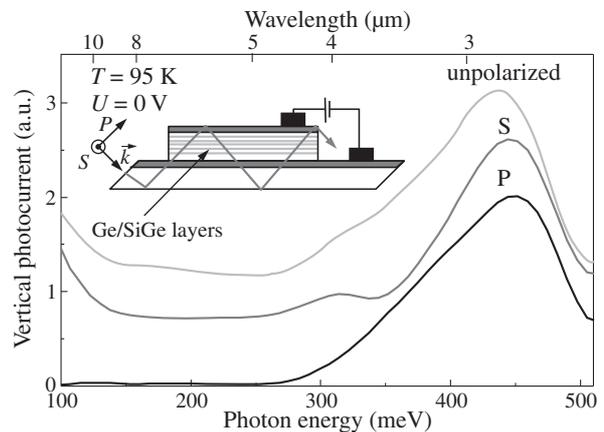

Fig. 1. Vertical photocurrent measured at $T = 95$ K for a *p*-polarized, *s*-polarized and unpolarized infrared excitation. The applied bias is 0 V. The curves are vertically shifted for clarity. The wedge coupling geometry is shown.

spectra are normalized to the corresponding polarized spectral intensity of the incoming light. The vertical photocurrent can be clearly detected without bias voltage. This is caused by asymmetry in the device introduced by the δ-doping planes and the existence of a built-in electric field. By increase of the bias voltage the PC signal becomes noise due to the strong increase of the dark current. An intense maximum with the PC onset at ≈ 280 meV (≈ 4.4 μm) is visible. It is nearly independent of the polarization excitation and attributed further to transitions from the states confined in Ge dots to continuum states at the Si valence band edge. No signal is detected in the long-wavelength range, except for the free carrier absorption in the s-polarization ($\lambda > 8$ μm) which stems from carriers in heavily doped Si contact layers.

In Fig. 2, the PC spectra of the lateral device measured at $T = 200$ K and $U = 5$ V are shown. The position of the main PC maximum is approximately the same as that of the vertical structure. In addition to the main peak, the lateral device exhibits a long wavelength PC response between 4 and 12 μm which is seen to be mainly polarized along the growth direction and is not observed in the vertical geometry. The long wavelength PC signal is clearly detected also in a normal incidence geometry and for s-polarization at temperatures as high as 200 K and disappears at $T > 220$ K.

In order to elucidate the nature of photoresponse, we performed 3D analysis of the band diagram of the heterostructure under study. Here we used a six-band $\mathbf{k} \times \mathbf{p}$ approximation (three valence bands and spin), based on the method of Bir and Pikus [6], which includes spin-orbit and strain effects. Recently this approach was successfully applied to simulate the electronic structure of strained Ge QDs on pure Si(001) surface [7]. The finite element calculations of three-dimensional spatial distribution of strain components were performed using the package COMSOL Multiphysics. The strain tensor elements are subsequently used as input to a strain-dependent Hamiltonian. We consider a pyramidal Ge nanocluster with four {105}-oriented facets and a (001) base embedded into the Si matrix. The pyramid lies on a 2 ML Ge wetting layer which, in turn, lies on a 15-nm $Si_{0.65}Ge_{0.35}$ buffer layer. The pyramid base length l is 12 nm, the pyramid heigh is 1.2 nm. The chosen geometrical parameters of the structure are inspired from the experimental observations.

From the calculations we find that there are only four confined hole states in Ge dot. The absence in wavefunction density of nodal surfaces perpendicular to the growth direction is clear evidence that the difference between all the found states is determined only by quantization in the plane of dot base. The ground and first excited states in QD are located about 354 and 273 meV from the Si barrier edge, respectively. The latter value is close to the PC onset in the vertical device and to the PC shoulder observed in the lateral structure (see Figs. 1 and 2). Thus, the photoresponse at $\lambda < 4$ μm can be associated with transitions from the bound states within the Ge dots to continuum states at the Si valence band edge. The calculated energy difference between the highest heave-hole subband in $Si_{0.65}Ge_{0.35}$ quantum well and the ground hole state in Ge QD, 140 meV, agrees well the long-wavelength PC onset in lateral device. Therefore, we may conclude that the long-wavelength in-plane photocurrent is caused by excitation of holes from QD to two-dimensional states of $Si_{0.65}Ge_{0.35}$ layer. Since this states are unbound in lateral direction, they can carry a current
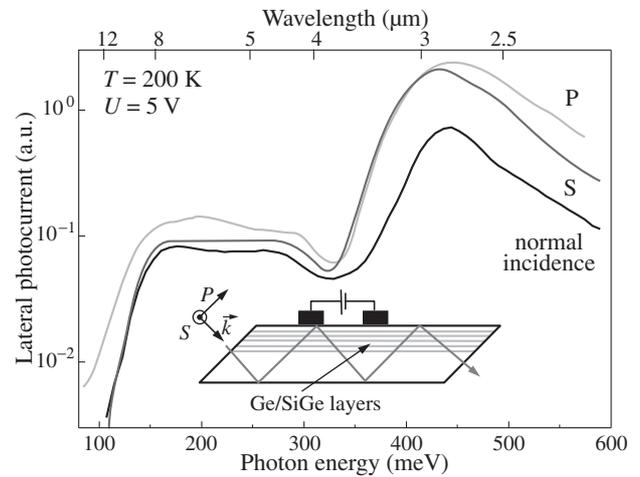

Fig. 2. Lateral photocurrent spectra measured at $T = 200$ K in multipass waveguide geometry (see inset) for two polarizations of incident light. The normal incidence photoresponse is also shown. The applied bias is 5 V.

if an external electric field is applied.

In summary, we report midinfrared photodetectors based on Ge self-assembled quantum dots grown on $Si_{0.65}Ge_{0.35}$ strained layer. The device photoresponse covers the spectral range from 2 to 12 μm. The demonstration of the normal incidence detection at $T = 200$ K shows the promise of the application of Ge/$Si_{0.65}Ge_{0.35}$/Si heterostructures with Ge QD for future high-temperature optoelectronics application. Further work is in progress to improve long-wavelength device operation.

References

[1] A.I. Yakimov *et al*, *Appl. Phys. Lett.* **75**, 1413 (1999).
[2] C. Miesner *et al*, *Appl. Phys. Lett.* **76**, 1027 (2000).
[3] T. Fromherz *et al*, *Appl. Phys. Lett.* **80**, 2093 (2002).
[4] N. Rappaport *et al*, *Appl. Phys. Lett.* **77**, 3224 (2000).
[5] A. I. Yakimov *et al*, *J. Appl. Phys.* **89**, 5676 (2001).
[6] G.L. Bir, G.E. Pikus, *Symmetry and Strain-Induced Effects in Semiconductors*, (New York: Wiley) 584, 1974.
[7] A.I. Yakimov *et al*, Phys. Rev. B **81** 115434 (2010).

Formation of Ge nanoislands on pit-patterned Si substrates studied by molecular dynamics simulations

P. L. Novikov[1,2], Zh. V. Smagina[1] and A. V. Dvurechenskii[1,2]

[1] A.V. Rzhanov Institute of Semiconductor Physics, SB RAS, Lavrentjeva 13, 630090 Novosibirsk, Russia
[2] Novosibirsk State University, Novosibirsk, Russia

Abstract. Study of Ge nanoislands formation on pit-patterned Si(001) substrate by molecular dynamics simulations is carried out. Energy surface of Ge/Si(001) structures with pits was mapped out. By the analysis of the energy surface the mechanism of adatoms diffusion on the pit-patterned surfaces was revealed. Energy of Si/Ge heterosystem with various morphologies, sizes and orientations of Ge nanoislands inside the pits was calculated. The size of the critical nucleus is estimated to be ∼20 nm.

Introduction

The challenge for investigators working in the field of material science is the formation of space arranged arrays of semiconductor quantum dots (QDs). These quasi zero-dimensio-nal systems exhibit abundant physical properties and offer great potential for device applications, such as light-emitting devices, QD-based lasers, spintronics, or even quantum computation. An effective way to solve the problem of the inhomogeneous size distribution and random location of QDs is utilization of lithographic techniques to prepare substrates with pre-patterned pits in well-defined positions [1–3]. The pits act as the nucleation sites for subsequently grown dots. However, even though extensive studies on growth of Ge dots on pit-patterned Si substrates have been carried out, still there exists a lack of knowledge about Ge QD formation mechanism and fundamental limits of the pit size favorable for space arrangement [3]. In our previous work [4] some peculiarities of diffusion mechanism on a pit-patterned surface were revealed using molecular dynamics (MD) simulations. For pits, assuming a shape of inverted square-base pyramids, it was established that an energy barrier appears at the pit edges, blocking the Ge fast migration through diffusion channels on Si(001)-(2 × 1) surface. In the present paper we study the effect of pit shape and Ge coverage on the surface diffusion. In addition, we analyze various morphologies of Ge inside pits to determine which one is energetically favorable.

1. Model

1.1. Energy surface calculation

MD simulation was used to study the properties of pit-patterned surface. The system under consideration included Si and Ge atoms, forming the pit-patterned structure, with interaction described by the empirical Tersoff potential [5]. By the numerical solution of Newton equation an equilibrium state of the system can be found. In particular, the equilibrium energy of a Ge adatom sticken to the surface at a certain point can be determined. Using such a probe Ge adatom, the energy surface is obtained through the scanning over the surface of the simulated structure. The procedure of energy surface calculation is similar to that described in [6]. Prior to energy calculations the simulated structures were allowed to relax.

The basic simulated structure was composed by 15×15 nm mesh of 20 ML-thick Si(001) with top Ge(001)-(2 × 1). The thickness of the Ge layer was varied from 1 to 4 monolayers (ML). The structure contained a pit, which had a shape of inverted square-base pyramid with (115)-oriented side walls. The pit was 4 nm wide. Periodical boundary conditions were imposed in the lateral directions.

1.2. Determination of thermodynamically stable morphology

Since the time-scale covered by MD simulations (∼100 ps) is much shorter as compared to the characteristic time of Ge nanoislands growth, an alternative approach was used to study the formation of Ge 3D-islands. First, a structure with an empty pit was made up, and its potential energy E_0 was calculated using Tersoff potential. Then a structure with a certain morphology of Ge inclusion inside the pit was considered, and its potential energy E_{Ge} was calculated in the similar way. Finally the energy density W was calculated by the following formula:

$$W = \frac{E_{Ge} - E_0}{N_{Ge}}, \qquad (1)$$

where N_{Ge} is the number of atoms in the Ge inclusion. W characterizes the energy added to the system due to filling the pit with Ge for the certain morphology of the Ge inclusion. As the energy is calculated per an atom, W does not change significantly at a small variation of Ge inclusion volume. Thus, if a set of different Ge morphologies of approximately the same volume is considered, by comparison of W calculated for each one it can be estimated which morphology is thermodynamically favorable.

The lateral size of the mesh involved in energy calculations was expanded up to 40 nm, which is comparable with the pit size in experiments.

Table 1. Energy density of Ge inclusions inside pit obtained by MD calculations for different Ge volumes and morphologies.

| Volume (nm³)	Energy density (eV/atom)	
	3D	2D
70	−3.68	−3.70
180	−3.75	−3.75
260	−3.82	−3.80
530	−3.78	−3.77
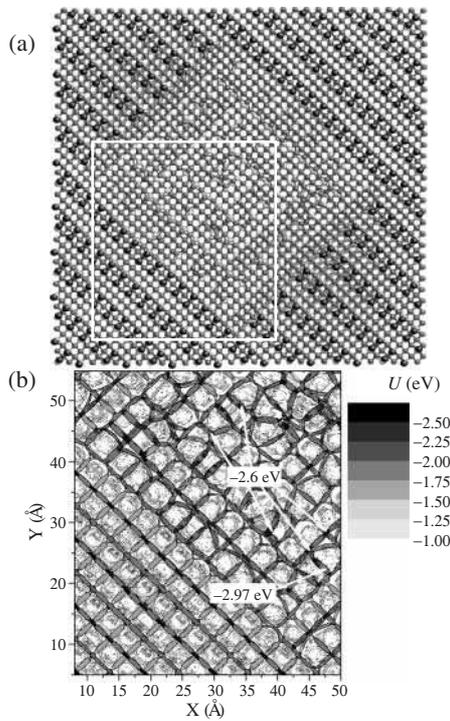
Fig. 1. (a) Simulated structure of 3ML-thick Ge(001)-(2 × 1) film on a pit-patterned Si(001) substrate (plan view). The red and blue balls represent the Ge and Si atoms, respectively. Ge atoms in dimer rows are painted in dark red. The pit has a shape of inverted square-base pyramid with (115)-oriented sidewalls. The energy surface was calculated within the region marked by the white rectangle. (b) Energy surface map of pit-patterned Si/Ge(001)-(2 × 1) structure. Color scale is used for indication of energy magnitudes. The energy values in the relevant points are shown with labels.

2. Results and discussion

Fig. 1 presents the simulated Si/Ge(001)-(2 × 1) surface with a pit (Fig. 1a) and the corresponding energy surface map (Fig. 1b). The quasi single-colored parallel paths on the map, outside the pit, present the diffusion channels. Being formed between the dimer rows at the planar surface, the diffusion channels are broken at the pit edge by the energy barrier of 0.9 eV. Ge atoms, which have reached the end of the diffusion channel, migrate with a lower rate by the sidewalls, where there are many traps for them (minima of −2.6 eV on the Fig. 1a). The similar picture was observed for the different Ge film thickness and the bigger inclination of the pit sidewalls. At all stages of Ge deposition the pits turn out to be the most favorable site for Ge adatoms accumulation. At further growth this may promote the nucleation of 3D Ge islands.

Structures included in energy calculation are shown in Fig. 2. Ge inclusion which would be formed in layer-by-layer (2D) growth mode is shown in Fig. 2c, the Ge 3D-nanoisland of hut-cluster shape — in Fig. 2b. Energy density values obtained by MD calculations are presented in Table 1. For Ge inclusion volume larger than 180 nm^3 (lateral size ∼18 nm) the energy density of 2D Ge inclusion exceeds that of hut-cluster. The size of ∼20 nm corresponds to the critical nucleus. This estimate gives the lower theoretical limit for the pit size favorable for space-arranged array formation. In the case of $Ge_{0.5}Si_{0.5}$ solution the critical size is increased up to 60 nm. It should be stressed that the difference in W values for 2D and
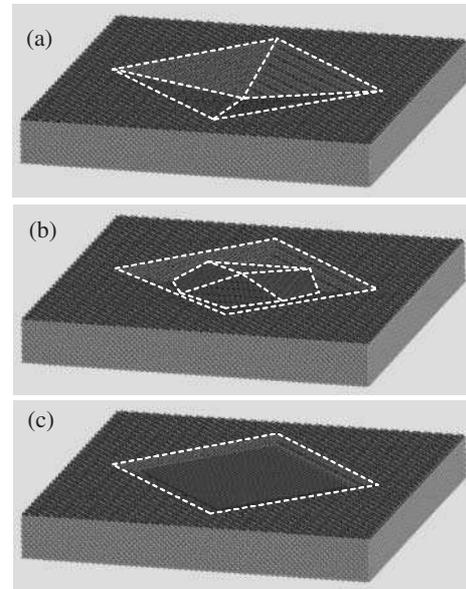

Fig. 2. Simulated Si/Ge structures involved in energy calculations (side view). (a) The reference structure with an empty pit. (b) Hut-cluster in the pit. (c) Ge inclusion with flat surface inside the pit.

3D morphologies, respectively, is much higher than the error of calculations. This difference is correlated for all Ge atoms, and when being multiplied by the number of Ge atoms N_{Ge}, it becomes much higher as compared with kT.

References

[1] G. Bauer and P. Schäffler, *Phys. Stat. Sol.* **203**, 3496 (2006).
[2] C. Dais, H.H. Solak, Ya. Ekinci, E. Muller, H. Sigg and D. Grützmacher, *Surf. Sci.* **601**, 2787 (2007).
[3] A. Pascale, I. Berbezier, A. Ronda and P.C. Kelires, *Phys. Rev. B* **77**, 075311 (2008).
[4] P. Novikov, J. Smagina, D. Vlasov, A. Deryabin, A. Kozhukhov and A. Dvurechenskii, *J. Cryst. Growth.*, (2011) (in press).
[5] J. Tersoff, *Phys. Rev. B* **37**, 6991 (1988).
[6] C. Roland and G.H. Gilmer, *Phys. Rev. B* **46**, 13428 (1992).

The electronic structure of SiGe quantum rings

P. Kuchinskaya[1], V. A. Zinovyev[1], A. V. Nenashev[1], V. A. Armbrister,[1] and A. V. Dvurechenskii[1,2]

[1] Institute of Semiconductor Physics, SB RAS, Lavrentieva av., 13, Novosibirsk 630090, Russia
[2] Novosibirsk State University, Pirogov str. 2, 630090 Novosibirsk, Russia

Abstract. SiGe quantum rings on Si(100) were growth by molecular beam epitaxy. Nanometer-sized rings formed during partial Si capping of self-assembled SiGe/Si(001) islands at the substrate temperature 680 °C. The morphology of these structures was investigated by atomic force microscopy. Two types of nanorings with very different diameters and vertical sizes were found. The electronic spectrum of the quantum rings was calculated by 6-band $\mathbf{k} \times \mathbf{p}$ method. The results of these calculations demonstrated, that SiGe nanorings are perspective objects for device application for THz range detection.

Introduction

Many researchers pay special attention to quantum rings (QRs), which have unique magnetic, transport and optical properties [1,2]. It was demonstrated that self-assembled nanometer-sized rings created during molecular beam epitaxy (MBE) of binary semiconductors (A_3B_5) can be used to terahertz (THz) radiation detection [3]. Recently, similar Ge/Si heterostructures with nanorings were obtained by the several experimental groups [4,5]. However, a systematic study of the electronic properties of the SiGe QRs is still lacking. This work is devoted to study of the formation of SiGe nanorings and the energy spectrum calculations of charge carriers localized in SiGe QRs.

1. Experimental findings

The samples were grown by MBE (Riber SiVA-21). After standard cleaning and in-situ oxide desorption, a 50 nm-thick Si buffer layer was deposited on Si (100) substrate. The array of self-assembled SiGe quantum dots (QDs) was formed by the following deposition of 8 monolayers of Ge with a growth rate of 0.007 nm/s at the substrate temperature of 680 °C. Then, SiGe QRs were created by capping the SiGe QDs with a 4nm-thick Si layer with a growth rate of 0.068 nm/s at the same temperature. The surface morphology of the grown samples is characterized by atomic force microscope (AFM). All measurements were performed in contact mode with microscope (SMM 2000K) equipped by sharp Veeco tips with 10 nm radius. AFM revealed two families of SiGe nanorings formed during MBE (Fig. 1): the first family with average ring diameter of about 400 nm, width of 95 nm, and height of 11 nm, the second one with the diameter of about 300 nm, width of 90 nm, and height of 6 nm. The in-plane density of the rings is $\sim 2 \times 10^8$ cm^{-2}.

2. Energy spectrum calculations

According to AFM data, the diameters of the grown SiGe rings (D) are always much bigger than their heights and widths, therefore the quantization of energy due to the finite length of the ring (πD) can be neglected. In this approximation the nanoring can be considered as an infinitely long quantum wire. The energy spectrum of localized hole states calculated for the quantum wire by 6-band $\mathbf{k} \times \mathbf{p}$ method. Two-dimensional problem was solved for different nanowire shapes (rectangle, triangle and trapezoid) with height 6 nm and width 90 nm. The Ge content of nanorings used in the calculations was 30%, which
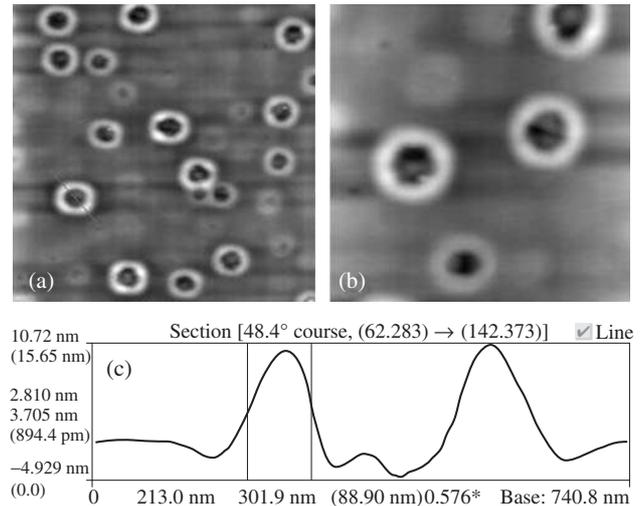

Fig. 1. (a) AFM image of the surface area (3×3 μm) with SiGe nanorings formed on the Si(100) at 680 °C, (b) the surface area (1.5×1.5 μm), (c) cross-sectional profile of the SiGe nanoring.

corresponds to average experimental value determined by x-ray scattering method for SiGe nanorings formed at 680 °C [6]. The energy levels of hole states in SiGe quantum ring were counted from the top of the Si valence band. The calculation showed that the energies of localized charge carriers are strongly dependent on the shape of nanoring cross-section. It was found, that the energy gap between ground and first excited state is about 1 meV for rectangle, 10 meV for triangle and 8 meV for trapezoid cross section shapes (see, Table 1).

Figure 2 shows calculated distributions of charge density for ground state and two excited states with corresponding energy levels in the case when a cross-section of the ring has shape of an isosceles trapezoid with the ratio between top and bottom bases 0.1. Notice, that this simulation geometry is very similar to the experimental AFM scan section profile of nanorings (Fig. 1). Energy gap between ground and exited state is

Table 1. The energy spectrum obtained for different nanowire shapes.

|	Rectangle	Triangle	Trapezoid
Ground state (meV)	198.6	192.5	195.4
First excited state (meV)	197.7	182.5	187.5
Second excited state (meV)	196.2	174.5	179.4
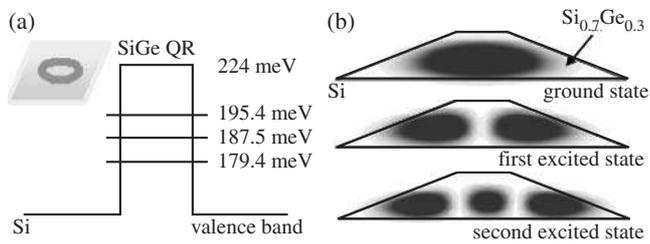
Fig. 2. Calculated energy levels for ground hole state and two excited hole states (a) and charge density distributions of corresponding energy levels (b) in the case when the cross-section of SiGe ring has shape of an isosceles trapezoid.

about 8 meV, which corresponds to the frequency 2.5 THz. Calculated energies for transitions between ground state and exited states allow us suggest, that obtained SiGe nanorings are perspective for developing of THz range detectors.

3. In summary

SiGe nanoring formation has been observed after partially capping SiGe islands on Si(001). This transformation is dependent on the cap layer thickness and substrate temperature at which the capping layer is deposited. The energy spectrum of localized states was calculated. The results of these calculations demonstrated that SiGe nanorings are perspective objects for device application for THz range detection.

References

[1] A. Lorke *et al*, *Phys. Rev. Lett.* **84**(10), 2223 (2000).
[2] T. Kuroda *et al*, *Phys. Rev. B* **72**, 205301 (2005).
[3] G. Huang *et al*, *Phys. Rev. Lett.* **94**, 101115 (2009).
[4] C.H. Lee *et al*, *Appl. Phys. Lett.* **94**, 141909 (2009).
[5] F.H. Li *et al*, *Nanotechnology* **18**, 115708 (2007).
[6] M. Stoffel *et al*, *Appl. Phys. Lett.* **94**, 253114 (2009).

First principle simulations of the vacancy mediated surface diffusion of Si-defect on the Me induced Si(111)$\sqrt{3} \times \sqrt{3}$ surface, Me = Al, Ga, In, Pb

Yu. V. Luniakov

Surface Physics Department, Institute for Automation and Control Processes, 690041 Vladivostok, Russia

Abstract. Using Nudged Elastic Band optimization the minimal energy paths for Si adatom moving on the ideal and vacancy defected metal induced Si(111)$\sqrt{3} \times \sqrt{3}$ surface have been obtained. The results of DFT calculations demonstrate that it is much more preferable for Si defect to move through vacancy than to exchange with Me adatom. The energy barriers for the direct Si and Me adatoms exchanges are considerably higher than that for Si-defect moving to the vacant T_4 position.

Introduction

One of the most interesting physical processes on the surfaces is the diffusion of the vacancies and adatoms that is responsible on the mobility of surfaces: motion of steps, islands or adsorbates. The most challenging effects are concerned with the mobility of the single surface defect because it is quite difficult to be traced experimentally or simulated theoretically. One of the distinctive example is high temperature STM observation of exchanges between group-III and Si atoms on Si(111)$\sqrt{3} \times \sqrt{3}$ surface [1–3]. The activation energies of the exchange are withing the range 1.2–1.7 eV and the prefactors are withing the range 10^{10}–10^{13} s^{-1}. The prefactor is largely dependent on the mechanism of the surface diffusion. As was shown by Kaxiras and Erlebacher [4], if adatoms are subjected to the collective concerted motion, the prefactors are march more smaller, i.e. $\approx 10^{-5}$ s^{-1} for Pb diffusion on Ge(111)-c(2 × 8) surface. The much larger prefactors for Si-Me adatom exchange on Si(111)$\sqrt{3} \times \sqrt{3}$ surface indicate that the mechanism is different from the concerted motion of adatoms. Another possible mechanism proposed by Hibino and Ogino [1] is that when metal adatom moved to T_4 site occupied by a Si adatom, the Si adatom looks like a vacancy and automatically moves to the T_4 site formerly occupied by the metal adatom. Even more simple mechanism is the vacancy mediated surface diffusion [5], when the diffusive motion of the adatoms can be explained by the presence of a low density of extremely mobile vacancies in the first layer of the surface. This mechanism is confirmed to be responsible to the of In

adatoms on Cu(100) surface [5]. Hannon has proposed that surface vacancies are responsible for mass transport between adatom islands on Cu(001) [6]. So the question about the most possible mechanism of adatom movement on the Me modified Si(111)$\sqrt{3} \times \sqrt{3}$ surface is still open for discussion. In order to testify whether the vacancy mediated surface diffusion is more favorable than direct Si — Me adatoms exchange we performed first prinsiple simulations of this processes for Pb, In, Ga and Al atoms for which the experimental results are available [1].

1. Methods of calculations

For the first principle simulations we employed the local density approximation (LDA) after Ceperley–Alder [7] in the Perdew–Zunger parametrization [8] for the exchange and correlation functional with projector-augmented wave pseudopotentials (PAW) [9], implemented in VASP ab-initio program [10–13]. The surface has been simulated by a periodic slab geometry with Si(111)$N\sqrt{3} \times N\sqrt{3}$ Me induced unit cells ($N = 2-6$), containing six silicon atomic layers and one Me adsorbate layer (Fig. 1). The dangling bonds of the bottom slab layer have been saturated by hydrogen atoms. The hydrogen atoms and bottom layer silicon atoms have been fixed and the rest atoms have been set free to move. A vacuum region of more than 10 Å has been incorporated within each periodic unit cell to prevent interaction between adjacent surfaces. Wave functions were represented using a plane-wave basis set with a kinetic energy cutoff of 250 eV. The Brillouin zone integration was performed with a Γ-point for large $4\sqrt{3}$ and $6\sqrt{3}$ supercells.

2. Results and discussions

It was conclusively determined that atomic structure of the Me induced Si(111)$\sqrt{3} \times \sqrt{3}$ is essentially the same for Al, Ga, In, and Pb adatoms: with coverage of 1/3 monolayer rest in the threefold symmetric T_4 sites above second-layer Si atoms. To check out the dependency of the vacancy formation energy
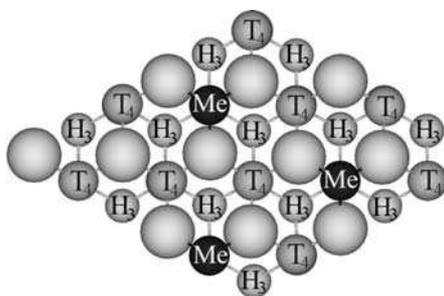

Fig. 1. Structural model of the Me induced Si(111)$2\sqrt{3} \times 2\sqrt{3}$-surface with vacancy defect. Me atoms are shown by the large black circles, the topmost Si atoms of the 1st layer are shown by the largest gray circles, the 2nd layer Si atoms are shown by the smaller gray circles, the 4th layer Si atoms are shown by the smallest gray circles.

Table 1. The dependency of the relative energies (in eV) of the surface with In adatom displaced from T_4 to T_4' or H_3 sites on the supercell size.

Energy (eV)	$2\sqrt{3} \times 2\sqrt{3}$		$4\sqrt{3} \times 4\sqrt{3}$		$6\sqrt{3} \times 6\sqrt{3}$	
Adsorption site	T_4'	H_3	T_4'	H_3	T_4'	H_3
Cell size	0.35	−0.05	0.59	0.11	0.66	0.11

(a)   (b)
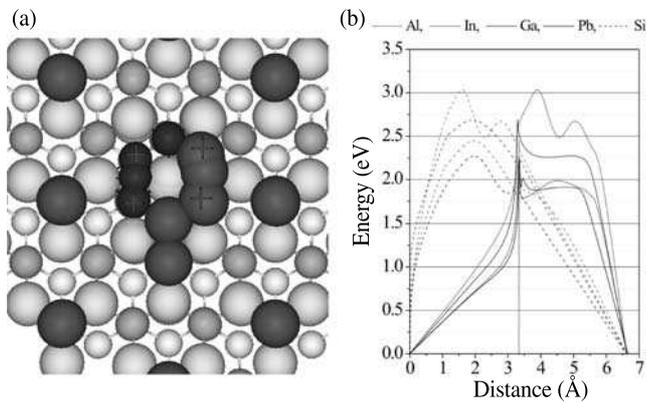
Fig. 2. (a) The possible Me and Si adatoms exchange path nearly on top Si atom and (b) the corresponding energy profiles for Me and Si adatoms, moving to meet each other. The solid line corresponds to the distance passed by Me, the dashed line corresponds to the distance passed by Si. The distances passed by Si or Me adatom have been projected to the line, connecting the neighboring T_4 sites beside Si and Me adatoms exchange.

on the size of a supercell we perform a series of calculation of Si(111)$N\sqrt{3} \times N\sqrt{3}$-In supercells containing one In vacancy (see Fig. 1). One of In atoms bordering to the vacancy was displaced from it's equilibrium position to the neighboring free T_4 site (hereinafter referred to as T_4') or to H_3 site. The resulting energies are summarized at table 1. We can see that when the superlattice is so small as $2\sqrt{3}$, the density of vacancies are too high, that gives the much smaller formation energies for In adatom moving to T_4' and H_3 sites. The energies for $4\sqrt{3}$ and $6\sqrt{3}$ supercells are in the right relative order and are different in less then 0.1 eV. So $4\sqrt{3}$ supercell Should be large enough for our simulations and all the following results have been attained using this supercell.

To simulate a movement of Si-defect on the ideal Si(111)$\sqrt{3} \times \sqrt{3}$-Me surface with Me = Al, Ga, In, Pb we have artificially chosen Si adatom path around on fop Si atom. On this path Si and Me adatoms are going to move towards each other passing around on top Si atom clockwise or counterclockwise (see Fig. 2(a)). The whole path has been divided onto a series of metastable configurations, every one have been fully optimized separately. To locate the barrier height we have carried out NEB optimization [14, 15] on a number of intermediate points nearby the closest metastable maximums where Si-defect and Me adatom are most close to each other around on top Si atom. Black crosses on Fig. 2(a) mark them. The full energy profiles for Si and Me adatoms are shown on Fig. 2(b), the energy barriers for Si-Me exchanges on the ideal Si(111)$\sqrt{3} \times \sqrt{3}$-Me sur-

(a)   (b)

Fig. 3. (a) The minimum energy path of Si defect migration obtained by NEB optimization and (b) the corresponding energy profiles. The designations are essentially the same as on Fig. 2.

face are summarized on table 2. We can see that the activation energies for Si-defect diffusion on the ideal Si(111)$\sqrt{3} \times \sqrt{3}$-Me surface is too much above the experimental results.

To investigate the influence of vacancy on the activation energy we perform NEB optimization of Si-adatom migration from the initial T_4 position to the neighboring site with the missing Me adatom (see Fig. 3(a)). The full energy profiles for Si-defect are shown on Fig. 3(b), the energy barriers for Si-defect moving on the $\sqrt{3} \times \sqrt{3}$-Me surface with vacancy are summarized on table 2, last column. We can see that the activation energies for Si-defect migration on the $\sqrt{3} \times \sqrt{3}$-Me surface is much better agree the experimental results if the movement is carried though vacancy.

References

[1] K.H. Hibino and T. Ogino, *Phys. Rev. B* **54**, 5763 (1996).
[2] E. Ganz, S.K. Theiss, I.-S. Hwang, and J.A. Golovchenko, *Phys. Rev. Lett.* **68**, 1567 (1992).
[3] K.H. Hibino and T. Ogino, *Surf. Sci.* **328**, L547 (1995).
[4] E. Kaxiras and J. Erlebacher, *Phys. Rev. Lett.* **71**, 2082 (1993).
[5] R. van Gastel *et al*, *Phys. Rev. Lett.* **86**, 1562 (2001).
[6] J.B. Hannon *et al*, *Phys. Rev. Lett.* **79**, 2506 (1997).
[7] D.M. Ceperley and B.J. Alder, *Phys. Rev. Lett.* **45**, 566 (1980).
[8] J.P. Perdew and A. Zunger, *Phys. Rev. B* **23**, 5048 (1981).
[9] G. Kresse, and D. Joubert, *Phys. Rev. B* **59**, 1758 (1999).
[10] G. Kresse and J. Hafner, *Phys. Rev. B* **47**, 558 (1993).
[11] G. Kresse and J. Hafner, *Phys. Rev. B* **49**, 14251 (1994).
[12] G. Kresse and J. Furthmuller, *Phys. Rev. B* **54**, 11169 (1996).
[13] G. Kresse and J. Furthmuller, *Comput. Mater. Sci.* **6**, 15 (1996).
[14] G. Henkelman, B.P. Uberuaga, and H. Jonsson, *J. Chem. Phys.* **113**, 9901 (2000).
[15] G. Henkelman and H. Jonsson, *J. Chem. Phys.* **113**, 9978 (2000).

Table 2. The dependency of the barrier height (in eV) for Si–Me adatom exhange on the ideal surface and for Si adatom moving to the vacant T_4 site though the Me vacancy.

Metal	Experimental [1,3]	Barrier for the ideal surface	Barrier for the vacancy surface
Al	1.42 ±0.07	3.11	1.58
Ga	1.67 ±0.11	2.79	1.58
In	1.56 ±0.15	2.67	1.52
Pb	1.20 ±0.17	2.41	1.33

Charging properties of Si₃N₄ based structures with embedded Si or Ge nanocrystals: Experiments and simulation

Zs. J. Horváth[1,2], P. Basa[1,3], T. Jászi[1,3], K. Z. Molnár[2], A. E. Pap[1], G. Molnár[1], L. Dobos[1], L. Tóth[1],
B. Pécz[1], *B. Pődör*[1,2] and P. Turmezei[2]

[1] Hungarian Academy of Sciences, Research Institute for Technical Physics and Materials Science,
Budapest, Hungary
[2] Óbuda University, Kandó Kálmán Faculty of Electrical Engineering, Institute of Microelectronics and Technology,
Budapest, Hungary
[3] Semilab Semiconductor Physics Laboratory Co. Ltd., Budapest, Hungary

Abstract. Non-volatile metal-silicon nitride-silicon dioxide-silicon (MNOS) memory structures with an embedded sheet of Si or Ge nanocrystals were prepared by low pressure chemical vapour deposition using chemical SiO₂ tunnel layers. It was obtained that Si or Ge nanocrystals improved the charging behaviour of the MNOS structures. To understand the physical origin of this phenomenon computer simulation was performed. The results of simulations are in agreement with the experimental results obtained on MNOS structures with Si or Ge nanocrystals.

Introduction

Information storage in non-volatile memories are based on changing the threshold voltage of field effect transistors (FETs) by appropriate voltage pulses. The actual mechanism is injection of charge by tunneling and its storage in a floating gate or in traps located in the insulator layer in MNOS or SONOS structures [1–4].

However, the reduction of the dimensions of floating gate memory FETs is limited mainly due to reliability problems connected with defects in the tunneling layer, because the reduction of lateral dimensions calls forth the reduction of oxide thickness. So, if there is a defect or week point in the thin oxide layer, the whole charge can be lost via it. Application of isolated semiconductor nanocrystals embedded in the insulator, as charge-storage media, is a possible and successful solution of this problem [1–4].

The loss of information via defects in oxide layer can also be avoided by using MNOS or SONOS structures. In these structures the charge is stored in defects located in the nitride layer, which are separated *a'priori*. However, we considered that the formation of semiconductor nanocrystals can improve the charge injection and storage behaviour of these structures. So, Ge or Si nanocrystals were embedded at the oxide/nitride interface, and — as expected — improved memory behaviour were obtained for different MNOS structures [3,4].

In this paper the charging behaviour of some of the studied MNOS structures containing Si or Ge nanocrystals embedded at the SiO₂/Si₃N₄ interface are analyzed, comparing the experimental results with tunneling probabilities calculated for structures with and without nanocrystals using WKB approximation [5].

1. Experiment and simulation

MNOS structures with embedded Si or Ge nanocrystals have been grown on n-type Si substrates. The results of two different series of samples are studied. In one series the structures consist of a 2.5 nm thick SiO₂ tunnel, a Si nanocrystal and a 40 nm thick Si₃N₄ control layers. The samples of the other series consist of a 2.5 nm thick tunnel SiO₂, a Ge nanocrystal and a 75 nm thick Si₃N₄ control layers. The effect of the dura-
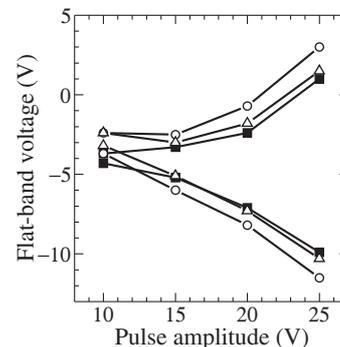
Fig. 1. Memory window of MNOS structures with embedded Ge nanocrystals prepared with nanocrystal deposition duration of 25 s (circles) and 50 s (triangles) as a function of charging pulse amplitude with pulse width of 100 ms. The results obtained on reference sample without nanocrystals are presented by squares.

tion of nanocrystal deposition has been investigated. Reference samples without nanocrystals were also prepared.

The SiO₂ layers with a thickness of 2.5 nm have been prepared by a chemical treatment using HNO₃ [3,4]. The Si nanocrystal layer and the Si₃N₄ control layer were deposited by LPCVD at 830 °C at a pressure of 30 Pa using SiH₂Cl₂ and NH₃ [3,4]. The Ge nanocrystals were grown by electron beam evaporation. During evaporation the substrate temperature was kept at 350 °C [3,4].

For deeper understanding the enhanced charging behaviour the tunneling probability of electrons to the conduction band of the nitride layer has been calculated using the WKB approximation [5].

2. Results and discussion

The enhanced charging properties of structures with embedded Ge nanocrystals can be seen in Fig. 1, which presents the memory window for samples with Ge deposition duration of 25 and 50 s as well as for the reference sample. The upper branches of the memory window were obtained for positive, while the lower branches for negative charging pulses. The samples with nanocrystals exhibited wider memory window, than the reference sample indicating enhanced charge injection
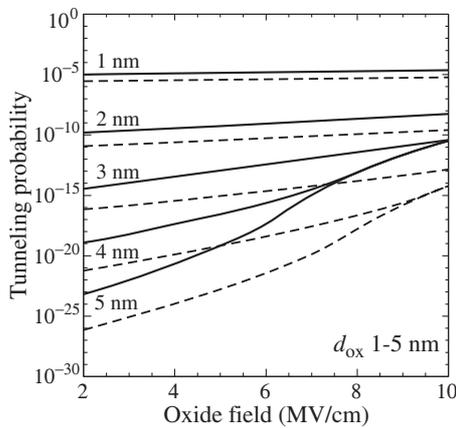
Fig. 2. Tunneling probability of electrons (solid lines) and holes (dashed lines) to the nanocrystals located at the SiO_2/Si_3N_4 interface, as a function of the electric field in the oxide layer and of the oxide thickness.

behaviour. Similar picture was obtained for the samples with Si nanocrystals: samples with nanocrystals exhibited wider memory window than the reference sample [3].

The calculated probability of electron or hole tunneling to the conduction or valence bands of the nitride layer, respectively, in MNOS structures without nanocrystals as a function of the oxide thickness and the electric field in the oxide layer exhibit maximum as a function of oxide thickness. The tunneling probability is higher and its maximum is closer to the SiO_2/Si_3N_4 interface for higher electric fields.

Fig. 2 presents the tunneling probability of electrons and holes to the nanocrystals located at the SiO_2/Si_3N_4 interface, as a function of the electric field in the oxide layer and the oxide thickness. As a matter of fact, this is the tunneling probability via the oxide layer by direct or Fowler–Nordheim tunneling [6]. For practical electric field values, the Fowler–Nordheim tunneling occurs at oxide thicknesses above 3 nm and at high electric fields only. The obtained probabilities are much higher than those obtained for tunneling to the nitride conductance or valence band in structures without nanocrystals, but at low electric fields only. For direct tunneling of electrons or holes via the oxide layer at medium electric fields to the nitride conduction or valence band, respectively, and for Fowler–Nordheim tunneling at high electric fields, the tunneling probabilities are the same to the nanocrystals, as to the nitride conduction band.

3. Conclusions

Charging behaviour of MNOS structures containing Si or Ge nanocrystals embedded at the SiO_2/Si_3N_4 interface have been studied by experiments and by calculating tunneling probabilities of electrons and holes to the nanocrystals or to the conductance/valence band of the nitride layer for structures with and without nanocrystals.

The presence of semiconductor nanocrystals at the SiO_2/Si_3N_4 interface enhances strongly the tunneling probability of electrons and holes for structures with thin oxide layers (3 nm or below) or at low electric fields, but they do not influence the charging behaviour of structures with thick oxide layers at high electric fields.

The results of calculations are in agreement with the experimental results obtained on MNOS structures with Si or

Ge nanocrystals embedded at the SiO_2/Si_3N_4 interface. The tunneling probability of both the electrons and holes increased due to the presence of nanocrystals yielding enhanced charging behaviour.

References

[1] Zs.J. Horváth, *Current Appl. Phys.* **6**, 145 (2006).

[2] B. Pődör, Zs.J. Horváth, P. Basa (Editors), *Semiconductor Nanocrystals. Proc. First Int. Workshop on Semiconductor Nanocrystals SEMINANO-2005*, Sept. 10–12, 2005, Budapest, Hungary; http://www.mfa.kfki.hu/conferences/seminano2005.

[3] Zs.J. Horváth, P. Basa, *Mater. Sci. Forum*, **609**, 1 (2009).

[4] Zs.J. Horváth, P. Basa, in: *Nanocrystals and Quantum Dots of Group IV Semiconductors*, (Eds. T.V. Torchinskaya, Yu.V. Vorobiev), American Scientific Publishers, Stevenson Ranch, California, USA, 225 (2010).

[5] K.I. Lundström, C.M. Svensson, *IEEE Trans. El. Dev.*, **ED-19**, 826 (1972).

[6] Zs.J. Horváth, G. Stubnya, P. Tütto, M. Németh-Sallay, J. Balázs, in: *Physics of Semiconductor Devices,* Allied Publisher Ltd., New Delhi, India, (Eds. V. Kumar and S.K. Agarwal), 383 (2000).

Phenomenon of dislocation nanoscale ordering during cyclic growth of three-dimensional SiGe islands on Si(100)

V. A. Zinovyev[1], A. Marzegalli[2], F. Boioli[2], R. Gatti[2], F. Montalenti[2], L. Miglio[2], M. Stoffel[3,4],
T. Merdzhanova[4], L. Wang[3], F. Pezzoli[3], A. Rastelli[3] and O. G. Schmidt[3]

[1] Institute of Semiconductor Physics, 630090 Novosibirsk, Russia
[2] Dipartimento di Scienza dei Materiali, Universita di Milano-Bicocca, via Cozzi 53, 20125 Milano, Italy
[3] Institute for Integrative Nanosciences, IFW Dresden, Helmholtzstrasse 20, 01069 Dresden, German
[4] Max-Planck-Institut für Festkörperforschung, Heisenbergstraße 1, 70569 Stuttgart-Germany

Abstract. An analytical model for investigating of the periodic dislocation nucleation during epitaxial growth of SiGe nanoislands on Si(001) substrates is proposed. This model, which includes suitable estimates of energy gain and cost produced by the dislocation nucleation events as well as mutual interactions between dislocations in the island, is able to predict correctly the spacing between tree rings, as measured either by atomic force microscope or by a He Ion microscope. Excepting the nucleation of the first few dislocations, which are strongly influenced by the island shape, the model predicts self-ordering of dislocations inside SiGe islands in a regularly spaced network.

Introduction

It has been discovered by in-situ transmission electron microscope (TEM) analysis during the epitaxial growth of three-dimensional (3D) SiGe island on Si (001) [1,2], that periodic dislocation nucleation occurs, and it is accompanied by sudden lateral expansions of the island and followed by a slow recovery of the original aspect ratio, during accumulation of the deposited material at the top. This phenomenon was named "cyclic growth". A more recent TEM study [3] reported an ordered pattern of 60° misfit lines. In the top view, they appear as concentric polygons at the basal plane of the island, suggesting a constant dislocation distance. Nevertheless it is still unknown whether plastic relaxation events are really periodic with increasing island base radius and what is the thermodynamic balance in volume that might lead to such periodicity. These issues will be clarified in this work, by comparing analytic calculations of critical island sizes for dislocation nucleation and accurate measurements of the footprints due to subsequent island lateral expansions, which were explained with the occurrence of subsequent plastic events in the island.

1. Experimental findings

Samples were grown by molecular beam epitaxy (MBE). After standard cleaning and in-situ oxide desorption, a 100 nm thick Si buffer was grown before the deposition of 15 ML Ge, at a substrate temperature of either 620 or 740 °C. With these growth parameters both coherent and plastically relaxed islands are observed on the surface [4,5]. The samples were then cooled to room temperature and chemically etched to remove selectively $Si_{1-x}Ge_x$ over Si. The surface morphology was then imaged by Atomic Force Microscopy (AFM) and by a Carl Zeiss Orion PlusTM helium-ion microscope (HeIM), revealing stepped-ring structures left below plastically relaxed islands (Fig. 1). Such observed structures are produced during the island cyclic growth [4].

From the microscopy images, we measured the distances between subsequent rings (ring width), starting from the central plateau and moving towards the periphery of the islands along two orthogonal directions. The two independent measurement techniques yield fully consistent results. It can be concluded that, within our growth conditions, the ring width
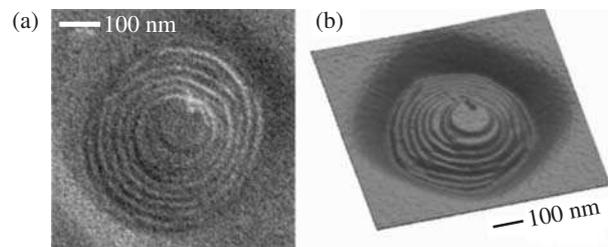
Fig. 1. (a) 3D view of an AFM image of a similar ring structure (the depth of the trench around the tree-ring is about 16 nm), (b) He-ion image of the Si surface obtained after removal of a dislocated SiGe island grown at 740 °C showing a characteristic ring structure.

shows a slight decrease from the island centre to the island borders, in the range from 10 to 20 nm for the sample grown at 620 °C and between 20 and 30 nm for the sample grown at 740 °C, converging to an almost constant value, 15 and 22 nm, respectively. The average Ge content in the islands determined using AFM [4] is $X = 0.36$ and $X = 0.48$ at 740 and 620 °C, respectively.

2. Analytical model

In order to interpret the experimental findings, we propose an analytical model of multiply dislocated islands, similar to the one commonly used in the calculation of the thermodynamic critical thicknesses of flat films, and recently adopted in the calculation of the critical dimension for the first dislocation nucleation in 3D SiGe islands on Si(001) [5]. This simple approach fully captures the essential features of the system, with no fitting of the involved parameters, just assuming closed circular loops of 60° type misfit segments, which are nucleated right at the perimeter of the growing island. It was assumed, that the dislocation nucleation occurs, when the energy lowering (E_{gain}) corresponding to the effective misfit reduction, provided by the dislocation becomes equal to the increase in energy (E_{cost}) due to the lattice distortion produced by the dislocation itself and due to interaction between the dislocation and other ones already present in the multi-dislocated island. By considering a 3D $Si_{1-x}Ge_x$ island with an aspect ratio ϱ, analytical expression for E_{gain} can formulated as $W(n) - W(n-1)$, where

$$W(n) = \frac{G}{1-\nu} F(\varrho, X) \left(\varepsilon_{xx}^2(n) + 2\nu \varepsilon_{xx}(n)\varepsilon_{yy}(n) + \varepsilon_{yy}^2(n) \right) V$$

is the elastic energy stored in an island when n dislocations are present. Here G is the shear modulus, ν is the Poisson ratio, V is the island volume, $\varepsilon_{xx}(n) = \varepsilon_{yy}(n) = \varepsilon_m - \frac{b_{\text{eff}}}{2} \sum_{i=1}^{n} \lambda_i/(\pi R^2)$ are the in-plane strain tensor components corresponding to the lattice misfit $\varepsilon_m = 0.0412\,X$, as reduced by the presence of n circular dislocations, $b_{\text{eff}} = b\cos(\pi/3)$ is the effective component of Burgers vector for a 60° misfit dislocation ($b = a_{\text{SiGe}}\sqrt{2}/2$), λ_i is the length of the dislocation, R is the island radius, $F(\rho, X)$ is the reduction factor of the elastic energy stored in the island and substrate (numerically evaluated by Finite Element Method). E_{cost} is evaluated by summing of two energy contribution related to the self-energy of the dislocation (E_{self}) and interaction energy between dislocations (E_{int}). E_{self} is analytically calculated as for the case of a flat film, by considering each segment of the circular loop is decomposed into two components, along the x and the y directions.

$$E_{\text{self}} = \lambda_i G \frac{\left(1 - \nu\cos^2\beta\right)b^2}{4\pi(1-\nu)} \ln\frac{\alpha R_{\text{cut-off}}}{b},$$

where β is the constant angle between dislocation line and Burgers vector b, α is the parameter taking into account the dislocation core energy (usually set to 2.7). $R_{\text{cut-off}}$ is the cut-off radius of the dislocation strain field, i.e. the average distance of the dislocation line from the free surface, taken as the height of a cylinder equal in volume and in base area to the island [5]. E_{int} is taken as the sum of the pair interaction energies between straight dislocation segments located near a free surface [6]:

$$E_{\text{int}} = \sum_{i=1}^{n} \frac{\lambda_n + \lambda_i}{2} E_{\text{I}}\left(d_{n,i}\right),$$

where

$$
\begin{aligned}
E_{\text{I}}(d) &= \frac{Gb^2/2}{4\pi(1-\nu)}\left[\ln\left(4a^2+1\right) - \frac{4a^2\left(12a^2+1\right)}{4a^2+1}\right] \\
&+ \frac{Gb^2/4}{4\pi(1-\nu)}\left[\ln\left(4a^2+1\right) + \frac{4a^2\left(4a^2+3\right)}{4a^2+1}\right] \\
&+ \frac{Gb^2/4}{4\pi(1-\nu)}\left[\ln\left(4a^2+1\right)\right].
\end{aligned}
$$

Here d_{ij} is the separation distance between dislocations, $a = d_{i,j}/R_{\text{cut-off}}$ is the dimensionless interaction radius. Since we assume that all dislocation loops nucleate exactly at the island edge, the ring width (and the dislocation spacing) as a function of the number of dislocations in the island is obtained directly by subtracting subsequent critical base radii for the dislocation nucleation.

3. Model vs Experiment

The model results in Fig. 2 show that the ring width initially decreases with the dislocation number, but after the nucleation of the very first dislocations the spacing between two subsequent loops becomes almost constant. It was found, that the interaction between dislocations contributes significantly to the spacing. We report the ring width between two plastic events vs the increasing number of rings for the same system, calculated with (solid line with boxes) and without (dashed line with circles) the interaction term. One can see that the solid
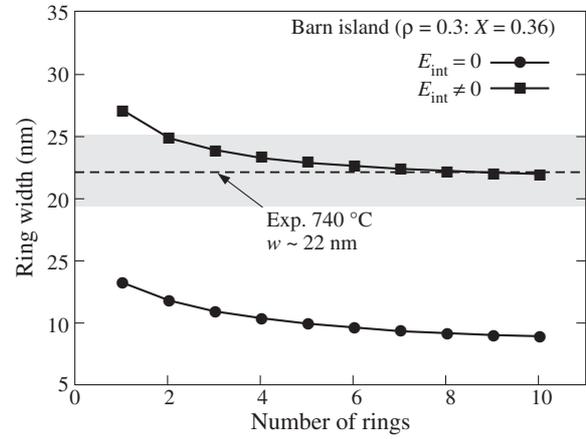
Fig. 2. Calculated distance between dislocations (ring width) versus the number of rings, with (full boxes, blue) and without (full circles, red) including the E_{int} term. Island aspect ratio to $\rho = 0.3$, in agreement with AFM measurements. Ge content $X = 0.36$, corresponding to the experimental data at T=740 °C.

curve correctly reproduces the experimental trend observed at 740 °C, as reported in Fig. 1, and converges to the ring width value of 22 nm, which is the experimental indication. The dashed curve obtained neglecting the repulsive term is shifted by a nearly constant value far below this experimental data, outside the relative error bar (the band in Fig. 2). Then the dislocation interaction in the thermodynamic balance is very important for an accurate prediction of the critical island radii and dislocation spacing. As one should expect, increasing the Ge content inside the elastic energy stored in the system is also increased and the dislocation spacing becomes smaller with the increasing misfit. In fact, by tuning the island Ge content X from 0.3 to 0.5, a downward shift of the ring width curve is obtained, in agreement with the experimental trend observed by decreasing the growth temperature. In particular, we observe that at any Ge concentration the ring width quickly converges to a nearly constant value, which is lower for higher island Ge content.

References

[1] M.C. Reuter, J. Tersoff, M. Hammar, R.M. Tromp, *Phys. Rev. Lett.* **73**, 300 (1994).
[2] F.M. Ross, J. Tersoff, M.C. Reuter, F.K. LeGoues, R.M. Tromp, *Microsc. Res. Tech.* **42**, 281 (1998).
[3] A. Portavoce, R. Hull, M.C. Reuter, F.M. Ross, *Phys. Rev. B* **76**, 235301 (2007).
[4] T. Merdzhanova, S. Kiravittaya, A. Rastelli, M. Stoffel, U. Denker, and O.G. Schmidt, *Phys. Rev. Lett.* **96**, 226103 (2006).
[5] R. Gatti, A. Marzegalli, V.A. Zinovyev, F. Montalenti, Leo Miglio, *Phys. Rev. B* **78**, 184104 (2008).
[6] A. Atkinson and S.C. Jain, *J. Phys.: Condens. Matter* **5**, 4595 (1993).

Transport in wide HgTe/HgCdTe quantum wells with Mexican hat spectrum

A. V. Germanenko[1], G. M. Minkov[1,2], O. E. Rut[1], A. A. Sherstobitov[1,2], S.A. Dvoretski[3] and N. N. Mikhailov[3]

[1] Ural State University, 620000 Ekaterinburg, Russia
[2] Institute of Metal Physics, Ural Branch of RAS, 620990 Ekaterinburg, Russia
[3] Institute of Semiconductor Physics, SB RAS, Lavrentieva av., 13, Novosibirsk 630090, Russia

Abstract. The transport phenomena in single quantum well structures based on the gapless semiconductor HgTe are investigated. The analysis of the Shubnikov–de Haas oscillations allows us to obtain the gate voltage dependence of the electron densities corresponding to different branches of the energy spectrum split due to the Rashba effect in asymmetric quantum well. The data are found in a good quantitative agreement with the results of numerical calculations performed with the use of the 6×6 matrix Hamiltonian. However, the central point of the paper relates to the features connected with the shape of the dispersion law. In biased structure, the energy versus quasimomentum curve has the form of Mexican hat. The existence of the electronlike and holelike states results in complicated magnetic field dependence of the Hall coefficient, which changes the sign from negative to positive with growing magnetic field within some gate voltage interval.

Introduction

After long hiatus in 90-s interest in gapless A_2B_6 semiconductors was rekindled in the new millennium [1–4]. The reason is the considerable achievements in technology of growing of the heterostructures allowing one to fabricate the systems with 2D gas of extremely high quality. On the other hand, the new interest is stimulated by the new phenomena arising in such a type structure resulting from the complicated energy spectrum of the parent material forming the quantum well.

In the present paper, the results of experimental investigations of the transport in wide single quantum well of mercury telluride are reported. The main attention is focused on the situation when the spectrum of the carriers has the form of Mexican hat due to mixing of the conduction and valence band states in biased heterostructure.

1. Experimental

Our HgTe quantum wells were realized on the basis of HgTe/ $Hg_{0.25}Cd_{0.75}Te$ heterostructure grown by means of MBE. The width of the quantum well is 20 nm. The 10 nm doping layer of indium is situated in the barrier above the quantum well at the distance of 10 nm from the upper interface. The samples were mesa etched into standard Hall bars. To change and control the carriers density in the quantum well, the field effect transistors have been fabricated on the basis of the Hall bars with parylene as an insulator and aluminium a gate electrode.

2. Results and discussion

To characterize the samples, the Shubnikov–de Haas (SdH) oscillations have been measured and analyzed. The typical oscillation picture is presented in Fig. 1a. It seen that it is rather complicated. The Fourier spectrum shown in Fig. 1b has two peaks, corresponding to the two branches of the electron energy spectrum split by spin-orbit interaction in asymmetric quantum well. Quantitative interpretation has been done in framework of the $k\hat{P}$ model. We started from the multiband Hamiltonian derived from Kane's model, making the usual assumption that the energy difference between the valence Γ_8 band and spin-orbit
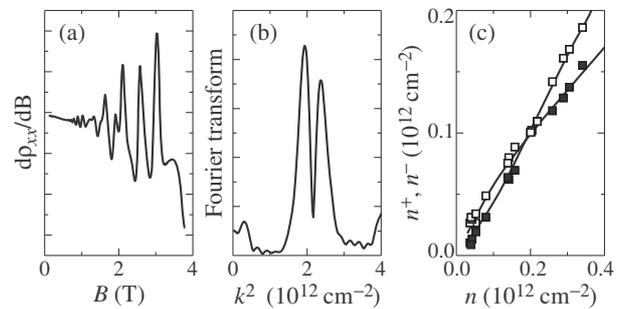
Fig. 1. (a) and (b) The magnetic field dependences of $d\rho_{xx}/dB$ and the results of the Fourier transformation, respectively, for $V_g = 0$ and $T = 4.2$ K. (c) The density of electrons corresponding to two "spin" branches of the energy spectrum as a function of the total electron density. Symbols are obtained from the Fourier analysis of the Shubnikov–de Haas oscillations, the lines are result of the numerical calculations within framework of 6×6 $k\hat{P}$-model.

split-off Γ_7 band is infinite. To consider the effects involving the heavy-hole states, the interaction with remote bands has been taken into account by a standard procedure of including additional terms with γ parameters in the Hamiltonian. An isotropic approximation has been used. The Shrödinger equation has been solved consistently with the Poisson equations. The method of direct numerical integration has been used (see, e.g., [5]). As seen from Fig. 1c this model agrees well with the results obtained from the analysis of the SdH oscillations.

Before discussing the Hall effect, it would be well to consider the dispersion law $\varepsilon(k)$ of 2D carriers in HgTe quantum well. As seen from Fig. 2 the degeneracy of the spectrum is lifted. This is result of the spin-orbit interaction in asymmetric quantum well. Another important feature of the spectrum is nonmonotonic run of the dispersion curves related to the valence band. The plot $\varepsilon(k_x, k_y)$ being plotted in three-dimensions looks like the Mexican hat turned over. Therewith, the states on the left and right of maximum are characterized by the different sign of the dynamic effective mass $\hbar^2 k \partial k/\partial \varepsilon(k)$. Finally, the energy spectrum of the HgTe quantum well is gaped.

Let us turn now to the main result of our paper — to the Hall
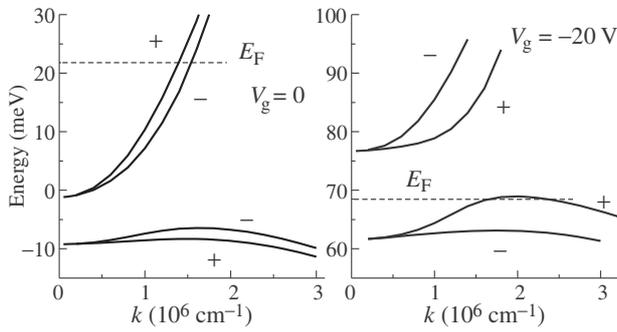
Fig. 2. The energy versus longitudinal quasimomentum dependence calculated for the structure investigated for two gate voltages. The dashed lines are the Fermi level. Signs + and − mark the branches of the energy spectrum split by spin-orbit interaction.
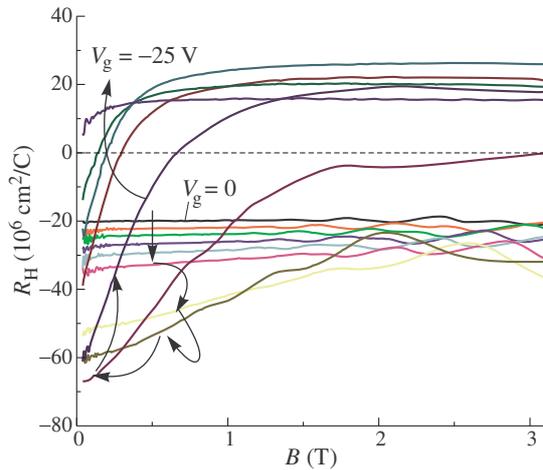

Fig. 3. The experimental magnetic field dependences of the Hall coefficient measured at $T = 4.2$ K for different gate voltages from $V_g = 0$ down to -25 V.

Fig. 4. The values of $k^2/2\pi$ plotted against the gate voltages. The symbols are obtained from the analysis of the B-dependences of the Hall coefficient as $k_e^2/2\pi = n$ and $k_h^2/2\pi = p$. The lines are calculation results. Inset illustrates the meaning of the holelike and electronlike states.

the energy spectrum in the theoretical model, the agreement between experiment and theory can be considered as rather good.

Thus, the existence of the electronlike and holelike states in biased HgTe/HgCdTe single quantum well heterostructure with the Mexican-hat energy spectrum results in complicated magnetic field dependence of the Hall coefficient. At the gate voltages, when the Fermi level lies within the hat, the Hall effect changes the sign from negative to positive with growing magnetic field.

Acknowledgements

References

[1] K. Ortner *et al*, *Phys. Rev. B* **66**, 075322 (2002).
[2] X.C. Zhang *et al*, *Phys. Rev. B* **69**, 115340 (2004).
[3] B. Andrei Bernevig *et al*, *Science* **314**, 1757 (2006).
[4] G.M. Gusev *et al*, *Phys. Rev. Lett.* **104**, 166401 (2010).
[5] V.A. Larionova and A.V. Germanenko, *Phys. Rev. B* **55**, 13062 (1997).

effect. At first glance it would seem that the Hall coefficient (R_H) should change sign from negative to positive when the Fermi level goes through the gap from the upper (electron) band to the lower (hole) one. However it is not the case in reality. As seen from Fig. 3 there is the range of the gate voltage from approximately -20 V to -12 V, where R_H behaves itself analogously to situation when two types of carriers — electrons and holes — take part in transport. The Hall coefficient changes the sign; it is negative at low magnetic field and positive at higher one. The transverse resistivity ρ_{xx} (not shown) increases monotonically with growing magnetic field.

It turns out that the classical hand-book formulae, which describes the transport for two types of carriers of different signs, fit the experimental curves $R_H(B)$ and $\rho_{xx}(B)$ fairly well. The found from the fit values of $k_e^2/2\pi = n$ and $k_h^2/2\pi = p$ as a function of gate voltage are shown in Fig. 4 by open and solid squares, respectively (for illustrative purpose the $k_h^2/2\pi$ values are negative). In order to show that the sign-alternative behavior of the Hall coefficient results from the existence of electronlike and holelike states on the Mexican-hat branch of the spectrum, the theoretical $[(k_e^-)^2 + (k_e^+)^2]/4\pi$ and $[(k_h^-)^2 + (k_h^+)^2]/4\pi$ versus V_g dependences are plotted as well. Taking into account an approximate approach to analysis of the Hall effect and magnetoresistivity and neglect of the wrapping of

Interaction correction to conductivity of 2D structures with strong spin-orbit interaction: suppression of the triplet channel

G. M. Minkov[1,2], A. A. Sherstobitov[1,2], A. V. Germanenko[2] and O. E. Rut[2]

[1] Institute of Metal Physics, Ural Branch of RAS, 620990 Ekaterinburg, Russia
[2] Ural State University, 620000 Ekaterinburg, Russia

Abstract. The interaction corrections to the conductivity in the quantum well structures $InP/In_{0.47}Ga_{0.53}As/InP$ with strong spin-orbit interaction are studied experimentally. The diffusion part of the interaction correction to the conductivity was found as correction to the σ_{xx}, which is absent in σ_{xy}. There was shown that the suppression of the triplet channel is not observed up to value of $1/\tau_s$, which is twenty times as larger as the temperature (where τ_s is the spin relaxation time). This result contradicts the theoretical prediction that only singlet channel remains at strong spin-orbit interaction.

The quantum corrections to the conductivity, namely the weak localization (WL) correction and correction due to electron-electron interaction, wholly determine the low temperature, $T \ll E_F, \hbar/\tau$, and magnetic field dependences of the conductivity (E_F and τ are the Fermi energy and transport relaxation time, respectively). Both these corrections crucially depend on the spin-orbit interaction strength. This interaction determines the spin relaxation time of the carriers, τ_s, also. When τ_s is less than or close to the phase relaxation time, τ_ϕ, the interference leads to appearance of the antilocalization behavior of the magnetoresistance. It becomes nonmonotonic. The magnetoresistivity being positive at low magnetic field transforms to the negative one at stronger magnetic field. At $\tau_s \ll \tau_\phi$ the only positive interference magnetoresistance remains, therewith the temperature dependence of interference correction changes from localization ($d\sigma/dT > 0$) to antilocalization one ($d\sigma/dT < 0$).

Spin-orbit interaction should change the interaction correction to the conductivity also. At the absence of spin relaxation this correction is

$$
\begin{aligned}
\delta\sigma_{ee} &= G_0 \left[1 - 3 \left(\frac{1 + \gamma_2}{\gamma_2} \ln(1 + \gamma_2) \right) \right] \ln T\tau \\
&= G_0 K_{ee} \ln T\tau,
\end{aligned}
\tag{1}
$$

where $G_0 = e^2/\pi h = 1.23 \times 10^{-5}$ Ohm^{-1}, $\gamma_2 = -F_0^\sigma/(1 + F_0^\sigma)$ is the interaction parameter. The first term in square brackets in Eq. (1) results from the interaction in singlet channel, while the second one results from the interaction in triplet channel. At $\hbar/\tau_s \ll T$ the contribution of the triplet channel should vanish, the correction cease to depend on the interaction constant and becomes

$$
\sigma_{ee} = G_0 \ln T\tau.
\tag{2}
$$

Such the behavior of the corrections to the conductivity was invoked to interpretation of the crossover to metallic temperature dependence of the conductivity with temperature decrease [1,2], which was observed in some 2D structures [3,4].

It should be noted that the suppression of triplet channel was predicted theoretically but, for the best of our knowledge, was never observed experimentally. It is not surprising because special structures are needed for reliable determination of the interaction correction and its dependence on spin-orbit interaction strength.

The heterostructure with 10 nm $In_{0.47}Ga_{0.53}As$ narrow gap single quantum well in InP with 12.5 nm Si doped layer sep-
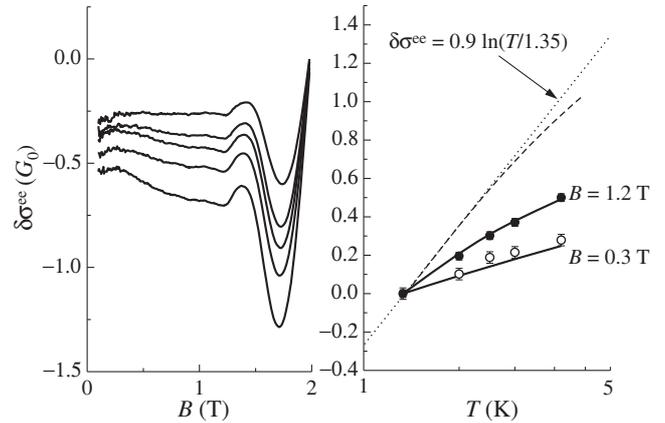
Fig. 1. (a),(b) The experimental magnetoresistance $\Delta\sigma = 1/\rho_{xx}(B) - 1/\rho_{xx}(0)$ for two electron densities; (c) The electron density dependence of τ, τ_ϕ and τ_s. $T = 1.35$ K.

arated by 12.5 nm undoped spacer (CBE06-173) was studied. The electrons in such well have simple, isotropic, nondegenerated energy spectrum. The effective g factor found from the angle dependence of the Shubnikov–de Haas oscillations amplitude is about 2. The electron density in the well was controlled with the help of the gate electrode. Part of the data was obtained after illumination of the samples. The results for both cases were mostly the same.

Because the suppression of the triplet term of the interaction correction is governed by the $T\tau_s$ value, the low field magnetoresistance was studied to find the spin relaxation time. The magnetoresistance curves for some conductivity values and their fit by theoretical expression [5] are presented in Figs. 1a and 1b. The obtained values of τ_ϕ, τ_s and τ are plotted in Fig. 1c.

To find the interaction correction to the conductivity from the experimental dependence of longitudinal, ρ_{xx}, and transverse, ρ_{xx}, magnetoresistance we have used the unique property of this correction in the diffusion regime, $T\tau \ll 1$, namely, it contributes to σ_{xx} while $\delta\sigma_{xy}^{ee} = 0$. To eliminate the WL contribution and the ballistic part of the interaction correction, which reduces to the renormalization of τ, we have found $\mu(B, T)$ from $\sigma_{xy}(B, T)$ and determined the interaction correction $\delta\sigma^{ee}$ as the difference between experimental value of σ_{xx} and calculated one $en\mu(T)/[1+\mu^2(T)B^2]$ (see Ref. [6] for detail). Results of such a data treatment for $\sigma(4.2 \text{ K}) = 29G_0$, $n = 2 \times 10^{11}$ cm^{-2} are presented in Fig. 2. Comparison with
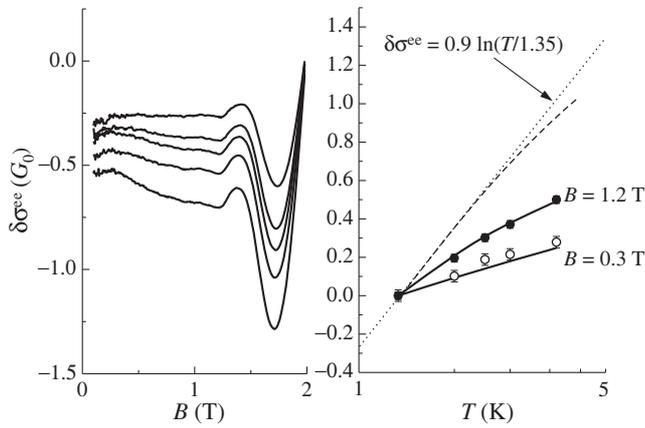
Fig. 2. (a) The magnetic field dependences of $\delta\sigma_{xx}^{ee}$ at $T = 4.2$, 3.0, 2.5, 2.0, and 1.35 K from bottom to top. (b) The temperature dependences of $\delta\sigma_{xx}^{ee}$ for two magnetic fields. Symbols are experimental results, solid lines are calculated with taking into account the Zeeman splitting only. The theoretical dependence for $B = 0$ (dashed line) takes into account the spin-orbit interaction only.

suppression of the triplet channel caused by the Zeeman effect is evident, while the suppression due to spin-orbit interaction does not reveal itself even for this case, when $1/\tau_s$ is 20–30 times as large as T. The reason of this contradiction with theoretical prediction is puzzle now.

References

[1] I.V. Gornyi *et al*, *Pis'ma Zh. Eksp. Teor. Fiz.* **68**, 314 (1998).
[2] G.M. Minkov *et al*, *Phys. Rev. B* **75**, 193311 (2007).
[3] S. Anissimova *et al*, *Nat. Phys.* **3**, 707 (2007).
[4] D.A. Knyazev *et al*, *Phys. Rev. Lett.* **100**, 046405 (2008).
[5] L.E. Golub, *Phys. Rev. B* **71**, 235310 (2005).
[6] G.M. Minkov, *Phys. Rev. B* **79**, 235335 (2009).
[7] I.V. Gornyi, *private communication*.

Fig. 3. The temperature dependences of $\delta\sigma_{xx}^{ee}$ for two magnetic fields. The symbols are the data. The solid lines are calculated dependences, which takes into account the Zeeman splitting only. The upper curve is the theoretical dependence for $B = 0$ taking into account the spin-orbit interaction only.

the theoretical dependences calculated with taking into account of suppression of the two triplets due to the Zeeman splitting (presented in the same figure by solid lines) demonstrates good quantitative agreement.

Note, the value of $1/\tau_s$ is three times larger than $T = 1.35$ K. Therewith the slope of σ_{xx} vs $\ln(T)$ dependence at low magnetic field is about 0.2. It means that the contribution of the interaction in the triplet channel constitutes about 0.8 from that in the singlet one, i.e. noticeable suppression is not observed. If one supposes that the spin-orbit interaction suppresses the triplet channel by the same manner as the Zeeman splitting, i.e., the logarithm in the second term in (1) should be replaced with $\ln T\tau\sqrt{1 + (T\tau_s)^{-2}}$ [7], the value of the triplet contribution at $T = 1.35$ K should be less than 0.1 [the dashed line in Fig. 2(b)].

It is possible that the suppression has to be observed at lower τ_s and lower temperature. Therefore, the measurement was extended down to $T = 0.6$ K, at higher electron density when τ_s is lower, $\tau_s \simeq 6 \times 10^{-13}$ s. Fig. 3 shows that the

In situ transmission electron microscopy analyses of thermally annealed self catalyzed GaAs nanowires grown by molecular beam epitaxy

S. Ambrosini[1,2,3], J. B. Wagner[4], T. Booth[5], A. Savenko[4,5], G. Fragiacomo[5], P. Boggild[5] and S. Rubini[1,2]

[1] TASC National Laboratory, 34149 Trieste, Italy

[2] Sincrotrone Trieste S.C.p.A, 34149 Trieste, Italy

[3] UNITS, Università degli Studi di Trieste, 34100 Trieste, Italy

[4] DTU CEN, Center for Electron Nanoscopy, Technical University of Denmark, DK-2800, Kgs. Lyngby, Denmark

[5] DTU Nanotech, Department of Micro and Nanotechnology, Technical University of Denmark, 2800 Kgs. Lyngby, Denmark

Abstract. Self catalyzed GaAs nanowires grown on Si-treated GaAs substrates were studied with a transmission electron microscope before and after annealing at 600 °C. At room temperature the nanowires have a zincblende structure and are locally characterized by a high density of rotational twins and stacking faults. Selected area diffraction patterns and high-resolution transmission electron microscopy images show that nanowires undergo structural modifications upon annealing, suggesting a decrease of defect density following the thermal treatment.

Introduction

GaAs nanowires (NWs) grown by catalyst assisted methods are typically affected by the presence of structural defects. Stacking faults are common, and the two GaAs polytypes, zincblend (ZB) and wurtzite (WZ) are often intermixed along the growth axis of a single nanowire. The two GaAs polytypes of GaAs have indeed a small cohesive energy difference (24 meV per III–V atom pair [1]). The occurrence of one or the other of the possible stacking has been recently predicted on thermodynamic basis in terms of the relative weight of the surface energies of the different phases involved in the NW growth, i.e. solid, liquid and gaseous [2]. Recently, wide effort has been devoted to careful tune the growth conditions in order to obtain pure ZB or pure WZ NWs [3, 4]. Self-catalyesd NWs typically display ZB structure but twins and stacking faults are generally present [5]. We give here a preliminary account of a study of the thermal stability of self-catalyzed GaAs NWs, especially with respect to the stability of stacking faults.

1. Experimental details

NWs have been synthesized by solid source molecular beam epitaxy using a Riber 32P apparatus: (111)B GaAs wafers have been deoxidized and 3–4 monolayers of Si (1 monolayer = 1.36 Å) have been epitaxially deposited. Air exposure and outgassing in ultra high vacuum completed the substrates preparation for self catalyzed NW growth [6]. NWs were grown at a growth temperature of 620 °C with an As to Ga beam-equivalent pressure ratio of 12. In these growth conditions a two-dimensional growth rate of 1 μm/hour is observed. A suspension of the as-grown nanowires in ethanol produced by sonication was then applied to a nickel Quantifoil TEM grid and examined in the transmission electron microscope (Tecnai G2 operating at 200 keV). The annealing step consisted of 10 minutes at 600 °C inside the TEM chamber using a sample holder with a platinum heating element (Gatan Inc.). High temperature mesurements were possible only in diffraction mode, while for high resolution the absence of thermal drift was mandatory: to acquire high resolution images, then,
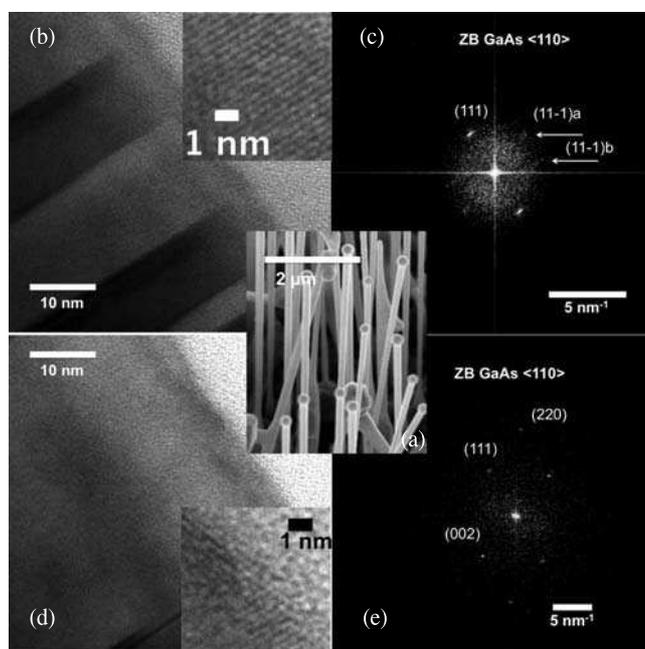
Fig. 1. (a) SEM image of GaAs NWs on (111)B GaAs substrates as grown; (b) HRTEM image of a NW in the ZB region at the base; (c) filtered FFT of (b); (d) HRTEM image of the same NW after the annealing step; (e) filtered FFT of (d). The insets in (b) and (d) show details of the crystal lattice. Notice that the FFTs are aligned with the HRTEM images.

30 minutes were waited after the annealing.

2. Results and discussion

In Fig. 1 the result of the annealing step on the NW body where it had pure ZB crystal structure is visible. In Fig. 1(a) a scanning electron microscope image of the NWs as grown on the (111)B GaAs substrate. In 1(b) the NW body with twinned zones of alternating contrast along the growth axis. The inset in 1(b) and the fast Fourier transform (FFT) of the image, visible in 1(c), confirms the stacking to be ZB, diffraction spots are indexed according to this structure. In 1(d) the HRTEM image
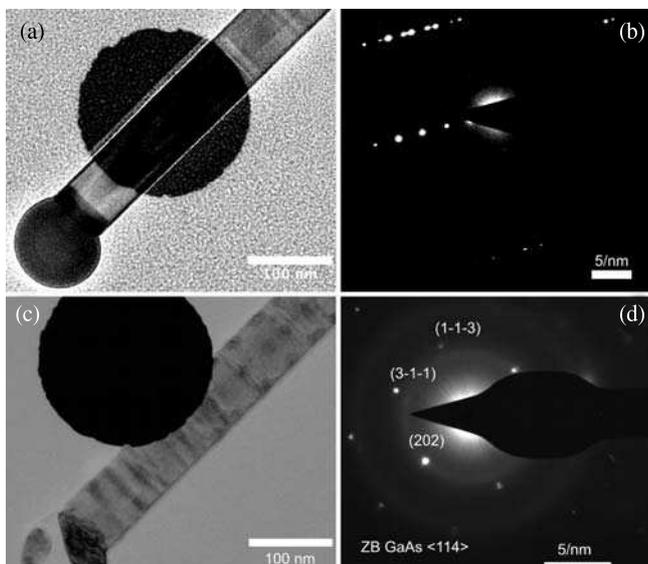
Fig. 2. Low magnification TEM images (left) and corresponding SAD patterns taken from the black circled zone (right) of a NW before (top) and after (bottom) the annealing step. Notice the black spots on the NW body in the region next to the SAD aperture in (c).

3. Conclusions

These preliminary results show that structural changes take place when self catalyzed GaAs NWs undergo thermal annealing. In particular, where the stacking was ZB, it remains ZB and where the structure was defected it seems to become simpler towards pure ZB. The incidental evidence of Ga diffusion within the NW body moreover confirms the effectiveness of post growth annealing procedures to affect NW structure. An annealing step in As atmosphere inside the growth chamber after the growth interruption and other TEM analyses performed with a lower electron beam energy are upcoming points of this investigation.

References

[1] C.Y. Yeh *et al*, *Phys. Rev. B* **46**, 10086 (1992).
[2] F. Glas *et al*, *Phys. Rev. Lett.* **99**, 146101 (2007).
[3] H. Shtrikman *et al*, *Nano Lett.* **9**, 215 (2009).
[4] H. Shtrikman *et al*, *Nano Lett.* **9**, 1506 (2009).
[5] G. Cirlin *et al*, *Phys. Rev. B* **82**, 35302 (2010).
[6] S. Ambrosini *et al*, *submitted to Nanoresearch* (2011).

of the same NW shows a greater uniformity possibly due to a tilt of the crystal after the annealing step, though the detail of the atomic lattice is still visible in the inset. In 1(e) the FFT of 1(d): spot indexes show the stacking to be ZB. Notice that the FFTs in 1(c) and 1(e) are aligned with the HRTEM image.

In Fig. 2 the low magnification image of a NW tip is visible, before in 2(a) and after in 2(c) the annealing step. In both 2(a) and 2(c), the black circle region shows where the SAD pattern in 2(b) and 2(d), respectively, were taken; notice that the diffractograms in 2(b) and 2(d) are 90° rotated with respect to 2(a) and 2(c). The diffractogram in 2(b) is compatible with a defected region with stacking faults and/or rotational twins, whereas the diffractogram in 2(d) is much simpler and strongly suggests the absence of multiple crystal phases in that area. Although a slight movement or rotation of the NW as result of the annealing step (same as previous image) could be the reason of the disappearance of some diffraction spots, distances and positions of the main diffraction peaks show pure ZB phase in the selected area. It should be pointed out that the slight different selected area between 2(a) and 2(c) is a result of the thermal drift at high temperature. Fig 2(c) shows other particulars, if compared with 2(a): first, the Ga nanoparticle on top of the NW has a different morphology; second, the presence of greater contrast spots on the NW body, close to the selected area, suggests a partial dewetting of the Ga nanoparticle. In this case, Ga atoms have migrated down the NW body and segregated in smaller Ga clusters; this should be taken into account in considering transport or electronic properties of annealed NWs. Their position inside the NW body couldn't though be resolved by this TEM analysis. With an energy difference of 24 meV per III–V atom pair between ZB and WZ GaAs polytypes and thermal energy employed for these experiments of 75 meV, structural changes in NWs are very likely to be triggered.

Characteristics of InAs-InSb heterostructured nanowires growth by chemical beam epitaxy: theory and experiment

M. A. Timofeeva[1], N. V. Sibirev[1], L. Lugani[2], D. Ercolani[2,3], M. V. Nazarenko[1], L. Sorba[2,3] and V. G. Dubrovskii[1,4]

[1] St Petersburg Academic University, St Petersburg, Russia
[2] NEST, Scuola Normale Superioreand CNR-INFM, Piazza S. Silvestro 12, I-56127, Pisa, Italy
[3] NEST, Istituto di Neuroscienze CNR, Piazza S. Silvestro 12, I-56127, Pisa, Italy
[4] Ioffe Physical-Technical Institute, St Petersburg, Russia

Abstract. We report the Au-assisted chemical beam epitaxy growth of defect-free zincblende InSb nanowires. The grown InSb segments are the upper sections of InAs/InSb heterostructures on InAs(111)B substrates. We found that the InAs part possesses cubic zincblende phase and the InSb part possesses hexagonal wurtzite phase. We developed a theoretical model which allows us to explain InAs/InSb NWs shape and crystal structure.

Introduction

Semiconductor nanowires (NWs) are anisotropic nanostructures orthogonal to the substrate surface with 10–100 nm in lateral dimensions. NWs have some unique properties that makes them promising for application in nanophotonic, nano-electronic and nanosensing devices. Nanowires are grown by different epitaxial techniques such as molecular beam epitaxy, metalorganic chemical vapor deposition and chemical beam epitaxy (CBE). One of theirs most attractive feature is the possibility of growing heterostructures with materials with very different lattice constants [1]. Among III–V semiconductor materials InSb has the smallest band gap and the largest bulk electron mobility [2,3]. The aim of our work was to investigate InAs/InSb NWs shape and to analyze their crystal structure.

1. Experiment

InAs-InSb NWs heterostructures were grown on InAs(111)B substrates by CBE techniques in a Riber Compact-21 system by Au-assisted growth using trimetilindium (TMIn), tertiarybuty-larsine (TBAs) and trimethylantimony (TMSb) as metalorganic (MO) precursors. InAs segment had been grown for 45 min at a temperature of 435 ± 10 °C, with MO line pressures of 0.3 and 1.0 Torr for TMIn and TBAs, respectively. Then the group — V precursor was switched from TBAs to TDMASb, with a pressure of 1.0 Torr, with no interruption or variation in the TMIn flux or substrate temperature. Fig. 1 shows scanning electron microscope (SEM) images of InAs/InSb NWs. The lower InAs part has a smaller diameter than upper InSb segment. Also it was found that InAs part grows in the hexagonal wurtzite phase (WZ) and InSb grows in cubic zincblende phase (ZB). It should be mentioned that sidewalls of the InSb part are rotated by 30° as compared to the InAs part.

2. Theory

We have developed a theoretical model of NWs growth which has enabled us to explain InAs/InSb NWs shape and crystal structure. The vertical NWs growth rate in quasi-stationary regime is determined by the material balance equation and the nucleation equation. It should take into account the direct impingement of the material to the droplet, re-evaporation of the growth material from the droplet, the nanowire growth and the diffusion flux. In terms of supersaturation in vapour Φ and in
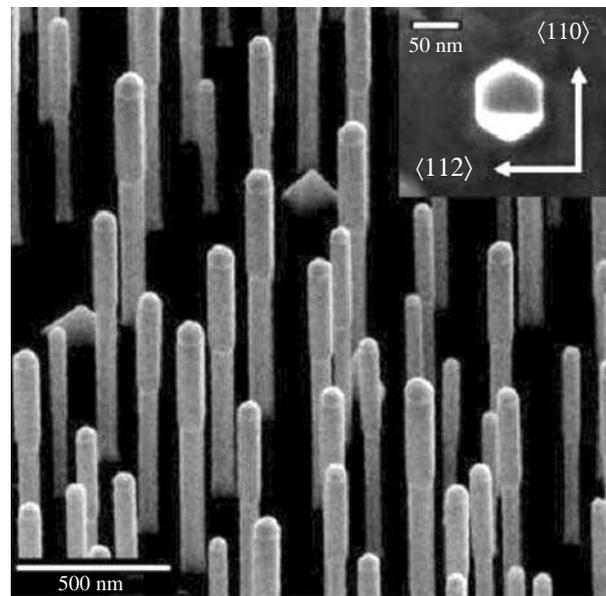
Fig. 1. SEM images of InAs/InSb NWs.

the droplet ξ the material balance equation can be presented in following form [4]:

$$\frac{dL}{dH} = \varepsilon \left[\Phi + 1 - (\xi + 1) \exp\left(\frac{R_{GT}}{R} \right) \right], \qquad (1)$$

here ε is a constant determined by the growth system properties, R_{GT} describes the desorption flux modification due to Gibbs–Thomson effect. To find the unknown supersaturation we write the nucleation equation [5]:

$$\frac{dL}{dH} = \frac{h}{t_G} \frac{V_{mono}(\xi) V_{poly}(\xi)}{V_{poly}(\xi) + V_{mono}(\xi)}, \qquad (2)$$

here V_{poly}, V_{mono} is the growth rate in polycentric and monocentric mode, respectively, h is the height of a monolayer and t_G is the microscopic growth time of 2D islands on the top facet [4]. Glas and co-authors [6] also showed that a lower surface energy of WZ NW sidewalls could lead to WZ formation instead of ZB crystal phase which is typical for bulk GaAs. They also show that the formation of WZ structure requires two conditions: (i) the nucleation at the triple line to gain the surface energy and (ii) high enough supersaturation of

liquid alloy to overcome the stacking fault [6,7]. This view has gained much support [8,9] and is now widely used for tuning the crystal phase of Au-catalyzed III–V NWs [9,10]. Joining equations (1) and (2) we get closed equation for R, Φ and ξ:

$$\Phi + 1 - (\xi + 1) \exp\left(\frac{R_{GT}}{R}\right) = \frac{h}{t_G} \frac{V_{mono}(\xi) V_{poly}(\xi)}{V_{poly}(\xi) + V_{mono}(\xi)}. \quad (3)$$

This allows us to find the supersaturation ξ. The dependence between supersaturation and radius gives the critical radius R_c of phase transition. For $R < R_c$ WZ phase dominates, and for $R > R_c$ ZB phase dominates. In Table 1 we present results for R_c for different growth temperatures [11].

Table 1. Results for maximal radius R_c.

Material	InAs			InSb		
T (°C)	380	400	420	380	400	420
R_c (nm)	86	73	62	5.2	5.2	5.2

The data presented in the table gives us opportunity to explain why the InAs part of NW possesses WZ phase and the InSb — ZB phase. In earlier work [11] we showed that the minimal surface energy for ZB NW sidewalls is reached at (110) and for WZ NW sidewalls at (1–100). This allows us to explain the rotation of the InSb part of NW. Simultaneous increase of the NW radius could be explained if we take into account high solubility of Sb in Au [12].

3. Conclusions

We have developed a theoretical model of NWs growth. According to this model we could predict crystal structure of NWs. This model allows us to describe InAs/InSb heterostructured NWs growth.

Acknowledgements

References

[1] V.G. Dubrovskii, G.E. Cirlin, V.M. Ustinov, *Semiconductors* **43**, 1585 (2009).

[2] S.J. Chung, K.J. Goldammer, S.C. Lindstrom, M.B. Johnson, and M.B. Santos, *J. Vac. Sci. Technol.* **B 17** 1151 (1999).

[3] H.A. Nilsson, P. Caroff, C.L. Thelander, M. Larsson, J.B. Wagner, L. Wernersson, L. Samuelson, and H.Q. Xu, *NanoLett.* **9** 3151 (2009).

[4] V.G. Dubrovskii *et al*, *Semicond. Sci. Technol.* **26**, 014034 (2011).

[5] N.V. Sibirev, and V.G. Dubrovskii, *Technical Physics Letters* **30** 9, 791 (2004).

[6] F. Glas, J.H. Harmand, and G. Patriarche, *Physical Rev. Lett.* **99**, 146101 (2007).

[7] V.G. Dubrovskii, N.V. Sibirev, *Phys. Rev. B* **77**, 035414 (2008).

[8] V.G. Dubrovskii *et al*, *Phys. Rev. B* **78**, 235301 (2008).

[9] J. Johansson *et al*, *Cryst. Growth and Design* **9**, 766 (2009).

[10] H.J. Joyce *et al*, *Nano Lett.* **10**, 908 (2010).

[11] N.V. Sibirev, M.A. Timofeeva, A.D. Bol'shakov, M.V. Nazarenko, and V.G. Dubrovskii, *Physics of the Solid State* **52** 7, 1531.

[12] T.B. Massalski, H. Okamoto, *Binary Alloy Phase Diagrams*, ASM International (1990).

Formation of GaAs$_{1-x}$N$_x$ nanolayer on GaAs by manipulations with N$_2^+$ and Ar$^+$ ion beams

V. M. Mikoushkin, V. V. Bryzgalov, A. A. Zhuravleva and A. P. Solonitsina

Ioffe Physical-Technical Institute, St Petersburg, Russia

Abstract. Nanofilms consisting mainly of dilute alloy GaAs$_{1-x}$N$_x$ with minor inclusions of GaN clusters were fabricated at high vacuum conditions on the surface of GaAs(100) by implantation of low-energy N$_2^+$ ions followed by Ar$^+$ ion bombardment. The elemental and chemical compositions were controlled *in situ* by Auger diagnostics in the course of the film fabrication. The nanofilms are characterized by high concentration of nitrogen $x \sim 0.04-0.09$ and by the thickness of about 4 nm.

Introduction

Surface nitridation of GaAs by low energy nitrogen ion beams seems to be an attractive way for passivation and insulation of the surface of GaAs based semiconductor structures and for some other applications [1–7]. An advantage of this technique is relative simplicity, compatibility with other vacuum technologies, and opportunity of *in situ* monitoring the elemental and chemical composition by different kinds of electron spectroscopy. In recent years, research in this direction has become very topical for solving the task of creating an ion implanted buffer GaN nanolayer on the surface of GaAs substrates for subsequent epitaxial growth of crystallographically perfect GaN layers for device structures [6,7] and even for direct fabricating GaN layers suitable for device applications [5]. In most studies, it was concluded that a nitride nanolayer formed by low energy implantation of the GaAs consists entirely of GaN [1,2,5,7] or at least contains predominantly Ga-N chemical bonds [3,6]. But recent research [8] with high resolution photoelectron spectroscopy and synchrotron radiation has revealed a significant fraction of GaAsN alloy besides GaN in the ion nitrated layers. In the present study, the fraction of GaAsN alloy has been radically increased in the implanted layer with the help of the developed Auger diagnostics for quantitative chemical analysis and special modification of the nitrated layer by the Ar$^+$ ion bombardment.

1. Experimental details

The experiment was carried out in an electron LHS-11 (Leybold AG) spectrometer with basic vacuum $P < 2 \times 10^{-10}$ Torr. GaAs(100) film with a thickness of about 100 nm grown by molecular beam epitaxy on a GaAs(100) substrate [9,10] was taken as a sample. The surface nitridation was effected by a beam of N$_2^+$ ions with the energy of $E_i = 2500$ eV after etching the surface with an Ar$^+$ ion beam. All stages of sample treatment were accompanied by measuring the Auger electron spectra in the regime allowed the known elemental sensitivity coefficients to be used for evaluating the elemental composition of samples. The concentration of nitrogen in the implanted layer was $[N] \sim 12$ at% and decreased to $[N] \sim 2.5$ at% upon the bombardment with Ar$^+$ ions with the energy of $E_i = 2500$ eV. The thickness of the ion implanted layer was estimated as the average projected range of nitrogen ions, $\langle x \rangle = 3.9$ nm, which was calculated for the given ion energy using the well known SRIM 2006 program. Since the mean free path of N KVV Auger electrons is $\lambda \sim 1.5$ nm, the information contained in the Auger electron spectra considered below refers to the near
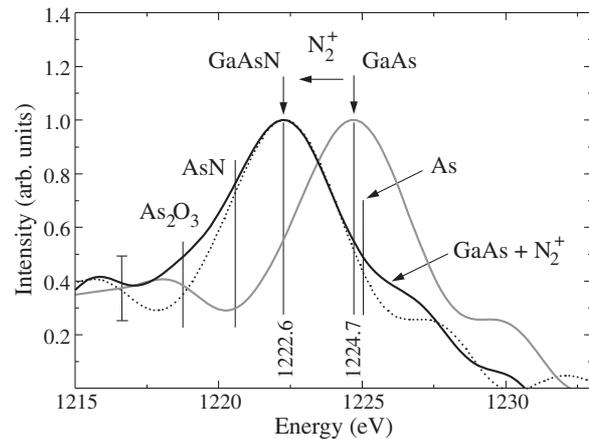
Fig. 1. AsLMM Auger spectra of GaAs (right curve) and GaAs implanted by nitrogen ions (left curve).

surface region of the probed layer without the substrate contribution.

2. Results and discussion

When colliding with the surface, molecular nitrogen ions dissociate, and chemically active atomic particles penetrate into the substrate to a projected range of several nanometers before they completely lose their kinetic energy. At the end of this process, the nitrogen atoms react with the GaAs matrix, substituting arsenic and resulting in formation of the following chemical phases: GaN, GaAsN and AsN. The last one was revealed in plasma nitridation of GaAs [11] but it was not observed in the most investigations involving the nitrogen ion implantation in GaAs [1,3,4,7,8–10] as well as in the present study. Fig. 1 shows that AsLMM Auger spectrum of nitrated layer is mainly described by one line without essential contributions of AsN, GaAs and As phases. This line was attributed to the remaining GaAsN phase.

Fig. 2 shows the N KVV Auger spectrum of a nitride layer after implantation (curve 1) as well as after the bombardment of the layer by Ar^+ ions for 3, 7, and 12 min, respectively (curves 2–4). These spectra clearly reveal the presence of two Auger lines centered at $E_A = 379.8$ and 382.8 eV. The position of the first component coincides with that of the line of a thick epitaxial layer of GaN [11]. The second line falls within the interval of $E_A = 381.5-383$ eV, in which a disordered GaAsN phase was observed in the early stages of plasma nitridation of the GaAs surface [11]. Thus, the formation of two nitride phases, GaN and GaAsN, was observed in nitrided lay-
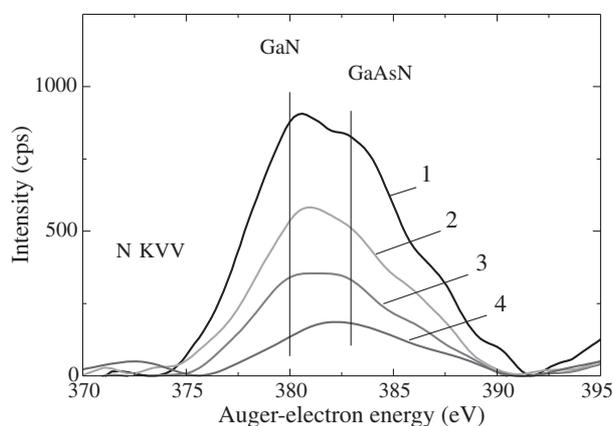
Fig. 2. N KVV Auger spectra of the nitride layer measured (1) after implantation and (2–4) after Ar^+ ion bombardment.
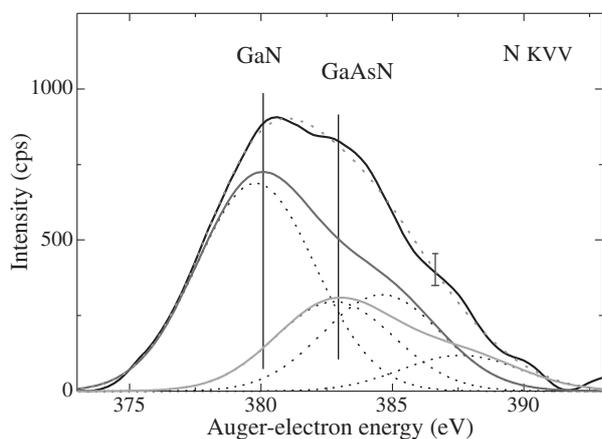
Fig. 3. N KVV Auger spectrum of a nitride layer and the result of its decomposition into components.

ers similarly to that revealed by high-resolution photo-electron spectroscopy [8].

A quantitative analysis of the revealed nitride phases was carried out by decomposition of the Auger spectra into components taken into account the double peak structure of N KLVV spectrum. Fig. 3 gives an example of this analysis. Area under the elementary spectra (thin solid curves) is proportional to the concentration of nitrogen atoms in the nitride phases. The results of the decomoisition showed that about 70% of nitrogen atoms enter into the GaN phase and about 30% of nitrogen is contained in the GaAsN phase after implantation. As can be seen from Fig. 2 (curves 2–4), the bombardment of the nitride layer by Ar^+ ions leads to a redistribution of the intensities of the main nitride components. Plots of the relative content of nitrogen in the GaN and GaAsN phases versus duration of the Ar^+ bombardment shown in Fig. 4 demonstrate the chemical effect of an argon ion beam on the nitride layer, which leads to a gradual disappearance of the GaN phase and a growth of the GaAsN phase. As a result, the distribution of nitrogen between these phases changes to the opposite.

At the same time, the thickness of the nitrated layer remains approximately constant because of knocking nitrogen atoms by argon impact into deeper layers and their mixing. The observed effect can be explained by intermixing the chemical phases due to ion cascades that are effectively generated by heavy argon ions [9,12]. Taking into account the total nitrogen concentration [N] in the layer, the variation of the content of the dominant
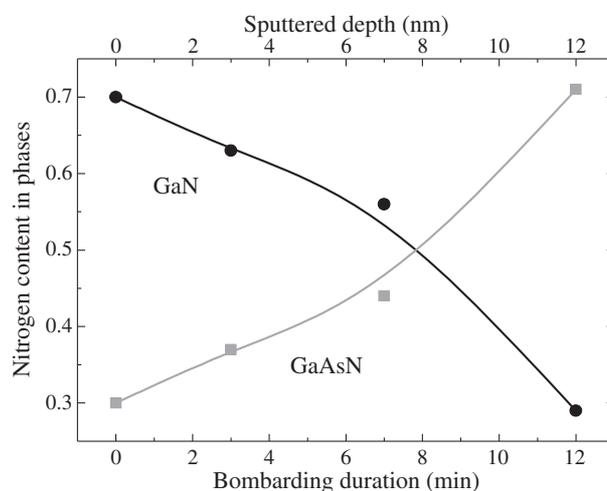
Fig. 4. Relative content of nitrogen in GaN and $GaAs_{1-x}N_x$ phases versus duration of the Ar^+ ion bombardment.

GaAsN phase was estimated to be $\sim 83 \rightarrow 99$ at% in the course of Ar^+ ion treatment. As the material is sputtered and the concentration [N] in the layer diminishes, the nitrogen content in $GaAs_{1-x}N_x$ alloy decreases from $x \sim 0.09$ to $x \sim 0.04$.

3. Conclusions

The implantation of N_2^+ ions at an energy of $E_i = 2500$ eV into an epitaxial film of GaAs(100) has been shown to form a surface nitride layer of about 4 nm thick. Auger diagnostics for quantitative chemical analysis of the nitrated layers has been developed using the values of NKVV Auger energies in GaN and GaAsN chemical phases measured in one experiment, with the accuracy being sufficient for separating their contributions into the experimental spectrum. Using this diagnostics showed that 70% of nitrogen atoms in the nitrided layer is contained in the GaN phase. The remaining 30% enter into a $GaAs_{1-x}N_x$ ($x \sim 0.09$) alloy. Nevertheless the alloy proved to be a dominant phase (>80 at%). It is established that the bombardment by accelerated argon ions produces a chemical effect on the nitride layer, which is related to a cascade mixing of the material. As a result, the domination of alloy becomes absolute (>98 at%), though the nitrogen concentration in alloy decreases.

References

[1] L.A. DeLouise, *J. Vac. Sci. Technol. A* **10**, 1637 (1992).
[2] J.S. Pan *et al*, *J. Mater. Res.* **13**, 1799 (1998).
[3] J.D. Hecht, F. Frost *et al*, *J. Appl. Phys.* **90**, 6066 (2001).
[4] Y.G. Li *et al*, *Appl. Surf. Sci.* **174**, 175 (2001).
[5] S. Meskinis, K. Slapikas *et al*, *Vacuum* **77**, 79 (2004).
[6] Z. Majlinger, A. Bozanic *et al*, *Vacuum* **84**, 41 (2009).
[7] P. Kumar, M. Kumar *et al*, *Appl. Surf. Sci.* **256**, 517 (2009).
[8] V.M. Mikoushkin *et al*, *Phys. St. Solidi (C)* **6**, 2655 (2009).
[9] Yu.S. Gordeev *et al*, *Tech. Phys.* **48**, 885 (2003).
[10] A.E. Zhukov *et al*, *Tech. Phys.* **46**, 1265 (2001).
[11] I. Aksenov, H. Iwai *et al*, *J. Appl. Phys.* **84**, 3159 (1998).
[12] V. M. Mikoushkin *et al*, *Bull. Russ. Acd. Sci.: Phys.* **72**, 609 (2009).

Photoluminescence studies of GaAs quantum nanostructures

Á. Nemcsics[1,2], J. Balázs[2], *B. Pődör*[1,2], J. Makai[2] and A. Stemmann[3]

[1] Microelectronics and Technology Institute, Kandó Kálmán Faculty of Electrical Engineering,
Óbuda University, Budapest, Hungary
[2] Research Institute for Technical Physics and Materials Science, Hungarian Academy of Sciences,
Budapest, Hungary
[3] Institut für Angewandte Physik und Zentrum für Mikrostrukturforschung, Hamburg, Germany

Abstract. We have studied the optical properties of droplet epitaxial quantum dots and quantum rings in the GaAlAs/GaAs system. Photoluminescence spectra measurements were performed in the temperature range from 4 to 300 K. The differences between the observed spectra and the electronic structure of quantum dots and quantum rings is briefly discussed.

Introduction

Self-assembled nanostructures, like quantum dots (QDs) and quantum rings (QRs) have recently been intensively investigated for basic physics and device applications. Notwithstanding the efforts of various groups there are still many open questions regarding the growth mechanisms of epitaxial nanostructures and their electrical and optical properties. Employing droplet epitaxy [1] to grow self-assembled lattice-matched quantum structures is a novel and interesting alternative method in comparison to the more common technology based on strain-driven quantum dot formation [7,8].

Here we report on some results of a photoluminescence study of the properties of uncovered droplet epitaxial QDs and QRs in the GaAs/GaAlAs system. The covered droplet epitaxial nanostructures have been investigated by several workers [4–6].

1. Experimental

Uncapped GaAs quantum dots and quantum rings were grown with droplet epitaxy onto an epitaxial (001) AlGaAs layer on the top of the GaAs substrate in a conventional solid source MBE system. To obtain quantum dots, the sample was cooled down to 200 °C after the growth of the AlGaAs layer. Then $\theta = 3.75$ ML gallium was deposited with a flux of 0.19 ML/s without arsenic flux. After gallium deposition we waited 60 s still without arsenic ambient pressure, followed by a processing under an arsenic pressure of 6.4×10^{-5} Torr for 120 s. Then the samples were annealed at 350 °C temperature under the same arsenic pressure for 10 minutes. The quantum ring growth process was somewhat different, the annealing was carried out at 300 °C at a substantially lower arsenic pressure of
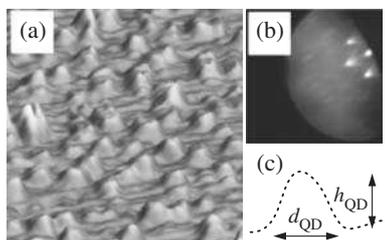
Fig. 1. (a) AFM picture of QDs, the density is 3.6×10^{10} cm^{-2}. (b) The RHEED pattern of the surface with QDs. (c) A typical AFM line scan across a QD, the height and base diameter are 7 and 40 nm respectively.
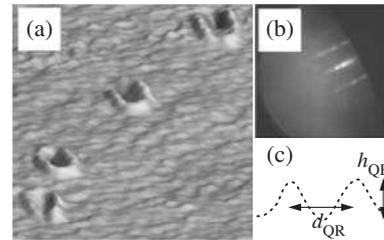
Fig. 2. (a) AFM picture of QRs, the density is 1.5×10^9 cm^{-2}. (b) The RHEED pattern of the surface with QDs. (c) A typical AFM line scan across a QR, the height and the mean base diameter are 2 and 60 nm respectively.

4×10^{-6} Torr. The growth of the quantum structures were monitored continuously in the [1–10] direction using RHEED. More details on the sample preparation were published in our earlier work [9]. After the growth of quantum objects, atomic force microscopy (AFM) and photoluminescence (PL) measurements were carried out.

Temperature dependence of photoluminescence (PL) was measured on the grown quantum structures between 4 and 300 K using a Janis refrigerator system. The PL was excited with the 488 nm line of an Ar$^+$ ion laser with radiated power of 47 mW. The chopped light beam was focused to the sample with a spot diameter of about 200 μm. The PL system consisted of an ORIEL Cornerstone monochromator, a Si avalanche photodiode detector and a Stanford DSP lock-in amplifier. The resolution was better than 0.5 nm.

2. Results and discussion

AFM pictures of GaAs quantum dots and quantum rings on the surface of the top GaAlAs layer of the GaAlAs/GaAs structure are shown in Figs. 1 and 2.

The shapes of the quantum dots were truncated pyramids with mean lateral dimensions and height of about 50 and 5 nm respectively. The mean diameter and height of quantum rings were about 60 nm and less than 5 nm respectively.

Representative PL spectra of quantum rings are shown in Figs. 3 and 4.

While in the PL spectra of QDs (not shown here) only the peaks belonging to GaAs could be identified, quantum confinement effects were observed in the PL spectra of quantum rings. Two peaks can be seen above the GaAs bandgap which are ascribed to transition between the first quantized level in
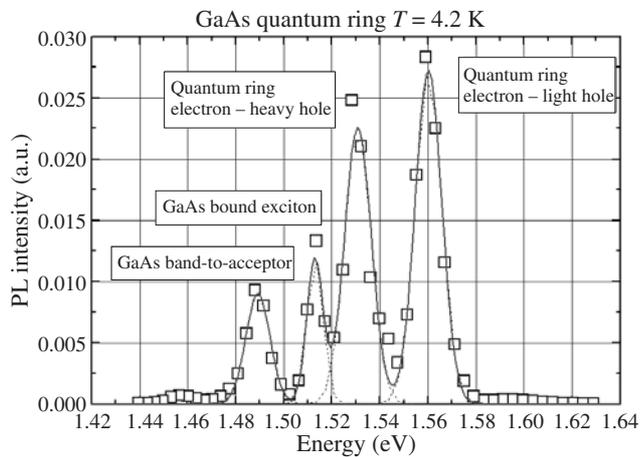
Fig. 3. PL spectrum of a QR sample at lHe temperature, exhibiting the fingerprint of quantized levels beside the lines characteristic to GaAs.
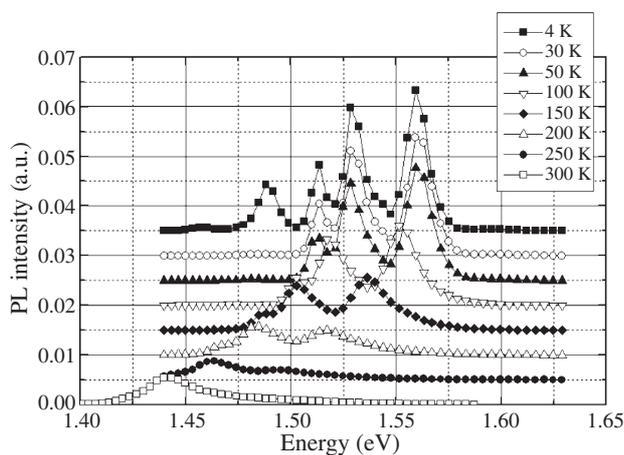
Fig. 4. Temperature dependent PL spectra of QRs. The evolution of the positions of the lines belonging to the QRs follows the temperature dependence of the GaAs bandgap.

References

[1]   N. Koguchi *et al*, *J. Cryst. Growth* **1** 1, 688 (1991).
[2]   K.Watanabe *et al*, *Jpn. J. Appl. Phys*. **39**, L79 (2000).
[3]   T. Mano *et al*, *Nano Lett.* **5**, 425 (2005).
[4]   Z. Gong *et al*, *Appl. Phys. Lett.* **87**, 093116 (2005).
[5]   K. Kuroda *et al*, *Appl. Phys. Lett.* **88**, 124101 (2006).
[6]   Y. Yamagiwa *et al*, *Appl. Phys. Lett.* **89**, 113115 (2006).
[7]   D. Leonard *et al*, *Appl. Phys. Lett.* **63**, 3203 (1993).
[8]   V. Bressler-Hill *et al*, *Phys. Rev. Lett.* **74**, 3209 (1995).
[9]   C. Heyn *et al*, *Appl. Phys. Lett.* **90**, 203105 (2007).
[10] R. Wiswanatha *et al*, *Phys. Rev. B* **72**, 055333 (2005).

the conduction band to the firs quantized levels in the heavy and light hole bands.

The above observations can be explained as follows. The nanostructures reported in the literature are either self-supported or confined in another materiel. Our uncapped structures are located between these two extremes. According to theoretical calculations in [10] a perceptible change in the bandgap of GaAs begins under the diameter of about 7 nm. The base diameter of QDs investigated here was much larger than, and their height was comparable with this value. Therefore quantum effects can hardly be expected. On the other hand the height of the QRs is significantly less than this value and energy quantization emerges.

To sum up uncapped GaAs quantum dots and quantum rings were grown by droplet epitaxy onto AlGaAs surfaces. Photoluminescence spectra were measured, and in the case of quantum rings two quantized peaks were found.

Acknowledgements

Investigation of electrical properties of individual GaAs-nanowires by scanning probe microscopy methods

M. S. Dunaevskii[1], P. A. Alexeev[1], M. Lepsa[2], G. Cirlin[1,3], Y. Samsonenko[1,3], M. Tchemycheva[4] and A. N. Titkov[1]

[1] Ioffe Physical-Technical Institute, St Petersburg, Russia
[2] Institute of Bio- and Nanosystems, Forschungszentrum Jülich 52428 Jülich, Germany
[3] St Petersburg Academic University, St Petersburg, Russia
[4] Institut d'Electronique Fondamentale, Université Paris-Sud, CNRS, France

Abstract. I-V curves of individual GaAs nanowires have been measured with scanning probe microscopy methods. The surface of these nanowires was covered either with a layer of natural oxide or with a layer of SiO_x. It was discovered a sharp, for two or three orders of magnitude, asymmetrical weakening of the currents in the I-V curves for GaAs-nanowires covered with SiO_x coating. The observed effect was partially attenuated when nanowires were illuminated by the red laser light from the energy region of interband absorption of GaAs.

Introduction

In the last decade, there was considerable interest addressed to the growth and use of semiconductor nanowires (NWs). These objects are crystalline rods with a diameter of 30 to 100 nm and lengths up to several microns. Nanowires have good prospects for use in a variety of new applications such as: the creation of optoelectronic light-emitting devices on silicon substrates [1], transistors and diodes [2], electron emitters [3], chemical and biological sensors [4], etc.

The structural properties of the NWs are studied in details, particularly by the methods of transmission electron microscopy. Less studied are electrical properties of NWs, in particular, mechanisms of doping of NWs. In general, the electrical properties of NWs are determined by: (i) the type and level of doping, (ii) the spatial distribution of impurities, (iii) the presence of p-n junctions (or heterojunctions), (iv) the influence of surface states, (v) the presence of elastic strain, etc.

1. Experimental results and discussion

In this work it is proposed the scanning probe microscopy (SPM) method of current-voltage measurements (I-V curves) using conductive SPM-probe positioned at the top of NWs. Indeed, conductive SPM-probe can be used as a small electrode, which can be placed into the different positions at the surface. When placed at the top of the individual NW (see Fig. 1a) it is possible to measure the current passing through the NW.

It was fulfilled a series of experiments on arrays of n-type GaAs-NW with different lengths and diameters. The surface of these NWs was covered either with a layer of natural oxide (Fig. 1a (1)) or with a layer of SiO_x (Fig. 1a (2)). At the Fig. 1b there can be seen n-type I-V curves measured on GaAs-NWs. It was investigated the influence of surface states on the electrical properties of NWs. It was discovered a sharp, two or three orders of magnitude, asymmetrical weakening of the currents in the I-V curves (see Fig. 1b) for GaAs-NW covered with SiO_x coating. The observed effect is partially attenuated when NWs were illuminated by the red laser light from the energy region of interband absorption of GaAs. The possible explanation of the observed effect could be the following: covering the GaAs-NW with SiO_x layer should lead to an increase of the density of
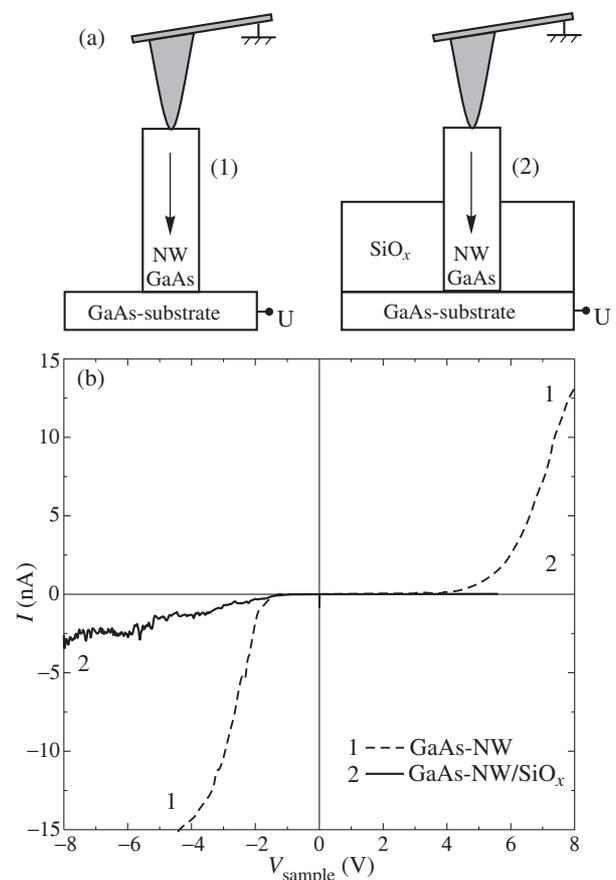
Fig. 1. (a) — Scheme of experiment and (b) — Current-voltage characteristics measured on GaAs-NW (1) and GaAs-NW covered with SiO_x (2).

surface states and the number of carriers escaped to the surface from the bulk of the NW.

Also, electrons at surface states may drift under the applied external electric field and could be accumulated at the interfaces encountered or oxide traps. Electric field of localized charges can cut-off the conduction channel in the NW, which explains the effect of reducing the current in buried NW. In thicker NWs effect may be stronger due to increased surface area and increased amount of surface trapped carriers. Illumination of
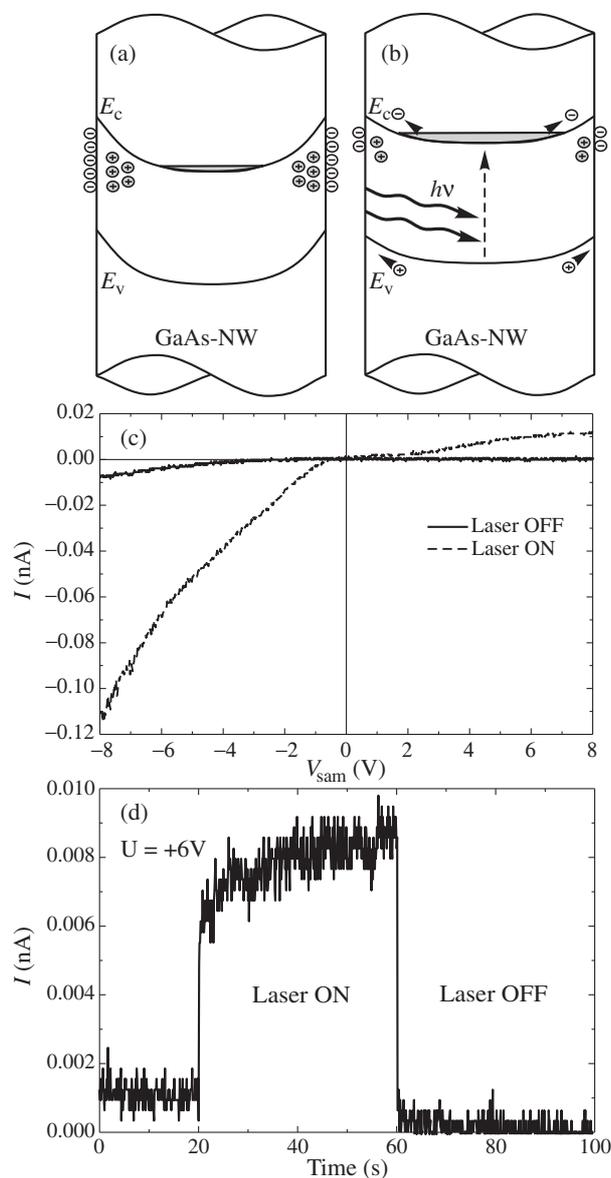
Fig. 2. a,b) — Illustration of light induced band bending change; (c) — I-V curves measured on NW in darkness and when illuminated by red laser; (d) — Change of the NW current when exposed to red laser light.

GaAs-NW with red laser light leads to depopulation of surface-state carriers and should weaken the observed effect.

Also, in this work it was studied the effect of light on the conductivity of the GaAs-NW. It was discovered the effect of the induced photocurrent in a GaAs-NW. When irradiated with light of the red laser with a wavelength = 630 nm current-voltage characteristics of the NWs significantly changed. When illuminated the slope of the I-V curve, which corresponds to the conductivity of NW, has increased by 10–30 times (Fig. 2c,d). Such a strong effect can be attributed to a specific feature of the NW — the "vicinity" of the surface. Indeed, the characteristic radius of GaAs-NW $R = 30-50$ nm is comparable with the characteristic thickness of the surface band bending zone in doped semiconductors. The illumination decreases band bending due to the effect of the birth and separation of electron-hole pairs (Fig. 2a,b) in the surface field. So, the exposure to light increases the carrier concentration near the surface of the

NWs. In addition, the illumination should reduce the number of charges localized at the NW-oxide boundary states, which should lead to increased values of the currents flowing through the NWs. The important role of surface charge states is also indicated by the fact that stronger currents associated with the light were observed in thin GaAs-NW ($d = 85$ nm), while in thicker GaAs-NW ($d = 120$ nm) the effect was weaker. Thus, all of the above may explain the increase of conductivity of GaAs-NW when illuminated by the red laser light. Additionally, the experiments were fulfilled to study the effect of illumination by the infrared laser (with the wavelength = 1.3 μm) on the conductivity of the GaAs-NW. In the latter case, when $E_{photon} > E_g$ the effect was not observed.

References

[1] Y. Li, J. Xiang, C.M. Lieber *et al*, *Nanoletters* **6**, 1468 (2006).
[2] M.T. Bjork, B.J. Ohlsson, L. Samuelson *et al*, *Appl. Phys. Lett.* **80**, 1058 (2002).
[3] R.B. Markus, T.S. Ravi, T. Gimmer *et al*, *Appl. Phys. Lett.* **56**, 236 (1990).
[4] C.M. Lieber *et al*, *Nature Biotechnology* **23**, 1294 (2005).

XPS spectra and surface characterization of nanostructured titanium implants

D. M. Korotin[1], S. Bartkowski[2], E. Z. Kurmaev[1], M. Neumann[2], E. B. Yakushina[3], R. Z. Valiev[3] and S. O. Cholakh[4]

[1] Institute of Metal Physics, Ural Branch of RAS, 620990 Ekaterinburg, Russia
[2] Faculty of Physics, University of Osnabrueck, 49069 Osnabrueck, Germany
[3] Institute of Physics of Advanced Materials, Ufa State Aviation Technical University,
12 K. Marx str.,450000 Ufa, Russia
[4] Ural Federal University, 620002 Ekaterinburg, Russia

Abstract. The results of XPS measurements of nanostructured (*ns*) and coarse-grained (*cg*) titanium are presented. For each set of measurements ion etching was performed and by such a way a full information about the surface and the near-surface layers of *ns*-Ti and *cg*-Ti is obtained. XPS Ti 2p show that the surface of both Ti-samples are covered by thick TiO_2 layer. The Ar^+-ion etching changes the near-surface composition of oxide layers increasing the contribution of TiO (Ti^{2+}). In accordance with electronic structure calculations, the Ti^{2+} substitution of Ca^{2+} in hydroxyapatite (the main component of tooth and bones) is thermodynamically favored and provides excellent biocompatibility of nanostructured Ti.

Introduction

Commercially pure titanium (*cp*-Ti) is widely used for a range of medical applications such as orthopedic and dental implants [1]. However, the mechanical strength, notably fatigue strength of *cp*-Ti is poorer to that of commonly used titanium alloys [2]. It is found that formation of a submicron or nano-scale grain structure with help of severe plastic deformation (SPD) can be used to enhance the strength of bulk coarse-grained (*cg*-Ti) by the formation of a submicron or nano-scale grain structure [3]. As result, the tensile strength of *cg*-Ti is increased from 700 to 1240 MPa, exceeding that for annealed Ti–6Al–4 V (940 MPa). SPD-treatment of *cg*-Ti allows to avoid the use of expensive (and often cytotoxic) alloying elements, as the required strength can be obtained by grain refinement, rather than by solid solution strengthening and precipitate hardening. It seems to be very important along with the improvement of mechanical properties to establish whether nanostructured titanium remains surface properties of coarse-grained titanium, well-acceptable for biomedical applications? In connection with this we have performed in present paper XPS study of the surface of *ns*-Ti and compared the obtained results with those of *cg*-Ti.

1. Experimental

The XPS measurements were performed on *cg*-Ti and *ns*-Ti samples using a Perkin Elmer PHI 5600 ci Multitechnique System with monochromatized Al Kα radiation (FWHM=0.3 eV). The binding energies were determined using the Au $4f_{7/2}$ core level (E_b(Au $4f_{7/2}$)=84.0 eV) as a reference. For each set of XPS measurements ion etching (with Ar^+ ions) was performed step by step with intervals of few minutes (from 1 to 84 min).

2. Results

XPS wide scans of *cg*-Ti and *ns*-Ti are presented in Fig. 1a. The XPS analysis shows that both implant surfaces consist of titanium, oxygen and carbon. As seen, O*1s*/C*1s* intensity ratio estimated from XPS survey spectra is increased from 1.36 to 1.69 after SPD treatment of *cg*-Ti. Therefore the SPD processing reduces the contamination of *ns*-Ti surface with hydro-
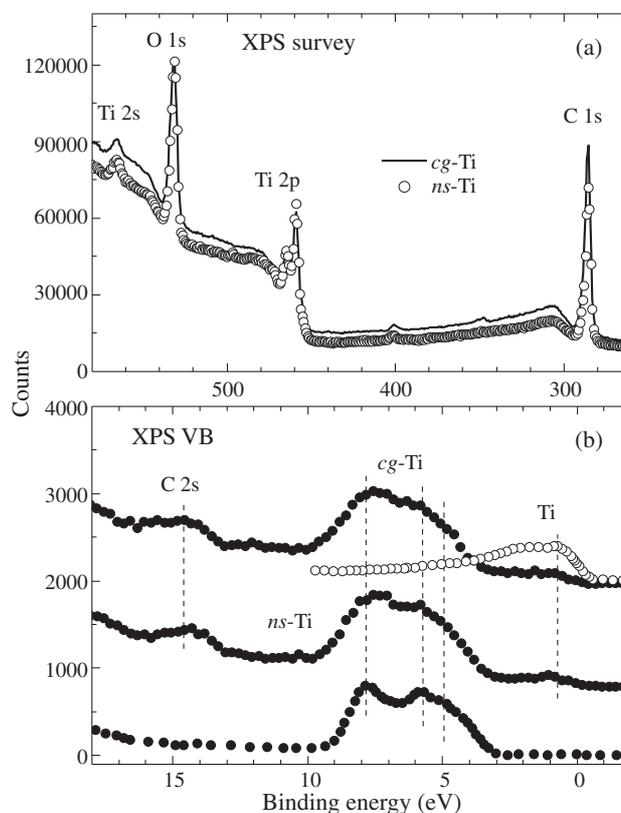
Fig. 1. XPS wide scans (a) and valence bands (b) of nanostructured and coarse-grained Ti.

carbons, and increases the surface energy and potential biocompatibility of the Ti-implant. In Fig. 1b the XPS valence bands of *cg*-Ti and *ns*-Ti are presented. They consist of five peaks located at 14.6, 7.8, 5.7, 5.0 and 0.7 eV. In agreement with previous studies we assign the feature located at 7.8 eV to O *2p*–Ti *3d* hybridized states while the 5.7 and 5.0 eV features have mainly O *2p* character [4]. One can see that the ratio of the peaks located at 7.8, 5.7 and 5.0 eV is found to be very
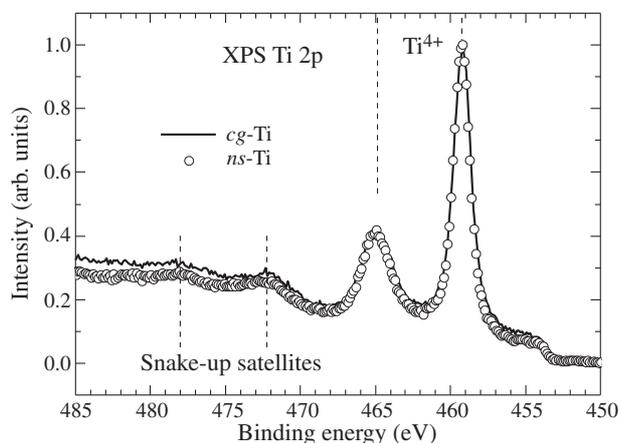
Fig. 2. High-energy resolved XPS Ti *2p*-spectra of *ns*-Ti and *cg*-Ti.


Fig. 3. XPS Ti *2p* of *ns*-Ti and *cg*-Ti in dependence of time of etching. The contributions of TiO$_2$, TiO and Ti metal constituent spectra correspond to optimal fitting of superimposed spectra to experimental curves for *cg*-Ti.

similar to that of TiO$_2$. C *2s*-states are fixed at $E = 14.6$ eV and the peak at 0.7 eV can be attributed to a contribution of *3d*-states of metallic Ti [5]; the relative intensity of this peak is not changed after SPD processing.

The results of high-energy resolved XPS Ti *2p* measurements are presented in Fig. 2. As seen, the Ti $2p_{3/2}$ and Ti $2p_{1/2}$ peaks are located at 459.2 and 464.9 eV both for *cg*-Ti and *ns*-Ti and can be attributed to Ti^{4+}. No Ti^{3+} shoulder at lower binding energy on the Ti $2p_{3/2}$ peak is detected, suggesting that all samples have a stoichiometric TiO$_2$ surface. As seen, XPS Ti *2p* spectra consist of high-energy shake up satellites at 477.8 and 472.4 eV which are typical for TiO$_2$ [7]. This is in agreement with theoretical thermodynamics which specify that the free energy of formation of TiO$_2$ is favored over other titanium oxides [8]. Therefore we can conclude that upon exposure to air the surface of *cg*-Ti and *ns*-Ti is covered with a TiO$_2$ film. This passive film protects the titanium surface from corrosion.

Ar$^+$ ion etching (Fig. 3c) strongly modifies the surface composition of the Ti oxide layers from domination of TiO$_2$ for untreated *cg*-Ti and *ns*-Ti (Fig. 3a) to TiO for ion etched *cg*-Ti and *ns*-Ti (after 84 min) (Fig. 3c). For an intermediate time of ion etching (39 min.) the superposition of TiO$_2$ and TiO contributions takes place (Fig. 3b).

We need to point out also that ion etching enhances the contribution of the Ti-metal signal compared to untreated *cg*-Ti and *ns*-Ti. The finding of a strong TiO (Ti^{2+}) contribution to the near-surface layers seems to be very important for understanding of biocompatibility of Ti based dental implants. According to a recent calculation of the electronic structure of Ti-substituted hydroxyapatite Ca$_{10}$(PO$_4$)$_6$(OH)$_2$ (the main building block of tooth enamel and bones) [6], the Ti^{4+} substitution and occupation is not thermodynamically favored while the divalent Ti substitution has a strong thermodynamic favorability.

3. Conclusion

To conclude we have performed a full surface characterization of nanostructured and coarse-grained Ti which includes the XPS measurements of core levels and valence bands. XPS Ti *2p*-spectra show that the surface of both Ti-samples is covered by thick TiO$_2$ (Ti^{4+}) oxide layer. It is found that the surface composition of Ti-oxides with is changed revealing increase of TiO contribution which provides the better biocom-

patibility of Ti implants due to substitution of Ti^{2+} for Ca^{2+} in hydroxyapatite.
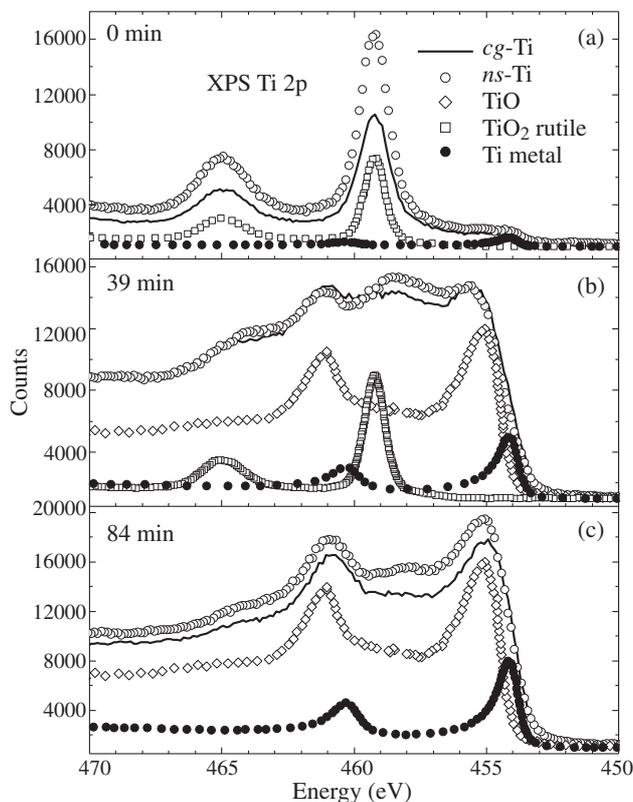
References

[1] X. Liu, P.K. Chu and C. Ding, *Mater. Sci. Eng.*, R: Rep. **47**, 119 (2004).
[2] H.J. Rack and J.L. Qazi, *Mater. Sci. Eng.*, C **26**, 1269 (2006).
[3] R.Z. Valiev, I.P. Semenova, V.V. Latysh, H. Rack, T.C. Lowe, J. Petruzelka *et al*, *Adv. Eng. Mater.* **10**, B15 (2008).
[4] U. Diebold, *Surface Science* Reports **48**, 53 (2003).
[5] H. Höchst, P. Steiner, G. Reiter and S. Hüfner, *Z. Phys. B Condensed Matter* **42**, 199 (1981).
[6] H.B. Jones, *Surface Science* Report **42**, 75 (2001).
[7] C.M. Chan, S. Trigwell and T. Ouerig, *Surf. Interface Anal.* **15**, 349 (1990).
[8] S. Yin and D.E. Ellis, *Phys. Chem. Chem. Phys.* **12**, 156 (2010).

The nonlinear optical properties of suspensions of dielectric α–Al$_2$O$_3$ nanoparticles. Theory and experiment

Y. Kulchin, V. Dzyuba and V. Milichko

Institute for Automation and Control Processes, FEB RAS, 690041 Vladivostok, Russia

Introduction

The purpose of this paper is to present an experimental study of nonlinear-optical response of suspension of dielectric Al$_2$O$_3$ nanoparticles in the weak laser radiation field (the intensity does not exceed 0.2 kW/cm^2) as well as the theoretical modeling of the nonlinear processes allowing to explain its causes.

1. Experimental details

To study the changes in optical characteristics of suspension of dielectric nanoparticles under the influence of weak laser radiation, we used the nanoparticles of dielectric α Al$_2$O$_3$ with a band gap of the bulk sample 7 eV. Shape and dimensions of the particles have been defined by atomic force microscopy and that were equal to 45:45:6 nm. The nanoparticles powder was used to prepare the suspension (0.13% volume particles concentration) in the immersion oil, which was placed in a quartz cell with dimensions 5:18 mm.

To investigate the processes of radiation refraction in the suspension which are characterized by intensity redistribution in the cross-section of passing laser beam we constructed the experimental setup (Fig. 1). In the experiments we used the solid-state sources of continuous linearly polarized laser radiation at wavelengths between 532 and 442 nm with a Gaussian intensity distribution, whose maximum power is 22 and 35 mW, respectively.

The standard z scan method was used for studying the effect of a weak laser radiation on the complex refractive index of the nanoparticles suspension. Z scanning feature in our experiment is that the maximum intensity of sources of continuous laser radiation did not exceed 0.24 and 0.09 kW/cm^2 for radiation with wavelengths 532 and 442 nm, respectively. Such intensity at least is less than four orders of intensities, which are widely used in most experimental works [1,2]. Z scan of weak continues laser radiation doesn't give the information about the specific cause of the changes of optical properties of nanoparticles suspensions, but gives the information about the combined effect of all possible physical factors. Thus, in this paper, we have to separate the nonlinear effects in a suspension of nanoparticles on thermal effects in the matrix.

The weak laser radiation allows excluding the organic ma-
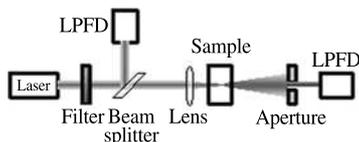
Fig. 1. Experimental setup for registration the integral and axis output power and for z scan experiments. LPFD is low-power photodetector of continuous radiation. Laser is semiconductor source of coherent radiation at wavelengths 532 and 442 nm.

$P_\text{in} = 6$ mW $P_\text{in} = 9$ mW
$P_\text{in} = 13$ mW $P_\text{in} = 16$ mW
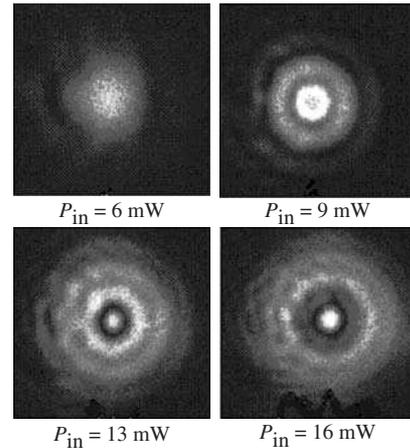
Fig. 2. Experimental results of radiation refraction in suspension, the profilometor photo of intensity distribution of wavelength 532 nm.

trix breakdown arising in the irradiation of pulsed light with the intensity 10 MW/cm^2 and eliminating the strong heating of organic matrix and the strong scattering of radiation. The limit of using radiation intensities is explained by strong scattering in the matrix under the action of heat and this obliges us to separate the nonlinear effects in the suspension of thermal effects in the matrix.

2. Results and discussion

From the results of determining the intensity distribution in the cross-section of output beam can be seen that the output power of paraxial part of beam (Fig. 2) has a pronounced nonlinear dependence.

The z scan with closed aperture [3] results showed the presence of nonlinear additions to the refractive index. The additive to the refractive index for dielectric nanoparticles suspension behaves non-monotonically for the two wavelengths depending on the input power value, hence the intensity at the focal point.

The z scanning with open apertures results did not show the presence of nonlinear absorption at a wavelength of 532 nm both in oil and in nanoparticles suspension. However, nonlinear absorption occurs in the immersion oil under the action of laser radiation at wavelength 442 nm. Thus, the dependence of the nonlinear additive to the refractive index as a function of input power of radiation was built by means of z scan results (Fig. 3). The experimentally calculated values of that additive are in the range $10^{-4}-10^{-5}$ and this is consistent with the theoretically calculated values for materials with similar electronic structure for these wavelengths [4].

As in the work the transmission spectrum of nanoparticles array was investigated (Fig. 4). It showed that nanoparticles suspended in oil have a broad absorption band with different
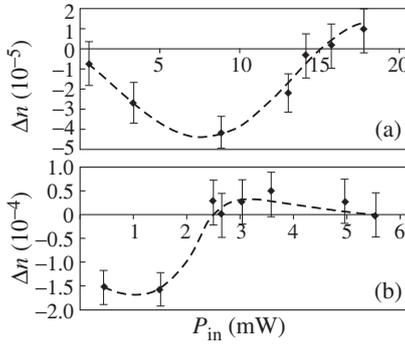
Fig. 3. The dependence of additive to refractive index on input power in nanoparticles array: a) 532 nm, b) 442 nm. Curves were obtained by subtracting the curve Δn for suspension of Δn for immersion oil.
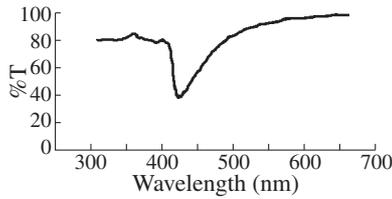
Fig. 4. Transmission spectrum of suspension α Al$_2$O$_3$ nanoparticles in immersion oil. Curve was obtained by subtracting the T spectrum for suspension of T spectrum for immersion oil.

densities of permitted states in the visible wavelength range [5]. It is in the range of using radiation frequencies that the nonlinear optical response is occurring.

3. Theoretical results

The theoretical description of the studied dielectric nanoparticles suspensions in the liquid matrix is based on the following assumptions: we assume that the used matrix is isotropic and has a linear optical properties in a limited spectral range, the concentration of nanoparticles are so small that we can neglect interparticle interaction. The real part of complex refractive index of nanoparticles suspensions in the field of a linearly polarized laser radiation, calculated in this paper, is of the form:

$$n(\omega, I) = n_0 + \sum\sum\left\{\left[1 - \frac{(I/I_{\mathrm{S}})\,\Gamma_{ng}^2}{(\omega - \omega_{ng})^2 + \Gamma_{ng}^2\,(1 + I/I_{\mathrm{S}})}\right]\right.$$

$$\left.\times\frac{A_{ng}\,(Q_1, Q_2)\,(\omega - \omega_{ng})\,\Delta\rho_{ng}^0}{(\omega - \omega_{ng})^2 + \Gamma_{ng}^2}\right\}$$

and

$$A_{ng}\,(Q_1, Q_2) = \frac{2\pi N}{\hbar n_0}\left[\frac{1}{3}|p_{ng}|^2 + Q_1\left(|p_1^{ng}|^2 - |p_2^{ng}|^2\right)\right.$$

$$\left. + Q_2\left(|p_3^{ng}|^2 - |p_2^{ng}|^2\right)\right],$$

where $\Delta\rho_{ng}^0$ is the equilibrium population difference, I_{S} is a saturation intensity, p_{ng} is the photoinduced dipole moment and Γ_{ng} is the width of the electron transitions in the absorption zone.

Using this formula we can determine the behavior of the nonlinear additive to the refractive index (Fig. 5), which is explained by following competing processes: the dipole moment
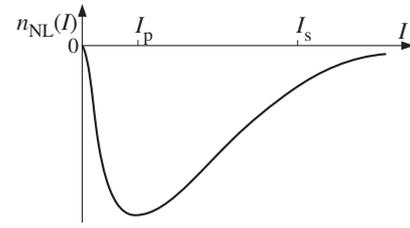
Fig. 5. Nonlinear part $n_{\mathrm{NL}}(I)$ of the suspension refractive index $n(\omega, I)$.

increases with increasing input radiation power, but the population difference between the allowed energy reduces.

It was theoretically found that the sign of the nonlinear additive to the refractive index of the dielectric nanoparticles suspension changes in the frequency range as follows:

Fig. 6. The dependence of nonlinear additive to refractive index on the frequent ranges.

where ω_n is frequency of electron transition from defect levels to the border zone between the excitons and the quantum-size levels, $\omega_p = \omega_n - \frac{\Delta\omega_1 - \Delta\omega_2}{2}$ and $\Delta\omega_1$, $\Delta\omega_2$ are the width of the allowed energy levels in band gap and levels of quantum-confined states, respectively.

4. Conclusion

The low-threshold non-linear process of changing the refractive index of the dielectric nanoparticles suspension under the action of weak visible laser radiation was investigated in this paper. We calculated the numerical values of the nonlinear additive to the refractive index referring to the experimental curves. The transmission spectrum of nanoparticles array was obtained. This allowed us to reveal features of the energy spectrum of carriers. We proposed the theoretical description both the causes of the observed low-threshold nonlinearity and the behavior of additives to the refractive index depending on the intensity.

References

[1] Quandou Wang *et al*, *Encyclopedia of Nanoscience and Nanotechnology* **8**, 101 (2004).
[2] P. Prem Kiran *et al*, *Journal of Applied Physics* **96**, 6717 (2004).
[3] Eric W. Van Stryland, Mansoor Sheik-Bahae, *Characterization Techniques and Tabulation for Organic Nonlinear Materials*, 655–692 (1998).
[4] V.P. Dzyuba *et al*, *Technical Physics Letters* **36** (11), 973 (2010).
[5] Yu.N. Kulchin *et al*, *Fizika i Tekhnika Poluprovodnikov* **43** (3), 349 (2009).

Electronic structure of Ge(111)-(2×1) surface in the presence of doping atoms. Ab initio analyses of STM data

S. V. Savinov, A. I. Oreshkin, S. I. Oreshkin and V. I. Panov

Moscow State University, Department of Physics, 119992, Moscow, Russia

Abstract. We present the result of experimental low temperature STM and theoretical first principles investigations of the electronic structure of the Ge(111)-(2×1) surface in the presence of donor doping atom at certain position in the surface bi-layer of (2×1) reconstruction. The results of ab initio calculations prove that despite of only slight geometrical crystal lattice distortion the influence of doping atom reflects in the appearance of slit state in the band gap and in the spatial oscillations of LDOS in vicinity of foreign atom.

Introduction

Electronic properties on elemental semiconductors (in particular Ge) have attracted substantial interest since they were historically the first semiconductors applicable in the technology. The cleavage along (111) natural cleavage plane allows one to obtain surface with well known (2×1) type of reconstruction [1]. This surface can serve as the test bench for both experimental STM/STS studies of individual atomic defects, and theoretical modeling.

In 1980s, both photoemission studies [2] of doped Ge single crystals and theoretical calculations [3] have revealed the existence of separate π occupied and π^* nonoccupied p_z derived bands for the Ge(111) surface electrons. For heavily doped Ge a partial occupation of π^* band was observed [2], i.e. there can be some electrons *above* Fermi level. The Ge(111) surface band gap has been determined by means of STM and STS [5]. Until now, however, there have been no reports on the observations of effects directly related to the existence of nonoccupied surface states π^* band on the Ge(111)-(2×1) surface.

Recently we have reported on our investigation of the nonoccupied surface states on *in situ* cleaved Ge(111)-(2×1) surfaces by means of low-temperature STM/STS under UHV conditions. The presence of the nonoccupied surface states is observed to induce LDOS spatial oscillations in the vicinity of domain boundary or individual impurity atom on Ge(111)-(2×1) surface in the energy range where π^* states exist. Experimen-
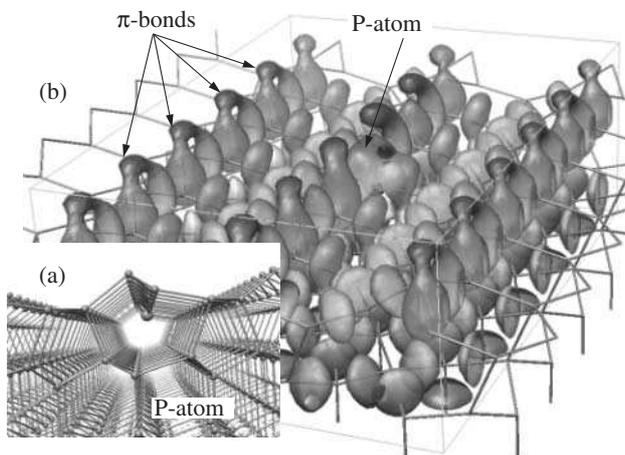
Fig. 1. a) The geometry of relaxed Ge(111)-(2×1) surface. P impurity atom is shown by big sphere. b) Spatial distribution of negative differential charge on Ge(111)-(2×1) surface around P impurity atom.
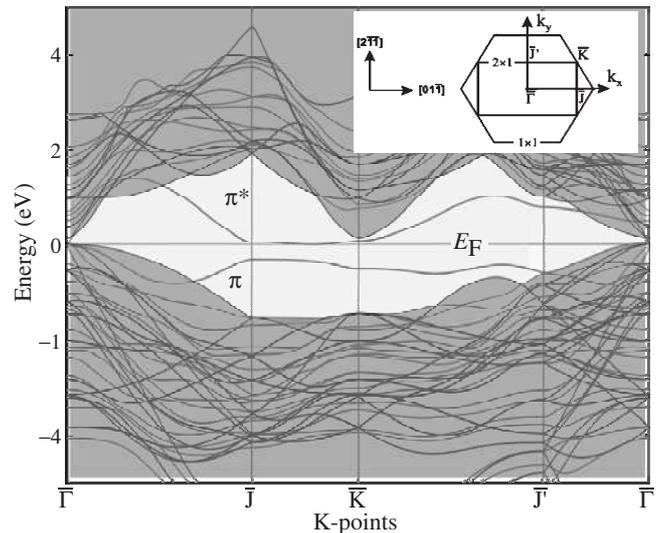
Fig. 2. Surface band structure of clean Ge(111)-(2×1) surface. Inset shows the relevant delails of Ge(111)-(2×1) surface model.

tal observation of quasi-1D surface screening around atomic defects on Ge(111)-(2×1) surface as well as the behaviour of impurity STM image on tunneling bias voltage were discussed in [8].

To clarify the physical nature of STM observed effects we have performed first principles calculations by means of DFT method in LDA approximation as implemented in SIESTA package [7]. Details will be published elsewhere. The use of strictly localized numeric atomic orbitals allows us to perform modeling of large surface cell, which amounts 4×21 cells of elementary 2×1 reconstruction (1512 atoms). The model structure consists of Ge(111)-(2×1) surface slab. The bottom surface Ge bonds are terminated with H atoms, and one Ge atom is substituted by phosphorus (P) atom. The geometry of the structure was fully relaxed, until atomic forces became less then 0.01 eV/Å. Afterwards the surface band structure and spatial distribution of LDOS were calculated.

1. Surface geometry, band structure and LDOS

The results of DFT modeling can be summarised as follows.

The atom of substitutional donor impurity P *does not* occupy the same place in the lattice as the Ge atom it substitutes, though the displacement is not very big (Fig. 1a). This is not unexpected, but at the same time we could not find in the literature any statement explicitly confirming this fact.

The model of Ge(111)-(2×1) surface reconstruction [1]
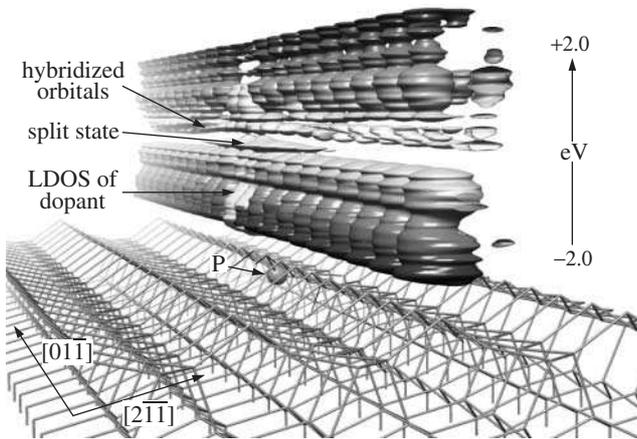
Fig. 3. Spatial distribution of surface LDOS.

with π-bonded chain rows can be directly confirmed by the analysis of spatial distribution of the system's charge. π bonds along chain rows are imaged as bridges in the distribution of negative differential charge (Fig. 1b).

Ge(111) surface reconstruction of (2×1) type causes the presence of occupied π and unoccupied π^* bands of surface states in the bandgap of projected bulk band structure. Surface states are highly dispersive along $\overline{\Gamma} - \overline{J}$ line of surface Brillouin zone. Bands are flat along $\overline{J} - \overline{K}$ line(Fig. 2). Worth noting that the bottom of π^* surface band is located in very close proximity to Fermi level, which in turn is aligned with the top of bulk valence band in case of Ge(111) surface.

The most important result of our DFT modeling relates to determination of spatial distribution of LDOS above the surface. Namely this quantity is relevant for STM observations interpretation. In the DFT framework surface LDOS can be expressed as

$$\rho\left(\overrightarrow{r_{x,y}},\ \mathrm{eV}\right) = \sum_i \left|\Psi(\overrightarrow{r_{x,y}})\right|^2 \tilde{\delta}\left(E - E_i\right)\Big|_{z=\mathrm{const}},$$

where Ψ are Khon–Sham wavefunctions, $\tilde{\delta}$ is smearing function and summing is evaluated at certain height above surface. This way we can calculate and plot surface LDOS $\rho(x, y, \mathrm{eV})$ (Fig. 3). To the best of our knowledge this is the first time when this type of data representation is used.

The LDOS distribution has quasi-1D character. Areas with high LDOS values are *completely localised above* upped π-bonded rows of (2×1) reconstruction, while low LDOS areas are located in between. This leads to STM imaging of only any other surface π-bonded row [5].

STM image of (sub-)surface impurity on Ge(111)-(2×1) surface looks (very roughly speaking) like quasi-1D protrusion at negative tunneling bias and as a depression at positive bias [8]. As it can be seen from Fig. 3 there is a state in the bandgap split off the conduction band. It is located just below the Fermi level. So, at negative bias it gives rise to excessive tunneling current above upper π-bonded row of (2×1) reconstruction. Its influence vanishes as bias goes deeper into filled bulk valence band. More detailed analysis reveals that split state originates from P donor impurity atom localised state.

Atomic orbitals of Ge atoms next to impurity atom are strongly hybridised in the bias voltage range, where π^* surface states band exists. On Fig. 3 it looks like some kind of upward "band bending". This results in decreasing of LDOS
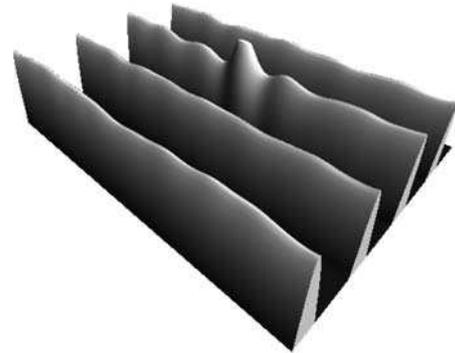
Fig. 4. Spatial oscillations of surface LDOS in vicinity of P donor impurity atom.

above upper π-bonded row in this range of positive bias, explaining the behaviour of impurity STM image.

In the DFT framework the contributions from different atomic orbitals and/or atoms to Khon–Sham wavefunction (KS WF) can easily be separated. This procedure does not have deep physical meaning, but allows to see, for example, the localization of impurity atom's WF. The illustration is given on Fig. 3, where contribution from atomic WF of P impurity atom is shown. Impurity WF are localized within two or three unit cells from impurity itself. We would like to note that we can readily analyze spatial localization of KS WF, and for some range of positive bias (range where π^* surface states band reside) KS WF are indeed localized near the surface.

Strong hybridization of atomic orbitals has one lot more important consequence. It leads to the appearance of spatial oscillations (SO) of surface (i.e. as measured by STM) LDOS in vicinity of impurity atom (Fig. 4). LDOS SO can be observed in a few atomic rows in vicinity of impurity atom.

The period of LDOS SO increases as tunneling bias increases in some range of positive bias.

This finding makes very important link between first principle description of solid state body and diagram technique based theoretical methods. The latter naturally predict the existence LDOS SO around atomic defects.

Acknowledgements

References

[1] C. Pandey, *Phys. Rev. Lett.* **47**, 1913 (1981).

[2] J.M. Nicholls, P. Maartensson, and G.V. Hansson, *Phys. Rev. Lett.* **54**, 2363 (1985).

[3] J.E. Northrup and M.L. Cohen, *Phys. Rev.* **B 27**, 6553 (1983).

[4] F. Bechstedt, A.A. Stekolnikov, J. Furthmuller, and P. Kackell, *Phys. Rev. Lett.* **87**, 016103 (2001).

[5] R.M. Feenstra, G. Meyer, F. Moresco, and K.H. Rieder, *Phys. Rev.* **B 64**, 081306 R (2001).

[6] D.A. Muzychenko, S.V. Savinov V.N. Mantsevich, N.S. Maslova, V.I. Panov *et al*, *Phys. Rev.* **B 81**, 035313 (2010).

[7] E. Artacho, D. Sanchez-Portal, P. Ordejon, A. Garcia and J.M. Soler, *Phys. Stat. Sol. (b)* 215, 809 (1999).

[8] P.I. Arseyev, N.S. Maslova *et al*, *JETP Lett.* **82**, 5, 312 (2005).

Modern achievements in X-ray spectra measurement and data treatment

M. D. Sharkov, K. Ju. Pogrebitsky, M. E. Boiko and S. G. Konnikov

Ioffe Physical-Technical Institute, St Petersburg, Russia

Abstract. A new schematic for an x-ray lab device to provide simultaneous performing two different x-ray experiments is assumed. The SAXS (Small-Angle X-Ray Scattering) technique application to determine the sample crystal perfection or grain sizes down to nanometers is described. SAXS measurement using two wavelengths to differ grain sizes from pore ones in the sample is suggested. A new EXAFS (Extended X-Ray Absorption Fine Structure) analysis method containing the procedure of the spectrum oscillations extracting based on the variation principle is developed. The limitations for the Fourier window width and position in EXAFS treatment are determined.

Introduction

Modern technologies require much information about the structure of materials. It is often important to obtain these data without destroying the samples. A solution of this task is provided, e.g., by x-ray analysis methods: EXAFS (Extended X-Ray Absorption Fine Structure) spectroscopy, SAXS (Small-Angle X-Ray Scattering), etc.

X-ray spectra can be measured at a synchrotron ring as well as at a special lab device. The synchrotrons provide high measurement rate and intensive beams but access to these facilities is difficult. In contrary to synchrotrons, the lab device allows one to measure x-ray spectra without much financial and time losses.

The SAXS technique is usually applied to detect clusters, small crystal and powder grains, and superlattice periodicity with sizes from several nanometers up to dozens of nm. The developed technique is sensitive even to far larger grains and scarcer superlattices, with sizes about 500 nm, as well as to nm sizes. Besides, the new technique provides a better precision in comparison with earlier practice.

Analysis of EXAFS spectra consists of several steps [1,2]. Some of them, like oscillations separation, are usually performed by methods which might lead to incorrect results. Other steps, like Fourier window definition, had not been studied until our recent works. The considered method is successful in solving these problems.

1. New "Butterfly" x-ray lab system

Figure 1 represents the standard x-ray lab device schematic [1]. The sample is irradiated by x-ray photons. Some of them are absorbed by the atoms of the sample. Other incident photons leave the sample surface for the surrounding vacuum and may be registered [2].

Our idea is to use the both windows of the x-ray source. This two-wing construction ("Butterfly") allows one to perform two experiments (e.g., measuring of XAFS and SAXS) simultaneously at a unique device.

2. SAXS measurement and analysis

To determine the perfection of a single crystal, Raman spectroscopy or observation of the x-ray diffraction rocking curve broadening are used ordinarily. Applying of these techniques meets the limitations connected with optical spreading of the
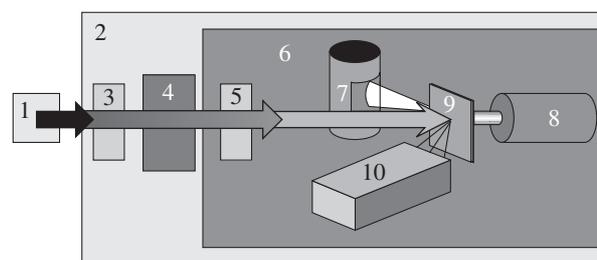
Fig. 1. A typical x-ray lab device schematic. Here 1 is X-ray generator, 2 is spectrometer vacuum volume, 3 is entrance slit, 4 is monochromator, 5 is exit slit, 6 is sample shield, 7 is x-ray detector, 8 is transmission x-ray detector, 9 is sample, 10 is channeltron.

light beam and of the investigated region of the crystal. Besides, rocking curve broadening is influenced by stresses in the sample and temperature factors.

The results of the x-ray porometry (those are the relations of the masses — not the sizes — for random pores and clusters) have been compared with the ones of the small-angle x-ray spectroscopy which is the way to detect directly the sizes of pores and clusters in the sample. X-rays of two and more different wavelengths may be used to avoid the Babinet uncertainness, i.e. to differ the pore sizes from the domain ones.

For example, a SiC sample has been investigated via the SAXS method [3]. SAXS pictures show smaller domains in the sample to tend to merge and form larger agglomerates in annealing, this fact corresponding to the theory.

3. EXAFS analysis

The new EXAFS spectrum analysis technique is developed [1,4]. It is assumed that EXAFS oscillations are extracted by the method based on the variation principle. The idea to extract the spectrum oscillations is to suggest a functional which is minimized by the sought smooth EXAFS component [4]. The view of the appropriate Euler-Lagrange equation is

$$\left(\frac{d^2}{dE^2} - C^2 \right) \mu_0 = C^2 \left(A - \mu \right)$$

with two parameters A and C. The boundary conditions of the first type are input for the task to be unambiguous.

The dependence of EXAFS treatment results on Fourier window limits has been studied for the spectra of some metals (V, Cr, Co, Cu) [1,5]. The most correct analysis results have appeared to be obtained when the bottom FT window limit is
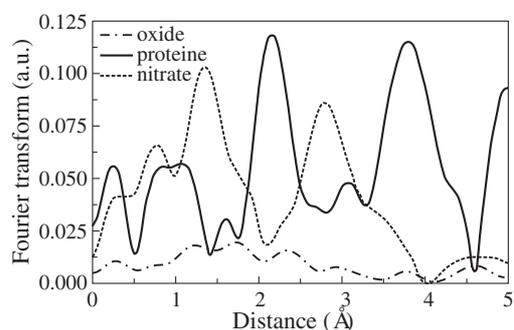
Fig. 2. FT of Cu K edge EXAFS for ceruloplasmin sample. Also the FT of Cu_2O and $Cu(NO_3)_2$ [7] are shown.

chosen between 40 and 80 eV above the absorption edge, and the Fourier window width is between the values of 300 and 700 eV.

Particularly, the human protein ceruloplasmin EXAFS spectrum has been treated by the described method. The protein molecule is known [6] to contain several thousands of atoms, and only 6 Cu within them. Nevertheless, the spectrum was obtained at the STAR lab device (Samsung Inc., Suwon, South Korea). Fig. 2 represents the results of EXAFS analysis for this spectrum.

The comparison of the Fourier transformed EXAFS oscillations for the protein, oxide, and nitrate allows one to formulate a hypothesis that the closest surrounding of Cu atoms in the protein structure are possible to be anions with the filled external electron shell (i.e. O^{2-}). The hypothesis [6] about the triangle of three Cu atoms with edges about 4 Å also seems to be valid.

Acknowledgements

References

[1] K.Ju. Pogrebitsky, M.D. Sharkov. *Semicond.* **44** 7, 723 (2010).

[2] *X-Ray Absorption: Principles, Applications, Techiniques of EX-AFS, SEXAFS, and XANES*, Vol. 92. Edited by D.C. Koningsberger and R. Prins. (Eindhoven, The Netherlands: Eindhoven University of Technology, N.-Y.) Chichester-Brisbane-Toronto-Singapore: John Wiley & Sons Inc., 673 p., 1988.

[3] M.E. Boiko, K.Ju. Pogrebitsky, M.D. Sharkov, A.P. Morovov, M.G. Vasin. *Proc. of the 8th PPXRD*, Glasgow, UK, 2009; M.E. Boiko, *Proc. of the XI International Conference on Small-Angle Scattering*, Upton, NY, USA, 1999.

[4] M.D. Sharkov, K.Ju. Pogrebitsky, S.G. Konnikov. *Tech. Phys.* **52** 8, 1089 (2007).

[5] M.D. Sharkov, K.Ju. Pogrebitsky, M.E. Boiko. *Proc. of the Advanced Research Workshop "NanoPiter-2010"*, St Petersburg, Russia, 2010.

[6] P. Bielli, L. Calabrese. *Cell. Mol. Life Sci.* **59**, 1413 (2002).

[7] G. Martens, P. Rabe, N. Schwentner, A. Werner. *Phys. Rev. Lett.* **39**, 1481 (1977).

Raman spectroscopy study of polymorph structure of GaAs nanowires

I. V. Shtrom[1,3], S. V. Karpov[1], M. B. Smirnov[1], B. V. Novikov[1], A. N. Smirnov[2], G. E. Cirlin[1−4], A. D. Bouravleuv[2,3] and Yu. B. Samsonenko[2−4]

[1] St Petersburg State University, Physical Faculty, St Petersburg, Russia
[2] Ioffe Physical-Technical Institute, St Petersburg, Russia
[3] St Petersburg Academic University, St Petersburg, Russia
[4] Institute for Analytical Instrumentation RAS, St Petersburg, Russia

Abstract. Raman spectra of GaAs nanowires grown on silicon substrates are presented. New spectral features not existing in the spectra of the zinc-blend polymorph (typical of the bulk material) are found. Their appearance is ascribed to co-existence of other crystalline phases: the 2H polymorph (isomorphous to wurtzite) and the 4H polymorph.

At normal pressure, the bulk semiconductor GaAs grows in a stable crystal structure isomorphous to zinc-blende — ZB. However, in mesoscopic size range characteristic for quantum points and nanowires (NWs), another polymorph of GaAs isomorphous to wurtzite (WZ) can also be stable [1]. Moreover, sometimes the polymorph transformation may result in formation of 4H-like structures [2]. Co-existence of the ZB and WZ structures in the GaAs NWs was recently confirmed by Raman [3,4] and photoluminescence [5] studies. No spectroscopic evidence for presence of the 4H segments was reported up to now.

1. Experimental

In this paper we represent Raman spectra of GaAs nanowires. The GaAs NWs were grown on Si(111) substrate during Au-assisted MBE technique [6]. Raman-spectra were recorded in the backscattering configuration by using the 514.5 nm line of an Ar^+ laser for excitation. The power of the incident light was about 200 mW (equivalent to 70 kW/cm^2). Raman spectra of GaAs NWs recorded in the $z(xx)\bar{z}$ geometry are shown in Fig. 1. Hereafter, z-axis is directed along the growth direction which corresponds to the [111] direction in ZB and to [0001] in WZ.

2. Result and discussion

Frequencies of fundamental vibrations of GaAs cover the interval from 0 up to 300 cm^{-1}. No Raman-active phonon modes of silicon Si substrate (see curve 1 in Fig. 1) fall into this interval. Thus they can be omitted. Several peaks detected in the spectral curves are labeled in Fig. 1 by italic figures. Their frequency positions are listed in Fig. 2. Two main peaks in Fig. 1 (labeled as 1 and 4) are well detectable at any excitation power. Unambiguously they can be attributed to the zone-centre TO and LO modes. Frequencies of these modes in bulk ZB phase are 271 and 293 cm^{-1} respectively [7]. Besides the TO and LO peaks, several additional Raman signals (labeled as 3 and 8) can be resolved in spectra shown in Fig. 1. Their origin can be explained in two ways. First explanation [8,9] relates two main additional Raman peaks (200 and 256 cm^{-1}) with scattering either on molecular vibrations of As$_4$ (210 and 255 cm^{-1} [10]), or on phonons of crystalline As, namely, on the double degenerate E_g mode (195 cm^{-1}) and the A$_{1g}$ mode (257 cm^{-1}) [11]. Alternatively, all observed additional Raman peaks can be assigned to fundamental phonon modes of different GaAs polytypes. For example, the peak 255 cm^{-1} was
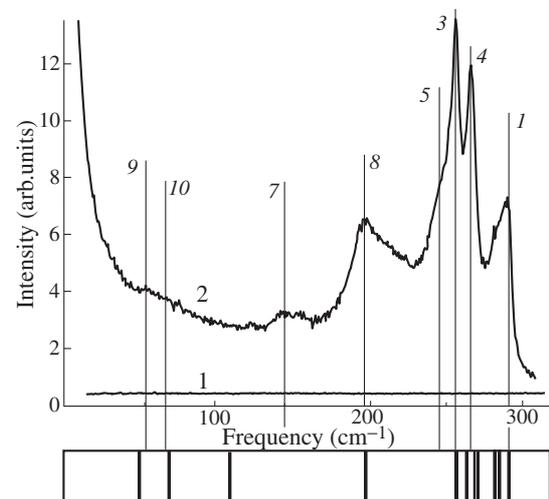
Fig. 1. A Raman-spectrum the sample with nanowires of GaAs, grown up on a silicon substrate. 1 — spectrum of substrate Si, $z(xy)\bar{z}$; 2 — NW GaAs, $z(xx)\bar{z}$; bottom part — possible frequency distribution of zone-centre modes of different GaAs polymorphs.

assigned to E_2-mode of WZ [4]. Similarly, peak 200 cm^{-1} can be related with Raman-active modes of 4H. Therefore it is suitable to discuss the selection rules for Raman scattering spectra of different GaAs polymorphs. Both WZ and 4H crystal structures are hexagonal and belong to space symmetry group C_{6v}^4(P6$_3$mc) with $Z = 2$ and $Z = 4$ respectively. Unit cell of WZ is twice bigger than elementary cell of ZB. Correspondingly, phonon branches of WZ along Γ-A direction can be represented as folded phonon branches of ZB along Γ-L. The folding scheme is shown in Fig. 2.

Unit cell of 4H is twice bigger than that of WZ; it corresponds to doubled c parameter. Correspondingly, the zone-edge A-phonons of WZ become zone-centre phonons in 4H structure. Some of them are Raman-active. In total, 24 fundamental modes of 4H are distributed irreducible representations of symmetry group as follows: $\Gamma = 4A_l(z) + 4B_l + 4E_1(x, y) + 4E_2$.

Frequency distribution and symmetry assignment of all fundamental phonons of three GaAs polymorphs are shown in Fig. 2. The folding representation is based on experimentally determined dispersion relation of cubic GaAs [7].

Crystal structures of the three polymorphs are different in the middle-range scale. This causes small differences in corre-
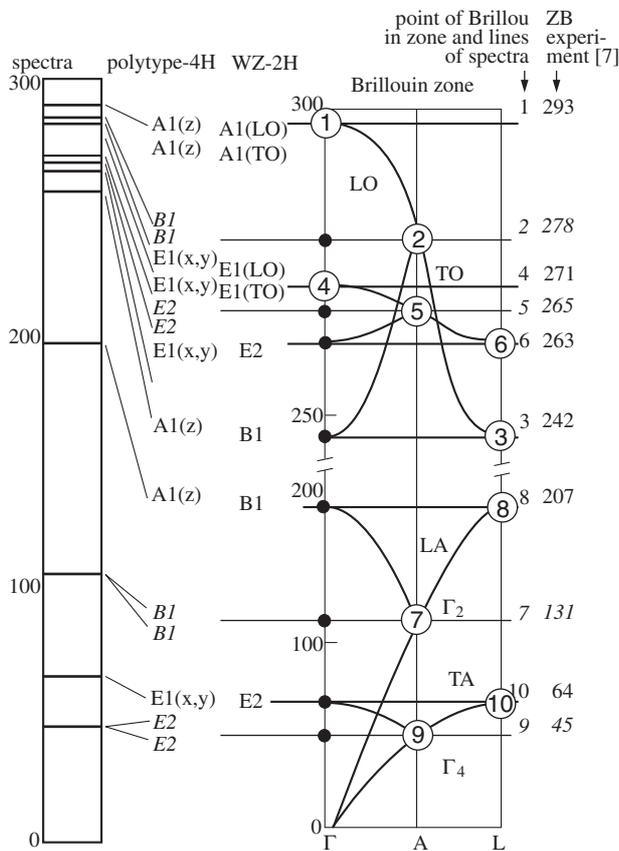
Fig. 2. Γ-L dispersion relation for ZB and correlation diagram between irreducible representations of ZB, WZ and 4H polytypes. Experimentally determined phonon frequency of ZB [7] are given on the right, frequency positions of observed Raman peaks are shown in the middle column.

sponding phonon frequencies. These differences are presented on Fig. 2 together with the correlation diagram connecting irreducible representations of ZB, WZ and 4H polytypes. In the same figure, the calculated frequencies are compared with frequencies derived from folding scheme based on experimental data [7].

It is necessary to notice that phonons which belong to representation B_1 in 2H structure are inactive in optical spectra. In the 4H structure they transform in A_1-phonons and become active both in Raman, and in IR spectra. Besides, Raman-spectrum of 4H includes new lines corresponding to phonons of E_2 symmetry representation. They are related to the zone-edge phonons of 2H, namely to the $\Gamma_4(A)$-phonons.

It is noticeable that owing to middle-range structural distinctions the two $\Gamma_4(A)$ phonons, which are four-fold degenerated in 2H structure, split in four twice degenerated E_2-modes in 4H structure.

In total, six new Raman lines — two types A_1 and four types E_2 can be expected in Raman spectrum of 4H in comparison with that of 2H. The zone-edge $\Gamma_2(A)$ phonons of 2H structure become zone-centre B_1-phonons 4H structure; they remain inactive in optical spectra. We will notice that they can become Raman-active at the further doubling of unit cell which would lead to appearance of $8H$ polytype. This analysis allows us to point out all frequency intervals in which Raman signals induced by structural polymorphism of GaAs NWs are expected. They are schematically presented in the bottom of Fig. 1.

According to schema shown in Fig. 1, we assign the Raman peak 3 to E_2-mode of WZ. Equally well it can be assigned to E_2-mode of 4H.

Instead of a narrow spectral line around $291\,\mathrm{cm}^{-1}$, related to $A_1(\mathrm{LO})$ phonon of bulk ZB, the high-frequency Raman spectrum of NWs exhibits a wide and complex spectral feature. It can be suggested that this feature includes contributions of LO-modes of other polymorphs as well as the disorder-induced Raman-scattering on phonons with non-zero wave vectors. Alternatively, the complex spectral structure observed in Raman spectrum of GaAs NWs in vicinity of LO signal was attributed either to the surface optical phonons [8] or to peculiarities of the long-range dipolar interactions [12].

Other peculiar feature of the observed Raman spectra is the line centered at $\sim198\,\mathrm{cm}^{-1}$. According to the phonon folding scheme, this line is related to the LA zone-edge phonon of ZB structure. In WZ structure, this phonon transform into zone-centre B_1 phonon which corresponds to silent mode inactive in IR and Raman spectra.

Emergence in Raman spectra of GaAs NWs of the lines at $\sim256\,\mathrm{cm}^{-1}$ obviously indicates co-existence of layers with WZ structure. Similarly, presence of spectral feature at $\sim198\,\mathrm{cm}^{-1}$ allows suggesting appearance of 4H structural segments. The additional Raman line at $\sim234\,\mathrm{cm}^{-1}$ (observed as a low-frequency shoulder of the line centered at $256\,\mathrm{cm}^{-1}$) is probably related with the zone-edge LO vibration of ZB. According to the phonon folding scheme this phonon transform into B_1-mode in WZ structure and becomes A_1-mode in 4H structure.

Similarly, a Raman line at $\sim72\,\mathrm{cm}^{-1}$ can be expected as manifestation of $E_2(\mathrm{low})$-phonon of WZ. This mode arises owing to folding of the transverse acoustic branch of ZB structure. Weak spectral features observed at ~150 and $\sim50\,\mathrm{cm}^{-1}$ well correlate with frequencies $\Gamma_2(A)$ and $\Gamma_4(A)$ zone-edge phonons of WZ structure.

3. Conclusions

Complex structure of Raman spectra of GaAs NWs can be related with structural polymorphism inherent to these nanostructures.

Analysis of frequency position and polarization properties of new spectral bands allows us to assign the line observed at $257\,\mathrm{cm}^{-1}$ to E_2-mode of WZ polymorph and the spectral feature observed at $198\,\mathrm{cm}^{-1}$ to A_1 mode of 4H polymorph.

References

[1] I. Zardo *et al*, *Phys. Rev.* **80**, 245324, (2009).
[2] I.P. Soshnikov *et al*, *Solid State Physics* **47**, 12, 2121 (2005).
[3] D. Spirkoska *et al*, *Phys. Rev. B* **80**, 245325 (2009).
[4] S.V. Karpov *et al*, *Solid State Physics*, in press (2011).
[5] B.V. Novikov *et al*, *Phys. Stat. Sol. (RRL)* **4**, 175 (2010).
[6] G.E. Cirlin *et al*, *Phys. Stat. Sol. (RRL)* **3**, 112 (2009).
[7] D. Strauch *et al*, *J. Phys.: Condens. Matter* **2**, 1457 (1990).
[8] N. Begum *et al*, *J. Appl. Phys.* **104**, 104311 (2008).
[9] R.L. Farrow *et al*, *Appl. Phys. Lett.* **31**, 768 (1977).
[10] A.J. Kornath *et al*, *J. Mol. Spect.* **255**, 189 (2009).
[11] R.N. Zitter *et al*, *The physics of Semimetals and Narrow Gap Semiconductors*, ed. D.L. Carter and R.T. Bate (Pergamon, New York) 285 (1971).
[12] G.D. Mahan *et al*, *Phys. Rev. B* **68**, 073402 (2003).

Visualization of the CdS/ZnSSe MQW heterostructure by scanning spreading resistance microscopy

D. E. Sviridov, V. I. Kozlovsky and N. V. Zabavin

P.N. Lebedev Physical Institute, RAS, 53 Leninsky pr., 119991 Moscow, Russia

Abstract. In this work, cross-sectional scanning spreading resistance microscopy (SSRM) was used to visualize the layers of the undoped CdS/ZnSSe multiple quantum well (MQW) heterostructure. Visualization mechanism and it's dependence on built-in AFM laser and halogen lamp (HL) illumination was studied. It was shown that the AFM laser can affect the current signal in QWs via nonequilibrium carrier generation in the GaAs substrate. Current-voltage (I-V) characteristics, measured when the probe was in contact with CdS or ZnSSe layers had the regions with saturation and negative differential resistance (NDR) which we interpret in terms of the tunneling of the electrons through potential barriers formed at the GaAs/ZnSSe and In-Ga/GaAs interfaces.

Introduction

Scanning spreading resistance microscopy (SSRM) of the cleavage surface is an effective atomic force microscopy (AFM) based technique for nanoscale heterostructure investigation [1]. This method can be used for visualization of the subsurface regions with different conductivity [2]. Here we presented the results of the undoped CdS/ZnSSe multiple quantum well (MQW) heterostructure cleavage investigation with SSRM. This structure can be used for example in e-beam [3], or optically pumped VECSELs [4]. It was shown that the current value strongly depends on the Schottky barrier height at the contact of the probe with the semiconductor layers and intrinsic carrier concentration in these layers. On the current-voltage (I-V) characteristics for the contacts of the probe with the layers of the structure there are regions with saturation and negative differential resistance, which are likely to be the result of additional potential barriers formation on GaAs/ZnSSe heterojunction and the second non-ohmic contact.

1. Experimental

The $CdS/ZnS_{0.07}Se_{0.93}$ MQW heterostructure was grown by metal-organic vapor phase epitaxy on semi-insulating GaAs substrate (n-type). Ten 5 nm thick QWs were separated by 140 nm thick barriers. The structure was undoped, but we suggest that it was slightly n-type due to the presence of the donor type native defects. The second contact was formed by the application of the liquid In-Ga eutectic to the cleavage. Measurements were carried out using AFM Solver P47-Pro (NT-MDT) at room temperature. We used the boron doped diamond coated probes (Nanosensors, GmbH) with the film resistivity $\rho = 0.01-0.02\ Ohm\,cm$. Probe was grounded. Potential could be changed from -10 to $+10$ V, and was applied to the second contact. To investigate the effect of built in AFM laser (BL) on the current measurements we switched it on and off during the scanning process and set the value of the feedback gain coefficient (FB) to zero to prevent the piezoscanner retraction. For additional external illumination we used halogen lamp ($h\nu = 1.2-3.1$ eV).

2. Results and discussion

A representative current image, obtained at -2 V sample potential, under three different conditions is shown in Fig. 1 (top) and the corresponding averaged line (SSRM current) is shown
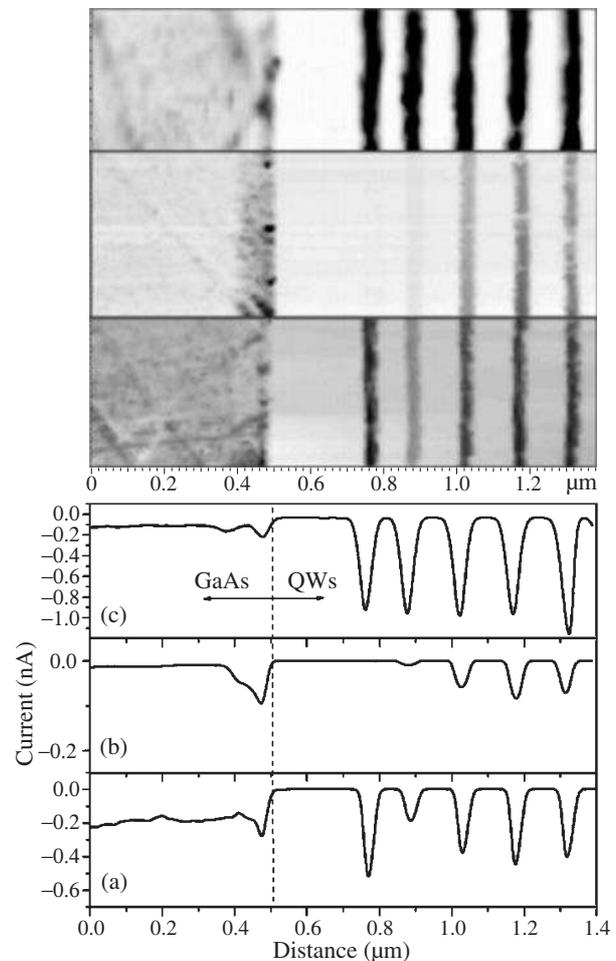
Fig. 1. Current image of the MQW heterostructure cleavage obtained at -2 V sample potential and three different conditions a) BL on and FB $\neq 0$, b) BL off and FB $= 0$, c) HL on and FB $= 0$ (top) and the corresponding averaged line (bottom).

in Fig. 1 (bottom). Section (a) was obtained with BL on and FB $\neq 0$, (b) BL off and FB $= 0$, (c) BL off, FB $= 0$ and halogen lamp on. The data presented shows that illumination strongly influences on the current value in all layers of the structure, even in the case of the BL, inspite of the fact that its photon energy (1.9 eV) is smaller than the CdS band gap energy (2.46 eV). In dark (section b) current value was comparaively small when the probe contacted with GaAs except for
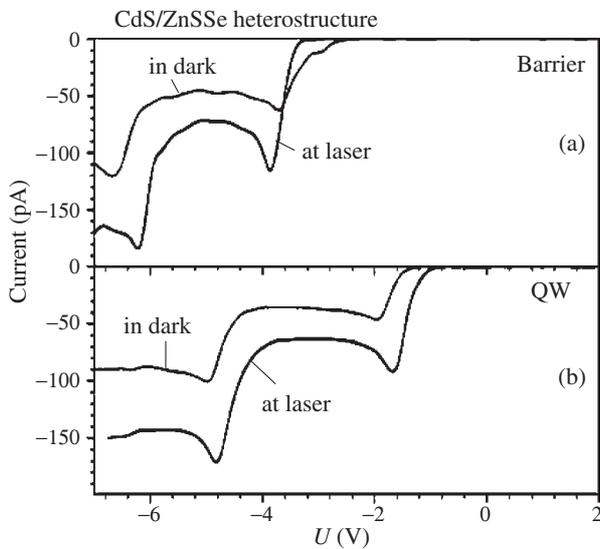
Fig. 2. IV characteristics of the probe-barrier (a) and probe-QW (b) contact in dark and under BL illumination.

References

[1] P. Eyben, M. Xu, N. Duhayon, W. Vandervorst, *J. Vac. Sci. Technol.* **B 20 (1)**, 471 (2002).

[2] J. Liu, K.C. Mandal and G. Koley, *Semicond. Sci. Technol.* **24**, 045012 (2009).

[3] V. Yu. Bondarev, V.I. Kozlovsky *et al*, *Quantum electronics,* **37 (9)**, 853 (2007).

[4] V.I. Kozlovsky, B.M. Lavrushin, Ya.K. Skasyrsky and M.D. Tiberi, *Quantum electronics,* **39 (8)**, 731 (2009).

the narrow region in the GaAs/ZnSSe heterojunction vicinity and increased from the first QW to the fifth. We could obtain current images of the QW region only at negative sample potential. The results, presented above, can be explained, if one suggests that in the case of undoped heterostructure the visualization of the QWs is mainly determined by the height of the Schottky barrier, formed when the probe is in contact with the cleavage surface, which in its turn depends on the chemical composition of the layers. This case is significantly different from the case of highly doped heterostructures, where the contrast is mainly formed by the variation in the conductivity. The Schottky barrier height, which is determined by the difference between the probe work function and the semiconductor electron affinity, is the same for all QWs. Then the inequality of the QWs on the current image in dark Fig. 1(b) can be explained in terms of inequality in carrier concentration. This inequality arises if QW are situated in the space charge region, formed in ZnSSe after the heterojunction formation. Under BL illumination the space charge region dissapears because of the diffusion of the photogenerated electrons from GaAs in ZnSSe. The carrier concentration becomes the same in all QWs as well as the current Fig. 1(a).

The I-V characteristics of the probe — QW and probe — barrier layer (Fig. 2) in dark and with BL illumination are step-like and have the regions with saturation and negative differential resistance. We suggest that except the Schottky barrier in the vicinity of the probe there are barriers at the GaAs/ZnSSe heterointerface and the second contact. When the bias to the second contact applied, current starts to increase due to Schottky barrier reduction and then saturates due to reverse biased barrier at the GaAs/ZnSSe interface. With the subsequent increase of the voltage this barrier apears to be tunneling transparent that results in the second increase of the current. The second saturation is likely due to the reverse biased Schottky barrier at the In-Ga/GaAs contact.

Folded acoustic phonons in Si/Ge superlattices with Ge quantum dots

A. B. Talochkin

Institute of Semiconductor Physics, SB RAS, Lavrentieva av., 13, Novosibirsk 630090, Russia

Abstract. Raman scattering by folded LA phonons in Si/Ge superlattices with Ge quantum dots grown by means of low-temperature molecular-beam epitaxy is studied. New features of folded LA modes related to their resonance enhancement and an unusual ratio of the intensities of doublet lines are observed. It is shown that the observed acoustic modes are related to acoustic vibrations localized in Ge quantum dots and induced by folded phonons of Si layers. Calculations carried out in the model of one-dimensional atomic chain allow us to explain the nature of localization of acoustic phonons caused by modification of the phonon spectrum of a thin quantum dot layer. It is found that the relative intensity of Raman lines belonging to one doublet of the folded modes turns out to be sensitive to the asymmetry of the relief of Ge quantum dot layers.

Introduction

Folding of acoustic phonons appeared in semiconductor super-lattices (SL) is the most impressive effect of modification of a phonon spectrum under the influence of an artificially made superperiodicity. This effect has been investigated in detail for different SLs by means of Raman scattering nearly 30 years ago [1–3]. A theory of this phenomenon in the continuum approximation was built by Rytov [4]; later it was extended for the case of semiconductor SLs [5,6]. It shown an excellent agreement with numerous experiments carried out in different SLs. In contrast, SLs with quantum dot (QD) layers reveal an unusual behavior of intensity of Raman scattering by folded longitudinal acoustic (FLA) phonons on the folding index m allowing one to observe large number of FLA modes (up to 10–20) in Raman spectra [7,8]. For ordinary SLs, their number is much less (2–4), which is determined in the theory by the sharp dependence $(1/m^2)$ of scattering intensity on m [5,6]. The nature of this anomalous behavior can not be explained in the framework of existing theory.

In this work, to elucidate an influence of QDs on SL phonon spectra we study Raman scattering by FLA phonons in Si/Ge SLs with Ge QDs.

1. Experimental

The studied multilayer Si/Ge structures with Ge QDs were grown by using "RIBER-Siva32" MBE installation. The Si (100) wafer n-doped (7.5 Ω cm) was used as a substrate. A 100 nm undoped Si buffer layer was first grown on a cleaned wafer at $T_s = 700$ °C. Then, the Ge layer with the effective thickness of 1.1 nm was grown at the substrate temperature of 250 °C. The grown Ge layer was coated with a 2 nm thick Si layer at the same temperature. Then, a 16 nm thick Si spacer was grown at $T_s = 450$ °C. The structure period that included the QD Ge layer and the 18 nm thick Si spacer was repeated 17 times. The Raman spectra were recorded using a triple diffraction grating spectrometer T64000 (Horiba Jobin Yvon) equipped with a ccd detector. The spectra were excited by the lines of an Ar laser at room temperature in a near-backscattering geometry.

2. FLA phonons in Si/Ge SL with Ge QDs

Fig. 1 shows the acoustic range of Si/Ge SL sample Raman spectrum. The FLA phonon lines and continuous phonon emission (CPE) spectrum indicated by a shaded area are shown separately. The latter component investigated in detail for different SLs previously is related to wave vector non-conservation in the scattering process. In our case, the broad CPE spectrum is related to Raman scattering in defect (relaxed) Ge islands. The doublets of well known FLA modes are observed. Their frequencies, as it was determined previously in the structures of this kind [7,8], are well described by the Rytov theory. The inset of Fig. 1 shows the dispersion of the FLA modes in the reduced Brillouin zone of size of π/D, where D is the SL period. The mesuared frequencies are shows in the inset of Fig. 1 by squares, and the phonon dispersion calculated using the Rytov theory for the sound velocity in SL $v^{LA} = 8.1 \times 10^5$ cm/s is denoted by a broken line. Thus determined sound velocity
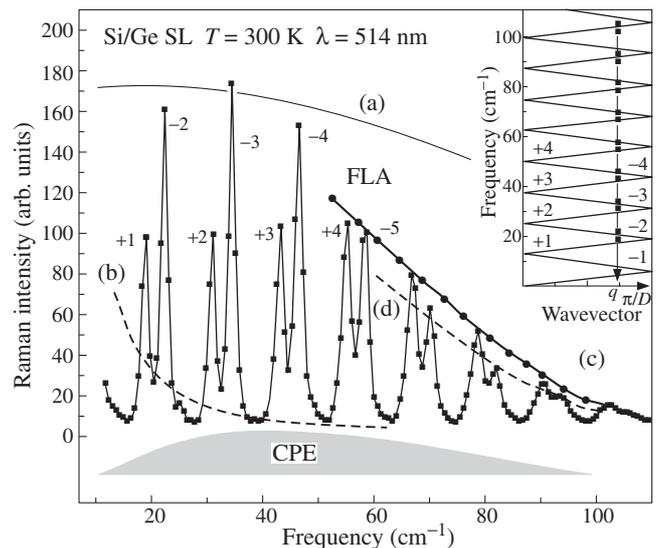
Fig. 1. The acoustic range of the Raman spectrum of Si/Ge SL with Ge QDs. The curves (a), (b), (c), and (d) indicate the results of calculations of the FLA envelop function. The inset shows the dispersion curve of the FLA phonons (broken line) in the SL reduced BZ calculated using the Rytov theory. The experimental frequencies of the FLA modes are denoted by squares.

only slightly differs from that of Si (8.43×10^5 cm/s) due to the small thickness of QD layers. As a result, the thick Si layers determine folding of acoustic phonons in SL and the observed frequencies of the FLA modes.

3. Localization of acoustic vibrations in Ge QDs

Fig. 2 shows the resonance dependences of Raman scattering by optical phonons for the bulk Ge (a) and pseudomorphic Ge QDs [9]. The resonance dependences of the FLA phonons (triangles) and the spectrum of CPE (circles) measured in our SL using the lines of the Ar laser is presented here. The obtained dependences reveal quite a different behavior related to localization of the observed phonon modes. The intensities of the FLA phonons display an enhancement precisely coinciding with the high-energy wing of the resonance curve obtained for the optical phonons of the strained Ge QDs. This means that the observed FLA modes are localized, similarly to Ge optical phonons, in Ge QDs. In turn, the contribution of phonons of the Si layers is negligible.

The nature of such an unusual localization can be understood taking into account an acoustic phonon spectrum modification in thin Ge QD layer. Indeed, because the average height of QDs is about $2a_0$ (a_0 is the Ge lattice constant) only the minimal frequency of LA phonons in them determined by quantization condition is $\omega_{min} \simeq 145$ cm^{-1}. Then, Ge QDs have not the natural LA vibrations in the considered frequency range $(0-100$ cm$^{-1})$. This means that the continuum approximation based on using the plane waves in the theory is not correct in our case. Hence, acoustic vibrations with frequencies less than ω_{min} can be excited in Ge QDs only under the effect of an external source, which is the phonons of the Si layers. The calculations carried out in the eight-atoms ($2a_0$) line chain model show that the amplitude of forced vibrations decreases linearly depending on the atomic number, and it does not penetrate nearly into an adjacent Si layer. Therefore, these vibrations are localized in Ge QDs similarly to Ge optical phonons, and we should use such decisions in QDs instead of the bulk plain waves.

Application of the QD localized acoustic vibrations in the theory of Raman scattering by FLA modes of SLs allows us to explain the unusual features of the observed spectra [10]. Raman intensity is proportional to the square of deformation related to acoustic waves. For vibrations localized in QDs, the deformation value is an order of magnitude larger than that of the Si FLA phonons. The envelope functions of FLA modes calculated for these two contributions are shown in Fig. 1 by curves (a) and (b) respectively. The first one (a) explains the large number of FLA modes observed in Raman spectra of SL with QDs even far from the resonance. The second contribution (b) dominates for ordinary SLs with close thicknesses of alternate layers. Thus, localization acoustic vibrations in QDs explains the observed considerable difference between these two cases.
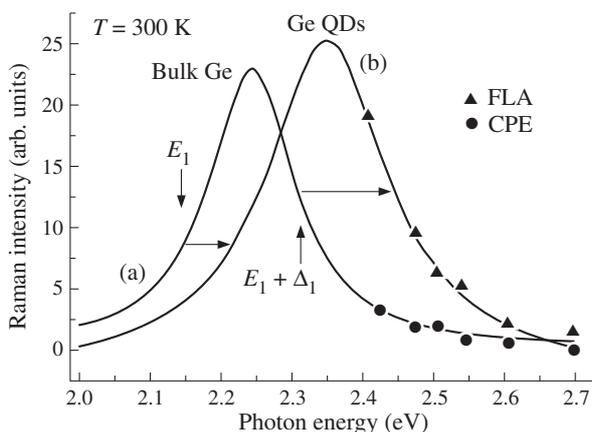
Usually, intensity of low-frequency line of each doublet is large than that of the high-frequency one. Our spectrum (Fig. 1) reveals the invert correlation between the line intensities for the three low-frequency doublets. Due to localization of forced acoustic vibrations in QDs the FLA waves of Si layers of opposite propagation direction interact with the different interfaces of Ge layers. One of them is plane as a result of wetting layer formation, and the other one has the sizable relief related to QDs. The diffraction losses appearing at reflection of Si FLA phonons from the last interfaces lead to decrease of wave amplitude excited in QDs. As a result, the intensity of corresponding phonon line of doublet turns out to be less than the other one related to interaction with the perfect interfaces. This effect vanishes for the doublets with high folding index (Fig. 1) because their wavelength is less than the distance between QDs, and diffraction losses became negligible. Thus, the diffraction losses related to the reflection of acoustic waves from the relief interface with QDs explain the observed ratio of intensities of the FLA phonon lines.

References

[1] D.J. Lockwood *et al*, *Phys. Rev. B* **35**, 2243 (1887).
[2] S.K. Yip and Y.C. Chang, *Phys. Rev. B* **30**, 7937 (1984).
[3] C. Colvard *et al*, *Phys. Rev. Lett.* **45**, 298 (1980).
[4] S.M. Rytov, *Akust. Zh.* **2**, 71 (1956).
[5] C. Colvard *et al*, *Phys. Rev. B* **31**, 2080 (1985).
[6] J. He, B. Djafari-Rouhani, and J. Sapriel, *Phys. Rev. B* **37**, 4986 (1988).
[7] A.G. Milekhin *et al*, *Nanotichnology* **13**, 55 (2002).
[8] P.H. Tan, D. Bougeard, G. Abstreiter, and K. Brunner, *Appl. Phys. Lett.* **84**, 2632 (2004).
[9] A.B. Talochkin and V.A. Markov, *Nanotechnology* **19**, 275402 (2008).
[10] A.B. Talochkin, *JETP* **111**, 1003 (2010).

Fig. 2. The resonance dependences of Raman scattering by optical phonon of bulk Ge (curve a) and pseudomorphic Ge QDs (curve b) obtained in [9]. The resonance curves of the FLA phonons (triangles) and the CPE spectrum (circles) measured from a Si/Ge SL with Ge QDs.

Thermooptical hysteresis properties of transparent dielectric metamaterials based on polymer nanocomposites

N. M. Ushakov[1,2], D. M. Kulbatskii[1], I. D. Kosobudskii[1,2], P. A. Muzalev[1,2] and V. Ya. Podvigalkin[1,2]

[1] Technical State University Saratov, Russia

[2] Kotelnikov Institute of Radio Engineering and Electronics (Saratov Branch) RAS, 410019 Saratov, Russia

Abstract. Thick films Ag-containing nanoparticles (NPs) in polymethylmethacrylate (PMMA) matrix have been produced by thermal decomposition metal-containing compounds in an argon-oxygen atmosphere and hydraulicking nanocomposition by sol gel method on silicon substrates. Optical absorption factor, dissipation factor and refractive index have been measured from 400 to 900 nm at the temperature field from 20 to 80 °C.

Introduction

The interaction of light with metal nanostructures in any transparent matrix has recently become a focus of considerable interest owing to the potential of harnessing strong, locally generated fields for a wide variety of applications [1–3]. At present time optical properties of polymer nanocomposites with nanoparticles stabilized in transparent dielectric polymethylmethacrylate matrix (PMMA) matrix have been studied for different nanoparticles (NPs) concentration and dimensions in matrix at the room temperature only. Nanocomposites based on Ag nanoparticles have a set of perspective applications (for example, see [3]). In this work, we report on results of the investigation of thermo-optical properties of nanocomposites based on 5–20 wt.% Ag nanoparticles in PMMA.

1. Experiment

In present work optical characteristics of nanocomposite thick films on glass with average thickness 70 microns were measured. Mass concentration of Ag NPs are from 5 to 20 wt.%, and their average sizes are from 15 up to 25 nm. The particle size of Ag was determined by transmission electron microscopy (TEM) on a JEOL JEM 300B microscope. The accelerating voltage was 75 kV.

The structure of Ag-PMMA samples were investigated using X-ray phase analysis method. In Fig. 1 difractogram of the 10 wt.% Ag based on PMMA is presented. Experimental results were demonstrated that Ag is the general metal component of the nano composite.

Optical transmission & reflection spectra of investigated

Fig. 2. Heating-cooling cycle of optical absorption coefficient for 10 wt.% Ag-PMMA nanocomposite at 570 and 820 nm.

samples were measured on spectrophotometer Lambda 950 (USA) in range 450–900 nanometers with specially created additional device consisting of heating element. For comparison absorption a factor for pure PMMA matrix was measured. The errors of measurement did not exceed 1%.

2. Results and discussion

Figure 2 presents the results of measured heating-cooling cycle of optical absorption coefficient for 10 wt.% Ag-PMMA nanocomposite at 570 and 820 nm.

The results of measurements heating-cooling cycle of refraction index for the 10 wt.% Ag-PMMA composite sample at 570 and 820 nm are presented in Figs. 3 and 4 respectively.

As absorption factor, as refraction index were demonstrated hysteresis properties from the temperature. It is enormous in comparison to what anyone else has done before.

As shown in Fig. 3 under heating of samples up from 20 to 70 °C optical absorption decreasing is observed at 570 nm, and from 50 to 70 °C optical absorption decreasing is observed at 820 nm. Then at the temperature band from 55 to 77 °C optical absorption decreases also. At that, optical absorption value at 570 nm is greatly more then at 820 nm. This results can be explained by the resonant interaction of light with plasmonic oscillations in metal nanospheres.

Fig. 1. Difractogram of the 10 wt.% Ag-PMMA composite.
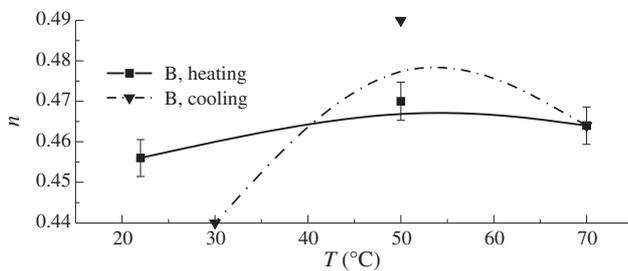
Fig. 3. Heating-cooling cycle of refraction index for the 10 wt.% Ag-PMMA composite sample at 570 nm.
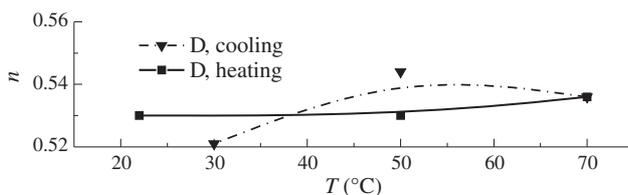
Fig. 4. Heating-cooling cycle of refraction index for the 10 wt.% Ag-PMMA composite sample at 820 nm.

In our opinion temperature region from 20 to 70 °C is a very interesting for a development of thermo-optical switches. Most of all the changing of optical absorption in the spectral range from 570 to 900 nm at 50 °C is observed. This spectral band is characteristic for exciton spectra. Maximum change in absorption factor and refractive index can be explained by sky line of exciton concentration at the border NPs-matrix under thermionic emission from nanoparticles and trapping ones in matrix.

Change of refraction index for composites on the basis of nanoparticles Ag reached values $\Delta n = 0.01$ in the range of temperatures from 25 to 70 °C.

References

[1] J.B. Pendry, *Contemp. Phys.* **45**, 191 (2004).
[2] M. Mayy, G. Zhu, Yu.A. Bamakov, and M.A. Noginov. *J. Appl. Phys* **105**, 084318 (2009).
[3] O.N. Gadomsky, K.K. Altunin, N.M. Ushakov, *JETP Lett.* **90** (4), 273 (2009).

The investigation of impedance parameters, texture and self-organization of oxide formations on titanium and aluminum surfaces

A. S. Zaichenko, S. A. Tsarev, P. L. Titov, A. V. Kirillov, S. A. Shegoleva, V. G. Kuryaviy and N. B. Kondrikov
Far East Federal University, Vladivostok, Russia

Abstract. An analysis of equivalent circuits, which were created by modeling of Al and Ti impedance specters, was carried out. The characteristics of equivalent circuits were given for Ti. An investigation of topological parameters of structures on Ti surface was made. The conclusion about type of nanotubes was got from FDP.

In this work the correlations between aluminum and titanium nanostructured anodic oxide surface texture and impedance parameters were studied. To develop well-ordered structure aluminum and titanium samples were REM microscopy was used as method of surface texture investigation. REM investigation was carried on Carl Zeiss CrossBeam 1540 EX, CarlZeiss EVO 60 with EDX and WDX for micro analysis and Hitachi S-5500. During the investigation of samples morphology nanotube arrays with different diameter, size and unity were founded (Fig. 1) [1]. The morphology data was compared with equivalent circuits created using mathematical modeling of impedance specters. The specters were recorded by electrochemical complex Solartron 1287 in 0.01 M Na_2SO_4 electrolyte, frequency ranges from 60000 to 0.1 Hz, 10 mV amplitude. The comparison of REM data and equivalent circuits showed that there was a zone in impedance specters that was specific for diffusion processes and well-described by Warburg impedance. Probably it caused by ion diffusion in nanotubes.

The diffusion plays key role in forming processes of such structures and can be promising for further research of nanostructures forming mechanisms. A Warburg element with unlimited length was chosen to characterize the diffusion in the equivalent circuit. We've chosen such element because tubes are open for ions on electrolyte side, which allows ions to have nonlocalized diffusion length that is greater than the length of nanotubes. This element was characterized by CPE-T parameter:

$$\mathrm{CPE-T} = \frac{\sqrt{(L^2/D)}}{Z}, \qquad (1)$$

where L is diffusion length, D is diffusion factor, Z is resistance caused by diffusion stage which is usually used for linear diffusion process describing.The value of $\mathrm{CPE-T}$ in the equivalent circuits showed us that it considerably depends on the length of nanotube and depends less on the diameter of nanotube. Except the Warburg impedance the capacitive parameters of system and the electrical resistance differed too, probably due to the different thickness of structurized oxide layer. A resistance of dense oxide layer is significantly greater than a resistance of structurized oxide layer, which is showed at Nikewist diagram on Fig. 2.

CPE elements with $\mathrm{CPE-P} \neq 0.5$ describe electrical capacities with account of deviations from flat condenser capacity. R elements describe corresponding resistances. All Values of equivalent circuits parameters were reduced to SI values in recalculation to 1 cm^2 of sample surface.
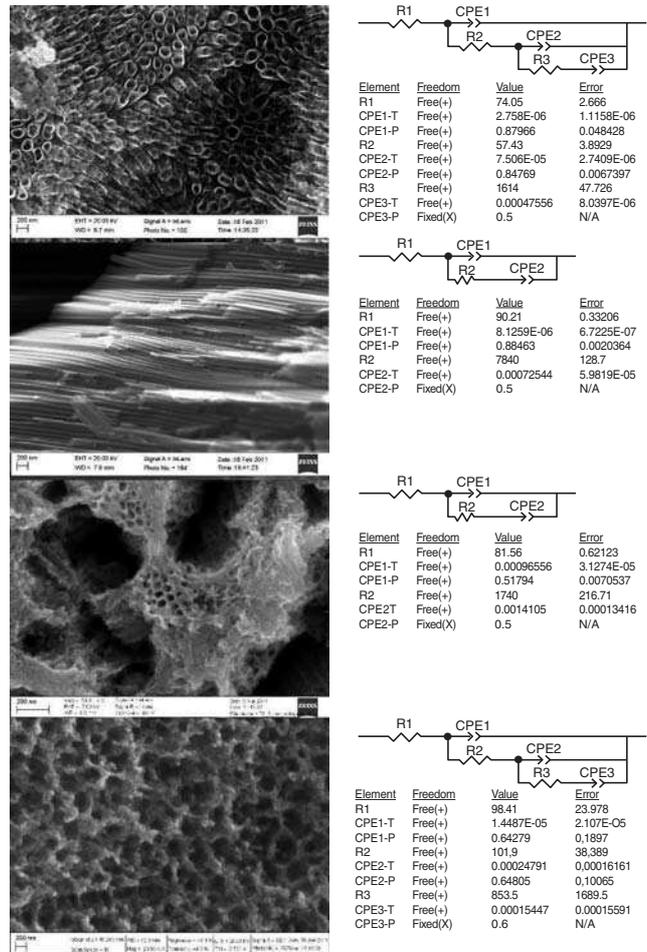
Fig. 1.

One of the goals of this work is to identify topological class of structures (Fig. 3a).

The corresponding Fraunhofer diffraction patterns (FDP) which were gained with fast Fourier transformation are showed on Fig. 3. The entire spectral-correlation method of complex electron-microscopic structures investigation can be found in monography [2]. The important conclusion about type of nanotubes was got from FDP. The type of FDP assimetry forms considerably nonadditive specter and has halo-diffraction pattern. Such system corresponds in global sense to modulation structures, which are strong nonlinear. This effect is uncommon due to the nearly identical diameters of tubes. The distribution of nanotubes on size would have Dirac delta-function
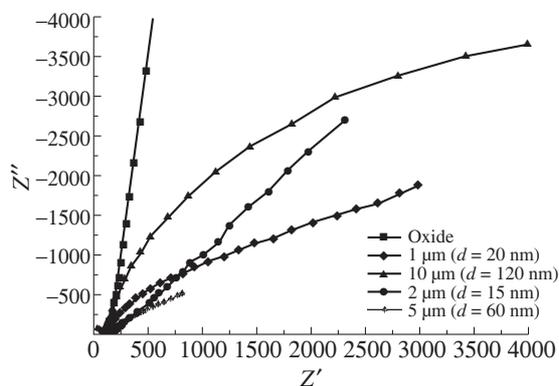
Fig. 2.
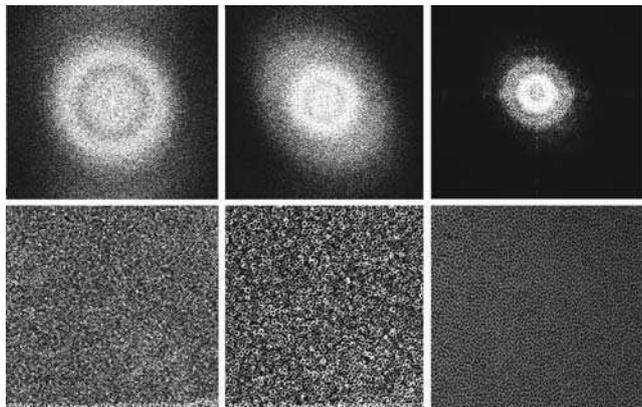
Fig. 3. Ti (left, middle) and Al (right) oxides and corresponding FDP.

Fig. 4.

type. Formally one can observe certain topological scaling looking at Fig. 4, which will entail a usage of fractal methods. The further calculations are given for titanium oxide. They will be realized in two approaches.

The first one is about simple modification of correlational methods of fractal dimension estimation by Grassberger–Prokachcho [3]. To do this the system of embedded circles, for which a dependence in double logarithmic scales between nanotubes quantity in corresponding sphere and the radius of sphere was calculated, was built. It rectifies well and gives angle tangent of 2.005. It showed us that fractal dimension of nanotube system is integer and equal to 2, but the system is fractal formation. The system of nanotubes according to corresponding physicochemical conditions is filling the dimension of the embedded space absolutely dense and uniform.

The second method is pursuing a somewhat different approach, which is showing the formation of flow lines crossing a general position. Crossing flow was ploted by scanning line with intersection of nanotubes in certain stripe. It comes out as flow projections of the centers of nanotubes on selected cross section. In what follows, the method is constructed similarly to the standard approach and obtained the corresponding dependence Rather good linear approximations with slope angle tangents slightly more than one and slightly less than one were carried out. The straight sum of linear subspaces is a simple sum of dimensions of these subspaces. This dimension is equal to 2.

The investigation of dissipative topological structure of nanotubes will be not full if we don't proceed to a local investigation from the global one. To find out ordering type in ex-

tremely little [4] we use specific method of nanotube cluster selection, where centres of nanotubes are schematically highlighted. The locality condition holds with hitting the first coordination sphere for any sample nanotube. 5 chosen clusters with different amount of nanotubes ($5 \leq n \leq 9$) differed with local order are showed at Fig. 4.
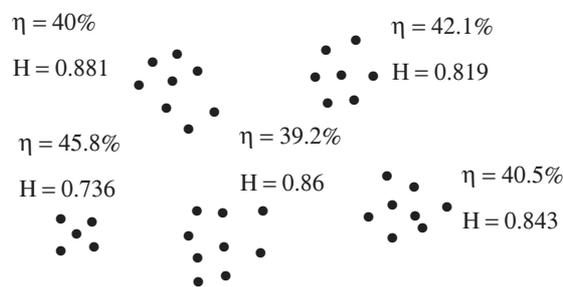
We also showed entropy levels as measures of disorder degree of these clusters at Fig. 3 and "coefficient of efficiency" (COE) which is around $39.2\% \leq \eta \leq 45.8\%$. If "COE" was 50% it would mean that "COE" corresponds to pure stochastic. The real "COE" showed that the order type is quasistochastic. In physicochemical point of view it showed the presence of dissipative process, which is close to Brownian process. Thereby generalizing the results of topology analysis of nanotube structure in a global approach and straight order analysis in the small, we come to a statement that nanotube system is dissipative structure of quasistochastic modulation type.

Taking into account the key role of physicochemical processes in electrochemical forming of nanotubes, the type of nanostructures depends on near-electrode layer processes features, especially on mass transfer processes. Impedance spectroscopy data showed the importance of diffusion in charge transfer processes, which can be one of key reasons of dissipative structure formation.

References

[1] S. Berger, *Selbstorganisierte nanostrukturierte anodische Oxidschichten auf Titan und TiAl...*: Dissertation, 2009. 212 p.

[2] V.V. Udin, *Stochastic magnetic structure of films with microporous structure*, M.:Nauka, 1987. 216 p.

[3] *Fractals in physics*, VI International Symposium in Trieste proceedings. On fractals in physics. M.:Mir, 1988. 672 p.

[4] V.V. Udin *et al*, *News RAS. Ser. Phys.* **73** 9, 1340 (2009).

Microchannel resistor sensor for liquid analysis

M. A. Parashchenko, N. V. Vandisheva, V. V. Kirienko, N. S. Filippov and S. I. Romanov
Institute of Semiconductor Physics, 630090 Novosibirsk, Russia

Abstract. This paper has been devoted to a creation of sensor based on ordered microchannel silicon resistor for electrophysical detection of liquids. Interactions of sensor with organic and inorganic liquids (acetic acid, ammonium hydroxide, ethyl alcohol, water-alcohol solution and deionized water) were studied by high frequency conductance measurements. It was established that the sensor had specific response for each liquid. It was shown that the proposed electrophysical method allowed identifying the liquids coming in contact with the sensor.

Introduction

The main aim of current trends in biotechnology is to get electrical sensors for analysis of various biological substances. Material that can be interest to create such devices is an ordered microchannel silicon which has single-type internal crystallographic surface and can be controllably obtained (Fig. 1).

Today, porous silicon and porous silicon oxides were used in manufacturing of different devices such as chemical [1–4], biological [5–7], gas [8] and humidity sensors [9–10] due to high adsorption ability. The principle of such sensors is similar. Test substances adsorbed on its large surface caused changes in structural and electronic properties of porous silicon. These changes can be detected by various physical methods, for example, measuring the electrical conductivity of the structure. It was reported that a silicon microchannel matrix was applied as a humidity sensor [9–10], but there was no mention of a sensor based on silicon membranes with ordered microchannels for electrical analysis of organic and inorganic liquids.

1. Experimental

In this work we have developed a sensor based on silicon resistor with ordered through microchannels which was tested on different liquids. A sensitive part of this sensor was a silicon microchannel matrix created by the anodic electrochemical etching of (100) oriented p-type silicon wafer with resistivity of 40 Ohm cm. In our study the silicon matrix 10×10 μm^2 with 195 μm thickness, 0.5 cm^2 square and 1.3 μm-thick walls was used. The microchannel matrix was fabricated in monolithic silicon wafer, then it was oxidized in dry oxygen at 900 °C and finally gold electrical contacts were placed on microchannel silicon surface. Fabricated sensor was set in a special sealed chamber with argon filled media. The chamber was connected to the measuring stand and all measurements were performed at room temperature. We investigated liquids used in biology and medicine. Deionized water as the primary solvent, acetic acid, ammonium hydroxide, ethyl alcohol and water-alcohol solution were chosen for experiments. Distribution of the liq-
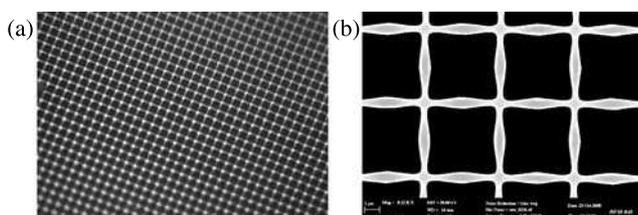
Fig. 1. Optical microscope photograph (a) and SEM image (b) of microchannel silicon matrix.
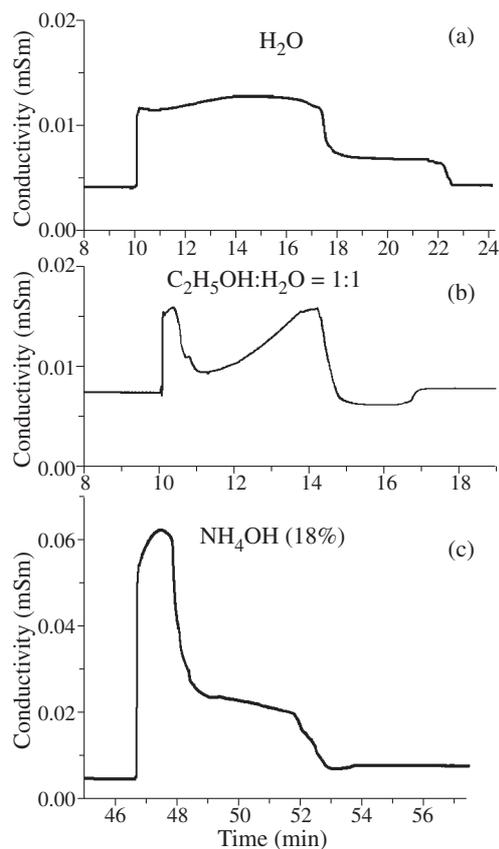
Fig. 2. Electrical response of the sensor to a 3 μl of deionized water (a), aqueous solution of ethanol (b), ammonium hydroxide (c).

uids on the sensitive element was performed by a graduated pipette.

2. Result and discussion

High frequency conductance measurements of the sensor during its interactions with organic and inorganic liquids were performed. It was clearly seen that impregnation of liquids into microchannels of the sensitive element led to different changes in conductivity of the structure (the sensor had its own specific response), which made it possible to distinguish liquids in microchannels (Fig. 2).

It was established that the fabricated sensor based on silicon microchannel resistor was an effective device for electrical detection of different organic and inorganic liquids. These sensors appear to have considerable promise for analytical and diagnostic devices in medicine and biology.

References

[1]   M. Archer *et al*, *Sensor and Actuators B*, 347 (2005).

[2]   H. Luth *et al*, *Materials Science and Engineering B* **69-70**, 104 (2000).

[3]   M.J. Sconing *et al*, *Sensors and Actuators B* **64**, 59 (2000).

[4]   M.J. Sconing *et al*, *Sensors* **2**, 11 (2002).

[5]   K.D. Hirschman *et al*, *Lab-on-a-Chip: Platforms, Devices, and Applications*, edited by Smith, Linda A.; Sobek, Daniel. Proceedings of the SPIE **5591**, 205 (2004).

[6]   M. Archer *et al*, *Biomedical Microdevices* **6:3**, 203 (2004).

[7]   C. RoyChaudhuri *et al*, *Smart Sensors and Sensing Technology*, Springer-Verlag Berlin Heidelberg 2008, 101 (2008).

[8]   V.S. Solntsev *et al*, *Semiconductor Physics, Quantum Electronics and Optoelectronics* **11**, 381 (2008).

[9]   Yun Wang *et al*, *IEEE Sensors Journals* **9**, (2009).

[10] Yun Wnag *et al*, *Sensors and Actuators B* **149**, 136 (2010).

Optical method of biological substance analysis based on silicon microchannel matrix

N. V. Vandysheva[2], E. V. Dmitrienko[1], I. A. Pyshnaya[1], A. A. Lomzov[1], D. V. Pyshnyi[1] and S. I. Romanov[2]

[1] Institute of Chemical Biology and Fundamental Medicine, SB RAS, Lavrentieva av., 8, 630090 Novosibirsk, Russia

[2] A.V. Rzhanov Institute of Semiconductor Physics, SB RAS, Lavrentjeva 13, 630090 Novosibirsk, Russia

Abstract. A simple optical method of biological substance detection has been proposed. This method is based on overlapping of silicon matrix microchannels by micro- and nanospheres consisted of light scattering and light absorbing materials. Biomolecules on the surface of the spheres bind them to microchannel surface due to specific chemical reactions. Therefore, registered intensity of transmitted light decreases.

Introduction

Detection of DNA hybridization is the basis of many applications in molecular diagnostics [1]. A number of optical methods have been reported for detecting hybridization using absorption spectroscopy [2], fluorescence [3] and surface plasmon resonance [4]. These methods employ complex and expensive equipment limiting their wide application in up-to-date diagnostics of different diseases.

In this report, we propose a simple optical method of biological substance detection based on overlapping of silicon microchannels by micro- and nanospheres consisted of light scattering and light absorbing materials (silica, latex, polystyrene etc.). The method has been approved for hybridization analysis of DNA. Specific complementary complexes formed by oligonucleotide probes covalently bound with silicon microchannel matrix and DNA targets immobilized on silica and latex microspheres are reliably detected.

1. Experimental

The silicon microchannel matrixes were made of (100) Si wafer through special techniques and had a highly ordered structure of square cross-section microchannels with {011} faces and ⟨100⟩ axis. The 110 μm-thick matrix with microchannels $15 \times 15\ \mu m^2$ and 80 μm-thick matrix with microchannels $7 \times 7\ \mu m^2$ were used. The surface of microchannel matrix and silica microspheres was sequentially modified with 3-aminopro-pyltrimethoxysilane and 2,4,6-trichlor-1,3,5,-triazin bifunctional reagent. Amino-containing oligonucleotide pro-
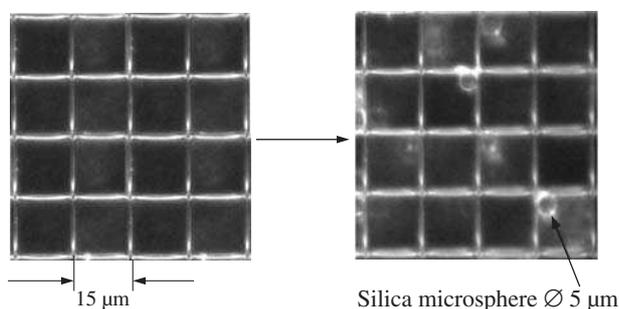
Fig. 1. Optical images of silicon microchannel matrix $15 \times 15\ \mu m^2$ before and after reaction of hybridization. The silica microspheres presence in microchannels evidence of positive reaction and, therefore, determine a structure of DNA targets.
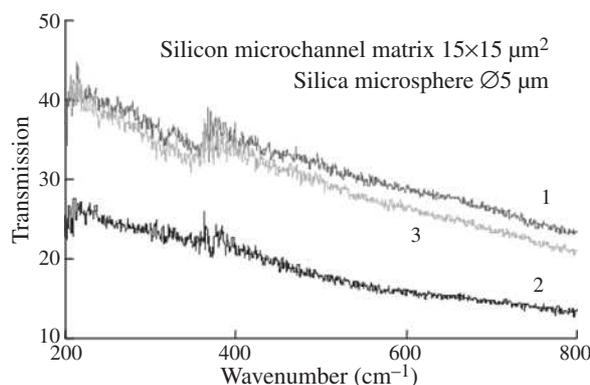
Fig. 2. Transmission spectra of silicon microchannel matrix (1) before and (2) after reaction of hybridization, (3) restored state of matrix with oligonucleotide probes after hybridization complexes denaturation and removal of microspheres with DNA targets.

bes were covalently immobilized on functionalized surface of microchannel matrix due to bifunctional reagent bonding with amino group of probe. The NH_2-oligonucleotides were covalently bound with aldehyde groups located on the microspheres surface through the Shiff bases formation followed by their reconstruction.

The hybridization complex formation between oligonucleotide probes immobilized on the microchannel matrix and microspheres surface was carried out in solution containing 20 mM tris-HCl, pH 7.5, 100 mM NaCl, 2 mM $MgCl_2$ during 30 min. Transmission spectra of hybridization complexes were recorded using UV-2100 Shimadzu spectrophotometer (Japan).

2. Results and discussion

Optical images of silicon microchannel matrix before and after hybridization reaction are shown in Fig. 1. It is evident that silicon microchannels $15 \times 15\ \mu m^2$ are overlapped by silica microspheres Ø 5 μm.

Transmission spectra of silicon microchannel matrix before and after hybridization reaction are shown in Fig. 2. It is obvious that the intensity of transmitted light was decreased by ~40% all through the wavelength range when the silica microspheres presented in microchannels (see spectra 1 and 2). Similar effect was observed with latex microspheres Ø 1.3 μm in microchannel matrix $7 \times 7\ \mu m^2$. In check experiments light intensity transmitted through microchannel matrix was not varied when non complementary DNA fragments were used, i.e.

the specific reaction did not occur.

On the basis of the proposed method it becomes possible to develop a simple optical device for diagnostics of DNA and different biological substances. The device can consists of light source, photodetector and a few lenses.

3. Conclusion

We have presented the simple optical method of biological substance detection approved for hybridization analysis of DNA. This method can be the basis of simple optical devices for diagnostics of DNA and different biological substances.

References

[1] K.R. Khrapko *et al*, *FEBS Lett.* **256**, 118 (1989).
[2] B. Eggins, *M.: Technosphera* (2005) 336 p.
[3] T. Vo-Dinh *et al*, *Anal. Chem.* **71**, 358 (1999).
[4] J. Homola *et al*, *Methods* **37**, 26 (2005).

Sensitive detectors of terahertz radiation based on $Pb_{1-x}Sn_xTe(In)$

D. E. Dolzhenko[1], L. I. Ryabova[1], A. V. Nicorici[2] and *D. R. Khokhlov*[1]

[1] M.V. Lomonosov Moscow State University, Moscow 119991, Russia
[2] Institute of Applied Physics, Moldavian Academy of Sciences, Kishinev MD-2028, Moldova

Abstract. Indium-doped lead telluride-based alloys reveal a range of unique features including pinning of the Fermi level and appearance of the persistent photoconductivity at low temperatures. Making use of these features allows construction of extremely sensitive direct detectors of terahertz radiation. We present physical principles of operation of terahertz photodetecting devices based on $Pb_{1-x}Sn_xTe(In)$. Noise Equivalent Power (NEP) as low as 6×10^{-20} W/Hz$^{1/2}$ at the wavelength of 350 μm and the operating temperature of 1.5 K is demonstrated. It is the lowest optical NEP value obtained so far in this spectral region.

Introduction

Recently, terahertz technologies have received a lot of attention due to attractive possibilities for numerous applications in medicine, ecological monitoring, security systems, high-resolution spectroscopy, and many other fields. One of the most challenging tasks in this area deals with applications in the space astronomy. At this time, there are several projects for launching space-based observatories operating in the terahertz spectral range, such as SPICA [1] which includes two terahertz instruments: SAFARI [2] and BLISS [3], MILLIMETRON [4], and other missions. These observatories will possess cryogenically cooled optics, so the requirements for detector sensitivity are very tough. For instance, the direct detector sensitivity goal for the BLISS instrument 3×10^{-20} W/Hz$^{1/2}$ requires improvement of the state-of-the-art by 2–3 orders of magnitude.

In this paper, we report on an alternative possibility based on unique features of a narrow-gap semiconductor — $Pb_{1-x}Sn_x$Te(In). Making use of these features allows construction of an extremely sensitive direct detector of terahertz radiation demonstrating NEP as low as 6×10^{-20} W/Hz$^{1/2}$ at the wavelength of 350 μm and much higher operating temperature of 1.5 K.

1. Main physical features of $Pb_{1-x}SnxTe(In)$

Doping of the lead telluride with indium in an amount exceeding concentration of other impurities and defects results in the Fermi level pinning effect [5]. Position of the pinned Fermi level E_0 may be tuned by alloying [6]. It crosses the gap in the tin content range ($0.22 < x < 0.28$) providing appearance of the semiinsulating state for this range of alloy compositions. Conductivity of the material in the semiinsulating state ($0.22 < x < 0.28$) is defined by activation from the impurity local level E_0, and therefore the free carrier concentration is very low $n, p < 10^8$ cm^{-3} at temperatures $T < 10$ K. This makes very attractive the idea to use this material as a photodetector.

External infrared illumination leads indeed to the substantial increment of the material conductivity at the temperatures $T < 25$ K [7]. High amplitude of photoresponse at the low temperatures is a consequence of the persistent photoconductivity effect. When the radiation is switched off, the conductivity relaxes very slowly. The chatacteristic relaxation time $\tau > 10^4$ s at $4.2 < T < 10$ K, then it sharply decreases with

the temperature rising, and $\tau \sim 10^{-2}$ s at $T \approx 20$ K. The effect is defined by the specifics of impurity states that form DX-like centers [8,9].

2. Spectral characteristics of the photoresponse

One of the key questions still not completely explored is the spectral characteristics of the photoconductivity. The problem arises from the fact that the background infrared illumination generates high concentration of long-lived non-equilibrium free electrons. In one of experimental approaches that were used to overcome this difficulty, a sample is completely screened from the background radiation, therefore the measurements can start from the "dark" conductivity state. This "low-background" approach was used in [10,11] for $Pb_{0.75}Sn_{0.25}$Te(In) in which the Fermi level is pinned at 20 meV below the conduction band edge. A series of cold filters were used to extract a certain spectral line in the terahertz range from the 300 K black-body radiation spectrum. It has been demonstrated that the persistent photoconductivity is observed in $Pb_{0.75}Sn_{0.25}$Te(In) for the wavelengths of the incident terahertz radiation of 90, 116 μm [10], 176, 241 μm [11].

3. Terahertz photodetectors

One of the ways to increase the signal-to-noise ratio of photodetectors is integration of the incident signal. In terms of this, the persistent photoconductivity effect observed in $Pb_{1-x}Sn_x$Te(In) gives a significant advantage for terahertz photodetecting systems based on these materials compared to the case of ordinary single photodetectors since it provides "internal" integration of the incident radiation flux. On the other hand, this advantage is valuable only if there exist a way to quench quickly the persistent photoconductivity. The most efficient way of such a quenching in $Pb_{1-x}Sn_x$Te(In) samples is application of strong radiofrequency pulses to sample contacts [12]. Using this technique, the long-living photoexcited free electrons may be localized for less than 10 μs. Therefore it became possible to operate in the regime of periodical accumulation and successive fast quenching of the photoresponse. Moreover, application of radiofrequency pulses in some special regime results in giant increment of the quantum efficiency up to $\sim$100 [13].

A laboratory model of the infrared radiometer based on $Pb_{1-x}Sn_x$Te(In) operating in the regime of periodical accumulation and successive fast quenching of the persistent photo-

conductivity, has been demonstrated in [12]. A helium-cooled filter provided effective cutting of the incident radiation spectrum at the wavelengths $\lambda > 18\ \mu$m. The photon flux detected in [12] was as low as N $\approx 2 \times 10^4$ s^{-1} that corresponds to NEP $\approx 2 \times 10^{-16}$ W for the detector area of 0.3×0.2 mm^2 and the oprating rate 3 Hz.

In this paper, we report on the same sort of measurements at the terahertz frequency of 350 μm. The Pb$_{0.75}$Sn$_{0.25}$Te(In) sample was mounted in a closed metallic vacuum cell which was immersed in the liquid helium. The cryogenic blackbody was located in the same cell, but it was separated from the sample compartment by a stop aperture of 1.1 mm in diameter. The stop aperture had a direct thermal contact with the helium bath. A combination of two terahertz filters pressed to the stop aperture was used to select the spectral transmission line. The first filter was a band-pass filter with the center at 350 μm and the Q-factor 4. The filter transmission coefficient was 0.7 in the band, being less than 0.001 outside the band, except for a small spectral region at the double frequency, at which the transmission was several percent. To exclude the influence of this second transmission line, a low-pass filter was used in combination with the first one. Its transmission edge corresponds to about 200 μm with the transmission coefficient 0.9 at low frequencies. The filters were produced by the QMC Instruments. The helium vapor pressure in the cell was kept at 10^{-1} mbar to allow effective sample and blackbody cooling. The blackbody was heated from 0.5 to 10 K above the cell temperature. The blackbody temperature T_b was controlled by a low-temperature Cu-Cu(Fe) thermocouple. The sample area was 0.3×0.2 mm^2. The sample temperature was varied from 4.2 to 1.5 K by pumping off the helium vapor.

Even in the absence of the blackbody radiation, a sawtooth-like conductivity signal has been detected. The source of the terahertz radiation were the walls of the cell. As the cell temperature T_c decreased from 4.2 to 1.5 K, the amplitude of the signal decreased accordingly. The signal amplitude was considerable even at the quenching frequency of 100 Hz.

In order to provide chopping of the incident radiation flux, the blackbody heater was loaded by AC voltage from the internal source of a SR830 (Stanford Research Instruments) lock-in amplifier. A diode was connected in series with the heater to provide modulation of the blackbody temperature at the not doubled local source frequency. The amplitude and the shape of the blackbody temperature modulation was controlled by the thermocouple. It turned out that it was possible to modulate effectively the blackbody temperature at the frequency of 0.3 Hz. The saw-tooth like signal from the sample was loaded to the lock-in input. The signal-to-noise ratio appeared to be 1 already at $T_b = 4.7$ K for $T_c = 4.2$ K and $T_b = 2.7$ K for $T_c = 1.5$ K. These values correspond to NEP $= 3 \times 10^{-17}$ W/Hz$^{1/2}$ at $T_c = 4.2$ K and NEP $= 6 \times 10^{-20}$ W/Hz$^{1/2}$ at $T_c = 1.5$ K. The latter value nearly hits the requirements for the future space instruments. These data look very promising especially taking into account that the operating temperature is much higher than that for the analogs.

4.　Summary

Application of the indium-doped lead-tin tellurides as base elements for the terahertz photodetectors gives a challenging opportunity to produce extremely sensitive systems. They have a number of advantageous features that allow them to compete successfully with the existing analogs. NEP as low as 6×10^{-20} W/Hz$^{1/2}$ at the wavelength of 350 μm and the operating temperature of 1.5 K has been demonstrated. This sensitivity nearly hits the goal for the future space observatories operating in the terahertz spectral range.

References

[1] T. Nakagawa, *Adv. Space Res.* **34**, 645 (2004).

[2] B. Swinyard, T. Nakagawa, H. Matsuhara, D. Griffin, M. Ferlet, P. Eccleston, A. di Giorgio, J. Baselmans, J. Goicoechea, K. Isaak, P. Mauskopf, L. Rodriguez, F. Pinsard, W. Raab, L. Duband, N. Luchier, N. Rando, A. Heras, T. Jagemann, N. Geis, S. Vives, *Proc. SPIE* **7010**, 70100I (2008).

[3] C.M. Bradford, M. Kenyon, W. Holmes, J. Bock, T. Koch, *Proc. SPIE* **7020**, 70201O (2008).

[4] W. Wild, N.S. Kardashev, *Experimental Astronomy* **23**, 221 (2009).

[5] V.I. Kaidanov, R.B. Mel'nik, I.A. Chernik, *Sov. Phys. Semicond.* **7**, 522 (1973).

[6] B.A. Akimov, L.I. Ryabova, O.B. Yatsenko, S.M. Chudinov, *Sov. Phys. Semicond.* **13**, 441 (1979).

[7] B.A. Akimov, N.B. Brandt, S.O. Klimonskiy, L.I. Ryabova, D.R. Khokhlov, *Phys. Lett.* **88A**, 483 (1982).

[8] B.A. Volkov, L.I. Ryabova, D.R. Khokhlov, *Phys. Uspekhi* **45**, 819 (2002).

[9] L.I. Ryabova, D.R. Khokhlov, *JETP Lett.* **80**, 133 (2004).

[10] D.R. Khokhlov, I.I. Ivanchik, S.N. Raines, D.M. Watson, J.L. Pipher, *Appl. Phys. Lett.* **76**, 2835 (2000).

[11] K.G. Kristovskiy, A.E. Kozhanov, D.E. Dolzhenko, I.I. Ivanchik, D. Watson, D.R. Khokhlov, *Phys. Solid State* **46**, 122 (2004).

[12] S.N. Chesnokov, D.E. Dolzhenko, I.I. Ivanchik, D.R. Khokhlov, *Infrared Phys.* **35**, 23 (1994).

[13] B.A. Akimov, D.R. Khokhlov, *Semicond. Sci. Technol.* **8**, S349 (1993).

Author Index